

T  
BPD  
Cum  
606,173  
Mar. 83

SUBMILLIMETRE SCATTERING ANTENNAS

A thesis submitted to the Faculty of Science  
of the University of London for the degree  
of Doctor of Philosophy

by

Howard John CUMMINS  
BSc(London)

Department of Physics  
The Royal Holloway College

June 1982

ProQuest Number: 10097507

All rights reserved

INFORMATION TO ALL USERS

The quality of this reproduction is dependent upon the quality of the copy submitted.

In the unlikely event that the author did not send a complete manuscript and there are missing pages, these will be noted. Also, if material had to be removed, a note will indicate the deletion.



ProQuest 10097507

Published by ProQuest LLC(2016). Copyright of the Dissertation is held by the Author.

All rights reserved.

This work is protected against unauthorized copying under Title 17, United States Code.  
Microform Edition © ProQuest LLC.

ProQuest LLC  
789 East Eisenhower Parkway  
P.O. Box 1346  
Ann Arbor, MI 48106-1346

ABSTRACT

Early attempts at constructing point contact detectors for submillimetre radiation led to the conclusion that the whisker itself exhibited long wire antenna properties. This discovery initiated the design of more advanced travelling wave antenna structures in a number of laboratories.

The objective of the present study has been to investigate an alternative approach to electromagnetic transduction, namely the standing wave antenna. In the context of this work the antenna is to be regarded not merely as a coherent flux collector, but as a device for efficiently converting the Poynting flux in a Gaussian beam waist into a conduction current. A basic study of coupled dipole arrays has been undertaken by a scattering technique that obviates the need for extracting power from the antenna terminals. A microcomputer controlled open resonator has been developed for making absolute measurements of the total scattering cross-section of arrays and the optical constants of various ultra thin substrate materials. Back-scattering measurements under travelling wave conditions were also undertaken to verify that these arrays exhibited useful radiation patterns in both the E and H-planes. The electrical properties of the antenna arrays were found to be predictable using established theory.

A photolithographic technique was employed to reproduce the antenna structures on thin mylar substrates previously metallized with silver.

Once antennas can be fabricated, there is a requirement for compatible transmission line structures which should ideally match the feed point impedances of the antennas so as to achieve maximum power transfer. In order to investigate the matching conditions, backscattering

measurements were made on arrays of identical dipoles each connected to a length of coplanar transmission line. Travelling wave vee-antennas have also been employed in an investigation of the dependence of the line velocity factor on substrate thickness. The electrical properties of the coplanar transmission lines were found to be in agreement with conventional theory and the ability of standing wave antennas to efficiently couple energy to them at a frequency of 891 GHz was verified.

CONTENTS		page no
ABSTRACT		1-2
CHAPTER ONE	INTRODUCTION	21-27
CHAPTER TWO	STANDING WAVE ANTENNAS AT SUBMILLIMETRE WAVELENGTHS	28-42
2.1.	Introduction	28
2.2.	Properties of metals in the sub- millimetre region	29
2.3.	The effects of surface impedance on submillimetre antennas	33
2.4.	Substrate effects on submillimetre antennas	39
CHAPTER THREE	THEORETICAL SCATTERING PROPERTIES OF ANTENNAS AND ANTENNA ARRAYS	43-84
3.1.	Introduction	43
3.2.	Bistatic Scattering	45
3.3.	Multiply loaded scatterers	48
3.4.	Planewave Scattering	51
3.5.	The relationship between scattering and antenna parameters	54
3.6.	Theoretical analysis of the back- scattering and total scattering cross-sections of single cylindrical dipoles	59
3.7.	Theoretical analysis of the back- scattering and total scattering cross-sections of antenna arrays	72
CHAPTER FOUR	THEORETICAL ASPECTS OF THE OPEN RESONATOR	85-102
4.1.	Introduction	85
4.2.	Theory of the open resonator	86
4.3.	Measurement of total scattering cross- sections using an open resonator	90
4.4.	Theoretical estimate of the resonator unloaded Q.	96
4.4.1.	Diffraction loss	96
4.4.2.	Power dissipated due to the finite conductivity of the mirrors	97
4.4.3.	Coupling loss	97
4.4.4.	Unloaded Q of the open resonator	99
4.5.	Design of the scanning submillimetre open resonator	100
CHAPTER FIVE	A COMPUTER CONTROLLED SUB- MILLIMETRE OPEN RESONATOR	103-122
5.1.	Introduction	103
5.2.	Mechanical Design	104
5.3.	Electrical Design	109
5.4.	Computer control system design	109

	page no
5.4.1. 12 Bit 8 Channel Analogue to Digital Converter	112
5.4.2. Stepping Motor interfaces	114
5.4.3. Rotary position transducer interface	115
5.4.4. Visual display unit interface for the AIM 65 microcomputer	116
5.4.5. Digital plotter interface	116
5.4.6. EPROM Programmer	119
5.5. Instrument operation	120
CHAPTER SIX THE HCN LASER SOURCE	123-137
6.1. Introduction	123
6.2. Laser details	123
6.3. Cavity Length Stabilisation	124
6.4. Laser output beam profile	134
CHAPTER SEVEN EXPERIMENTAL INVESTIGATIONS WITH THE SUBMILLIMETRE OPEN RESONATOR	138-195
7.1. Experimental investigation of the mode spectrum of the unloaded open resonator	138
7.2. Influence of higher order modes on scattering cross-section measurements	153
7.3. Mirror modulation of the open resonator cavity	161
7.4. Determination of the scattering widths of a long thin wire at submillimetre wavelengths using the open resonator	168
7.5. Measurement of the refractive index and absorption coefficients of dielectric materials at 891 Ghz	172
7.6. Measurement of broadside total scattering cross-sections of short- circuited arrays	175
7.7. Measurement of the H-plane total scattering cross-section	183
CHAPTER EIGHT THE PHOTOLITHOGRAPHIC REPRODUCTION OF SUBMILLIMETRE ANTENNAS	196-210
8.1. Antenna design and manufacture	196
8.2. Physical Properties and choice of the antenna materials	197
8.3. Production process	200
8.3.1. Substrate preparation	200
8.3.2. Resist coating	200
8.3.3. Resist drying	202
8.3.4. Resist exposure	202
8.3.5. Developing and drying	202
8.3.6. Etching and resist removal	202
8.3.7. Inspection	202
8.4. Results	204

	page no
CHAPTER NINE      THE INVESTIGATION OF BACK- SCATTERING FROM LINEAR ARRAYS OF SHORT CIRCUITED DIPOLES	211-278
9.1. Angular spectrum from backscattering measurements	211
9.2. H-plane backscattering pattern from arrays of short-circuited halfwave dipole elements	214
9.2.1. Simple diffraction theory for the H-plane scattering by an antenna array	216
9.2.2. Experimental investigation of the variation of H-plane back- scattering from antenna arrays at 891 GHz	217
9.3. E-plane backscattering pattern from arrays of short-circuited dipole elements	234
9.3.1. Theoretical consideration of E-plane backscattering from an array of short circuited dipole elements	235
9.3.2. Experimental investigation of the variation of E-plane back- scattering from antenna arrays at 891 GHz	265
CHAPTER TEN      PROPERTIES OF COPLANAR TRANSMISSION LINES AT 891 GHz	279-320
10.1. Transmission line analysis from scattering measurements	279
10.2. Transmission lines for submillimetre wavelengths	281
10.2.1. Coplanar transmission line	283
10.2.2. Theoretical analysis of coplanar transmission line	283
10.3.. Experimental investigation of coplanar lines from backscattering measurements	288
10.4. Experimental investigation of the variation of velocity factor of coplanar lines with substrate thickness using vee-antennas	298
CHAPTER ELEVEN    CONCLUSIONS AND FURTHER WORK	321-345
REFERENCES	346-351
ACKNOWLEDGMENTS	352

	page no
APPENDICES: I	353-354
II	355-369
III	370-404
IV	405-408
V	409-411
VI	412-415

TABLES

2.1. The onset frequency of the anomalous region listed for various metals of interest	31
2.2. Surface impedances of various metals at 891 GHz with their DC electric conductivities $\sigma_{dc}$ .	33
5.1. Plotting commands	117-118
6.1. HCN laser line output powers	123
7.1. OpenResonator mode positions	140
7.2. Relative mode strengths	143
7.3. Dielectric properties at 891 GHz measured with the open resonator	175
8.1. Dielectric material properties	198
8.2. Substrate processing times	203
9.1. Broadside lobe full beamwidth, $\theta_B$	228
9.2. Angle of grating lobes from broadside, $\theta_D$	228
9.3. Grating lobe relative intensities	234
9.4. E-plane backscattering results for linear arrays of 10 short-circuited dipole elements. Inter-element separation is $0.25\lambda$ .	266
10.1. Experimental results obtained from dipole arrays terminated with coplanar transmission lines	297
11.1. Physical constants for a bismuth bolometer on a mylar substrate used in the calculations	338
11.2. Semiconductor properties	341

FIGURES

1.1. Clear weather attenuation of electromagnetic radiation as a function of frequency between 10 GHz and 1000 THz	23
2.1. Biconical antenna with its equivalent transmission line representation.	34
2.2. Geometry of a dipole antenna	37
2.3. Velocity ratio $C/V$ for an infinite sheet of thickness $2d$ for $TE_0$ and $TE_1$ modes	41



	page no
2.4. Velocity ratio C/V for an infinite sheet of thickness 2d for $TM_0$ and $TM_1$ modes	41
3.1. (a) Transmitting array (b) Receiving array, and (c) Diffracting array	44
3.2. Bistatic scattering	47
3.3. Multiply loaded scatterer	49
3.4. Broadside scattering from a cylindrical dipole	62
3.5. Normalised backscattering cross section $SIGMA = \sigma_{BS}/\lambda^2$ , for a cylindrical short-circuited dipole antenna of halflength H and radius $3.5 \times 10^{-3}\lambda$ . $K = 2\pi/\lambda$ .	63
3.6. Normalised total scattering cross section $SIGMA = \sigma_s/\lambda^2$ , for a short circuited dipole antenna of halflength H and radius $= 1.5 \times 10^{-2}\lambda$ . $K = 2\pi/\lambda$ .	64
3.7. Normalised total scattering cross section $SIGMA = \sigma_s/\lambda^2$ , for a short circuited dipole antenna of halflength H and radius $= 3.5 \times 10^{-3}\lambda$ . $K = 2\pi/\lambda$ .	65
3.8. Normalised total scattering cross section $SIGMA = \sigma_s/\lambda^2$ for a short circuited dipole antenna of halflength H and radius $= 3.5 \times 10^{-4}\lambda$ . $K = 2\pi/\lambda$ .	66
3.9. Normalised total scattering cross section $SIGMA = \sigma_s/\lambda^2$ for a centre loaded dipole of halflength H. Load impedance = $73 + j0\Omega$ radius = $15 \times 10^{-3}\lambda$ . $K = 2\pi/\lambda$ .	67
3.10. Normalised total scattering cross section $SIGMA = \sigma_s/\lambda^2$ for a centre loaded dipole of halflength H. Load impedance = $73 + j0\Omega$ radius = $3.5 \times 10^{-3}\lambda$ . $K = 2\pi/\lambda$ .	68
3.11. Normalised total scattering cross section $SIGMA = \sigma_s/\lambda^2$ for a centre loaded dipole of halflength H. Load impedance = $73 + j0\Omega$ radius = $3.5 \times 10^{-4}\lambda$ . $K = 2\pi/\lambda$ .	69
3.12. Variation of Q with antenna width $a/\lambda$ for planar dipole antennas.	71
3.13. H-plane scattering from a parasitic linear array	73
3.14. Normalised broadside scattering cross section $SIGMA = \sigma_s/\lambda^2$ , for a 20 element array of short circuited dipole elements of halflength D and inter-element separation $0.25\lambda$ mutual impedance effect neglected. Element radius = $3.5 \times 10^{-3}\lambda$ .	75

3.15.	Normalised broadside scattering cross section $\text{SIGMA} = \sigma_s/\lambda^2$ for a 20 element array of short circuited dipole elements of halflength D and inter-element separation = $0.25\lambda$ . Mutual impedance effects accounted for. Element radius = $3.5 \times 10^{-3}\lambda$ .	76
3.16.	Normalised total scattering cross section $\text{SIGMA} = \sigma_s/\lambda^2$ , for an array of 15 short-circuited halfwave dipoles with inter-element separation = D.	77
3.17.	Normalised total scattering cross section $\text{SIGMA} = \sigma_s/\lambda^2$ , for an array of 15 short-circuited fullwave dipoles with inter-element separation = D.	78
3.18.	Mutual impedance variation with separation, d, for two parallel half-wave dipoles, non staggered	80
3.19.	Variation of total scattering cross section $\text{SIGMA} = \sigma_s/\lambda^2$ , for 20 short circuit halfwave dipoles of inter-element spacing $0.25\lambda$ with angle of incidence, $\text{ANGLE}^\circ$ .	81
3.20	Variation of total scattering cross section $\text{SIGMA} = \sigma_s/\lambda^2$ , for 20 short circuited half-wave dipoles of inter-element separation $0.5\lambda$ with angle of incidence, $\text{ANGLE}^\circ$ .	82
3.21.	Variation of total scattering cross section $\text{SIGMA} = \sigma_s/\lambda^2$ , for 20 short circuit halfwave dipoles of inter-element spacing $0.75\lambda$ with angle of incidence, $\text{ANGLE}^\circ$ .	83
3.22.	Variation of total scattering cross section $\text{SIGMA} = \sigma_s/\lambda^2$ , for 20 short circuit halfwave dipoles of inter-element spacing $1.0\lambda$ with angle of incidence, $\text{ANGLE}^\circ$ .	84
4.1.	Geometry of the open resonator with spherical mirrors.	87
4.2.	Electric field distributions for interferometers with circular mirrors	88
4.3.	Theoretical transverse distribution of the electric field in a $\text{TEM}_{00}$ mode at the centre of an open resonator. $\lambda_0 = 337 \mu\text{m}$ , $R_0 = 0.768 \text{ m}$ and $d = 0.16 \text{ m}$ .	89
5.1.	Schematic diagram of the open resonator	106
5.2.	Open resonator extracted from vacuum tank which also acts as a radiation shield.	107

	page no
5.3. Schematic diagram of the sample movements	108
5.4. Open resonator construction.	110
5.5. Stepping motor drive board rack and power supply unit.	110
5.6. Linear position transducer power supply and meter unit and Slo-syn stepping motor unit	111
5.7. Electrical testing of the open resonator	111
5.8. AIM 65 Microcomputer and Peripheral Crate	113
5.9. Close up of Peripheral Crate	113
5.10. Schematic diagram of the microcomputer controlled submillimetre open resonator	121
6.1. Block diagram of the servo loop	126
6.2. Servo system pyroelectric detector pre-amplifier	127
6.3. Servo system main amplifier	128
6.4. Laser stabiliser circuit diagram	129
6.5. Laser output monitoring arrangement	132
6.6. Variation of laser output with time for both stabilised and unstabilised cases	133
6.7. 8 Metre HCN laser	135
6.8. Laser stabilising circuitry rack units.	135
6.9. Schematic of experimental arrangement used to measure output beam profile of the HCN laser	136
6.10. Output beam profile of HCN laser	137
7.1. Experimental arrangement used to investigate the mode spectrum of the open resonator	139
7.2. Open resonator mode spectrum with mirror apertures equal to 10 cm	141
7.3. Open resonator mode spectrum with modes identified. Mirror apertures equal to 3 cm	142
7.4. Variation of the mode spectrum of the open resonator with mirror separation $d$ . Mirror aperture $\phi = 3$ cm	144-147
7.5. Variation of the mode spectrum of the open resonator with mirror separation $d$ . Mirror aperture $\phi = 2$ cm	148-152
7.6. Variation of the mode spectrum of the open resonator with sample position, $S$ , when loaded with a linear array of 15 short circuited dipole elements of length $0.5\lambda$ separation by $0.75\lambda$ . Mean mirror separation = 17 cm. Mirror apertures = 3 cm.	154-159

	page no
7.7. Variation of open resonator loaded Q with longitudinal sample position. Sample was a linear array of 15 short circuited dipole elements of length $0.5\lambda$ separated by $0.75\lambda$ .	160
7.8. (i) Resonance curve (ii) Differentiated resonance curve	162
7.9. Use of a Piezoelectric ceramic cylinder to modulate the input mirror of the open resonator	163
7.10. Piezoelectric cylinder drive circuitry employed to produce the mirror modulation and reference signal	165
7.11. Voltage variation across the Piezoelectric ceramic cylinder produced by the circuit shown in Figure 7.10.	166
7.12. Left: Mirror chopped response curve (Gain = 72dB, $\tau = 2s$ , $f_{chop} = 7Hz$ ) Right: Radiation chopped response curve (Gain = 46dB, $\tau = 0.5s$ , $f_{chop} = 13 Hz$ )	166
7.13. Scattering cross-section of a circular cylinder with $\vec{H}$ parallel to the cylinder axis (— theoretical (geometrical optics + one correction term), $\bar{I}$ experimental at 891 GHz)	171
7.14. Variation of normalised total scattering cross-section with inter-element space, for linear arrays of 15 half-wave ( $L = 0.5\lambda$ ) and fullwave ( $L = 1.0\lambda$ ) short circuited dipole elements	177
7.15. Variation of normalised total scattering cross-section with element half-length for linear arrays of 20 short circuited dipoles having inter-element spacing of $0.25\lambda$ .	178
7.16. Variation of $R_{in}/R_o \lambda$ with dipole element half-lengths from $0.01\lambda$ to $0.75\lambda$ .	181
7.17. Variation of $R_{in}/R_o \lambda$ with dipole element half-lengths from $0.01\lambda$ to $0.85\lambda$ .	182
7.18. (a) Variation of scattering cross-section with angle of incidence $\theta$ for $3.5 \mu m$ mylar substrate ( $\ominus$ ) and the same substrate with a 10 element linear array of short circuited halfwave dipoles separated by $1\lambda$ ( $\bar{I}$ ) (b) Variation of H plane scattering cross-section for the array above obtained by taking the difference between the curves in Figure 7.18 (a)	184
7.19. Multiple reflection in a thin dielectric interface	185

	page no
7.20. Variation of intensity reflection coefficient with angle of incidence for a mylar substrate of thickness $3.5 \mu\text{m}$ and refractive index 1.76. Electric field vector is perpendicular to the plane of incidence.	188
7.21. Multiple reflection between two thin parallel films, $d \ll t$ .	190
7.22. Variation of intensity reflection coefficient for two parallel substrates with substrate separation for $0^\circ$ angle of incidence. Substrate thicknesses = $3.5 \mu\text{m}$	191
7.23. Variation of intensity reflection coefficient for two parallel substrates with substrate separation for $25^\circ$ angle of incidence. Substrate thicknesses = $3.5 \mu\text{m}$ .	192
7.24. Variation of intensity reflection coefficient for two parallel substrates with substrate separation for $50^\circ$ angle of incidence. Substrate thicknesses = $3.5 \mu\text{m}$ .	193
7.25. Experimental variation of effective cross-section, $\sigma_{\text{eff}}$ , of two parallel mylar substrates with substrate separation. Angle of incidence = $10^\circ$ , substrate thickness = $3.5 \mu\text{m}$ .	195
8.1. Photograph of the clean box in which the reproduction process was undertaken	201
8.2. Photomicrograph taken in transmitted light of a linear array of short-circuited halfwave dipoles (length = $168 \mu\text{m}$ ) separated by half wavelength ( $168 \mu\text{m}$ ). Reproduced on $3.5 \mu\text{m}$ mylar	205
8.3. Photomicrograph taken in reflected light of the EBL master mask plate used to re-produce the above array	205
8.4. Photomicrograph, taken in transmitted light of an array of halfwave dipoles (length = $168 \mu\text{m}$ ) attached to lengths of short-circuited coplanar transmission line	206
8.5. Photomicrograph, taken in transmitted light of an element from the array shown in Figure 8.4.	206
8.6. Photomicrograph, taken in reflected light of a vee antenna	207
8.7. Photomicrograph, taken in reflected light, of the apex of the vee antenna in Figure 8.6.	207

	page no
8.8. Electron micrograph of a linear antenna array. Magnification = 200	209
8.9. Electron micrograph of an element from the above array. Magnification = 4000	209
8.10. Electron micrograph of antenna metalisation. Magnification = 7500	210
8.11. Electron micrograph of antenna metalisation. Magnification = 10000	210
9.1. Experimental arrangement employed for backscattering measurements	212
9.2. E and H plane scattering geometry for a dipole array in the ZY plane. X axis is array normal	215
9.3. H plane scattering geometry for a dipole array of N elements of inter-element separation d	215
9.4. Variation of H-plane electric field distribution for a linear array of 10 isotropic elements of inter-element separation $0.25\lambda$ .	218
9.5. Variation of H-plane electric field distribution for a linear array of 10 isotropic elements of inter-element separation $0.5\lambda$ .	219
9.6. Variation of H-plane electric field distribution for a linear array of 7 isotropic elements of inter-element separation $0.62\lambda$ .	220
9.7. Variation of H-plane electric field distribution for a linear array of 5 isotropic elements of inter element separation $0.75\lambda$ .	221
9.8. Variation of H-plane electric field distribution for a linear array of 5 isotropic elements of inter-element separation $1.0\lambda$ .	222
9.9. H-plane backscattering pattern for a linear array of 10 short circuited halfwave dipole elements of inter-element separation $0.25\lambda$ . Reproduced on a $3.5 \mu\text{m}$ mylar substrate. Element width = $10 \mu\text{m}$ .	223
9.10. H-plane backscattering pattern for a linear array of 10 short circuited halfwave dipole elements of inter-element separation $0.5\lambda$ . Reproduced on a $3.5 \mu\text{m}$ mylar substrate. Element width = $10 \mu\text{m}$ .	224

- 9.11. H-plane backscattering pattern for a linear array of 7 short circuited halfwave dipole elements of inter-element separation  $0.62\lambda$ . Reproduced on a  $3.5 \mu\text{m}$  mylar substrate. Element width =  $10 \mu\text{m}$ . 225
- 9.12. H-plane backscattering pattern for a linear array of 5 short circuited halfwave dipole elements of inter-element separation  $0.75\lambda$ . Reproduced on a  $3.5 \mu\text{m}$  mylar substrate. Element width =  $10 \mu\text{m}$ . 226
- 9.13. H-plane backscattering pattern for a linear array of 5 short circuited halfwave dipole elements of inter-element separation  $1.0\lambda$ . Reproduced on a  $3.5 \mu\text{m}$  mylar substrate. Element width =  $10 \mu\text{m}$ . 227
- 9.14. Theoretical H-plane backscattering pattern for a linear array of 10 short circuited half-wave dipole antennas of inter-element separation  $0.25\lambda$ . Element width =  $0.03\lambda$ . 229
- 9.15. Theoretical H-plane backscattering pattern for a linear array of 10 short circuited half-wave dipole elements of inter-element separation  $0.5\lambda$ . Element width =  $0.03\lambda$ . 230
- 9.16. Theoretical H-plane backscattering pattern for a linear array of 7 short circuited half-wave dipole antennas of inter-element separation  $0.62\lambda$ . Element width =  $0.03\lambda$ . 231
- 9.17. Theoretical H-plane backscattering pattern for a linear array of 5 short circuited half-wave dipole elements of inter-element separation  $0.75\lambda$ . Element width =  $0.03\lambda$ . 232
- 9.18. Theoretical H-plane backscattering pattern for a linear array of 5 short circuited half-wave dipole antennas of inter-element separation  $1.0\lambda$ . Element width =  $0.03\lambda$ . 233
- 9.19. E-plane scattering geometry for a single dipole element. Element half-length =  $L$  236
- 9.20. (a) Variation of the backscattered electric field  $E(\theta)/E_0$  with angle of incidence  $\theta$  for a short circuited dipole element of halflength  $0.25\lambda$ . 238  
(b) Variation of electric field distribution  $E(\theta)/E_0$  with azimuthal angle  $\theta$  for a transmitting antenna of halflength  $0.25\lambda$ . 239

	page no
9.21. (a) Variation of the backscattered electric field $E(\theta)/E_0$ with angle of incidence $\theta$ for a short circuited dipole element of halflength $0.5\lambda$ .	240
(b) Variation of electric field distribution $E(\theta)/E_0$ with azimuthal angle $\theta$ from a transmitting antenna of halflength $0.5\lambda$ .	241
9.22. (a) Variation of the backscattered electric field $E(\theta)/E_0$ with angle of incidence $\theta$ for a short circuited dipole element of halflength $0.55\lambda$ .	242
(b) Variation of electric field distribution $E(\theta)/E_0$ with azimuthal angle $\theta$ for a transmitting antenna of halflength $0.55\lambda$ .	243
9.23. (a) Variation of the backscattered electric field $E(\theta)/E_0$ with angle of incidence $\theta$ for a short circuited dipole element of halflength $0.65\lambda$ .	244
(b) Variation of the electric field distribution $E(\theta)/E_0$ with azimuthal angle $\theta$ for a transmitting antenna of halflength $0.65\lambda$ .	245
9.24. (a) Variation of the backscattered electric field $E(\theta)/E_0$ with angle of incidence $\theta$ for a short circuited dipole element of halflength $0.7\lambda$ .	246
(b) Variation of electric field distribution $E(\theta)/E_0$ with azimuthal angle $\theta$ for a transmitting antenna of halflength $0.7\lambda$ .	247
9.25. (a) Variation of the backscattered electric field $E(\theta)/E_0$ with angle of incidence $\theta$ for a short circuited dipole element of half-length $0.75\lambda$ .	248
(b) Variation of electric field distribution $E(\theta)/E_0$ with azimuthal angle $\theta$ for a transmitting antenna of halflength $0.75\lambda$ .	249
9.26. (a) Variation of the backscattered electric field $E(\theta)/E_0$ with angle of incidence $\theta$ for a short circuited dipole element of halflength $0.8\lambda$ .	250
(b) Variation of electric field distribution $E(\theta)/E_0$ with azimuthal angle $\theta$ for a transmitting antenna of halflength $0.8\lambda$ .	251
9.27. (a) Variation of the backscattered electric field $E(\theta)/E_0$ with angle of incidence $\theta$ for a short circuited dipole element of halflength $0.85\lambda$ .	252



- (b) Variation of electric field distribution  $E(\theta)/E_0$  with azimuthal angle  $\theta$  for a transmitting antenna of halflength  $0.85\lambda$ . 253
- 9.28. (a) Variation of backscattered electric field  $E(\theta)/E_0$  with angle of incidence  $\theta$  for a short circuited dipole element of halflength  $1.0\lambda$ . 254
- (b) Variation of electric field distribution  $E(\theta)/E_0$  with azimuthal angle  $\theta$  for a transmitting antenna of halflength  $1.0\lambda$ . 255
- 9.29. (a) Variation of the backscattered electric field  $E(\theta)/E_0$  with angle of incidence  $\theta$  for a short circuited dipole element of halflength  $1.05\lambda$ . 256
- (b) Variation of electric field distribution  $E(\theta)/E_0$  with azimuthal angle  $\theta$  for a transmitting antenna of halflength  $1.05\lambda$ . 257
- 9.30. (a) Variation of the backscattered electric field  $E(\theta)/E_0$  with angle of incidence  $\theta$  for a short circuited dipole element of halflength  $1.1\lambda$ . 258
- (b) Variation of electric field distribution  $E(\theta)/E_0$  with azimuthal angle  $\theta$  for a transmitting antenna of halflength  $1.1\lambda$ . 259
- 9.31. E-plane backscattering pattern for a linear array of 10 short circuited dipole elements of halflength  $0.25\lambda$ . Inter-element spacing =  $0.25\lambda$ , element width =  $0.03\lambda$ . 260
- 9.32. E-plane backscattering pattern for a linear array of 10 short circuited dipole elements of halflength  $0.5\lambda$ . Inter-element spacing =  $0.25\lambda$ , element width =  $0.03\lambda$ . 261
- 9.33. E-plane backscattering pattern for a linear array of 10 short circuited dipole elements of halflength  $0.75\lambda$ . Inter-element spacing =  $0.25\lambda$ , element width =  $0.03\lambda$ . 262
- 9.34. E-plane backscattering pattern for a linear array of 10 short circuited dipole elements of halflength  $0.8\lambda$ . Inter-element spacing =  $0.25\lambda$ , element width =  $0.03\lambda$ . 263
- 9.35. Experimental E-plane backscattering pattern for a linear array of 10 short-circuited dipole elements of halflength  $0.25\lambda$  separated by  $0.25\lambda$ . Element width =  $10 \mu\text{m}$ . 267

	page no
9.36. Experimental E-plane backscattering pattern for a linear array of 10 short-circuited dipole elements of halflength $0.5\lambda$ separated by $0.25\lambda$ . Element width = $10 \mu\text{m}$ .	268
9.37. Experimental E-plane backscattering pattern for a linear array of 10 short circuited dipole elements of halflength $0.55\lambda$ . Element width = $10 \mu\text{m}$ .	269
9.38. Experimental E-plane backscattering pattern for a linear array of 10 short-circuited dipole elements of halflength $0.65\lambda$ . Element width = $10 \mu\text{m}$ .	270
9.39. Experimental E-plane backscattering pattern for a linear array of 10 short-circuited dipole elements of halflength $0.7\lambda$ . Element width = $10 \mu\text{m}$ .	271
9.40. Experimental E-plane backscattering pattern for a linear array of 10 short circuited dipole elements of halflength $0.75\lambda$ . Element width = $10 \mu\text{m}$ .	272
9.41. Experimental E-plane backscattering pattern for a linear array of 10 short circuited dipole elements of halflength $0.8\lambda$ separated by $0.25\lambda$ . Element width = $10 \mu\text{m}$ .	273
9.42. Experimental E-plane backscattering pattern for a linear array of 10 short-circuited dipole elements of halflength $0.85\lambda$ separated by $0.25\lambda$ . Element width = $10 \mu\text{m}$ .	274
9.43. Experimental E-plane backscattering pattern for a linear array of 10 short-circuited dipole elements of halflength $1.0\lambda$ separated by $0.25\lambda$ . Element width = $10 \mu\text{m}$ .	275
9.44. Variation of the velocity factor $V/C$ for the current on a dipole plotted against the effective thickness $t_{\text{eff}}$ of the supporting substrate for various substrate relative permittivities, $\epsilon_r$ .	277
10.1. Cross-section of typical dielectric waveguides for millimetre wave integrated circuits (a) rod guide (b) image guide (c) insular guide	282
10.2. Strip transmission lines	284
10.3. Coplanar line geometry	286
10.4. Numerical value of $\frac{\tilde{F}(\beta)}{\beta} \Big  \frac{f(\beta)}{Q} \Big ^2$ plotted against $\beta a$	286

- 10.5. (a) Variation of input reactance with dipole halflength H 289
- (b) Variation of input resistance with dipole halflength H 289
- 10.6. Variation of effective backscattering cross-section,  $F$ , with the length of a short-circuited  $115\ \Omega$  transmission line loading a halfwave dipole of input impedance  $73 + j\ 42\ \Omega$ . The length of line is expressed in guide wavelengths and the variation for various line attenuations is given 292
- 10.7. Variation of effective backscattering cross-section,  $F$ , with the length of a short circuited  $138\ \Omega$  transmission line loading a  $0.62\lambda$  length dipole of input impedance  $200 + j\ 300\ \Omega$ . The length of line is expressed in guide wavelengths and the variation for various line attenuations is given. 293
- 10.8. Variation of backscattered signal response with length of transmission line for an array of  $10, 0.5\lambda$  length dipoles connected to  $115\ \Omega$  short circuited coplanar transmission line 295
- 10.9. Variation of backscattered signal response with length of transmission line for an array of  $10, 0.62\lambda$  length dipoles connected to  $138\ \Omega$  short circuited coplanar transmission line 296
- 10.10. Geometry of the vee-antenna 299
- 10.11. Technique employed to support the vee antennas 302
- 10.12. H-plane backscattering pattern for a vee antenna reproduced on a  $1.5\ \mu\text{m}$  thick mylar substrate 303
- 10.13. E-plane backscattering pattern for a vee antenna reproduced on a  $1.5\ \mu\text{m}$  thick mylar substrate 304
- 10.14. H-plane backscattering pattern for a vee antenna reproduced on a  $3.5\ \mu\text{m}$  thick mylar substrate 305
- 10.15. E-plane backscattering pattern for a vee antenna reproduced on a  $3.5\ \mu\text{m}$  thick mylar substrate 306
- 10.16. Variation of velocity factor with substrate thickness for a  $\text{TE}_0$  mode excited on a mylar substrate ( $\epsilon_r = 3.1$ ) at  $891\ \text{GHz}$  ( $337\ \mu\text{m}$ ). 309
- 10.17. Variation of scattering cross section factor with the length of short circuited transmission lines of various characteristic impedance connected to a vee antenna of input impedance  $200\ \Omega$ . The length of line is expressed in guide wavelengths. Attenuation is ignored. 310

10.18.	Variation of backscattered signal from a vee antenna with the length of terminating short circuited transmission line reproduced on 1.5 $\mu\text{m}$ thick mylar	312
10.19.	Variation of backscattered signal from a vee antenna with the length of terminating short circuited transmission line reproduced on 3.5 $\mu\text{m}$ thick mylar	313
10.20.	Variation of backscattered signal from a vee antenna with the length of terminating short circuited transmission line reproduced on 4 $\mu\text{m}$ thick mylar	314
10.21.	Variation of backscattered signal from a vee antenna with the length of terminating short circuited transmission line reproduced on 6 $\mu\text{m}$ thick mylar	315
10.22.	Variation of backscattered signal from a vee antenna with the length of terminating short circuited transmission line reproduced on 8 $\mu\text{m}$ thick mylar	316
10.23.	Variation of backscattered signal from a vee antenna with the length of terminating short circuited transmission line reproduced on a 8.9 $\mu\text{m}$ thick mylar	317
10.24.	Variation of backscattered signal from a vee antenna with the length of terminating short circuited transmission line reproduced on 12.5 $\mu\text{m}$ thick mylar	318
10.25.	Variation of the velocity factor V/C with the substrate thickness T for the above coplanar line geometry	319
11.1.	End-fire antenna array structure on thin dielectric substrate	323
11.2.	Asymptotic current distribution in a symmetrically fed dipole antenna of halflength L	325
11.3.	Radiation (electric field) patterns for transmitting and reflecting dipole antennas of halflength L	328
11.4.	Proposed design for a co-linear dipole array with series connected microbolometers	330
11.5.	(a) A bismuth layer is deposited on substrate. A silver layer is deposited over the bismuth and covers half of the substrate	331
	(b) Detail of substrate layers. A photo-resist layer covers the metalisation	331

- 11.5. (c) The mask is aligned over the substrate so that the microbolometer elements lie on the bismuth side of the bismuth/silver interface 331
- (d) The finished antenna/bolometer structure after etching and resist removal 332
- 11.6. Schematic diagram of a R.F. sputter etching plant 334
- 11.7. Proposed microbolometer geometry 337
- 11.8. Variation of radiation absorption length,  $K$ , with acceptor impurity concentration in p - type silicon 342
- 11.9. Variation of radiation absorption length,  $K$ , with donor impurity concentration in n -type silicon 343
- A.3.1 TTL to ADC 117 drive board interface (for 4 step/rev stepping motors) 371
- A.3.2. TTL to ADC 800 drive board interface (for 800 step/rev stepping motors) 372
- A.3.3. Dual 24 volt 6 amp power supply circuit diagram. Each output fed one ADC 117 and one ADC 800 drive board 373
- A.3.4. Circuit diagram for the linear variable differential transformer displacement transducer power supply and meter unit 374
- A.3.5. Peripheral crate buffer module 375
- A.3.6. 4K RAM board 376
- A.3.7. 4K EPROM board 377
- A.3.8. (a) 8 Channel 12 bit A - D converter address decoding circuitry 379
- (b) 8 channel 12 bit A - D converter. 8 channel input analogue multiplexer and converter IC circuit 380
- A.3.8. (c) 8 channel 12 bit A - D converter. Analogue channel address select and status latching circuitry 381
- (d) 8 channel 12 bit A - D converter. Data bus input/output tristate buffering 382
- A.3.9. (a) Dual stepping motor interface address decoder 384
- (b) Stepping motor interface parallel loaded down counter, forward/reverse latch and clock circuit. There were two such circuits in the dual interface. 385

A.3.9.	(c)Dual stepping motor interface peripheral status register tristate output buffer	386
A.3.10.	(a) Quad stepping motor interface address decoding and input data bus buffering circuitry	388
	(b) Stepping motor interface parallel loaded down counter, motor drive board oscillator enable latching and forward/reverse latch circuitry. There are 4 such circuits in the quad interface	389
	(c) Quad stepping motor interface peripheral status register tristate buffering	390
A.3.11.	(a) Rotary position transducer interface address decoding and output tristate buffering circuitry	392
	(b) Rotary position transducer V-scan to natural binary decoding and display circuitry.	393
A.3.12.	(a) VDU interface address decoder, data latch and strobe generator circuit	396
	(b) CRT controller circuit	397
A.3.13.	(a) Digital plotter interface address decoder and data strobe circuitry	399
	(b) Digital plotter interface data latch and busy output tristate buffer	400
A.3.14.	EPR0M programmer circuit	404
A.6.1.	Geometry of the vee-antenna	413
A.6.2.	(a) Vee-antenna conductors mapped into spherical-polar co-ordinates	413
	(b) Vee-antenna conductors mapped into $u + iv$ co-ordinates. ( $u + iv = \tan \frac{\theta}{2} \exp i \phi$ )	413

## CHAPTER ONE

### INTRODUCTION

In terms of wavelength, submillimetre waves may be said to span the two decade range from 1 to 0.01 millimetre or, alternatively, in terms of frequency from 300 GHz to 30 THz. The short wavelength limit then corresponds approximately to the wavelength of the CO<sub>2</sub> laser, although some people consider this to be within the infrared. At the longer wavelength end, electron beam and semiconductor devices find application as sources. Within the region itself, coherent radiation is obtained from optically pumped<sup>1</sup> and electrically excited<sup>2</sup> molecular gas lasers. Electron beam devices called backward wave oscillators have also been used to generate frequencies up to 1.5 THz.

Although the submillimetre region has been extensively studied from a purely scientific viewpoint, technologically, it is underdeveloped. This is possibly due to the lack of compact coherent sources and detectors. Also the applicability of conventional circuit ideas, which are employed at lower frequencies, have not been fully explored. Such knowledge is essential if integrated circuit systems are to be built for these frequencies.

The submillimetre region is characterised by high atmospheric attenuation<sup>3</sup>. Figure 1.1, shows the clear attenuation of electromagnetic radiation as a function of frequency between 10 GHz and 1000 THz at sea level. It is clear that the atmospheric attenuation ranges between 100 and 1000 dB Km<sup>-1</sup> over most of the submillimetre spectrum. However, applications may still exist for submillimetre radiation in inter-satellite communication links where atmospheric attenuation is not a problem. The use of submillimetre waves would have advantages over optical waves in this application. The inherently wider beamwidth would help reduce search and acquisition times. Also a greater improvement in beam holding capability would result.

However, the beamwidth would still be narrow enough to ensure a high security link which lower frequencies might not provide.

The atmospheric attenuation at submillimetre frequencies could be used to advantage for terrestrial communication links where the resulting short range could reduce the susceptibility to interception and jamming<sup>4</sup>.

Submillimetre radiation is used for investigations into the composition of the upper atmosphere<sup>5 6 7</sup>. Measurements have included concentration of water, ozone, oxides of nitrogen and nitric acid, even with concentrations as low as 1 part in  $10^{11}$ . Radio astronomy has now extended into the submillimetre region. Atmospheric attenuation is overcome by using balloons, rockets and aircraft as observing platforms and high altitude ground based observatories through atmospheric "windows". Submillimetre waves are particularly suited for plasma diagnostics in plasmas where electron densities lie in the range  $10^{19}$  to  $10^{21} \text{ m}^{-3}$ . Such concentrations exist in thermonuclear discharges, where this wavelength region has found particular application<sup>8 9 10</sup>. One possible use for short wavelength radiation is the scale modelling of electromagnetic problems where large structures are involved. For example, a phase sensitive radar at 891 GHz ( $337\mu\text{m}$ ) has been developed by E.M.I. Electronics for use in radar modelling<sup>11</sup>.

Techniques for guided wave propagation used at microwave and optical frequencies face severe limitations in the submillimetre region. Optical guides make use of the low loss transmission properties of glasses, for which there is no equivalent in the submillimetre as dielectric loss is generally high. The use of metallic waveguiding techniques employed at lower frequencies is also excluded because of high surface resistance losses and the manufacturing difficulties created by the small size of the components. This has led to the realisation that at these high frequencies free space modes of propagation offer to become the optimum radiation guiding technology.<sup>12</sup>



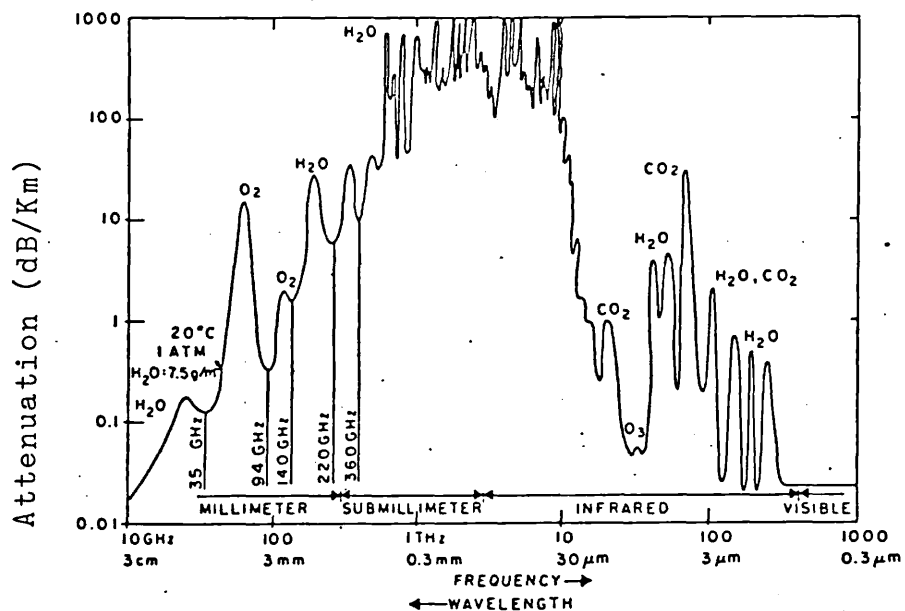


Figure 1.1. Clear weather attenuation of electromagnetic radiation as a function of frequency between 10 GHz and 1000 THz. (Ref. 3).

Free space modes of propagation are known as "beam modes"<sup>13</sup>. Any wavefront can be described by a set of "beam modes" just as a complicated waveform may be described by a Fourier series. The distribution of field amplitude in the cross-section of each of these modes has a specific form, unchanging as the beam propagates, apart from rescaling. This analysis is useful when considering sub-millimetre optical systems where the assumptions of geometrical optics, that the cross-section of the beam is at least two orders of magnitude greater than the wavelength, might not apply.

The input beam may be constructed from a series of "beam modes" which can be individually propagated through the optical system and then summed to produce the resulting output beam. Clearly techniques of matching devices to these "beam modes" are required.

Low loss transmission is essential at submillimetre frequencies as the power available from sources is usually limited. The advantages of "beam mode" propagation systems can be summarized as :-

- (1) low loss transmission
- (2) easily manufactured components
- (3) low cost

Four types of receiver system may be used for the detection of submillimetre radiation, video, heterodyne down converting, heterodyne up converting and imaging. The first two techniques are the most useful, the others having been relatively little investigated in the submillimetre region. Small size detectors and mixers, such as planar schottky barrier diodes<sup>14</sup> and microbolometers<sup>15 16</sup>, that lend themselves to inclusion in integrated circuit devices, are of considerable interest at these frequencies. Also, small thermal detectors such as microbolometers can be designed to have fast response times. Such devices are usually 1-10  $\mu\text{m}^2$  in size. However, for a single mode propagation system, if the physical area of the detector is  $\lesssim \lambda^2$  then not even a

single mode can effectively be received as  $\lambda^2$  is the order of the diffraction limited area of the focused spot of radiation. Some form of antenna that effectively matches the geometry of the incoming radiation "beam mode", and a means of matching the impedance of the detector to that of the radiation coupling system, is therefore required.

The long wire antenna properties<sup>17</sup> of whiskers used with point-contact detectors have been used to maximise the responses of these detectors at submillimetre wavelengths. The angular antenna patterns of such structures are not very favourable for efficient coupling from the radiation field, but the addition of reflectors around the wire can significantly simplify and improve the directivity of the antenna pattern<sup>18</sup>. However, this type of antenna/detector is difficult to fabricate into an array and is very fragile.

Travelling wave antennas generally have awkwardly shaped or oriented antenna patterns which causes problems when one tries to integrate these into planar circuitry. Resonant standing wave antennas may overcome these disadvantages. They can be arranged in arrays so that the main lobe is perpendicular to the plane of the array. This is convenient, for example, when the antennas are integrated onto the surface of high resistivity semiconductor substrates. Arrays would be preferable to single antennas. The effective receiving cross section of a resonant halfwave dipole, when perfectly matched to its load, is  $0.13\lambda^2$ . Therefore to obtain substantial receiving cross sections an array of such antennas would be desirable.

The aim of this investigation was to study the properties of standing wave antennas from their scattering properties. This technique was chosen because the planar detectors, suitable for integrating with submillimetre antennas, that have been developed to date are difficult and expensive to reproduce. Also, they have low responsivities. Attempting to investigate antennas from their transmission properties is not possible as waveguiding technology is not well enough developed at these frequencies to permit the efficient feeding of power to transmitting antennas.

It is therefore easier to investigate the scattering properties of antennas at submillimetre wavelengths than their reception or transmission properties. The experimental work was done at a frequency of 891 GHz (337 $\mu$ m) using a HCN laser as the radiation source. This frequency was chosen because it is at the longer wavelength end of the submillimetre region where extensions to higher frequencies of millimetre source technologies is likely to create future interest. Also as a coherent radiation source, the HCN laser is rugged and cheap to run. This frequency is within an atmospheric "window" where attenuation is  $\sim 50$  dB/Km<sup>19</sup> at sea level and, therefore, might be useful for short range communication links.

The work embarked upon is introduced in Chapter 2 with a consideration of whether standing wave antennas are possible at these high frequencies. The physical aspects of electromagnetic scattering from antennas are developed in Chapter 3 by considering the relationships between the scattering, transmitting and receiving patterns of antennas. Also, the antenna parameters, such as antenna gain and terminal impedance, are found in terms of the scattering parameters. The theoretical analysis of multiple loaded scatterers due to Harrington<sup>20</sup> is introduced. The theoretical results obtained from computer programs developed using this theory are given. Chapter 4 introduces the submillimetre open resonator which is one of the measurement techniques employed in this investigation. It has the advantage of giving absolute determinations of the total scattering cross-sections of short circuited antennas. The theoretical aspects of the resonator and the measurement technique is developed. From the design parameters a practical design was obtained. A microcomputer control system was developed to control the open resonator and a detailed description is given in Chapter 5. It was found that the amplitude stability of the HCH laser was insufficient to enable measurements to be made over long experimental runs. A current stabilised power supply and a servo loop system to stabilise the laser cavity were employed to overcome this difficulty. They are described in Chapter 6.

Chapter 7 reports the results of experimental investigations with the open resonator. The instrument was used to measure the dielectric properties of various dielectric materials at 891 GHz. The results obtained were used to select a suitable substrate material for supporting the antenna arrays. Chapter 7 also includes the measurements obtained on various arrays of short circuited antenna elements. The techniques employed for producing the submillimetre antennas are reported in Chapter 8.

It was found that the standing-wave structure of the radiation in the open resonator precluded its use for measurements on the angular variation of scattering. In Chapter 9 the experimental arrangement employed to investigate the backscattering responses of the antennas is described. The angular variation of scattering is compared with the theoretical predictions. The results of coupling dipole antennas to lengths of short circuited coplanar transmission line is reported in Chapter 10. The properties of the coplanar transmission line were found by analysing the variation of scattering response of the antenna with transmission line length.

Chapter 11 contains the conclusions drawn from the experimental programme and suggests possible avenues for further work in this area.

## CHAPTER TWO

### STANDING WAVE ANTENNAS AT SUBMILLIMETRE WAVELENGTHS

#### 2.1. Introduction

The small size and delicacy of submillimetre antennas necessitates supporting them on a suitable substrate. The properties and geometry of the supporting substrate can either be employed to enhance the antenna performance, or be made to interfere as little as possible with the action of the antenna. As an example of the former strategy, Mizuno et al.<sup>21</sup>, have modelled, at 10 GHz, a design for the submillimetre region consisting of a resonant dipole, with an associated director element, on a dielectric plate. As well as supporting the antenna the substrate also acts as a dielectric plate antenna. This results in an increase in gain of more than 10 dB over that of an isolated dipole antenna. The disadvantage of this type of antenna is that the direction of maximum response lies in the plane of the dielectric plate, which may not be desirable in some applications.

In the present investigation, resonant antennas on thin dielectric substrates were studied. This type of structure promises to have a large gain in a direction perpendicular to the plane of the substrate, which would be desirable in applications requiring two-dimensional arrays, such as imaging systems for example. The effective aperture or absorption cross section of an antenna,  $A_e$ , is defined as

$$A_e = \frac{W}{P_i} \quad (2.1.)$$

$W$  is the power delivered to the load impedance at the antenna terminals and  $P_i$  is the power density of the incident radiation. The effective aperture is dependent on the load impedance and the direction and polarisation of the incident wave. For the general case, where polarisations and impedances are not matched,  $T_{ai}$ <sup>22</sup> has

evaluated (2.1) as

$$A_e = \frac{pq\lambda^2 D(\theta, \phi)}{4\pi} \quad (2.2.)$$

$D(\theta, \phi)$  is the directivity or gain of the antenna in the direction of the incident field,  $q$  and  $p$  are, respectively, the impedance and polarisation mismatching factors, and  $\lambda$  is the free space wavelength. Therefore, the amount of power an antenna extracts from a given power density of incident radiation is proportional to the square of the wavelength.

At submillimetre wavelengths, antenna arrays will be vastly superior to single dipoles for the efficient coupling of radiation to detectors. Single dipole antennas are possibly of some interest as they could be used quite effectively with parabolic focusing systems, provided that the spot size can be made sufficiently small. High gain antenna systems do suffer from the disadvantage that they are consequently highly directive, so accurate antenna alignment is required. In this chapter, the factors which affect the properties of resonant submillimetre antennas are considered and may be summarised as :-

- (i) the finite surface impedance of the best electrical conductors at submillimetre wavelengths
- (ii) the properties of the supporting dielectric substrate
- (iii) the physical dimensions of the antenna

## 2.2. Properties of metals in the submillimetre region

As frequency increases, the electromagnetic fields and currents in a metal become concentrated in an increasingly thinner surface layer, whilst outside the metal the finite value of the velocity of light becomes apparent. The wave character of the electromagnetic field emerges more clearly as the wavelength decreases causing surface reactance effects to become important. At high frequencies the classical skin effect becomes inadequate. The inertia of the electrons leads to relaxation effects,

whilst the particle nature of the electrons manifests itself in the anomalous skin effect. The onset of the anomalous skin effect occurs when the skin depth becomes smaller than the mean free path of the electrons. The frequency at which this happens for different metals is of particular interest, as the incident radiation is more strongly absorbed than expected from the theory of the classical skin effect. Consequently antenna losses would be greater than calculated from classical theory.

The frequency at which the onset of the anomalous skin effect occurs is  $\nu_a$  (Hz) and is given by<sup>23</sup>

$$\nu_a = \frac{1}{2\pi} \left( \frac{\lambda p}{v} \right) \frac{1}{\tau^3} \quad (2.3.)$$

where

- $\tau$  = Drude relaxation time (s)
- $v$  = Fermi surface electron velocity ( $\text{ms}^{-1}$ )
- $\lambda p$  = Wavelength of electromagnetic radiation oscillating at the plasma frequency of the electrons in the metal (m).

now

$$\lambda p^2 = \frac{m_e}{\mu_o n_e e^2} \quad (2.4.)$$

$m_e$  = effective mass of the electrons in the metal (Kg)

$e$  = electron charge ( $= 1.6 \times 10^{-19}\text{C}$ )

$\mu_o$  =  $4\pi \times 10^{-7} \text{Hm}^{-1}$

$n_e$  = electron density ( $\text{m}^{-3}$ )

In Table 2.1, the onset frequency of the anomalous region is listed for various metals of interest. Data used to construct this table was taken from reference 24.



Table 2.1

Temperature = 300K

Metal	$\tau$ $\times 10^{-14}$ s	$v$ $\times 10^6$ ms $^{-1}$	$\lambda_p$ $\times 10^{-8}$ m	$n_e$ $\times 10^{28}$ m $^{-3}$	$m_e$ $\times 10^{-31}$ Kg	$v_a$ GHz
Cu (Copper)	2.7	1.57	2.38	8.47	11.83	1855
Ag (Silver)	4.0	1.39	2.41	5.86	10.01	746
Au (Gold)	3.0	1.40	2.41	5.90	10.01	1747
Al (Aluminium)	6.5	2.30	1.75	18.1	12.74	43
Sn (Tin)	0.23	1.90	1.58	14.8	11.84	$9 \times 10^5$
Bi (Bismuth)	0.023	1.87	0.31	14.1	0.43	$3.6 \times 10^7$
Pb (Lead)	0.14	1.83	2.02	13.2	17.31	$7.1 \times 10^6$
Zn (Zinc)	0.49	1.83	1.29	13.2	7.10	$6.7 \times 10^4$

It can be seen that copper, tin, bismuth, lead, zinc and gold all exhibit classical behaviour at 891 GHz, the frequency of the HCN laser used in the investigations. However, silver and aluminium exhibit anomalous behaviour at this frequency. However, silver is still one of the best metals to use as it has the lowest resistance loss of all the metals, provided that the higher surface reactance is not detrimental to the antenna response. By calculating the surface impedance of the metals, it is possible to estimate the attenuation and phase velocity of the currents supported on antennas for 891 GHz. Hence, the feasibility of resonant antennas at such a high frequency can be deduced.

The surface impedance,  $Z_s$ , of a metal having a skin depth  $\delta$  is given by

$$Z_s = \omega \mu \delta \quad (2.5.)$$

$\omega$  = angular frequency =  $2\pi f$

$\mu$  = permeability of the metal

$\delta$  is complex and is given by

$$\delta = \delta' + j \delta'' \quad (2.6.)$$

in the classical regime

$$\delta' = \delta'' = \frac{1}{2} \delta_k \quad (2.7.)$$

for a classical conductor  $\delta_k$  is given by

$$\delta_k = \left( \frac{2}{\omega \mu \sigma} \right)^{\frac{1}{2}} \quad (2.8.)$$

$\sigma$  being the DC conductivity of the metal.

Therefore

$$Z_s = \sqrt{\frac{\omega\mu}{2\sigma}} + j \sqrt{\frac{\omega\mu}{2\sigma}} \quad (2.9.)$$

In the anomalous regime<sup>23</sup>

$$\delta^3 = \left\{ \frac{-2}{b} \right\} \left\{ \frac{v}{\omega_a} \right\} \lambda p^2 \quad (2.10.)$$

$\omega_a$  is the angular frequency of onset of the anomalous regime and is equal to  $2\pi\nu_a$  the constant  $b$  is dependent on whether electrons are scattered diffusely, in which case  $b \sim 7.3$ , or specularly, for which  $b \sim 10.3$ , from the metal surface.

also  $\delta'' = \sqrt{3} \delta'$  (2.11.)

from 2.11 the complex skin depth  $\delta$  in the anomalous region becomes

$$\delta = \left\{ \frac{1}{4b} \left( \frac{v}{\omega_a} \right) \lambda p^2 \right\}^{\frac{1}{3}} + j \sqrt{3} \left\{ \frac{1}{4b} \left( \frac{v}{\omega_a} \right) \lambda p^2 \right\}^{\frac{1}{3}} \quad (2.12.)$$

By employing equations and data in Table 2.1 it is possible to estimate the surface impedance of the metals listed. As the metals are not ferromagnetic the permeability of the metal,  $\mu$ , can be taken to be the free space value,  $\mu_0 = 4\pi \times 10^{-7} \text{ Hm}^{-1}$ . The value for the constant  $b$  was taken to be 8.8. The surface impedances at 891 GHz for the metals in Table 2.1 are listed along with their DC electrical conductivities,  $\sigma_{dc}$ , in Table 2.2.

Table 2.2.

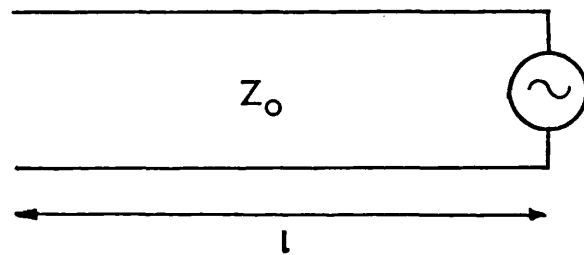
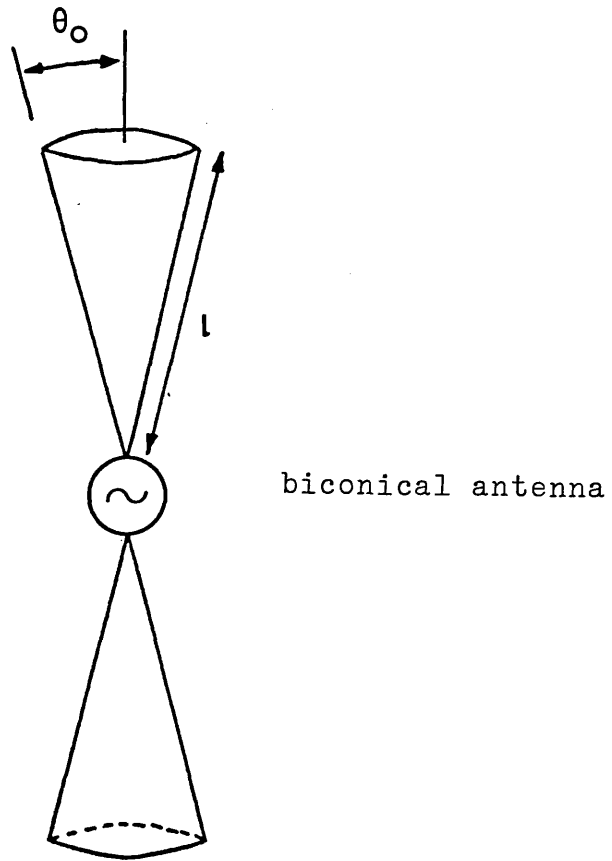
Surface impedances of various metals at 891 GHz with their DC electrical conductivities  $\sigma_{dc}^{2,3}$  Temperature = 300 K.

Metal	$\frac{\sigma_{dc}}{\Omega^{-1}m^{-1}}$	Surface Impedance $Z_s = R_s + j X_s (\Omega)$
Cu (Copper)	$6.4 \times 10^7$	$0.234 + j 0.234$
Ag (Silver)	$6.8 \times 10^7$	$0.121 + j 0.211$
Au (Gold)	$4.8 \times 10^7$	$0.270 + j 0.270$
Al (Aluminium)	$4.0 \times 10^7$	$0.438 + j 0.759$
Sn (Tin)	$8.6 \times 10^6$	$0.63 + j 0.63$
Bi (Bismuth)	$9.3 \times 10^5$	$1.94 + j 1.94$
Pb (Lead)	$5.2 \times 10^6$	$0.82 + j 0.82$
Zn (Zinc)	$1.8 \times 10^7$	$0.44 + j 0.44$

2.3. The effects of surface impedance on submillimetre antennas.

At wavelengths less than one millimetre conductor losses become prohibitive in metal waveguiding structures. However, this is not true for antennas, as losses tend to be lower on a large open structure, where fields are not enclosed by a large area of conductor as in a closed single mode waveguide. Antenna and waveguide problems become much more difficult when surface impedance is included. Whatever modes exist may no longer be orthogonal. Because of this, conventional techniques, such as separation of variables, are no longer applicable. Hence, the effects of finite surface impedance have not, so far, been precisely calculated in most cases.

The resistive component of the surface impedance of the antenna gives rise to attenuation of the surface currents. If the surface resistance is too high then the currents will be heavily damped, lowering the Q of the antenna and so producing poor antenna properties. The reactive component of the surface impedance reduces the velocity factor of the wave on the antenna. This reduction can destroy the main beam of the antenna pattern<sup>37</sup>. To estimate the



equivalent transmission line  
representation

Figure 2.1. Biconical antenna with its equivalent transmission line representation.

effects of finite surface impedance on antennas in the submillimetre region one can consider, for example, a dipole antenna operating at 891 GHz.

A cylindrical dipole may be approximated to a biconical antenna having a small half cone angle  $\theta_0$ . Figure 2.1 shows a biconical antenna with its equivalent transmission line representation. The propagation constant of the unperturbed line is  $\omega\sqrt{LC}$  where L and C are the inductance capacitance per unit length. The surface impedance appears as an additional series impedance per unit length,  $R + jX$ . The distributed resistance attenuates the wave and the attenuation constant  $\alpha$  is (to the first order)

$$\alpha = (R/2) \sqrt{C/L} \text{ nepers/unit length} \quad (2.13.)$$

The characteristic impedance of the line,  $Z_0$ , is equal to  $\sqrt{L/C}$  for the loss free case. For a biconical antenna the impedance of the equivalent transmission line is <sup>25</sup>

$$Z_0 = \frac{\eta \text{Ln cot}(\theta_0/2)}{\pi} \quad (2.14.)$$

where  $\eta$  is the characteristic impedance of free space ( $\eta = 377 \Omega$ ). The change in propagation constant due to the distributed reactance is  $\Delta\beta$

$$\Delta\beta = \frac{(X/2)}{Z_0} \quad (2.15.)$$

In some antenna configurations, the slowing of propagation increases directivity, as occurs in the Hansen-Woodyard condition<sup>26</sup>. By graphical methods these authors found that an increased directivity could be obtained if, for an ordinary end-fire array where the phase change between elements was  $-k_0d$ , the phase was changed to  $-k_0d \pi/n$ , where  $n$  is the number of elements,  $d$  is the element spacing, and  $k_0$  is  $2\pi/\lambda_0$ . This theory has been extended to include other types of antennas. However, the directivity is increased at the expense of antenna efficiency. However, in thin wire standing wave antennas, any slowing reduces the main beam amplitude. This can be understood by considering

the far field power density  $K$  of a dipole antenna of halflength  $L$  carrying a current with propagation constant  $\beta$ . The current distribution has a sinusoidal variation with  $Z$  of the form<sup>27</sup>

$$\begin{aligned} I &= I_m \sin \beta (L - Z) \quad Z \geq 0 \\ I &= I_m \sin \beta (L + Z) \quad Z < 0 \end{aligned} \quad (2.16.)$$

for the above case

$$K(\beta, \theta) = 120 k_o^2 \beta^2 I_m^2 \left[ \frac{\sin^2 [L(\beta + k_o \cos \theta)] \sin^2 [L(\beta - k_o \cos \theta)]}{(\beta^2 - k_o^2 \cos^2 \theta)^2} \right] \sin^2 \theta \quad (2.17.)$$

$k_o$  is the free space propagation constant. Figure 2.2 shows the geometry of the situation.

We find the effect of changing the phase velocity by evaluating the derivative of maximum power density with respect to  $\beta$ .

$$\left. \frac{dK(\beta, \theta)}{d\beta} \right|_{\theta_{\max}} = \frac{\partial K}{\partial \beta} + \frac{\partial K}{\partial \theta} \frac{d\theta_{\max}}{d\beta} \quad (2.18.)$$

At a maximum  $\delta K / \delta \theta = 0$ . Using this fact and equations 2.17 and 2.18 it can be shown (see Appendix 1) that

$$\frac{dK}{d\beta} = \frac{2K}{\beta} - \frac{2K \cos \theta}{k_o \sin^2 \theta} - \frac{4K (\beta - k_o \cos \theta)}{(\beta^2 - k_o^2 \cos^2 \theta)} \quad (2.19.)$$

this gives the relation

$$\frac{\delta K}{K} = \frac{2\delta\beta}{\beta} - \frac{\delta\beta}{k_o} \left\{ \frac{2 \cos \theta}{\sin^2 \theta} \right\} - \frac{4\delta\beta (\beta - k_o \cos \theta)}{(\beta^2 - k_o^2 \cos^2 \theta)} \quad (2.20.)$$

according to which the decrease in power density is proportional to the increase in propagation constant.

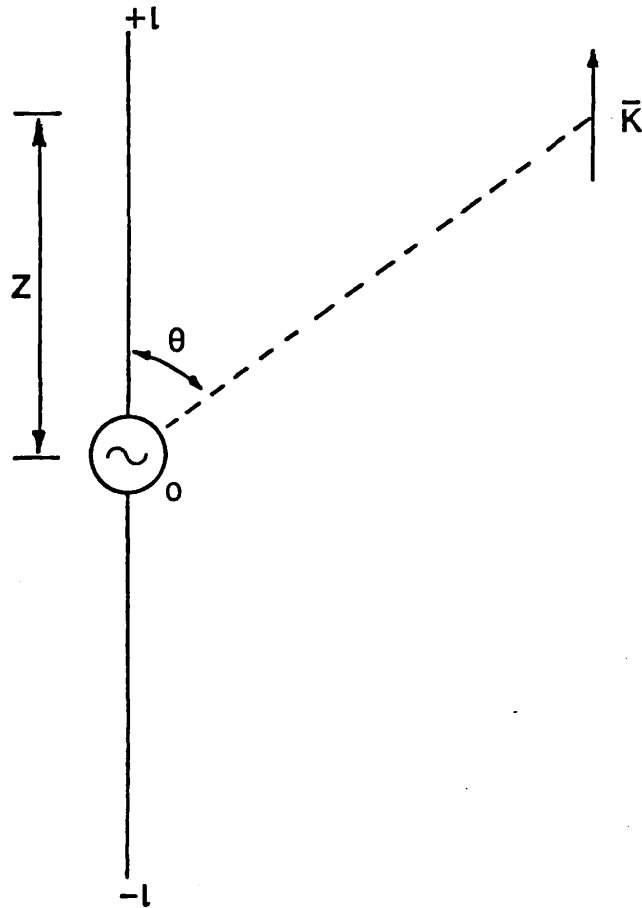


Figure 2.2. Geometry of a dipole antenna.

This does not conflict with the well known Hansen-Woodyard result which neglects the square of the element factor, i.e.  $\sin^2\theta$ . For example, the radiation pattern for a halfwave dipole has its maximum value at  $\theta = 90^\circ$ . Hence from equation 2.19, putting  $\theta = 90^\circ$ ,

$$\frac{\delta K}{K} = \frac{-2\delta\beta}{\beta} \quad (2.21)$$

Therefore a 1% increase in  $\delta\beta$  will only result in a 2% decrease in the maximum power density although the beam-width will be reduced by 5%.

Carrying out the same analysis for a thin wire travelling wave antenna leads to the relation<sup>37</sup>

$$\frac{\delta K}{K} = \frac{\delta\beta}{k_0} \left( - \frac{2 \cos \theta}{\sin \theta} \right) \quad (2.22.)$$

The power density is dramatically reduced if  $\theta$  is small which is generally true for the main lobe of a travelling wave antenna. For example, the pattern for a  $10 \lambda$  antenna has its peak at  $17^\circ$ <sup>37</sup>. In this case a 1% increase in  $\beta$  causes the beam power to reduce by 22%. Hence, a dipole antenna has better submillimetre characteristics than the long wire antenna as a substantial reduction in propagation constant is necessary to destroy the main beam of a resonant dipole antenna.

For a halfwave planar antenna of width,  $W$ , equal to  $\lambda/30$  the characteristic impedance of the equivalent biconical transmission line is from equation 2.14 found to be  $\approx 325 \Omega$  (corresponding to  $\theta_0 = 3.81^\circ$ ).

For a cylindrical antenna of radius  $a$ , the additional impedance per unit length,  $R + jX$ , arising from the surface impedance of the metal,  $R_s + j X_s$ , is given by

$$R + jX = (R_s + j X_s) / 2\pi a \quad (2.23.)$$

The equivalent radius of a planar antenna of width  $W$  is  $W/4$ . An order of magnitude assessment suggests that, for aluminium, using the surface impedance from Table 2.2 and equations 2.13, 2.15 and 2.23,  $\alpha = 0.013$  nepers/ $\lambda_0$  (0.11 dB/ $\lambda_0$ ) and  $\Delta\beta = 0.022/\lambda_0$  ( $\sim 2\%$ ). Therefore, even



if a metal with a high surface impedance like aluminium is used a resonant antenna is still feasible at 891 GHz. The radiation lobe of the dipole would only be reduced by 7%, due to the surface resistance and reactance effects, from the loss free value. The surface currents are low enough to propagate without significant loss.

#### 2.4. Substrate effects on submillimetre antennas.

It is important to ascertain whether a horizontal dipole on the surface of a dielectric can still act as an effective antenna. Mizuno et al<sup>28</sup> have shown that short, thin dipoles on thin dielectrics are effective but have rather low gains. However, the infrared antennas reported to date<sup>29-31</sup> have been long dipoles on thick substrates. Several researchers have studied how waves propagate along conductors on dielectric half spaces<sup>32-34</sup>, but the problem has not been completely solved. It has already been demonstrated<sup>32,33</sup> that, for a single wire, there is a propagation mode with a phase velocity of  $V = C(\sqrt{(\epsilon_r + 1)/2})^{-1}$ , where C is the velocity of light and  $\epsilon_r$  the dielectric constant of the halfspace. Because the wave propagates faster than the speed of light in the dielectric, it will tend to radiate into the dielectric, as has recently been demonstrated by Rees et al<sup>35</sup>. This loss can be decreased by reducing the wire thickness. Also the radiation patterns of antennas on thick dielectric substrates are greatly distorted as a result of preferential radiation into the dielectric as has already been demonstrated<sup>35</sup>.

One needs to know (a) how narrow a conductor must be to support a propagating mode and whether a high gain pattern will result, and (b) how thin the substrate must be to avoid modes being set up in the dielectric with their subsequent loss.

There will exist a certain amount of coupling between electro magnetic radiation incident on the antenna structure and the TE and TM modes in the dielectric substrate supporting the antenna. Power reradiated by the antenna will only excite the TE modes in the

dielectric substrate as the electric field is directed in the plane of substrate. The zero order TE and TM modes have no cut off frequency, but for the higher order modes there exists a critical thickness of dielectric below which a given mode cannot propagate. The critical thickness,  $d$ , of the  $n^{\text{th}}$  mode is the same for both TE and TM modes and is given by <sup>36</sup>

$$\frac{2d}{\lambda} = \frac{n}{2\sqrt{\epsilon_r - 1}} \quad \epsilon_r > 1 \quad (2.24.)$$

$\epsilon_r$  is the dielectric constant of the substrate. Figures 2.3 and 2.4 show the velocity ratio  $C/V$  for an infinite sheet of dielectric of thickness  $2d$  for TE and TM modes respectively. The velocity of light in vacuo is  $C$ ,  $\lambda$  is the wavelength, and  $V$  is the velocity of radiation in the dielectric.

It is evident that by keeping the substrate thin and the dielectric constant low, it is possible to reduce substrate loss as

- (a) only zero order TE or TM modes will be excited
- (b) as  $V$  is nearly equal to  $C$  there will be less radiation directed into the dielectric

As stated previously, the width of the planar antenna is also important in keeping losses low. By modelling dipole antenna at X band for the far infrared<sup>37</sup>, it has been demonstrated that when conductor widths are too large the resulting antenna have only weakly resonant properties. In fact, the resulting patterns resemble slab diffraction rather than antenna patterns. A useful criterion to adopt is, that the antenna width must be less than  $\lambda/30$  for resonant currents to propagate. However, to reduce conductor loss, it is necessary to increase the width of the antenna with increasing frequency.

For a dipole antenna of width  $W$  the attenuation,  $\alpha$ , per free space wavelength  $\lambda_0$  of propagating currents is

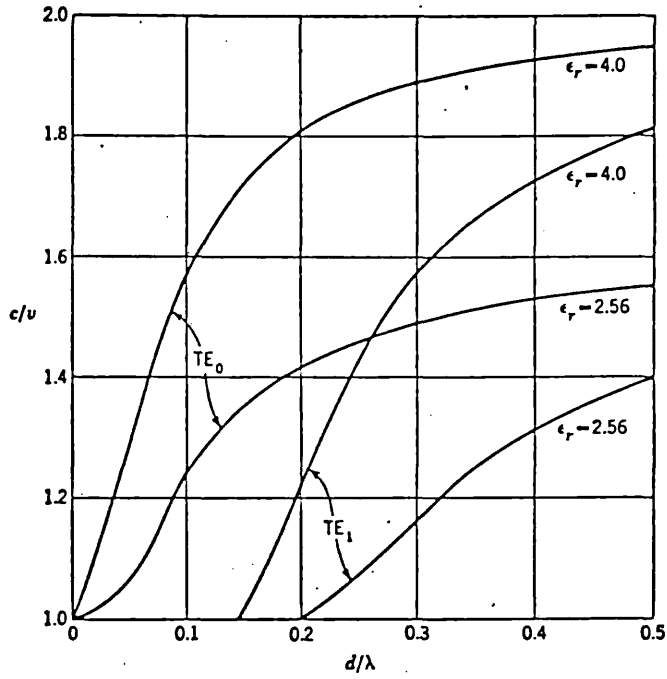


Figure 2.3. Velocity ratio  $C/V$  for an infinite sheet of thickness  $2d$  for  $TE_0$  and  $TE_1$  modes<sup>36</sup>.

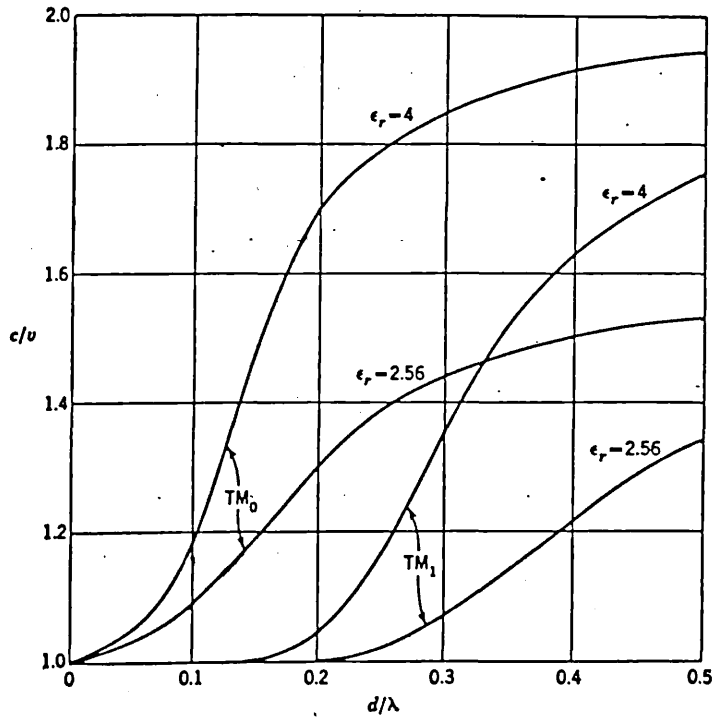


Figure 2.4. Velocity ratio  $C/V$  for an infinite sheet of thickness  $2d$  for  $TM_0$  and  $TM_1$  modes<sup>36</sup>.

given approximately by

$$\alpha = \frac{R_s \lambda_0}{\pi W Z_0} \quad \text{nepers} / \lambda_0 \quad (2.25.)$$

$Z_0$  is the characteristic impedance of the antenna, and  $R_s$  is the surface impedance. For a dipole antenna of width  $\lambda/30$  the characteristic impedance,  $Z_0$ , is  $\approx 330 \Omega$ . For a good conductor, say silver,  $R_s \approx 2.4 \times 10^{-7} \sqrt{f}$ . Therefore, by re-arranging equation 2.25 we can obtain an expression for the cut off frequency above which a dipole antenna will no longer be effective in terms of the maximum tolerable current attenuation  $\alpha_c$ .

$$f_c = \left\{ \frac{330 \pi \alpha_c}{2.4 \times 10^{-7} \times 30} \right\}^2 \quad (2.26.)$$

It seems unlikely that resonant currents would propagate if  $\alpha$  was greater than 0.05 nepers /  $\lambda_0$ , as this would correspond to a 30% reduction in the radiation lobe. This corresponds to a frequency of 51.8 THz for a dipole antenna having a silver conductor of width  $\lambda/30$ . It therefore seems unlikely that resonant dipole antennas would be effective at frequencies beyond 50 THz (or a wavelength  $< 6 \mu\text{m}$ ).

## CHAPTER THREE

### THEORETICAL SCATTERING PROPERTIES OF ANTENNAS AND ANTENNA ARRAYS

#### 3.1. Introduction

In Chapter 1 it was stated that, it is more straightforward to investigate submillimetre antennas from their scattering rather than their reception and transmission properties. This is because of various technical difficulties associated with the latter two techniques. Before commencing with a detailed theoretical analysis of the scattering of radiation by an antenna or antenna array, it is first necessary to establish the general inter-relationships that exist between the scattering, transmission and reception properties of antennas.

It is well known that the transmitting and receiving patterns for any antenna (or antenna plus connecting network) are similar. This is a consequence of the reciprocity theorem. The reradiation (scattering) pattern however, is usually different from the pattern which characterize reception and transmission<sup>38</sup>. This follows from the fact that the current distribution on an array is different in the receiving and transmitting cases.

To see this, consider the array and connecting network illustrated in Figure 3.1. We place in series with the load in Figure 3.1 (b) a voltage source,  $E_1$ , of such magnitude that it just balances the open-circuit voltage from the network. In this case, the current through the load will be zero. The element currents, however, will clearly in general not be zero. They will, rather, adopt a current distribution, termed the idling current distribution, of a shape dependent on the incident field, the array and the connecting network. The array can now be brought back to its normal state if we add another voltage,  $E_2$ , in series with  $E_1$  to cancel it. However,

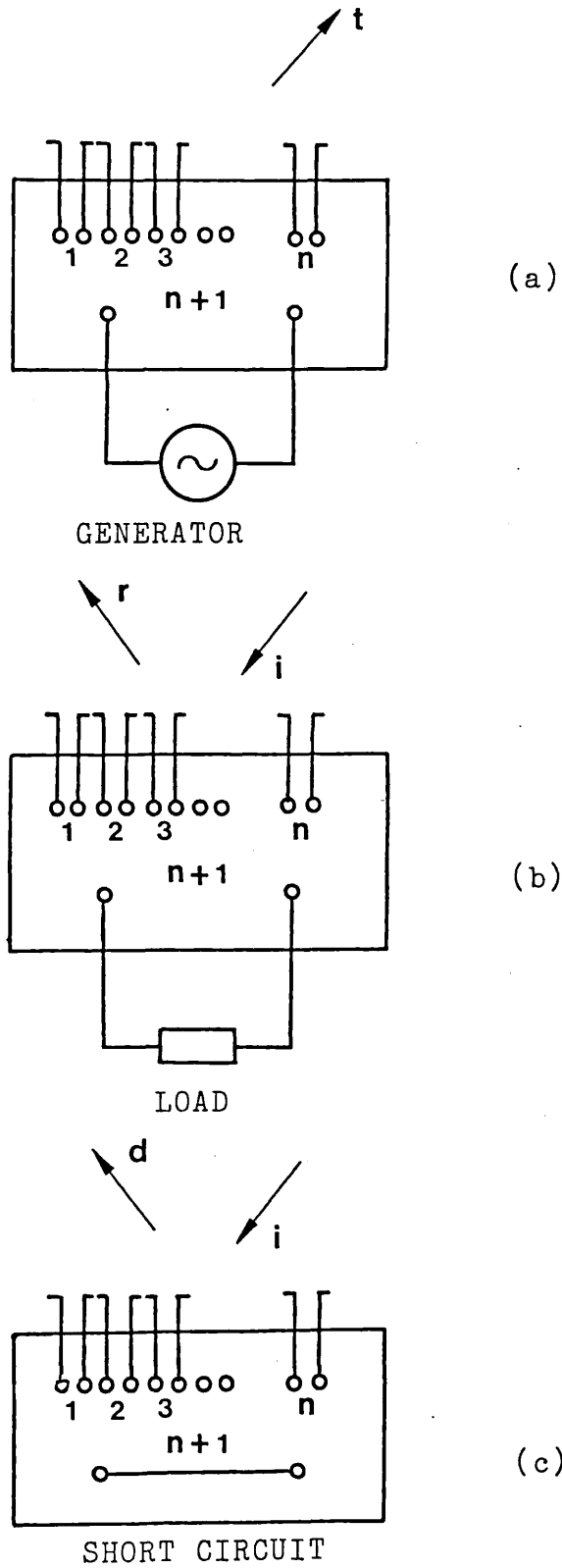


Figure 3.1. (a) Transmitting array  
(b) Receiving array, and  
(c) Diffracting array

$E_2$  will produce, on the array, a pure transmitting current distribution. Thus, the receiving current distribution on the array is formed by the superposition of the idling current distribution and the transmitting current distribution. The antenna current distribution determines the spatial field around the antenna. Only when the transmitting and idling currents have the same shape, which cannot be expected in general, will the scattering take place with the same polar diagram as in transmission and reception.

However, from the study of the scattering properties of antennas, detailed information about the standing current distribution can be obtained. Predications of the transmission and reception properties of the antennas can then be made. The important parameters for investigation are the total scattering cross section and the differential scattering cross section of the antennas. This chapter discusses the general case of Bistatic, backscattering and total scattering by multiply loaded scatterers. It is based on the analysis due to Harrington<sup>20</sup>, whose theory is applicable to reciprocal and non-reciprocal media, active and passive loads, near-field and far-field scattering and an arbitrary number of scatterers.

### 3.2 Bistatic Scattering

Consider the case of Bistatic scattering by a singly loaded object. The geometry is illustrated in Figure 3.2. Terminals  $t$  represent those of the transmitting antenna to which a generator is connected so as to energise the scatterer. Terminals  $r$  represent those of the receiving antenna, used to investigate the scattered field. An arbitrary load impedance,  $Z_L$ , is connected to the scattered terminals,  $s$ . As this is a linear three port system, the matrix expression relating terminal voltages and currents may be written as

$$\begin{bmatrix} V_r \\ V_t \\ V_s \end{bmatrix} = \begin{bmatrix} Z_{rr} & Z_{rt} & Z_{rs} \\ Z_{tr} & Z_{tt} & Z_{ts} \\ Z_{sr} & Z_{st} & Z_{ss} \end{bmatrix} \begin{bmatrix} I_r \\ I_t \\ I_s \end{bmatrix} \quad (3.1.)$$

When the scatterer and  $Z_L$  are absent, we have a two port system, for which

$$\begin{bmatrix} V_r^{\circ} \\ V_t^{\circ} \end{bmatrix} = \begin{bmatrix} Z_{rr}^{\circ} & Z_{rt}^{\circ} \\ Z_{tr}^{\circ} & Z_{tt}^{\circ} \end{bmatrix} \begin{bmatrix} I_r \\ I_t \end{bmatrix} \quad (3.2.)$$

where the superscript  $^{\circ}$  denotes an absent scatterer. Subtracting equation 3.2 from equation 3.1 we have

$$\begin{bmatrix} \Delta V_r \\ \Delta V_t \\ V_s \end{bmatrix} = \begin{bmatrix} \Delta Z_{rr} & \Delta Z_{rt} & Z_{rs} \\ \Delta Z_{tr} & \Delta Z_{tt} & Z_{ts} \\ Z_{sr} & Z_{st} & Z_{ss} \end{bmatrix} \begin{bmatrix} I_r \\ I_t \\ I_s \end{bmatrix} \quad (3.3.)$$

$$\text{where } \Delta V_i = V_i - V_i^{\circ} \quad (3.4.)$$

are the voltage changes at r and t produced by the introduction of the scatterer, and

$$\Delta Z_{ij} = Z_{ij} - Z_{ij}^{\circ} \quad (3.5.)$$

are the resulting impedance changes. At the terminals of the scatterer there exists the constraint

$$V_s = -Z_L I_s \quad (3.6.)$$

To obtain the open circuit voltage at r,  $I_r$  is taken to be zero

$$I_r = 0 \quad (3.7.)$$

Therefore, from equations 3.6, 3.7 and 3.3

$$\begin{bmatrix} \Delta V_r \\ \Delta V_t \\ 0 \end{bmatrix} = \begin{bmatrix} \Delta Z_{rr} & \Delta Z_{rt} & Z_{rs} \\ \Delta Z_{tr} & \Delta Z_{tt} & Z_{ts} \\ Z_{sr} & Z_{st} & Z_{ss} + Z_L \end{bmatrix} \begin{bmatrix} 0 \\ I_t \\ I_s \end{bmatrix} \quad (3.8.)$$

Solving equation 3.8 for  $\Delta V_r$  gives

$$\Delta V_r = \left\{ \Delta Z_{rt} - \frac{Z_{rs} Z_{st}}{Z_{ss} + Z_L} \right\} I_t \quad (3.9.)$$



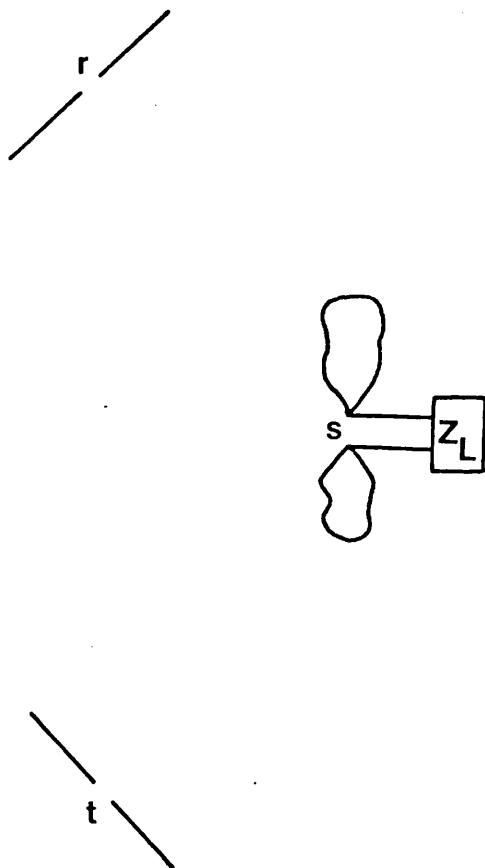


Figure 3.2. Bistatic scattering.

The solution for  $\Delta V_t$  is the equation for backscattering. Equation 3.9 gives only that component of voltage at the receiver due to the introduction of the loaded scatterer. In addition, there may be a component of voltage at the receiver due to direct coupling from the transmitter. The first term in equation 3.9 is due to scattering by the open voltage scatterer ( $Z_L = \infty$ ). The second term shows the effect of varying  $Z_L$ .  $\Delta Z_{rt}$ ,  $Z_{rs}$ ,  $Z_{st}$  and  $Z_{ss}$  may be calculated by any convenient method. The variational method due to Hu and given in 3.6 is a useful one. In 3.5 it will be shown how equation 3.9 may be used to calculate total and backscattering cross sections of antennas.

### 3.3. Multiply loaded scatterers

Figure 3.3 represents a scatterer with N terminal pairs, or ports, to which an N port linear impedance network is connected. It is convenient to use symbolic matrix notation to keep the equations compact, and to emphasise the similarity to the one port case. We therefore define impedance matrix of the scatterer

$$\begin{bmatrix} Z_{ss} \end{bmatrix} = \begin{bmatrix} Z_{11} & Z_{12} & \dots & Z_{1N} \\ Z_{21} & Z_{22} & \dots & Z_{2N} \\ \dots & \dots & \dots & \dots \\ Z_{N1} & Z_{N2} & \dots & Z_{NN} \end{bmatrix} \quad (3.10.)$$

The scatterer voltage and current matrices as

$$\begin{bmatrix} V_s \end{bmatrix} = \begin{bmatrix} V_1 \\ V_2 \\ \vdots \\ V_N \end{bmatrix} \quad \begin{bmatrix} I_s \end{bmatrix} = \begin{bmatrix} I_1 \\ I_2 \\ \vdots \\ I_N \end{bmatrix} \quad (3.11.)$$

and the receiver-scatterer and transmitter-scatterer impedance matrices as

$$\begin{bmatrix} Z_{rs} \end{bmatrix} = \begin{bmatrix} Z_{r1} & Z_{r2} & \dots & Z_{rN} \end{bmatrix}$$

$$\begin{bmatrix} Z_{ts} \end{bmatrix} = \begin{bmatrix} Z_{t1} & Z_{t2} & \dots & Z_{tN} \end{bmatrix}$$

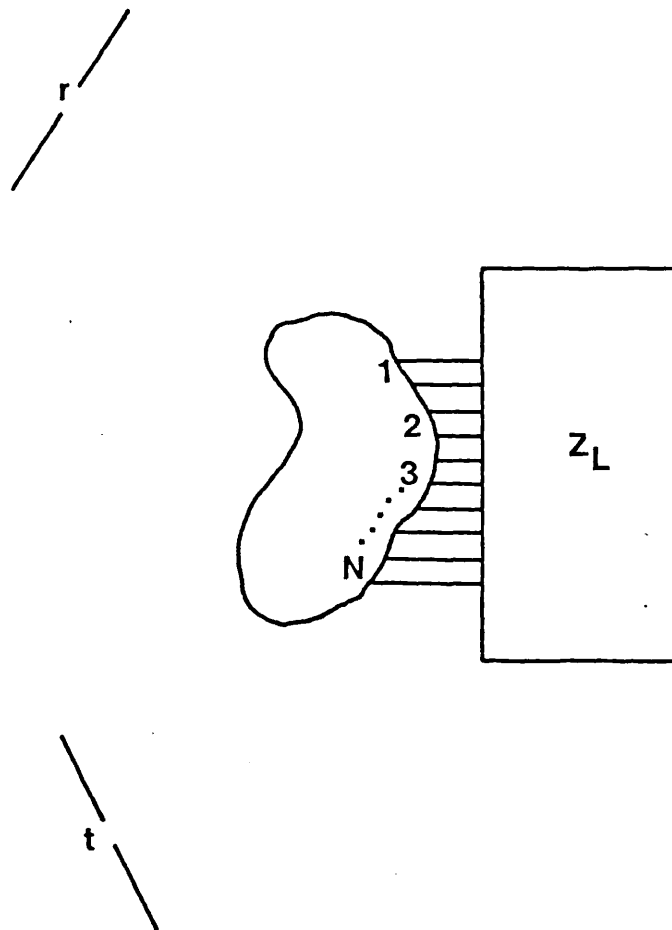


Figure 3.3. Multiply loaded scatterer.

$$\begin{bmatrix} Z_{sr} \end{bmatrix} = \begin{bmatrix} Z_{1r} \\ Z_{2r} \\ \vdots \\ Z_{Nr} \end{bmatrix} \quad \begin{bmatrix} Z_{st} \end{bmatrix} = \begin{bmatrix} Z_{1t} \\ Z_{2t} \\ \vdots \\ Z_{Nt} \end{bmatrix} \quad (3.12.)$$

for the case of the multiply loaded scatterer, the equivalent equation of 3.1 is

$$\begin{bmatrix} V_r \\ V_t \\ [V_s] \end{bmatrix} = \begin{bmatrix} Z_{rr} & Z_{rt} & [Z_{rs}] \\ Z_{tr} & Z_{tt} & [Z_{ts}] \\ [Z_{sr}] & [Z_{st}] & [Z_{ss}] \end{bmatrix} \begin{bmatrix} I_r \\ I_t \\ [I_s] \end{bmatrix} \quad (3.13.)$$

Equations 3.2 to 3.5 remain the same in form. The scatterer load is described by an N by N matrix  $[Z_L]$ .

The constraints at the scatterer terminals are

$$[V_s] = - [Z_L] [I_s] \quad (3.14.)$$

restricting consideration to simple Bistatic scattering, the equivalent of equation (3.7) is

$$\begin{bmatrix} \Delta V_r \\ \Delta V_t \\ 0 \end{bmatrix} = \begin{bmatrix} \Delta Z_{rr} & \Delta Z_{rt} & [Z_{rs}] \\ \Delta Z_{tr} & \Delta Z_{tt} & [Z_{ts}] \\ [Z_{sr}] & [Z_{st}] & [Z_{ss} + Z_L] \end{bmatrix} \begin{bmatrix} 0 \\ I_t \\ [I_s] \end{bmatrix} \quad (3.15.)$$

Solving equation 3.15 for  $\Delta V_r$  gives

$$\Delta V_r = \left\{ \Delta Z_{rt} - [Z_{rs}] [Z_{ss} + Z_L]^{-1} [Z_{st}] \right\} I_t \quad (3.16.)$$

equation 3.16 has the same form as equation 3.9 except for matrices replacing the single elements in equation 3.9.

### 3.4. Planewave Scattering

When the transmitter and receiver are far from the scatterer, the special case of planewave scattering is obtained. Numerical evaluation of the impedance parameters is more simple because proximity effects are eliminated. For example,  $Z_{ss}$  depends only on the scatterers geometry, and not on the transmitter and receiver.

In general, the incident wave can be expressed in terms of two field components, denoted  $E_1^i$  and  $E_2^i$ . These are transverse to the radius vector and taken to be orthogonal. The scattered wave in any particular direction can also be expressed in terms of two orthogonal components, say  $E_1^s$  and  $E_2^s$ . The scattered components vary as  $\exp(-j kr_r)/r_r$ , where  $r_r$  is the distance to the receiver. To obtain a representation independent of  $r_r$ , we define

$$\begin{bmatrix} E_1^s r_r e^{j kr_r} \\ E_2^s r_r e^{j kr_r} \end{bmatrix} = \begin{bmatrix} S_{11} & S_{12} \\ S_{21} & S_{22} \end{bmatrix} \begin{bmatrix} E_1^i \\ E_2^i \end{bmatrix} \quad (3.17.)$$

These S parameters are more convenient than the commonly defined cross section parameters as they contain phase information. They are related to the cross-section parameters as follows.

The bistatic cross section,  $\sigma_{BI}$ , is defined as the area for which the incident wave contains sufficient power to produce, by omnidirectional radiation, the same wave intensity in the direction of the receiver. This is expressed as

$$\sigma_{BI} = 4 \pi r_r^2 \left| \frac{E^s}{E^i} \right|^2 \quad (3.18.)$$

where  $|E^i|^2 = |E_1^i|^2 + |E_2^i|^2$ , and similarly for  $|E^s|^2$ . As defined,  $\sigma_{BI}$  is a function of the polarisation of the incident wave. Let  $a$  be a complex quantity which specifies the polarisation

according to

$$a = \frac{E_2^i}{E_1^i} \quad (3.19.)$$

From equation 3.17 and 3.18

$$\sigma_{BI} = \frac{4 \pi |S_{11} + a S_{12}|^2 + |S_{21} + a S_{22}|^2}{1 + |a|^2} \quad (3.20.)$$

When the transmitter and receiver coincide, the special case of backscattering is obtained and  $\sigma_{BI}$  becomes  $\sigma_{BS}$ , the backscattering cross section. The total scattering cross section,  $\sigma_s$ , which is defined as the ratio of the total power scattered by the antenna to the incident power density, can be obtained from  $\sigma_{BS}$ . This will be discussed in 3.5.

To show how the  $S_{mn}$  parameters are related to the Z parameters, let terminals  $t$  be defined as a pair of points in free space separated by a distance  $L_t$  in the direction of  $E_n^i$ . A current element  $I_t$  applied across  $L_t$  produces at the origin, which is chosen on the scatterer, a field,

$$E_n^i = \frac{\eta I_t L_t e^{-j k r_t}}{2_j \lambda r_t} \quad (3.21.)$$

where  $\eta$  is the intrinsic impedance of free space ( $\approx 377 \Omega$ ),  $\lambda$  is the wavelength and  $r_t$  is the distance to the transmitter. Let terminals  $r$  also define a pair of points in free space separated by  $L_r$  in the direction  $E_m^s$ . The voltage change across  $L_r$  due to the scatterer is

$$\Delta V_r = E_m^s L_r \quad (3.22.)$$

Hence, as defined by equation 3.17, the  $S$  parameters are given by

$$S_{mn} = r_r e^{jk r_r} \frac{E_m^s}{E_n^i}$$

$$= \frac{2j\lambda}{\eta L_t L_r} r_r r_t e^{jk(r_r + r_t)} \frac{\Delta V_r}{I_t} \quad (3.23.)$$

Defining the far zone parameters

$$\Delta Z_{rt}' = \left\{ \begin{array}{c} r_r \\ \frac{L_r}{L_r} \end{array} e^{jkr_r} \right\} \left\{ \begin{array}{c} r_t \\ \frac{L_t}{L_t} \end{array} e^{jkr_t} \right\} \Delta Z_{rt} \quad (3.24.)$$

$$Z_{rs}' = \left\{ \begin{array}{c} r_r \\ \frac{L_r}{L_r} \end{array} e^{jkr_r} \right\} Z_{rs} \quad (3.25.)$$

$$Z_{st}' = \left\{ \begin{array}{c} r_t \\ \frac{L_t}{L_t} \end{array} e^{jkr_t} \right\} Z_{st} \quad (3.26.)$$

Equation 3.9 can be used to write equation 3.23 as

$$S_{mn} = \frac{2j\lambda}{\eta} \left\{ \Delta Z_{rt}' - \frac{Z_{rs}' Z_{st}'}{Z_{ss} + Z_L} \right\} \quad (3.27.)$$

Each  $Z'$  parameter depends on  $m$  and  $n$ , i.e. upon the polarisation of the incident wave. Hence, by establishing equations 3.17 and 3.27, the characteristics of the scatterer are defined in terms of  $Z'$  parameters, which are independent of the particular transmitter and receiver and the distances to them. The equivalent expression to equation 3.27 for a multiply loaded scatterer is

$$S_{mn} = \frac{2j\lambda}{\eta} \left\{ \Delta Z_{rt}' - [Z_{rs}'] [Z_{ss} + Z_L]^{-1} [Z_{st}'] \right\} \quad (3.28.)$$

It is normal to define and measure bistatic cross sections with the transmitter, receiver and scatterer polarisations adjusted to maximize the cross section. Choosing  $E_1^i$  of equation 3.19 so that  $I_s$  is a maximum when  $a = 0$ , then  $E^i$  is  $E_1^i$ . Also  $E_1^s$  is chosen so that it is the entire scattered field hence  $S_{21} = 0$ . From equation 3.20

and 3.27

$$\sigma_{BI} = \frac{16 \pi \lambda^2}{\eta^2} \left| \Delta Z_{rt}' - \frac{Z_{rs}' Z_{st}'}{Z_{ss}' + Z_L} \right|^2 \quad (3.29.)$$

For a multiply loaded scatterer

$$\sigma_{BI} = \frac{16 \pi \lambda^2}{\eta^2} \left| \Delta Z_{rt}' - \begin{bmatrix} Z_{rs}' \end{bmatrix} \begin{bmatrix} Z_{ss}' + Z_L \end{bmatrix}^{-1} \begin{bmatrix} Z_{st}' \end{bmatrix} \right|^2 \quad (3.30.)$$

The backscattering cross section,  $\sigma_{BS}$ , is equal to the bistatic cross section when the transmitter and receiver are coincident. Equations 3.29 and 3.30 give the equations for the backscattering case by replacing the subscript r by t.

### 3.5. The relationship between scattering and antenna parameters.

An antenna structure is a type of electromagnetic scatterer. The  $Z'$  parameters of planewave scattering are simply related to commonly defined antenna parameters. In this section these relations will be derived for a one port antenna and then generalised to a multiport scatterer. In antenna theory, a one port antenna (one feedpoint or loadpoint) is characterised by an input impedance (equal to  $Z_{ss}$  in scatterer theory), a transmitting gain

$$\begin{aligned} G(\theta, \phi) &= \frac{\text{radiation intensity in } (\theta, \phi) \text{ direction}}{\text{total radiated power}} \\ &= \frac{4 \pi r^2 |E^r|^2 / \eta}{|I_s|^2 R_{ss}} \end{aligned} \quad (3.31.)$$

where  $E^r$  is the radiation field at a distance  $r$  produced by current  $I_s$  at the input terminals, and a receiving aperture

$$\begin{aligned} A(\theta, \phi) &= \frac{\text{power delivered to a matched load}}{\text{power density of incident wave}} \\ &= \frac{|I_s|^2 R_{ss}}{|E^i|^2 / \eta} \end{aligned} \quad (3.32.)$$



where  $E^i$  is the incident plane wave. The polarisation is chosen to produce the maximum current  $I_s$  in the conjugate matched load,  $Z_L = Z_{ss}^*$  (astrisk denotes conjugate). If all media are reciprocal, then<sup>39</sup>

$$A(\theta, \phi) = \frac{\lambda^2}{4\pi} G(\theta, \phi) \quad (3.33.)$$

$G$  and  $A$  are related to the  $Z'$  parameters. A current source  $I_s$  applied to the scatterer terminals produces a field at the receiver terminals

$$E_r = \frac{V_r}{L_r} = \frac{Z_{rs} I_s}{L_r} \quad (3.34.)$$

Substituting into equation 3.31 gives

$$G(\theta_r, \phi_r) = \frac{4\pi r_r^2 |Z_{rs} I_s / I_r|^2}{|I_s|^2 R_{ss} \eta} \quad (3.35.)$$

where the subscripts  $r$  on  $(r, \theta, \phi)$  denote specialisation to the receiver co-ordinates. From equation 3.25 we obtain

$$G(\theta_r, \phi_r) = \frac{4\pi}{\eta R_{ss}} |Z_{rs}'|^2 \quad (3.36.)$$

which gives a relationship between  $G$  and  $Z_{rs}'$ . For

the receiving case, a current source  $I_t$  applied across the transmitter terminals  $L_t$  produces a field at the scatterer. The current produced in a conjugate matched load ( $Z_L = Z_{ss}^*$ ) at the scatterer terminals is

$$I_s = \frac{V_s \hat{\theta}}{Z_{ss} + Z_L} = \frac{I_t Z_{st}}{2 R_{ss}} \quad (3.37.)$$

From equation 3.37, 3.33 and 3.21

$$A(\theta_t, \phi_t) = \left| \frac{I_t Z_{st}}{2 R_{ss}} \right|^2 R_{ss} \left| \frac{2\lambda r_t}{I_t L_t} \right|^2 \eta \quad (3.38.)$$

where subscripts  $t$  on  $(r, \theta, \phi)$  denote specialisation to the transmitter co-ordinates. From equation 3.26 and 3.38

$$A(\theta_t, \phi_t) = \frac{\lambda^2}{\eta R_{ss}} |Z_{st}'|^2 \quad (3.39.)$$

which gives the relationship between A and  $Z_{st}'$ .

Provided that  $\Delta Z_{rt}'$  is small compared with the second term in 3.29, which, in general, it is, except for antennas with large open circuit scattering cross sections, then, from equations 3.29, 3.36 and 3.39

$$\sigma_{BI} \approx 4A (\theta_t, \phi_t) G (\theta_r, \phi_r) \left| \frac{R_{ss}}{Z_{ss} + Z_L} \right|^2 \quad (3.40.)$$

When all media are reciprocal, equation 3.33 may be used in equation 3.40 to write

$$\sigma_{BI} = \frac{\lambda^2}{\pi} G (\theta_t, \phi_t) G (\theta_r, \phi_r) \left| \frac{R_{ss}}{Z_{ss} + Z_L} \right|^2 \quad (3.41.)$$

For the backscattering case, in which the receiver and transmitter coincide 3.41 becomes

$$\sigma_{BS} \approx \frac{\lambda^2}{\pi} G^2 (\theta, \phi) \left| \frac{R_{ss}}{Z_{ss} + Z_L} \right|^2 \quad (3.42.)$$

The total scattering cross section,  $\sigma_s$ , an antenna is defined as

$$\sigma_s = \frac{\text{total power scattered by the antenna}}{\text{power density of incident wave}}$$

provided that the open circuited scattering cross section of an antenna is not large then, the power dissipated in the radiation resistance is generally taken to be equal to the reradiated (scattered) power.<sup>40</sup> Hence, for an antenna at the origin illuminated by a transmitter at co-ordinates  $(r_t, \theta_t, \phi_t)$ .

$$\sigma_s (\theta_t, \phi_t) = \frac{|I_s|^2 R_{ss}}{|E^i|^2 / \eta} \quad (3.43.)$$

As a conjugate matched load cannot be assumed then

$$\begin{aligned} I_s &= \frac{V_s^o}{Z_{ss} + Z_L} \\ &= \frac{I_t Z_{st}}{Z_{ss} + Z_L} \end{aligned} \quad (3.44.)$$

Substituting equations 3.21 and 3.44 into 3.43 and simplifying with equation 3.26

$$\sigma_s (\theta_t, \phi_t) = \frac{\lambda^2}{\eta} \frac{4 R_{ss}}{(Z_{ss} + Z_L)^2} |Z_{st}'|^2 \quad (3.45.)$$

Equation 3.29 for the backscattering case is

$$\sigma_{BS} (\theta_t, \phi_t) = \frac{16 \pi \lambda^2}{\eta^2} \left| \Delta Z_{tt}' - \frac{Z_{ts}' Z_{st}'}{Z_{ss} + Z_L} \right|^2 \quad (3.46.)$$

If all media are reciprocal,  $Z_{ts}' = Z_{st}'$ , so by combining equations 3.45 and 3.46

$$\frac{\sigma_{BS} (\theta_t, \phi_t)}{\lambda^2} = \frac{16 \pi}{\eta^2} \left\{ \frac{\sigma_s}{\lambda^2} \right\} \eta \left( \frac{Z_{ss} + Z_L}{4 R_{ss}} \right)^2 \quad (3.47.)$$

assuming  $\Delta Z_{tt}'$  is negligible compared with the second term in equation 3.46, which it will be, provided that the open circuit scattering cross section of the antenna is small. Re-arranging equation 3.47 to obtain the total scattering cross-section in terms of the backscattering cross section.

$$\frac{\sigma_s (\theta_t, \phi_t)}{\lambda^2} = \left\{ \frac{\sigma_{BS} (\theta_t, \phi_t)}{\lambda^2} \frac{1}{\pi} \right\}^{\frac{1}{2}} \left| \frac{R_{ss}}{Z_{ss} + Z_L} \right| \quad (3.48.)$$

In the case of the scattering antenna terminated with a conjugate matched load ( $Z_L = Z_{ss}^*$ ) we obtain

$$\frac{\sigma_s (\theta_t, \phi_t)}{\lambda^2} = \left\{ \frac{\sigma_{BS} (\theta_t, \phi_t)}{4 \pi \lambda^2} \right\}^{\frac{1}{2}} \quad (3.49.)$$

If  $Z_L = 0$  then

$$\frac{\sigma_s (\theta_t, \phi_t)}{\lambda^2} = \left\{ \frac{\sigma_{BS} (\theta_t, \phi_t)}{\pi \lambda^2} \right\}^{\frac{1}{2}} \left| \frac{R_{ss}}{Z_{ss}} \right| \quad (3.50.)$$

For multiply loaded scatterers, the elements of the  $[Z_{rs}']$  matrix may be related to the antenna gain by equation 3.36, where  $G$  is now the gain obtained by feeding only one port of the antenna and leaving all other ports open circuited. Similarly, the elements of the  $[Z_{st}']$  matrix are each related to the receiving aperture by equation 3.39, obtained by matching only one port and leaving all others open circuited. For a multiply loaded scatterer, the backscattering cross section is obtained from equation 3.30 with the transmitter and receiver coincident.

$$\sigma_{BS}(\theta_t, \phi_t) = \frac{16\pi\lambda^2}{\eta^2} \left| \Delta Z_{tt}' - [Z_{ts}'] [Z_{ss} + Z_L]^{-1} [Z_{st}'] \right|^2 \quad (3.51.)$$

Because of reciprocity,  $[Z_{ts}'] = [\tilde{Z}_{st}']$  ( $\tilde{\phantom{x}}$  denotes transpose). The total scattering cross section<sup>40, 41</sup> now becomes

$$\sigma_s(\theta_t, \phi_t) = \frac{\left| \begin{bmatrix} [\tilde{I}_s] & [Z_{ss}] & [I_s] \end{bmatrix} \right|^2}{|E^i|^2 / \eta} \quad (3.52.)$$

where the radiation impedance matrix  $[Z_{ss}]$  allows for quadrature currents arising from the inter-element interactions. The analogous equation for a multiport scatterer, corresponding to equation 3.44 is

$$[I_s] = [Z_{ss} + Z_L]^{-1} [V_s^o] \quad (3.53.)$$

$$= I_t [Z_{ss} + Z_L]^{-1} [Z_{st}] \quad (3.54.)$$

For an array of parasitic dipole elements,  $Z_L = 0$ . Also if all media are reciprocal then  $[Z_{ss}]$  is a symmetric matrix, so

$$[I_s] = I_t [Z_{ss}]^{-1} [Z_{st}] \quad (3.55.)$$

and

$$[\tilde{I}_s] = I_t [\tilde{Z}_{st}] [Z_{ss}]^{-1} \quad (3.56.)$$

Substituting equation 3.21, 3.55 and 3.56 into equation 3.52, and simplifying the result with equation 3.26

generalised to the multiport case

$$\sigma_s = \frac{4\lambda^2}{\pi} \left| [Z_{st}]' [Z_{ss}]^{-1} [Z_{st}] \right| \quad (3.57.)$$

Provided that the scattering cross section of the open circuited array is small, then  $\Delta Z_{tt}'$  can be neglected compared with the other terms on the right in equation 3.51. Hence, from equation 3.51 with  $Z_L = 0$ , and equation 3.57

$$\frac{\sigma_s(\theta_t, \phi_t)}{\lambda^2} = \left\{ \frac{\sigma_{BS}(\theta_t, \phi_t)}{\pi \lambda^2} \right\}^{\frac{1}{2}} \quad (3.58.)$$

The techniques employed to numerically analyse scattering arrays of parasitic dipole elements are discussed in the next section.

### 3.6. Theoretical analysis of the backscattering and total scattering cross-sections of single cylindrical dipoles.

The solution to the broadside backscattering cross section,  $\sigma_{BS}$ , of a centre-loaded cylindrical antenna has been calculated by Hu<sup>42</sup>. The principal results are now given. By considering the interaction between a fictitious short dipole and the cylindrical dipole, the backscattering cross-section is obtained in terms of the self and mutual impedance of the two antennas.

The backscattering cross section,  $\sigma_{BS}$ , is given by the equation

$$\frac{\sigma_{BS}}{\lambda^2} = \frac{1}{900\pi} \left| (Z_{11}' - Z_1') - \frac{Z_{12}'^2}{Z_{22}' + Z_L} \right|^2 \quad (3.59.)$$

where  $Z_L$  is the load impedance, and  $Z_{11}' - Z_1'$ ,  $Z_{12}'$  and  $Z_{22}'$  are the far field impedance parameters, which depend only on the geometry of the cylindrical antenna and are independent of the load. This equation is identical to equation 3.46 but with the impedance parameters altered to the notation used by Hu<sup>42</sup>.

The impedances are determined by a variational method. The current distribution on the cylindrical antenna is assumed to be of the form

$$I(Z) = \frac{I(0) \cos \beta Z - \cos \beta L}{1 - \cos \beta L} \quad (3.60.)$$

Where  $\beta$  is the propagation constant of the current on the antenna,  $L$  is the antenna halflength and  $I(0)$  is the terminal current.

The impedances

$$Z_{11}' - Z_1' = -j 30 \left[ \frac{H^2}{E + jF} \right] \quad (3.61.)$$

$$Z_{12}' = j 30 \left[ G - \frac{H(C + jD)}{(E + jF)} \right] \quad (3.62.)$$

$$Z_{22}' = j 30 \left[ (A + jB) - \frac{(C + jD)^2}{(E + jF)} \right] \quad (3.63.)$$

The primed impedances depend on the quantities  $A, B, C, D, E, F, G$  and  $H$  which are the results of the current integrals for the antennas, where<sup>42</sup>

$$A = \frac{1}{(1 - \cos L)^2} \left\{ S(4L) + 4 \cos L(L \cos L - \sin L) \left[ \ln \frac{4L}{\alpha} - C(2L) \right] - \frac{8}{\pi} \sin^2 L - \cos^2 L \sin 2L \right\}$$

$$B = \frac{1}{(1 - \cos L)^2} \left\{ -C(4L) - (4L \cos^2 L - 2 \sin 2L) S(2L) + \sin^2 2L \right\}$$

$$C = \frac{1}{1 - \cos L} \left\{ (\sin L) S(4L) + (1 - \cos L) C(4L) + 4 \cos L(1 - \cos L - L \sin L) C(2L) + 4 \cos L(1 - \cos L) C(L) + 4 \sin L(L \cos L - \sin L) \ln \frac{4L}{\alpha} + 4(1 - \cos L)^2 \ln \frac{2L}{\alpha} - \frac{8}{\pi} \alpha \sin L(1 - \cos L) - (\sin 2L)^2 \right\}$$

$$D = \frac{1}{1 - \cos L} \left\{ (1 - \cos L)S(4L) - (\sin L)C(4L) \right. \\ \left. + 4 \cos L(1 - \cos L - L \sin L)S(2L) \right. \\ \left. + 4 \cos L(1 - \cos L)S(L) + 2 \sin^2 L \sin 2L \right\}$$

$$E = 2 \cos L(1 - \cos L)S(4L) + 2 \sin L(1 - \cos L)C(4L) \\ + 4(1 - \cos L)^2 S(2L) - 4L (\sin^2 L)C(2L) \\ + 8 \sin L(1 - \cos L)C(L) \\ + |4L \sin^2 L - 8 \sin L(1 - \cos L)| \ln \frac{4L}{\alpha} \\ - \frac{24}{\pi} \alpha(1 - \cos L)^2 - 2 \sin^2 L \sin 2L$$

$$F = 2 \sin L(1 - \cos L)S(4L) - 2 \cos L(1 - \cos L)C(4L) \\ - 4L (\sin^2 L)S(2L) - 4(1 - \cos L)^2 C(2L) \\ + 8 \sin L(1 - \cos L)S(L) + 4 \sin^4 L$$

$$G = \frac{2}{1 - \cos L} (\sin L - L \cos L)$$

$$H = 2 |2(1 - \cos L) - L \sin L|$$

with

$$L = \beta l, \quad \alpha = \beta a \\ C(x) = \int_0^x \frac{1 - \cos u}{u} du, \quad S(x) = \int_0^x \frac{\sin u}{u} du.$$

a is the antenna radius

The program listed in Appendix 2.1 was used to analyse the backscattering and total scattering broadside responses of cylindrical dipole antennas. The scattering geometry is illustrated in Figure 3.4. Figure 3.5 shows the variation of normalised backscattering cross section, "sigma", with electrical halflength KH, for a cylindrical dipole antenna. The load impedance,  $Z_L = 0$ , and the radius of the antenna was  $3.5 \times 10^{-3} \lambda$ . The total broadside scattering cross section can be found using equation 3.48. Figures 3.6, 3.7 and 3.8 show the variation of the total broadside scattering cross section with electrical halflength, KH, for a short circuited cylindrical dipole, for different antenna radii. It is evident

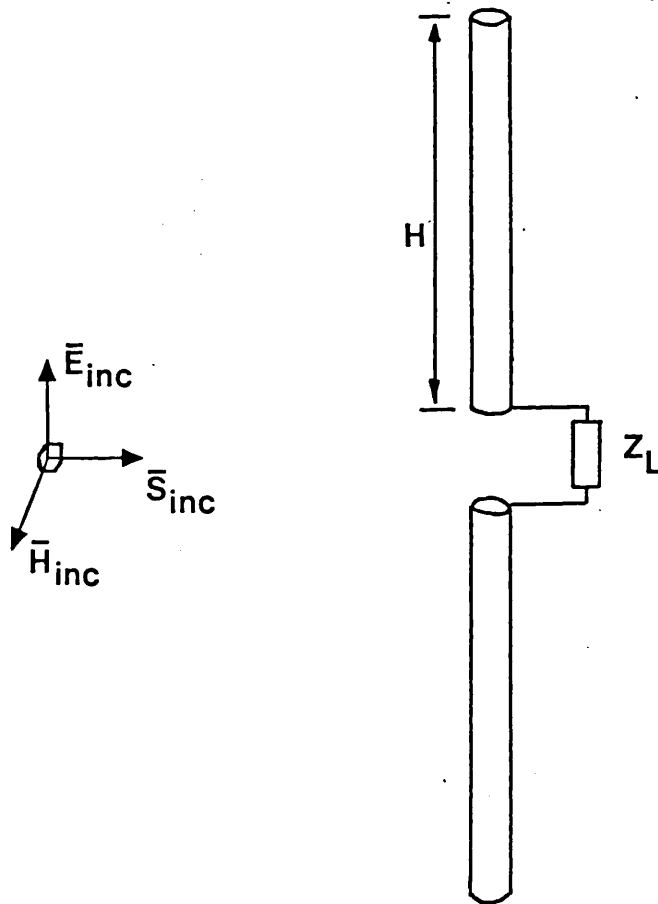


Figure 3.4. Broadside scattering from a cylindrical dipole.



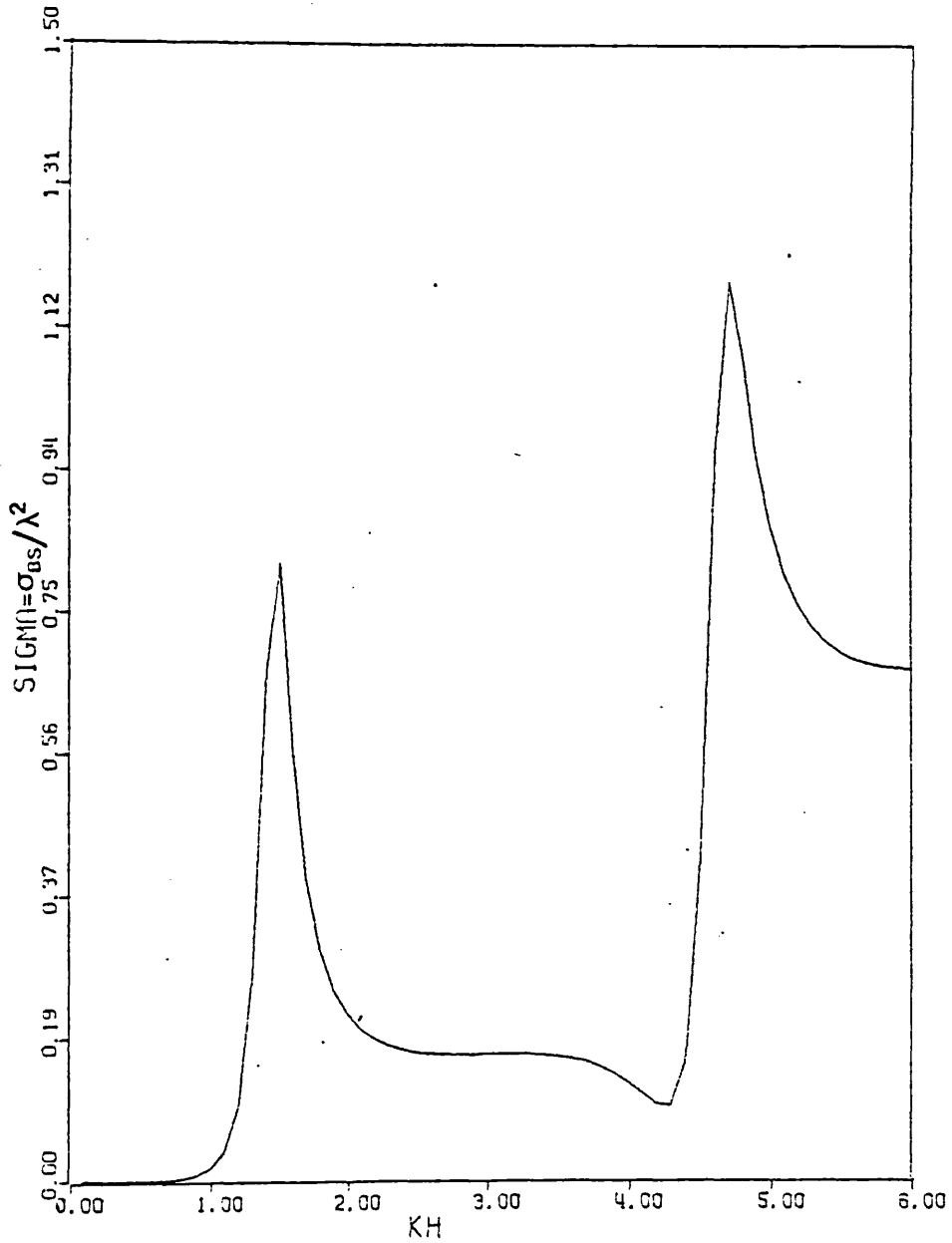


Figure 3.5. Normalised backscattering cross section SIGMA,  $=\sigma_{BS}/\lambda^2$ , for a cylindrical short-circuited dipole antenna of halflength H and radius  $3.5 \times 10^{-3}\lambda$ .  $K = 2\pi/\lambda$ .

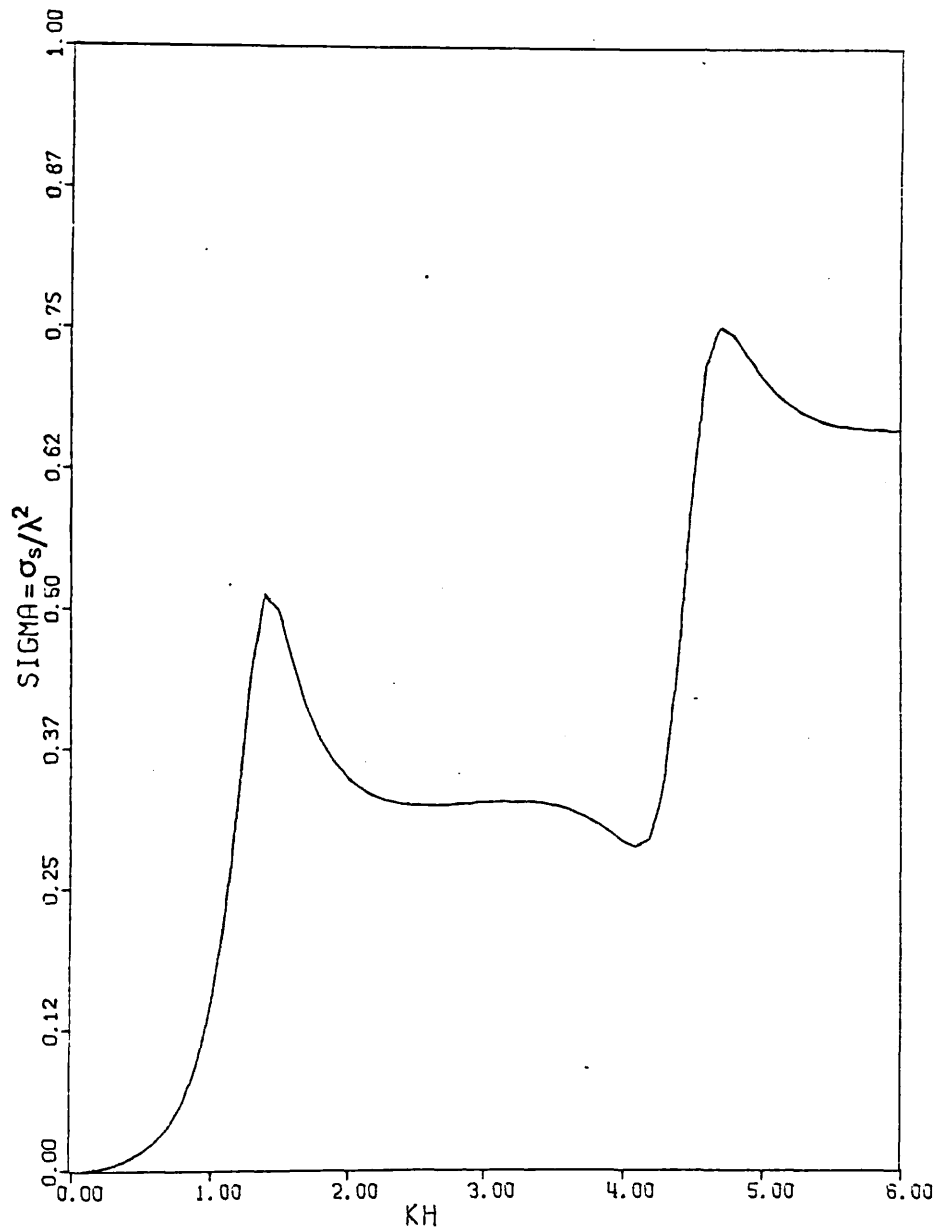


Figure 3.6. Normalised total scattering cross section  
 $SIGMA = \sigma_s / \lambda^2$ , for a short circuited  
dipole antenna of halflength  $H$  and  
radius =  $1.5 \times 10^{-2} \lambda$ .  $K = 2\pi / \lambda$ .

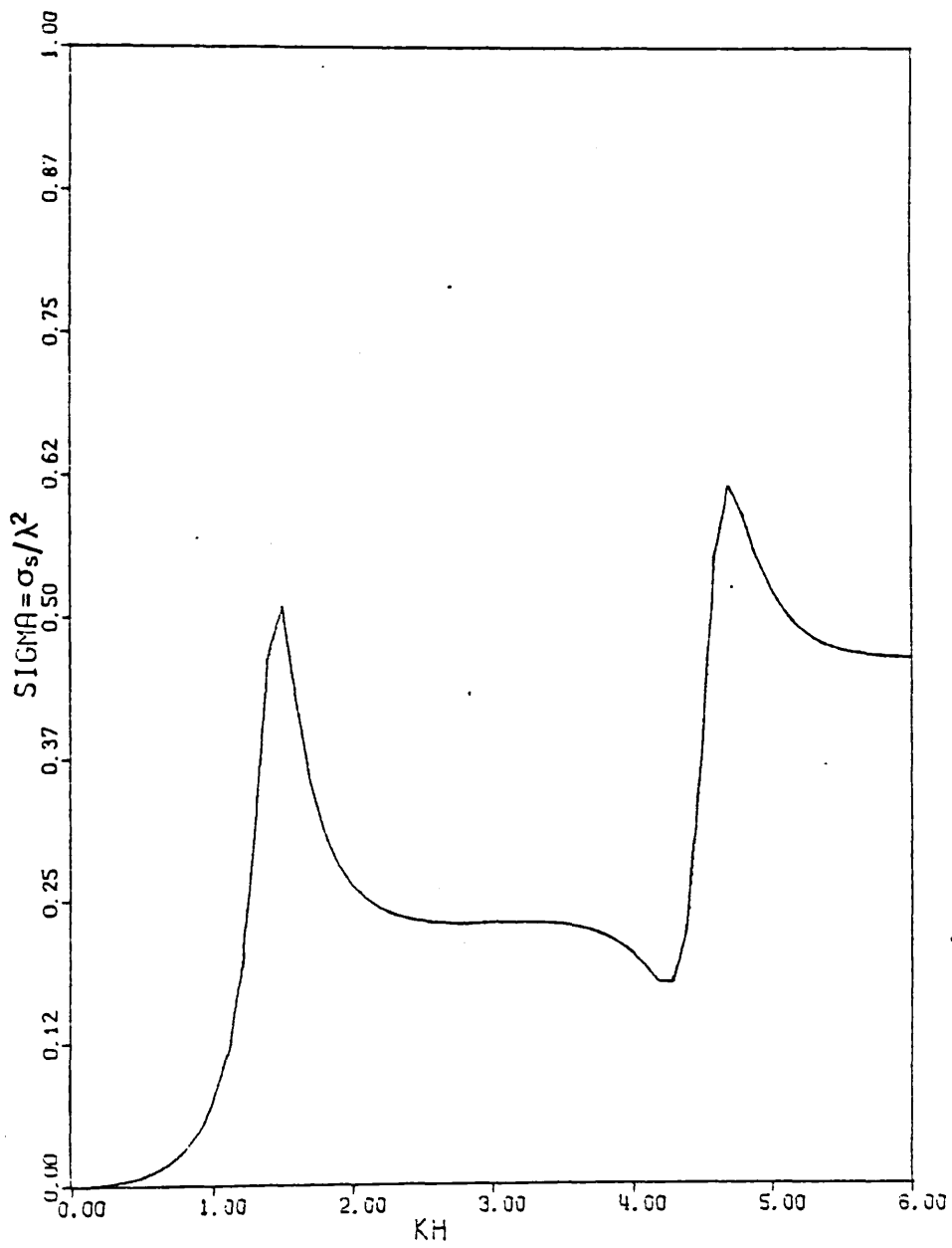


Figure 3.7. Normalised total scattering cross section  $SIGMA = \sigma_s / \lambda^2$ , for a short circuited dipole antenna of halflength  $H$  and radius  $= 3.5 \times 10^{-3} \lambda$ .  $K = 2\pi / \lambda$ .

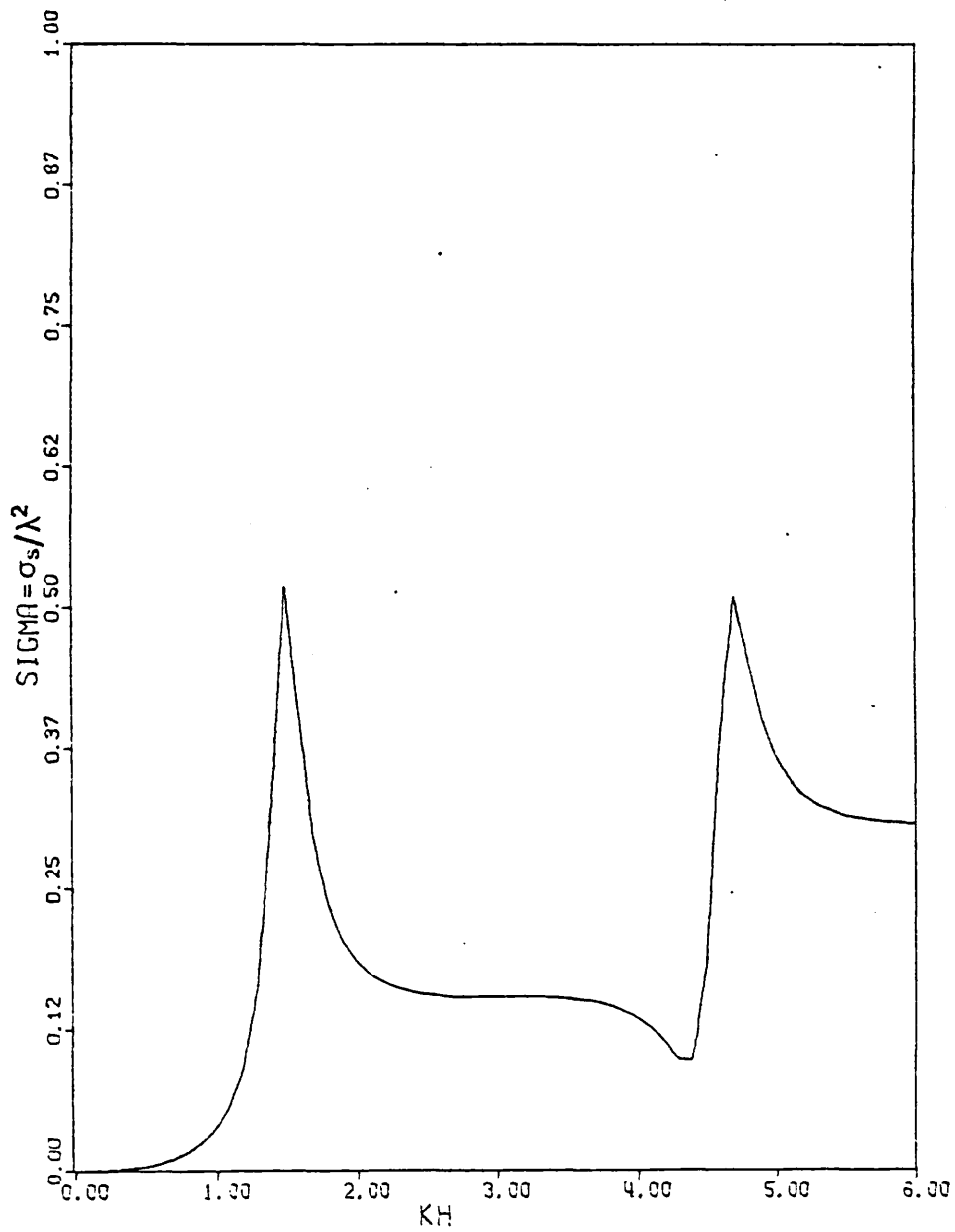


Figure 3.8. Normalised total scattering cross section  $SIGMA = \sigma_s / \lambda^2$  for a short circuited dipole antenna of halflength  $H$  and radius  $= 3.5 \times 10^{-4} \lambda$ .  $K = 2\pi / \lambda$ .

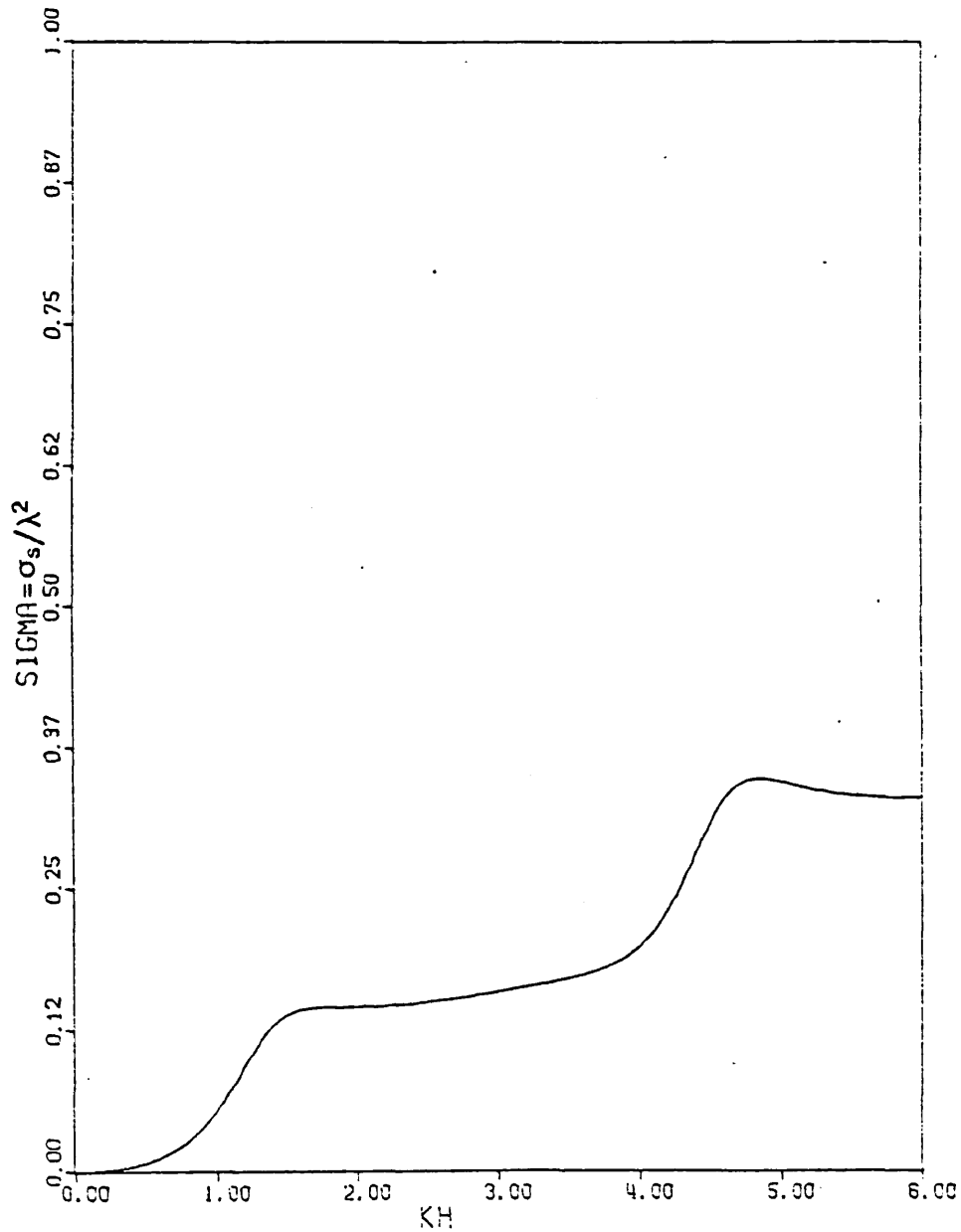


Figure 3.9. Normalised total scattering cross section  $SIGMA = \sigma_s / \lambda^2$  for a centre loaded dipole of halflength  $H$ . Load impedance =  $73 + j0 \Omega$  radius =  $15 \times 10^{-3} \lambda$ .  $K = 2\pi / \lambda$ .

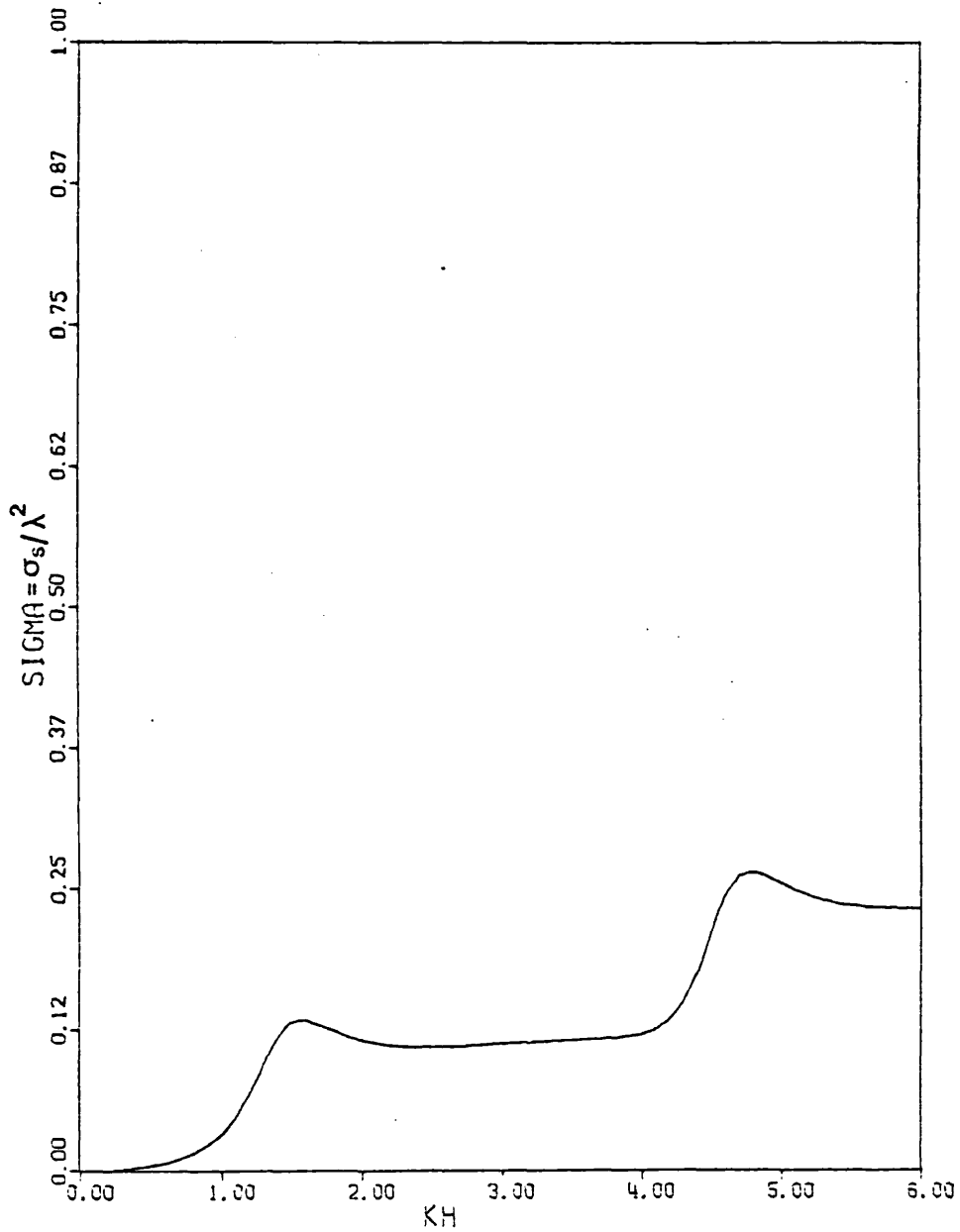


Figure 3.10. Normalised total scattering cross section  $SIGMA = \sigma_s / \lambda^2$  for a centre loaded dipole of halflength  $H$ . Load impedance =  $73 + j0 \Omega$ . radius =  $3.5 \times 10^{-3} \lambda$ .  $K = 2\pi / \lambda$ .

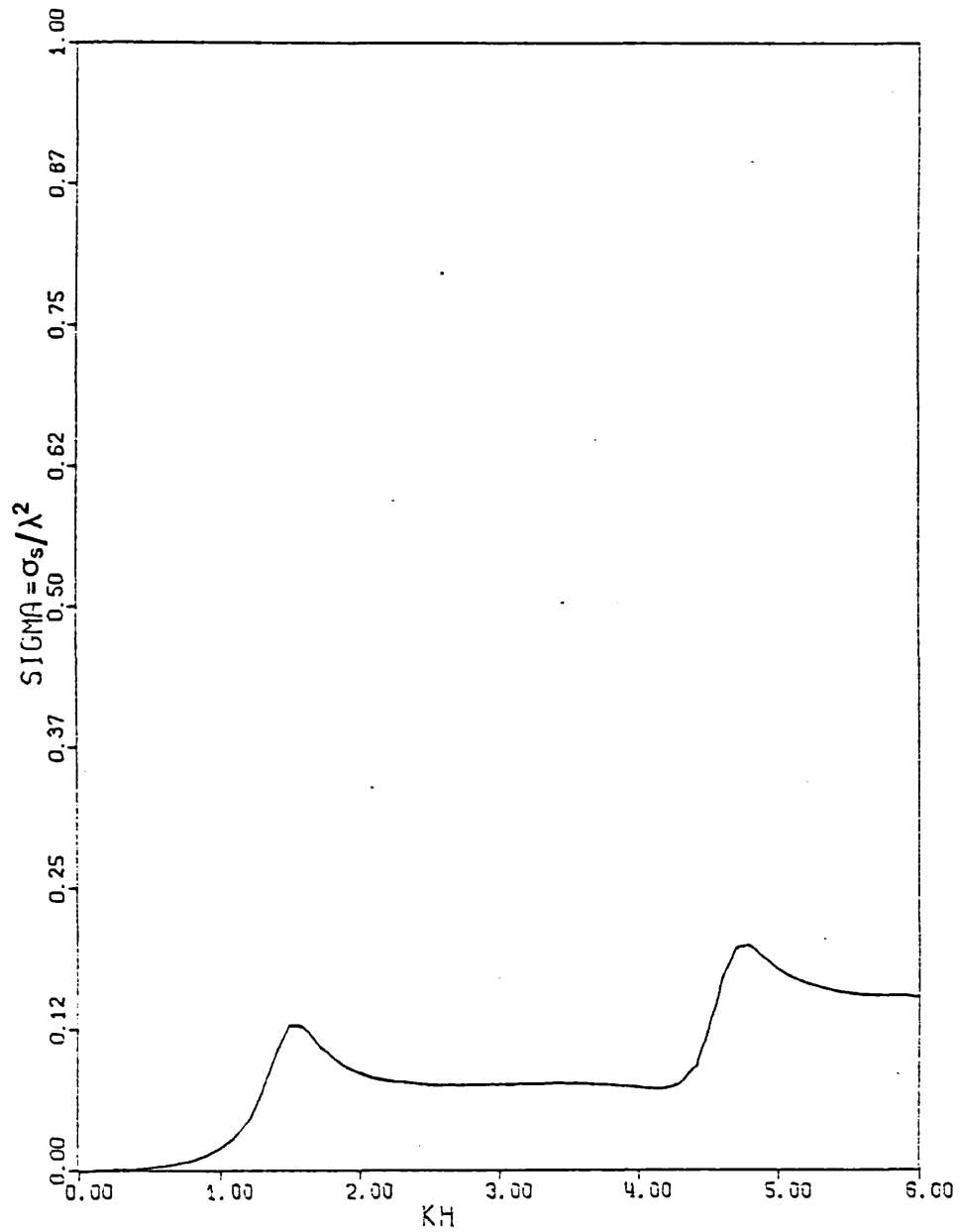


Figure 3.11. Normalised total scattering cross section  $SIGMA = \sigma_s / \lambda^2$  for a centre loaded dipole of halflength  $H$ . Load impedance =  $73 + j0\Omega$  radius =  $3.5 \times 10^{-4}\lambda$ .  $K = 2\pi/\lambda$ .

that the smaller the antenna radius the sharper are the resonances. The Q of a cylindrical antenna is given by<sup>43</sup>

$$Q = \frac{\pi Z_o}{8 R_a} \quad (3.64.)$$

Where  $R_a$  is the radiation resistance.

For a loaded antenna,  $Z_o$  is the characteristic impedance of the antenna where

$$Z_o = 120 \left| \ln \left( \frac{2H}{a} \right) - 1 \right| \quad (3.65.)$$

H is the antenna halflength and a is the radius of the antenna. Clearly as a becomes smaller so  $Z_o$ , and hence Q, increases.

Figures 3.9, 3.10 and 3.11 show the variation of the total scattering cross-sections with electrical halflength, KH, for cylindrical dipoles of various radii, all centre loaded with a 73  $\Omega$  resistive load. It is again evident that, the smaller the antenna radius the sharper are the resonances. Also, the reduction in scattering cross section due to the effects of positive loading can be seen.

One can analyse flat strip dipoles using the theory developed for cylindrical dipoles, by replacing the flat strip dipoles by cylindrical dipoles having radii equal to one fourth the strip width<sup>44, 45</sup>, and equal length. Figure 3.12 shows the variation of antenna Q with strip width for a planar halfwave dipole<sup>45</sup>.



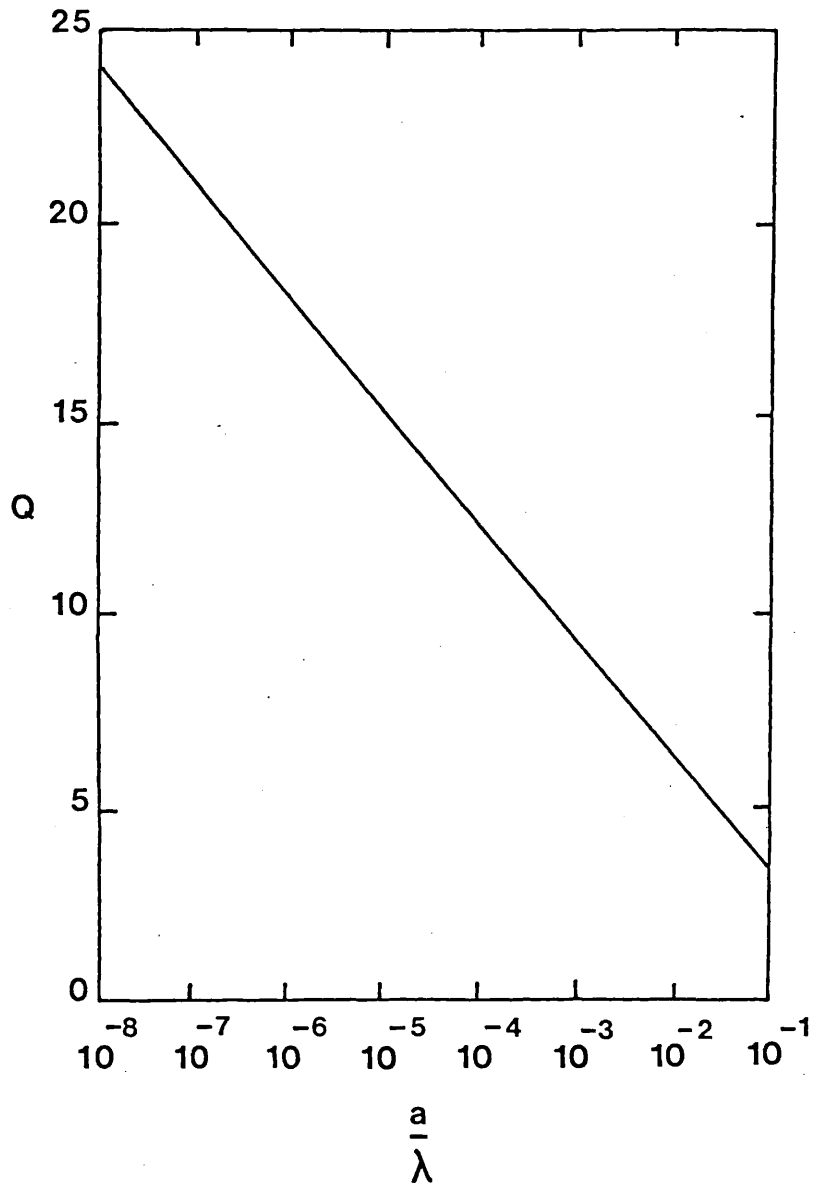


Figure 3.12. Variation of Q with antenna width  $a/\lambda$  for planar dipole antennas<sup>39</sup>.

3.7. Theoretical analysis of the backscattering and total scattering cross-sections of antenna arrays.

It has been shown that for multiply loaded scatterers such as antenna arrays, the backscattering cross section is given by

$$\frac{\sigma_{BS}}{\lambda^2} = \frac{1}{900 \pi} \left| \Delta Z_{tt}' - [Z_{ts}'] [Z_{ss} + Z_L]^{-1} [Z_{st}'] \right|^2$$

where  $[Z_{ts}']$  = impedance matrix from transmitter/receiver to scatterer

$[Z_{st}']$  = impedance matrix from scatterer to receiver/transmitter

because of reciprocity

$$[Z_{ts}'] = [\tilde{Z}_{st}']$$

(~ denotes transpose)

$[Z_{ss}]$  = antenna array impedance matrix (containing self and mutual impedance terms of the array)

$[Z_L]$  = load impedance matrix (containing self and mutual impedance terms of the load)

$\Delta Z_{tt}'$  = impedance change at transmitter/receiver due to the presence of the scatterer from that when the scatterer is absent.

$\Delta Z_{tt}'$  may be neglected as it is small compared to the other terms, for the cases considered here. The total scattering cross section for an array of parasitic elements may be obtained from the backscattering cross section from equation 3.58. The scattering geometry is illustrated in Figure 3.13.

As the broadside array cross-sections are of interest for experimental work in the open resonator, the self impedance and mutual impedance parameters for the  $[Z_{ss}]$  and  $[Z_{st}]$  matrix are taken from the results of Hu<sup>42</sup>. The mutual impedance parameters for the radiation impedance matrix,  $[Z_{ss}]$ , are taken to be the mutual impedances obtained by Brown and King<sup>46</sup>. These neglect

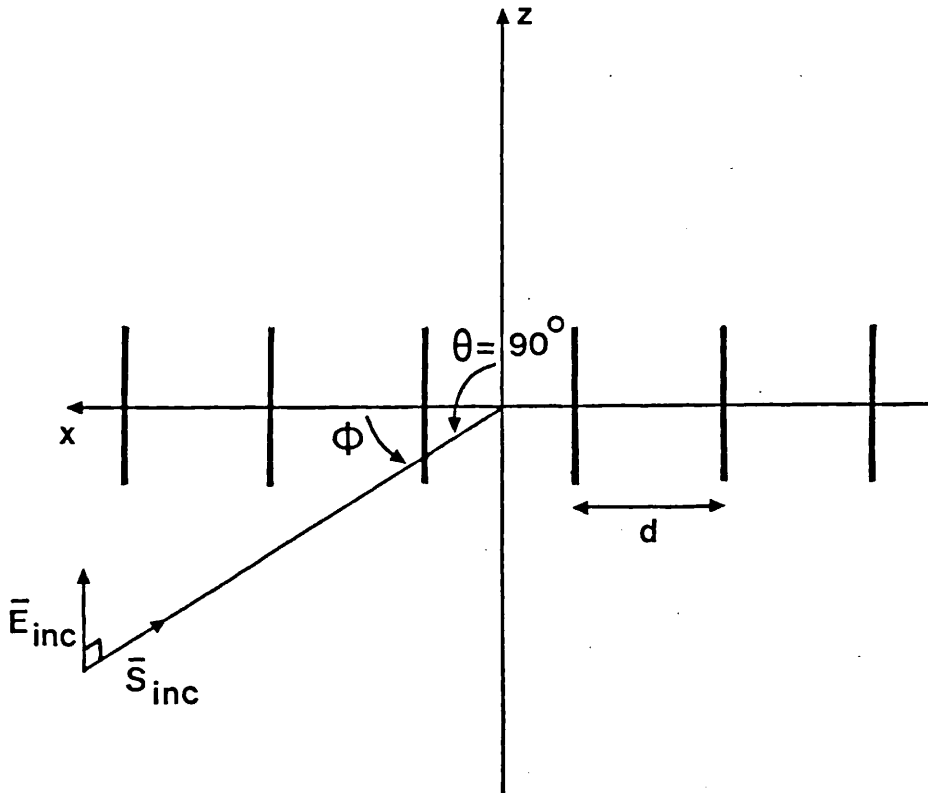


Figure 3.13. H - plane scattering from a parasitic linear array.

the effects of antenna thickness which is known to be small. These mutual impedance parameters are given in equations 3.66 and 3.67. They are referred to the input terminals of the array elements, which is required by equation 3.51, rather than the current antinodes which is sometimes quoted.

$$R_m = \frac{30}{\sin^2 G} \left[ 2\{2 + \cos 2G\} \text{Cik}d - 4 \cos^2 G \{ \text{Cik}(\sqrt{d^2 + a^2} - a) + \text{Cik}(\sqrt{d^2 + a^2} + a) \} + \cos 2G \{ \text{Cik}(\sqrt{d^2 + (2a)^2} - 2a) + \text{Cik}(\sqrt{d^2 + (2a)^2} + 2a) \} + \sin 2G \{ \text{Sik}(\sqrt{d^2 + (2a)^2} + 2a) - \text{Sik}(\sqrt{d^2 + (2a)^2} - 2a) - 2\text{Sik}(\sqrt{d^2 + a^2} + a) + 2\text{Sik}(\sqrt{d^2 + a^2} - a) \} \right] \quad (3.66.)$$

and

$$X_m = \frac{30}{\sin^2 G} \left[ - 2\{2 + \cos 2G\} \text{Sik}d + 4\cos^2 G \{ \text{Sik}(\sqrt{d^2 + a^2} - a) + \text{Sik}(\sqrt{d^2 + a^2} + a) \} - \cos 2G \{ \text{Sik}(\sqrt{d^2 + (2a)^2} - 2a) + \text{Sik}(\sqrt{d^2 + (2a)^2} + 2a) \} + \sin 2G \{ \text{Cik}(\sqrt{d^2 + (2a)^2} + 2a) - \text{Cik}(\sqrt{d^2 + (2a)^2} - 2a) - 2\text{Cik}(\sqrt{d^2 + a^2} + a) + 2\text{Cik}(\sqrt{d^2 + a^2} - a) \} \right]. \quad (3.67.)$$

The program listed in Appendix 2.2 was used to calculate the total backscattering cross sections of the various arrays consisting of parasitic (short circuited) dipole elements. Figure 3.14 shows the variation of broadside total scattering cross section for a 20 element linear array, with element halflength  $D$ , consisting of parasitic elements. The inter-element spacing is  $0.25\lambda$  and the mutual impedance effects are neglected. Figure 3.15 shows the effect of including mutual impedances in the radiation impedance matrix. The mutual impedances between elements reduces the sharpness of the resonance response of the antenna, as each element is effectively loaded to some extent by the others.

The variation of broadside total scattering cross section with inter-element spacing,  $D\lambda$ , for linear arrays of 15 parasitic elements are shown in Figures 3.16 and 3.17. Figure 3.16 shows the variation for short circuited

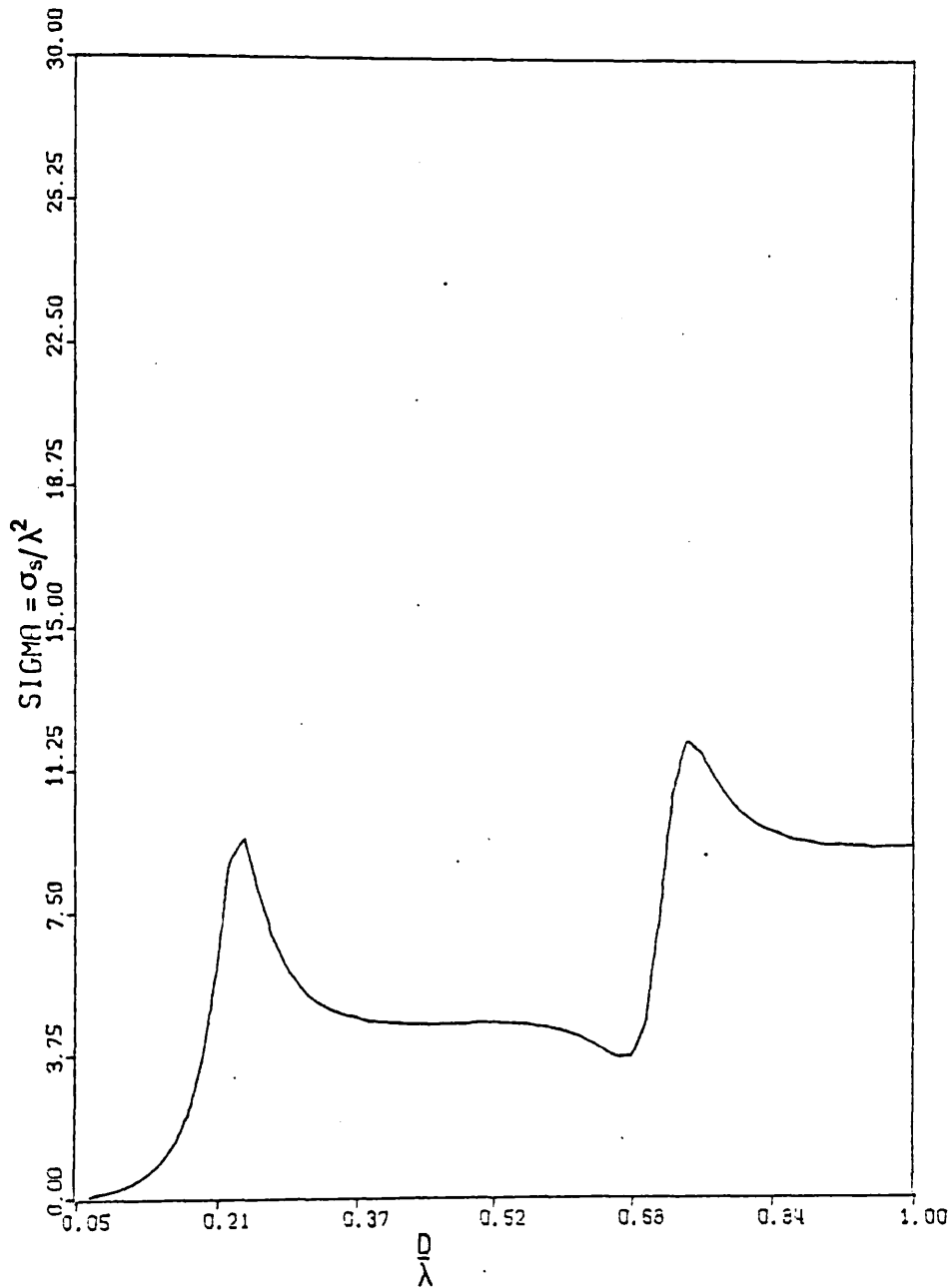


Figure 3.14. Normalised broadside scattering cross section  $SIGMA = \sigma_s/\lambda^2$ , for a 20 element array of short circuited dipole elements of halflength  $D$  and inter-element separation  $0.25\lambda$  mutual impedance effect neglected. Element radius =  $3.5 \times 10^{-3}\lambda$ .

Figure 3.15. Normalised broadside scattering cross section SIGMA,  $=\sigma_s/\lambda^2$  for a 20 element array of short circuited dipole elements of halflength  $D$  and inter-element separation  $= 0.25\lambda$ . Mutual impedance effects accounted for. Element radius  $= 3.5 \times 10^{-3}\lambda$ .

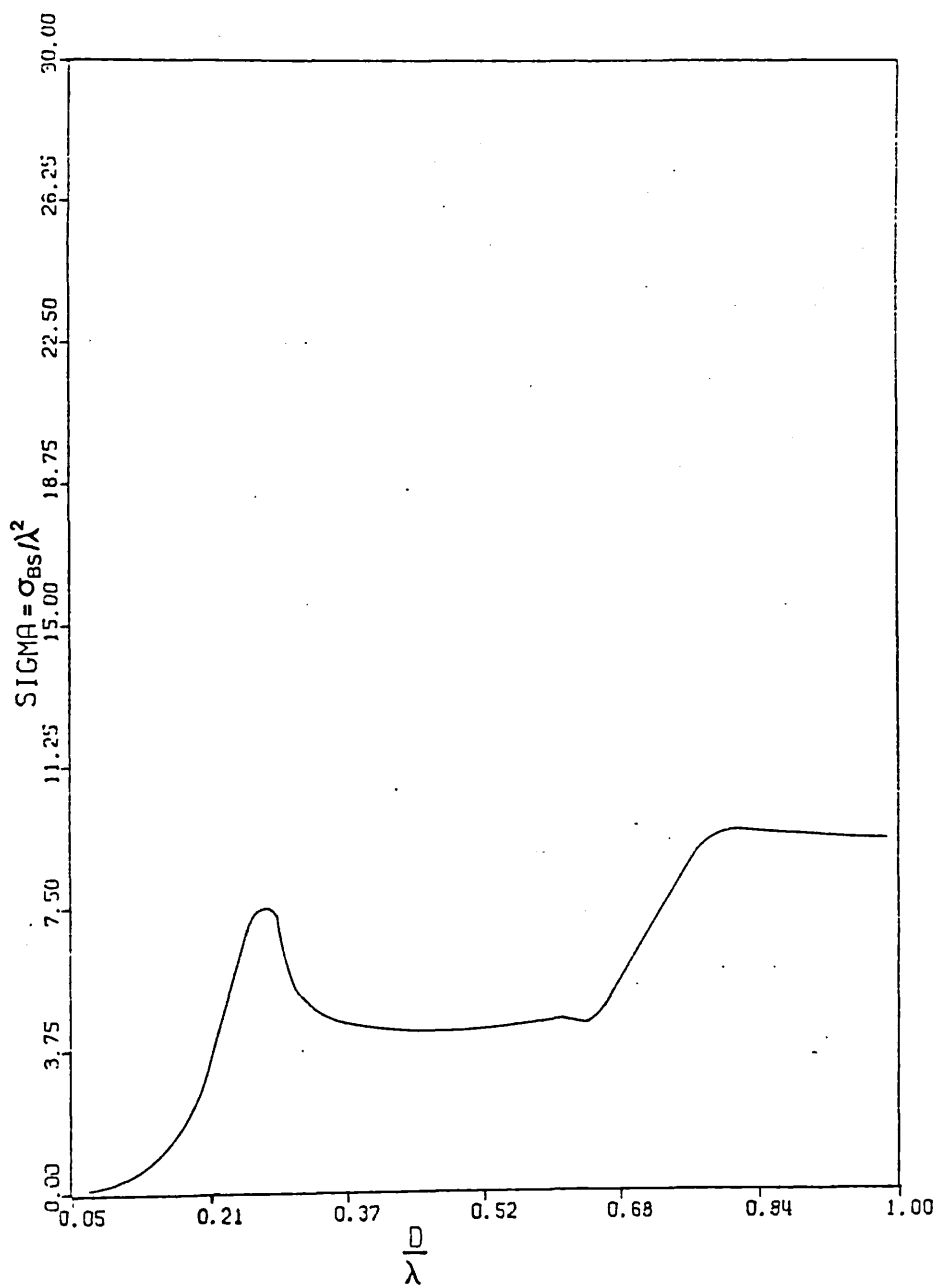


Figure 3.16. Normalised total scattering cross section  $SIGMA = \sigma_s/\lambda^2$ , for an array of 15 short-circuited halfwave dipoles with inter-element separation =  $D\lambda$ .

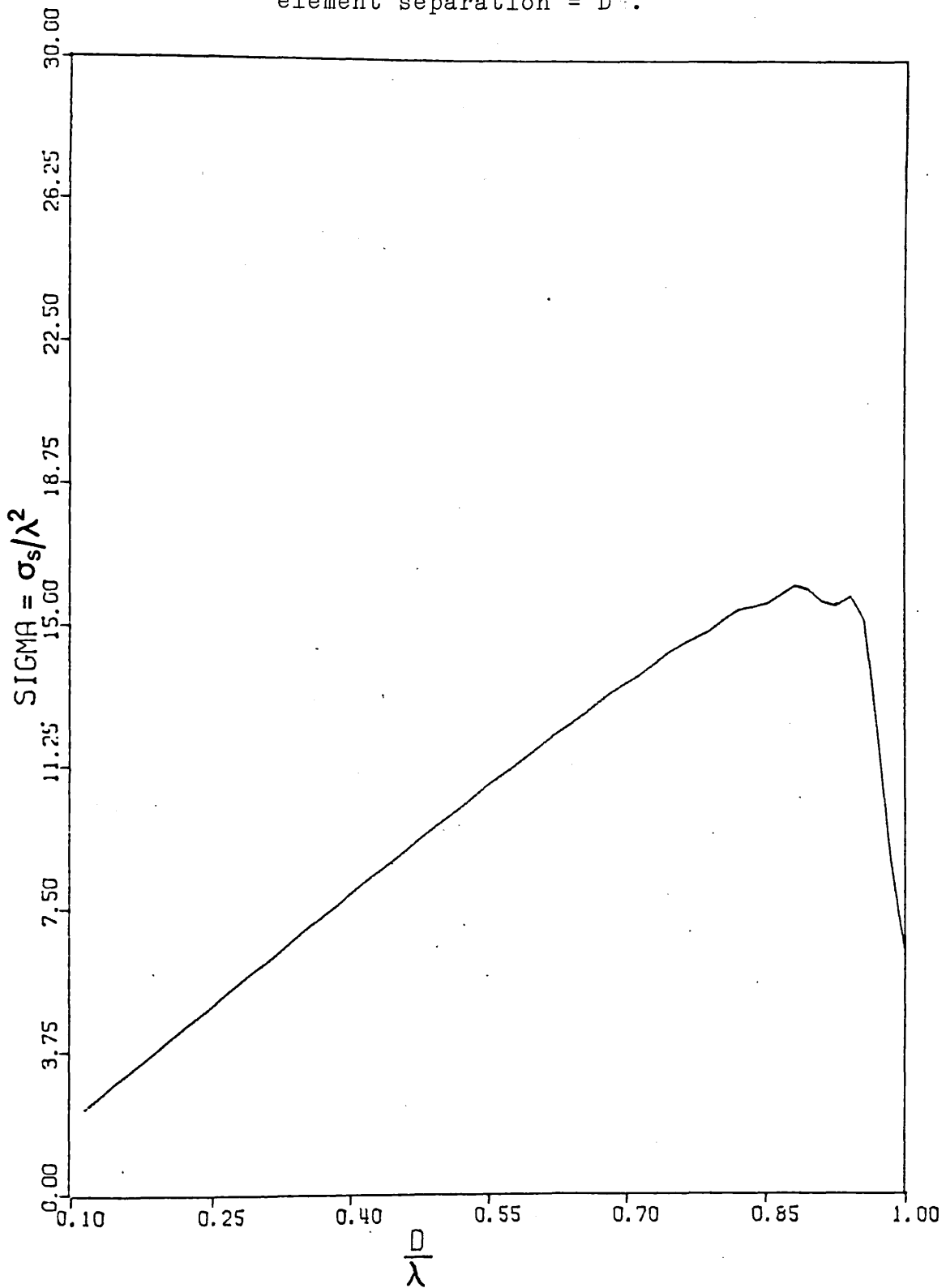
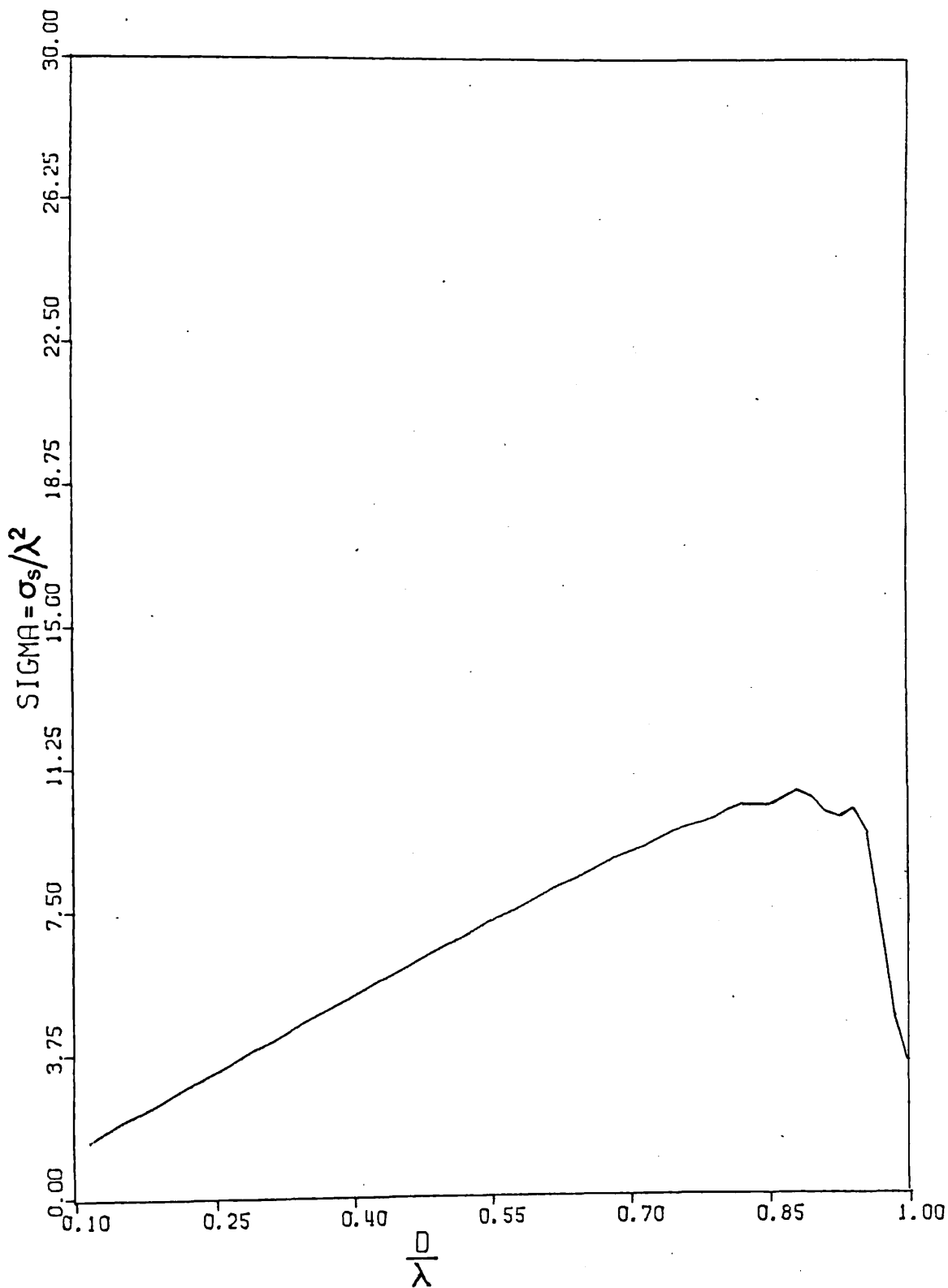


Figure 3.17. Normalised total scattering cross section  $SIGMA = \sigma_s / \lambda^2$ , for an array of 15 short-circuited fullwave dipoles with inter-element separation =  $D$ .





halfwave dipoles and Figure 3.17 the variation for fullwave dipoles.

The form of the curves in Figure 3.16 and 3.17 is determined by the mutual impedances between the antenna elements. For example, consider the parasitic halfwave dipole array. Figure 3.18 shows the variation of mutual impedance with inter-element spacing for two parallel halfwave antennas, non staggered<sup>47</sup>. Ignoring mutual coupling between elements, the normalised total scattering cross section for 15 parasitic elements would be 7.73 (see Figure 3.16). When the resistive component of mutual impedance is negative, the cross section of the antenna is higher than the non-interaction average, as there is greater positive current interaction between the array elements and their nearest neighbours. The sign of the reactive component also determines the phase of the current interactions and so also affects the cross section enhancement.

To investigate the polar H-plane variation of the total scattering cross section of a linear parasitic array, the expressions from Hu<sup>42</sup> for the mutual impedances between the scatterer and transmitter/receiver,  $|Z_{st}|$ , are weighted with a term dependent on the phase of excitation experienced by each element. This then allows for the phase variation of the element currents across the array when it is excited off axis. For the geometry shown in Figure 3.13, the impedance weighting factor for the  $m^{\text{th}}$  element in the array is given by  $e^{j(m-1)kd \cos \phi}$ , where  $k = 2\pi/\lambda$ ,  $d$  is the inter-element spacing and  $\phi$  is the angle of incidence. Hence

$$\left[ Z_{st}^{\phi} \right] = \left[ Z_{st} \right] \left[ e^{j(m-1)kd \cos \phi} \right] \quad (3.68.)$$

Figures 3.19 and 3.22 show the H plane variation of total scattering cross section for a linear array of 20 parasitic halfwave dipoles for inter-element spacings  $0.25\lambda$ ,  $0.5\lambda$ ,  $0.75\lambda$  and  $1.0\lambda$ .

The program used to produce these is listed in Appendix 2.3.

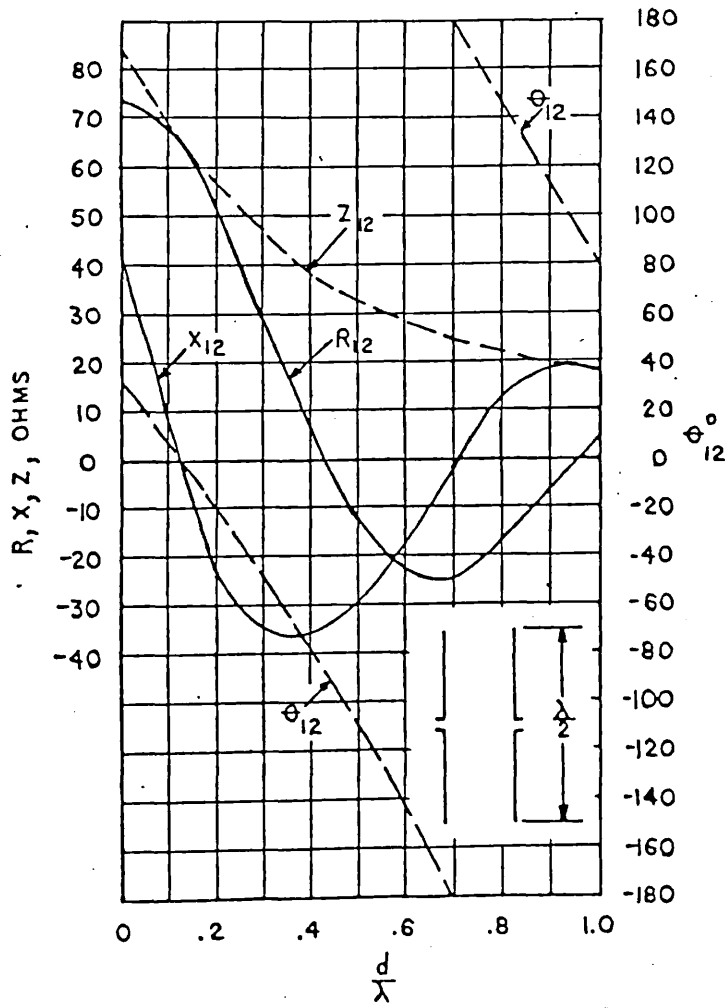


Figure 3.18. Mutual impedance variation with separation,  $d$ , for two parallel halfwave dipoles, non staggered (after King<sup>47</sup>).

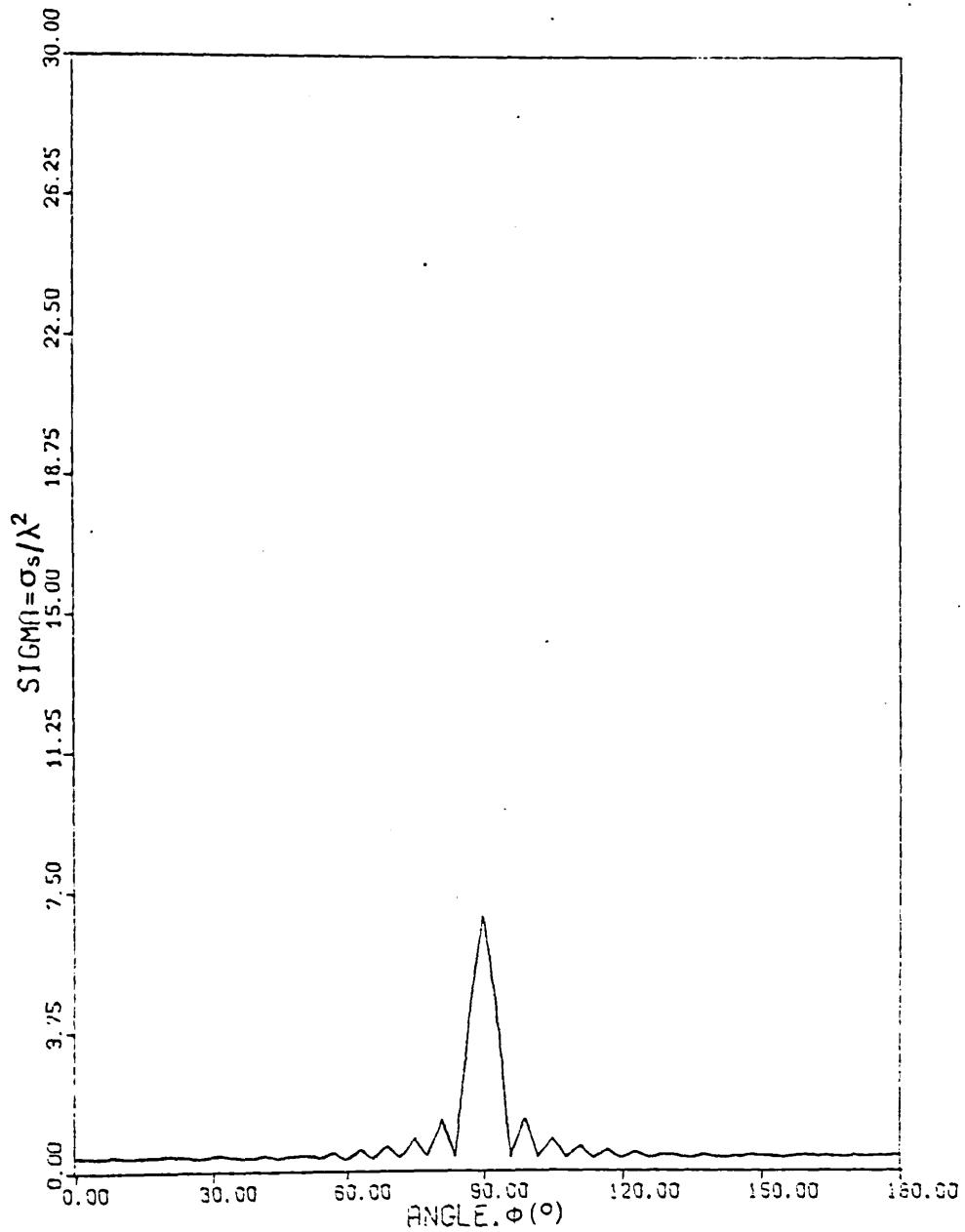


Figure 3.19. Variation of total scattering cross section  $SIGMA = \sigma_s / \lambda^2$ , for 20 short circuit halfwave dipoles of inter-element spacing  $0.25\lambda$  with angle of incidence, ANGLE  $^\circ$ .

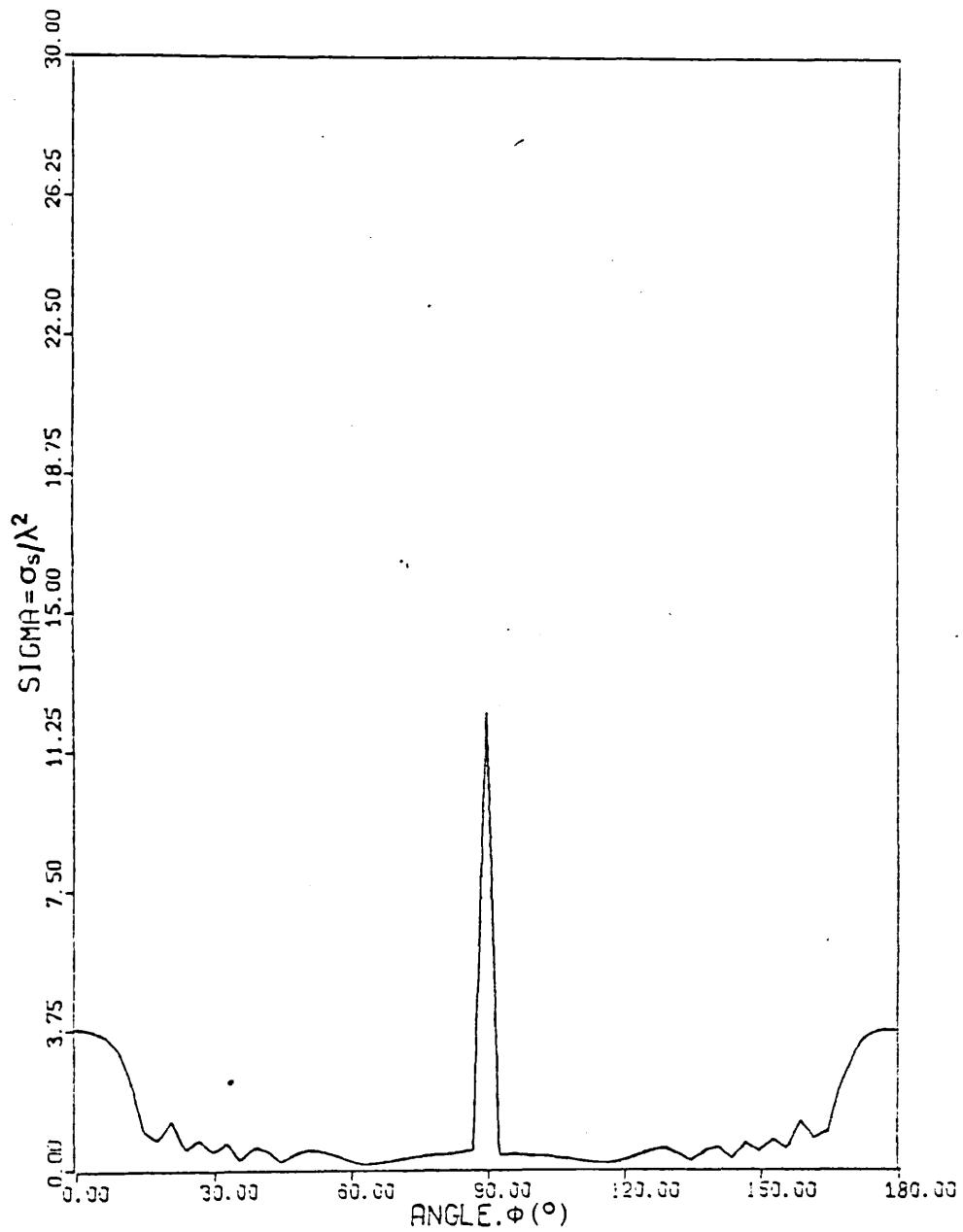


Figure 3.20. Variation of total scattering cross section  $SIGMA = \sigma_s / \lambda^2$ , for 20 short circuited half-wave dipoles of inter-element separation  $0.5\lambda$  with angle of incidence,  $ANGLE^\circ$ .

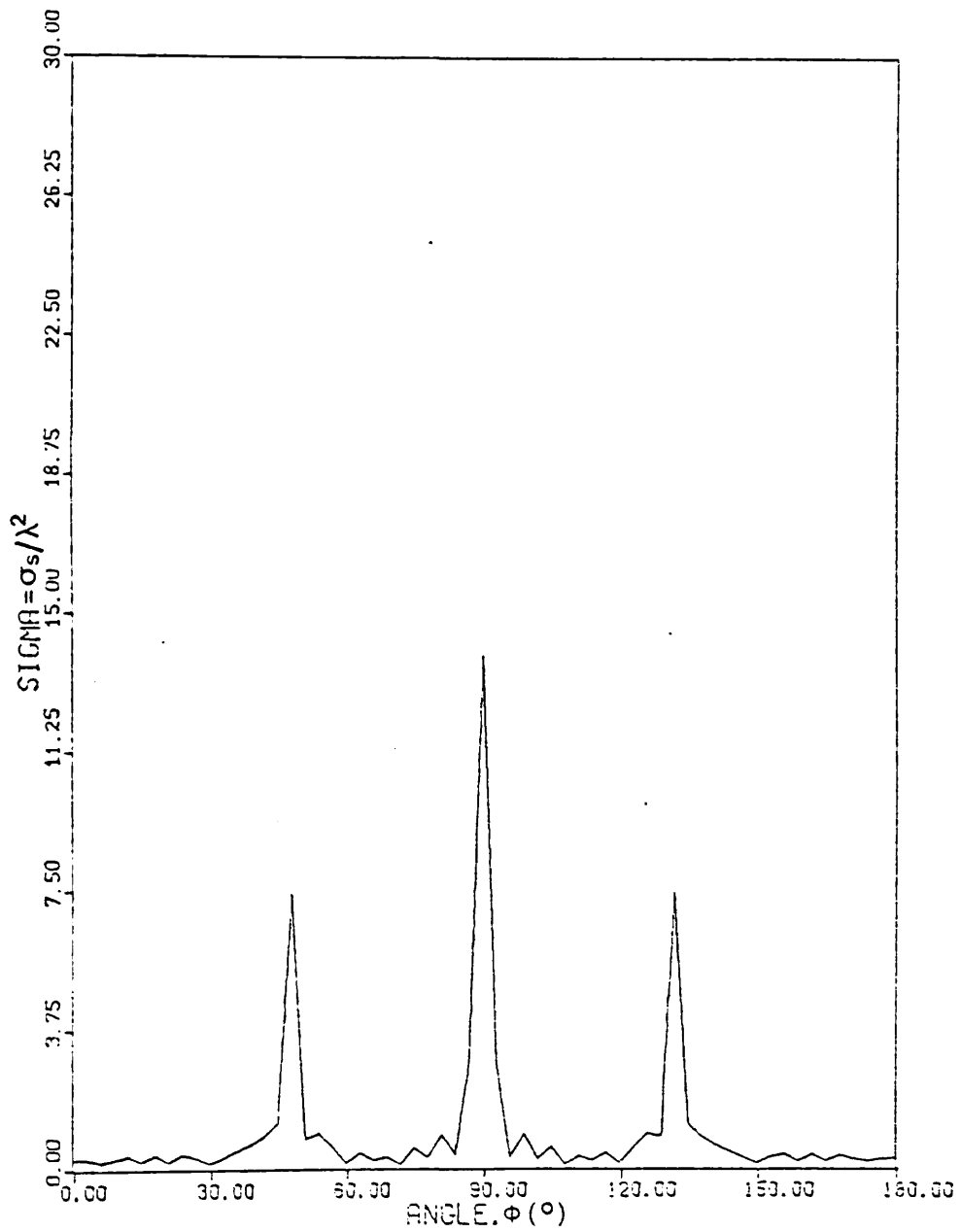


Figure 3.21. Variation of total scattering cross section  $\text{SIGMA} = \sigma_s / \lambda^2$ , for 20 short circuit halfwave dipoles of inter-element spacing  $0.75\lambda$  with angle of incidence,  $\text{ANGLE } \phi$ .

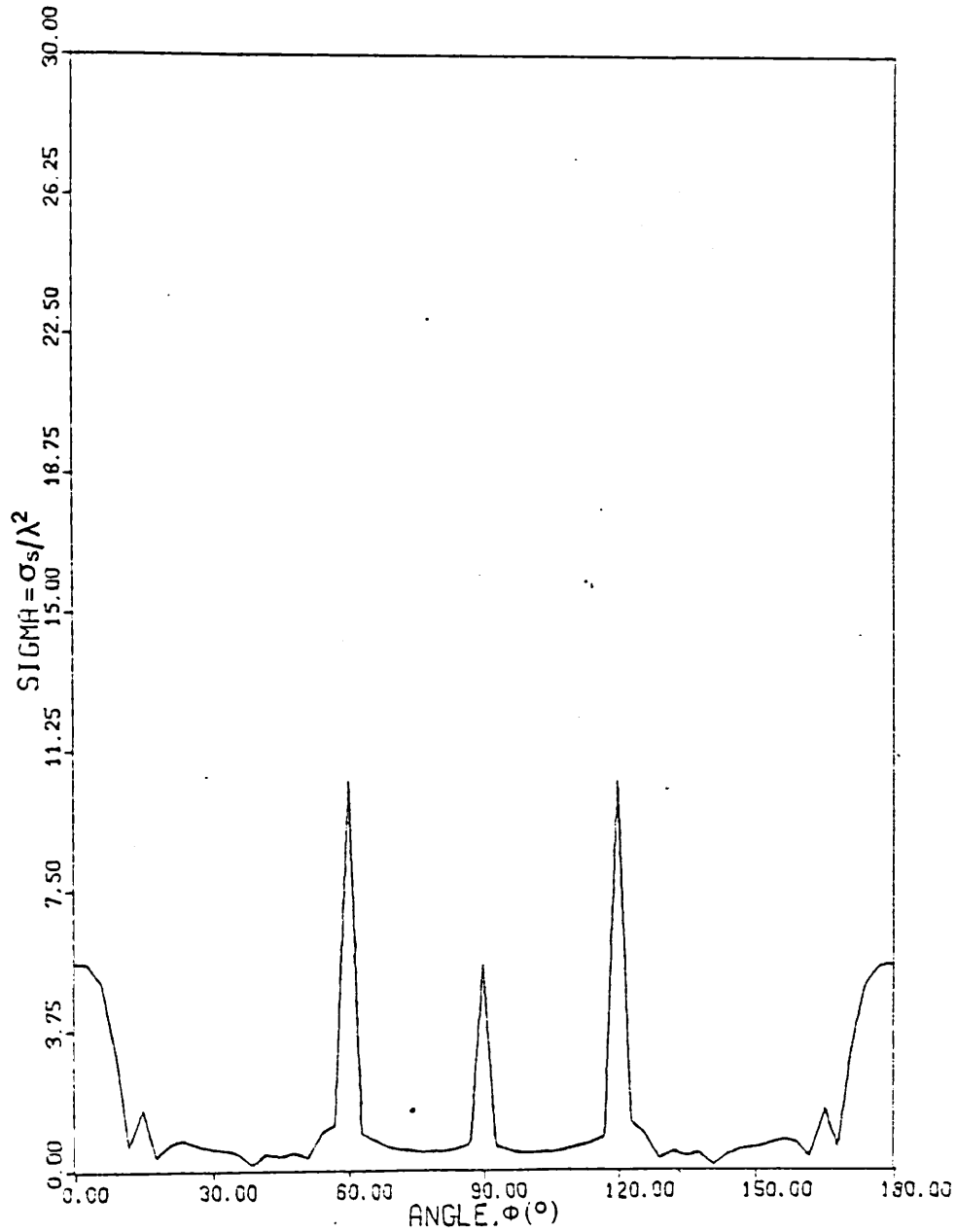


Figure 3.22. Variation of total scattering cross section  $\text{SIGMA} = \sigma_s / \lambda^2$ , for 20 short circuit halfwave dipoles of inter-element spacing  $1.0\lambda$  with angle of incidence,  $\text{ANGLE}^{\circ}$ .

CHAPTER FOUR  
THEORETICAL ASPECTS OF THE  
OPEN RESONATOR

4.1. Introduction.

The open resonator, usually with planar or spherical mirrors, has been used in the microwave and millimetre wave spectral regions for the measurement of extinction and scattering cross sections<sup>48-53</sup>, dielectric constants and loss tangents of solids and gases<sup>54,55</sup>, and the propagation constants of dielectric lines<sup>56</sup>. These measurements are calculated from a knowledge of the resonant frequency, resonator dimensions and the changes in the quality factor (Q) produced by introducing the material into the open resonator. This method eliminates the need for absolute power measurements. The technique has the advantage of being direct in concept and absolute in all its measurement régimes. A method pioneered by Cullen<sup>48</sup> for measuring the scattering cross sections of single metallic spheres suspended within an x-band open resonator, has provided a means of measuring the total scattering cross sections of parasitic dipole arrays at submillimetre wavelengths. By observing the variation with dipole and array dimensions, and testing the agreement between theory and experiment, it has been possible to verify that resonant currents flow on the dipoles when their dimensions are correct.

Also the ability of the open resonator to measure the dielectric properties of materials<sup>54,57</sup> was useful in evaluating and choosing suitable substrates, upon which to reproduce the antennas.

The open resonator has proved to be a useful measuring and diagnostic instrument for the submillimetre region. In this Chapter the underlying principle and the theoretical aspects of the open resonator are developed.

Also, the design parameters of an instrument for use at a fixed frequency of 891 GHz (an HCN laser) are obtained.

#### 4.2. Theory of the open resonator.

The open resonator is illustrated in Figure 4.1, and consists of two spherical mirrors of radius of curvature  $R_0$ , separated by a distance  $d$ . Such a system will act as a resonator with very high Q-factor. The resonator can support an infinite set of modes and the mode spectrum is given by Kogelnik and Li<sup>58</sup> as

$$\frac{f_{pLq}}{f_0} = (q + 1) + b(2p + L + 1) \quad (4.1.)$$

where  $f_{pLq}$  is the frequency of the  $TEM_{pLq}$  mode,  $f_0$  is the frequency separation between adjacent axial modes, given by

$$f_0 = \frac{c}{2d} \quad (4.2.)$$

and  $b$  is the frequency separation between adjacent azimuthal modes, where

$$b = (1/\pi) \arccos(1 - d/R_0) \quad (4.3.)$$

The axial mode number  $q$  measures the number of half-wavelengths contained within the axial distance  $d$ . The radial variation of the field is determined by  $p$  and the angular variation by  $L$ .

The electric field distributions for the various modes of a resonator with circular mirrors are shown in Figure 4.2. The  $TEM_{00q}$  modes, which have gaussian intensity profiles in the transverse plane, as shown in Figure 4.3, are the most useful for making measurements with the resonator. In this mode the field varies with the transverse radial distance,  $r$ , according to the formula

$$|E| = E_0 \exp(-r^2/\omega^2). \quad (4.4.)$$

In the central plane of symmetry ( $Z=0$ ), the parameter  $\omega$ , often called the "beam radius", has a minimum value  $\omega_0$  given by

$$\omega_0^2 = (\lambda_0 / 2\pi) \sqrt{d(2R_0 - d)} \quad (4.5.)$$



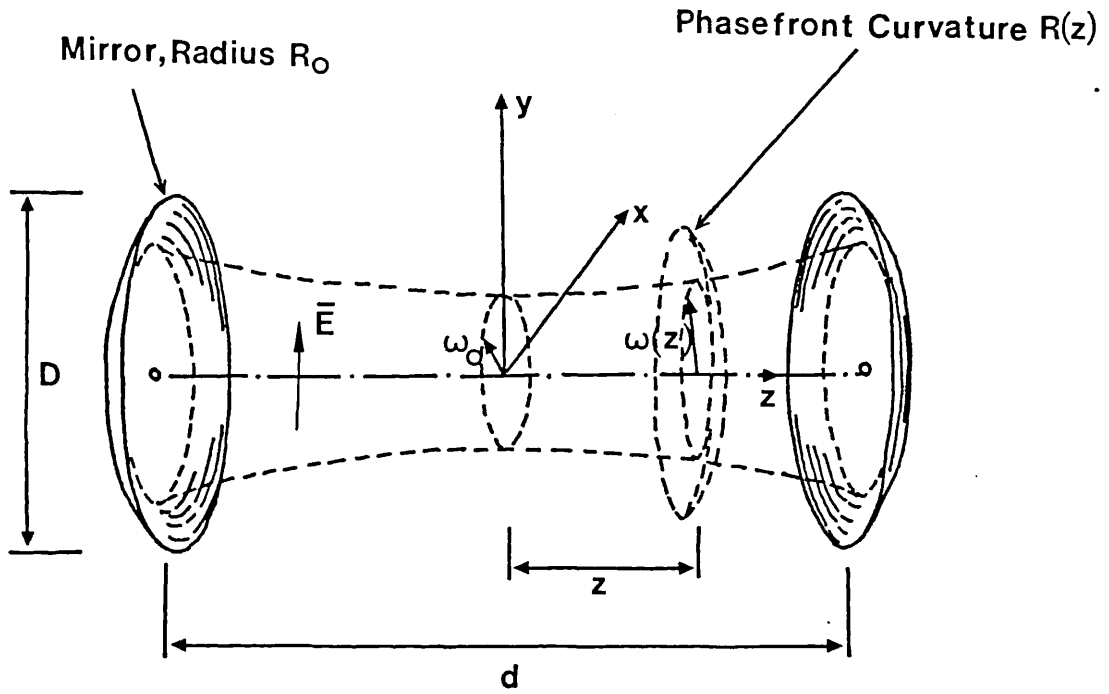


Figure 4.1. Geometry of the open resonator with spherical mirrors.

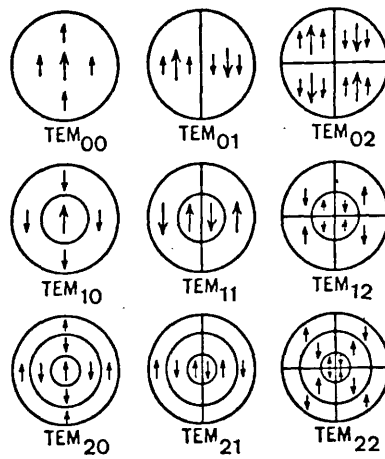
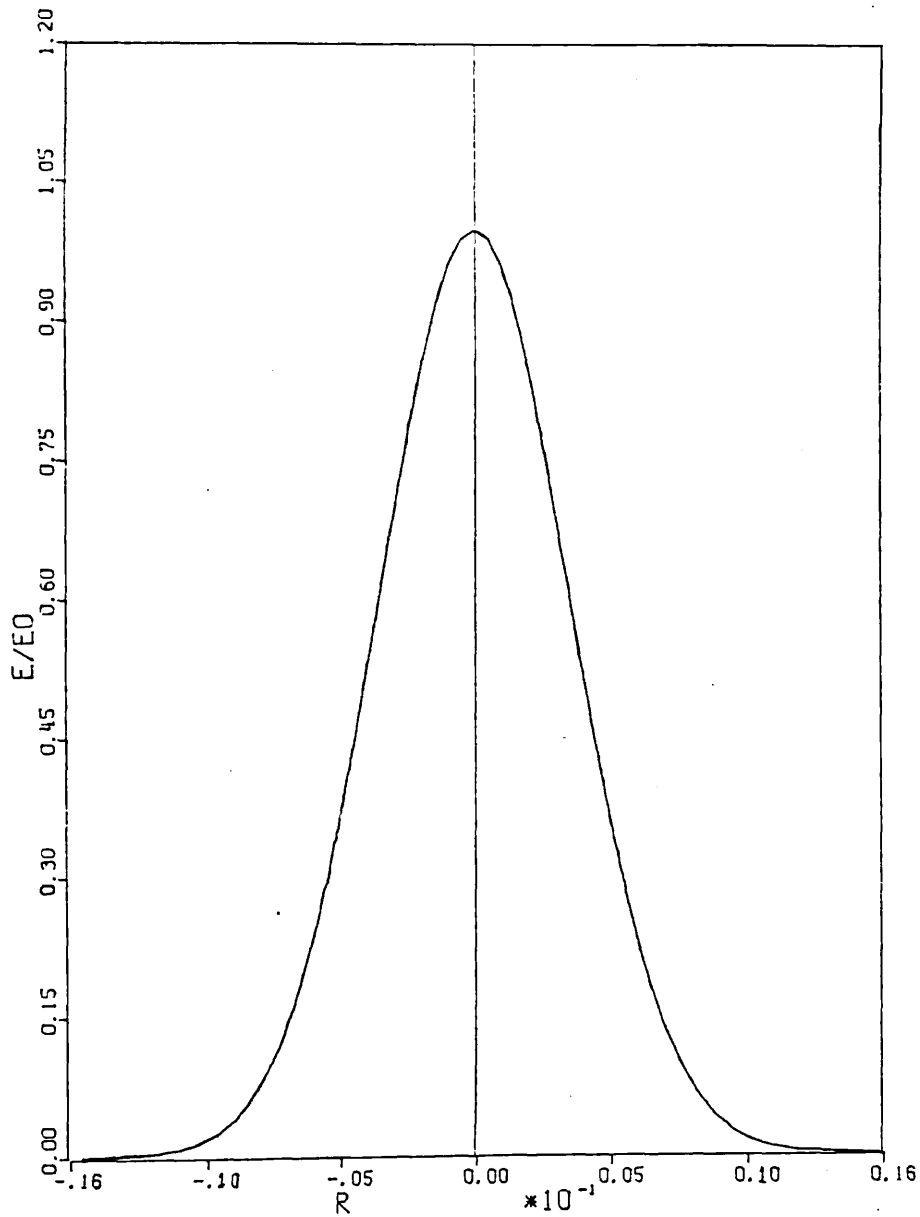


Figure 4.2. Electric field distributions for interferometers with circular mirrors (after Kogelnik and Li)

Figure 4.3. Theoretical transverse distribution of the electric field in a  $TEM_{00}$  mode at the centre of an open resonator.  $\lambda_0 = 337 \mu\text{m}$ ,  $R_0 = 0.768 \text{ m}$  and  $d = 0.16 \text{ m}$ .



The beam radius  $\omega(Z)$  and the radius of curvature of the phase front  $R(Z)$  at a distance  $Z$  along the axis are given by the following relations;

$$\omega^2(Z) = \omega_0^2 \left[ 1 + \left( \lambda_0 Z / \pi \omega_0^2 \right)^2 \right] \quad (4.6.)$$

$$\text{and } R(Z) = Z \left[ 1 + \left( \pi \omega_0^2 / \lambda_0 Z \right)^2 \right] \quad (4.7.)$$

The theory underlying the above formulae is presented in a review articles by Kogelnik and Li<sup>58</sup>.

#### 4.3. Measurement of total scattering cross-sections using an open resonator.

The open resonator technique provides a measure of the total power loss from the resonator due to an object being placed within it. This information is derived from measurements of the resonator Q-factor. The total loss comprises both the power scattered and absorbed by the object. The extinction cross section is a useful measure of the total power reradiated and absorbed by an object, when illuminated by a uniform electromagnetic wave. The extinction cross section,  $\sigma_T$ , is defined by

$$\sigma_T = \frac{\text{total power scattered and absorbed}}{\text{incident power density}} \quad (4.8.)$$

and is the sum of the total scattering,  $\sigma_s$ , and absorption cross section,  $\sigma_A$ ,

$$\sigma_T = \sigma_s + \sigma_A \quad (4.9.)$$

When  $\sigma_A$  is zero as, for example, it would be in the case of a short circuited antenna array, the extinction cross section becomes equal to the total scattering cross section. Therefore, this technique may be used to measure the total scattering cross sections of antennas when absorption is negligible. The separation and radius of curvature of the mirrors are chosen to make  $\omega_0$ , the "beam waist", large compared with the dimensions of the scattering obstacle. Also, the scatterer must be placed where the phasefront curvature is infinite,

which is at the centre of the instrument when the mirrors have equal curvature. The scattering object can then be considered to be illuminated by a plane wave. However, the field in the resonator has a standing-wave structure; the object is to deduce the power scattered under travelling-wave conditions. This can be done for any obstacle whose symmetry is such that the total power scattered and absorbed is unchanged if the direction of the incident plane wave is reversed. If there is any difference in extinction cross sections between waves travelling in the positive and negative directions then the cross section measured in the open resonator will be the average of these.

The procedure is to measure the Q-factor of the resonator without the obstacle, and then to repeat the Q-factor measurement with the obstacle in each of two positions,  $\lambda/4$  apart. If these three Q-factors are denoted respectively by  $Q_0$ ,  $Q_1$  and  $Q_2$ , the scattering cross section is given by<sup>49</sup>

$$\sigma_T = \frac{\pi d}{4} \sqrt{d(2R_0 - d)} \left[ \left\{ \frac{1}{Q_1} - \frac{1}{Q_0} \right\} + \left\{ \frac{1}{Q_2} - \frac{1}{Q_0} \right\} \right] \quad (4.10.)$$

The relationship between the power scattered and absorbed under travelling-wave and standing-wave conditions, which is the basis of equation 4.10, may be obtained as follows<sup>48</sup>.

Let  $\bar{E}_1$  and  $\bar{H}_1$  represent a plane wave travelling in the positive direction along the Z axis of the open resonator (see Figure 4.1.), and let  $\bar{E}_{S_1}$  and  $\bar{H}_{S_1}$  represent the scattered electromagnetic field due to the presence of the obstacle. The total power emerging from a closed surface,  $S_0$ , completely surrounding the object is

$$P_1 = \frac{1}{2} \operatorname{Re} \int_{S_0} (\bar{E}_1 + \bar{E}_{S_1}) \times (\bar{H}_1^* + \bar{H}_{S_1}^*) \cdot d\bar{S} \quad (4.11.)$$

where an asterisk denotes the complex conjugate.

$$P_1 = \frac{1}{2} \operatorname{Re} \int_{S_0} (\bar{E}_1 \times \bar{H}_1^* + \bar{E}_1 \times \bar{H}_{S_1}^* + \bar{E}_{S_1} \times \bar{H}_1^* + \bar{E}_{S_1} \times \bar{H}_{S_1}^*) \cdot d\bar{S} \quad (4.12.)$$

Similarly, for a wave travelling in the negative direction a similar equation may be written, with the subscript 2 used to distinguish this case.

$$P_2 = \frac{1}{2} \operatorname{Re} \int_{S_0} (\bar{E}_2 + \bar{E}_{S_2}) \times (\bar{H}_2^* + \bar{H}_{S_2}^*) \cdot d\bar{S} \quad (4.13.)$$

$$P_2 = \frac{1}{2} \operatorname{Re} \int_{S_0} (\bar{E}_2 \times \bar{H}_2^* + \bar{E}_2 \times \bar{H}_{S_2}^* + \bar{E}_{S_2} \times \bar{H}_2^* + \bar{E}_{S_2} \times \bar{H}_{S_2}^*) \cdot d\bar{S} \quad (4.14.)$$

Suppose the two fields are now superimposed. If  $\bar{E}_1$  and  $\bar{E}_2$  are equal at the origin of the axial co-ordinate Z, the resultant field will vary as  $\cos kz$ . The power scattered and absorbed by the obstacle when situated in the standing wave will be denoted by  $P_c$ . The total electric field is

$$\bar{E}_c = \bar{E}_1 + \bar{E}_2 + \bar{E}_{S_1} + \bar{E}_{S_2} \quad (4.15.)$$

and the total magnetic field is

$$\bar{H}_c = \bar{H}_1 + \bar{H}_2 + \bar{H}_{S_1} + \bar{H}_{S_2} \quad (4.16.)$$

Therefore, the total power scattered and absorbed by the object is

$$P_c = \frac{1}{2} \operatorname{Re} \int_{S_0} (\bar{E}_c \times \bar{H}_c^*) \cdot d\bar{S} \quad (4.17.)$$

$$P_c = \frac{1}{2} \operatorname{Re} \int_{S_0} (\bar{E}_1 + \bar{E}_2 + \bar{E}_{S_1} + \bar{E}_{S_2}) \times (\bar{H}_1^* + \bar{H}_2^* + \bar{H}_{S_1}^* + \bar{H}_{S_2}^*) \cdot d\bar{S} \quad (4.18.)$$

Moving the obstacle through a distance  $\lambda/4$  along the Z axis corresponds to reversing the sign of  $\bar{E}_2$  and  $\bar{H}_2$  relative to  $\bar{E}_1$  and  $\bar{H}_1$ . Thus, in relation to the object, the field now varies as  $\sin kz$ . The power scattered and absorbed will be denoted by  $P_s$ . Since the signs of the incident fields  $\bar{E}_2$  and  $\bar{H}_2$  have been effectively reversed, the signs of the scattered field  $\bar{E}_{S_2}$  and  $\bar{H}_{S_2}$  must also be reversed. Hence the total electric field is given by

$$\bar{E}_S = \bar{E}_1 - \bar{E}_2 + \bar{E}_{S_1} - \bar{E}_{S_2} \quad (4.19.)$$

and the total magnetic field given by

$$\bar{H}_S = \bar{H}_1 - \bar{H}_2 + \bar{H}_{S_1} - \bar{H}_{S_2} \quad (4.20.)$$

Letting the total power scattered and absorbed be denoted by  $P_s$ , then

$$P_s = \frac{1}{2} \operatorname{Re} \int_{S_0} (\bar{E}_S \times \bar{H}_S^*) \cdot d\bar{S} \quad (4.21.)$$

$$P_s = \frac{1}{2} \operatorname{Re} \int_{S_0} (\bar{E}_1 - \bar{E}_2 + \bar{E}_{S_1} - \bar{E}_{S_2}) \times (\bar{H}_1^* - \bar{H}_2^* + \bar{H}_{S_1}^* - \bar{H}_{S_2}^*) \cdot d\bar{S} \quad (4.22.)$$

It is straightforward to show that

$$2(P_1 + P_2) = P_c + P_s \quad (4.23.)$$

In practice, with a non-ideal resonator, it is evident that there will be losses associated with it when no scattering object is present. For a non-ideal resonator, if the Q-factor is  $Q_0$  without the scatterer present, and  $Q'$  with the scatterer present, then

$$\frac{1}{Q'} = \frac{1}{Q_0} + \frac{1}{Q} \quad (4.24.)$$

where  $Q$  is the Q-factor that would be measured if the scatterer were placed in a resonator with no intrinsic loss.

The Q-factor for any resonant system may be defined as,

$$\begin{aligned}
 Q &= \frac{2\pi f \times \text{energy stored}}{\text{power dissipated}} \\
 &= \frac{2\pi f E}{P} \quad (4.25.)
 \end{aligned}$$

The total energy, E, stored in the resonator volume  $V_o$  is given by

$$E = \int_{V_o} \frac{|\bar{S}|}{C} dV \quad (4.26.)$$

where C is the velocity of light and  $|\bar{S}|$  is the time averaged poynting flux. For a  $TEM_{00}$  mode the variation of electric field is given by equation 4.4. If the mirror separation is d then, the energy stored is given very accurately by

$$E = \int_{-\frac{d}{2}}^{+\frac{d}{2}} \int_0^{\infty} \int_0^{2\pi} \frac{|E_o|}{2\eta c} e^{-\frac{2r^2}{w^2}} r dz dr d\theta \quad (4.27.)$$

It is assumed that the mirror aperture radius is large compared with the beam radius, so that the energy stored can be considered to equal that stored in a resonator with infinite mirrors. Integrating with respect to  $\theta$  and r gives

$$E = \frac{|E_o|^2}{2\eta c} \int_{-\frac{d}{2}}^{+\frac{d}{2}} \frac{\pi w^2}{2} dz \quad (4.28.)$$

From equation 4.6,

$$E = \frac{|E_o|^2}{4\eta c} \pi w_o^2 \int_{-\frac{d}{2}}^{+\frac{d}{2}} \left| 1 + (\lambda_o Z / \pi w^2)^2 \right| dz \quad (4.29.)$$

Integrating with respect to Z, equation 4.29 becomes

$$E = \frac{E_o^2}{2\eta} \frac{\pi d w_o^2}{2c} \quad (4.30.)$$



In making measurements with this technique it is assumed that the incident poynting flux  $|\bar{S}_0| = E_0^2/2\eta$ , and so equation 4.30 becomes

$$E = |\bar{S}_0| \frac{\pi d \omega_0^2}{2 c} \quad (4.31.)$$

Substituting equation 4.31 for E in equation 4.25

$$Q = \frac{\pi^2 \omega_0^2 d |\bar{S}_0|}{\lambda_0 P} \quad (4.32.)$$

The power dissipated in an ideal open resonator into which an object is placed will be entirely due to power scattered and absorbed by the obstacle. The extinction cross section is given by

$$\sigma_T = \frac{P_1 + P_2}{|\bar{S}_0|} \quad (4.33.)$$

from equation 4.23

$$\sigma_T = \frac{P_c + P_s}{2 |\bar{S}_0|} \quad (4.34.)$$

Therefore, if an object is placed in an ideal open resonator at a point Z, where the field is a maximum, then the Q-factor of the resonator,  $Q_c$  is

$$Q_c = \frac{\pi^2 \omega_0^2 d |\bar{S}_0|}{\lambda_0 P_c} \quad (4.35.)$$

If the object is moved to a point  $Z + \lambda/4$ , where the field is a minimum, the Q-factor of the resonator,  $Q_s$  is

$$Q_s = \frac{\pi \omega_0^2 d |\bar{S}_0|}{\lambda_0 P_s} \quad (4.36.)$$

From equations 4.36, 4.35 and 4.34

$$\sigma_T = \frac{\pi \omega_0^2 d}{2\lambda} \left\{ \frac{1}{Q_c} + \frac{1}{Q_s} \right\} \quad (4.37.)$$

For a non-ideal open resonator of unloaded Q-factor  $Q_0$

$$\sigma_T = \frac{\pi^2 \omega_0^2 d}{2 \lambda_0} \left[ \left\{ \frac{1}{Q_1} - \frac{1}{Q_0} \right\} + \left\{ \frac{1}{Q_2} - \frac{1}{Q_0} \right\} \right] \quad (4.38.)$$

where  $Q_1$  and  $Q_2$  are measured with the obstacle at  $Z$  and  $Z + \lambda/4$  and  $Z$  is in the planewave region. The obstacle need not necessarily be placed at a field maximum or minimum. Substituting equation 4.5 into equation 4.38 the result in equation 4.10 is obtained.

#### 4.4. Theoretical estimate of the resonator unloaded Q.

There are three principal sources of loss in the unloaded open resonator. These are (1) diffraction loss caused by the finite sizes of the mirrors, (2) mirror surface loss due to the finite mirror conductivity, and (3) coupling loss produced by the methods employed for coupling energy into and out of the resonator. These are now dealt with in turn.

##### 4.4.1. Diffraction loss

The diffraction loss  $\alpha$  produced by a mirror of aperture diameter  $D$  is given by the expression<sup>49</sup>

$$\alpha = \exp \left\{ -\frac{D^2}{2\omega^2} \right\} \quad (4.39.)$$

, where  $\omega$  is the beam radius of the radiation at the mirror. If no other losses exist, then the unloaded  $Q$  of the resonator will be diffraction limited to  $Q_{DIFF}$  where

$$Q_{DIFF} = \frac{2 \pi d}{\lambda_0 \alpha} \quad (4.40)$$

$\lambda_0$  is the free space wavelength.

4.4.2. Power dissipated due to the finite conductivity of the mirrors.

At a distance  $r$  from the axis of the open resonator, the magnetic field has the value

$$H(r) = H_0 \exp \left\{ -\frac{r^2}{\omega^2} \right\} \quad (4.41.)$$

where  $\omega$  is the beam radius at the mirror and  $H_0$  is the on axis value of magnetic field. The power dissipated in an element of area on the mirror  $r dr d\theta$  is given by,

$$P = \frac{1}{2} R_s |H(r)|^2 r dr d\theta \quad (4.42.)$$

where  $R_s$  is the surface resistance of the metal with which the mirror is coated. The total power dissipated is given very accurately by

$$P_{TOT} = \frac{1}{2} R_s \int_0^{\infty} 2\pi r |H_0|^2 \exp \left\{ -\frac{2r^2}{\omega^2} \right\} dr \quad (4.43.)$$

Integrating equation 4.42 and multiplying by two to get the total power dissipated in both mirrors we find

$$P_{DISS} = R_s \frac{\pi \omega^2}{2} |H_0|^2 \quad (4.44.)$$

The on axis time averaged poynting flux within the cavity is

$$|\bar{S}_0| = \frac{1}{2} \eta |H_0|^2 \quad (4.45)$$

From equations 4.25, 4.31, 4.44 and 4.45 the surface resistance loss on the mirrors limit the unloaded  $Q$  to  $Q_{DISS}$ , where

$$Q_{DISS} = \frac{\pi d \eta}{\lambda_0 R_s} \quad (4.46.)$$

assuming that no other losses are present.

4.4.3. Coupling Loss.

The two principal methods of coupling radiation to an open resonator at submillimetre wavelengths are

beam splitter coupling and hole coupling.

For a beam splitter coupled resonator, the unloaded Q will be limited to  $Q_{\text{COUP}}$  if no other losses are present<sup>56</sup>.

$$Q_{\text{COUP}} = \frac{2 \pi d}{S \lambda_0} \quad (4.47.)$$

where  $S^2$  is the coupling factor of the beam splitter.

$$S = \frac{\sqrt{2} (\epsilon_r - 1) \pi t}{\lambda_0} \quad (4.48.)$$

,  $t$  is the plate thickness and  $\epsilon_r$  the relative permittivity.

For an open resonator with coupling holes at the centre of each mirror the major loss will be from hole radiation. For a circular aperture, the radiation intensity  $K$  is given by<sup>27</sup>

$$K = \frac{2 E_0^2 \pi^2 a^4}{\eta \lambda_0^2} \cos^4 \frac{\theta}{2} \left| \frac{J_1(ka \sin \theta)}{ka \sin \theta} \right|^2 \quad (4.49.)$$

where  $a$  is the hole radius. If  $ka \gg 1$  (about ten times is the lower limit) then most of the power goes into the main beamwidth  $\theta_0$  given by

$$\theta_0 = \frac{1.22 \lambda}{a} \quad (4.50.)$$

the power dissipated,  $W$ , is

$$W = 2 \int_0^{\theta_0} \int_0^{2\pi} K \sin \theta \, d\theta \, d\phi \quad (4.51.)$$

The factor two in equation 4.51 arises because there are two coupling holes, one in each mirror. Substituting equation 4.49 into 4.51 and integrating

$$W = \frac{1}{2} \frac{E_0^2 \pi a^2}{\eta} [1 - (J_0^2 \theta_0 + J_1^2 \theta_0)] \quad (4.52.)$$

where  $\theta_0 = ka \sin \theta_0$ . As  $E_0 = \eta H_0$  then we can compare

the mirror dissipation with the hole radiation.

$$\frac{W}{P_{DISS}} = \frac{Q_{DISS}}{Q_{COUP}} = \frac{\eta a^2}{R_s \omega^2} [ 1 - (J_0^2 \theta_0 + J_1^2 \theta_0) ] \quad (4.53.)$$

$\omega$  is the beam radius at the mirrors.

#### 4.4.4. Unloaded Q of the open resonator.

The dimensions of the open resonator were chosen to avoid mode degeneracies between the  $TEM_{00}$  and the higher order modes. For mirror radii of 0.768 m and spacing 0.16 m, equation 4.1 suggested that mode degeneracies would not be a problem. However, it was discovered that this was incorrect, so one of the mirrors was stopped down to an aperture diameter of 2cm to eliminate the higher order modes. The beam radius  $\omega_0$  at the centre of the resonator, assuming the dimensions above, is derived from equation 4.5. It is  $4.50 \times 10^{-3}$  m which is  $\approx 13$  wavelengths at 337  $\mu$ m. The spot radius at the mirrors is found from equation 4.6 and is  $4.88 \times 10^{-3}$  m. From equations 4.39 and 4.40,  $\alpha$  from equation 4.39 is found to be  $2.25 \times 10^{-4}$  and this limits  $Q_{DIFF}$  to  $1.32 \times 10^7$ .

The mirrors were coated with aluminium for which the surface resistance  $R_s$ , at 891 GHz, is  $0.438\Omega$  from table 2.2. From equation 4.46 it is found that the unloaded Q factor due to finite mirror surface resistance,  $Q_{DISS}$ , is  $2.56 \times 10^6$ .

It was decided to use coupling holes rather than a beam splitter system for coupling energy in and out of the open resonator. The beamsplitter has the disadvantage of reducing the usable volume of the resonator and may distort the beam profile. 1mm diameter coupling holes were decided upon. From equation 4.50 the value for the beamwidth  $\theta_0$  is 0.411 radians. Hence,  $\theta_0 = 7.45$ . Now,  $J_0$  (7.45)

= 0.3 and  $J_1(7.45) = 0.09$ . Therefore, from equation 4.53

$$\frac{Q_{DISS}}{Q_{COUP}} = 32.5$$

as  $Q_{DISS}$  equals  $2.56 \times 10^6$  then  $Q_{COUP}$  is equal to 78,700..

From the values obtained for the diffraction, mirror and coupling losses, it is evident that coupling loss is the dominant mechanism which determines the unloaded resonator Q. From the above considerations the open resonator was expected to have an unloaded Q in the region of 70,000.

#### 4.5. Design of the scanning submillimetre open resonator.

The radiation source employed for the experimental measurements is a CW HCN laser providing 10 mW of power at 337  $\mu\text{m}$  (corresponding to a frequency of 891 GHz). The output coupling is by means of a vertical beamsplitter and the output radiation is therefore horizontally polarised. The laser is also mode peak locked for high amplitude and frequency stability. The laser system is more fully described in Chapter 6.

The laser could be used to provide a swept frequency source by scanning the laser cavity through the gain profile of the cavity medium. However, this technique does not provide sufficient frequency deviation to enable measurements to be made of the open resonator Q's encountered, which are typically  $\approx 10^5$ . It is therefore necessary to employ a scanning open resonator and keep the laser frequency fixed.

The mode spectrum of the open resonator is given by equation 4.1. For a  $\text{TEM}_{00q}$  mode, equation 4.1 simplifies to

$$\frac{f}{f_0} = (q + 1) + \frac{1}{\pi} \arccos(1 - d/R_0) \quad (4.54.)$$

where  $f_0 = C/2d$  and  $f = f_{00q}$

differentiating equation 4.54 with respect to  $d$

$$\frac{\delta f}{\delta d} = -\frac{f}{d} + \frac{C}{2\pi d R_0 \sqrt{(1 - (1 - d/R_0)^2)}} \quad (4.55.)$$

The second term on the righthand side of equation 4.55 is small compared with the first term. Therefore

$$\frac{\delta f}{f} = -\frac{\delta d}{d} \quad (4.56.)$$

and as  $\delta f/f = Q^{-1}$ , neglecting the sign

$$Q = \frac{d}{\delta d} \quad (4.57.)$$

The resonance curve of the resonator can be obtained by mechanically scanning one of the mirrors. The  $Q$  is obtained from the mirror separation and the difference in mirror separations between -3 dB power points, for a given mode. With the upper limit of the unloaded resonator  $Q$  known, the amount of mirror movement required to scan through a fundamental  $TEM_{000}$  mode may be estimated. For an unloaded  $Q$  of 70,000 and a mirror separation of 0.16 m a scanning distance of 2.3  $\mu\text{m}$  would be required to sweep between the -3 dB points of the resonance curve. In order to sweep from baseline through to baseline a movement of twice this amount would be required. When the resonator is loaded with a scattering object,  $Q$ 's as low as 10,000 may have to be measured, so a scanning distance of 32  $\mu\text{m}$  might conceivably be necessary.

A number of possible techniques for scanning the mirror were considered. Loudspeaker type movements suffer from the disadvantage of being mechanically unstable and sensitive to external vibration. Piezo electric cylinders could have been used, but the drive voltages required to sweep through a single mode of an unloaded resonator were found to be too high. As an example, for a Vernitron PZT-5A ceramic ring 3" long and 0.2" thick, a potential of 600 volts would be required to produce a 1.15  $\mu\text{m}$  movement.

Because the open resonator is a scanning one, mode degeneracies can be a problem<sup>60</sup>. A facility permitting continuous adjustment of the mirror separation to avoid mode degenerate regions was required. It was decided to employ a crossed roller slide for the mirror scanning system, and was quite adequate for supporting one of the resonator mirrors and the Golay detector. The slide was driven by a 1mm pitch precision leadscrew. The leadscrew was driven by an 800 step per revolution stepping motor through a 25:1 anti-backlash reduction gearbox. The theoretical resolution on the mirror drive was 0.05  $\mu\text{m}$  per step.

The mechanical and electronic aspects of the open resonator are discussed in Chapter 5.



## CHAPTER FIVE

### A COMPUTER CONTROLLED SUBMILLIMETRE OPEN RESONATOR.

#### 5.1. Introduction.

The mechanical complexity of the open resonator, coupled with the repetition of the actions required when making measurements, suggested the use of an automatic control system for running the instrument. This would speed up the measurement process, as the required manual re-adjustments of the sample and the scanning mirror, normally carried out by the operator between measurements, could be made by the automatic control system. It was decided that a microcomputer should be used to control the instrument. The main requirement of the microcomputer was, that it could support a high level language with floating point arithmetic and be capable of controlling peripheral interfaces from the high level language. Therefore, the control of the instrument, the logging of the data, and the subsequent processing of this data to calculate values for the measured total scattering cross sections, could be done with programs written in a high level language. This had the advantage that the software could be written quickly and changed easily, so making the instrument software reconfigurable. For example, the instrument could be changed from one measuring the total scattering cross sections of scatterers to one making dielectric constant and loss tangent measurements on materials, by simply loading another program.

The AIM 65 microcomputer manufactured by Rockwell was chosen to run the instrument. This was a single board microcomputer having a full size QWERTY keyboard, and a 20 column thermal printer onboard for providing hardcopy. It was available with a maximum of 4K of onboard RAM and had a powerful 8K monitor in ROM which allowed mnemonic machine code entry. The machine also supported an 8K

BASIC interpreter which fulfilled the high level language specification stated previously.

A number of peripheral units were built for interfacing the AIM 65 to the open resonator system. These also included some general purpose interfaces which were necessary for the efficient running of the system, such as the VDU interface, EPROM programmer, and the digital plotter interface. The mechanical movements for the mirror and sample positions, and the sample orientation, were driven by stepping motors. Position transducers were used to measure and monitor their relative movements. The mechanical and electronic details are fully described in the subsequent sections.

### 5.2. Mechanical Design.

Figure 5.1 illustrates the geometry of the open resonator. Radiation from the HCN laser was focussed through a 1mm diameter coupling hole in the fixed mirror, with an f-2 polythene lens housed in a brass telescope tube. The scanning mirror and Golay cell detector were mounted on a cross roller slide. Radiation was coupled via a 1mm coupling hole through to the detector. This slide was moved by a 1mm pitch leadscrew which was driven with an 800 step stepping motor through a 25:1 antibacklash reduction gearbox. This gave a theoretical resolution of 0.05  $\mu\text{m}$  per step for the mirror drive.

The supporting framework for the resonator components can be seen from the photograph in Figure 5.4. It consisted of two 12.5 inch diameter, 1 inch thick, aluminium plates spaced with four 17 inch long invar spacers. The fixed mirror was attached to one of the end plates which had a 2½ inch diameter hole in the centre to allow radiation to be coupled through into the resonator. All motor drives were supported on milled solid aluminium mounting flanges which were mechanically clamped to the invar spacers. The frame of the instrument, described above, could be slid into and out of a vacuum tank which also

served as a radiation shield for the instrument. A photograph of the instrument in its extracted position, and the tank is shown in Figure 5.2.

The geometry of the sample supporting movements is illustrated in Figure 5.3. These movements allowed the sample to be moved in the longitudinal and transverse directions between the resonator mirrors. The longitudinal slide, with a 1mm pitch leadscrew, was driven by a 800 steps per revolution stepping motor through a 12.5 to 1 antibacklash reduction gearbox. The transverse slide, with a 1mm pitch leadscrew, was driven with a stepping motor, having 200 steps per revolution, through a 12.5 to 1 antibacklash reduction gearbox. The theoretical resolutions on the longitudinal and transverse drives were, 0.1  $\mu\text{m}$  per step and 0.4  $\mu\text{m}$  per step, respectively.

Linear variable differential transformer displacement transducers (LVDT's), were mounted to monitor the mirror, and sample longitudinal and transverse, movements. The resolution of these transducers is theoretically infinite. However, as the output voltages of these transducers were digitised by a 12 bit analogue to digital converter with polarity indication (giving a resolution of 0.5mV/bit), then the theoretical resolution of the transducer was 0.125  $\mu\text{m}$ . A rotary position transducer was mounted so as to measure the angle of incidence of the sample with respect to the axis of the resonator. The output of this transducer had an 8 bit resolution per revolution. Hence, the angle of incidence could be measured with a resolution of 1.4<sup>o</sup>. The movements used to control the angle of incidence and sample polarisation were geared rotary mounts having a clear aperture of 2 inches diameter. The stage was kinematically supported and controlled through a worm drive, with turns ratio of 120:1. The shafts were driven by 4 step per revolution stepping motors giving a theoretical resolution of 0.75<sup>o</sup> per step.

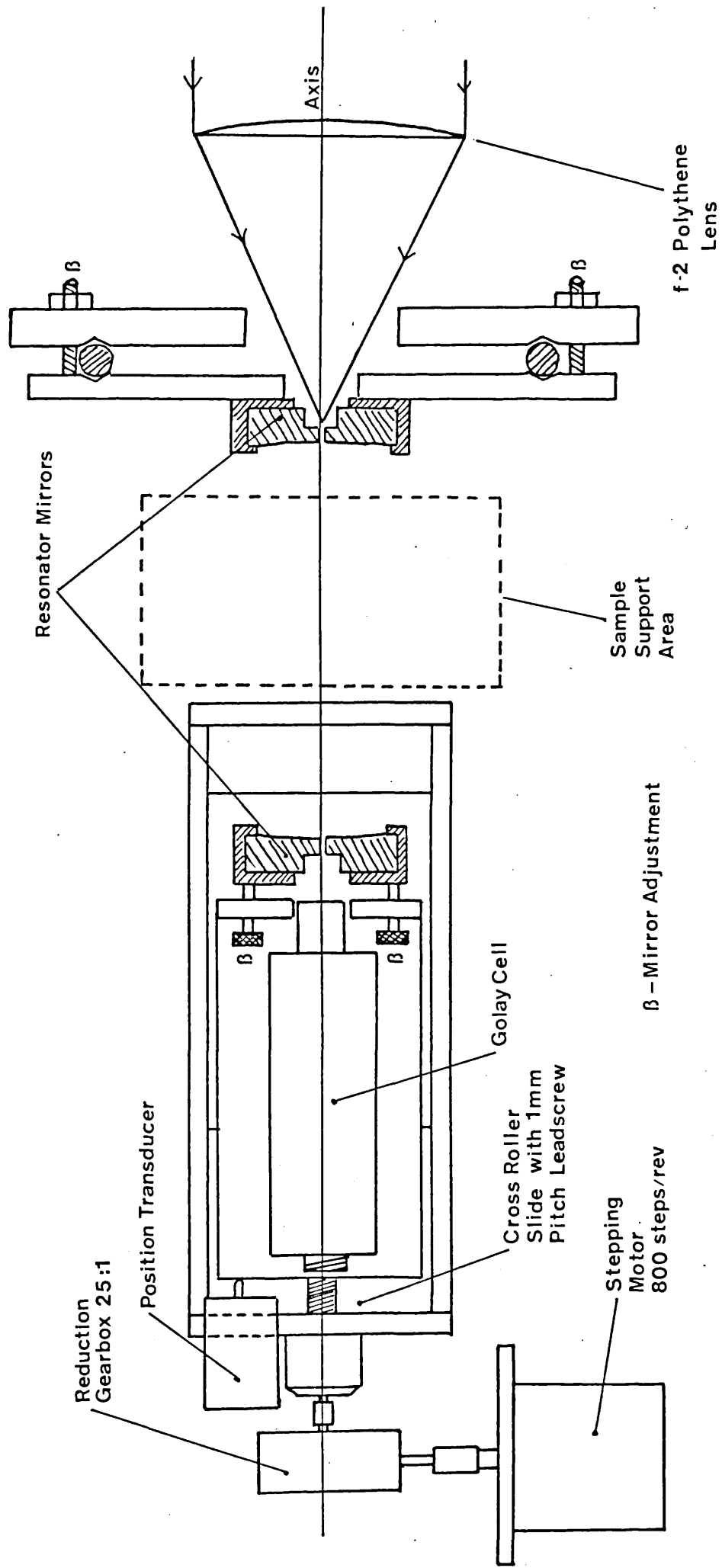


Figure 5.1. Schematic diagram of the open resonator.

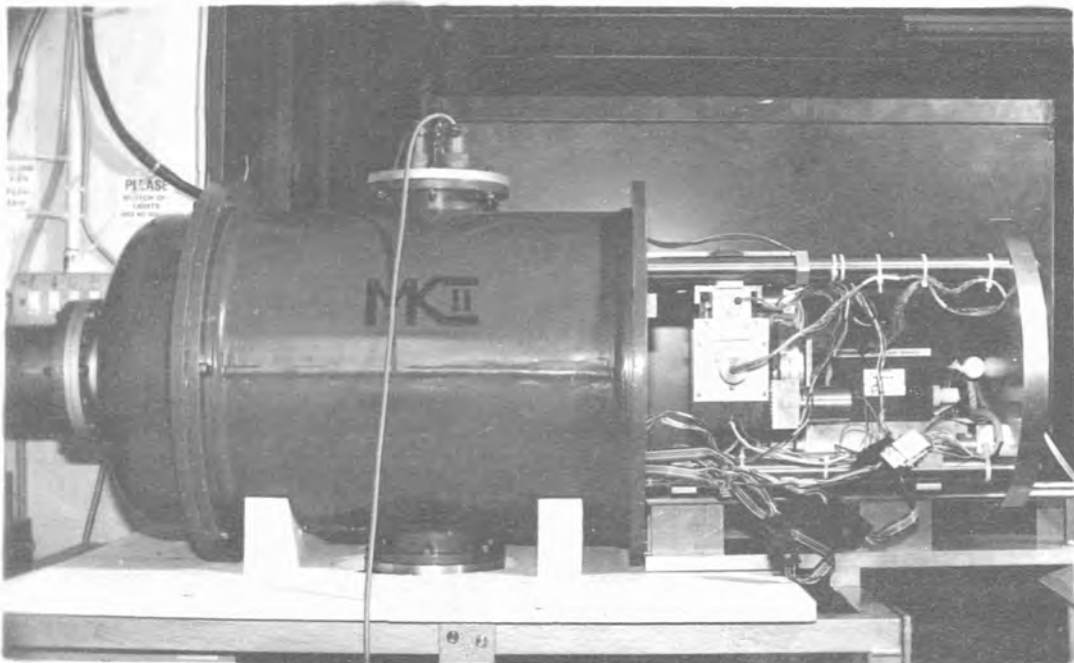
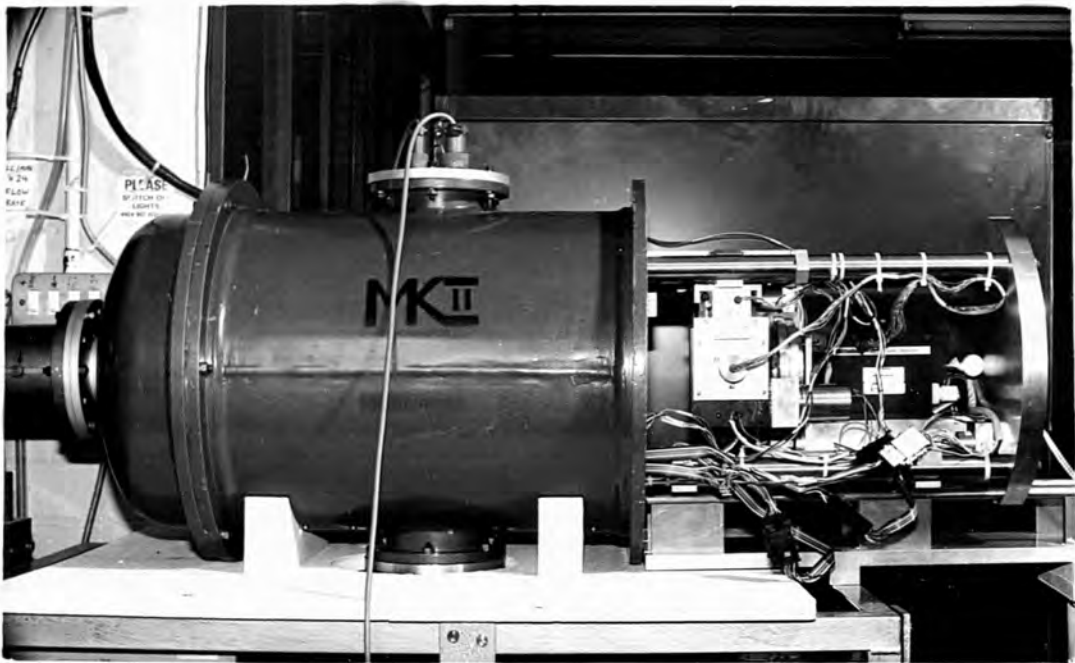


Figure 5.2. Open resonator extracted from vacuum tank which also acts as a radiation shield.



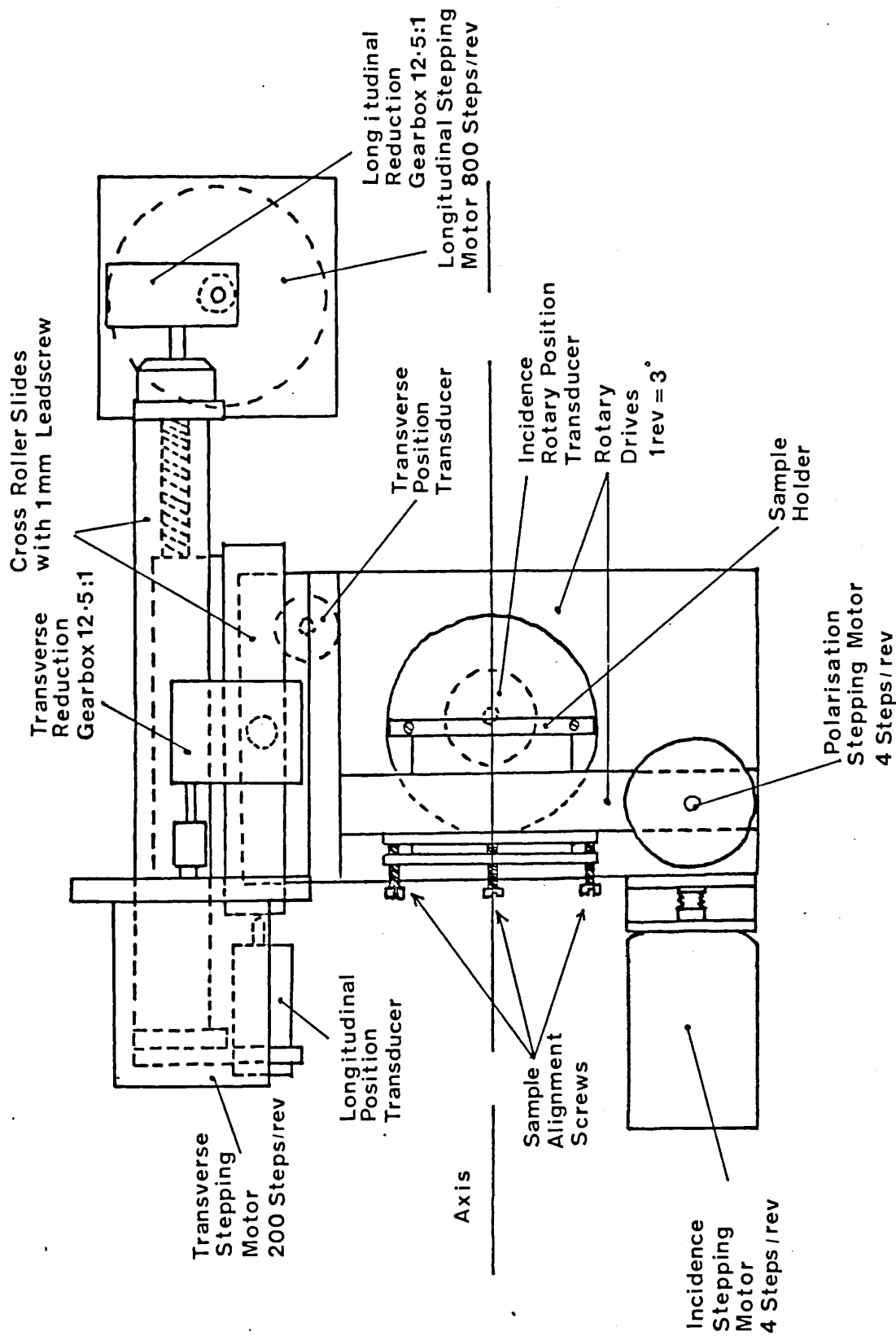


Figure 5.3. Schematic diagram of the sample movements.

### 5.3 Electrical Design.

In this section the electrical designs relating to the stepping motors and linear position transducers are described. Figures 5.5 and 5.6 show respectively, the rack units which hold the stepping motor drive boards and power supplies, and the linear position transducer power supplies and meter unit. The circuit diagram for the stepping motor drive board to computer peripheral interface circuit is shown as Figures A.3.1 and A.3.2 in Appendix 3. These circuits converted the input and output signals for the computer peripheral unit, which were 5 volt TTL level signals, to the 24 volt CMOS levels required by the stepping motor interfaces. Figure A.3.3 in Appendix 3 is the circuit for the dual 24 volt 6 amp power supply for the stepping motors. This power supply had to be well smoothed and regulated to prevent spurious stepping by the motors.

The circuitry illustrated in Figure A.3.4 in Appendix 3 supplied the precision 10 volt, reference voltage required by the LVDT's. The outputs from these transducers were 200 mV per 0.001 inches when fed into 10 K $\Omega$  loads. A digital panel meter could be switched to monitor the output voltages from any one of the three transducers or the transducer supply voltage. The transducer output voltages were fed via co-axial cables to the analogue to digital converter. The 10 volt supply voltage was maintained by a band gap reference integrated circuit, and buffered with a power amplifier to obtain sufficient current for the transducers. The photograph in Figure 5.7 shows the open resonator undergoing electrical testing before it was commissioned.

### 5.4. Computer Control System Design.

All the peripherals, with the exception of the EPROM programmer, which was interfaced through the system "Versatile Interface Adapter" (VIA), were interfaced onto the system address and data busses. They therefore



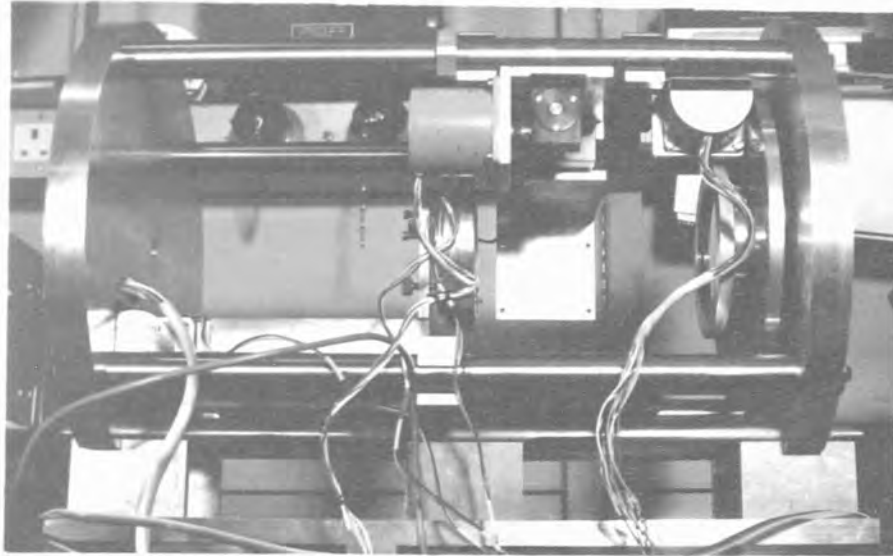


Figure 5.4. Open resonator construction.

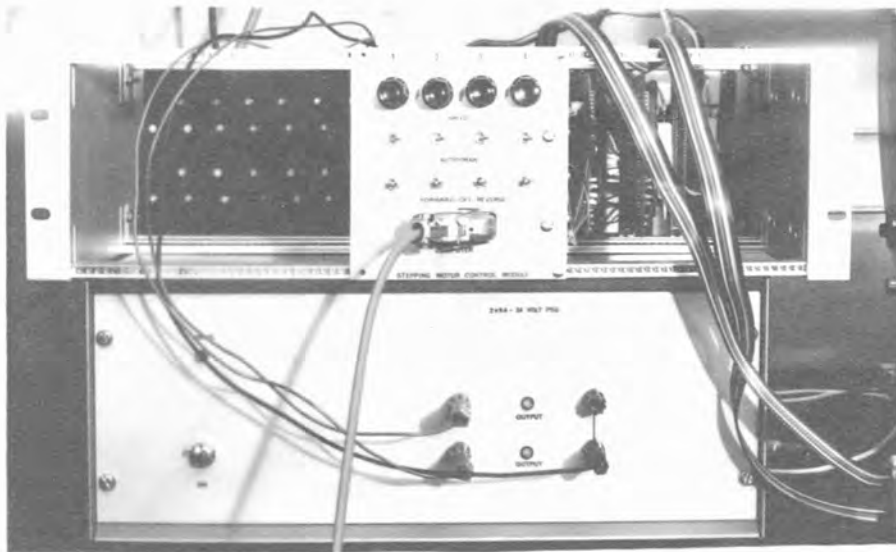
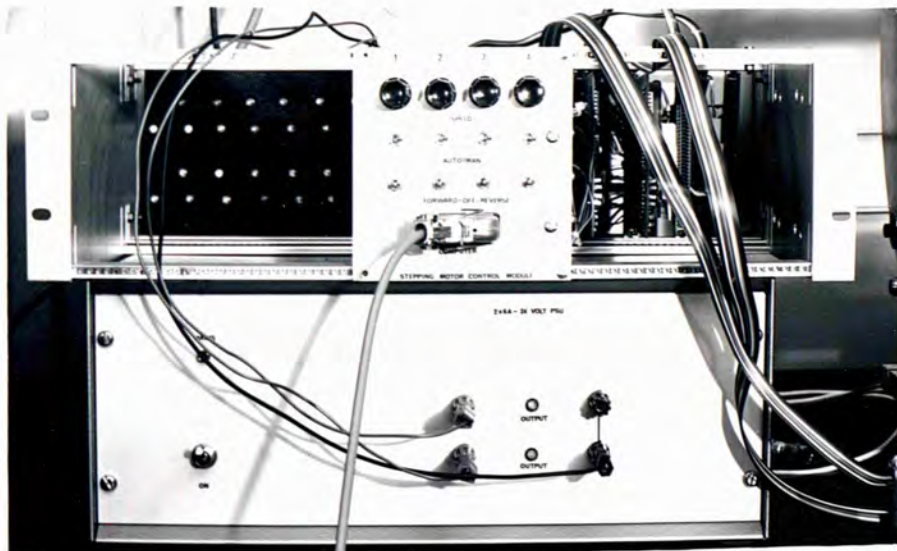
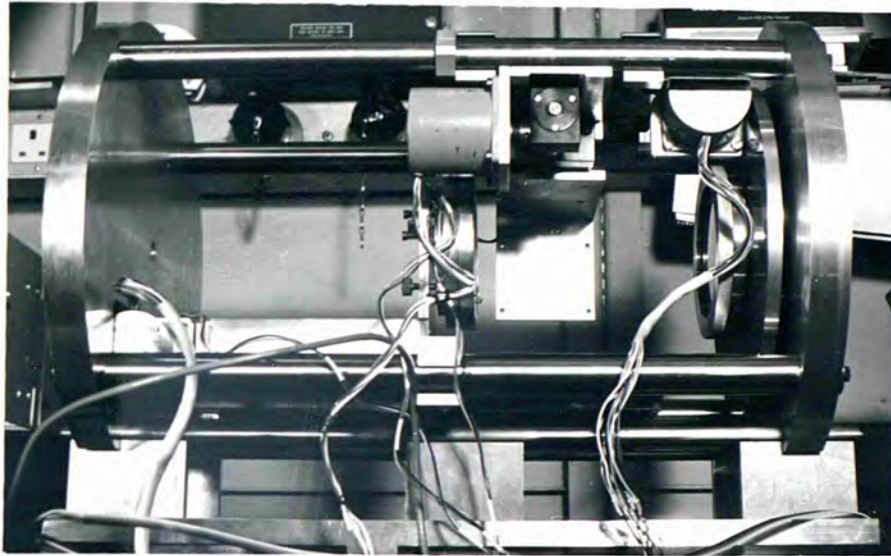


Figure 5.5. Stepping motor drive board rack and power supply unit.



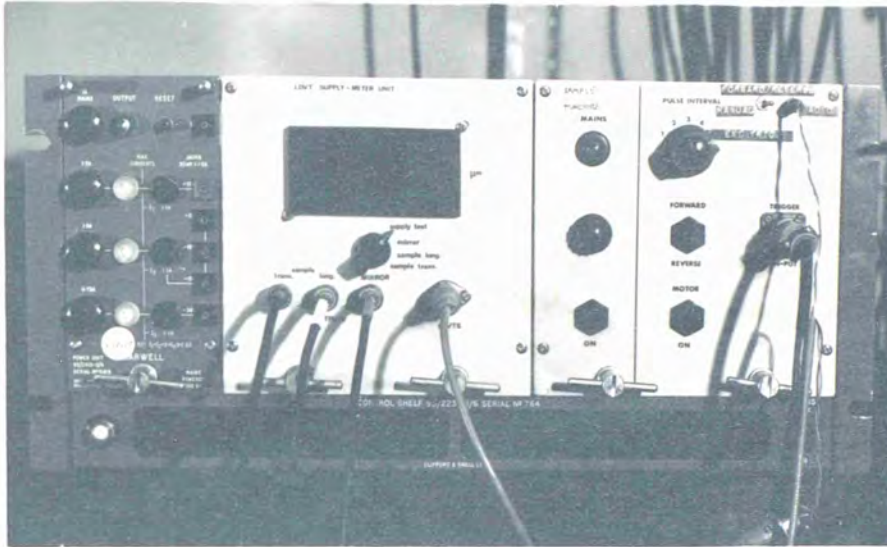


Figure 5.6. Linear position transducer power supply and meter unit and Slo-syn stepping motor unit.

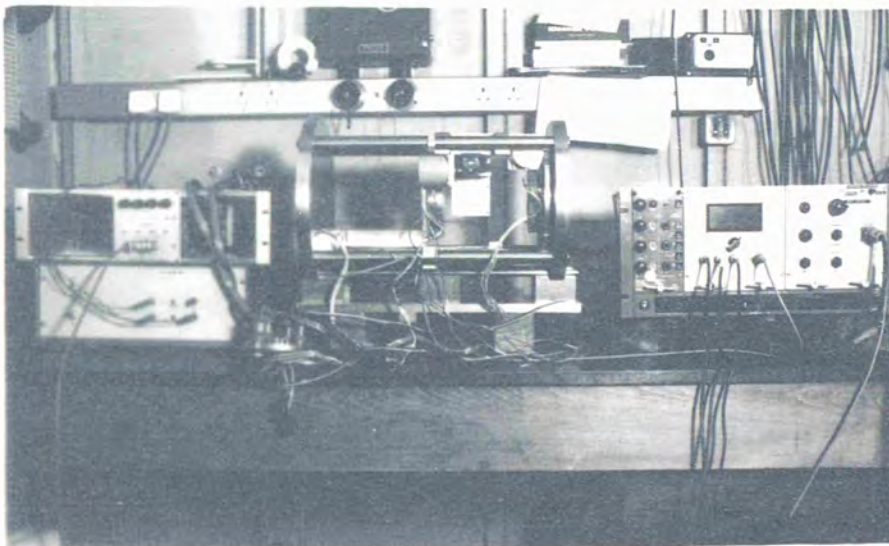
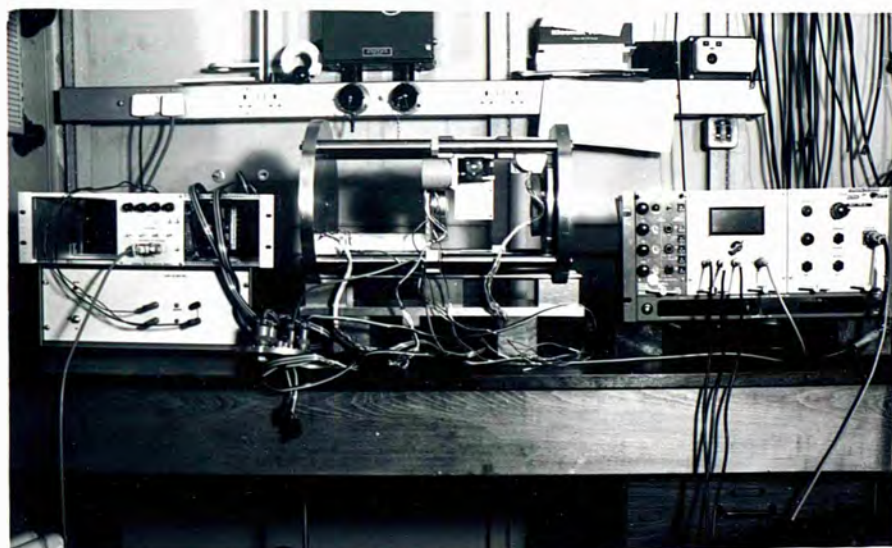
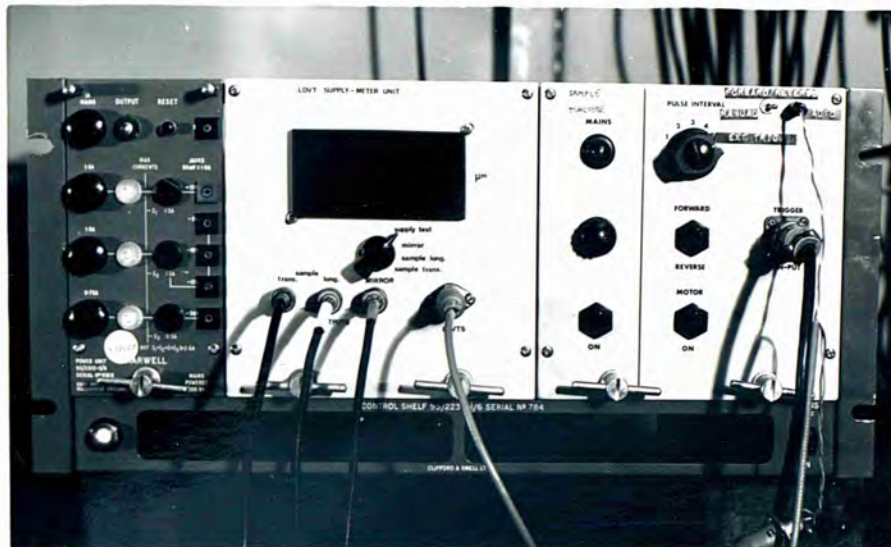


Figure 5.7. Electrical testing of the open resonator.



appeared as memory locations to the microcomputer and, as such, could be controlled directly from the high level BASIC language PEEK and POKE commands. Although this approach made the system more hardware intensive it had the advantage that the software could be completely written in BASIC, so reducing programming time and allowing rapid reconfiguration of the system. Figure A.3.5 in Appendix 3 shows the circuit diagram for the peripheral crate buffer module. This buffered the address and data bus lines, available from the AIM 65 expansion connector, so they could feed up to 9 peripheral boards. The photograph in Figure 5.8 shows the AIM 65 microcomputer and peripheral crate. A close up photograph of the peripheral crate can be seen in Figure 5.9. The AIM 65 had 4K of onboard RAM. This was extended to 12K with two 4K RAM boards which plugged into the peripheral crate. The circuit for the 4K RAM boards is shown in Figure A.3.6 in Appendix 3. The address ranges of the RAM boards were from  $1000_{16}$  to  $1FFF_{16}$  and from  $2000_{16}$  to  $2FFF_{16}$ . A 4K EPROM board was also built to hold the machine code routines for the VDU interface and the BASIC arctangent function, which was not available on the BASIC ROM. Figure A.3.7 in Appendix 3 shows the 4K EPROM board circuit. The address range of the ROM board was from  $9000_{16}$  to  $9FFF_{16}$ . The address ranges that can be accessed on the peripheral crate were selected by means of the dual in line switches on the buffer module. The peripheral units are described in subsequent sub-sections.

#### 5.4.1. 12 Bit 8 Channel Analogue to Digital Converter.

A multichannel design was chosen for the analogue to digital (A - D) converter because a number of analogue signals had to be monitored by the microcomputer. These were, the Golay detector output and the three LVDT outputs.

The A - D converter design was based on the Intersil ICL 7109 12 bit A - D converter integrated circuit. This



Figure 5.8. AIM 65 Microcomputer and Peripheral Crate.

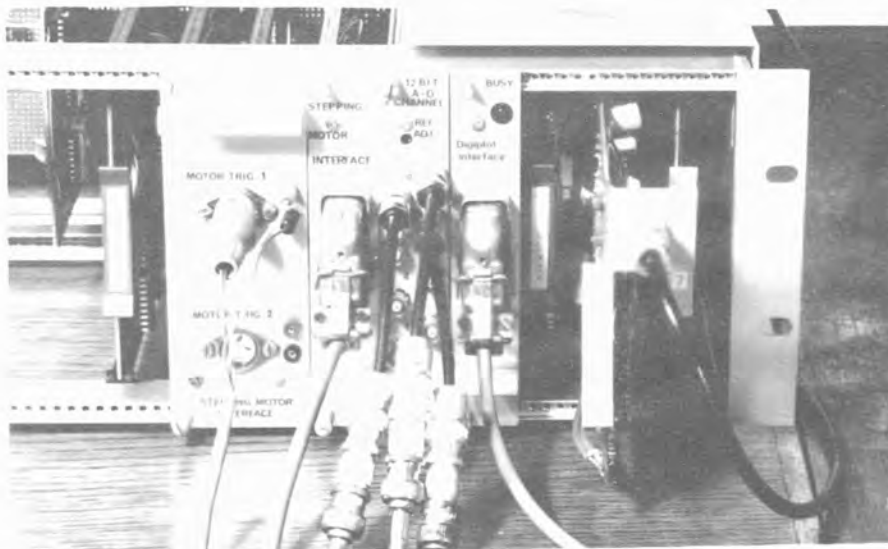
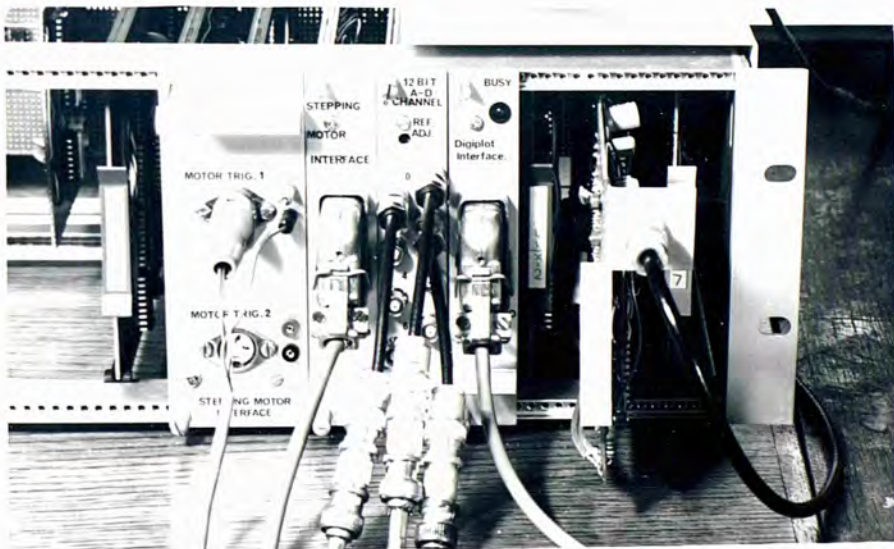


Figure 5.9. Close up of Peripheral Crate.



CMOS LSI chip featured 12 bit binary outputs with overrange and polarity bits. In the design a 2.048 volt reference input was used to give a range of  $\pm 4.096$  volts and 1mV per bit sensitivity. The 8 analogue inputs were multiplexed with a CMOS 4051 analogue multiplexer. Each input could range from -5 to +5 volts so covering the A - D converter range of -4.096 to +4.096 volts. The overrange bit was set if the input exceeded this input range in either the positive or negative directions. Figures A.3.8 (a), (b), (c) and (d) in Appendix 3 show the circuit designs for the A - D converter. The peripheral address allocations and BASIC commands are given in Appendix 3.

#### 5.4.2. Stepping Motor Interfaces.

Two types of stepping motor interfaces were designed and built for use with the Astrosyn and Slo-syn stepping motor drives that were used in the instrument. The Slo-syn motor was used to drive the transverse sample movement and Astrosyn motors were used on all the other drives.

The dual stepping motor interface was capable of controlling two stepping motor drive units of the Slo-syn type. These were modified to allow for external clock pulse inputs and forward/reverse capability. The design allowed the microcomputer to initiate up to 255 motor steps to occur with a single command, as 8 bits were available on the data bus. Opto-isolators were used in the signal pulse interfaces between the peripheral and motor drive boards to ensure noise immunity and allow flexibility in interfacing. The forward/reverse signals were available at the outputs of open collector gates, to drive the relays used to provide external forward/reverse control in the motor drive units. By reading the value of the status register of the peripheral, it was possible to ascertain the direction setting of the individual motors and whether or not a stepping sequence was in operation. The circuit designs for this inter-



face are shown in Figures A.3.9 (a), (b) and (c) in Appendix 3. The address allocations and BASIC commands for the dual stepping motor interface are given in Appendix 3.

The quad stepping motor interface was designed to interface the AIM 65 microcomputer to the four Astrosyn stepping motor drive boards. The "on board" oscillator frequency was available on the drive board edge connectors for monitor and control purposes. The motors could be turned on and off, and the direction of rotation changed, by external control signals. The circuit designed for controlling the stepping motors is shown in Figures A.3.10 (a), (b) and (c) in Appendix 3. The design allowed the microcomputer to initiate up to 256 motor steps on each motor. A parallel loaded down counter, clocked from the frequency monitor board outputs, could be loaded with the required number of steps and a flip flop set, which turned motor on and started the clock pulses. These clock pulses would cause the counter to count down, resetting the flip-flop when the counter reached zero, so turning the motor and the clock off. Forward and reverse direction control was obtained by latching bit 0 of the data bus by means of D type flip flops. The number of steps required was loaded into the 8 bit up/down counter appropriate to the stepping motor. If the up/down counter was loaded with N then the number of steps executed was N + 1. The address allocations and basic commands used for this peripheral are described in Appendix 3. By reading the status register, it was possible to verify whether or not stepping sequences were occurring on any of the motors.

#### 5.4.3. Rotary Position Transducer Interface.

This interface was designed to interface the rotary position transducer, used to measure the angle of incidence of the sample with respect to the resonator axis, to the AIM 65 microcomputer. The circuit diagram

for this interface is shown in Figure A.3.11 (a) and (b) in Appendix 3. The position transducer was of the brush contact type and employed a V scan system to eliminate code ambiguities. It had a resolution of 8 bits per turn. The circuit used for converting the V-scan code to natural binary code, which was displayed on the LED unit, is shown in Figure A.3.11 (b) in Appendix 3. The binary output is read as an 8 bit word by the micro-computer.

#### 5.4.4. Visual Display Unit Interface for the AIM 65 Microcomputer.

The design for the visual display unit (VDU) was based around the Thomson - CSF SF.F. 96364 CRT processor integrated circuit. The video output was CCIR compatible (i.e. 50 Hz, 625 lines). The circuit employed was identical to the SF. KEX. 68364. 4-0. 4 page VDU circuit described in the Thomson - CSF manual on the CRT processor IC, and is shown in Figure A.3.12 (b) in Appendix 3. The 4 page character ROM was replaced by a 1 page version due to non availability, with the result that some functions were not available. The circuit for the hardware interface between the AIM 65 and the VDU controller is shown in Figure A.3.12 (a) in Appendix 3. The VDU had full wrap-around pageing of the four pages. Each page was capable of supporting 16 lines of 64 characters length. The software routines, that were written so as to make the VDU interface compatible with the AIM 65, are described in Appendix 3. They were stored in EPROM on the EPROM board, which was described earlier.

#### 5.4.5. Digital Plotter Interface.

The Wantabe instruments "Digi-Plot" intelligent plotter was used with the AIM 65 microcomputer to provide graph plotting functions. The command table for the digital plotter is given in Table 5.1. Figures A.3.13 (a) and (b) in Appendix 3 shows the interface circuitry for the digital plotter. The 7 bit ASCII instruction codes

TABLE 5.1.  
PLOTING COMMANDS

Command name	Input format	Function (All coordinates are integers in units of 0.1 mm)
LINE TYPE	Lp (Terminator)	Sets type of line for vector drawing; p = 0 indicates a solid line, and p = 1 indicates a broken line. Once specified, the same line type is maintained until reset. However, when the power is switched on the solid line setting is always assumed. This setting affects the DRAW and RELATIVE DRAW commands.
LINE SCALE	Bℓ (Terminator)	Specifies the pitch of a broken line. The lengths of the line segments and gaps are both equal to ℓ, which must be not more than 127; thus the pitch is actually 2ℓ. Once specified, the setting holds until reset. LINE SCALE and LINE TYPE commands may appear independently. (See note 1.)
DRAW	D x <sub>1</sub> , y <sub>1</sub> , x <sub>2</sub> , y <sub>2</sub> ..... x <sub>n</sub> , y <sub>n</sub> (Terminator)	If (x <sub>0</sub> , y <sub>0</sub> ) is the present position, draws series of vectors: (x <sub>0</sub> , y <sub>0</sub> ) → (x <sub>1</sub> , y <sub>1</sub> ) → (x <sub>2</sub> , y <sub>2</sub> ) → ... → (x <sub>n</sub> , y <sub>n</sub> ) Here all points x <sub>i</sub> , y <sub>i</sub> are specified in absolute coordinates by up to 4-digit integers. In other words (100, 100) represents the point x = 10mm, y = 10mm. (See note 2 on vector interpolation)
MOVE	M x, y (Terminator)	Moves with the pen up to position (x, y) in absolute coordinates. If a series of points x <sub>1</sub> , y <sub>1</sub> , x <sub>2</sub> , y <sub>2</sub> , ..... x <sub>n</sub> , y <sub>n</sub> are specified as for the DRAW command, the pen performs the same movement with the pen raised.
RELATIVE DRAW	I Δx <sub>1</sub> , Δy <sub>1</sub> , Δx <sub>2</sub> , Δy <sub>2</sub> ..... Δx <sub>n</sub> , Δy <sub>n</sub> (Terminator)	If (x <sub>0</sub> , y <sub>0</sub> ) is the present position, draws a series of vectors: (x <sub>0</sub> , y <sub>0</sub> ) → (x <sub>0</sub> + Δx <sub>1</sub> , y <sub>0</sub> + Δy <sub>1</sub> ) → (x <sub>0</sub> + Δx <sub>1</sub> + Δx <sub>2</sub> , y <sub>0</sub> + Δy <sub>1</sub> + Δy <sub>2</sub> ) → ... → (x <sub>0</sub> + ∑ <sub>n=1</sub> <sup>n</sup> Δx <sub>i</sub> , y <sub>0</sub> + ∑ <sub>n=1</sub> <sup>n</sup> Δy <sub>i</sub> ) In other words, the parameters specify the increments for each vector rather than the absolute coordinates.
RELATIVE MOVE	R Δx, Δy (Terminator)	Moves with the pen up from present position (x <sub>0</sub> , y <sub>0</sub> ) to (x <sub>0</sub> + Δx, y <sub>0</sub> + Δy). As for RELATIVE DRAW, a series of increments may be specified.
AXIS	X p, q, r (Terminator)	Draws a coordinate axis; p = 0 specifies a Y axis, and p = 1 specifies an X axis. (The axes must be parallel to the axes of the plotter.) A segment of length q is drawn, and then a graduation; this is repeated r times. For example, if X1, 150, 6 is specified, an axis is drawn in the X direction with 6 segments of length 15mm, making a total length of 90mm. When the axis is completed, the pen remains down and waits for the next command. (See note 3 for example.)
HOME	H (Terminator)	Returns with the pen raised to the origin set when power was turned on. Thus this command is equivalent to M0, 0 except that if the alarm lamp is on, it goes off when the HOME command is obeyed, and the pen returns to the origin.

TABLE 5.1.  
PLOTTING COMMANDS

Command name	Input format	Function (All coordinates are integers in units of 0.1 mm)
ALPHA SCALE	$S_n$ (Terminator)	<p>Specifies the size of characters and marks, by an integer from 0 to 15.</p> <p>Characters are 7 units high and 4 units wide, with a space 3 units wide between characters.</p> <p>Thus each character fits in a square of side 7 units, where a unit is specified by <math>(n + 1) \times 0.1</math> mm. For example, for <math>n = 0</math>, the characters are 0.7 mm x 0.4 mm, with 0.3 mm spacing, and for <math>n = 14</math>, they are <math>(0.7 \times 15 =) 10.5</math> mm x <math>(0.4 \times 15 =) 6</math> mm, with <math>0.3 \times 15 = 4.5</math> mm spacing.</p> <p>When marks are drawn, their size is determined similarly: the basic size, 0.4 mm square is multiplied by <math>n + 1</math>. Once specified, the character size remains the same until reset. Initially, when power is switched on, the setting <math>n = 3</math> is assumed.</p>
ALPHA ROTATE	$Q_n$ (Terminator)	<p>The orientation of characters is specified by <math>n</math>, which is an integer in the range 0 to 3. The direction of writing is rotated anticlockwise from the X-axis through <math>0^\circ</math> for <math>n = 0</math>, <math>90^\circ</math> for <math>n = 1</math>, <math>180^\circ</math> for <math>n = 2</math> and <math>270^\circ</math> for <math>n = 3</math>.</p> <p>ALPHA SCALE and ALPHA ROTATE commands may appear independently. Once specified the character orientation is constant until reset; when the power is switched on, <math>n = 0</math> is always assumed.</p>
PRINT	$P C_1 C_2 C_3 \dots C_n$ (Terminator)	<p>The character string <math>C_1 C_2 \dots C_n</math> is drawn. Codes, other than hexadecimal 00 to 0D, which do not map into printable characters are ignored. (for example, DLE, NAK, SYN, ETB).</p> <p>Spaces, however, are left blank in the normal way. There are a total of 95 printing characters. (See Table 2.)</p>
MARK	$N_n$ (Terminator)	<p>Draws the special symbol (mark) specified by <math>n</math>, which is an integer from 1 to 6: 1 = ●, 2 = ◊, 3 = ◻, 4 = △, 5 = ⊗, 6 = ⊙. The magnification factor specified by the ALPHA SCALE command also applies to marks. (See note 5)</p>

were latched by the interface and were strobed into the plotter. The strobe was generated by a monostable in the interface. The busy signal, generated by the plotter while plotting and processing instructions, set data bit 0 on the data bus when the peripheral was read by the microcomputer.

As an example, the input sequence for the draw command would be :

Command Code	D	(ASCII code for D)
Parameter	200	(ASCII code for 2, 0 and 0)
Delimiter	,	(ASCII code for ,)
Parameter	200	(ASCII code for 2, 0 and 0)
Terminator	<CR>	(Carriage return)

The plotting area of the digital plotter was 360 mm x 260 mm and the programmable step size was 0.1 mm.

#### 5.4.6. EPROM Programmer.

The EPROM programmer was designed to program electrically programable read only memories (EPROMS) of the 2708 type. These 1 K by 8 bit EPROMS are ultra-violet light erasable. The EPROM programmer was used in conjunction with the AIM 65 user and system VIA's. The address lines of the 2708, A0 to A7, were connected to port B on the user VIA and address lines A8 and A9 were connected to tape 1A and 2B outputs respectively, which corresponded to bits 4 and 5 on port B of the system VIA. The data input/output lines of the 2708 were connected to port A of the user VIA. The power supply built into the programmer provided the +12V, +5V, -5V and the +30V programming voltages. The design was based upon one which appeared in Reference 61. The circuit diagram is shown in Figure A.3.14 in Appendix 3.

The EPROM programmer software package is listed in Appendix 3. It was written in machine code and enabled the user to initialise the EPROM programmer, program and verify the contents of the EPROM using the AIM 65 function keys (see operation flowchart in Appendix 3).

The programmed EPROMS were used on the EPROM board described earlier. Memory locations  $0C00_{16}$  to  $0FFF_{16}$  of the AIM 65 memory were copied to the EPROM by the programming procedure.

#### 5.5. Instrument Operation.

A schematic diagram of the microcomputer controlled submillimetre open resonator is shown in Figure 5.10. The program listed in Appendix 4 was developed to measure the total scattering cross sections of structures placed within the volume of the open resonator and is given as an example of the program required to operate the instrument.

The program was designed to scan the resonator mirror through a TEM<sub>00</sub> mode and sample the Golay detector response. The detector output voltage was measured and digitised by the A-D converter and stored, along with the mirror position at which the detector reading was taken. The outputs of the mirror and sample position transducers were measured and digitised with the A-D converter. From the stored data, the baseline average was subtracted, and the halfwidth of the resonance curve obtained. The loaded Q of the resonator mode was calculated from the halfwidth and mirror separation. The mirror could be scanned forwards and backwards over the mode resonance and the average Q calculated. This averaged out any leadscrew errors. The number of scans per resonance measurement was set by the operator. The sample was then moved through a quarter of a wavelength. The sample displacement was monitored by the sample longitudinal linear position transducer. The mirror scanning process was repeated to obtain the second loaded Q value. The sample could then be changed or moved in some required way. The above measurements were then repeated. In the example program in Appendix 4, the angle of incidence of the sample with respect to the resonator axis was altered so the variation of total scattering cross section with angle of incidence could be investigated. After the required number of measure-

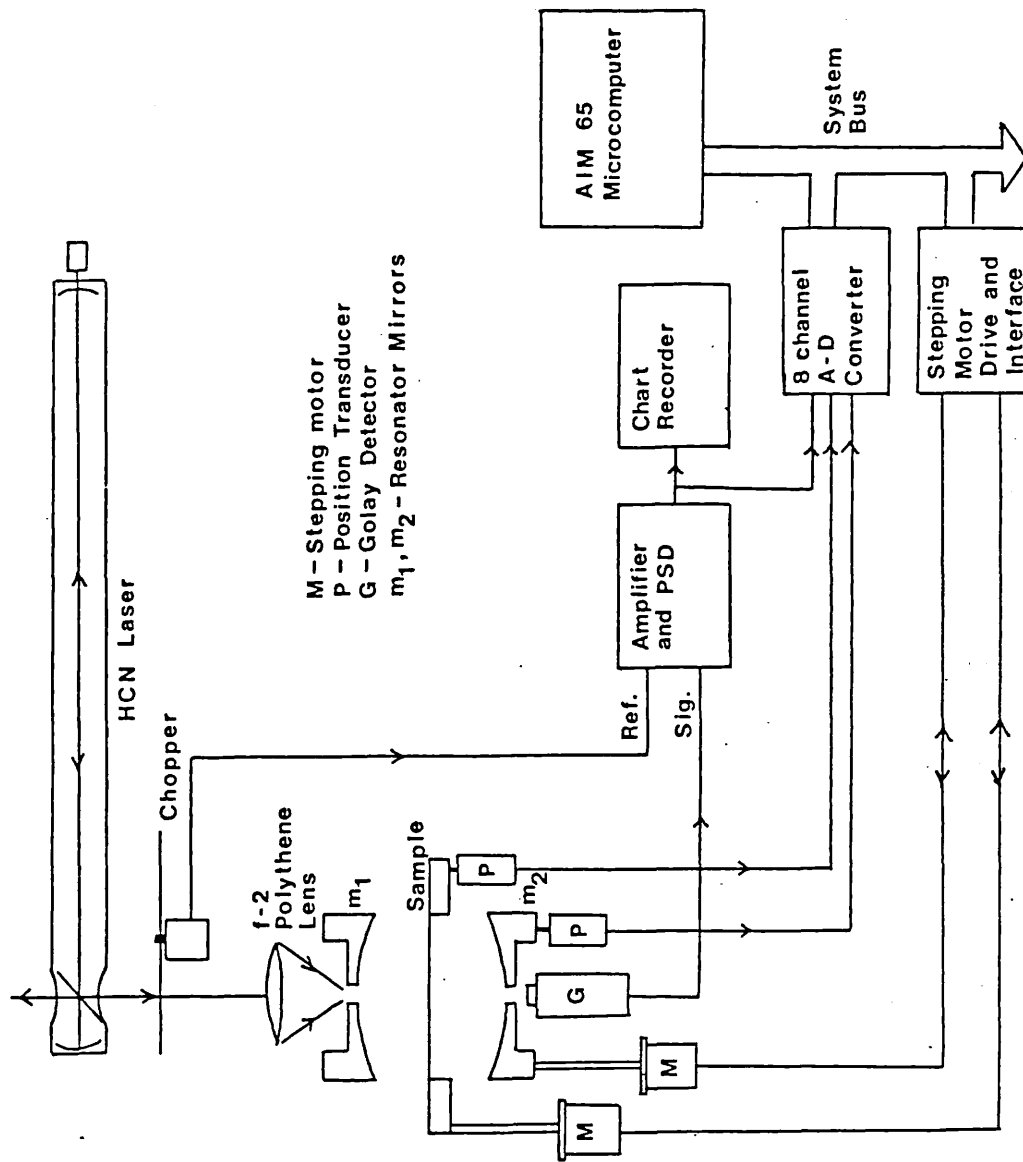


Figure 5.10 Schematic diagram of the microcomputer controlled submillimetre open resonator.

ments were obtained, the unloaded Q value of the resonator, which had previously been measured with the sample removed would be entered. From the resonator dimensions, the unloaded Q value, and the loaded Q values measured and stored by the program, the total scattering cross-sections were calculated. The scattering cross-sections could then be printed out, along with the value of the parameter that was being varied.

The Q factor of the resonator could be measured to an accuracy of 3% for Q values in the range 20,000 to 65,000. It was estimated that the scattering cross sections were measured with an accuracy of 10%. Because each measurement of scattering cross-section took approximately 15 minutes, the HCN laser, used as the coherent radiation source for the resonator, had to be capable of maintaining a stable output over a period of several hours. The laser stabilisation techniques that were employed are described in Chapter 6.



CHAPTER SIX  
THE HCN LASER SOURCE.

6.1. Introduction.

The coherent radiation source developed for the investigation was a 10 mW CW HCN laser operating at 891 GHz. This source was chosen because the output frequency is at the low frequency end of the submillimetre region, where it is expected future interest will lie. The HCN laser is also rugged and cheap to run. A servo system was developed for stabilising the laser cavity<sup>62</sup>.

The principal output line of the HCN laser occurs at a frequency of 891 GHz, corresponding to a wavelength of 337  $\mu\text{m}$ . Additional lines are found at wavelengths of 373  $\mu\text{m}$ , 310  $\mu\text{m}$  and 309  $\mu\text{m}$ . The output powers of these various lines are listed in Table 6.1.

Table 6.1.

HCN laser line output powers	
Wavelength ( $\mu\text{m}$ )	Output power (mW)
309	} 1.0 (combined)
310	
337	10
373	0.1

6.2. Laser Details.

The laser tube was 7.6 m long and 15 cm in diameter. The beamsplitter output consisted of a 12.5  $\mu\text{m}$  thick mylar film held in a vertical plane at an angle of 45° to the laser axis by a stretching frame with elliptical aperture. Two horizontally polarised co-linear output beams were produced by this arrangement. Atmospheric pressure was held off by 125  $\mu\text{m}$  thick mylar vacuum windows. The laser was excited by a discharge current of 1A in a continuous flow methane, nitrogen and

helium mixture (partial pressures 1: 2: 10 respectively). The total tube pressure was 66.7 Pa (0.5 torr) and the corresponding voltage drop was 2.2 KV. A very stable striated discharge was obtained with a water cooled hollow cathode situated in a tube sidearm. An essential requirement for stable output was a discharge with stationary striations. This could only be achieved with the correct hollow discharge. Under these conditions the active mode linewidth would be in the region of 100 KHz<sup>63</sup> which is much less than the bandwidth of the unloaded open resonator (which was 14 MHz corresponding to an unloaded Q of 65,000).

A current stabilised power supply capable of delivering up to 6 KV at 3 KW was used to supply DC power to the laser. A 500  $\Omega$ , 1 KW ballast resistor was connected in series with the laser tube to limit the initial starting current. Although rigidly clamped by four invar spacers, the cavity length varied by up to 100  $\mu\text{m}$  per hour due to thermal expansion. As a result the laser drifted off tune, making long term measurements impossible.

### 6.3. Cavity Length Stabilisation.

In order to obtain useful output powers from far infrared molecular lasers (of which the HCN laser is an example) it is necessary to employ cavity lengths in excess of a metre. This is because the gain per unit length tends to be low<sup>63</sup>, being of the order of 0.01 - 0.1  $\text{m}^{-1}$ . One of the main factors affecting the stability of a continuous wave (cw) HCN laser comes from the instability in the laser body structure due to fluctuating ambient temperature. This can be overcome by employing temperature regulated silica or steel spacing rods<sup>64, 65</sup>. Although this is very effective, these techniques are however complicated and expensive, especially if the laser is of appreciable length. The method now described overcomes these disadvantages.

The laser cavity can be stabilised by locking it to the mode peak by employing a cavity modulation technique. This was achieved by using a hemispherical laser cavity configuration with the lighter 3" diameter plane mirror supported in the cone of a 5" loudspeaker. The DC correction voltage generated by the servo system was applied to the loudspeaker to correct for changes in cavity length. A small AC modulating voltage was also applied to the loudspeaker to achieve cavity modulation. The modulating voltage applied to the loudspeaker caused modulation of the laser output of a few per cent. The detected modulation was amplified and applied to a phase sensitive detector along with the modulating signal which acted as the reference. The correction voltage generated by the phase sensitive detector was fed back to the loudspeaker along with the modulating signal. A modulation frequency of 40 Hz was chosen as this was high enough to lie outside the bandwidth of the Golay detectors employed in the investigation.

The output from one of the laser ports was focused on to a Mullard RPY 89 pyroelectric detector in order to detect the modulated output from the laser. The Mullard RPY 80 series of pyroelectric detectors were found to have voltage responsivities in the submillimetre region comparable to those quoted by the manufacturers for the near infrared. The silicon windows used to protect the detector elements were found to attenuate the laser radiation only slightly.

A block diagram of the servo system is shown in Figure 6.1. To prevent the plasma discharge from going to ground via the loudspeaker, the servo loop circuitry was floating and the amplified detector signal was coupled using an opto-isolator. The circuits for the Mullard pyroelectric detector pre-amplifier and the main amplifier are shown in Figures 6.2 and 6.3 respectively. A full circuit of the laser stabiliser is shown in Figure 6.4. The theory of operation is next discussed.

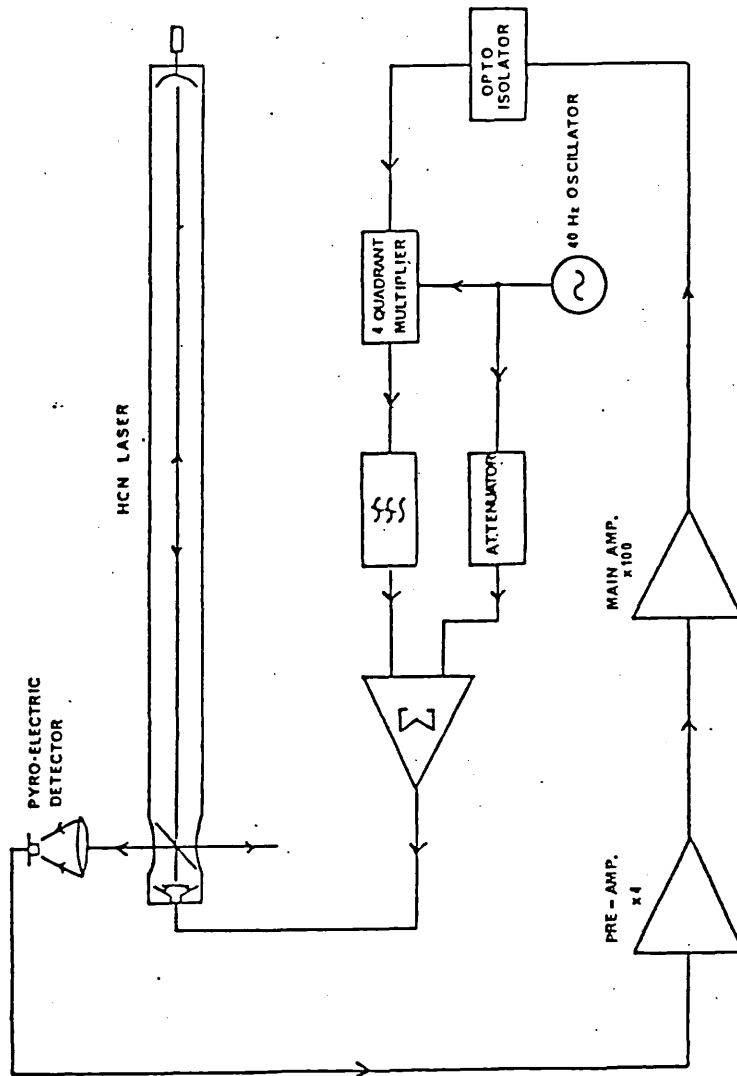


Figure 6.1 Block diagram of the servo loop.

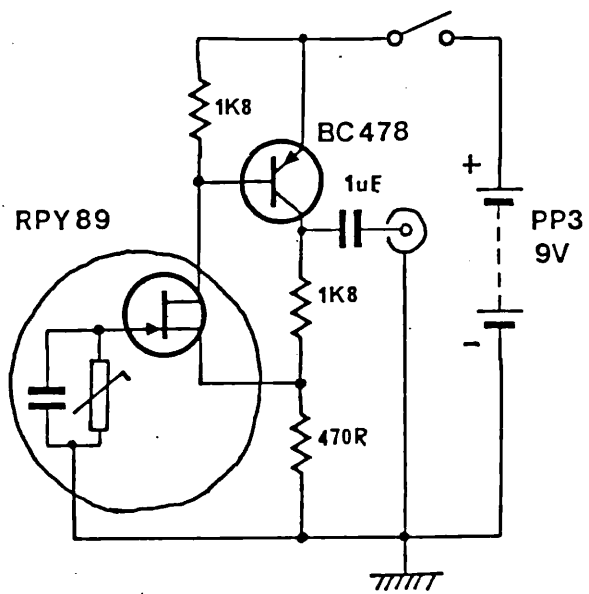


Figure 6.2 Servo system pyroelectric detector pre-amplifier.



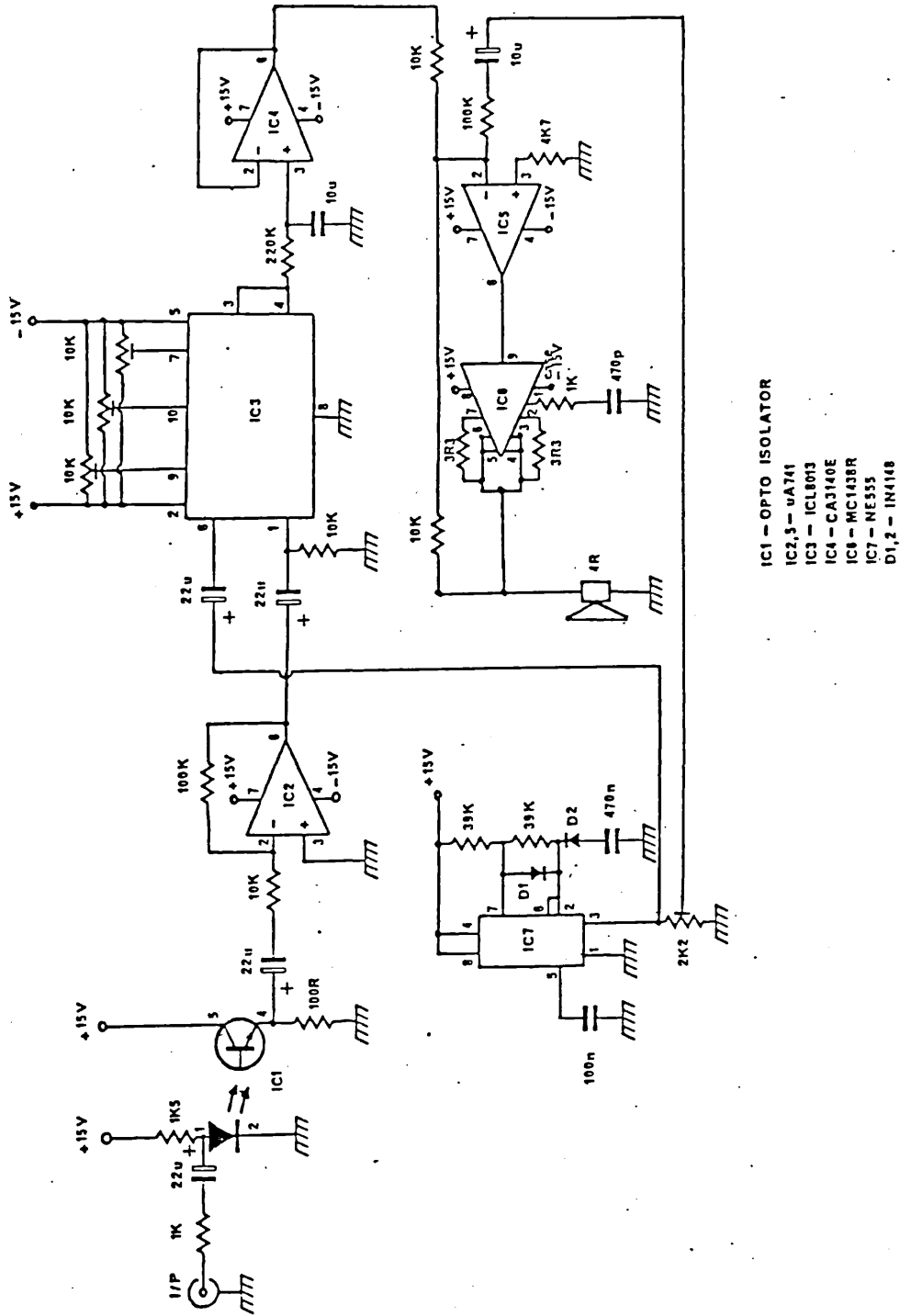


Figure 6.4 Laser stabiliser circuit diagram.

The cavity mode resonance curve of the laser can be approximated to a parabola of the form

$$I = I_0 (1 - a x^2) \quad (6.1.)$$

where  $I$  is the laser intensity when the mirror is displaced a distance  $x$  from the mode peak mirror position.  $I_0$  is the peak laser intensity and  $a$  is a constant ( $a = 2.5 \times 10^9 \mu\text{m}^{-2}$  for our laser). The loudspeaker is modulated by a small AC signal of frequency  $\omega_m$  which produced a mechanical modulation of the mirror,  $m$ , represented by

$$m = m_0 \cos \omega_m t \quad (6.2.)$$

If the mirror is displaced by a distance  $e$ , then from equations 6.1 and 6.2 the output intensity is given by

$$I = I_0 [1 - a (e + m_0 \cos \omega_m t)^2] \quad (6.3.)$$

After detection the AC component of this signal is

$$V_{\text{SIG}} = K I_0 a (e^2 + 2em_0 \cos \omega_m t + m_0^2 \cos^2 \omega_m t) \quad (6.4.)$$

where  $K$  is the detector sensitivity.

After voltage amplification  $A_v$ , the signal is then multiplied by a reference signal,  $V_{\text{REF}}$ , in a four quadrant multiplier.

$$V_{\text{REF}} = V_R \cos \omega_m t \quad (6.5.)$$

The output of the four quadrant multiplier is given by

$$V_o = V_R A_v K I_0 a (e^2 \cos \omega_m t + 2 e m_0 \cos^2 \omega_m t + m_0^2 \cos^3 \omega_m t) \quad (6.6.)$$

The  $\cos^2 \omega_m t$  term gives rise to a DC error signal, proportional to  $e$ , of amplitude

$$V_{\text{DC}} = V_R A_v K I_0 a e m_0 \quad (6.7.)$$

The error signal was extracted by feeding the four quadrant multiplier output through a low pass filter with  $f_c = 0.07$  Hz. The output of the filter was



buffered and fed back to the loudspeaker so as to compensate for the displacement error.

For this particular servo loop the open loop DC output voltage corresponding to an error of  $1 \mu\text{m}$  was  $0.84 \text{ V}$ . Hence, the loop amplification factor (A) was equal to  $0.84 \text{ V } \mu\text{m}^{-1}$ . The feedback factor B is supplied by the loudspeaker sensitivity which was  $168 \mu\text{m V}^{-1}$ . The stability factor for the servo loop  $S = (AB)^{-1}$ , was calculated to be  $0.7\%$ . The loop time constant, which was governed by the time constant of the low pass filter, was  $2.2$  seconds.

To ascertain the performance of the laser stabilisation system the experimental arrangement shown in Figure 6.5 was employed. The phase sensitive detector output was monitored on a chart recorder with an integration time constant of  $10$  seconds. Figure 6.6 shows the variation of laser output power with time for both the stabilised and un-stabilised cases. The servo loop stability of the system was measured and found to be  $0.9\%$ . The servo loop reduced the output drift rate from  $44\%$  per hour to  $4.8\%$  per hour. The amplitude modulation produced by the  $40 \text{ Hz}$  cavity modulation was also measured and found to be  $5\%$  of the total output amplitude. The cavity modulation gave rise to a theoretical residual frequency modulation of  $26 \text{ KHz}$ .

Clearly this technique offered a marked improvement in the output stability provided that the small amount of amplitude and frequency modulation could be tolerated. The modulation frequency could be increased but was limited here by the frequency response of the monitor detector. In applications where the laser might be employed as a local oscillator, the degree of frequency modulation produced by the stabiliser could prove detrimental. However, in applications where good amplitude stability is the major requirement this technique is most successful.

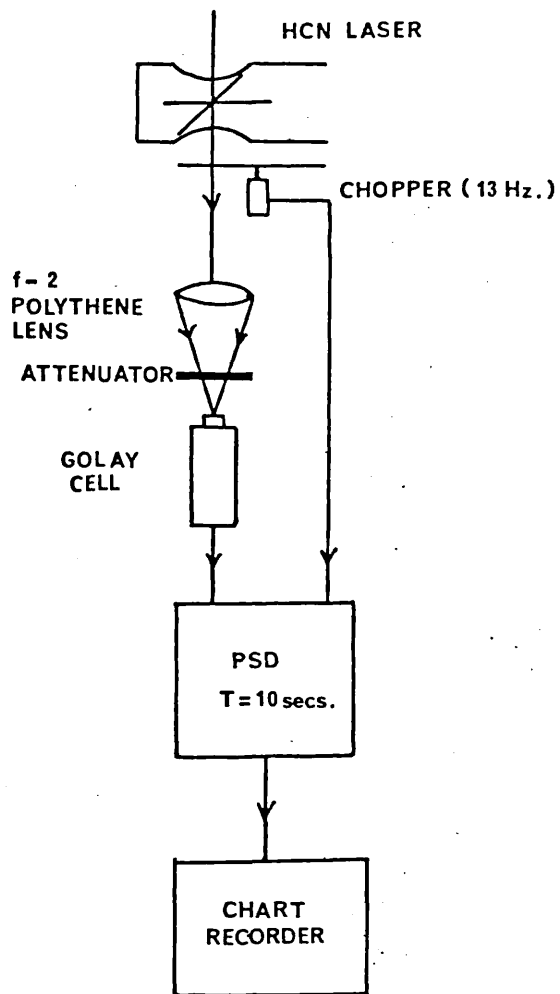


Figure 6.5 Laser output monitoring arrangement.

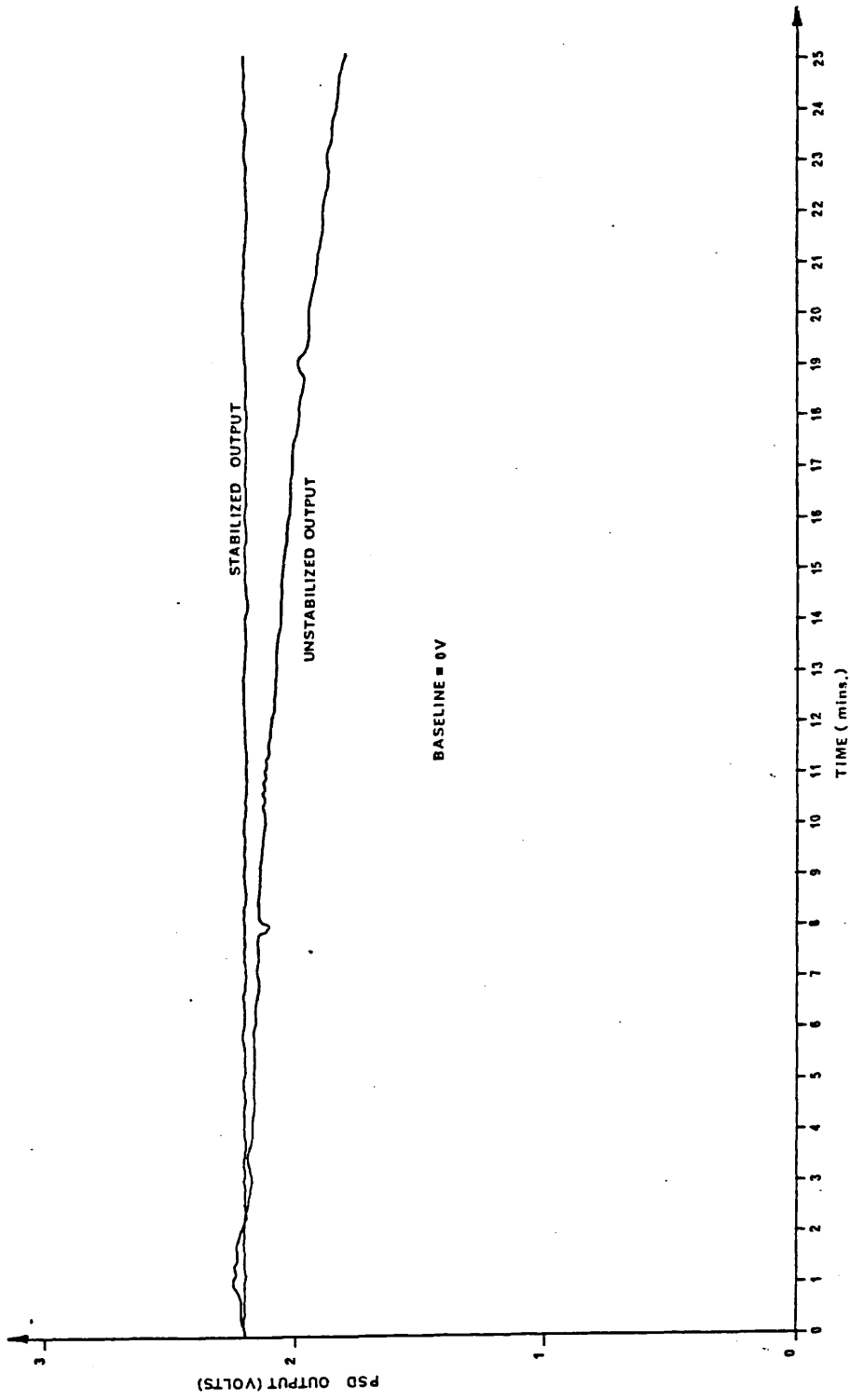


Figure 6.6 Variation of laser output with time for both stabilised and unstabilised cases.

The photographs shown in Figures 6.7 and 6.8 are of the HCN laser employed for the investigations and the laser stabilising circuitry rack unit, respectively.

#### 6.4. Laser Output Beam Profile.

The laser beam output profile was measured with the experimental arrangement shown in Figure 6.9. A Golay detector was mounted on a carriage which could be tracked across the laser output port. A slit 3 mm wide was cut in an aluminium plate and used to limit the aperture of the Golay detector. The aluminium plate was covered with a microwave absorbing material (ecosorb AN-75) to eliminate reflection problems which may have arisen. The mechanical chopper for the Golay detector was also mounted on the same carriage in front of the aluminium plate. The carriage was tracked across the output beam of the laser and the Golay signal measured at 0.125 inch intervals. Figure 6.10 shows the output beam profiles obtained. The laser beam width at half power and beam divergence were found to be  $21 \pm 3$  mm and  $5 \pm 1$  milliradians, respectively.

The output beam polarisation was also measured by removing the slotted aluminium plate and rotating a wire grid analyser (consisting of fine gold metallic lines 100  $\mu$ m thick spaced 100  $\mu$ m apart on polythene film) in front of the Golay detector. The polarisation was found to be 98% plane polarised in the horizontal plane. The output power stability, beam profile and polarisation purity obtained from the laser system were most satisfactory, and it is felt that the results obtained from the experimental investigations to be described later substantiate this conclusion.

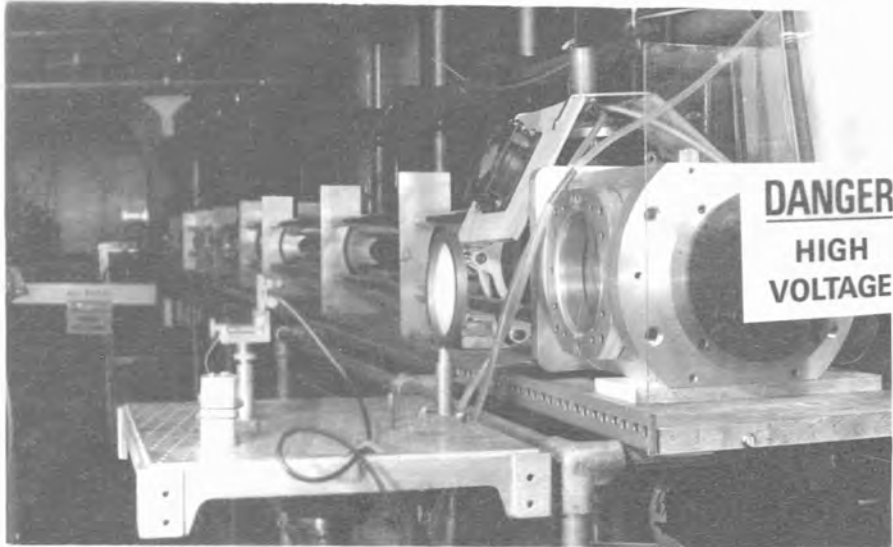


Figure 6.7. 8 Metre HCN Laser.

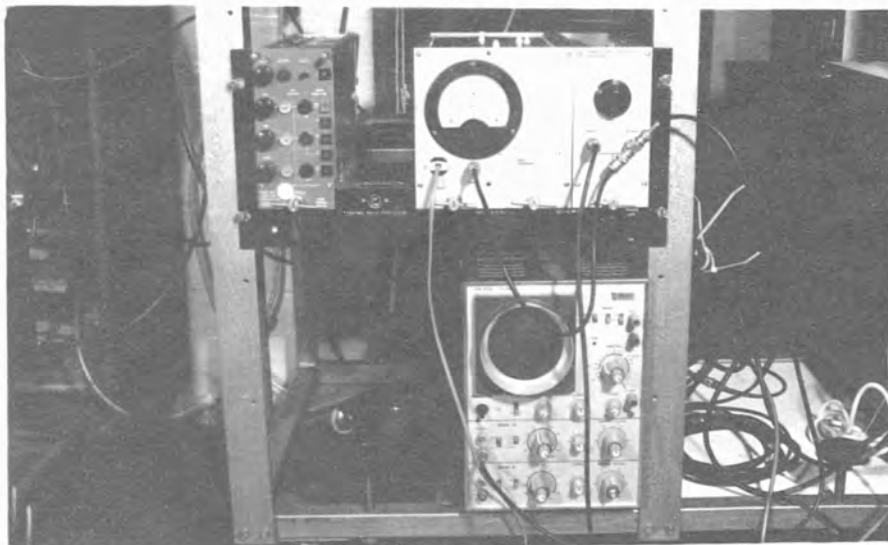
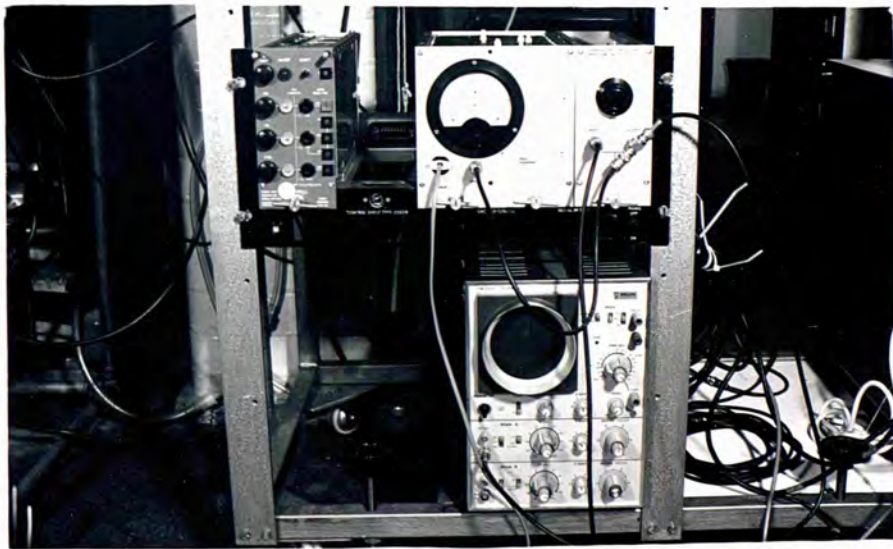
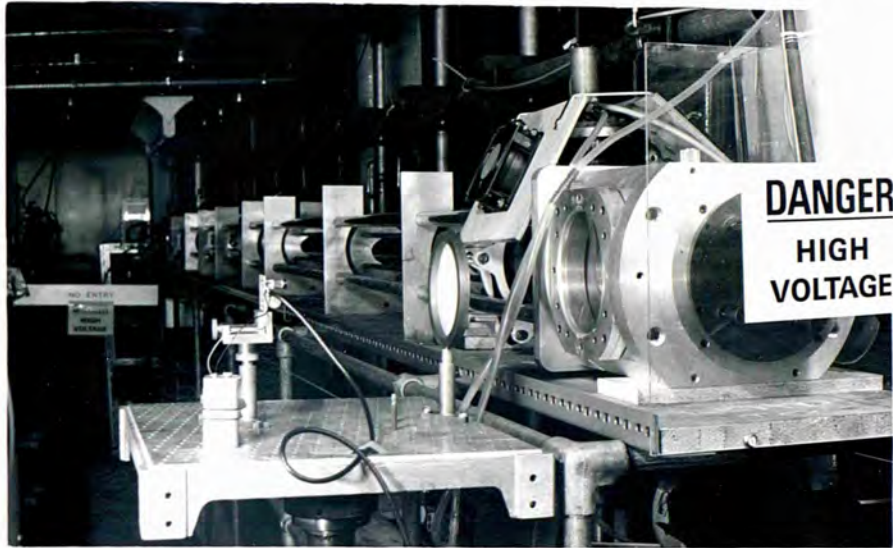


Figure 6.8. Laser Stabilising Circuitry Rack Units.



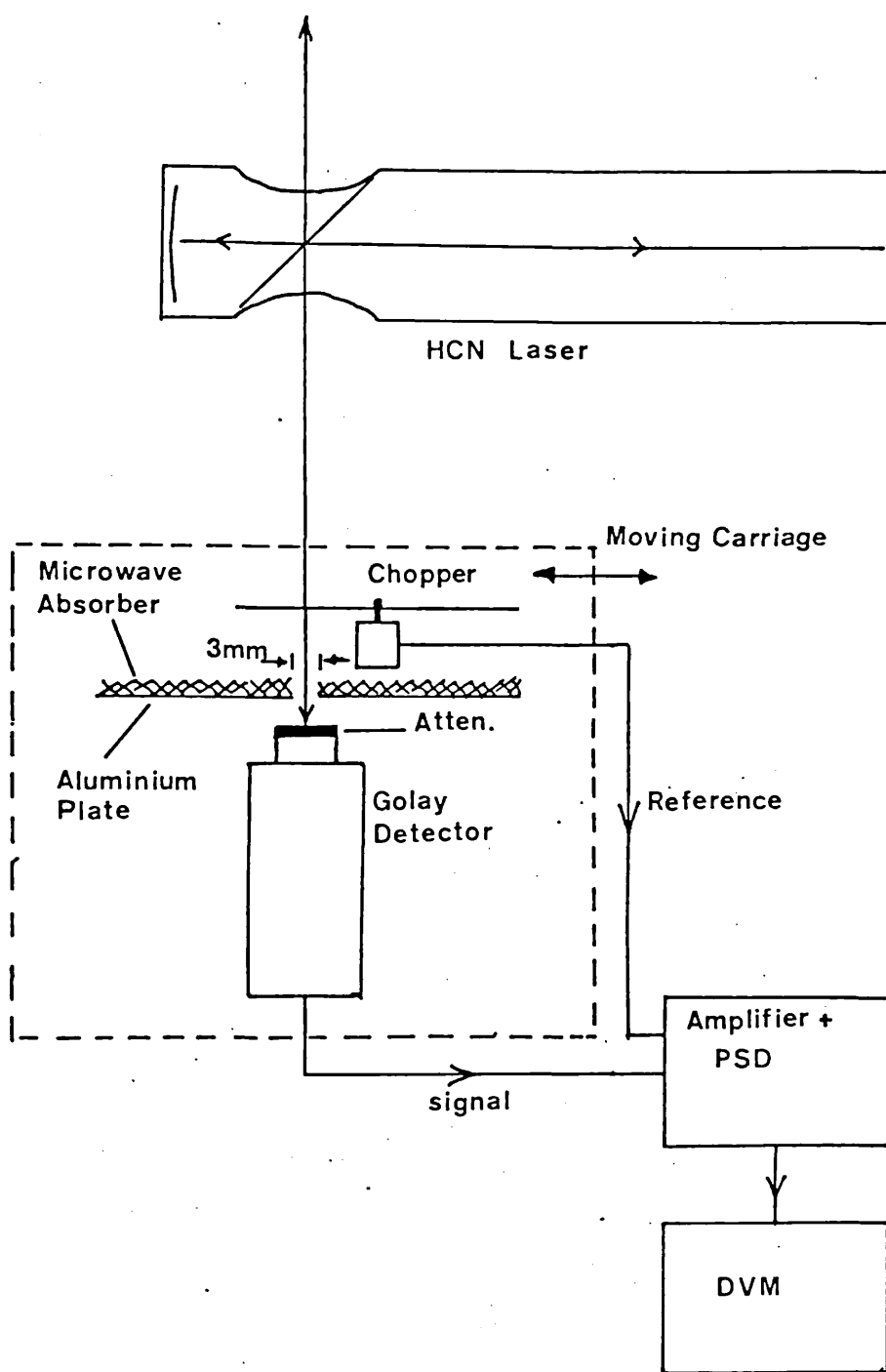


Figure 6.9 Schematic of experimental arrangement used to measure output beam profile of the HCN laser.

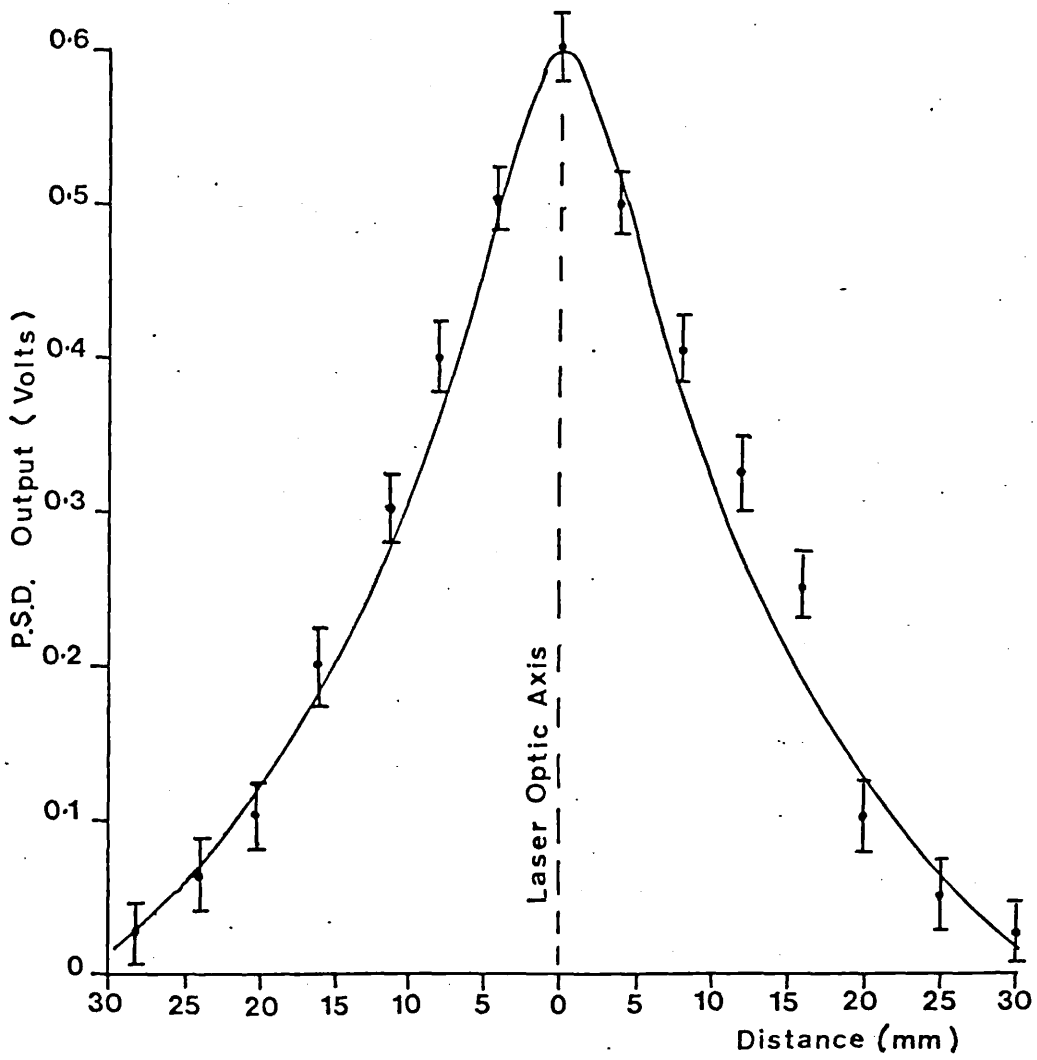


Figure 6.10 Output beam profile of HCN laser.



CHAPTER SEVEN

EXPERIMENTAL INVESTIGATIONS WITH  
THE SUBMILLIMETRE OPEN RESONATOR

7.1. Experimental Investigation of the Mode Spectrum  
of the Unloaded Open Resonator.

In order to investigate the mode spectrum of the open resonator, the experimental arrangement illustrated in Figure 7.1 was employed. The mirror scanning stepping motor was driven continuously and the Golay detector output signal, after phase sensitive detection, was recorded on a Y-T chart recorder.

The mode spectrum of the open resonator is given by equation 4.1.<sup>58</sup> in Chapter 4. This can be rewritten as

$$f_{plq} = (q + 1) \frac{c}{2d} + b (2p + L + 1) \frac{c}{2d} \quad (7.1.)$$

where  $f_{plq}$  is the resonant frequency of the  $plq^{\text{th}}$  mode and  $b = 1/\pi \arccos(1-d/R_0)$ . As  $b$  only varies slowly with the mirror separation  $d$  it can be regarded as a constant. Because the frequency of the HCN laser is fixed the resonances of the  $plq^{\text{th}}$  mode will occur at mirror separations  $S$  where

$$S = \frac{\lambda_{\text{HCN}} (q + 1)}{2} + \frac{\lambda_{\text{HCN}} b (2p + L + 1)}{2} \quad (7.2.)$$

If, on the chart recorder output, the  $\text{TEM}_{00}$  modes are separated by a distance  $D$ , which corresponds to an absolute distance of  $\lambda_{\text{HCN}}/2$ , then the distance between  $\text{TEM}_{plq}$  mode and the  $\text{TEM}_{00q}$  modes on the chart recorder output will be  $\delta$  where

$$\delta = Db(2p + L) \quad (7.3.)$$

The resonator used in the investigation had a  $b$  value of 0.21 at a mean mirror separation of 0.16 m and with mirror radii equal to 0.768 m. Table 7.1 gives  $\delta/D$

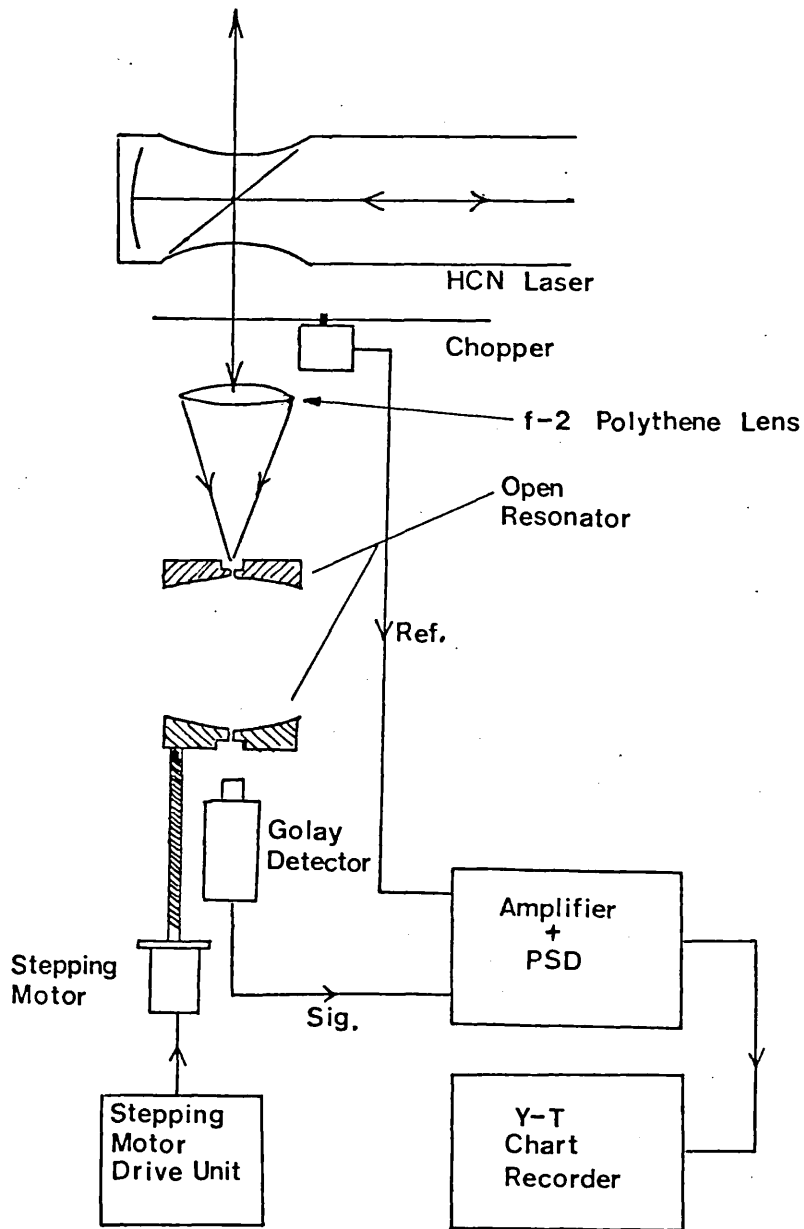


Figure 7.1. Experimental arrangement used to investigate the mode spectrum of the open resonator.

for the various modes

Table 7.1. Open Resonator Mode Positions

p	L	2p + L	$\delta/D$
0	1	1	0.21
0	2	2	0.42
1	0	2	0.42
0	3	3	0.63
1	1	3	0.63
0	4	4	0.84
2	0	4	0.84
2	1	5	1.05
2	2	6	1.26

Figure 7.2 shows the experimentally observed mode spectrum for the resonator with mirror apertures both equal to 10 cm. The mode spectrum was swamped with higher order modes, making meaningful mode identification difficult. The measurement of the resonator Q and the corresponding determination of scattering cross-section was found to be impossible. By reducing the apertures of both mirrors to 3 cms with cork irises to suppress many of the higher order modes, the mode spectrum shown in Figure 7.3 was obtained.

Since the resonator was excited via a coupling hole at the centre of the mirrors, only modes where the field is maximum at the centre would be strongly excited and conversely, modes where the field is a minimum at the centre of the mirrors would be weakly excited. Table 7.2 gives the relative strengths of the various modes tabulated in Table 7.1.

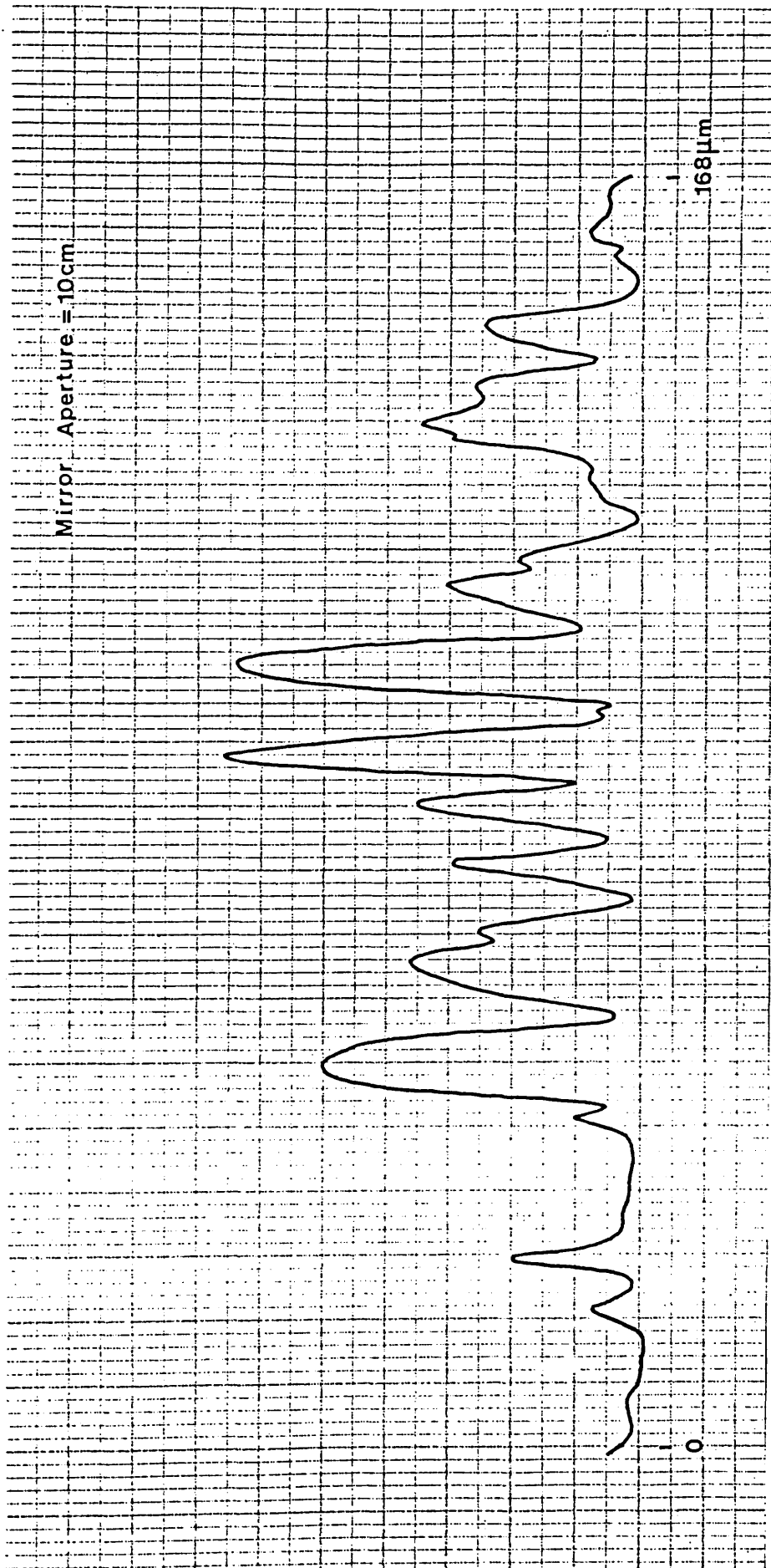


Figure 7.2. Open resonator mode spectrum with mirror apertures equal to 10 cm.

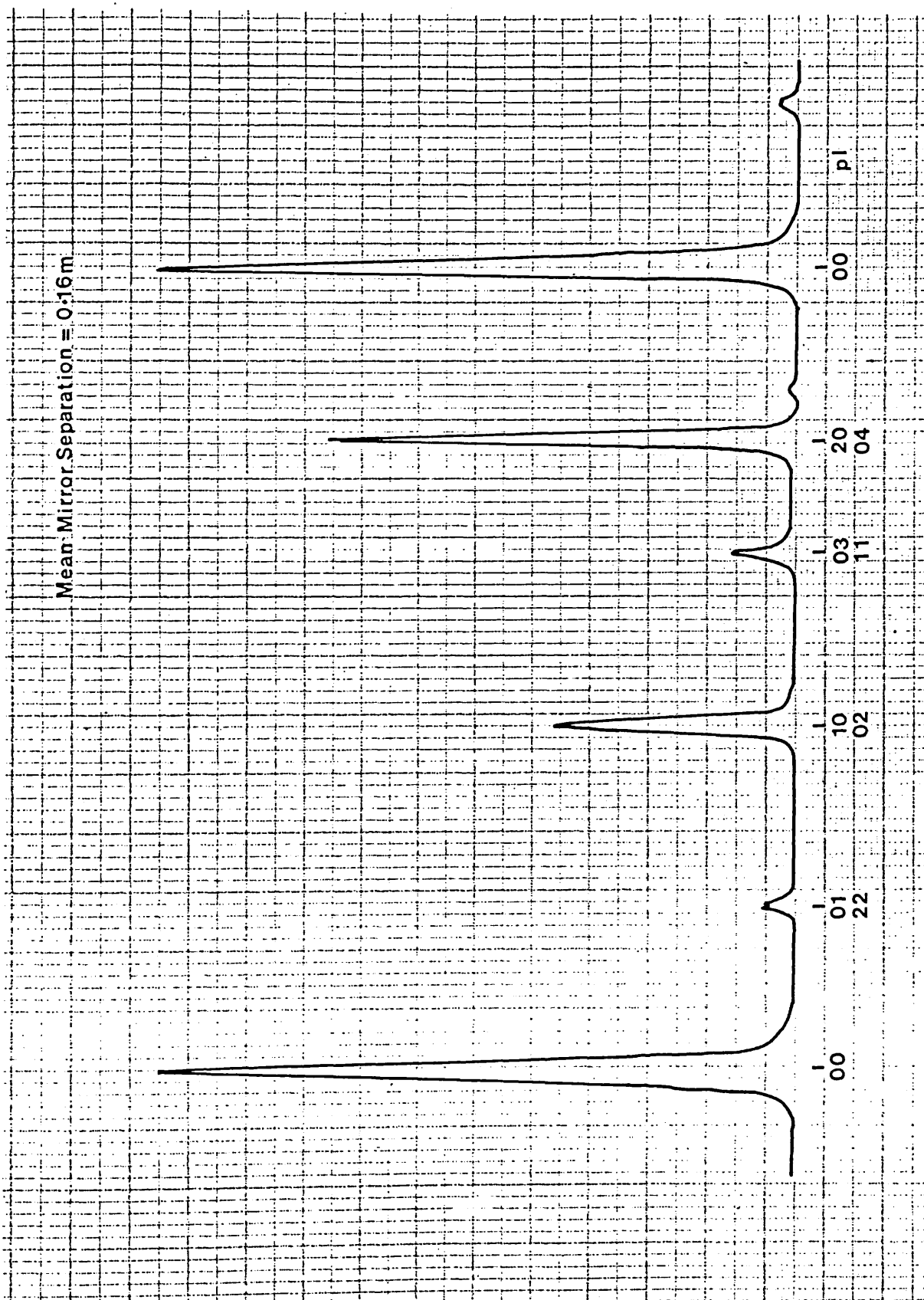


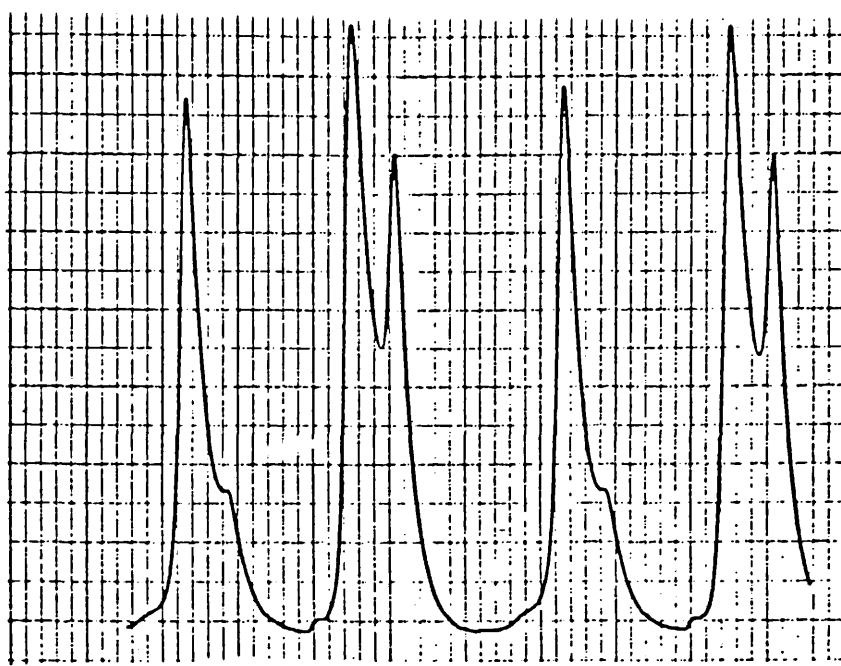
Figure 7.3. Open resonator mode spectrum with modes identified. Mirror apertures equal to 3 cm.

Table 7.2. Relative Mode Strengths  
(W = Weak, S = Strong)

p	L	$\delta/D$	Strength
0	0	0	S
0	1	0.21	W
0	2	0.42	W
1	0	0.42	S
0	3	0.63	W
1	1	0.63	W
0	4	0.84	W
2	0	0.84	S
2	1	1.05	W
2	2	1.26	W

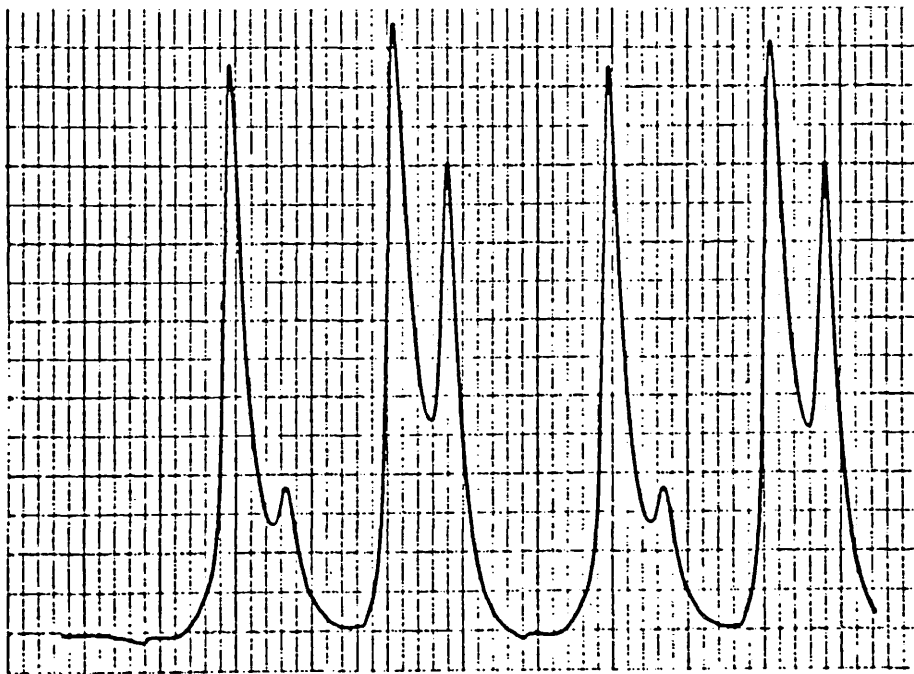
The higher order modes are only weakly excited anyway<sup>49</sup>. From calculations of the mode separations and a knowledge of their strengths, mode assignments on the recorded spectrum were made. A typical mode spectrum complete with the assignments, is shown in Figure 7.3. The agreement with theory is good. The variation of the mode positions with mirror separation was studied for various mirror apertures. The mirror apertures were stopped down using cork irises<sup>66</sup>. Mode spectra for mirror apertures of 3 cm and 2 cm, and various mirror separations are shown in Figures 7.4 and 7.5 respectively. In the case of a 3 cm aperture it was evident that mode degeneracies would be a problem for most mirror separations. By reducing both mirror apertures to 2 cm it was possible to restrict the modes excited to the TEM<sub>00</sub> and the TEM<sub>10</sub> modes. It can be seen from Figure 7.5 that the mode degeneracies were eliminated for mirror apertures of 2 cm as the higher order modes were no longer excited.

Figure 7.4. Variation of the mode spectrum of  
the open resonator with mirror  
separation  $d$ .  
Mirror aperture  $\phi = 3$  cm



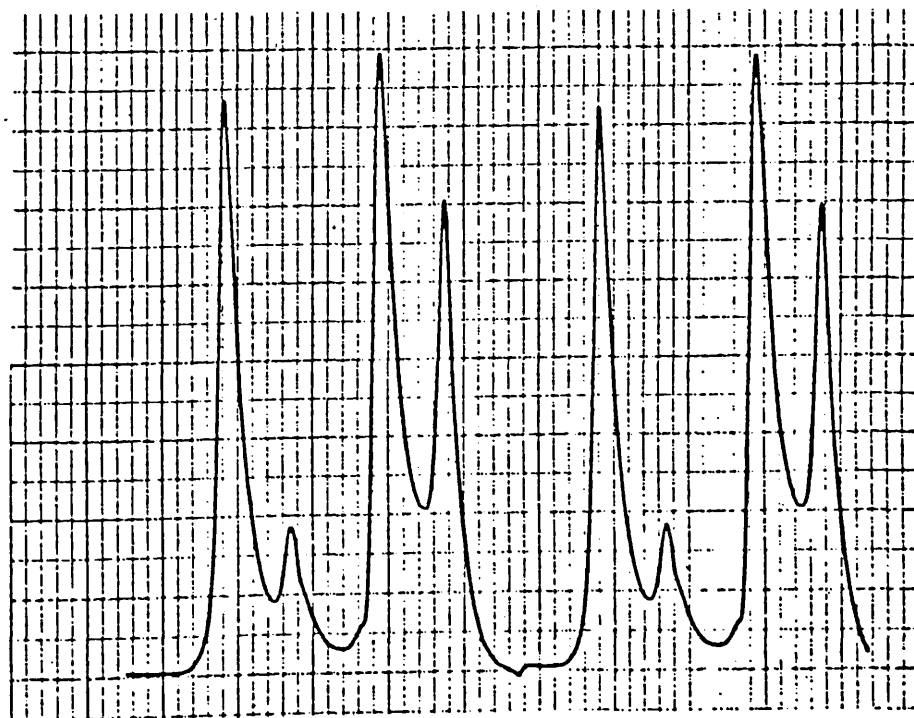
$d = 16.2 \text{ cm}$

$\phi = 3 \text{ cm}$



$d = 15.2 \text{ cm}$

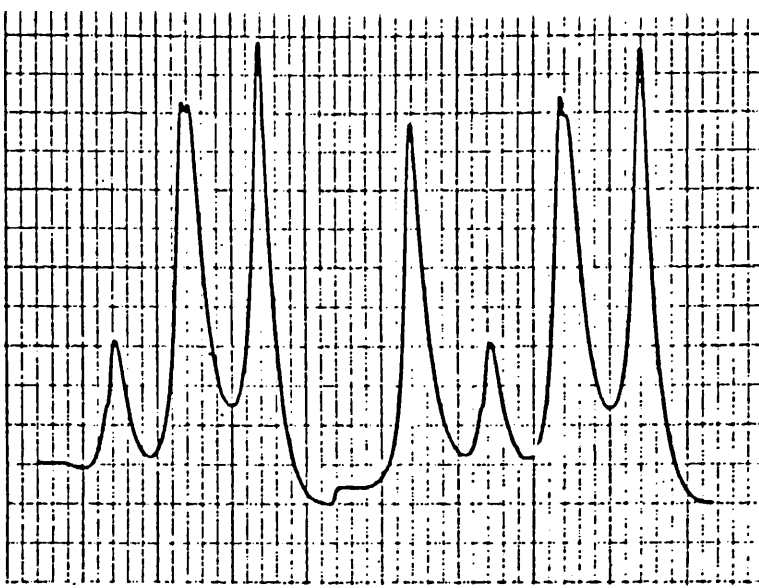
$\phi = 3 \text{ cm}$



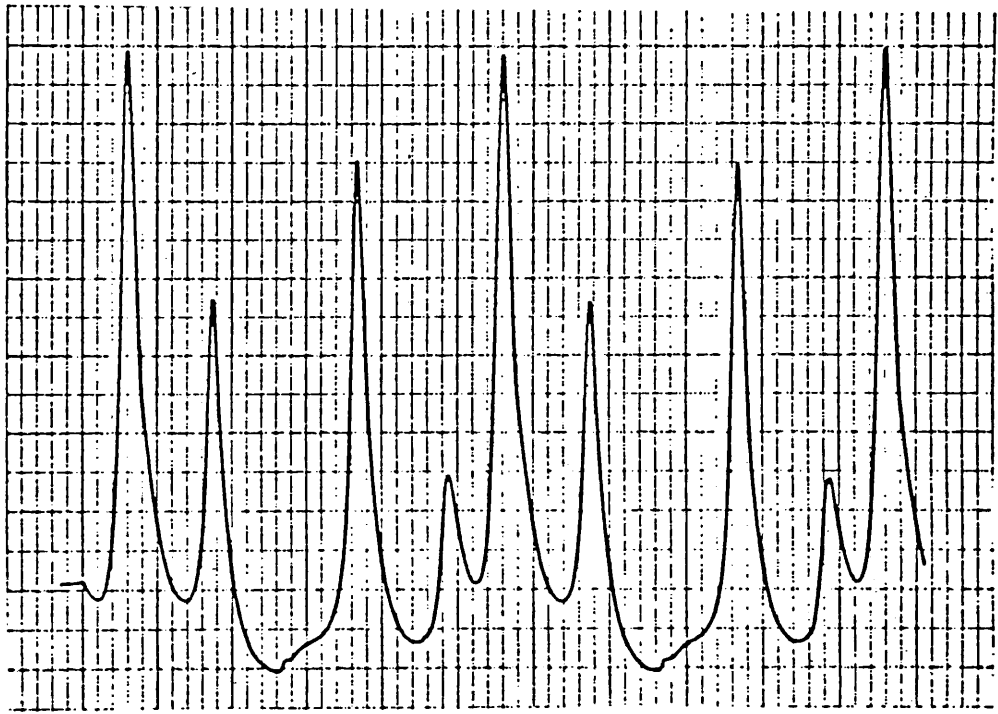
$d = 14.2 \text{ cm}$

$\phi = 3 \text{ cm}$

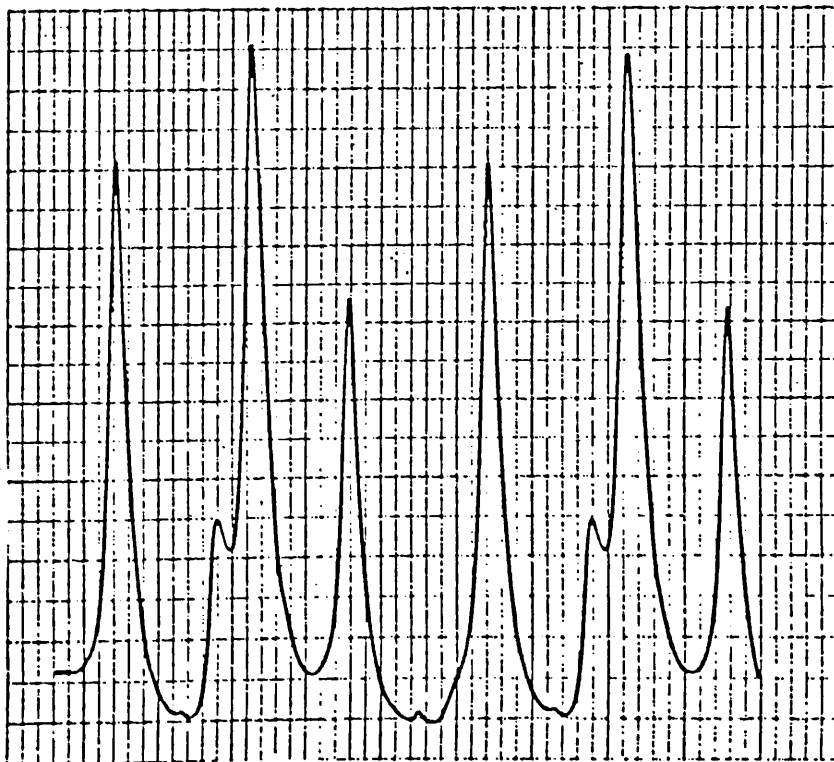




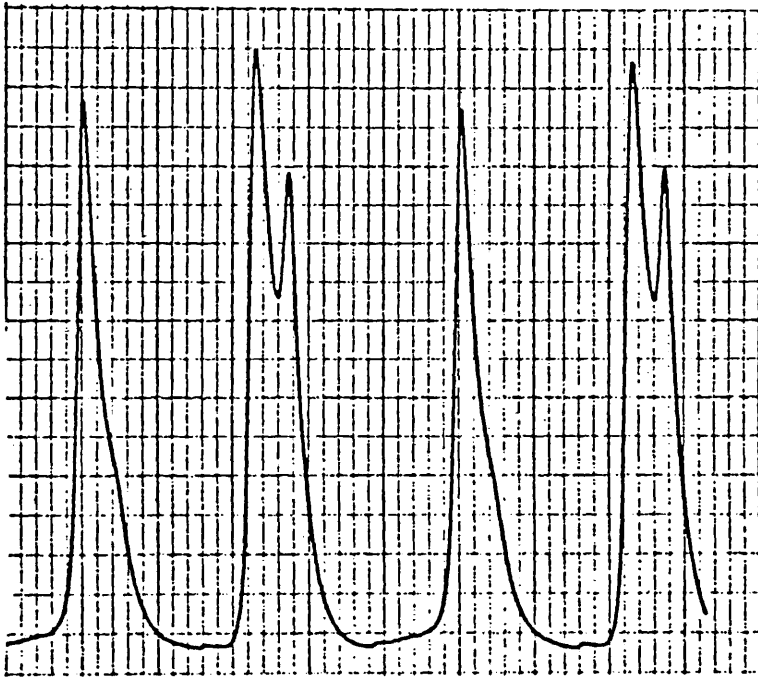
$d = 13.2 \text{ cm}$        $\phi = 3 \text{ cm}$



$d = 12.2 \text{ cm}$        $\phi = 3 \text{ cm}$



$d = 11.2$        $\phi = 3 \text{ cm}$



$d = 10.2 \text{ cm}$

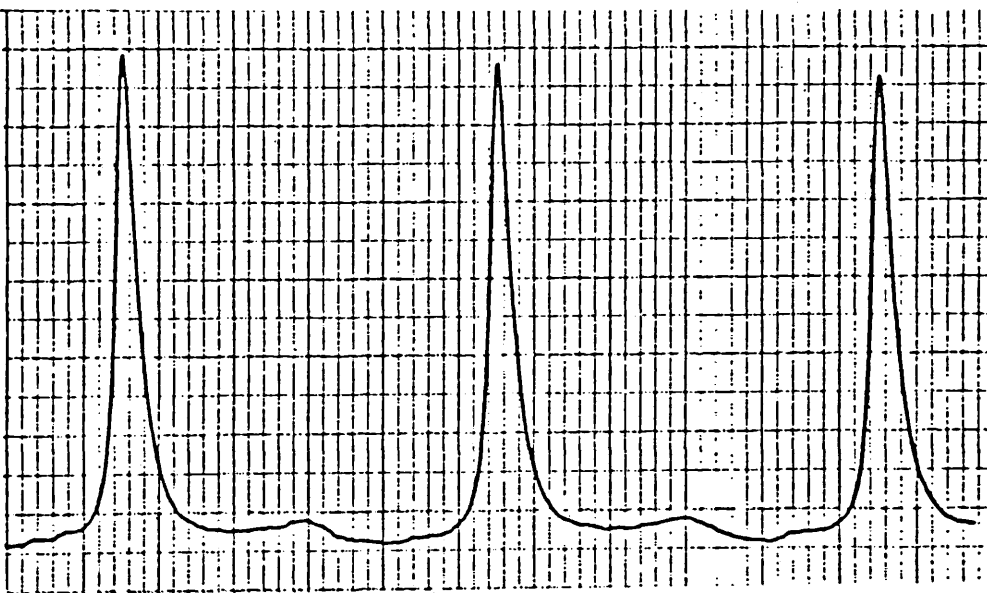
$\phi = 3 \text{ cm}$

Figure 7.5. Variation of the mode spectrum of the open resonator with mirror separation  $d$ .  
Mirror aperture  $\phi = 2$  cm.



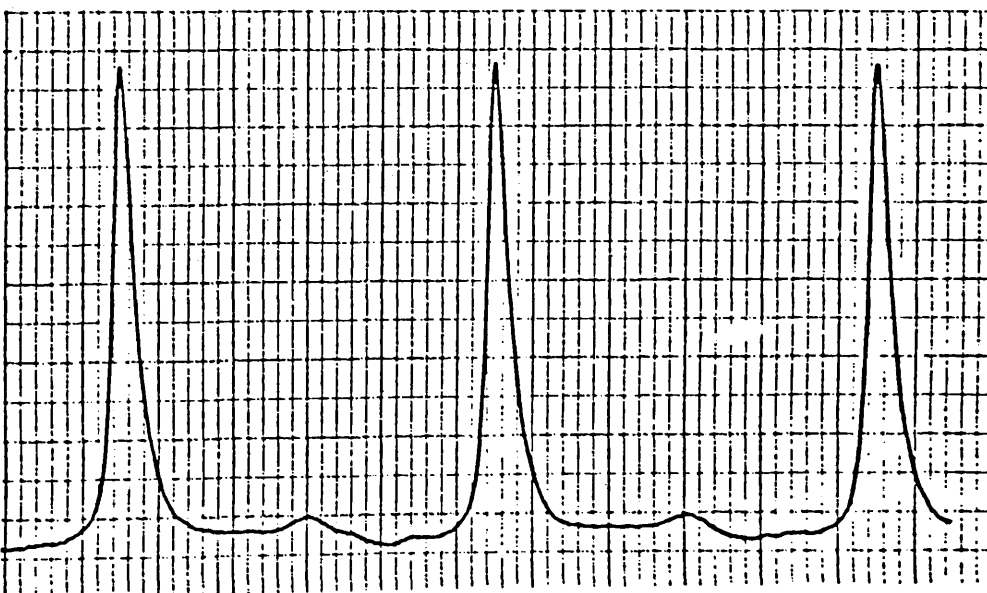
$d = 19.0 \text{ cm}$

$\phi = 2 \text{ cm}$



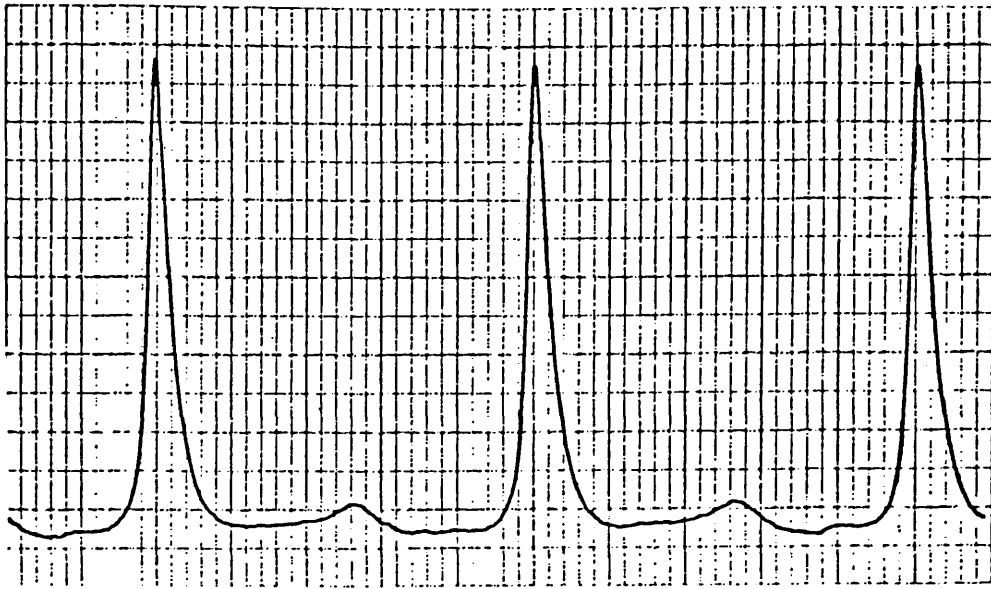
$d = 18.1 \text{ cm}$

$\phi = 2 \text{ cm}$



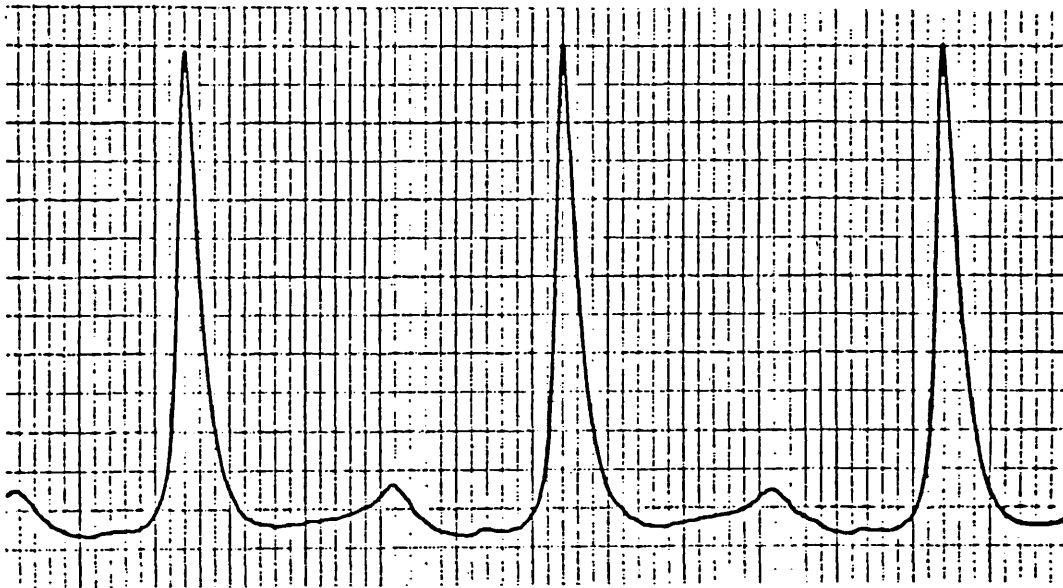
$d = 17.1 \text{ cm}$

$\phi = 2 \text{ cm}$



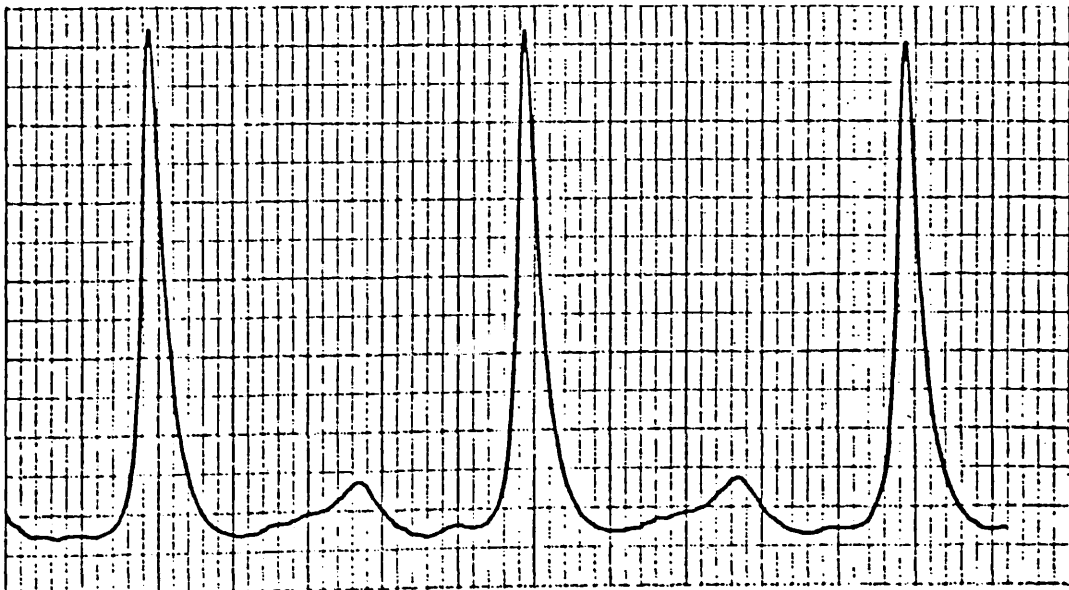
$d = 16.1 \text{ cm}$

$\phi = 2 \text{ cm}$



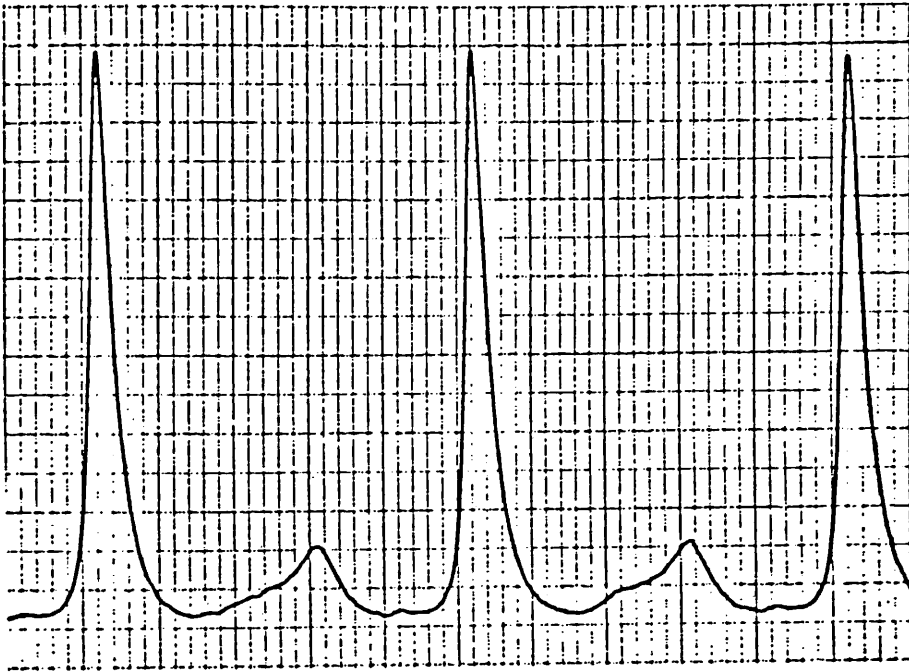
$d = 14.85 \text{ cm}$

$\phi = 2 \text{ cm}$



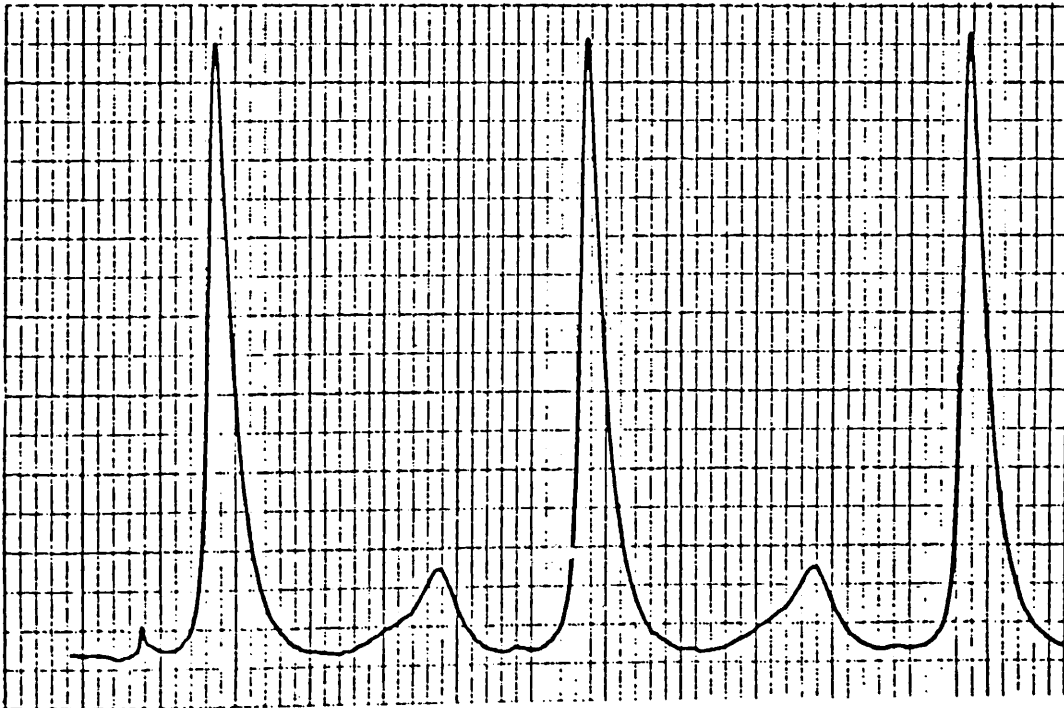
$d = 14.1 \text{ cm}$

$\phi = 2 \text{ cm}$



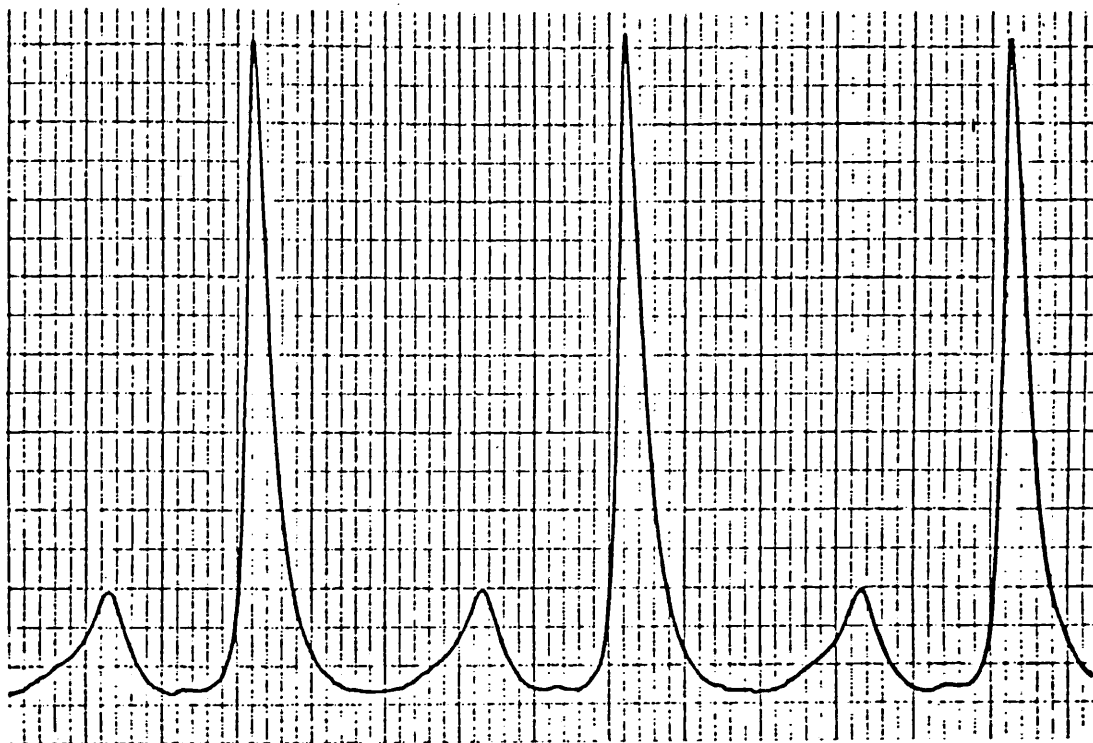
$d = 13.1$

$\phi = 2 \text{ cm}$



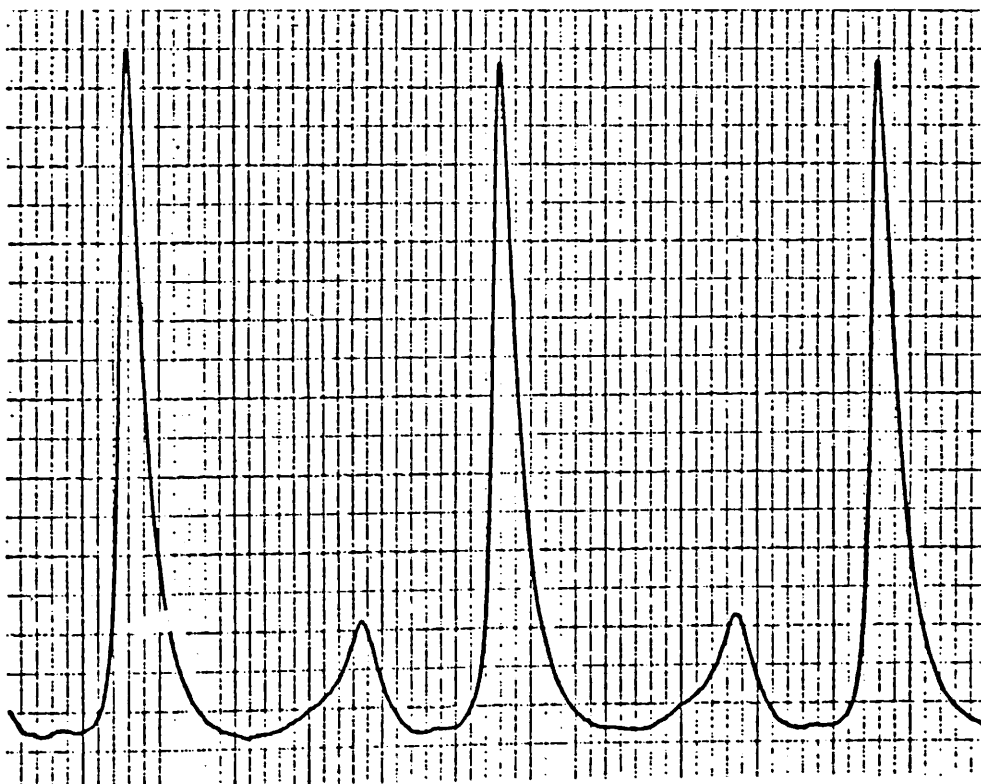
$d = 12.1$

$\phi = 2 \text{ cm}$



$d = 11.1$

$\phi = 2 \text{ cm}$



$d = 10.6$

$\phi = 2 \text{ cm}$

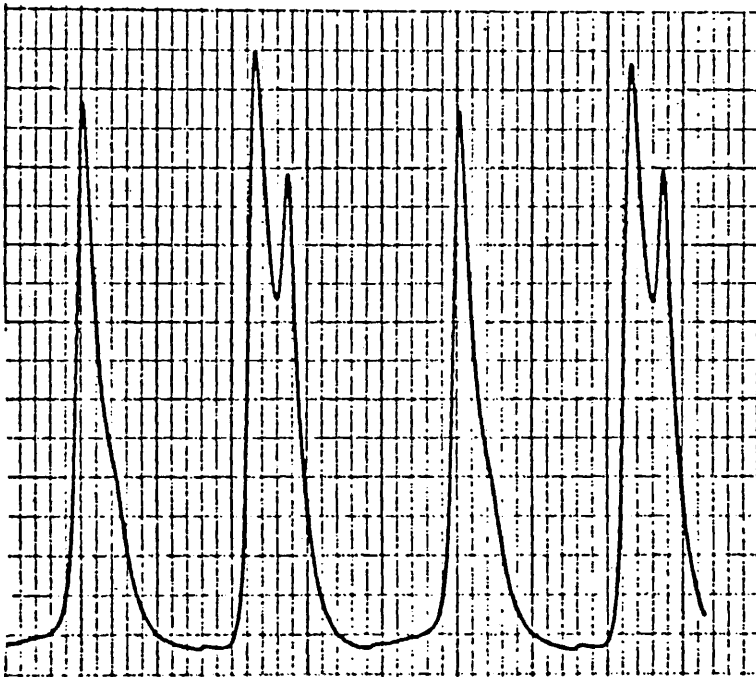
## 7.2. Influence of higher order modes on scattering cross-section measurements.

Figure 7.6 shows the mode spectra of the open resonator at a mirror separation of 0.17 m and how they are modified by changing the longitudinal position of the scattering object. The scattering object was a linear array of 15 short-circuited dipole elements of length  $0.5\lambda$  separated by  $0.75\lambda$ , reproduced on a  $3.5 \mu\text{m}$  thick mylar substrate. The scattering obstacle was found to couple energy to, and so perturb, the higher order modes. Some of these modes became degenerate with the fundamental  $\text{TEM}_{00}$  mode, making accurate determinations of the scattering cross-sections difficult<sup>60</sup>. Even nearly degenerate modes caused the resonance curves of the fundamental modes to become distorted, reducing the accuracy of the halfwidth measurements. As has been demonstrated in Section 7.1, by reducing the aperture of one of the mirrors to 2 cm, it was possible to excite only the  $\text{TEM}_{00}$  mode and weakly excite the  $\text{TEM}_{10}$  mode. The unloaded Q of the open resonator with the apertures of both mirrors reduced to 2 cm was 40,000. With only one mirror aperture reduced to 2 cm an unloaded resonator Q of 65,000 was measured. Therefore, all measurements were made with only one mirror stopped down as the higher unloaded Q obtained under this condition increased the measurement accuracy.

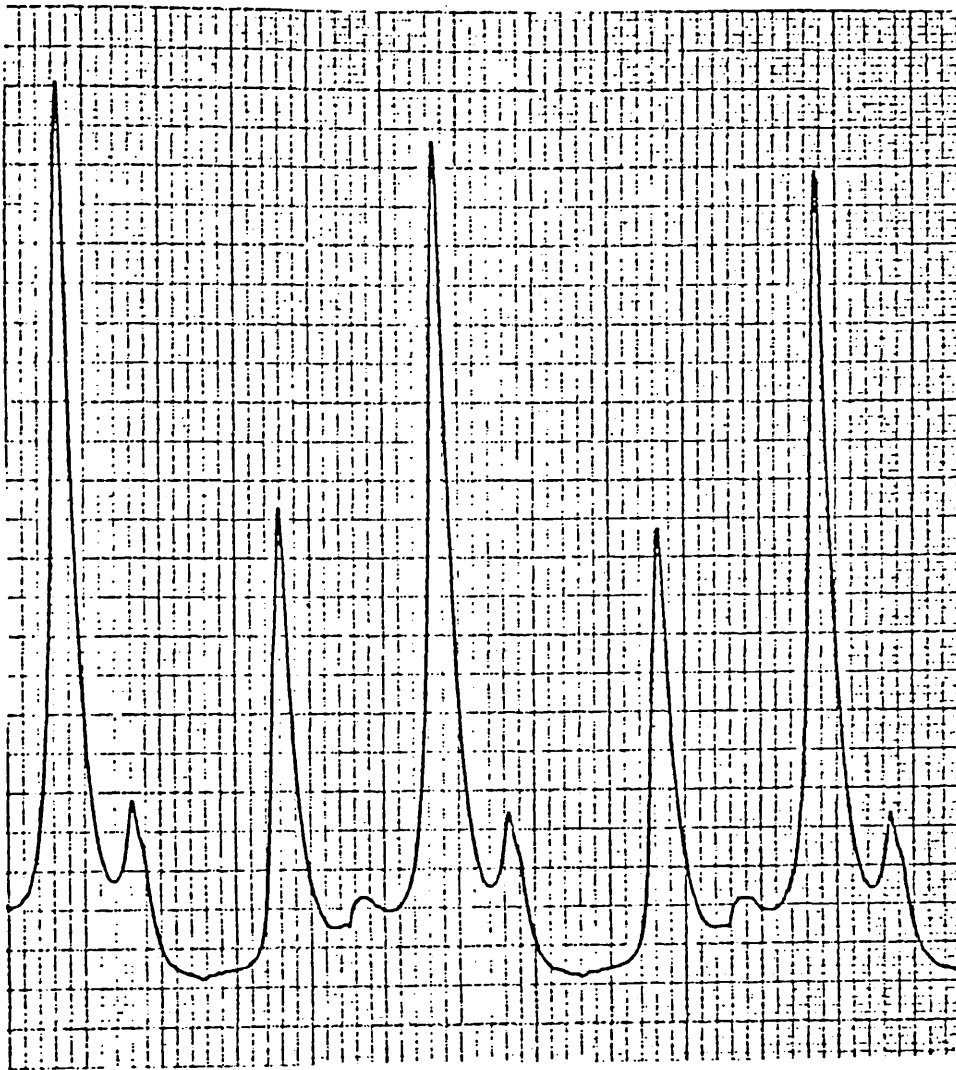
The variation of the loaded Q of the resonator with axial position of the scattering array is shown in Figure 7.7. The sample separations between consecutive loaded Q maxima and minima were found to be  $168 \pm 3 \mu\text{m}$ . This is half the HCN laser wavelength ( $337 \mu\text{m}$ ), verifying the standing wave field distribution within the resonator cavity. A wire grid analyser was rotated in front of the detector to verify that the horizontal linear polarisation was maintained within the resonator cavity. It was found that the field was  $\sphericalangle 98\%$  horizontally polarised.



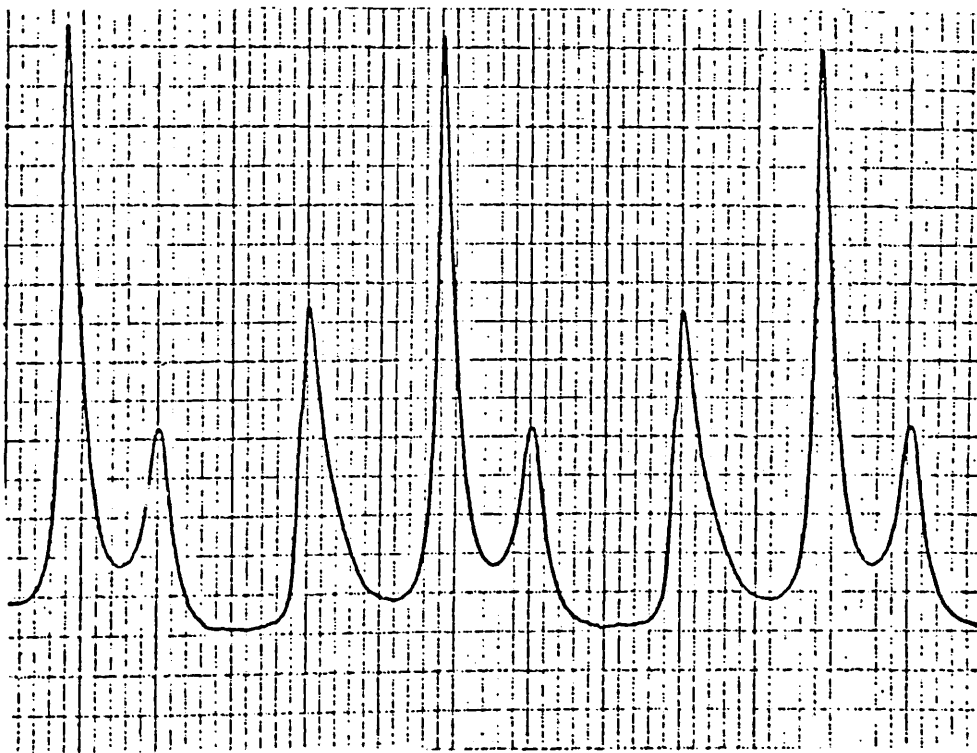
Figure 7.6. Variation of the mode spectrum of the open resonator with sample position,  $S$ , when loaded with a linear array of 15 short circuited dipole elements of length  $0.5\lambda$  separated by  $0.75\lambda$ .  
Mean mirror separation = 17 cm .  
Mirror apertures = 3 cm.



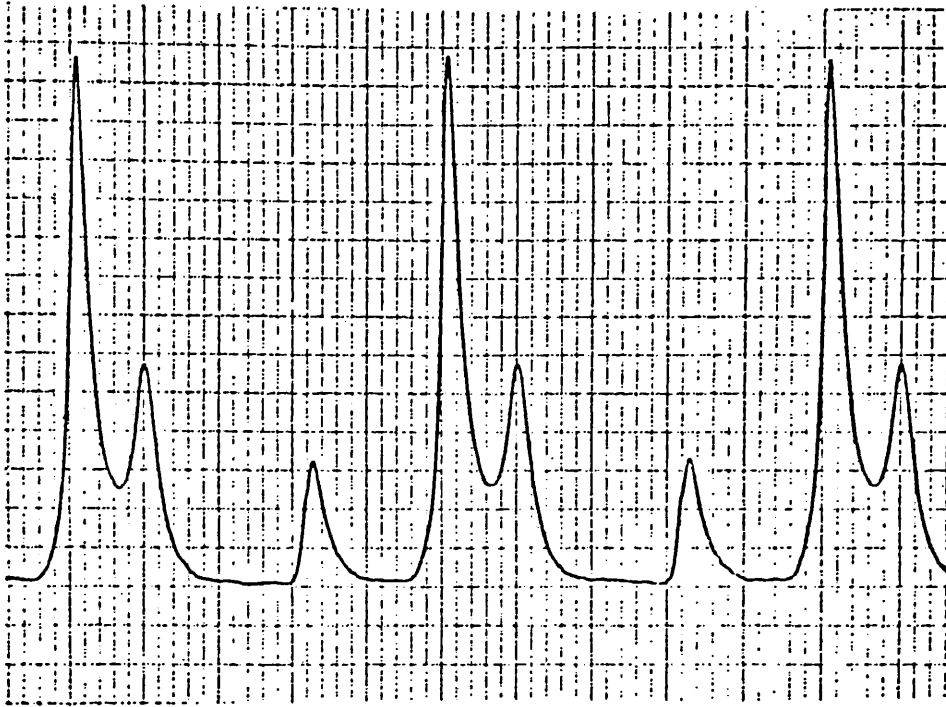
$d = 17 \text{ cm}$        $\phi = 3 \text{ cm}$   
Mode spectrum of unloaded cavity.



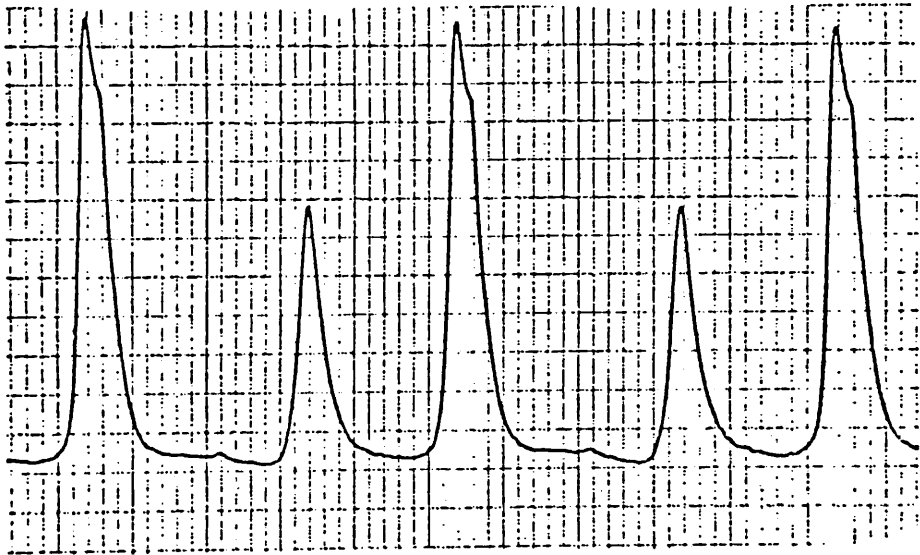
$S = 72 \mu\text{m}$        $d = 17 \text{ cm}$        $\phi = 3 \text{ cm}$



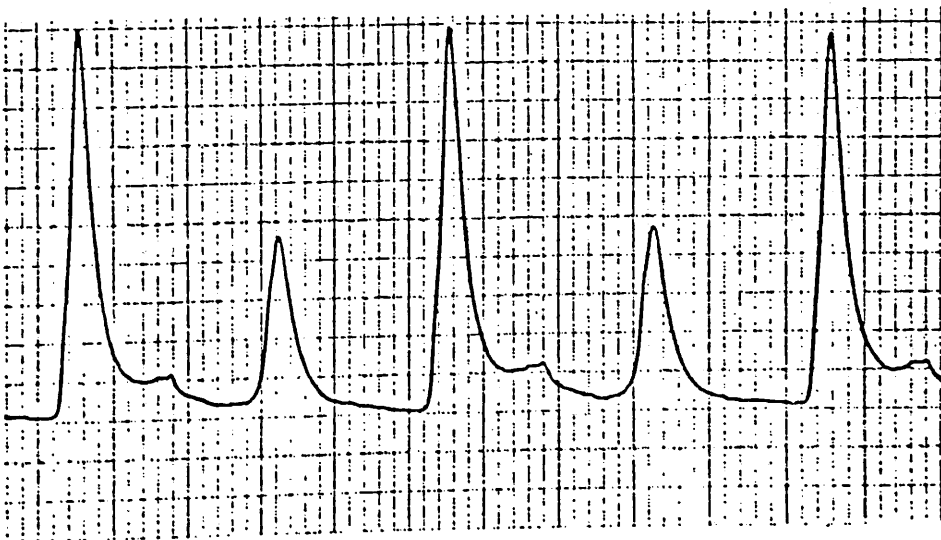
$S = 92 \mu\text{m}$        $d = 17 \text{ cm}$        $\phi = 3 \text{ cm}$



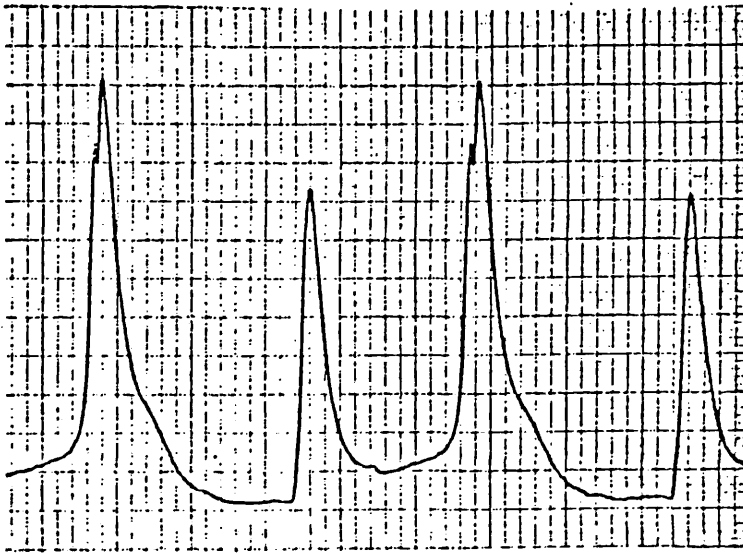
$S = 112 \mu\text{m}$        $d = 17 \text{ cm}$        $\phi = 3 \text{ cm}$



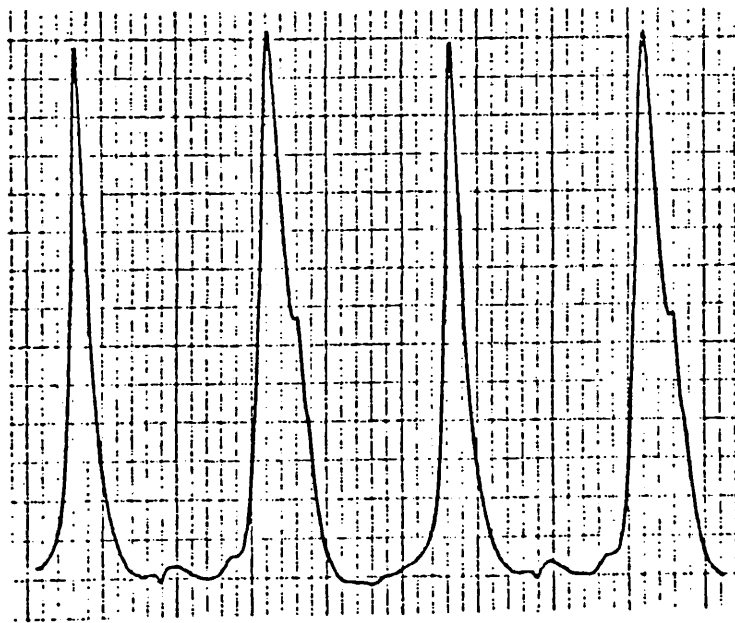
$S = 132 \mu\text{m}$        $d = 17 \text{ cm}$        $\phi = 3 \text{ cm}$



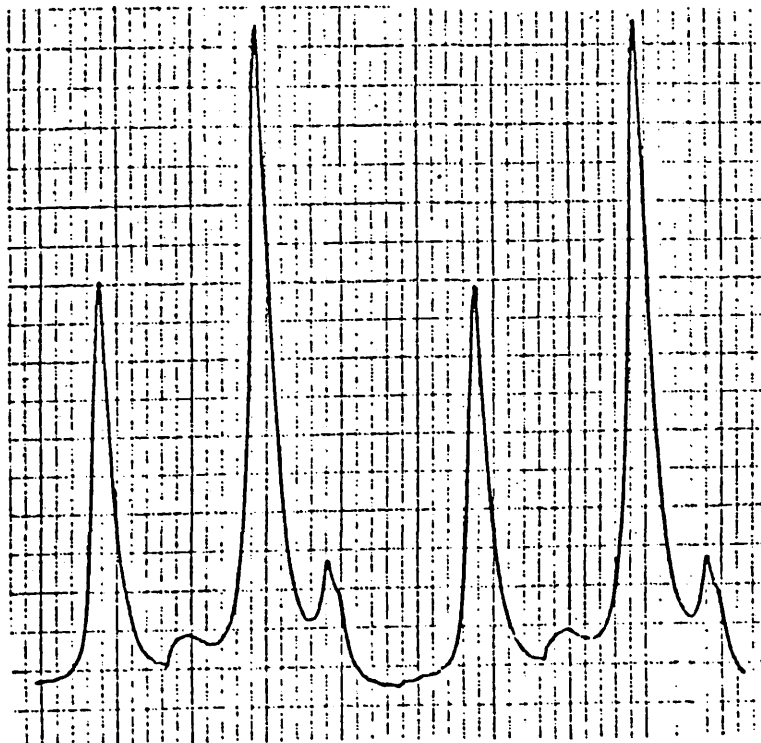
$S = 152 \mu\text{m}$        $d = 17 \text{ cm}$        $\phi = 3 \text{ cm}$



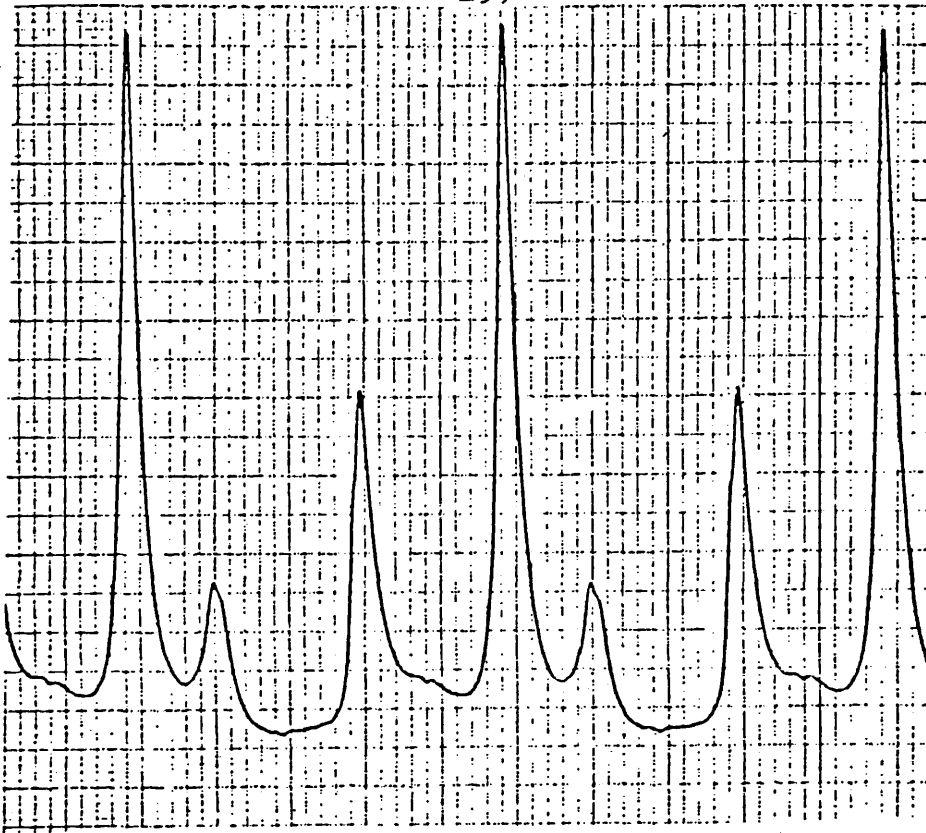
$S = 172 \mu\text{m}$        $d = 17 \text{ cm}$        $\phi = 3 \text{ cm}$



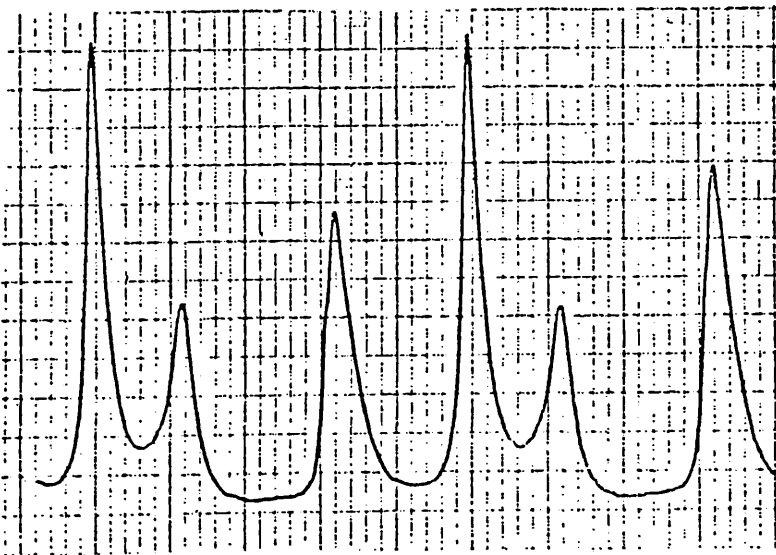
$S = 192 \mu\text{m}$        $d = 17 \text{ cm}$        $\phi = 3 \text{ cm}$



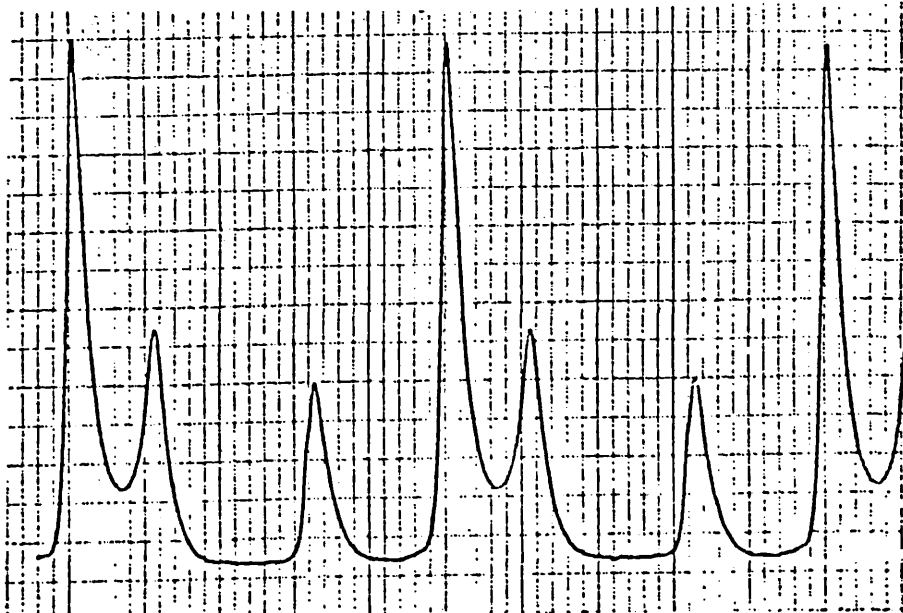
$S = 212 \mu\text{m}$        $d = 17 \text{ cm}$        $\phi = 3 \text{ cm}$



$S = 232 \mu\text{m}$        $d = 17 \text{ cm}$        $\phi = 3 \text{ cm}$



$S = 252 \mu\text{m}$        $d = 17 \text{ cm}$        $\phi = 3 \text{ cm}$



$S = 261 \mu\text{m}$        $d = 17 \text{ cm}$        $\phi = 3 \text{ cm}$

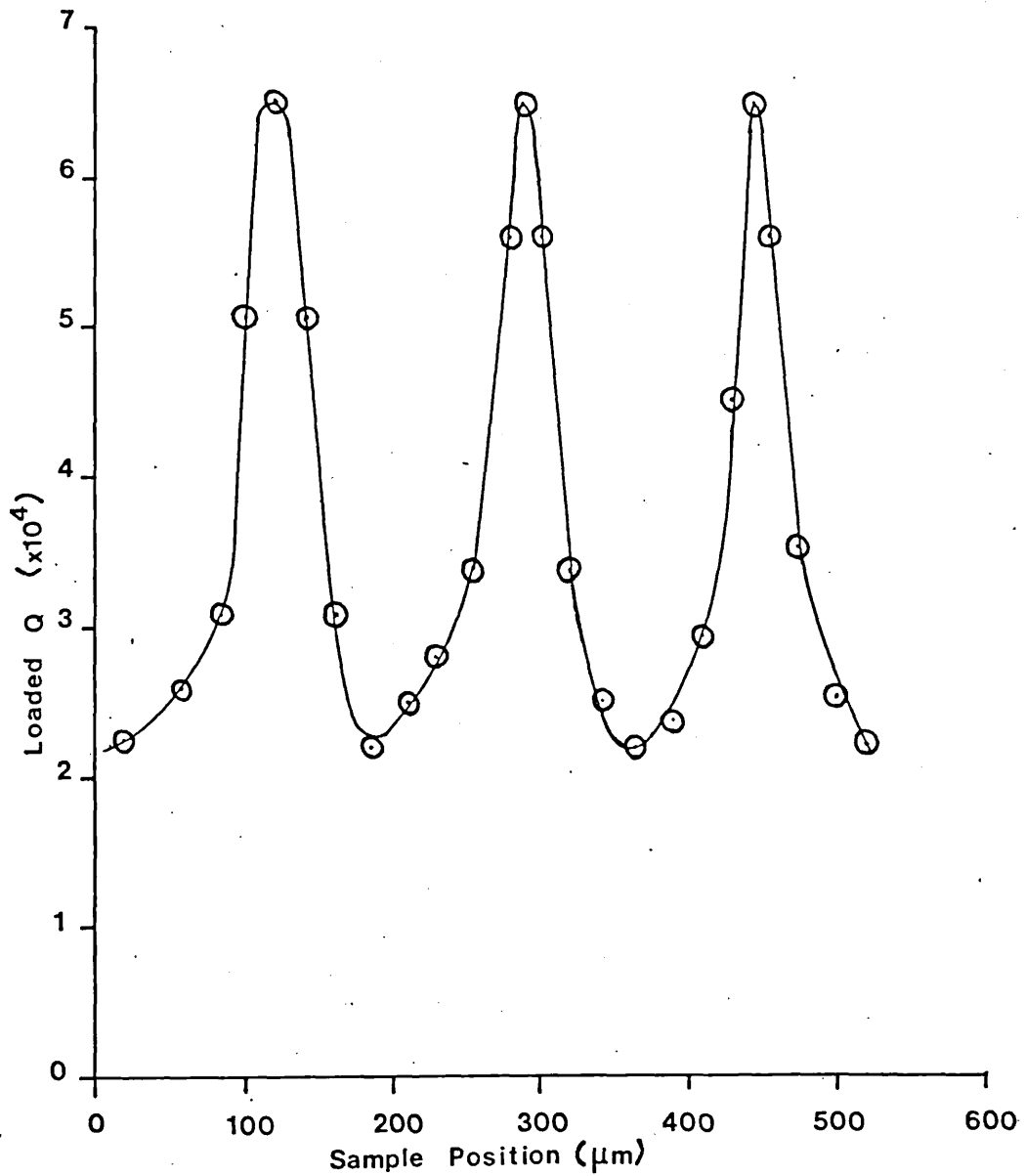


Figure 7.7. Variation of open resonator loaded Q with longitudinal sample position. Sample was a linear array of 15 short circuited dipole elements of length  $0.5\lambda$  separated by  $0.75\lambda$ .

### 7.3. Mirror modulation of the open resonator cavity.

A common technique employed in NMR spectroscopy is to differentiate the resulting frequency response curve. When this technique is applied to a resonator mode it results in a signal as shown in Figure 7.8(ii). The separation of the positive and negative peaks gives the resonance halfwidth and the zero crossing point corresponds to the centre frequency. As these points are easily distinguished, it is possible to obtain the Q very accurately because it is no longer necessary to measure the half power positions of the resonance curve shown in Figure 7.8(i).

The long response time of the Golay detector (30 ms) necessitated the use of relatively slow mechanical scan rates for the resonator mirror. Hence a differentiator with a long time constant would have been required. As the stability of a long time constant differentiator would have been poor, it was decided to employ a mirror modulation technique to obtain directly the differentiated output signal. Instead of chopping the output radiation from the laser, the mirror separation of the resonator cavity was now modulated. The phase and amplitude of the Golay detector output signal was obviously dependent upon the slope of the resonance curve at each sampled mirror position. The Golay output signal was phase detected with the mirror modulating waveform acting as a phase reference. The resulting output was the derivative of the resonance curve.

A Piezoelectric ceramic cylinder was used to modulate the position of the input mirror of the open resonator. The arrangement is illustrated in Figure 7.9. In order to estimate the required amplitude of mirror movement, it was decided that a modulation of about 10% of the unloaded open resonator halfwidth was required to obtain a sufficiently high output signal. The Golay detector output produced by a 10% mirror



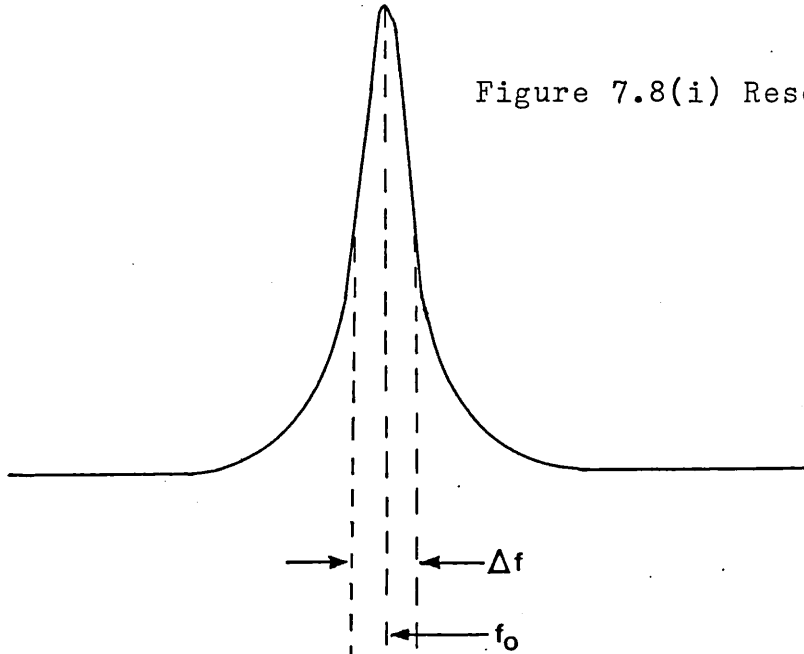


Figure 7.8(i) Resonance curve.

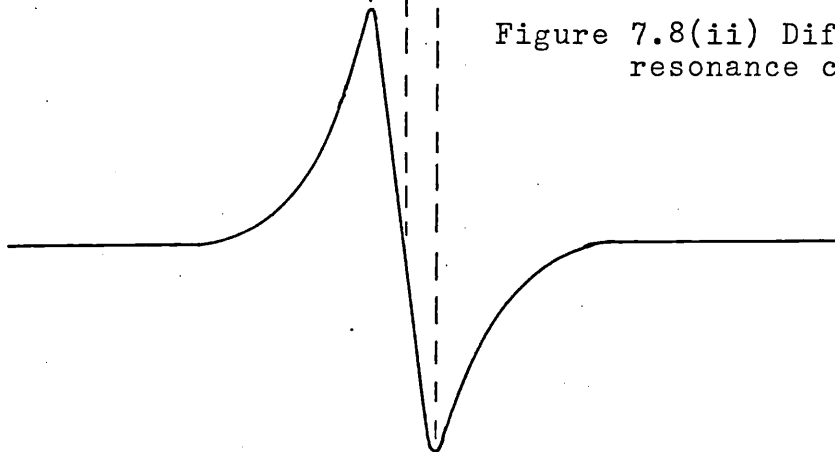


Figure 7.8(ii) Differentiated resonance curve.

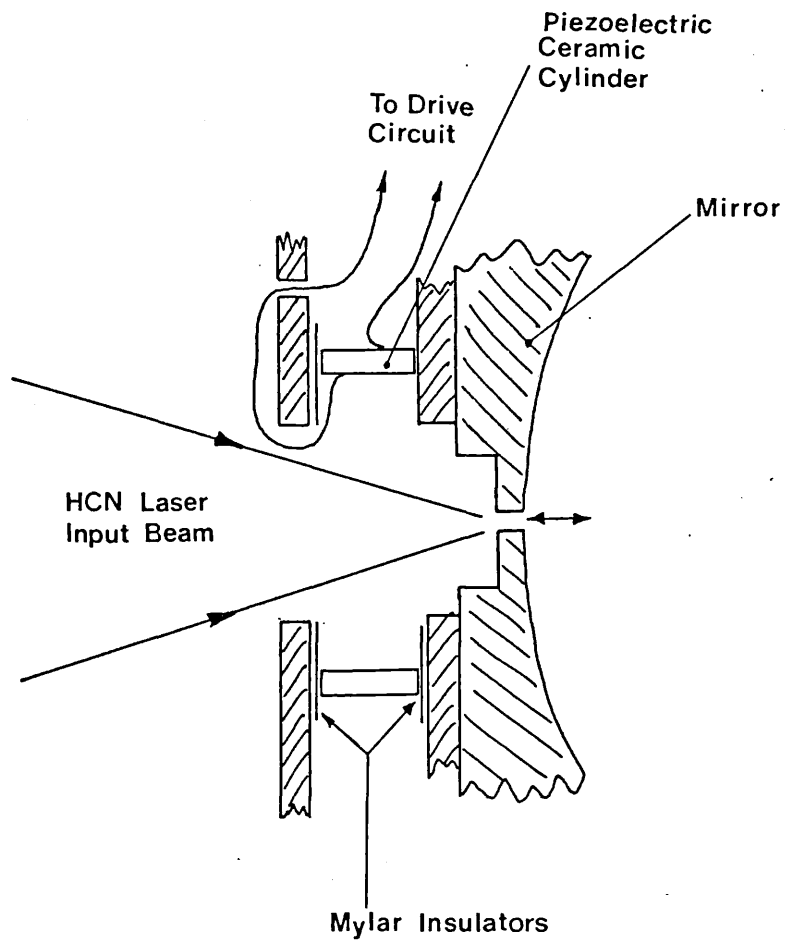


Figure 7.9. Use of a Piezoelectric ceramic cylinder to modulate the input mirror of the open resonator.

modulation when the mirror position corresponded to a half power point on the resonance curve (0.01 V peak to peak chopped radiation signal) was 1 mV peak to peak. The Q factor of the unloaded open resonator in this instance was  $6.5 \times 10^4$ . The corresponding half-width distance was 2.28  $\mu\text{m}$  at a mirror separation of 0.15 m. Therefore, a mirror movement of 0.23  $\mu\text{m}$  ( $2.3 \times 10^{-5}$  cm) was required for a 10% modulation.

For a Piezoelectric cylinder of length  $a$  and wall thickness  $t$ , the voltage required to produce a change in cylinder length  $\delta a$  is  $V$  where

$$V = \frac{\delta a t}{a d_{31}} \quad (7.4.)$$

The Piezoelectric constant for the cylinder used,  $d_{31}$ , was  $3.5 \times 10^{-6}$  cm/KV. The cylinder length was 2.54 cm and the wall thickness  $t$  was 0.6 cm. For a change in length of 0.23  $\mu\text{m}$  ( $2.3 \times 10^{-5}$  cm) a voltage of 1.5 KV was required. The outside diameter of the cylinder was 3 inches and the cylinder capacitance was 8000 pF. The circuit designed to drive the Piezoelectric cylinder and generate the reference signal for the Eye Unicam SP51 Golay amplifier/P.S.D. is shown in Figure 7.10.

The operation of the circuit in Figure 7.10 is as follows. The Piezoelectric cylinder was charged up to the 1.5 KV input voltage through a 4.7 M $\Omega$  current limiting resistor. The time constant of this circuit was 40 ms. The Thyristors were triggered every 140 ms by the unijunction transistor oscillator. The Piezoelectric cylinder was discharged through a 1 K $\Omega$  2 watt resistor. When the current through the Thyristors dropped below 10 mA the Thyristors turned off and the ceramic cylinder charged up again. The time constant of the discharge circuit was approximately 10  $\mu\text{s}$ . The voltage variation across the ceramic cylinder is shown in Figure 7.11. The unijunction oscillator timing capacitor output voltage was fed into a 741 operational amplifier threshold comparator.



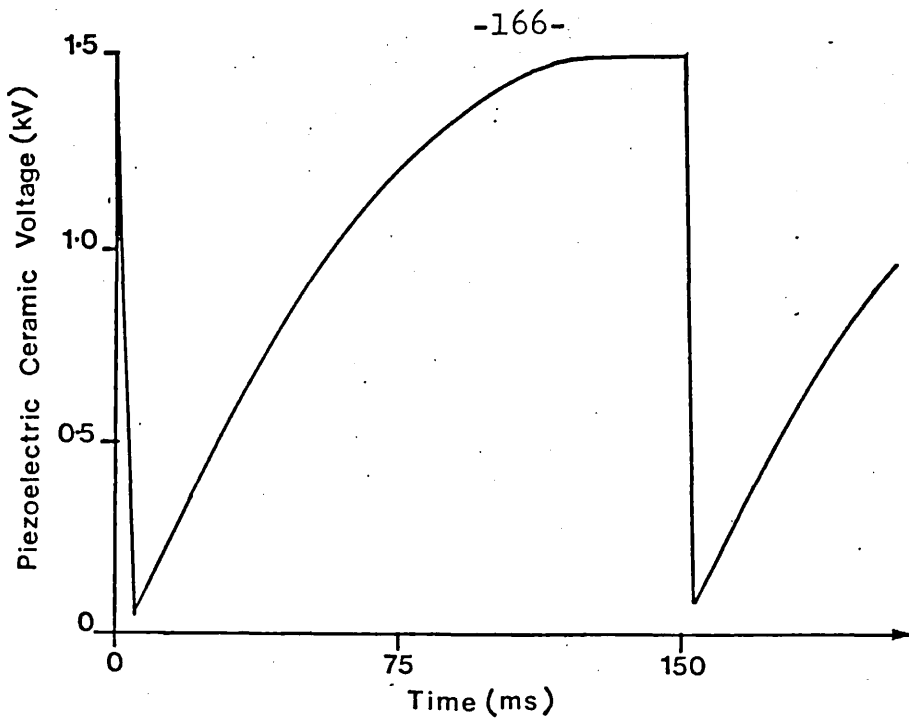


Figure 7.11. Voltage variation across the Piezo-electric ceramic cylinder produced by the circuit shown in Figure 7.10.

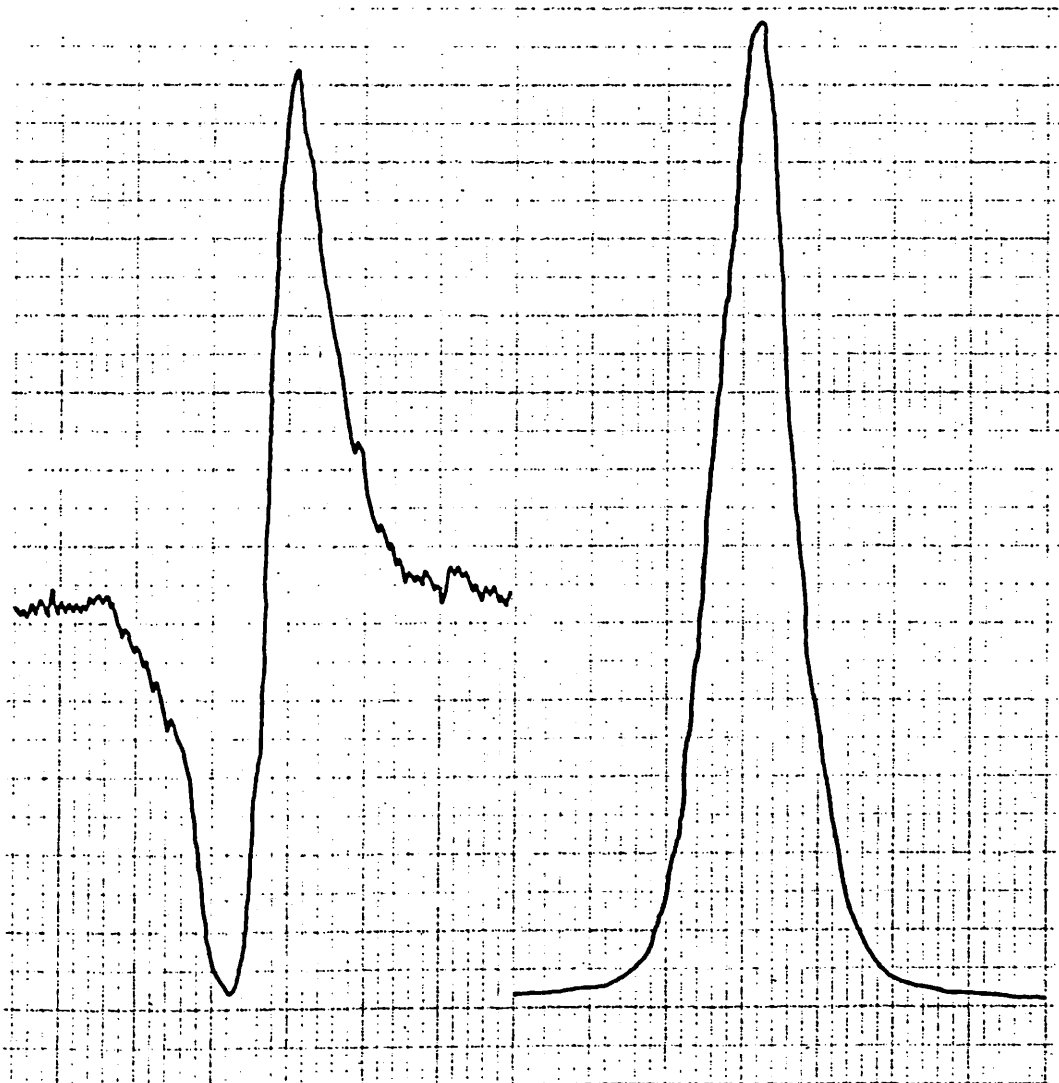


Figure 7.12. Left: Mirror chopped response curve  
(Gain = 72dB,  $\tau = 2s$ ,  $f_{\text{chop}} = 7\text{Hz}$ ).

Right: Radiation chopped response curve  
(Gain = 46dB,  $\tau = 0.5s$ ,  $f_{\text{chop}} = 13\text{Hz}$ )

The output of the threshold comparator was fed into a phase inverting circuit which could be switched in or out so as to produce a reference phase of  $0^\circ$  or  $+180^\circ$  relative to the cylinder modulation voltage. The output of the phase inverting circuit fed a 555 timer voltage controlled pulse position modulating circuit which fed a 1:1 mark to space ratio signal to a relay driver. The phase of the reference signal was adjustable and could be varied between  $0^\circ$  and  $+170^\circ$  relative to the output of the phase inverting circuit. The relay contacts substituted for the reed contacts on the mechanical Golay chopper. These provided the reference signal for the SP51 Golay amplifier. Figure 7.12 shows the experimental response curves derived from the normal mechanically chopped and the vibrating mirror modulated radiation. As the Golay output signal was lower for the mirror modulation case, more gain was required on the Golay amplifier. A PSD time constant of 2 seconds and an amplifier gain of 72 dB was necessary to achieve a satisfactory signal-to-noise ratio for the mirror modulation case, as opposed to a time constant of 0.5 seconds and an amplifier gain of 46 dB in the case of mechanically chopped radiation.

Although the vibrating mirror method has several advantages over the conventional resonance curve measurement technique with regard to increasing the accuracy of measurement of  $\Delta d$  and  $d$ , it was found that the higher signal-to-noise ratio obtained with the conventional method outweighed the theoretical improvement in accuracy. Also, the signal-to-noise ratio deteriorated as the loaded resonator  $Q$  decreased because the gradient of the sides of the resonance curve decreased. Although interesting in its own right, this technique was not adopted for use in the final instrument.

7.4. Determination of the scattering widths of a long thin wire at submillimetre wavelengths using the open resonator.

To ascertain whether or not the conventional open resonator measurement technique was operating successfully at this wavelength, it was decided to measure the scattering cross-sections of some common objects for which the cross-sections were accurately known. At X-band Cullen<sup>49</sup> employed metal spheres for this purpose and obtained excellent agreement with Mie scattering theory, thereby verifying the technique. The range of sphere diameters employed by Cullen ranged from  $0.3\lambda$  to  $0.04\lambda$  at X-band. As spheres of corresponding diameter at 891 GHz ( $337 \mu\text{m}$ ) would have been difficult to support and locate, it was decided to verify the open resonator calibration by measuring the scattering widths of fine wires at this wavelength. The theoretical variation of the scattering width with wire diameter is well known and therefore could be employed as the reference measurement. Also, the open resonator measurement technique has been used to make the same measurement at X-band with some success<sup>67</sup>.

The open resonator technique is limited to the measurement of the extinction cross-section of a class of scatterers possessing reflection symmetry in a plane perpendicular to the direction of propagation of the incident wave. It can therefore be used to measure the cross-section of a two-dimensional object such as an infinitely long cylinder.

The field at the beam waist in an open resonator has the form,

$$E_x = E_0 \exp \left\{ -\frac{r^2}{\omega_0^2} \right\} \quad (7.5.)$$

where  $r$  is the perpendicular distance from the axis of the Gaussian beam and  $\omega_0$  is the beam radius at the waist. This can be factorised as

$$E_x = \exp \left\{ -\frac{x^2}{\omega_0^2} \right\} \exp \left\{ -\frac{y^2}{\omega_0^2} \right\} \quad (7.6.)$$

where the x-y plane is perpendicular to the beam axis. If the axis of the cylinder is parallel to say the x-axis then in the vicinity of the wire, all the scattered field components will have  $\exp(-x^2/\omega_0^2)$  as a factor. However, if  $\omega_0$  is sufficiently large in comparison to the radius of the wire and the wavelength, the y, z dependent part of the scattered field will be essentially the same as that for an incident plane wave.

The total incident power in the beam is

$$p = \frac{\pi}{2} \omega_0^2 S_0 \quad (7.7.)$$

where  $S_0$  is the incident poynting flux and

$$S_0 = \frac{1}{2} \frac{E_0^2}{\eta} \quad (7.8.)$$

$\eta$  = intrinsic impedance of free space.

Here,  $E_0$  is the maximum amplitude of the Gaussian field distribution. The power removed from the beam per unit length of the cylinder is

$$d P_s = \sigma S_0 \exp \left\{ -\frac{2x^2}{\omega_0^2} \right\} dx \quad (7.9.)$$

Here,  $\sigma$  is the total scattering and absorption width of the cylinder. If the cylinder is perfectly conducting, then this is just the scattering width.

The total power removed from the beam is

$$P_s = \sigma S_0 \int_{-\infty}^{+\infty} \exp \left\{ -\frac{2x^2}{\omega_0^2} \right\} dx \quad (7.10.)$$

$$= \sigma S_0 \sqrt{\frac{\pi}{2}} \omega_0 \quad (7.11.)$$

Hence, the effective extinction cross-section of the cylinder, referred to the on axis power density is<sup>67</sup>

$$\sigma_{\text{eff}} = \sqrt{\frac{\pi}{2}} \omega_0 \sigma \quad (7.12.)$$



The quantity of  $\sigma_{\text{eff}}$  is that measured in the open resonator and the beam waist radius  $\omega_0$  can be found from equation 4.5 in Chapter 4.

The scattering cross-section was measured for a series of fine annealed copper wires in the range 32-50 SWG (corresponding to a range of diameters from 274.3  $\mu\text{m}$  to 25.4  $\mu\text{m}$  respectively). The surface reactance of copper at 891 GHz (see Table 2.2 in Chapter 2) is  $0.234 + j 0.234 \Omega$ . This is sufficiently low to allow the currents to propagate without significant attenuation.

The copper wires were positioned in the central planewave region intersecting the resonator axis and with the axis of the wire orientated vertically in the resonator. Hence the magnetic field vector,  $H$ , was parallel to the wire. The length of the wires used was 80 mm so the wire continued well beyond the mirror aperture of 20 mm. The wire therefore appeared of infinite length. The unloaded  $Q$  of the open resonator was measured each time with the wire absent. Three measurements were taken of the effective scattering cross section,  $\sigma_{\text{eff}}$ , for each wire. The scattering width was calculated from equation 7.12. The experimental measurements of normalised scattering width  $\sigma/4a$  plotted against the normalised radius  $ka$  are shown in Figure 7.13. The cylinder radius is  $a$  and  $k = 2\pi/\lambda$ . The solid line in Figure 7.13 represents the theoretical results for  $\vec{H}$  parallel to the axis of the cylinder as obtained by Wu<sup>68</sup>.

The agreement between theory and experiment is very good. Hence, the application of the technique to the measurement of scattering cross-sections at submillimetre wavelengths was verified.

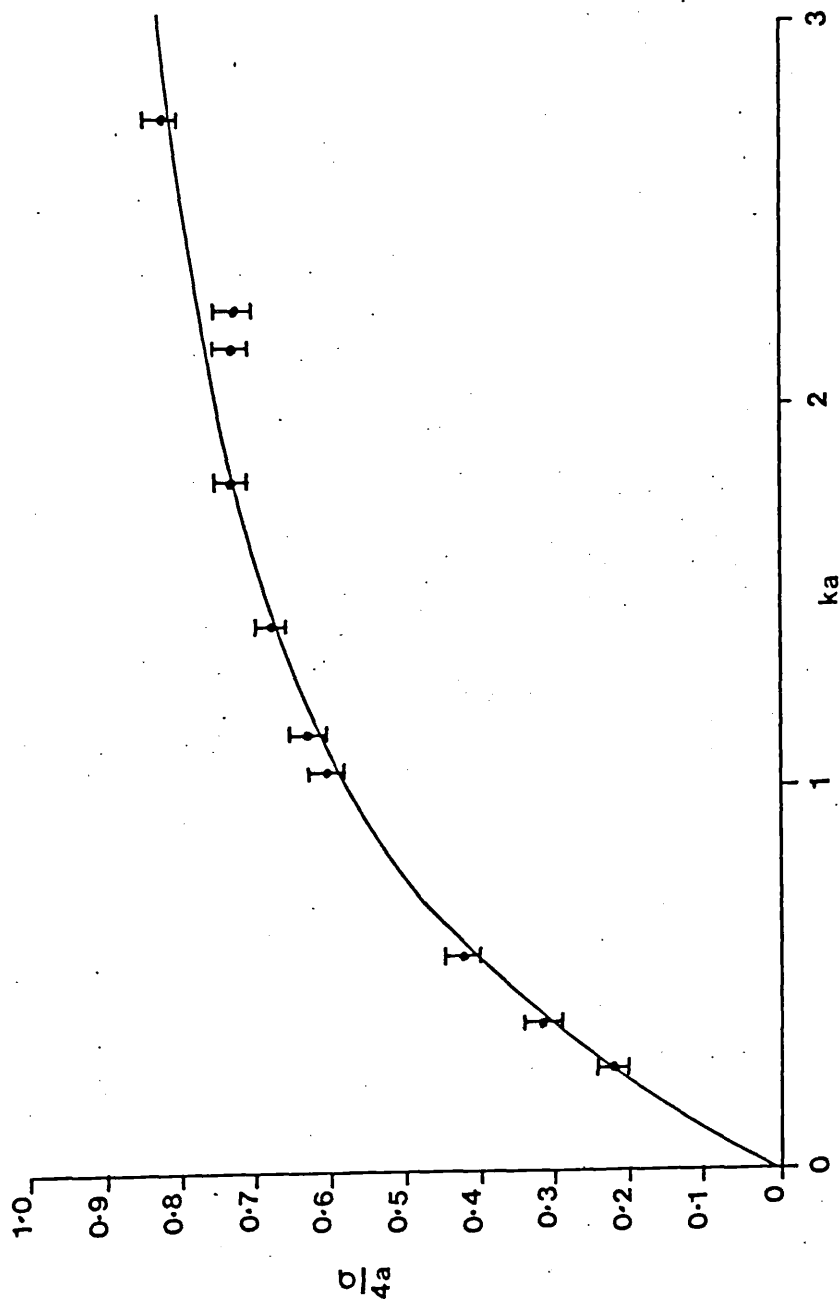


Figure 7.13. Scattering cross-section of a circular cylinder with  $\vec{H}$  parallel to the cylinder axis (— theoretical (geometrical optics + one correction term), I experimental at 891 GHz)

7.5. Measurement of the refractive index and absorption coefficients of dielectric materials at 891 GHz.

The first application of an open resonator to the measurement of permittivity appears to have been made by Degenford and Coleman<sup>6,9</sup>. In their method, a plane sheet of dielectric material was placed at the centre of the resonator, but with its normal making a small angle  $\theta$  with the axis of the resonator. The reason for the tilt was to simplify the theory by allowing reflected waves to escape from the resonator. By eliminating reflections in this way, the theory becomes very simple, amounting effectively to the condition that the optical path length between the mirrors should be an integral number of half wavelengths. Provided that thin dielectric samples,  $< \lambda/30$  thick, are employed, and the dielectric constant is low, then the effect of reflections is small<sup>6</sup>. A small amount of tilt would have the effect of increasing the effective thickness of the dielectric sample, but for small angles this increase would be negligible. For example, a tilt of  $3^\circ$  would increase the effective thickness by 0.13%.

If the  $TEM_{00q}$  mode of the open resonator is resonant at a mirror separation of  $d$  we can use the approximation that

$$d = (q + 1) \frac{\lambda}{2} \quad (7.13.)$$

where  $\lambda$  is the free space wavelength.

If we now place a dielectric sheet of thickness  $t$  and refractive index  $\mu$  into the cavity, then the  $TEM_{00q}$  mode will be resonant when the mirror separation is  $d'$ . As the change in optical path length is  $(1 - \mu)t$  then

$$d' = d + (1 - \mu)t \quad (7.14.)$$

The difference in the positions of the  $TEM_{00q}$  modes

when the dielectric is removed from the resonator is  $x$ ,

$$\text{where } x = d - d' \quad (7.15.)$$

hence

$$x = (\mu - 1)t \quad (7.16.)$$

Obtaining a mode spectrum with the dielectric successively in place and removed and by noting the relative positions of the  $TEM_{00}$  modes in the two spectra, the refractive index  $\mu$  may be found.

The absorption coefficient  $\alpha$  may also be found, provided that the power loss due to reflections is much lower than that due to absorption. If  $P_0$  is the power incident on a thickness of dielectric  $t$ , then the power dissipated in the dielectric is given by  $P$  where

$$P = P_0 (1 - \exp(-\alpha t)) \quad (7.17.)$$

It is assumed that the dielectric sheet is thin compared with the wavelength, say  $< \lambda/30$ . With the sample positioned at a maximum field point in the standing wave distribution, the power dissipated in the sheet is given by equation 7.17. Here  $P_0$  is obtained by integrating the Poynting flux distribution over the area of the dielectric which is assumed to be infinite in extent.

$$P_0 = \sqrt{\epsilon_r} |S_0| \int_0^\infty \int_0^{2\pi} \exp\left\{-\frac{2r^2}{\omega_0^2}\right\} r \, dr \, d\theta \quad (7.18.)$$

The error made in assuming an infinite area of dielectric is small, because the Gaussian beam profile falls off rapidly with radius  $r$ . Hence

$$P_0 = \frac{\sqrt{\epsilon_r} |S_0| \pi \omega_0^2}{2} \quad (7.19.)$$

$\epsilon_r$  is the relative permittivity of the dielectric and is equal to the square of the refractive index  $\mu$ .

The presence of the dielectric reduced the quality factor of the open resonator  $Q_M$ . If  $Q_o$  is the unloaded quality factor then

$$\frac{1}{Q_M} = \frac{1}{Q_o} + \frac{P}{\omega E} \quad (7.20.)$$

where  $\omega = 2\pi f$  and  $E$  is the energy stored in the resonator. From equation 4.31 in Chapter 4

$$E = \frac{|S_o| \pi d \omega_o^2}{2c} \quad (7.21.)$$

hence

$$\frac{1}{Q_M} = \frac{1}{Q_o} + \frac{(\sqrt{\epsilon_r} |S_o| \frac{\pi \omega_o^2}{2} (1 - \exp(-\alpha t)))}{\left\{ \frac{2\pi f |S_o| \pi d \omega_o^2}{2c} \right\}} \quad (7.22.)$$

$$\frac{1}{Q_M} = \frac{1}{Q_o} + \frac{\sqrt{\epsilon_r} (1 - \exp(-\alpha t))}{2\pi d/\lambda} \quad (7.23.)$$

substituting  $\mu$  for  $\sqrt{\epsilon_r}$  and re-arranging for  $\alpha$

$$\alpha = -\frac{1}{t} \ln \left[ 1 - \frac{\left\{ \frac{1}{Q_m} - \frac{1}{Q_o} \right\}}{\left\{ \mu \lambda / 2\pi d \right\}} \right] \quad (7.24.)$$

Various thin dielectric samples were measured to determine which materials would be the most suitable for antenna substrates. The results obtained are given in Table 7.3 where they are also compared with the values quoted by other Authors.

Table 7.3

Dielectric Properties at 891 GHz measured with the open Resonator					
Material	Measured		Previously published		Ref.
	$\mu$	$\alpha(\text{cm}^{-1})$	$\mu$	$\alpha(\text{cm}^{-1})$	
High Density Polythene	1.46 $\pm 0.03$	0.59 $\pm 0.01$	1.44	0.4	70
Low Density Polythene	1.62 $\pm 0.05$	0.21 $\pm 0.01$	1.50	0.2	70
PTFE (Teflon)	1.45 $\pm 0.05$	0.77 $\pm 0.01$	1.39	0.8	70
Mylar (Melinex)	1.76 $\pm 0.03$	1.97 $\pm 0.04$	1.75	2.0	71
Fused Silica	2.18 $\pm 0.01$	3.15 $\pm 0.05$	2.14	3.3	72
Crystal Quartz (Z - Cut)	2.08 $\pm 0.04$	0.07 $\pm 0.01$	2.13	0.1	73

Agreement with the previously published results was found to be quite good. The optical properties of polymers in the submillimetre region are dependent upon internal stresses within the material caused by the method of manufacture, and this may possibly explain some of the discrepancies.

#### 7.6. Measurement of broadside total scattering cross-sections of short-circuited arrays.

The open resonator technique measures the extinction cross-sections (the combined scattering and absorption cross-sections) of objects placed within it. However, as no power is absorbed by an ideal short-circuited antenna, then the extinction cross-section is equal to the total scattering cross-section of the antenna. The beam radius,  $\omega_0$ , of the  $\text{TEM}_{00}$

mode in the planewave region at the centre of the open resonator was  $5 \times 10^{-3}$  m ( $15 \lambda$  at  $337 \mu\text{m}$ ) for a mirror separation of 0.16 m. This dimension consequently limited the size of the antenna arrays that could be investigated. The unloaded Q of the open resonator was  $\sim 65,000$ , and the total scattering cross-section of a single halfwave dipole was calculated to be  $5.85 \times 10^{-8}$  m<sup>2</sup> at 891 GHz. As the minimum detectable cross-section using the open resonator was calculated to be  $0.7 \times 10^{-7}$  m<sup>2</sup>, then arrays of 5 or more elements were desirable in order to achieve sufficiently accurate results. The process for producing these arrays, and the choice of materials used is described in Chapter 8. The  $3.5 \mu\text{m}$  mylar substrates had equivalent scattering cross-sections of  $3 \times 10^{-8}$  m<sup>2</sup> and this was allowed for when computing the cross-sections of the arrays alone.

Figures 7.14 and 7.15 show the experimental results obtained. The continuous line represents the theoretical results predicted by the computer code developed from the theory of multiple scatterers due to Harrington<sup>20</sup>, which was presented in Chapter 3. Figure 7.14 shows the variation with inter-element separation of the total scattering cross-section  $\sigma_s$ , for arrays with 15 elements of halfwave and fullwave lengths. The variation with element length for arrays of 20 elements is shown in Figure 7.15, the inter-element separation being kept constant at  $0.25\lambda$ .

The agreement between theory and experiment for the variation with inter-element spacing was very good. This indicates that the mutual interaction between the elements in the array has been properly accounted for, and does not appear to have been affected by the substrate. However, for the variation with length, the agreement is less

Figure 7.14. Variation of normalised total scattering cross-section, with inter-element spacing, for linear arrays of 15 halfwave ( $L = 0.5\lambda$ ) and fullwave ( $L = 1.0\lambda$ ) short circuited dipole elements.

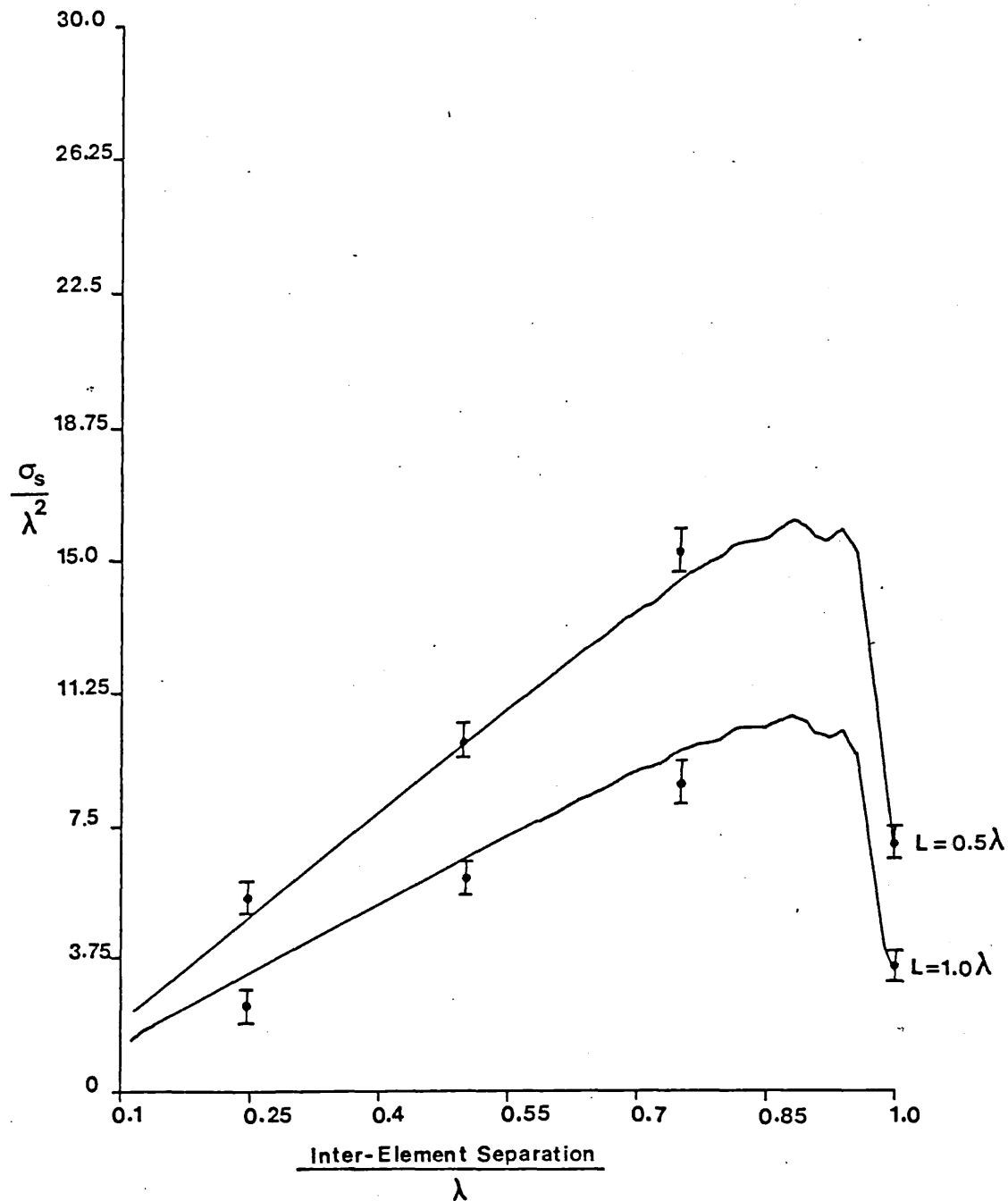
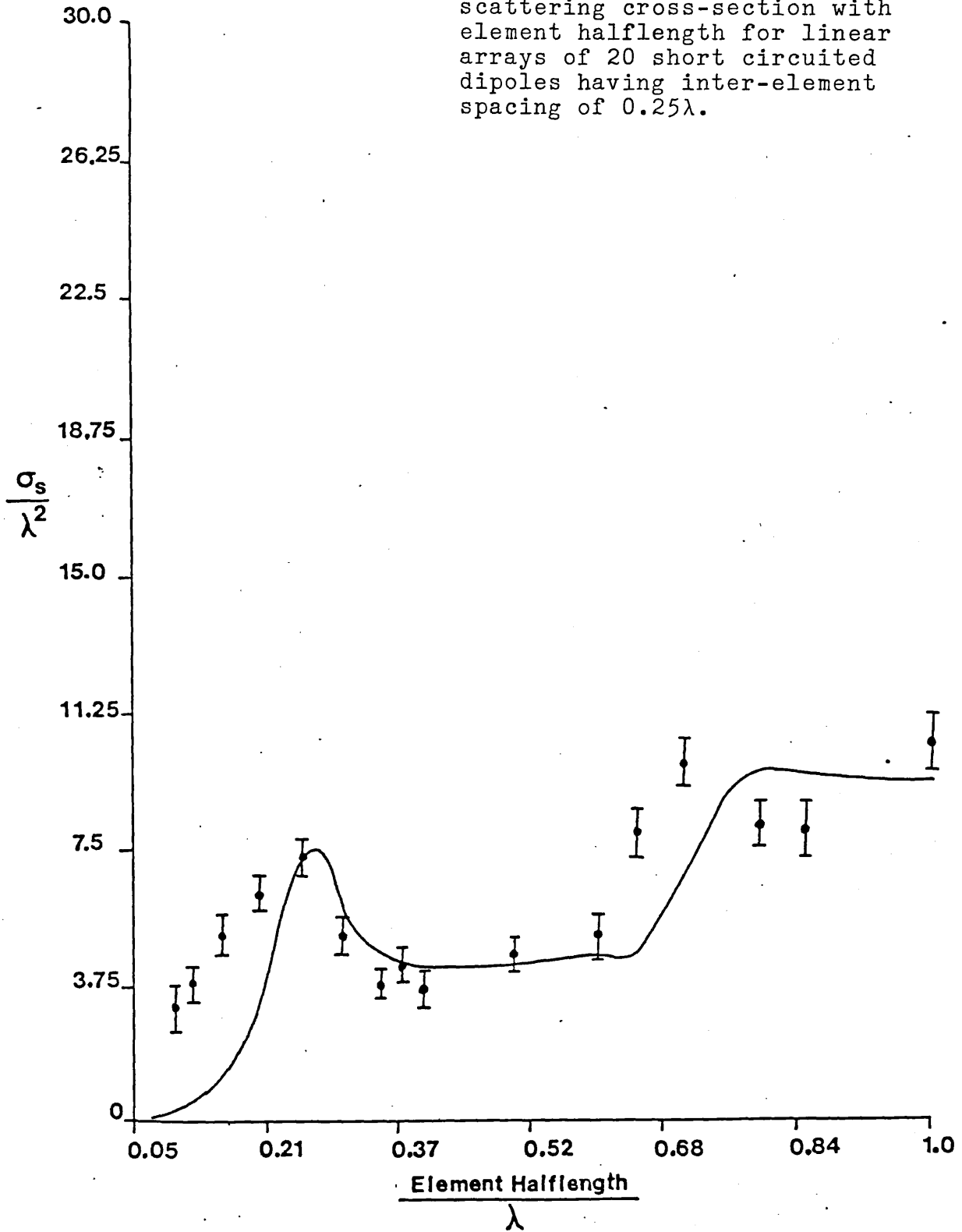




Figure 7.15. Variation of normalised total scattering cross-section with element halflength for linear arrays of 20 short circuited dipoles having inter-element spacing of  $0.25\lambda$ .



satisfactory - particularly for very short and also very long dipoles.

If  $R_o$  is the ohmic resistance per unit length of a dipole element, then the power loss  $P_o$  in the antenna carrying a current distribution  $I(Z)$  is given by the integral

$$P_o = \frac{1}{2} R_o \int_{-L}^{+L} |I(Z)|^2 dZ \quad (7.25.)$$

where  $L$  is the element halflength.

Now, for a scattering element of halflength  $L$ , the current distribution assumed by Hu is given by

$$I(Z) = \frac{I_o [\cos \beta Z - \cos \beta L]}{[1 - \cos \beta L]} \quad (7.26.)$$

where  $\beta$  is the propagation constant of the current on the antenna. Substituting equation 7.26 into 7.25

$$P_o = \frac{1}{2} \frac{I_o^2 R_o}{|1 - \cos \beta L|^2} \int_{-L}^{+L} |\cos \beta Z - \cos \beta L|^2 dZ \quad (7.27.)$$

Integrating 7.27

$$P_o = \frac{1}{2} \frac{I_o^2 R_o}{(1 - \cos \beta L)^2} \left| L + 2L \cos^2 \beta L + \frac{\sin 2\beta L}{2\beta} - \frac{4 \sin \beta L \cos \beta L}{\beta} \right| \quad (7.28.)$$

From the conservation of energy, this power must equal that dissipated in the increase in antenna input resistance effectively due to the ohmic loss. Let the increase in antenna input resistance be denoted by  $R_{in}$ . Then

$$P_o = \frac{1}{2} I_o^2 R_{in} \quad (7.29.)$$

Equating equations 7.28 and 7.29

$$R_{in} = R_o \left[ \frac{L + 2L \cos^2 \beta L + \frac{\sin 2\beta L}{2\beta} - \frac{4 \sin \beta L \cos \beta L}{\beta}}{(1 - \cos \beta L)^2} \right] \quad (7.30.)$$

Figures 7.16 and 7.17 show  $R_{in}/R_o \lambda$  plotted against element halflength, assuming that  $\beta$  is equal to the free space value  $2\pi/\lambda$ . For a cylindrical antenna of radius  $a$ , provided that the radius is much greater than the skin depth, the resistance per unit length  $R_o$  is given by

$$R_o = \frac{R_s}{2 \pi a} \quad (7.31.)$$

where  $R_s$  is the surface resistance of the metal. A planar dipole of width  $W$  can be approximated to a cylindrical antenna of radius  $a$  equal to  $W/4$ . Hence 7.31 becomes

$$R_o = \frac{2 R_s}{\pi W} \quad (7.32.)$$

The dipole elements used throughout this investigation had widths of  $\lambda/30$  so

$$R_o = \frac{60 R_s}{\pi \lambda} \quad (7.33.)$$

For a planar antenna of width  $\lambda/30$  reproduced in silver, for which  $R_s = 0.121 \Omega$ ,  $R_o$  is  $2.31 \Omega$  per wavelength. From Figure 7.16 it is evident that  $R_{in}/R_o \lambda$  does not exceed unity over the range of half-lengths  $0.01\lambda$  to  $0.8\lambda$ . Hence the increase in antenna input resistance for the dipole elements described is not greater than  $2.31 \Omega$  over this range. As this is small compared to the terminal input resistances, which vary from  $20 \Omega$  to  $1500 \Omega$  over this range of halflengths, then the effects of the finite surface impedance are negligible. For

EQUIVALENT LOSS INPUT RESISTANCE

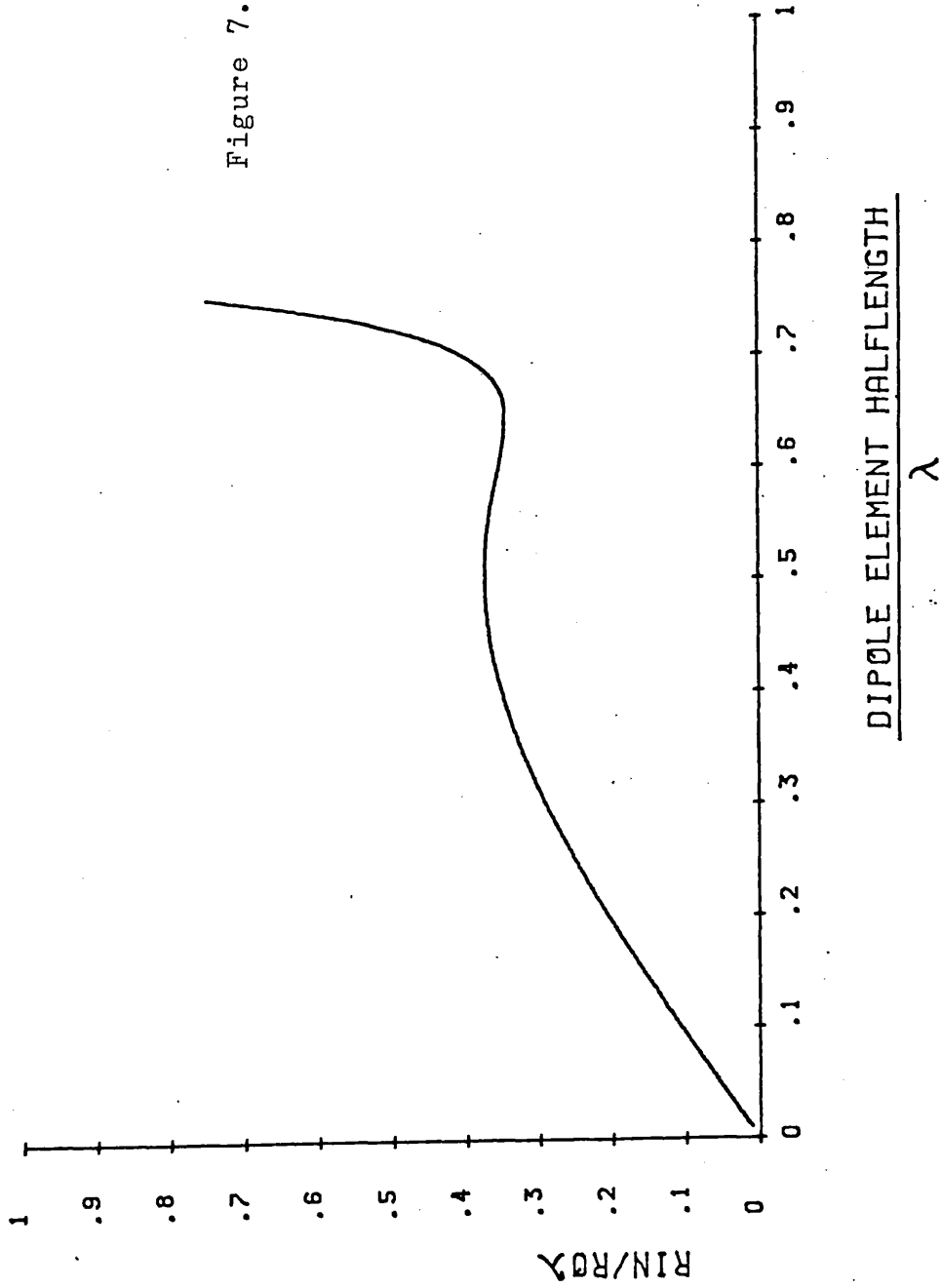


Figure 7.16. Variation of  $R_{in}/R_0 \lambda$  with dipole element half-lengths from  $0.01\lambda$  to  $0.75\lambda$ .

EQUIVALENT LOSS INPUT RESISTANCE

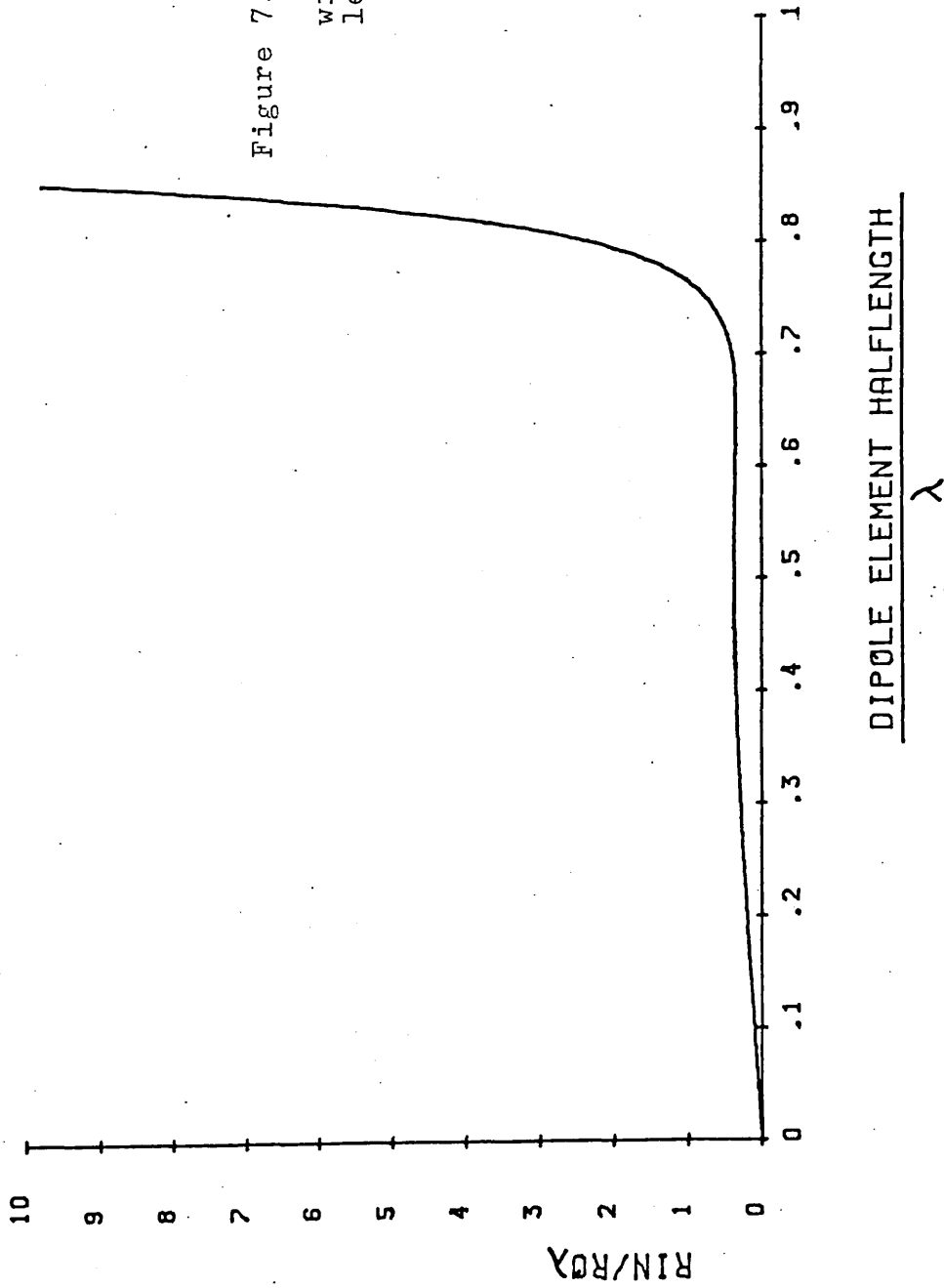


Figure 7.17. Variation of  $R_{in}/R_{0\lambda}$  with dipole element half-lengths from  $0.01\lambda$  to  $0.85\lambda$ .

half-lengths between  $0.8\lambda$  and  $1.0\lambda$   $R_{in}$  increases rapidly. However, the input resistance of the antenna also increases rapidly over this region and so the effect of the increasing component of the input resistance due to the loss may not be as detrimental as it might first appear.

In the case of short dipoles, the poor agreement between the theoretical and experimental cross-sections may result from the current distribution on the elements breaking down as the width of the elements become comparable to the element half-length. For long dipoles it is evident that the surface impedance is responsible for the disagreement.

The agreement between theory and experiment for the half-lengths of most practical interest, between  $0.25\lambda$  and  $0.5\lambda$ , validates the assumption that the currents are flowing in phase in the elements for broadside incidence and are not appreciably affected by the presence of the substrate. The effect of the substrate on the current density in the elements is examined in Chapter 9 when more data on the current distribution in the element is available. Furthermore, the finite surface impedance does not appear to have caused significant change in the measured cross-sections. The application of the open resonator technique to the absolute measurement of broadside scattering cross-sections of arrays has been demonstrated. The fact that the technique is absolute will be of use in the calibration of the backscattering measurements obtained by a different technique to be described in a later Chapter.

#### 7.7. Measurement of the H-plane total scattering cross-section.

An attempt to measure the variation of the H-plane scattering cross-section was made, using the open resonator. The mount which was employed to vary

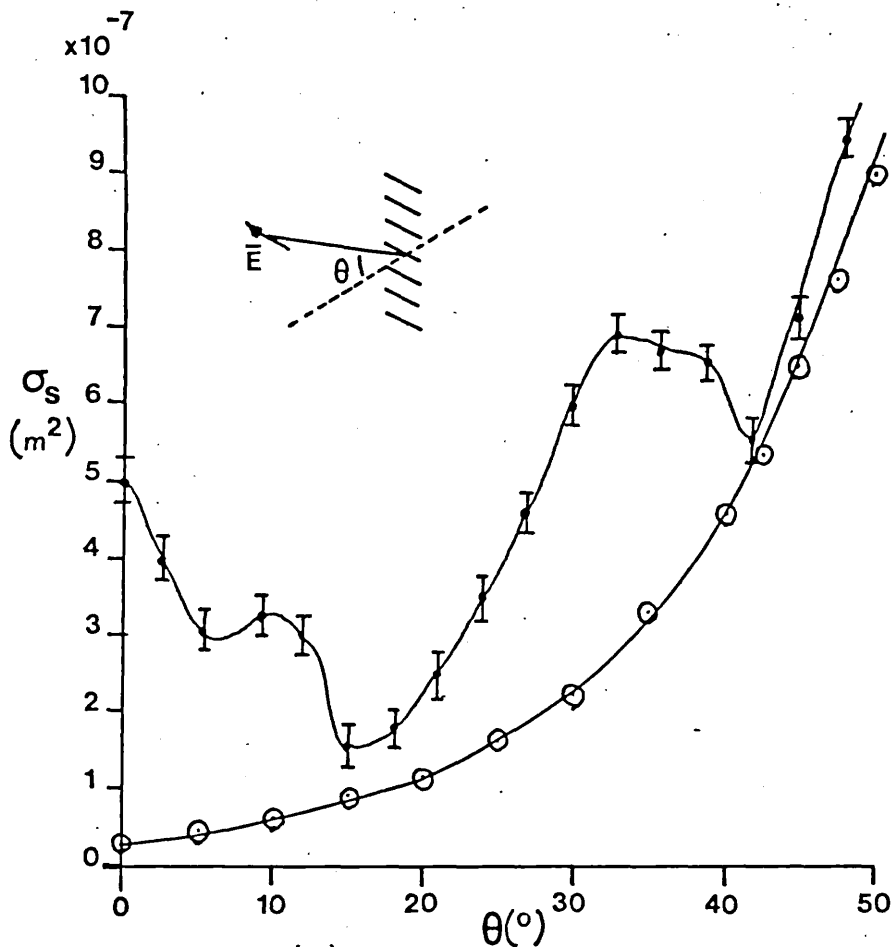


Figure 7.18 (a). Variation of scattering cross-section with angle of incidence  $\theta$  for 3.5  $\mu\text{m}$  mylar substrate ( $\ominus$ ) and the same substrate with a 10 element linear array of short circuited halfwave dipoles separated by  $1\lambda$  ( $-|$ )

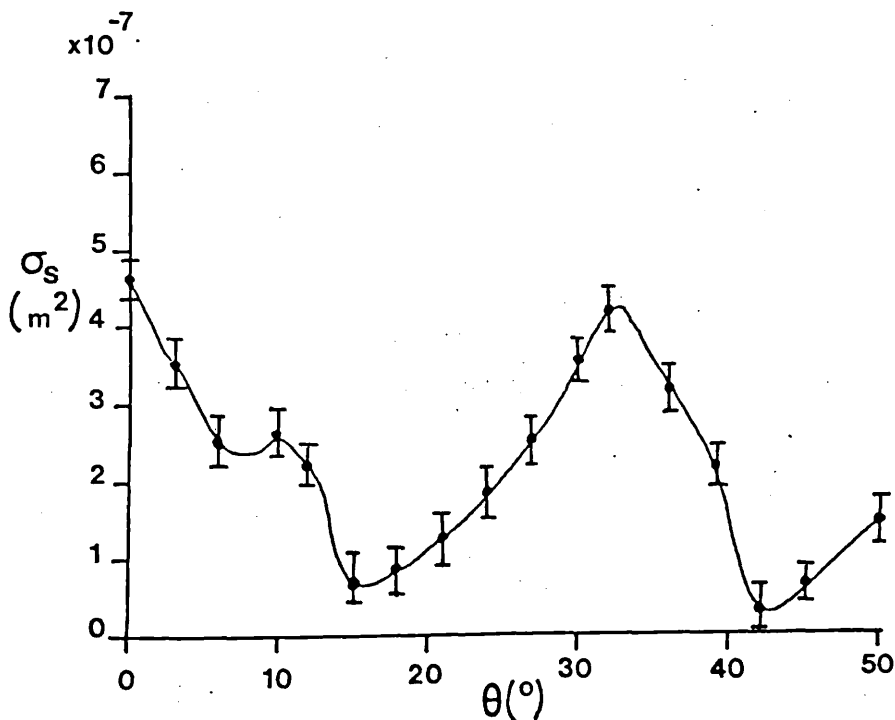


Figure 7.18 (b). Variation of H plane scattering cross-section for the array above obtained by taking the difference between the curves in Figure 7.18 (a).

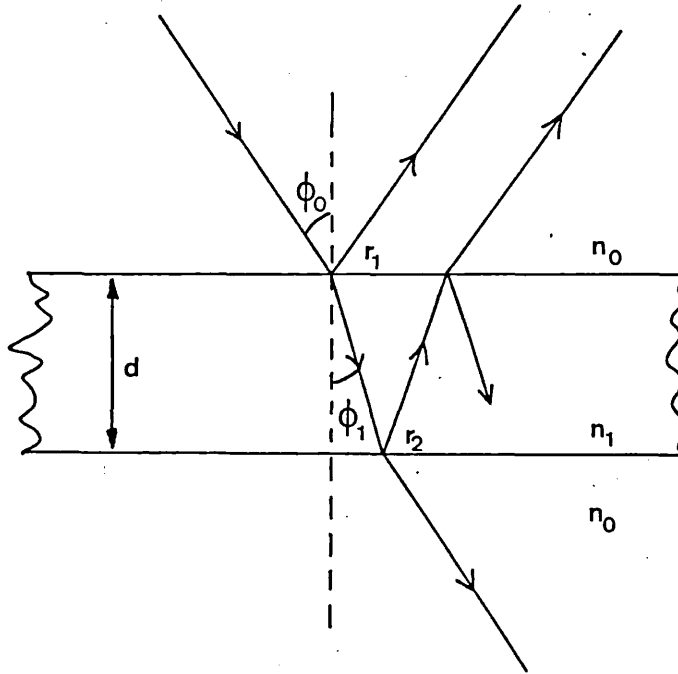


Figure 7:19. Multiple reflection in a thin dielectric interface.



the polarisation of the sample was removed and a mount having a larger elliptical aperture was substituted in order to prevent vignetting of the sample by the supporting structure. The antenna arrays were supported on 3.5  $\mu\text{m}$  thick mylar attached to 70 mm aperture stainless steel support rings. The maximum angle that the sample could make with the axis of the open resonator was  $52^\circ$ . Figure 7.18 shows the results obtained. The bottom curve in Figure 7.18 (a) shows the variation of the equivalent scattering cross-section of the mylar substrate with the angle of incidence. As the polarisation of the field in the resonator is perpendicular to the plane of incidence then the Fresnel amplitude reflection coefficient,  $r_{1s}$ , for the substrate is<sup>73,74</sup>

$$r_{1s} = \frac{\eta_0 \cos \phi_0 - \eta_1 \cos \phi_1}{\eta_0 \cos \phi_0 + \eta_1 \cos \phi_1} \quad (7.34.)$$

where  $\eta_0$  and  $\eta_1$  are the respective refractive indices of air and the substrate.  $\phi_0$  is the angle of incidence made by the incident beam with the normal to the plane of the substrate, and  $\phi_1$  is the angle of refraction within the substrate. The intensity reflection coefficient  $R_s$  is given by

$$R_s = \frac{2 r_{1s}^2 (1 - \cos 2\delta)}{1 + r_{1s}^4 - 2 r_{1s}^2 \cos 2\delta} \quad (7.35)$$

where  $\delta = \frac{2\pi}{\lambda} \eta_1 d \cos \phi_1$  is the phase

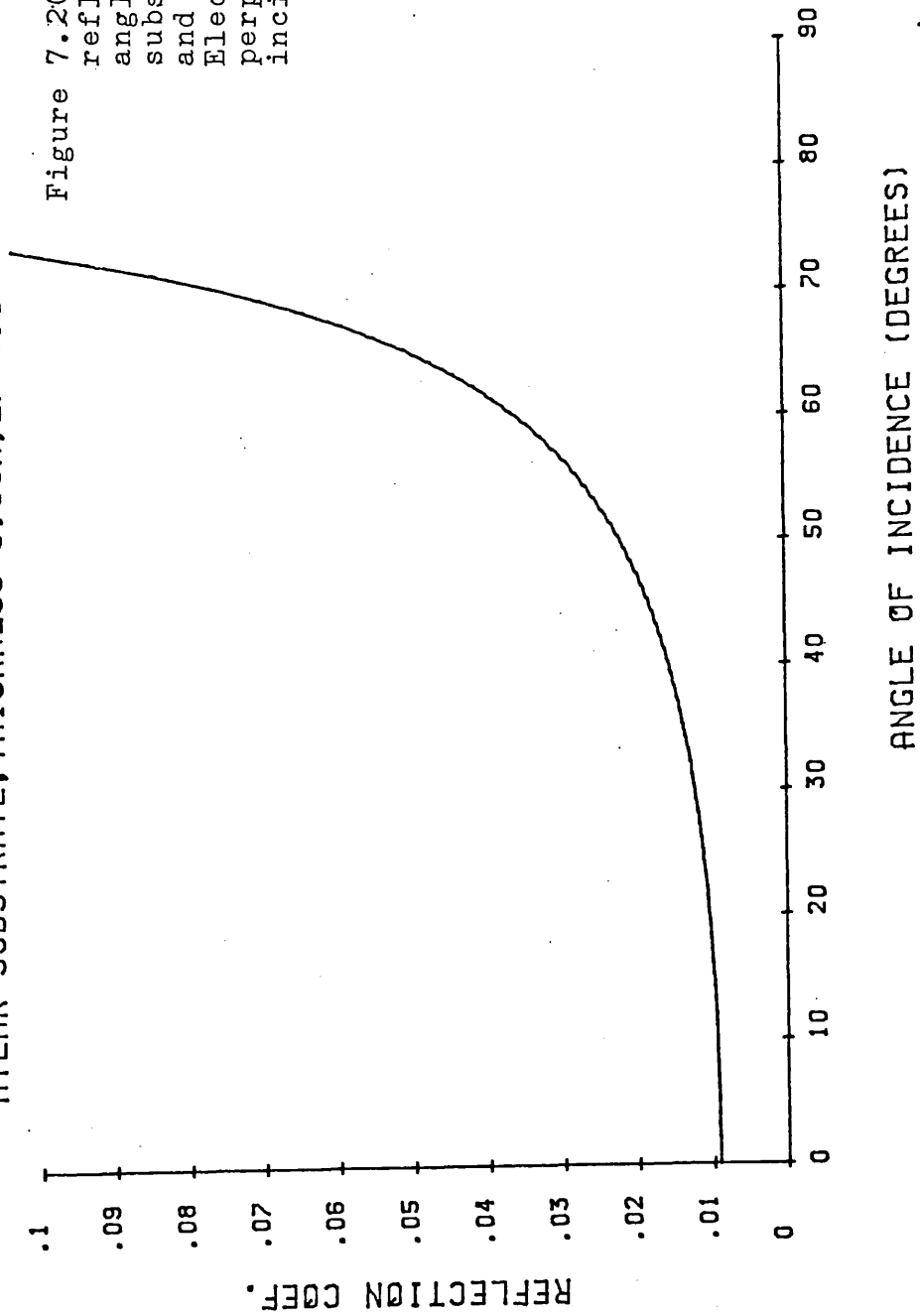
difference between adjacent emerging beams, the geometry is shown in Figure 7.19. The substrate thickness is  $d$ . The variation of intensity reflection coefficient with angle of incidence for a 3.5  $\mu\text{m}$  thick mylar substrate of refractive index 1.76, is shown in Figure 7.20. The reflection coefficient remains constant for angles of incidence up to  $30^\circ$  and then increases rapidly thereafter. A similar variation is noted experimentally for the equivalent scattering cross-section, although the agreement is

by no means exact. However, the multiple reflections within the cavity itself will affect the result and these have not been accounted for. The experimental variation is possibly a result of the combined effects of increasing effective thickness, which increases the absorption, and the enhanced reflection coefficient. Together these reduce the resonator  $Q$  from the normal incidence value and so the effective uncorrected cross-section increases. The top curve in Figure 7.18 (a) shows the variation of the total measured scattering cross-sections of the substrate alone plus a linear array of 10 short circuited dipoles separated by  $1\lambda$ . The geometry of the array, with respect to the field is shown inset. Figure 7.18 (b) gives the variation of the total scattering cross-section of the array, taken to be the difference between the two curves in Figure 7.18 (a). Although the agreement between the measured and theoretical cross-sections for broadside incidence ( $\theta = 0^\circ$ ) was good,  $\sigma_s/\lambda^2$  theoretical = 4.37,  $\sigma_s/\lambda^2$  experimental =  $4.13 \pm 0.25$ , the rest of the H-plane pattern did not agree with that theoretically predicted. The pattern obtained has neither a clearly defined main lobe, nor does it exhibit grating lobes. The beamwidth of an antenna is an important measure of its directional properties. The 3 dB beamwidth is defined as the angular difference between the half-power points on the main antenna lobe. The full beamwidth is defined as the angular difference between the nulls on either side of the main lobe. The theoretical 3 dB beamwidth of the main lobe for the array studied here is  $3^\circ$ , the measured 3 dB beamwidth was  $20^\circ$ .

This disagreement is a result of the standing wave power distribution in the open resonator which effectively makes the excitation non-uniform. For an array of dipoles in a travelling wave the current amplitudes ultimately excited in each element by a wave crest are equal, provided that the incident field has a spatially uniform amplitude distribution in a

MYLAR SUBSTRATE, THICKNESS=3.5UM, ER=3.1

Figure 7.20. Variation of intensity reflection coefficient with angle of incidence for a mylar substrate of thickness 3.5  $\mu$ m and refractive index 1.76. Electric field vector is perpendicular to the plane of incidence.



transverse plane. The successive phase differences between the element currents is dependent upon the angle of incidence of the travelling wave. However, in the standing wave as the angle of incidence is varied, it is possible for some elements to find themselves in a zero field for all times and so will not receive any excitation. However, these particular elements will receive a maximum excitation when the array is moved by  $\lambda/4$ , as required by the measurement technique. It is evident that the standard procedure for the determination of cross-section is only valid for arrays orientated in the broadside position. Not only are the dipole excitations non-uniform but also the mutual interactions will be quite different.

An attempt was made to eliminate or at least minimise the effect of substrate reflection by using a second parallel mylar substrate, the position of which could be continuously varied with respect to the array. The thickness of this second substrate was identical to that supporting the array. This was intended to minimise the substrate reflections in a manner similar to that of a stub tuner in a microwave circuit. If  $R_s$  is the intensity reflection coefficient of a single substrate, given by equation 7.35 then for two identical parallel substrates of separation  $t$ , much greater than their thicknesses  $d$ , the combined intensity reflection coefficient,  $R_T$ , is given by

$$R_T = \frac{2 R_s (1 - \cos 2D)}{1 + R_s^2 - 2 R_s \cos 2D} \quad (7.36.)$$

where  $D = \frac{2\pi \eta_0 t}{\lambda} \cos \phi_0$  is the phase difference between adjacent beams emerging from the combination.  $\phi_0$  is the angle of incidence made by the incident beam with the normal to the plane of the substrates. The geometry is illustrated in Figure 7.21. Figures 7.22, 7.23 and 7.24 show the variation of intensity reflection coefficient with substrate separation for angles of incidence of  $0^\circ$ ,  $25^\circ$  and  $50^\circ$  respectively, for two



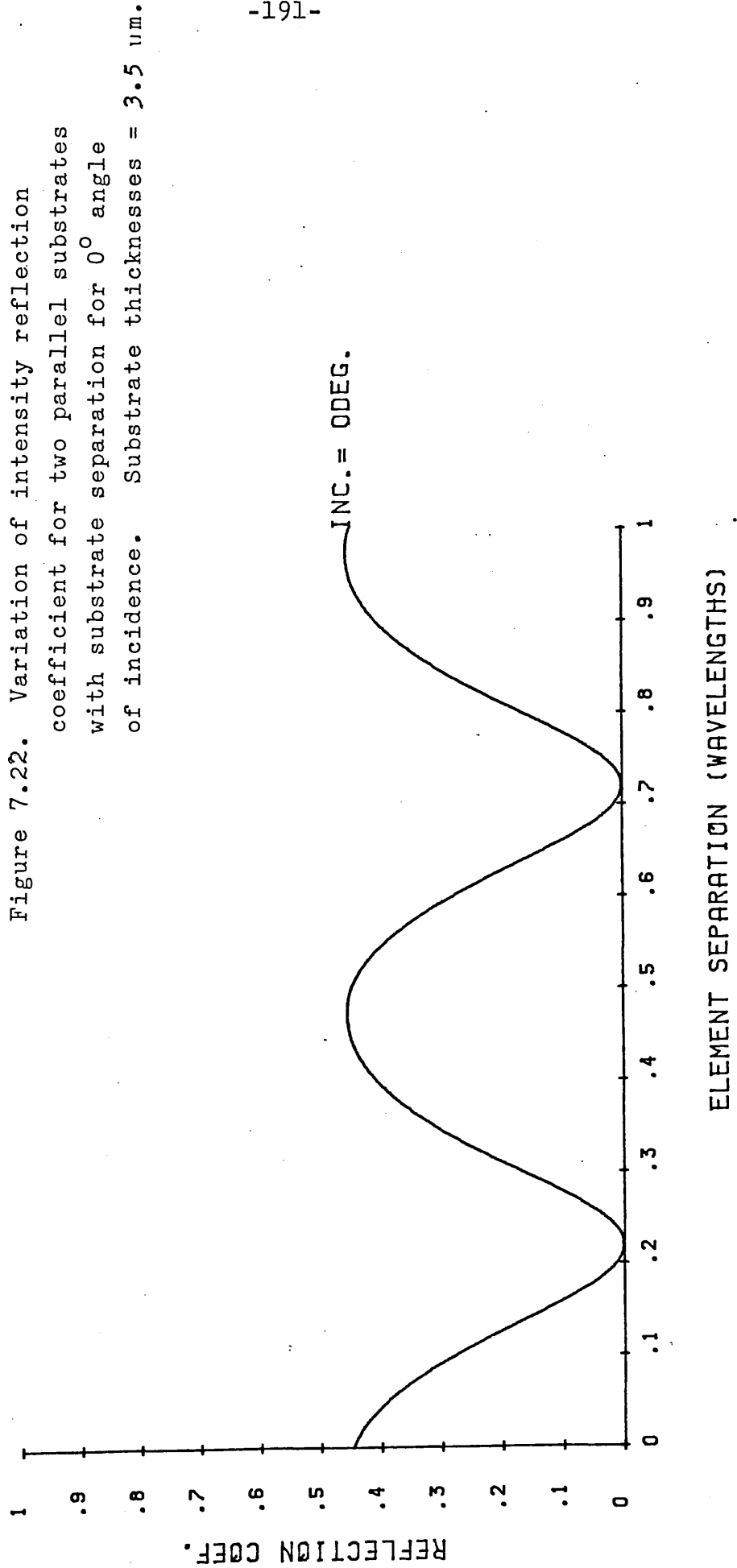


Figure 7.23. Variation of intensity reflection coefficient for two parallel substrates with substrate separation for 25° angle of incidence. Substrate thicknesses = 3.5 μm.

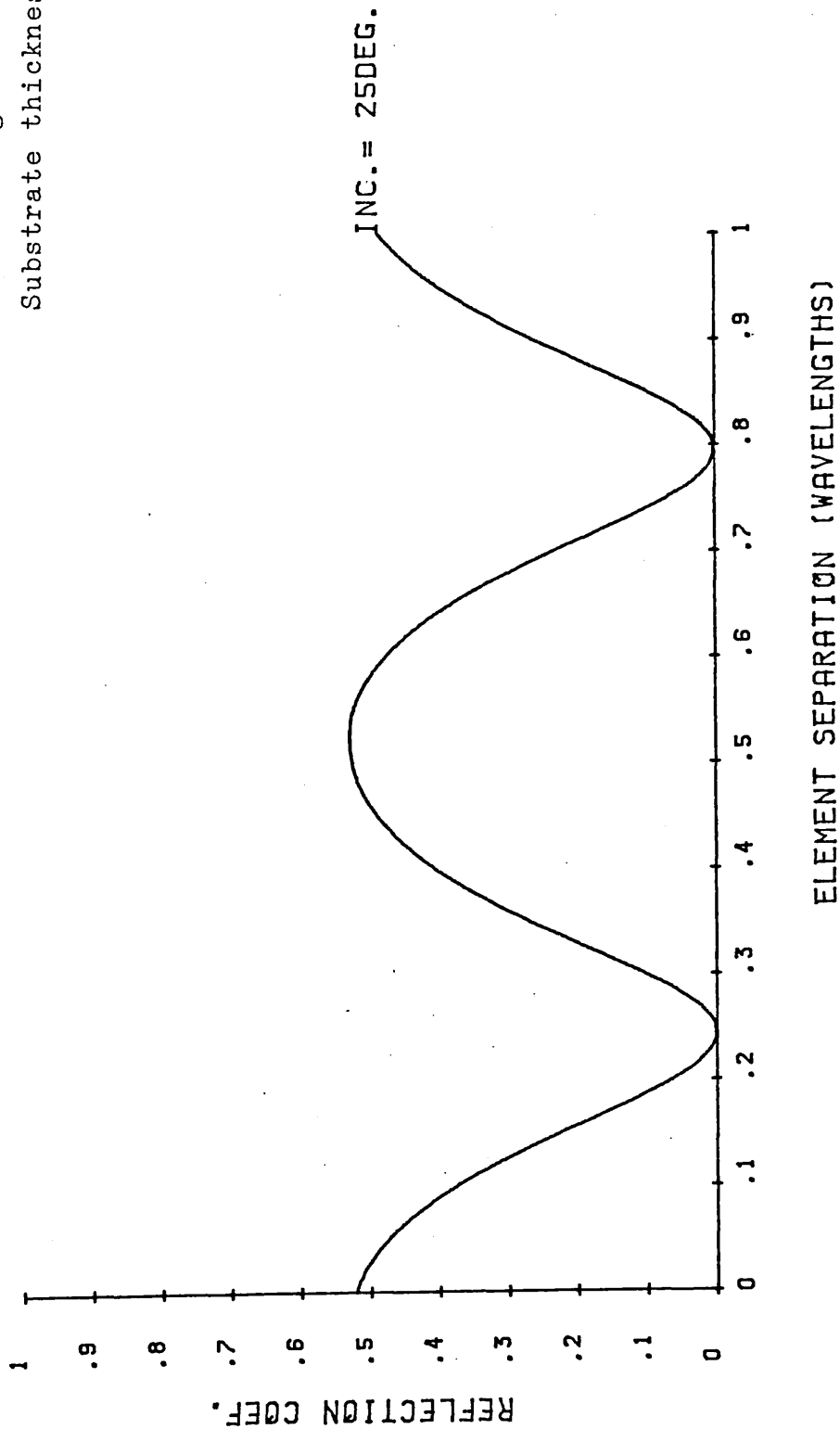
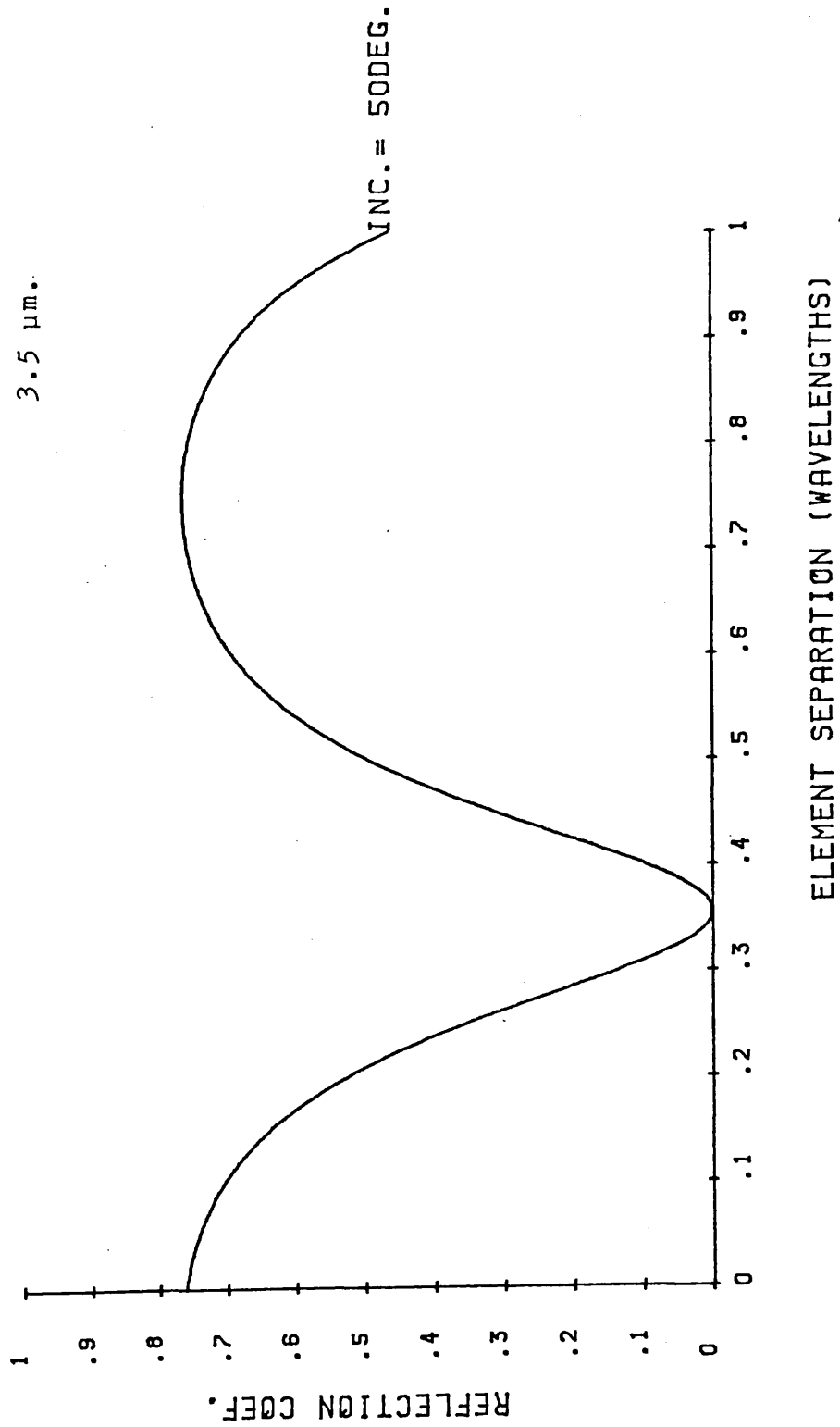


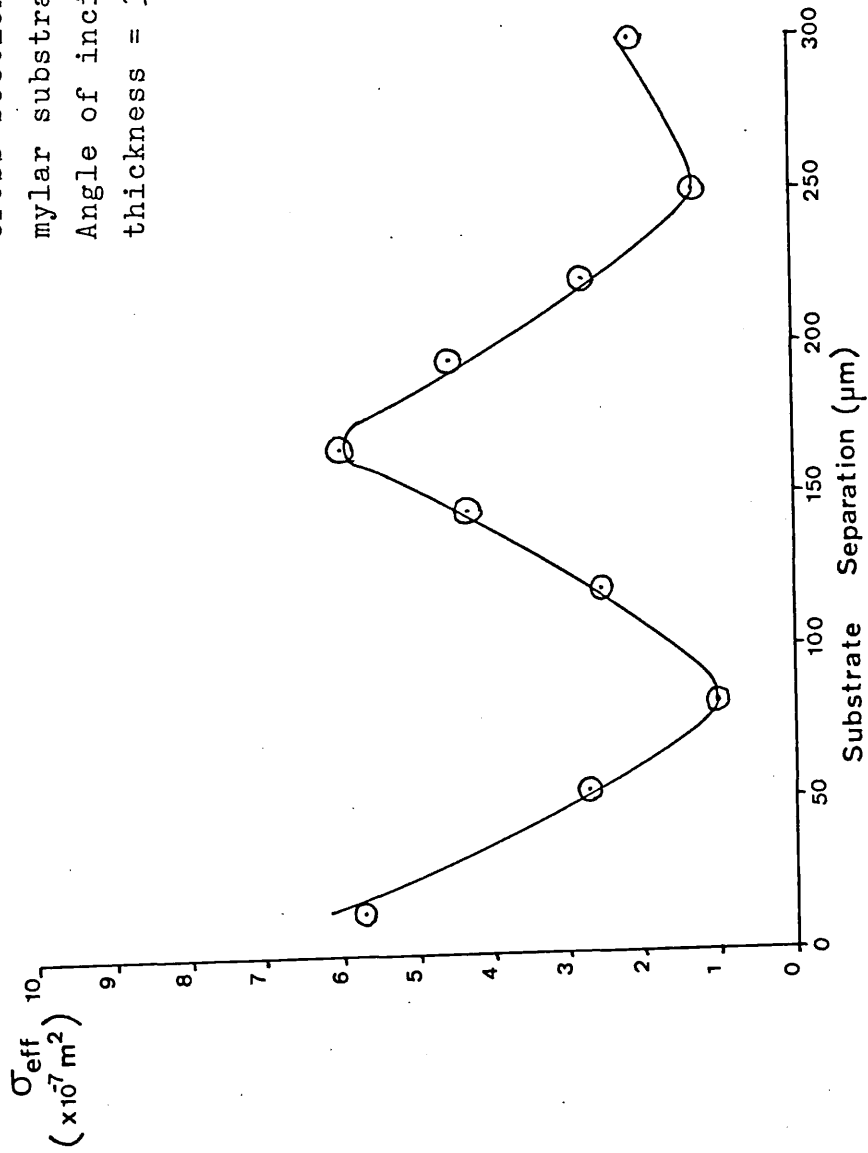
Figure 7.24. Variation of intensity reflection coefficient for two parallel substrates with substrate separation for 50° angle of incidence. Substrate thicknesses = 3.5 μm.





parallel 3.5  $\mu\text{m}$  thick mylar substrates. It can be seen that the substrate reflection can be reduced to zero for certain substrate separations. However, it was found that because a large component of the effective substrate cross-section was due to the absorption by the mylar alone, the chief effect of the second substrate was to further increase the effective extinction cross-section of the substrate. The second substrate was supported on a ring with a 40 TPI thread on the outside. This could be screwed in and out of the substrate holder to vary the substrate separation. The resolution was 635  $\mu\text{m}$  per turn. Figure 7.25 shows the variation of effective cross-section with substrate separation. The two mylar substrates used were 3.5  $\mu\text{m}$  and the angle of incidence was  $10^\circ$ . The unloaded  $Q$  of the open resonator was 65000. It is clear that substrate absorption is significant as the lowest attainable effective cross-section was  $1 \times 10^{-7} \text{ m}^2$  - a factor of two greater than that of a single halfwave dipole at this wavelength. The angular response of an array was obtained from backscattering measurements in a travelling wave. These experiments will be described in Chapter 9.

Figure 7.25. Experimental variation of effective cross-section,  $\sigma_{\text{eff}}$ , of two parallel mylar substrates with substrate separation. Angle of incidence =  $10^\circ$ , substrate thickness =  $3.5 \mu\text{m}$ .



## CHAPTER EIGHT

### THE PHOTOLITHOGRAPHIC REPRODUCTION OF SUBMILLIMETRE ANTENNAS.

#### 8.1. Antenna Design and Manufacture.

As was stated in Chapter 2, the small size and delicacy of submillimetre antennas necessitates supporting them on a suitable substrate. The properties of these antennas are dependent upon :-

- (a) The finite surface impedance of the metallic films used for the antenna metalisation.
- (b) The electrical and mechanical properties of the supporting substrate material.
- (c) The dimensional accuracy of the antenna geometry.

Clearly the above factors affect the choice of antenna metalisation, substrate material and method of reproduction. The antennas were reproduced using a photofabrication process, the details of which will be discussed in Section 8.3. The substrate material was first vacuum coated with metal which was then covered with a layer of positive photoresist. The pattern of the antenna metalisation was reproduced in the photoresist by exposure to ultraviolet light through a positive mask. The masks themselves were produced by electron beam lithography. The mask patterns obtained using this technique had absolute dimensional tolerances of  $\pm 0.1 \mu\text{m}$  and linewidth control of  $\pm 0.1$  to  $0.2 \mu\text{m}$ . Masks produced by this technique enabled the required accuracy in the antenna dimensions to be obtained. The mask patterns were produced in bright chrome on  $63.5 \text{ mm} \times 63.5 \text{ mm} \times 1.5 \text{ mm}$  thick low expansion glass plates. The mask patterns were generated by describing the shapes, orientations and repetitions required using the GAELIC<sup>75,76</sup> language. This language has been designed specifically for describing the mask patterns required in integrated circuit layouts. An example program with the hard copy output of the mask pattern is given in Appendix 5. The widths of the dipole antennas employed in the investigation were

10  $\mu\text{m}$  so as to keep the widths  $< \lambda/30$ , thus ensuring adequate response as discussed in Chapter 2.

## 8.2. Physical Properties and Choice of the Antenna Materials.

Table 8.1 lists the absorption coefficients and dielectric constants of various possible substrate materials, which were measured at 891 GHz in the open resonator as described in Chapter 7, along with their mechanical properties<sup>77</sup>.

The low absorption and dielectric constant of P.T.F.E. would make it an ideal substrate material. However, it was found that the vacuum coated metal films did not adhere sufficiently well to this material, due to its "non-stick" properties. The polythenes were not suitable because their low melting points also made them difficult to vacuum coat due to a vapour barrier being set up. Crystal quartz would make an ideal substrate as it has a very low absorption and good mechanical stability and strength. However, it could not be conveniently produced in sufficiently thin samples for the wavelength employed in this investigation. A process was developed, however, for reproducing arrays on quartz substrates because this material could be more suitable for practical devices. Mylar substrates were found to be a good compromise as from Table 8.1 it can be seen that this material has a low absorption coefficient and dielectric constant. Also, it has the best mechanical properties of all the plastic substrates considered in terms of stability and strength. Mylar was found to be easy to handle and vacuum coat, also it was available in thin sheets ranging in thickness from 1.5  $\mu\text{m}$  to 100  $\mu\text{m}$ .

The surface impedances of various metals at 891 GHz is listed in Table 2.2 in Chapter 2. As was previously stated, a metal having a low surface impedance is necessary in order to minimize the antenna losses. A resonant dipole antenna produced from aluminium would

TABLE 8.1  
DIELECTRIC MATERIAL PROPERTIES

Material	Relative Permittivity at 891 GHz	Absorption Coefficient at 891 GHz	Tensile Strength	10 <sup>5</sup> x Coefficient Linear Expansion
	$\epsilon_r$	$\alpha$	MN m <sup>-2</sup>	°C
P.T.F.E.	2.10	0.8	13 - 33	10
High density polythene	2.13	0.4	20 - 36	10 - 20
Low density polythene	2.62	0.2	4 - 15	10 - 20
Mylar	3.09	2.0	66	6
Crystal quartz (z cut)	4.56	0.1	8.3	1.4
Fused silica	4.75	3.3	30 - 90	0.045

have a surface resistance loss of  $0.11 \text{ dB } \lambda^{-1}$  which is still low enough to maintain good antenna characteristics.

Aluminium was not used, however, because of its high surface resistance. Also it was found that aluminium films were attacked by the alkaline solutions used to develop the photoresist. This caused the photoresist to come away even in un-exposed areas. Wet chemical etching<sup>7,8</sup> was employed to remove the unwanted areas of metallisation from the substrates. Only acid etches could be used because alkaline etches were found to attack the photoresist. Aqua regia (3 parts HCL to 1 part  $\text{HNO}_3$  by volume) was used to try to etch gold films. However, this etch was too violent and so tended to disrupt and undercut the structure. Cyanide etches were considered too dangerous to use.

Copper films were also tried. The temperature required to vacuum evaporate copper was higher than that required for silver or gold. Hence, it was found that the copper films were generally thinner and had a higher density of pin hole defects than the silver or gold films. Copper films could be etched with Ferric Chloride solution but undercutting was severe. Reducing the concentration of etchant was found to reduce the undercutting but dirty backgrounds resulted.

Silver was the obvious choice for the antenna metallisation because it has the lowest surface resistance of all the metals listed in Table 2.2. It was found to vacuum coat the mylar well with very few pin hole defects, the silver films were etched with a 50% weight by volume solution of Ferric Nitrate ( $\text{Fe}(\text{NO}_3)_3 \cdot 9\text{H}_2\text{O}$ ). This etchant reproduced edges and corners accurately with the minimum of undercutting. The backgrounds were also very clean.

It was essential that the thickness of the evaporated metallisation was greater than the skin depth for the

metal at the frequency used, so as to minimise conductor loss. The skin depth for silver at 891 GHz was calculated as 0.02  $\mu\text{m}$ . The average thickness of the silver films employed was 0.1  $\mu\text{m}$  approximately five times the skin depth at this frequency.

### 8.3. Production Process.<sup>79</sup>

The antennas could be satisfactorily reproduced on a variety of substrates using silver. These were, mylar films of various thicknesses ranging from 1.5  $\mu\text{m}$  to 20  $\mu\text{m}$ , quartz discs 15 mm in diameter and 100  $\mu\text{m}$  thick and crystal quartz slabs 25 mm x 10 mm x 3 mm thick.

#### 8.3.1. Substrate Preparation.

For mylar films, the mylar was stretched in a stretching frame and heat shrunk in an oven at 120°C to remove any creases. The films were vacuum coated with silver to a thickness of 0.1  $\mu\text{m}$  at pressures  $< 10^{-6}$  torr. After vacuum coating, the films were transferred to stainless steel support rings (O.D. 55 mm, I.D. 50 mm and 2.5 mm thick). The rings supported the substrates during the lithographic process and also the finished antenna structure during evaluation. The rings were glued to the non-silvered side of the mylar film with cyanoacrylate adhesive. The ring and film were cut from the stretching frame once the adhesive had set.

Quartz substrates were cleaned by boiling in semiconductor grade trichlorethane and dried in an oven at 120°C. The substrates were vacuum coated on one side with silver to a thickness of 0.1  $\mu\text{m}$ . After preparation, the substrates were stored in a dessicator until required.

The subsequent processes were carried out in the laminar flow clean box (class 100) shown in Figure 8.1, under a 40 watt yellow fluorescent tube safelight.

#### 8.3.2. Resist Coating.

The substrates were coated with a positive photoresist (Shipley Chemicals AZ - 1350) by spin or dip coating.

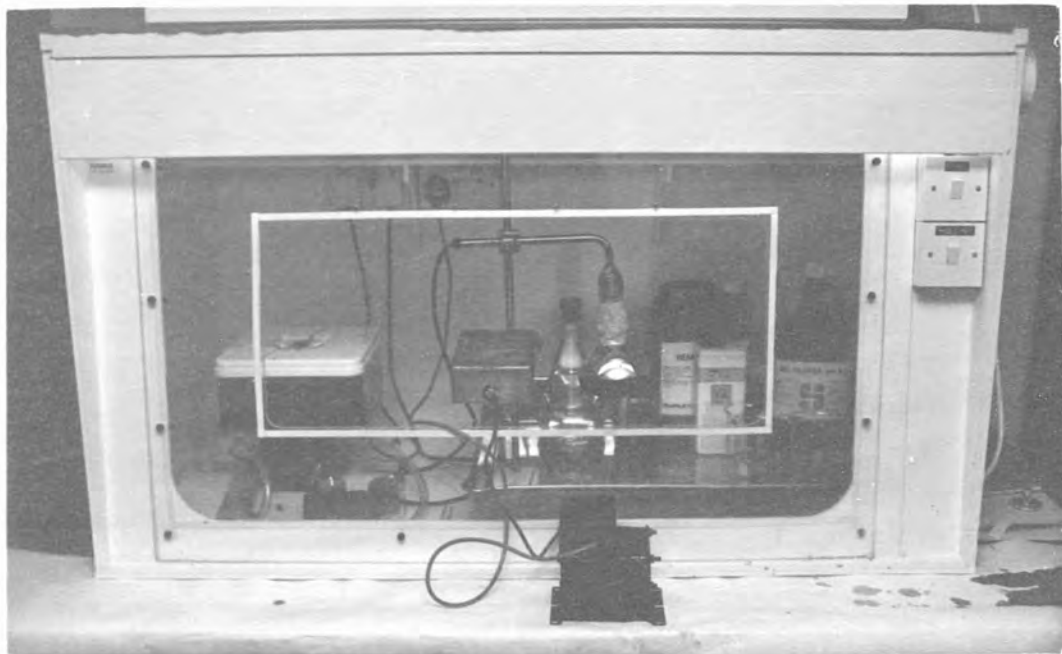
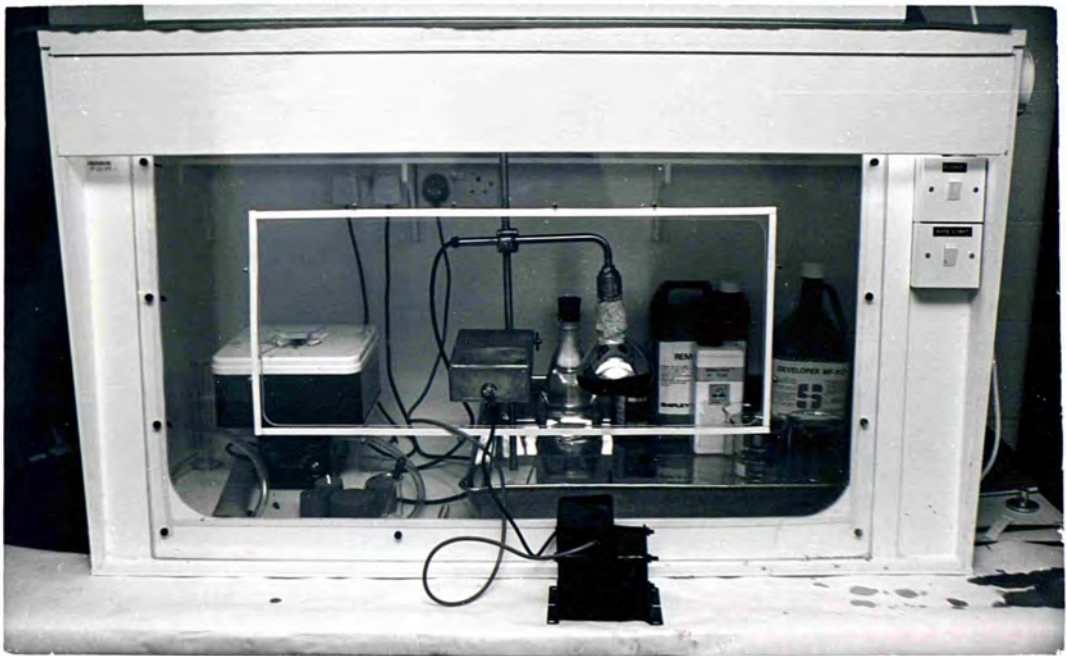


Figure 8.1. Photograph of the clean box in which the reproduction process was undertaken.





The method employed depended on the geometry of the substrate. The coating details are given in Table 8.2 for the various types of substrate.

#### 8.3.3. Resist Drying.

The photoresist was dried for 10 minutes with the substrate placed at a distance of 10 cm from a 250 watt infrared lamp (with red filter).

#### 8.3.4. Resist Exposure.

After drying, the selected mask was contacted with the substrate and the required antenna positioned and aligned. A simple contact printer with a vacuum mask chuck was made for this purpose. The photoresist was then exposed to an intense ultra violet source through the mask. The source employed was a 1600 candle power 125 watt mercury arc lamp, placed at a distance of 10 cm from the substrate. The exposure times are listed in Table 8.2.

#### 8.3.5. Developing and Drying.

After exposure, the resist coated substrates were developed in Shipley Chemicals MF - 312 developer (1:1. diluted with distilled water) and then dried under the infrared lamp. This procedure hardened the resist.

#### 8.3.6. Etching and Resist Removal.

Once dry, the excess silver was etched away by immersing the substrate in a 50% WT./Vol. solution of Ferric Nitrate. The etching took only a few seconds and the substrates were quickly washed under a stream of running water. The substrates were then dried under the infrared lamp. The resist covering could be removed by washing the substrate with acetone.

#### 8.3.7. Inspection.

The completed antenna structures were examined under a x100 microscope with a measuring graticule to check

TABLE 8.2.

Substrate processing times

Process	Mylar film	100 $\mu$ m thick quartz discs	75 x 10 x 3 mm quartz slabs
Resist coating	spin at 2000 rpm for 30 seconds	spin at 3000 rpm for 30 seconds	dip coat; pull out at 10 mm per second
Exposure time *	25 seconds	15 seconds	35 seconds
Developing time †	20-25 seconds	15 seconds	30-40 seconds

\* Substrate placed 10 cm from 1600 candle power 125 watt mercury arc lamp.

† MF-312 (Shipley Chemicals) developer 1:1 diluted with distilled water. Constant agitation.

the antenna dimensions and detect any flaws that might have occurred during the process. It was found that the quartz substrates had more background dirt than the mylar substrates. This was probably due to silver being trapped in any residue pits left by the polishing process.

#### 8.4. Results.

The photomicrograph shown in Figure 8.2, taken in transmitted light, is of a linear array of short circuited halfwave dipoles separated by a half wavelength, reproduced on a 3.5  $\mu\text{m}$  thick mylar substrate. The length of the dipoles is 168  $\mu\text{m}$  and the width 10  $\mu\text{m}$ . A photograph taken in reflected light of the electron beam generated master mask plate used to produce the above array is shown in Figure 8.3.

Figure 8.4. shows an array of halfwave dipoles connected to lengths of short circuited coplanar transmission lines. This type of array was used in the backscattering experiments described in Chapter 10, which were performed in order to determine the properties of the coplanar transmission line at this frequency.

The photograph in Figure 8.5 is of a single element of the array shown in Figure 8.4. It demonstrates that the photolithographic technique employed was capable of reproducing complex structures with minimal undercutting, and so maintain the accurate dimensions set by the masks.

Vee antennas were also employed in investigation to specifically determine the variation of line velocity factor with substrate thickness. This is described further in Chapter 10. The vee antennas terminated in various lengths of short circuited coplanar transmission line, were reproduced on thicknesses of mylar ranging from 1.5  $\mu\text{m}$  to 12.5  $\mu\text{m}$  thick. The photomicrographs shown in Figures 8.6 and 8.7 were taken in reflected light, are of a complete vee antenna and

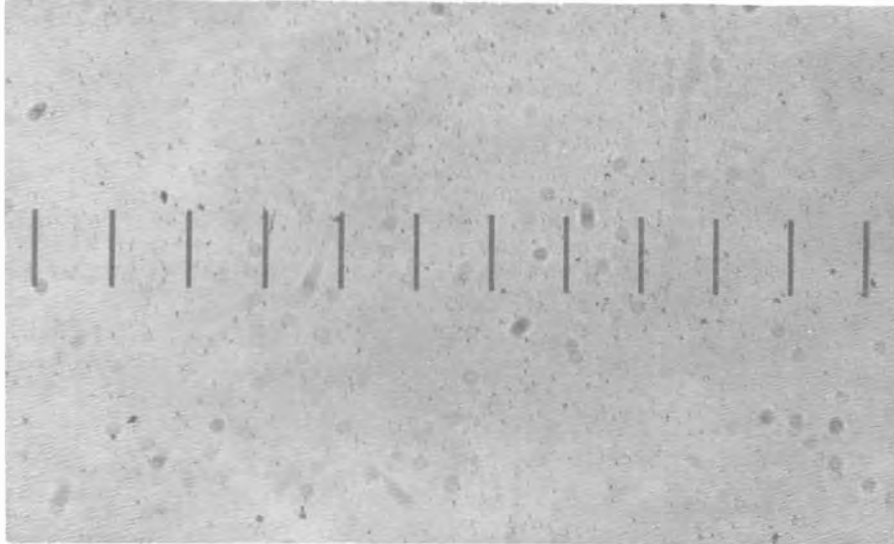


Figure 8.2. Photomicrograph taken in transmitted light of a linear array of short-circuited halfwave dipoles (length =  $168 \mu\text{m}$ ) separated by half wavelength ( $168 \mu\text{m}$ ). Reproduced on  $3.5 \mu\text{m}$  mylar.

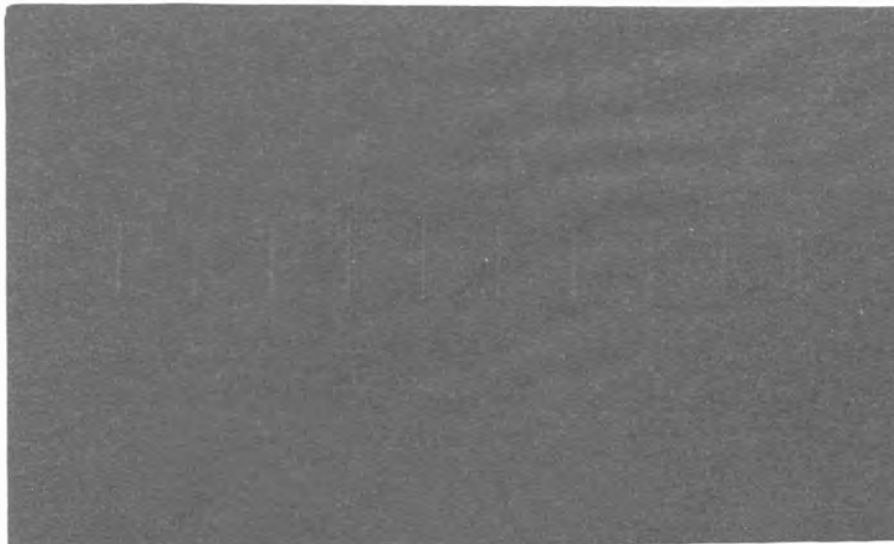


Figure 8.3. Photomicrograph taken in reflected light of the EBL master mask plate used to reproduce the above array.

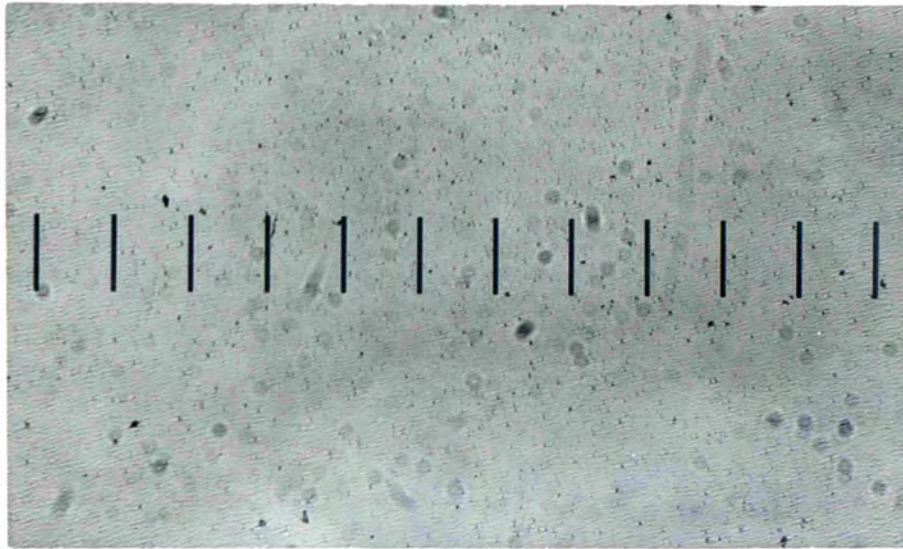




Figure 8.4. Photomicrograph, taken in transmitted light of an array of halfwave dipoles (length =  $168 \mu\text{m}$ ) attached to lengths of short-circuited coplanar transmission line.

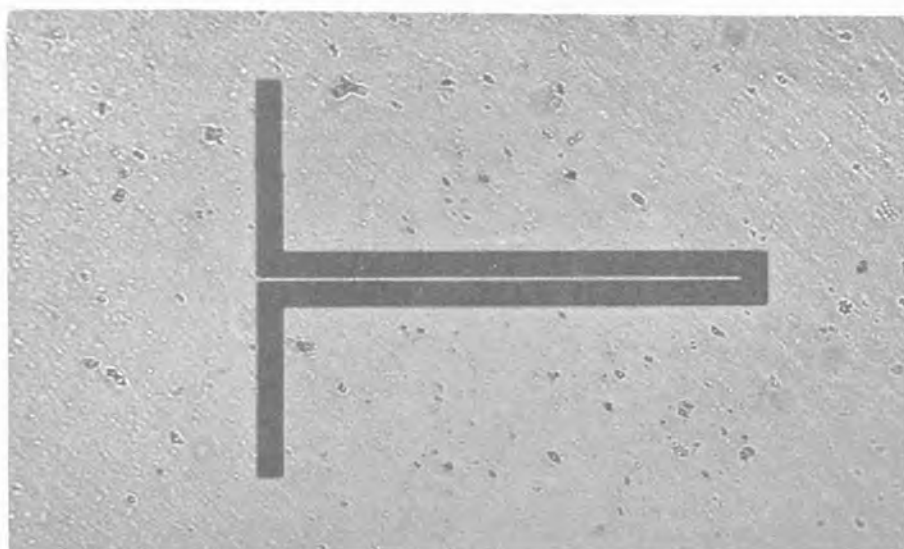
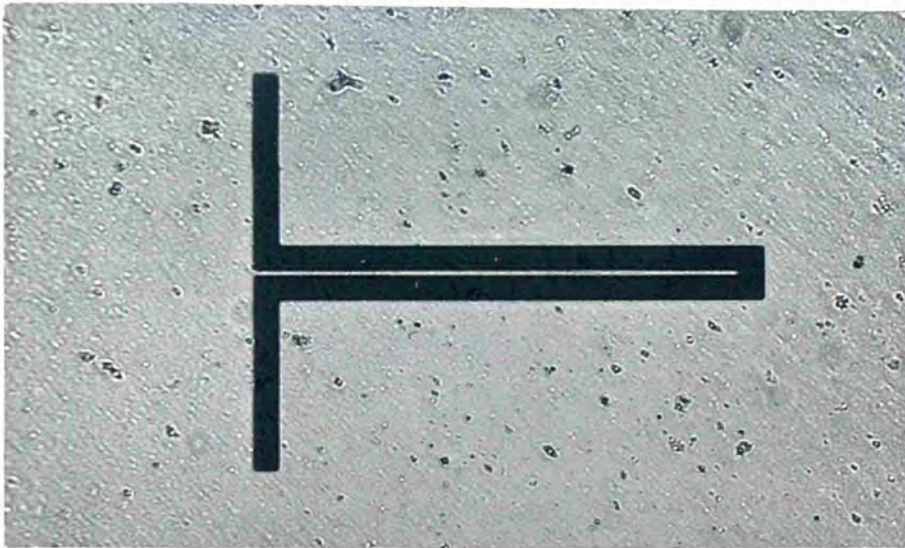
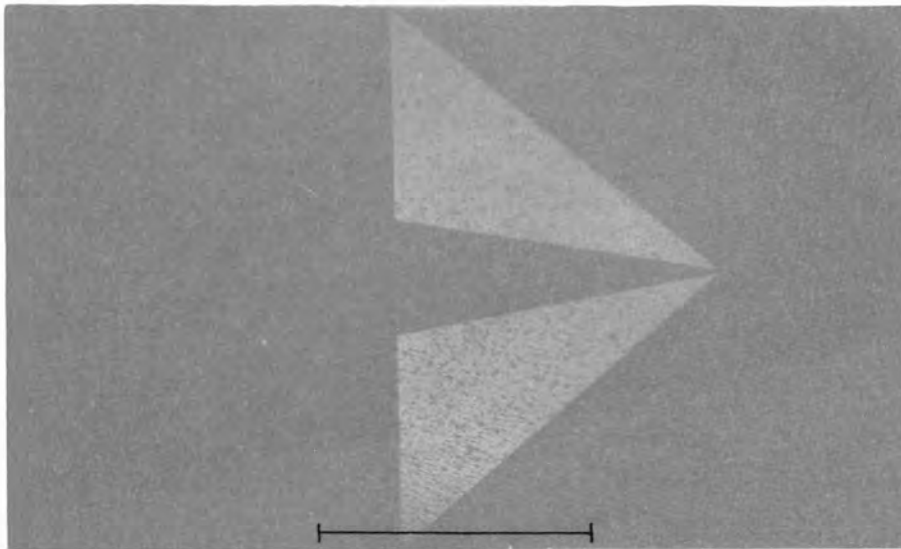


Figure 8.5. Photomicrograph, taken in transmitted light of an element from the array shown in Figure 8.4.

T T T T T T T T T T

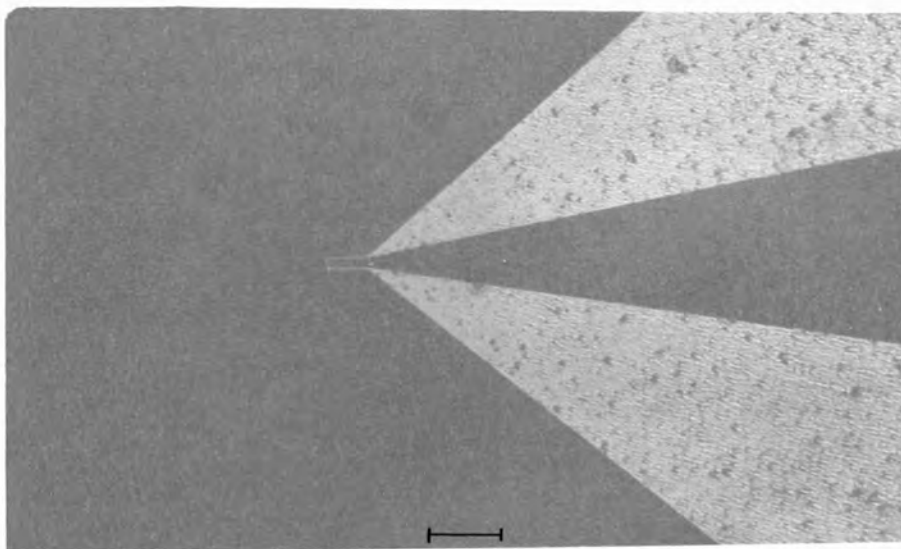






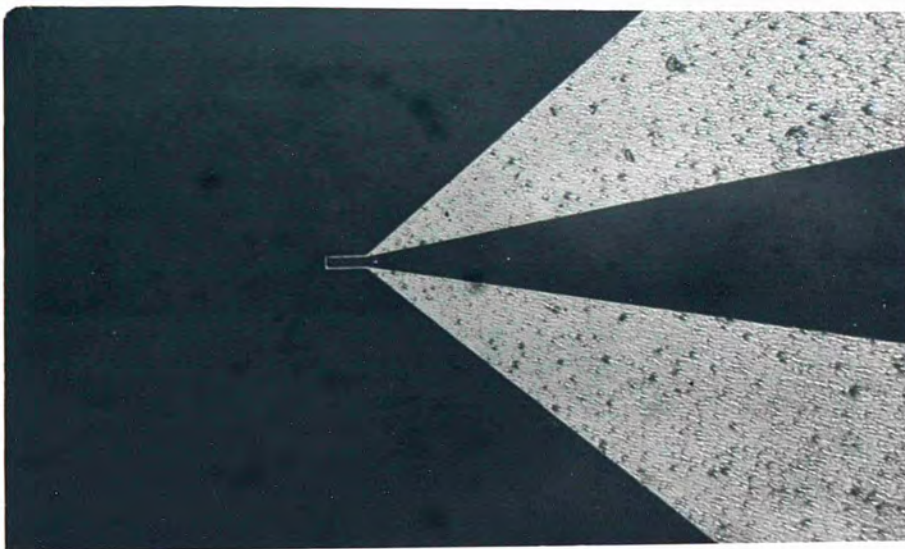
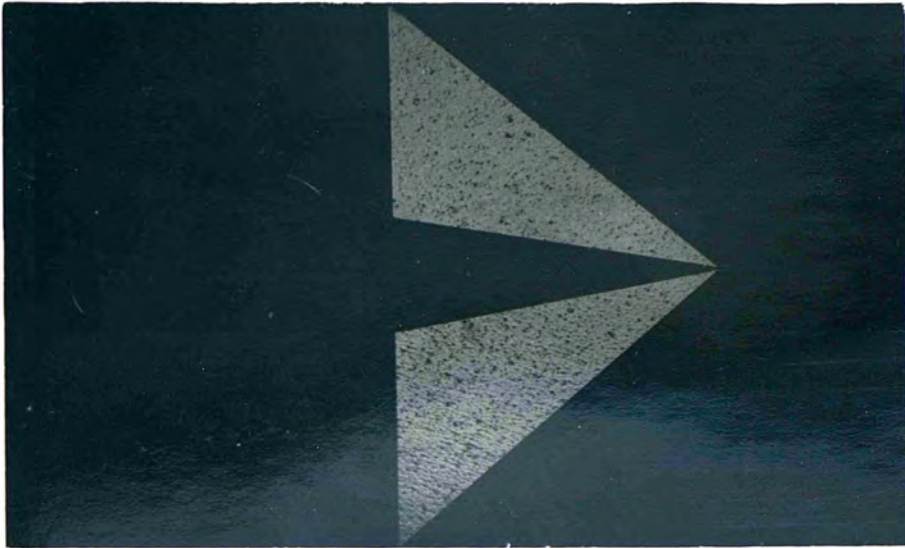
1 mm

Figure 8.6. Photomicrograph, taken in reflected light of a vee antenna.



100  $\mu$ m

Figure 8.7. Photomicrograph, taken in reflected light, of the apex of the vee antenna in Figure 8.6.



the region close to the apex of the vee respectively. The mottled effect is due to slight irregularities in the mylar substrate and small amounts of residual photoresist still clinging to the metalisation. Figures 8.8, 8.9, 8.10 and 8.11 show electron micrographs of a linear array of dipole antennas under magnifications of x200, x4000, x7500, x10000 respectively. The conclusion drawn from these studies was submillimetre antennas could be satisfactorily reproduced by optical lithography. The wet etching technique employed, reproduced the antennas with good line definition, and minimal undercutting, and therefore good line width control. Unfortunately this technique was limited to silver metalisation.

The wet etching technique was unsatisfactory when layers of different metalisations, such as silver and bismuth, were needed. Clearly, junctions between different materials would be required in practical devices; for example, when bolometric or resistive loads are to be employed. The differential etch rate of the various metallic films in a common attacking etch was found to produce 'lift off' problems associated with the top film. Also undercutting of the fastest etching metal was severe. Also specific etches for different metals are difficult to find and even then unlikely to be compatible with the photoresist used. A "dry etching" technique<sup>80</sup> might be more suitable for complex device manufacture. This is discussed more fully in Chapter 11.

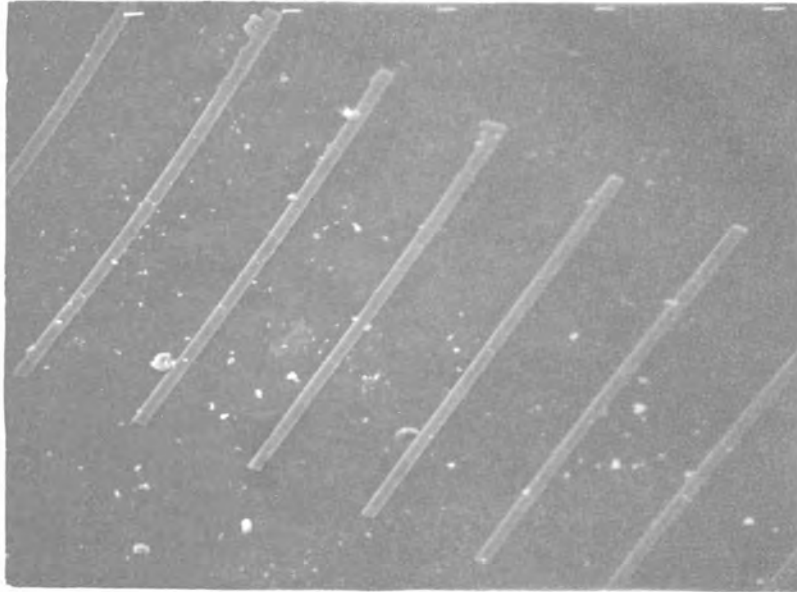


Figure 8.8. Electron micrograph of a linear antenna array. Magnification = 200.

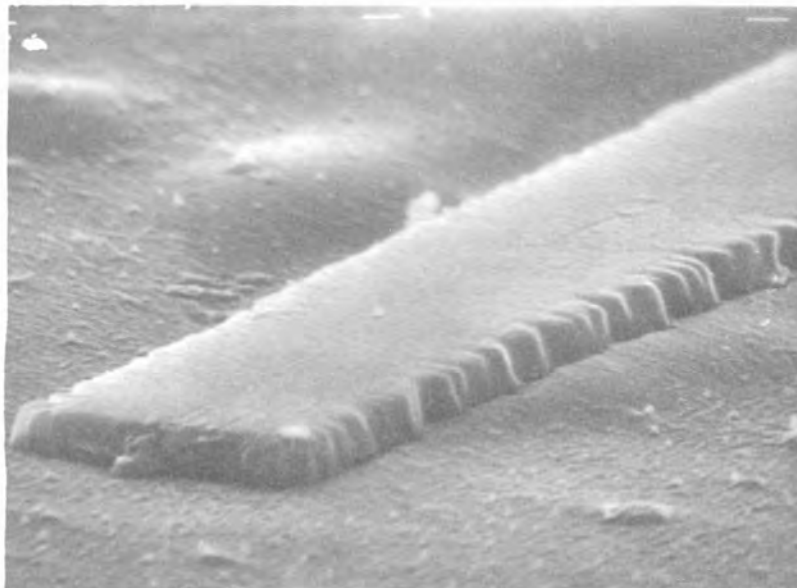


Figure 8.9. Electron micrograph of an element from the above array. Magnification = 4000.

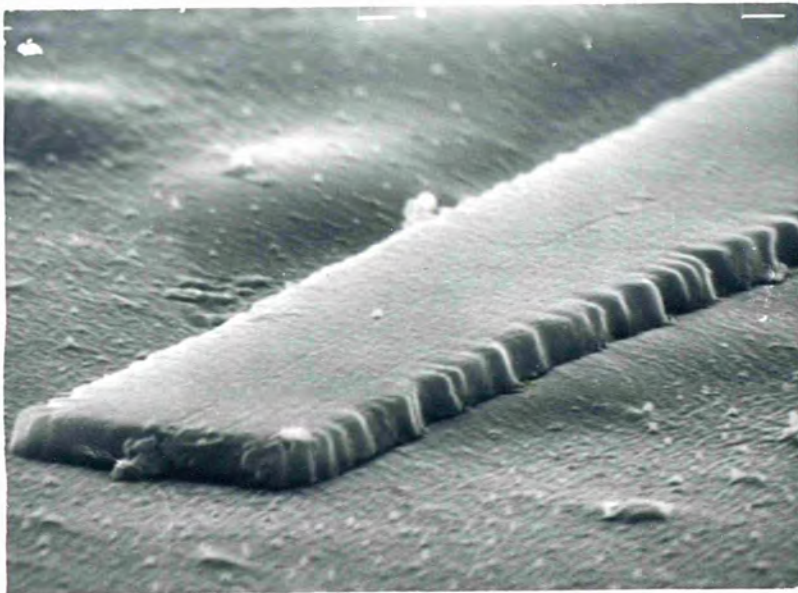
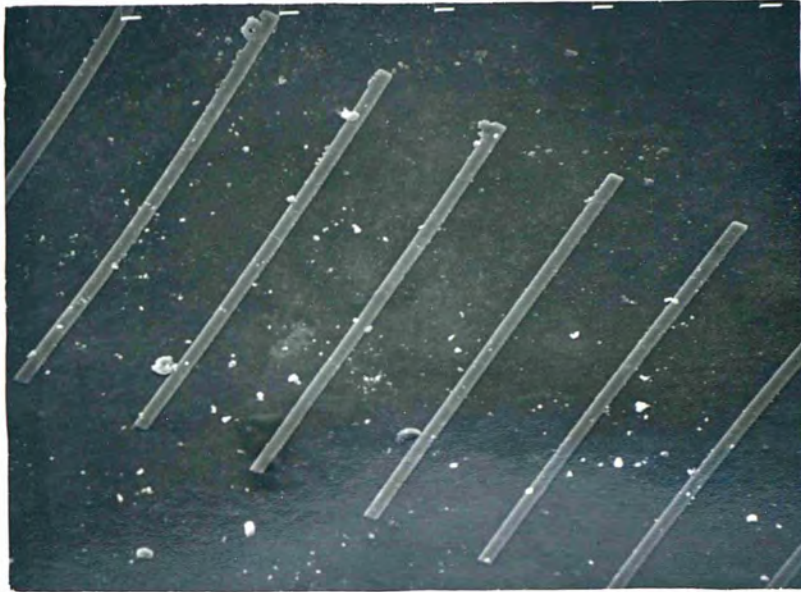




Figure 8.10. Electron micrograph of antenna metallisation. Magnification = 7500.



Figure 8.11. Electron micrograph of antenna metallisation. Magnification = 10000.



CHAPTER NINE  
THE INVESTIGATION OF BACKSCATTERING  
FROM LINEAR ARRAYS OF SHORT  
CIRCUITED DIPOLES

9.1. Angular Spectrum from Backscattering Measurements.

The periodic structure of the electromagnetic field in the open resonator precluded a determination of the angular dependence of the scattering. The backscattering cross-section,  $\sigma_{BS}$ , of an obstacle is defined by the equation

$$\sigma_{BS} = \frac{P_s}{S_i} \quad (9.1.)$$

$P_s$  is the power that a fictitious isotropic scatterer would be required to radiate in order to maintain a field at the source equal to that produced by the actual obstacle. The magnitude of the Poynting flux of the incident plane wave from the source is  $S_i$ .

The apparatus employed to obtain the backscattering measurements is shown in Figure 9.1. The laser radiation was chopped by a mechanical chopper. The beamsplitter coupled a portion of the energy to a monitor detector. The remaining energy was focussed on to the scatterer which was located in a rotary mount and driven by a stepping motor. The backscattered energy was directed on to a Golay cell detector by a small plane mirror placed behind the secondary mirror of the f-3 cassegrain focussing arrangement. After amplification and phase sensitive detection, the output signal was fed to a chart recorder and digital voltmeter (DVM). The optical arrangement was essentially bistatic as the incident and scattered beams were not co-incident. However, as the angular difference was only 2.5 degrees, the arrangement was considered to be a backscattering one.

The focussing system employed to illuminate the scattering array was required to produce a uniform plane wave excitation over the array aperture. Also, the detector



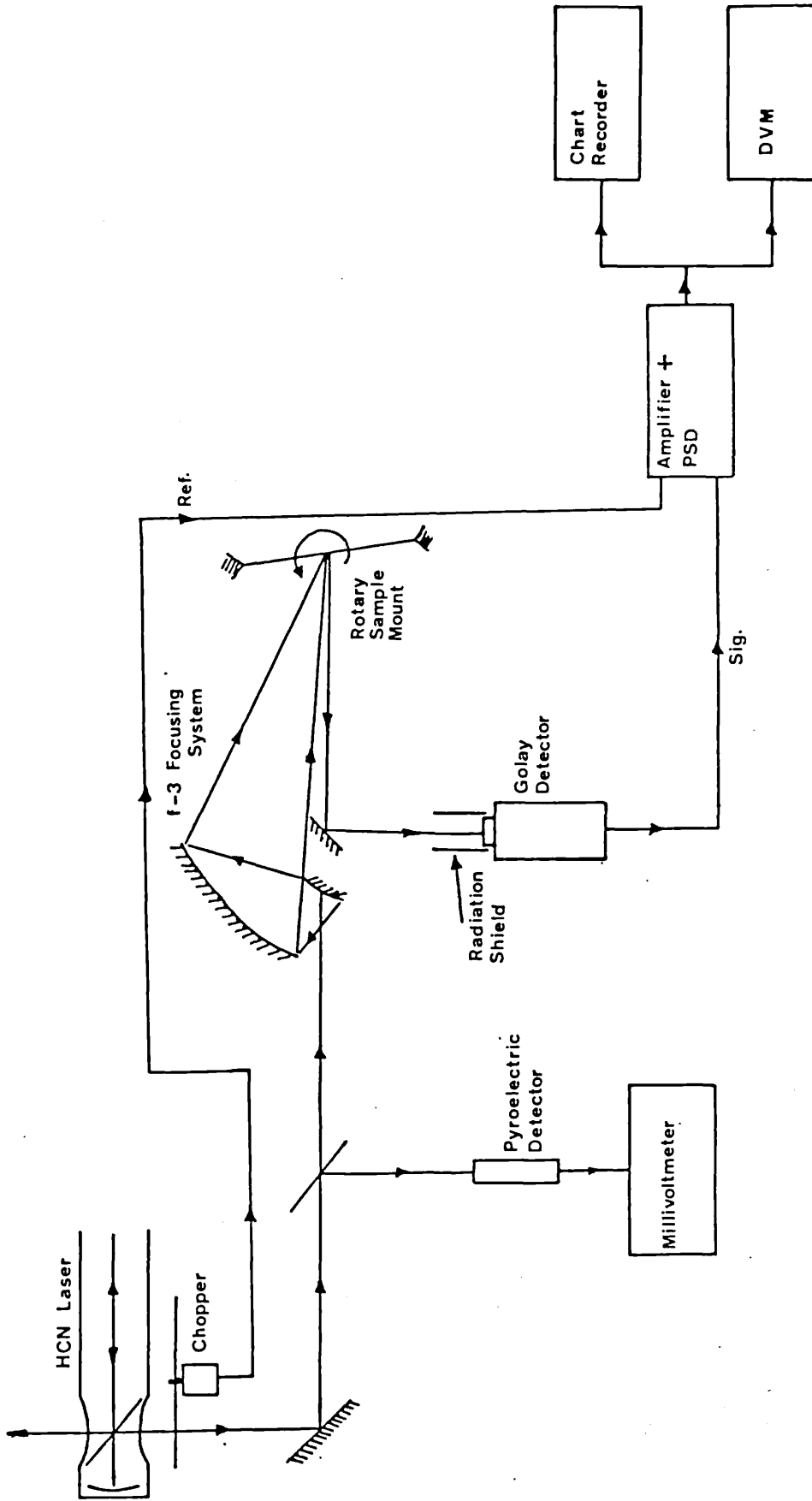


Figure 9.1. Experimental arrangement employed for the backscattering measurements.

must lie in the far-field of the scattering array in order to obtain measurements of the far-field patterns<sup>81</sup>.

As the Gaussian beam from the laser output was truncated by the input aperture of the focussing system it is perhaps wise to assume that the focal spot size will be diffraction limited and the wave will be effectively plane over the diameter of the first Airey disc. The focal spot diameter  $d$  is given by

$$d = f \theta \quad (9.2.)$$

where  $f$  is the focal length and  $\theta$  the angular width of the first Airey ring and is given by

$$\theta = \frac{1.22\lambda}{D} \quad (9.3.)$$

The diffraction limiting aperture  $D$  was taken to be that of the secondary mirror which was equal to 20 mm. Hence for  $\lambda = 337 \mu\text{m}$ , was calculated to be 0.02 radians. The focal length of the cassegrain focusing system was 95 mm and the value calculated from equation (9.2.) for the diameter of the plane wave region of the focal spot was 1.95 mm. This diameter consequently limited the size of the arrays that could be investigated to less than 6 wavelengths long.

The minimum permissible distance between the detector and scatterer occurs at the Fresnel - Fraunhofer boundary and is given by  $2D^2/\lambda$  where  $D$  is the aperture of the scattering antenna. As the apertures of the scattering arrays used in this investigation did not exceed 1.9 mm then the minimum distance between the detector and scatterer at a wavelength of 337  $\mu\text{m}$  was 22 mm. As the scatterer to detector distance was 80 mm the detector was well within the far-field of the array.

A helium-neon laser beam was aligned co-axially with the HCN laser such that the cassegrain optics produced a visible focal spot co-incident with the far-infrared focus. This feature was essential for accurate positioning of the arrays at the beam waist. This assumption was verified by locating the far-infrared focus using a temperature sensitive liquid crystal film which was sandwiched between thin polyester sheets of low thermal mass.

The output signal from the Golay detector will be proportional to the backscattered signal provided that the Golay detector is used in its square law region. If the power density at the scattering antenna is  $P_d$  and the backscattering cross-section is  $\sigma_{BS}$  then the power produced at the Golay detector is  $P_d'$  where

$$P_d' = \frac{P_d \sigma_{BS}}{4 \pi r^2} \quad (9.4.)$$

and  $r$  is the distance from the Golay detector to the scatterer. Hence the output voltage of the detector is  $V$  where

$$V = \frac{K P_d \sigma_{BS}}{4 \pi r^2} \quad (9.5.)$$

$K$  is the voltage responsivity (in units of volts/watt) of the detector. Therefore

$$V = C \sigma_{BS} \quad (9.6.)$$

where  $C$  is a constant given by

$$C = \frac{K P_d}{4 \pi r^2} \quad (9.7.)$$

The value of the constant  $C$  depends upon the test range, the detector sensitivity and the incident power density. The output power of the laser was monitored with a pyroelectric detector to verify that it remained constant during the experiment.

## 9.2. H-Plane Backscattering Pattern from Arrays of Short-circuited Halfwave Dipole Elements.

Figure 9.2 shows the scattering geometry of a linear array and defines the H-plane and E-plane geometries<sup>82</sup>. The position of beamwidth of the main lobe and the grating lobes of an array can be calculated by conventional diffraction theory. This simple theory was used to verify the grating lobe positions derived from the more complex theory developed in Chapter 3. However, the more simple diffraction theory does not predict the relative amplitudes of the various sidelobes, whereas the more exact theory does.

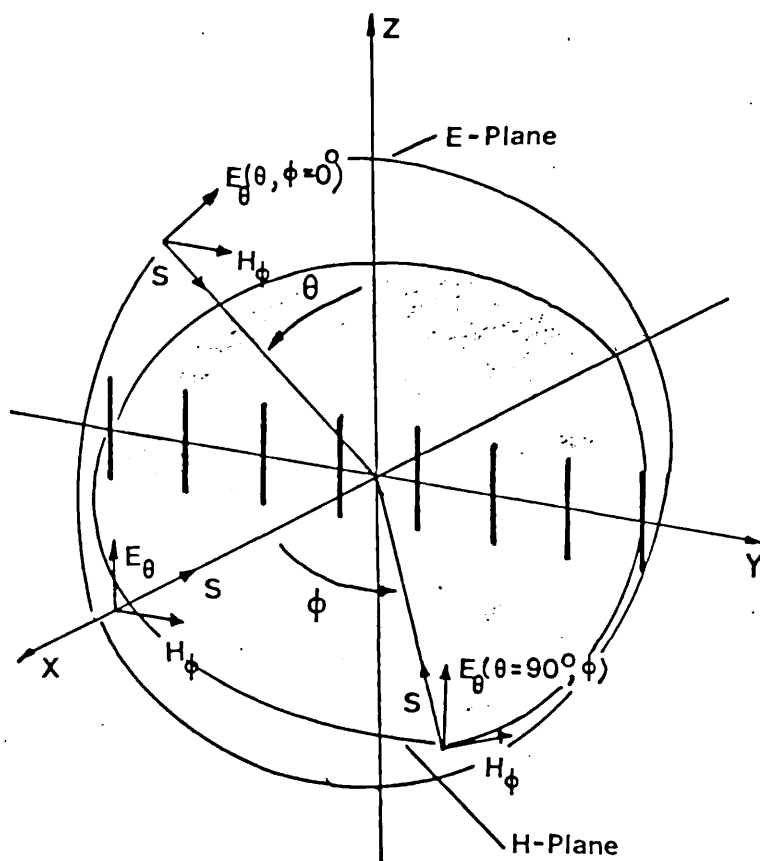


Figure 9.2. E and H plane scattering geometry for a dipole array in the ZY plane. X axis is array normal.

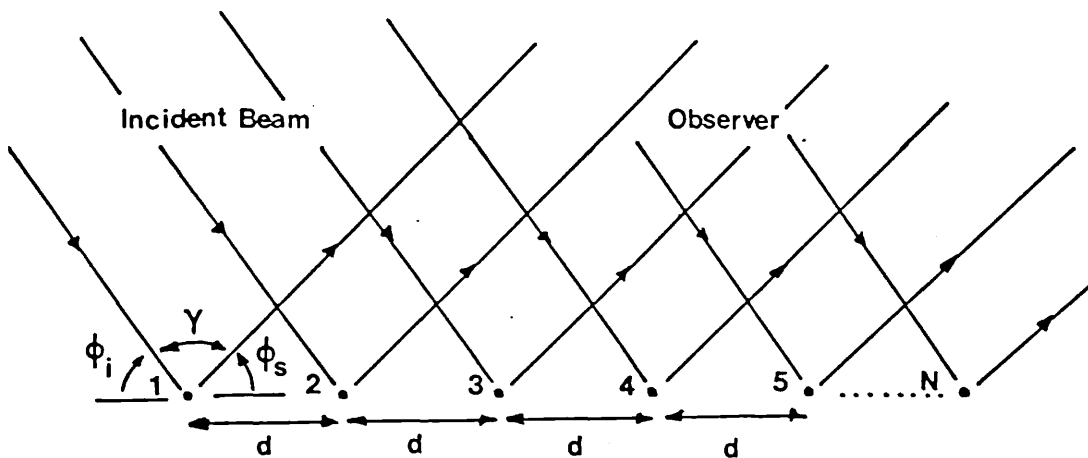


Figure 9.3. H plane scattering geometry for a dipole array of N elements of inter-element separation d.

9.2.1. Simple Diffraction Theory for the H-Plane Scattering by an Antenna Array.

The geometry for an array of  $N$  elements of inter-element spacing  $d$  is shown in Figure 9.3. Let  $\phi_i$  be the angle the incident beam makes with the plane of the array and let  $\phi_s$  be the angle the observer of the scattered signal makes with the plane of the array. The resultant field  $E_R$  produced by an array of  $N$  elements, separated by a distance  $d$  and each having a successive phase difference  $\alpha$ , at an angle  $\phi_s$  to the plane of the array is given by<sup>83</sup>

$$E_R = E_o \left[ \frac{\sqrt{N}}{N} \frac{\sin (N (\theta \pm \alpha) / 2)}{\sin ((\theta \pm \alpha) / 2)} \right] \quad (9.8.)$$

where 
$$\theta = \frac{2 \pi d}{\lambda} \cos \phi_s \quad (9.9.)$$

Now, in the case of a scattering array the phase difference of excitation between successive elements is governed by the angle of incidence of the illuminating beam. From Figure 9.3 it can be deduced that

$$\alpha = \frac{-2 \pi d}{\lambda} \cos \phi_i \quad (9.10.)$$

Substituting equations 9.9 and 9.10 into 9.8 yields the result

$$E_R = E_o \left[ \frac{\sqrt{N}}{N} \frac{\sin [N \pi d / \lambda (\cos \phi_s - \cos \phi_i)]}{\sin [\pi d / \lambda (\cos \phi_s - \cos \phi_i)]} \right] \quad (9.11.)$$

hence

$$E_R = E_o \frac{\sqrt{N}}{N} \frac{\sin \left[ \frac{N \pi d}{\lambda} \left\{ -2 \sin \left\{ \frac{\phi_s + \phi_i}{2} \right\} \sin \left\{ \frac{\phi_s - \phi_i}{2} \right\} \right\} \right]}{\sin \left[ \frac{\pi d}{\lambda} \left\{ -2 \sin \left\{ \frac{\phi_s + \phi_i}{2} \right\} \sin \left\{ \frac{\phi_s - \phi_i}{2} \right\} \right\} \right]} \quad (9.12.)$$

The case of interest is the backscattering case. From Figure 9.3 it can be seen that  $\phi_s + \phi_i + \gamma = \pi$ . For the backscattering case  $\gamma = 0$  and so  $\phi_s + \phi_i = \pi$ . Hence equation 9.12 becomes

$$E_R = E_o \left[ \frac{\sqrt{N}}{N} \frac{\sin \left\{ N \pi d / \lambda \left\{ 2 \sin \frac{\pi}{2} \sin \left\{ \frac{\phi_s - \phi_i}{2} \right\} \right\} \right\}}{\sin \left\{ \frac{\pi d}{\lambda} \left\{ 2 \sin \frac{\pi}{2} \sin \left\{ \frac{\phi_s - \phi_i}{2} \right\} \right\} \right\}} \right] \quad (9.13.)$$

Now  $\sin \frac{\pi}{2} = 1$  and  $\phi_s = \pi - \phi_i$ . As  $\sin (\frac{\pi}{2} - \phi_i)$   
 $= \cos \phi_i$  then equation 9.13 becomes

$$E_R = \frac{E_o}{\sqrt{N}} \frac{\sin (\frac{N \pi d}{\lambda} 2 \cos \phi_i)}{\sin (\frac{\pi d}{\lambda} 2 \cos \phi_i)} \quad (9.14.)$$

The variation of  $E_R$  with  $\phi_i$  is plotted in Figure 9.4 to 9.8 for the arrays of interest. The broadside full power beamwidth can be obtained from equation 9.14. A minimum will occur when the term  $2 \pi N d \cos \phi_i / \lambda$  is equal to  $m \pi$ , where  $m$  is an integer. Taking  $m = 1$  as the first order minimum then the value for  $\phi_i$  at which this occurs is

$$\phi_i = \cos^{-1} \left\{ \frac{\lambda}{2Nd} \right\} \quad (9.15.)$$

The broadside full beamwidth  $\theta_{FW}$  is given by

$$\theta_{FW} = 2 \left\{ \frac{\pi}{2} - \cos^{-1} \left\{ \frac{\lambda}{2Nd} \right\} \right\} \text{ radians} \quad (9.16.)$$

If  $\lambda/2Nd$  is small, which is generally the case, then equation 9.16 can be approximated to

$$\theta_{FW} = \left\{ \frac{\lambda}{Nd} \right\} \text{ radians} \quad (9.17.)$$

The predicted angular positions of the grating lobes, that appear when the spacing between elements is greater than half a wavelength, exactly agreed with the simple diffraction theory given above and also the more complex scattering theory of Chapter 3. These grating lobes occur in those directions where the radiation from all the elements adds in phase.

### 9.2.2. Experimental Investigation of the Variation of H-plane Backscattering from Antenna Arrays at 891 GHz

The H-plane backscattering patterns obtained for linear arrays of short-circuited halfwave dipoles of width  $10 \mu\text{m}$  and of various inter-element separations, reproduced on  $3.5 \mu\text{m}$  mylar substrates, are shown in Figures 9.9 to 9.13. The corresponding theoretical H-plane backscattering patterns obtained from computer code developed from the

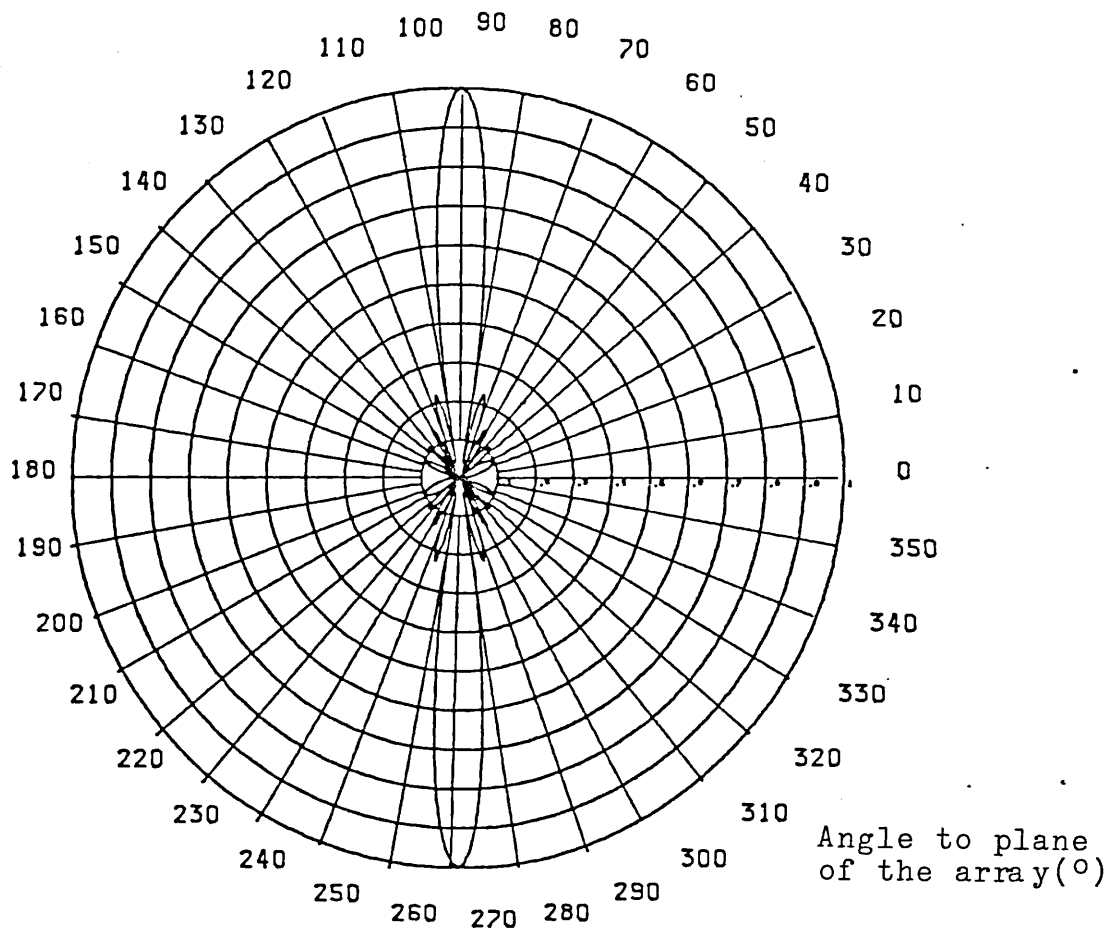


Figure 9.4. Variation of H-plane electric field distribution for a linear array of 10 isotropic elements of inter-element separation  $0.25\lambda$ .

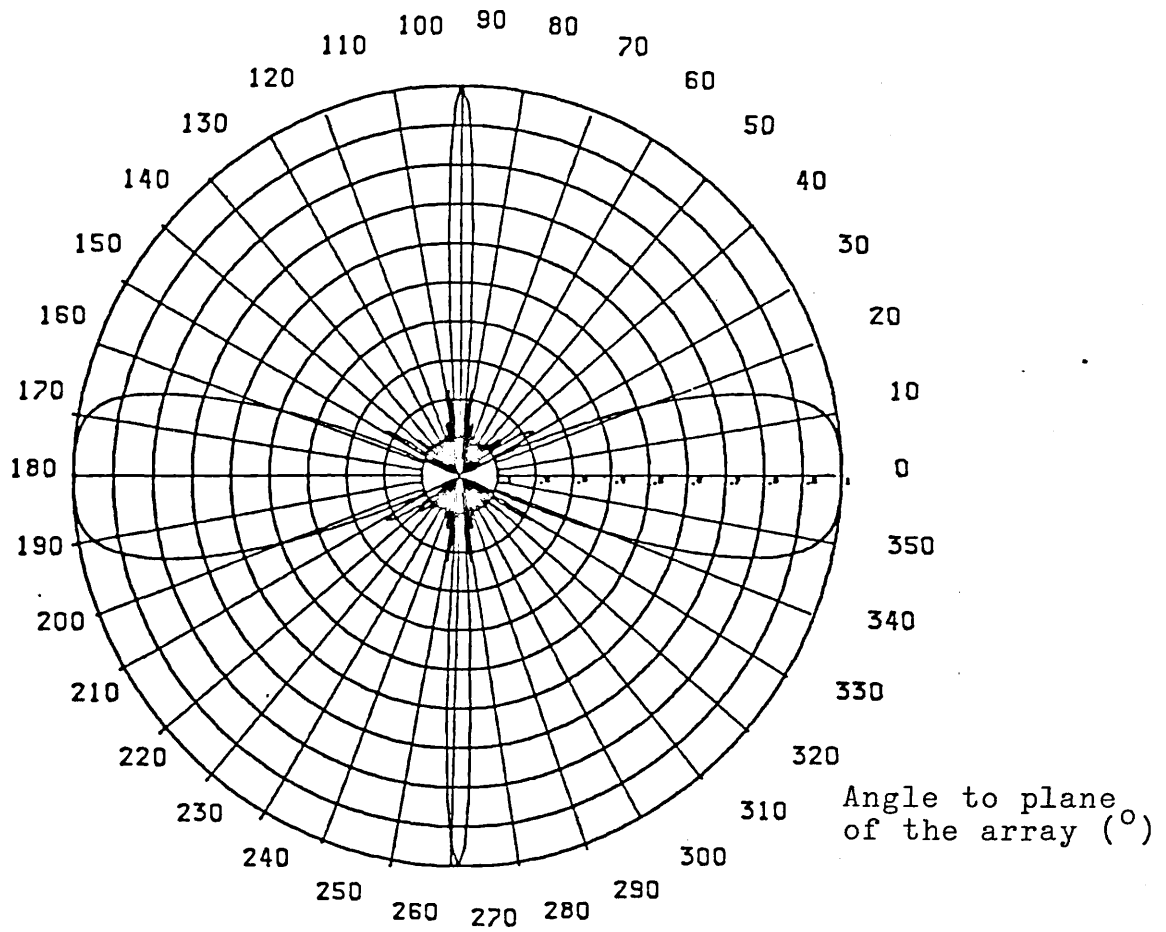
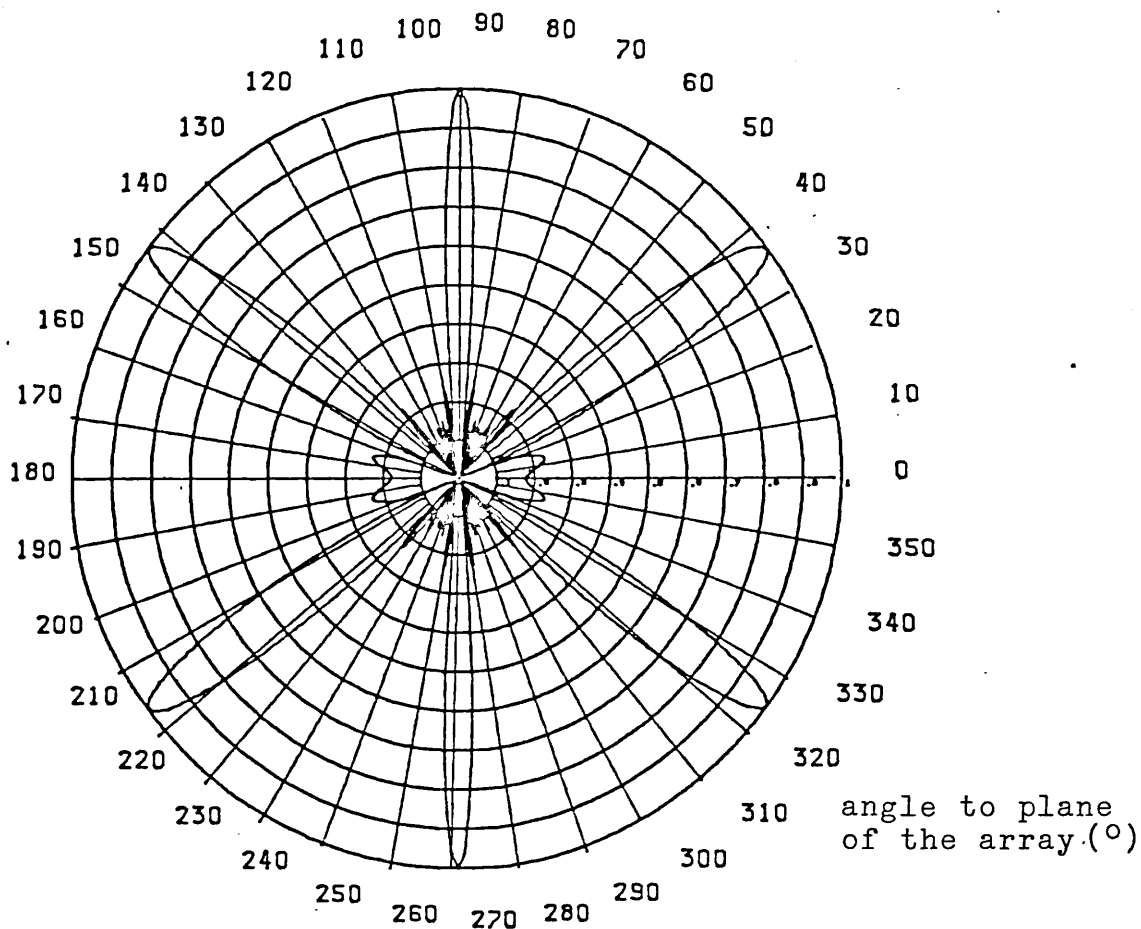


Figure 9.5. Variation of H-plane electric field distribution for a linear array of 10 isotropic elements of inter-element separation  $0.5\lambda$ .





$N=7:D=0.62$

Figure 9.6. Variation of H-plane electric field distribution for a linear array of 7 isotropic elements of inter-element separation  $0.62\lambda$ .

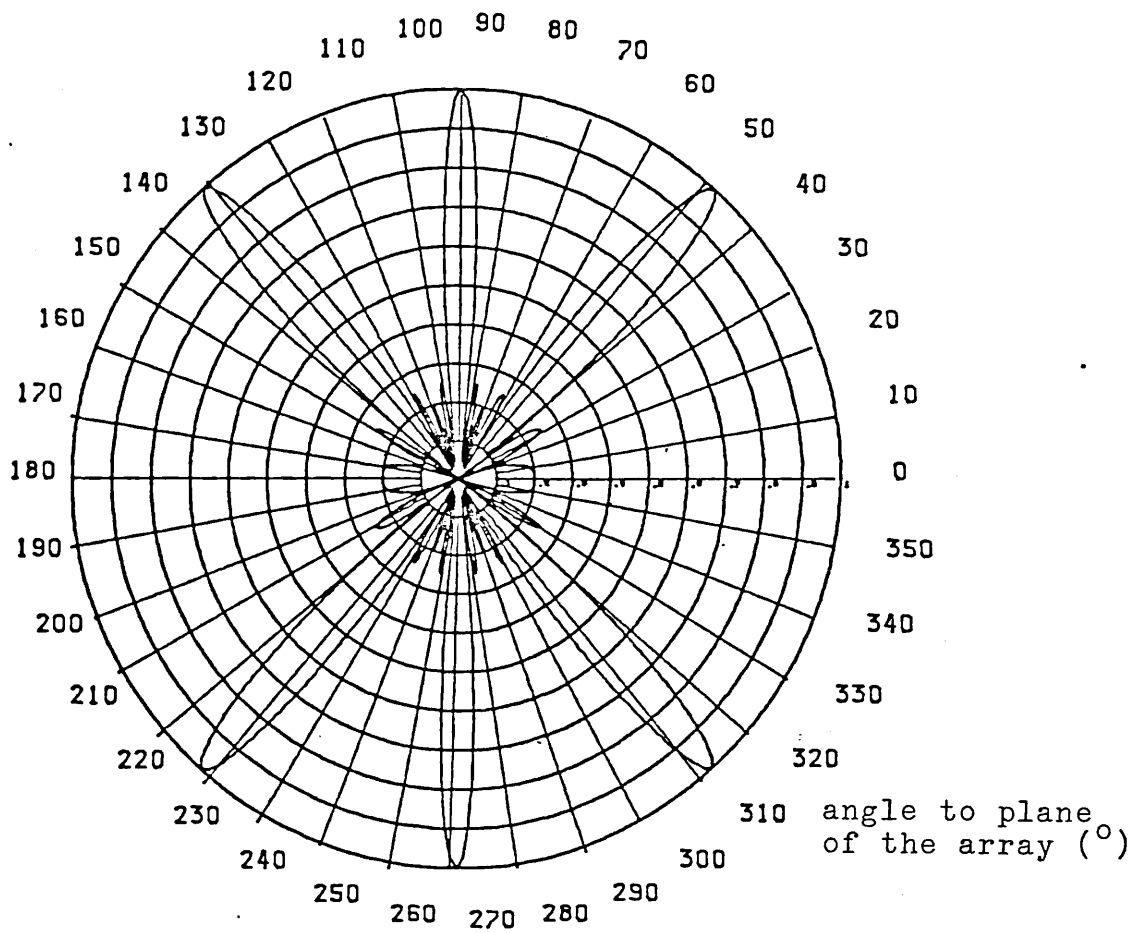
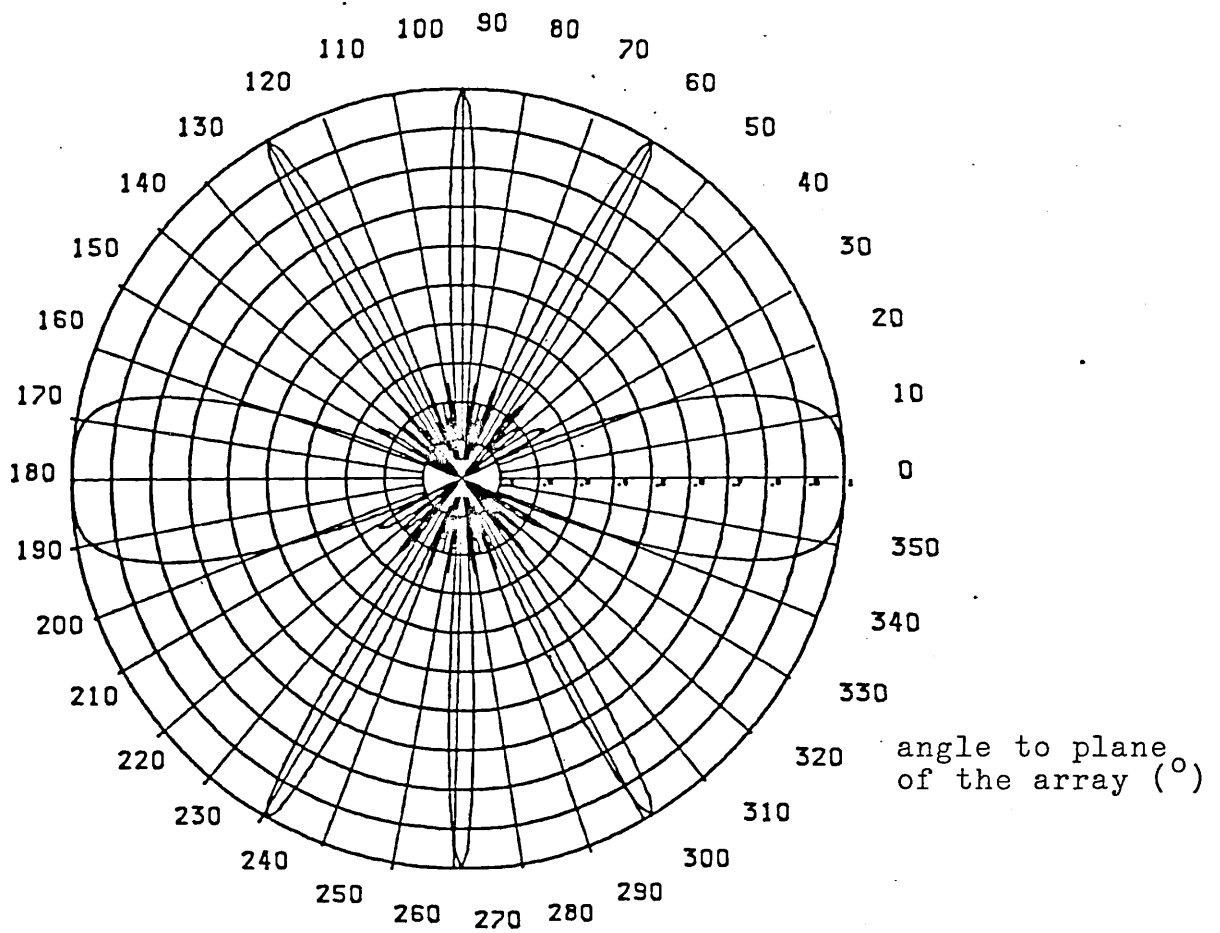


Figure 9.7. Variation of H-plane electric field distribution for a linear array of 5 isotropic elements of inter element separation  $0.75\lambda$ .



$N=5:D=1.0$

Figure 9.8. Variation of H-plane electric field distribution for a linear array of 5 isotropic elements of inter-element separation  $1.0\lambda$ .

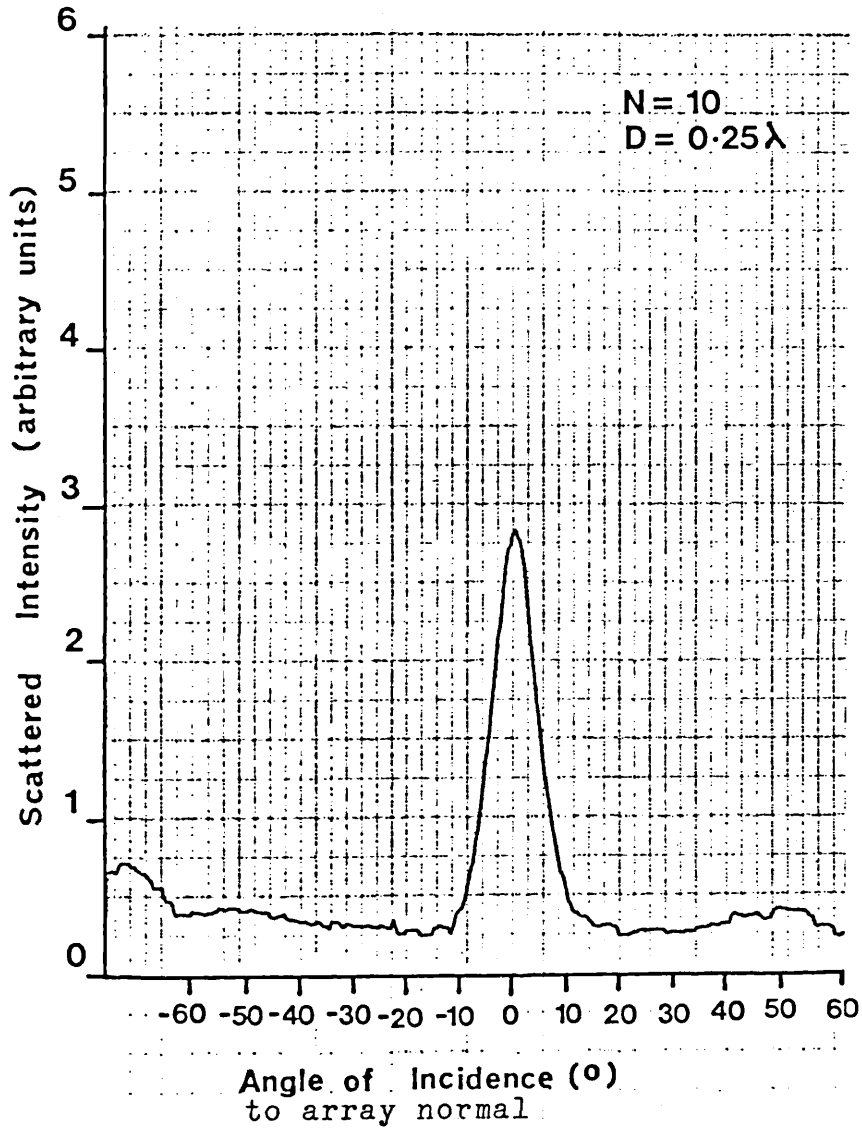


Figure 9.9. H-plane backscattering pattern for a linear array of 10 short circuited halfwave dipole elements of inter-element separation  $0.25\lambda$ . Reproduced on a  $3.5 \mu\text{m}$  mylar substrate. Element width =  $10 \mu\text{m}$ .

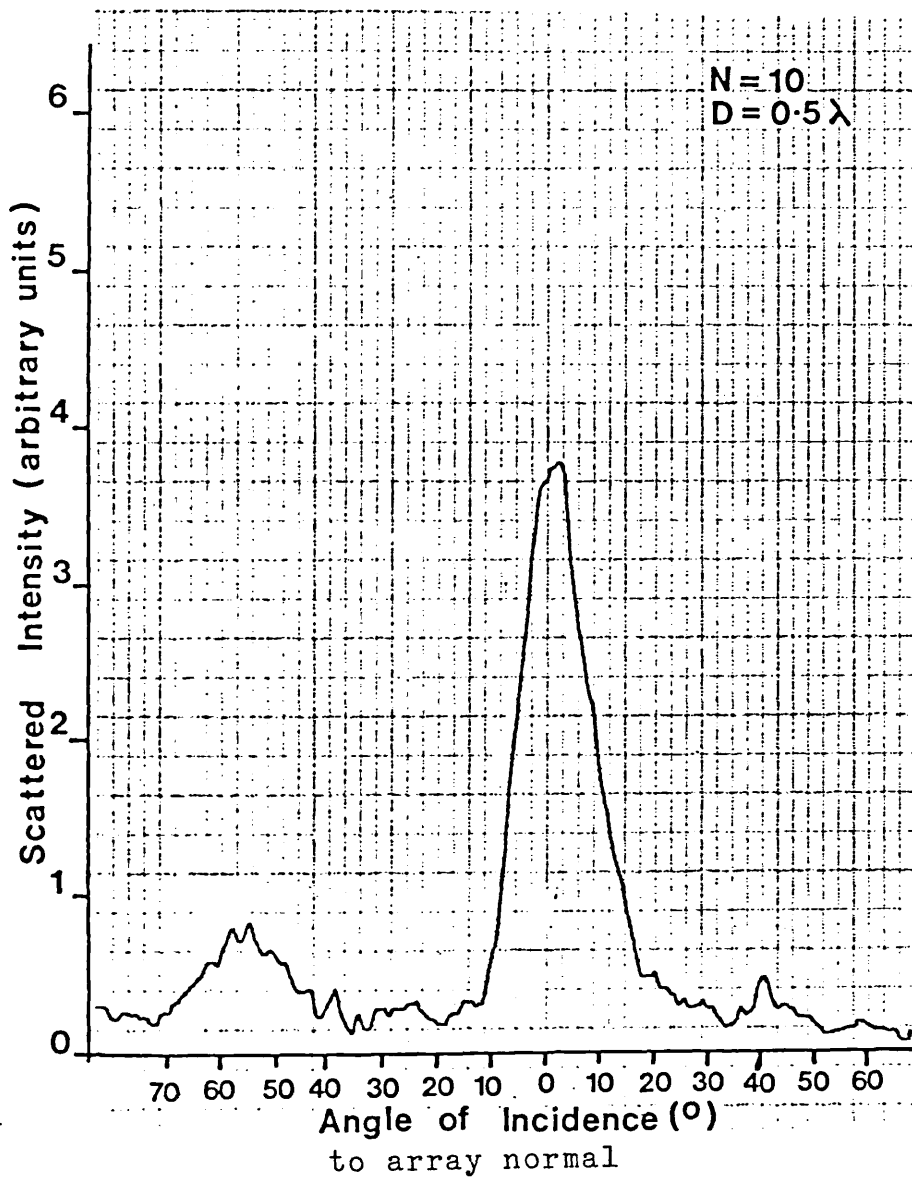


Figure 9.10. H-plane backscattering pattern for a linear array of 10 short circuited halfwave dipole elements of inter-element separation  $0.5\lambda$ . Reproduced on a  $3.5 \mu\text{m}$  mylar substrate. Element width =  $10 \mu\text{m}$ .

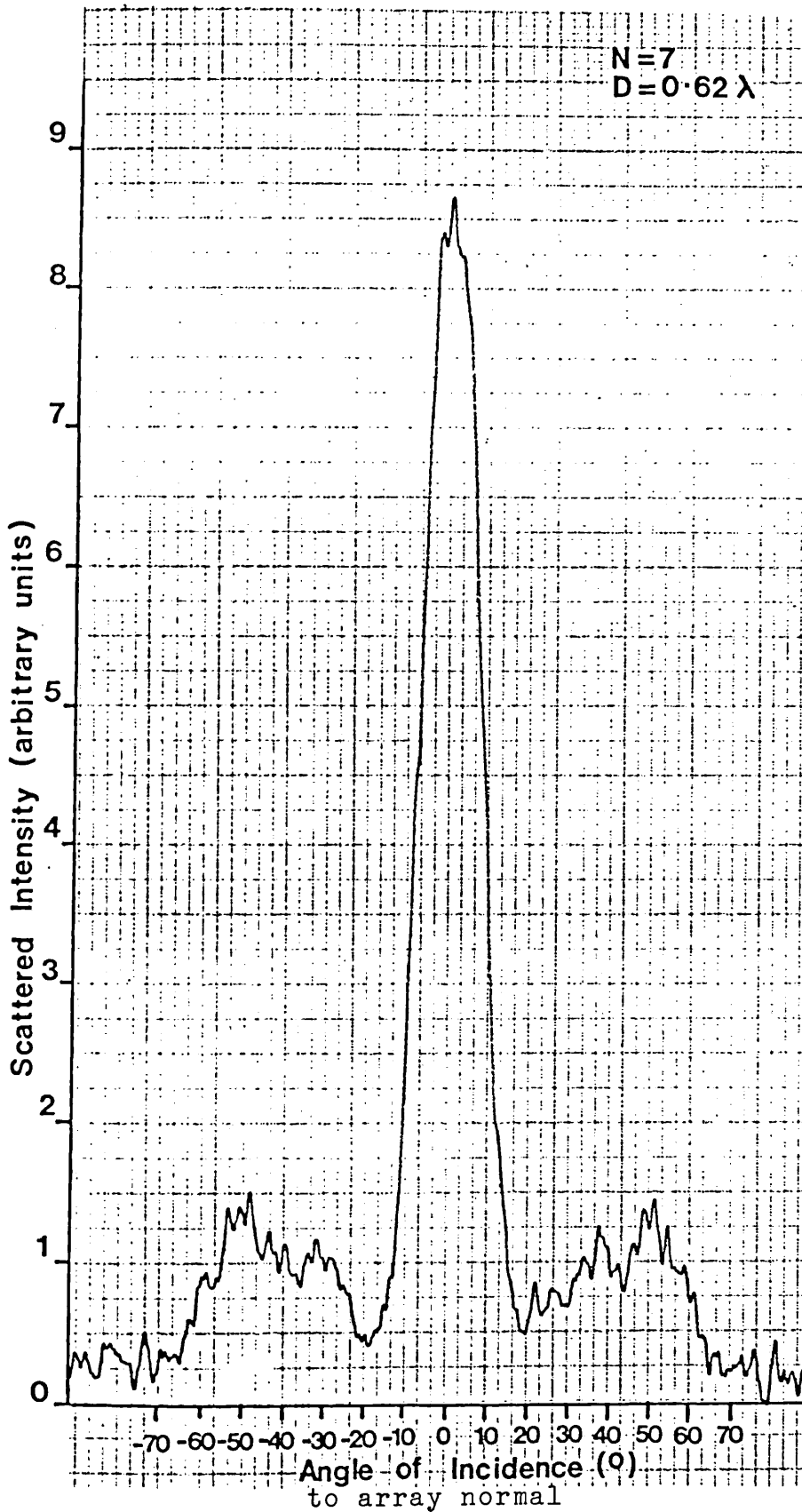


Figure 9.11. H-plane backscattering pattern for a linear array of 7 short circuited halfwave dipole elements of inter-element separation  $0.62\lambda$ . Reproduced on a  $3.5\ \mu\text{m}$  mylar substrate. Element width =  $10\ \mu\text{m}$ .

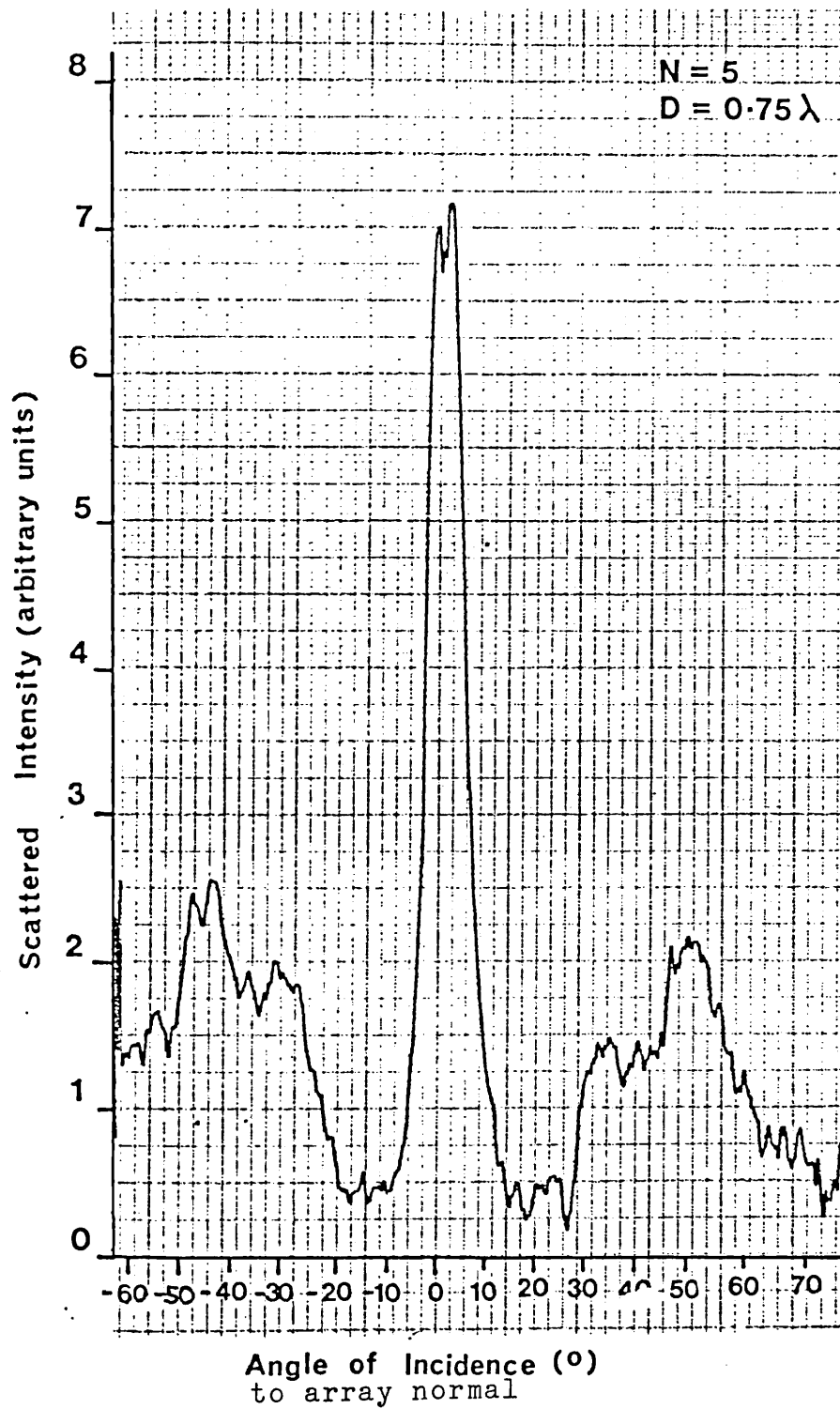


Figure 9.12. H-plane backscattering pattern for a linear array of 5 short circuited halfwave dipole elements of inter-element separation  $0.75\lambda$ . Reproduced on a  $3.5 \mu\text{m}$  mylar substrate. Element width =  $10 \mu\text{m}$ .

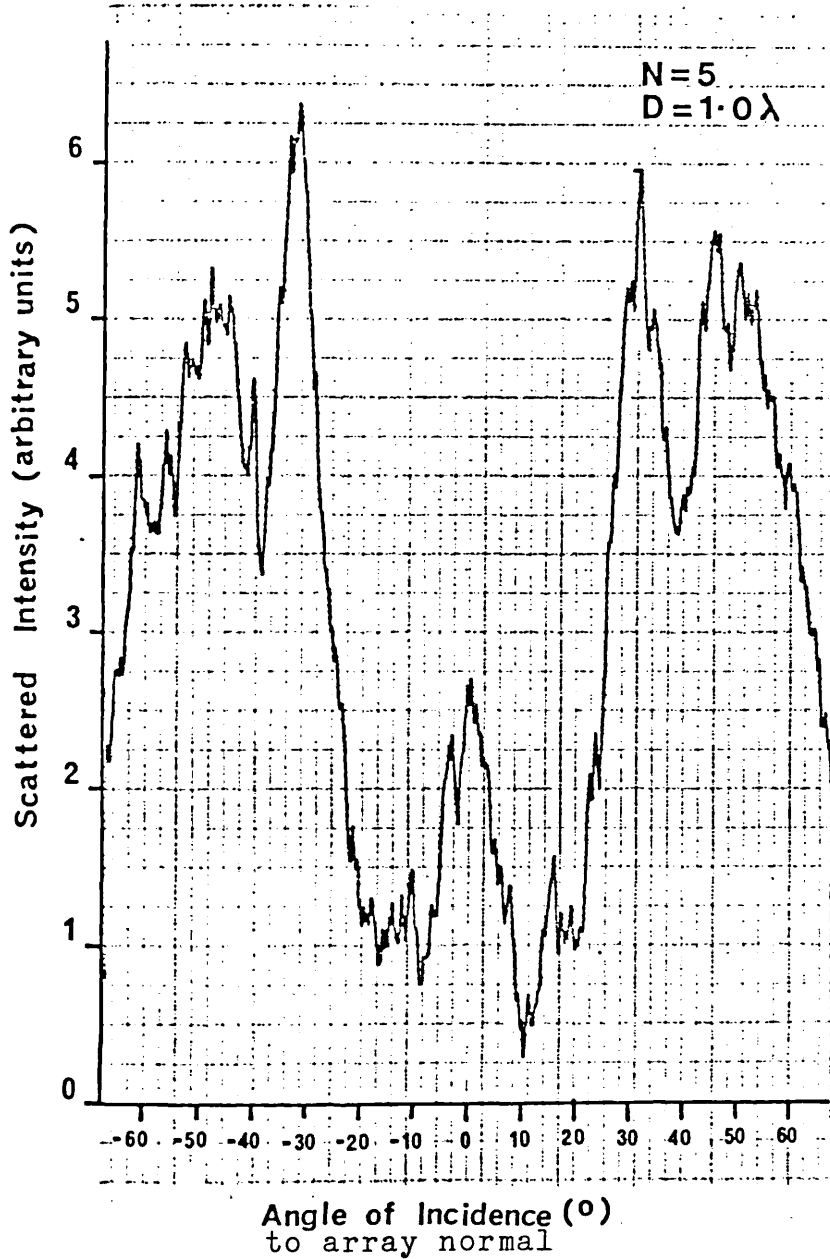


Figure 9.13. H-plane backscattering pattern for a linear array of 5 short circuited halfwave dipole elements of inter-element separation  $1.0\lambda$ . Reproduced on a  $3.5 \mu\text{m}$  mylar substrate. Element width =  $10 \mu\text{m}$ .



theory given in Chapter 3, are shown in Figures 9.14 to 9.18. The principal results obtained for the arrays investigated are given in Tables 9.1, 9.2 and 9.3. The experimental results are an average of three independent measurements.

TABLE 9.1.

Broadside Lobe Full Beamwidth, $\theta_B$			
Number of Elements	Inter-Element Separation	$\theta_B$	
		Theoretical	Experimental
10	0.25 $\lambda$	22.9°	20° ± 2°
10	0.5 $\lambda$	11.5°	25° ± 2°
7	0.62 $\lambda$	13.2°	20° ± 2°
5	0.75 $\lambda$	15.3°	18° ± 2°
5	1.0 $\lambda$	11.4°	15° ± 2°

TABLE 9.2.

Angle of Grating Lobes from Broadside, $\theta_D$			
Number of Elements	Inter-Element Separation	$\theta_D$	
		Theoretical	Experimental
10	0.25 $\lambda$	None	None
10	0.5 $\lambda$	90°	Angle too large to measure
7	0.62 $\lambda$	52°	50° ± 3°
5	0.75 $\lambda$	42°	45° ± 3°
5	1.0 $\lambda$	30°	31° ± 3°

Figure 9.14. Theoretical H-plane backscattering pattern for a linear array of 10 short circuited half-wave dipole antennas of inter-element separation  $0.25\lambda$ . Element width =  $0.03\lambda$ .

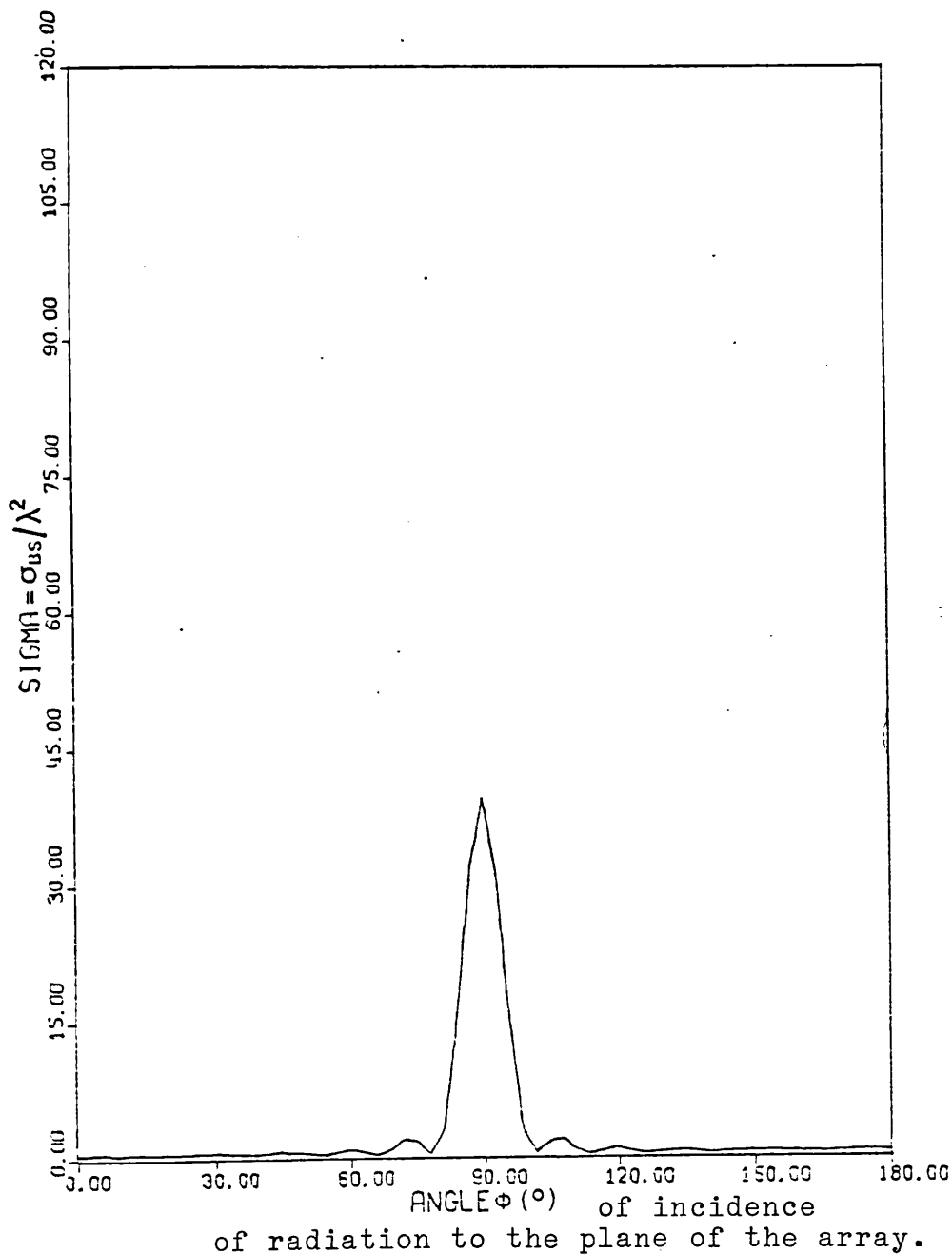


Figure 9.15. Theoretical H-plane backscattering pattern for a linear array of 10 short circuited half-wave dipole elements of inter-element separation  $0.5\lambda$ . Element width =  $0.03\lambda$ .

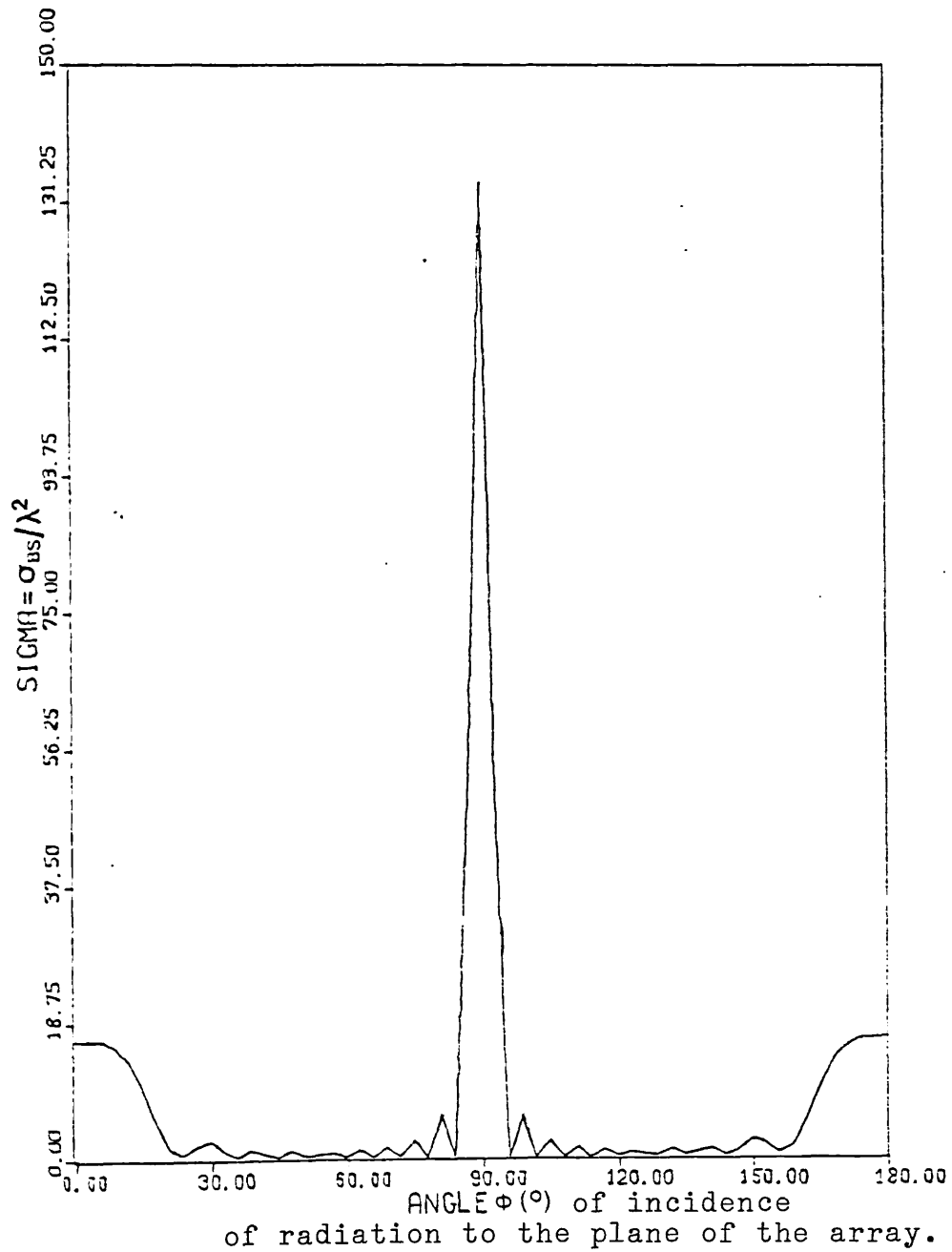


Figure 9.16. Theoretical H-plane backscattering pattern for a linear array of 7 short circuited half-wave dipole antennas of inter-element separation  $0.62\lambda$ . Element width =  $0.03\lambda$ .

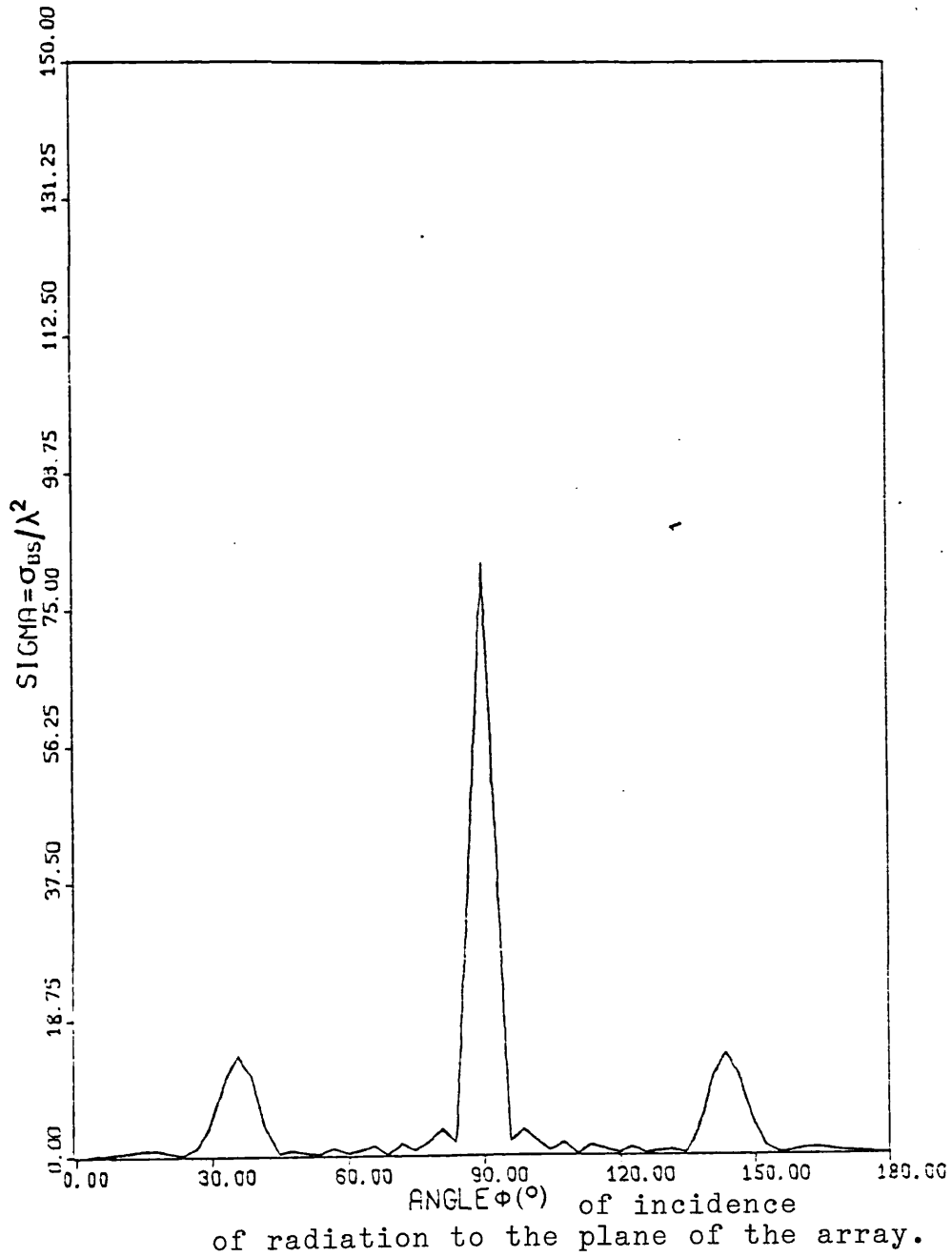


Figure 9.17. Theoretical H-plane backscattering pattern for a linear array of 5 short circuited half-wave dipole elements of inter-element separation  $0.75\lambda$ . Element width =  $0.03\lambda$ .

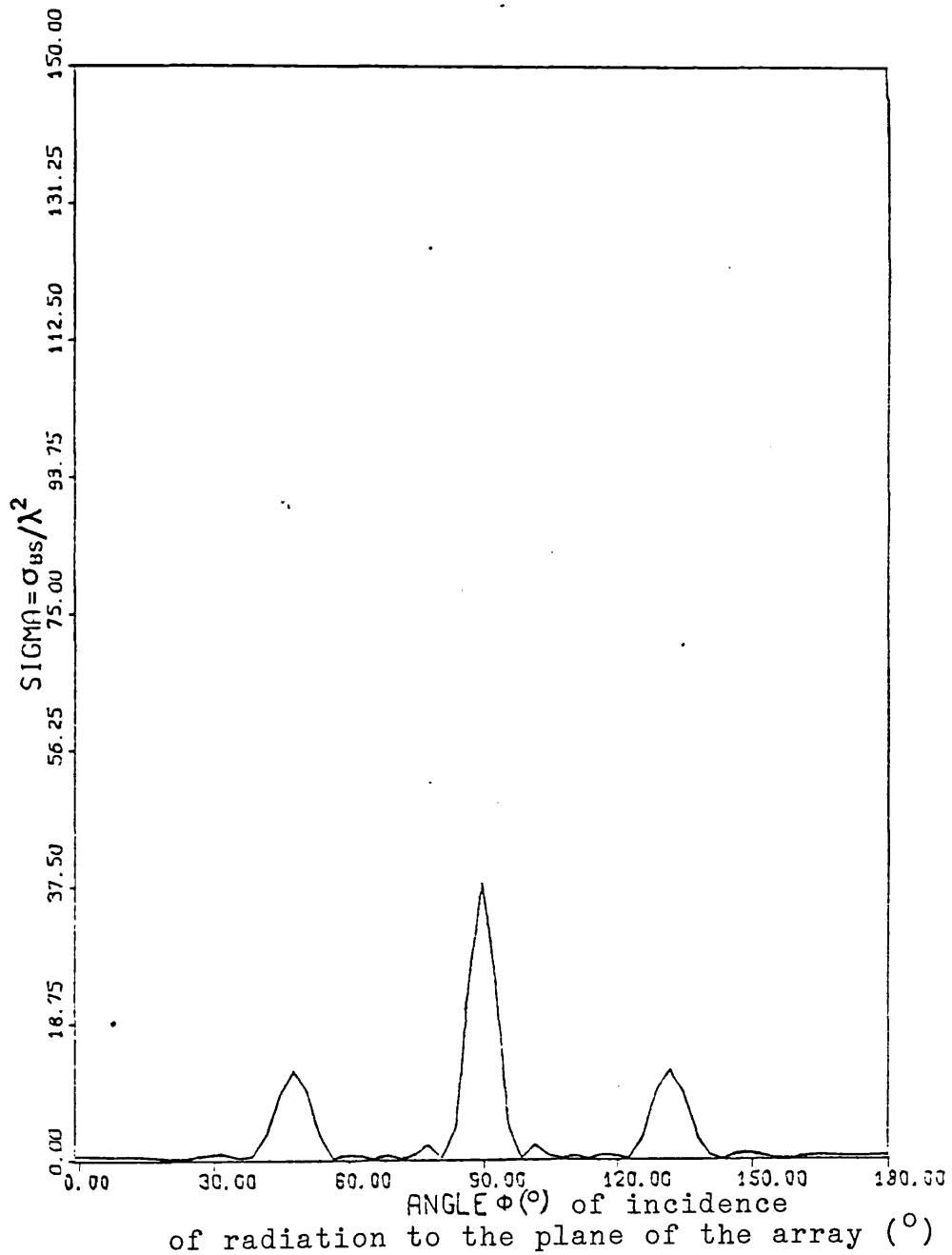


Figure 9.18. Theoretical H-plane backscattering pattern for a linear array of 5 short circuited half-wave dipole antennas of inter-element separation  $1.0\lambda$ . Element width =  $0.03\lambda$ .

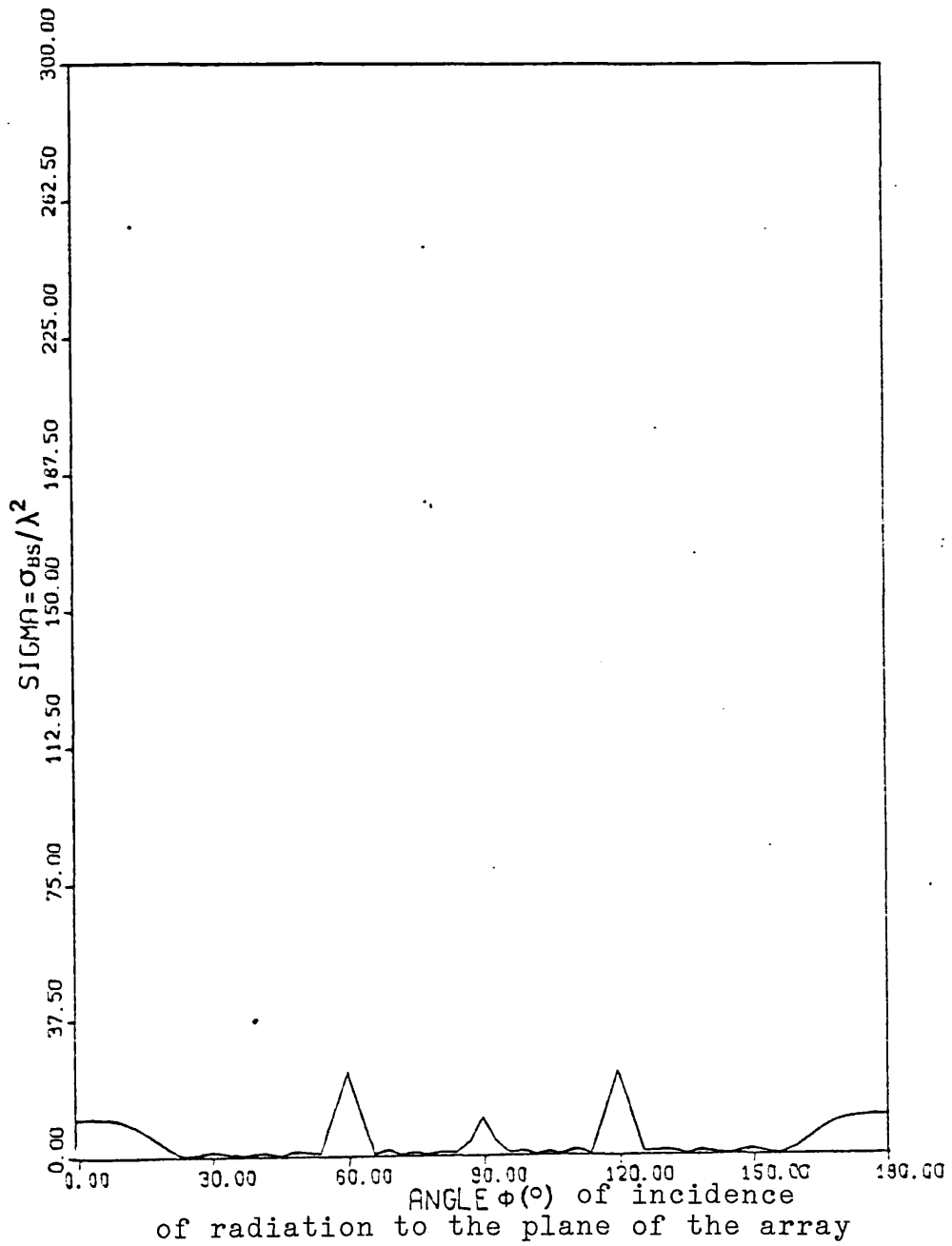


TABLE 9.3.

Grating Lobe Relative Intensities					
Array		Normalised back-scattering cross section $\sigma/\lambda^2$		$\frac{\text{Broadside Lobe Intensity}}{\text{Grating Lobe Intensity}}$	
Number of Elements	Inter-Element Separation	Broadside Lobe	Grating Lobe	Theoretical	Experimental
7	0.62 $\lambda$	81.5	13.8	5.9	5.8 $\pm$ 0.2
5	0.75 $\lambda$	38.2	12.4	3.1	3.2 $\pm$ 0.2
5	1.0 $\lambda$	10.5	23.2	0.45	0.43 $\pm$ 0.03

The agreement between theory and experiment for the positions of the grating lobes and their relative intensities with respect to the broadside lobe is excellent. However, the experimentally measured full beamwidths do not agree with the theoretically predicted values. This is due to the finite angular width of the incident illuminating beam which was  $7^\circ$ , rather than too small a spot size. However, the measured beamwidths are of the correct order of magnitude and the beamwidths do decrease with increasing inter-element separation, as would be theoretically expected.

### 9.3. E-Plane Backscattering Pattern from Arrays of Short-Circuited Dipole Elements.

The E-plane backscattering pattern of a linear short-circuited dipole element is very strongly dependent upon the current distribution in the element produced by the incident field. By investigating the variation of the backscattering pattern in the E-plane it was possible to verify the form of this current distribution. As previously stated, at submillimetre wavelengths, it is necessary to employ an antenna array to achieve sufficient scattering. Although the magnitude of the current distribution will be modified by mutual interactions between adjacent elements it is usually assumed that the form of the current distri-

bution, which in turn governs the form of the radiation pattern, is not appreciably modified from that of a single isolated element<sup>25</sup>.

9.3.1. Theoretical consideration of E-plane Backscattering from an Array of Short Circuited Dipole Elements.

The E-plane pattern for an array of elements of linear extent, and orientated as shown in Figure 9.2, is identical to that of a single element as there is no array factor multiplication to be considered in the E-plane as is the case in the H-plane.

Figure 9.19 illustrates the geometry of a single short-circuited dipole element of halflength  $L$ . A current distribution of the form given in equation 7.26 in Chapter 7 is assumed. To obtain the current in a parasitic antenna it must be noted that for an element of finite length the current must vanish at the ends, which must, therefore, act as virtual sources of waves on the conductor. The electric charge associated with a uniform current if it were propagating on the element due to the uniform exciting field would tend to concentrate at the ends, and the increasing force due to it would oppose the flow of charge. Therefore, the incident uniform field may be considered as a uniform distribution of generators producing a uniform current, and the ends of the conductor act as point generators which produce a sinusoidal current distribution on the antenna. The total current in a wire extending from  $Z = -L$  to  $Z = L$  due to a uniform field is thus

$$I(Z) = A + B \cos \beta Z$$

There can be no sine term because  $I(-Z) = I(Z)$  from symmetry considerations. As the current vanishes at the ends  $I(-L) = I(L) = 0$ . Hence

$$A = -B \cos \beta L \quad \beta = \frac{-A}{\cos \beta L} \quad (9.18.)$$

therefore

$$\begin{aligned} I(Z) &= B (\cos \beta Z - \cos \beta L) \\ &= A \frac{\cos \beta L - \cos \beta Z}{\cos \beta L} \end{aligned} \quad (9.19.)$$



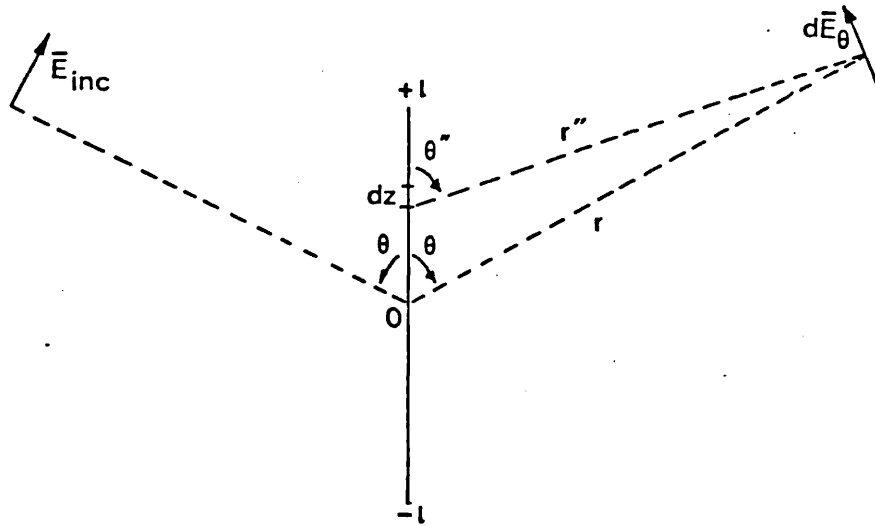


Figure 9.19. E-plane scattering geometry for a single dipole element. Element halflength =  $L$ .

In terms of the current at the centre of the wire,  $Z = 0$ , equation 7.26 is obtained. Rewriting equation 7.26

$$I(Z) = I_0 \frac{\cos \beta Z - \cos \beta L}{1 - \cos \beta L} \quad (9.20.)$$

The propagation constant  $\beta$  of the current is assumed to be equal to that of free space,  $k = 2\pi/\lambda$ . The theoretical variation in the E-plane of the backscattered field is considered in Appendix V. It is assumed here that the form of the current distribution is not affected by the angle of incidence of the field in the E-plane. This assumption was found to be valid by Van Vleck<sup>84</sup> for the first few resonant lengths. However, as indicated in Appendix V the amplitude of the current,  $I_0$ , on the dipole varies with the E-plane angle of incidence  $\theta$  according to the relationship.

$$I_0(\theta) = I_0(90^\circ) \sin \theta \quad (9.21.)$$

The backscattered field distribution is found to be of the form

$$E_\theta = E_0 (\cos (KL \cos \theta) \sin kL - \frac{\sin (kL \cos \theta) \cos kL}{\cos \theta}) \quad (9.22.)$$

where  $L$  is the element halflength and

$$E_0 = \frac{j 2 \eta I_0(\theta = 90^\circ) e^{-jkr}}{4 \pi r (1 - \cos kL)} \quad (9.23.)$$

Figures 9.20 (a) to 9.30 (a) show the variation of the backscattered field distribution  $E(\theta)/E_0$  with angle of incidence  $\theta$  for a short-circuited dipole element having various element halflengths.

Figures 9.20 (b) to 9.30 (b) show the variation of the transmitted field of thin centre driven dipoles of equivalent halflength,  $L$ , as their scattering counterparts shown in Figures 9.20 (a) to 9.30 (a). The transmitting current distribution is assumed to be of the form

$$I(Z) = I_0 \sin k (L - |Z|) + L > Z > -L \quad (9.24.)$$

and the radiation field expressed in the spherical polar

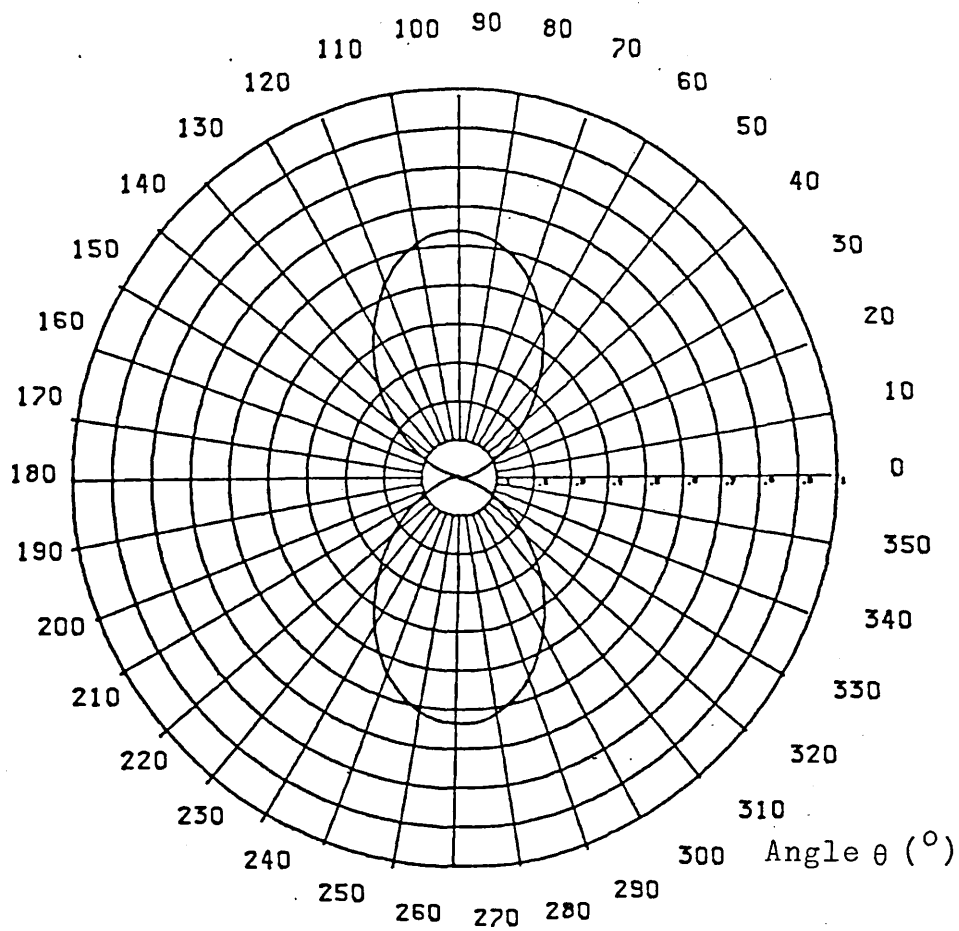
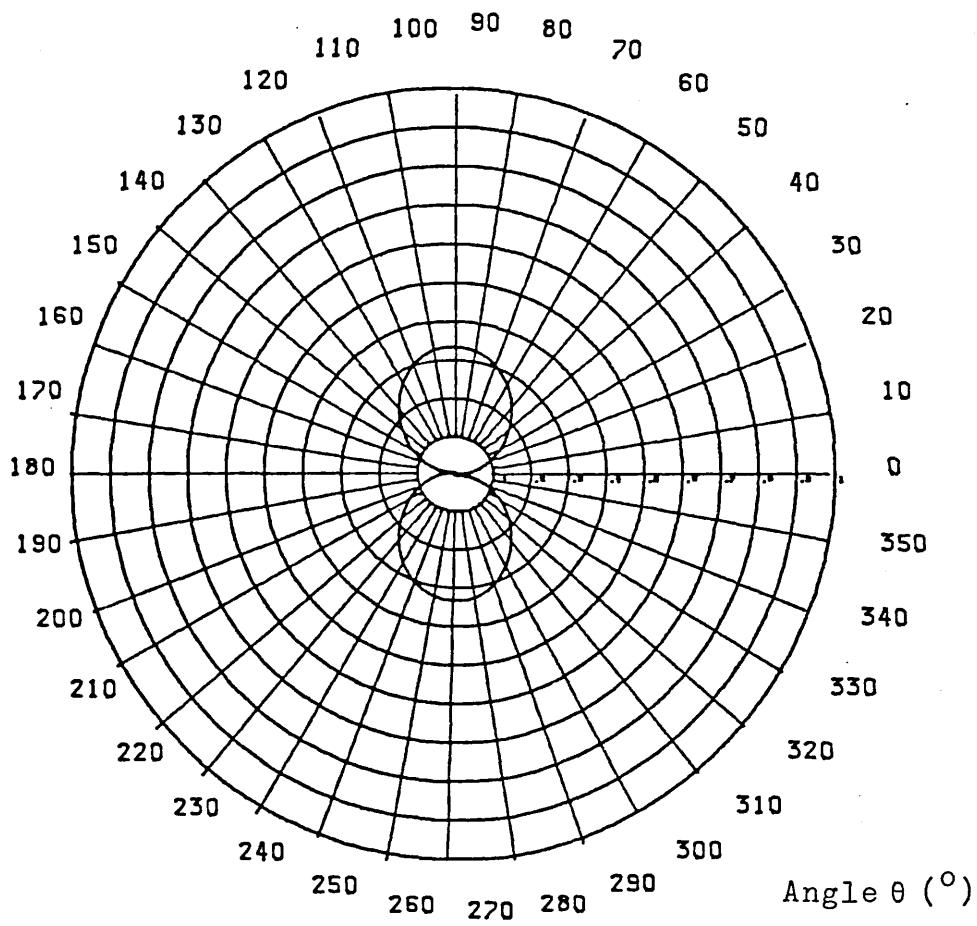
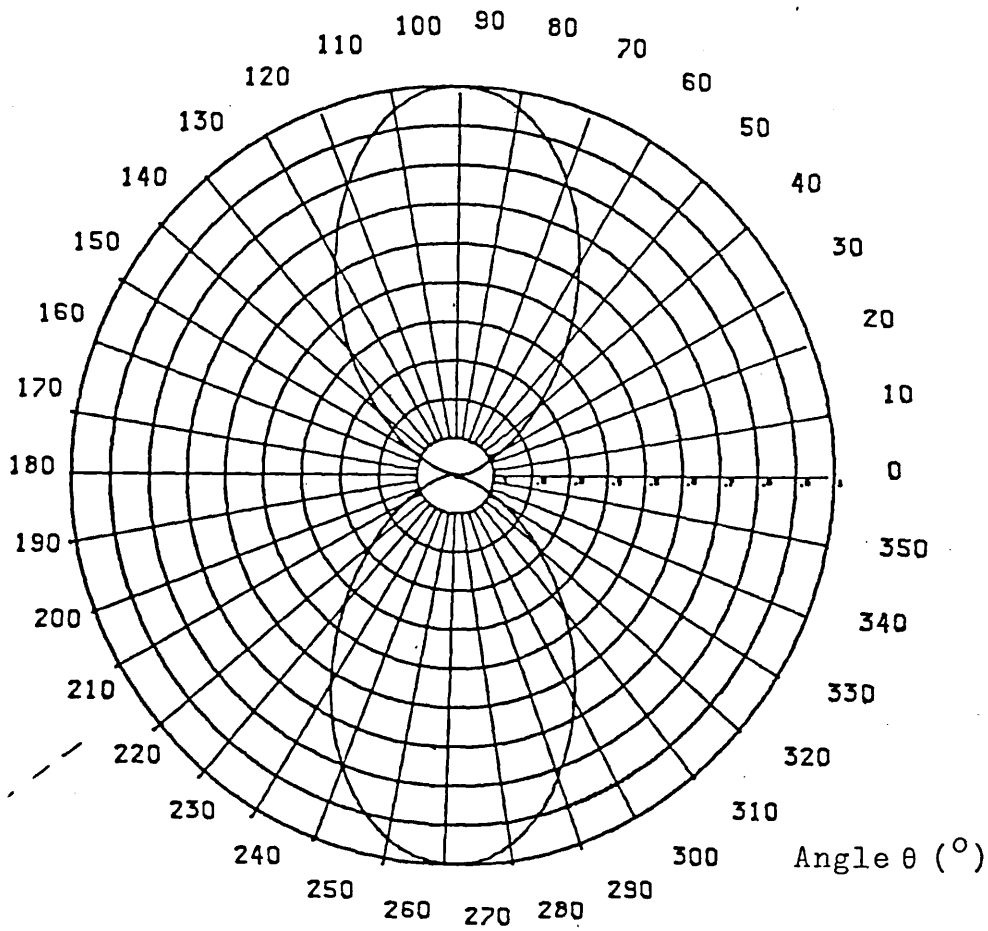


Figure 9.20 (a). Variation of the backscattered electric field  $E(\theta)/E_0$  with angle of incidence  $\theta$  for a short circuited dipole element of halflength  $0.25\lambda$ .



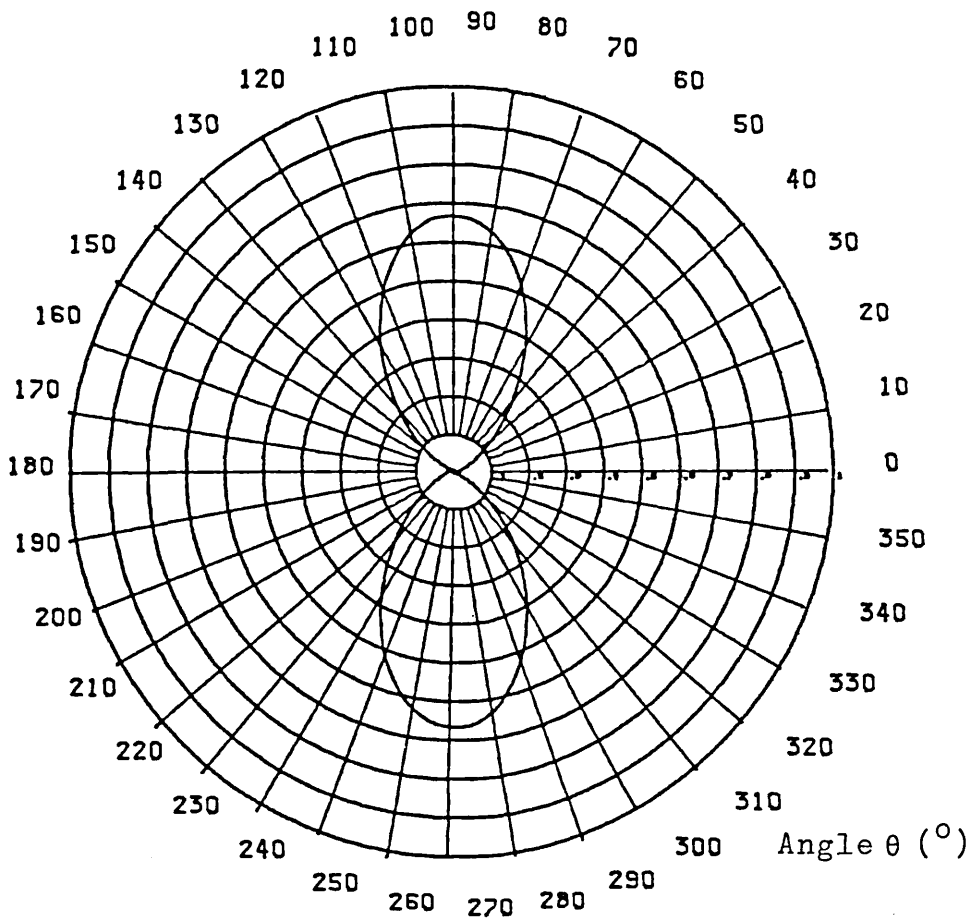
HALFLENGTH=0.25λ

Figure 9.20 (b). Variation of electric field distribution  $E(\theta)/E_0$  with azimuthal angle  $\theta$  for a transmitting antenna of halflength  $0.25\lambda$ .



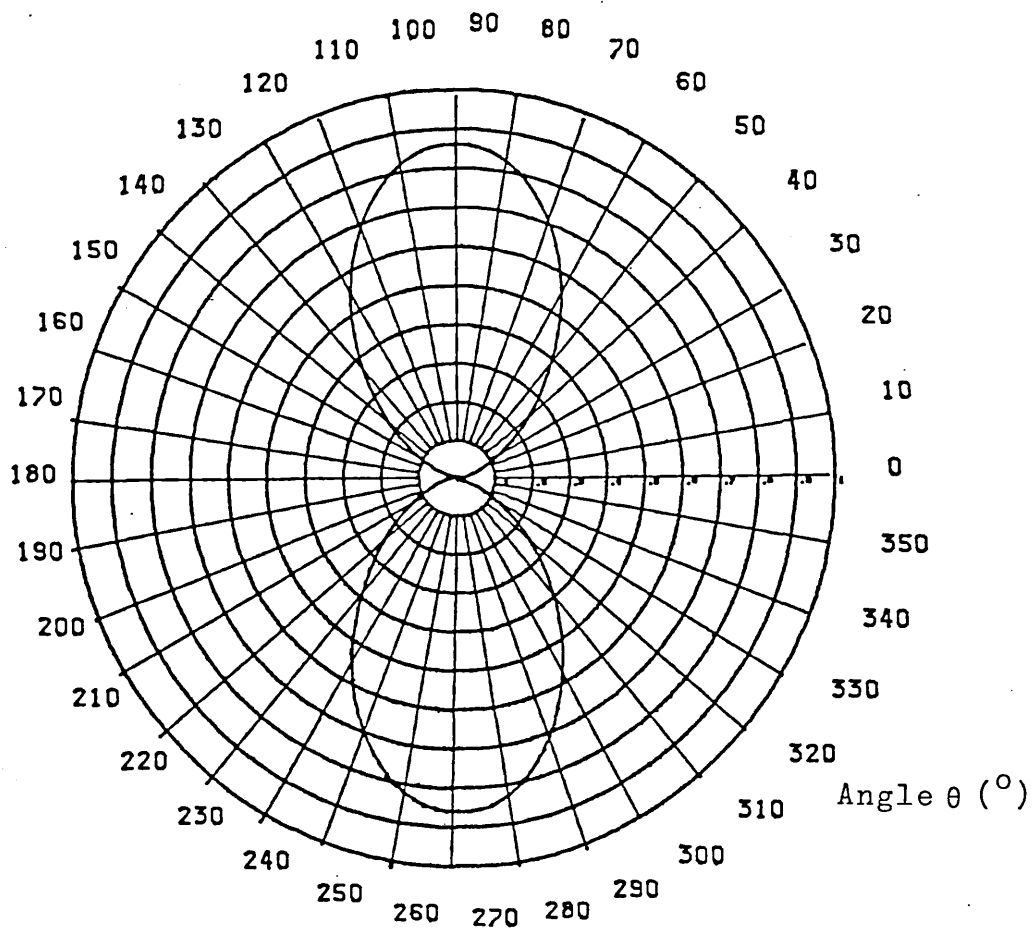
HALFLENGTH= $0.5\lambda$

Figure 9.21 (a). Variation of the backscattered electric field  $E(\theta)/E_0$  with angle of incidence  $\theta$  for a short circuited dipole element of halflength  $0.5\lambda$ .



HALFLENGTH= $0.5\lambda$

Figure 9.21 (b). Variation of electric field distribution  $E(\theta)/E_0$  with azimuthal angle  $\theta$  from a transmitting antenna of halflength  $0.5\lambda$ .



HALFLENGTH=0.55λ

Figure 9.22. (a) Variation of the backscattered electric field  $E(\theta)/E_0$  with angle of incidence  $\theta$  for a short circuited dipole element of halflength  $0.55\lambda$ .

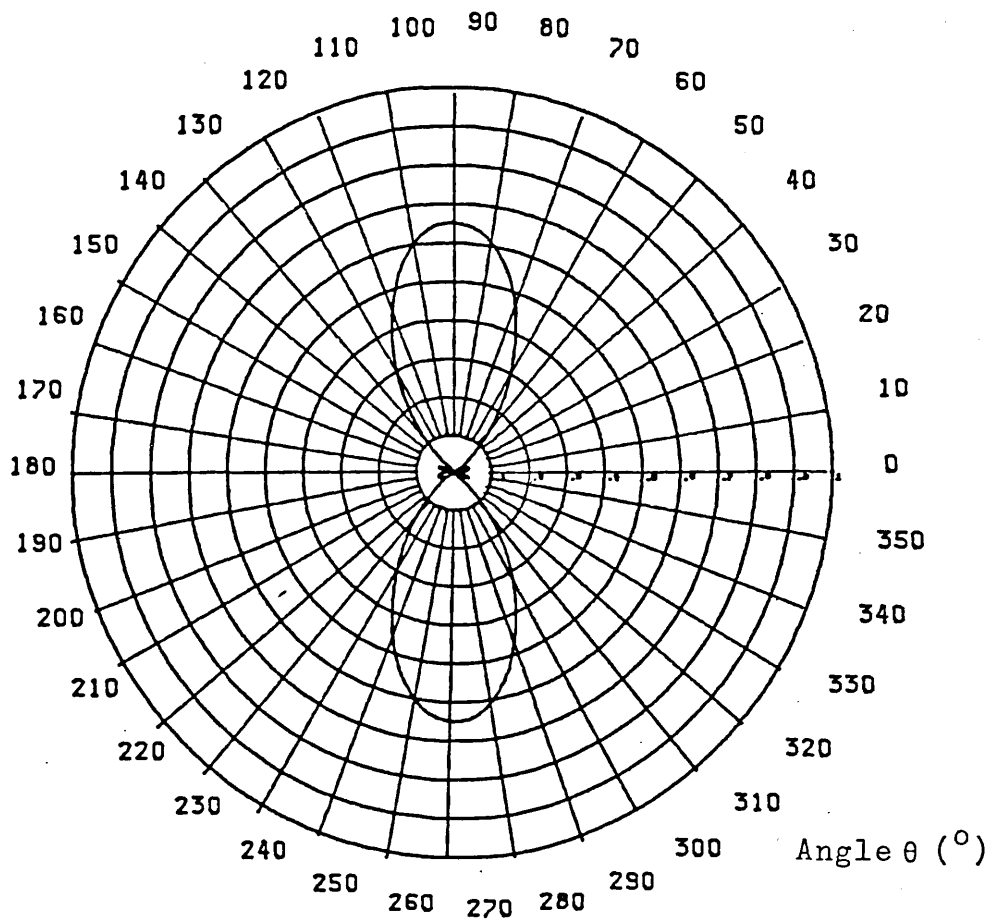
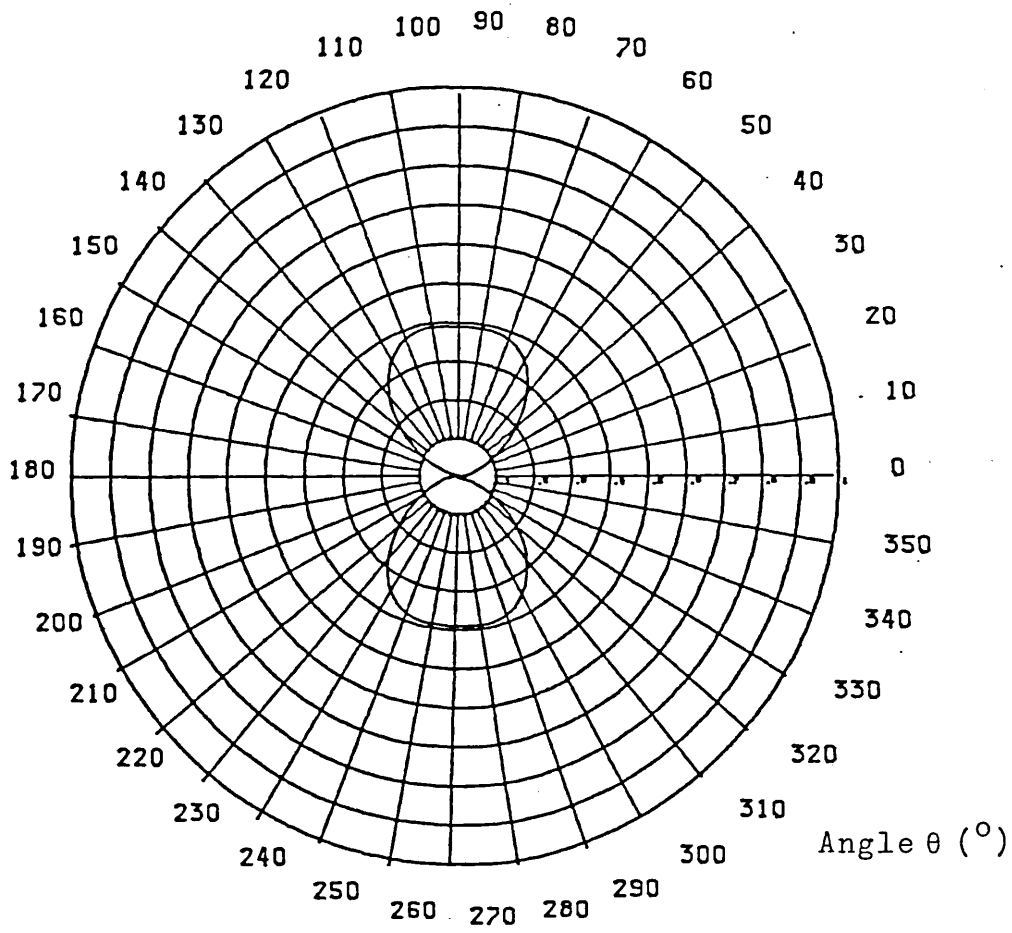


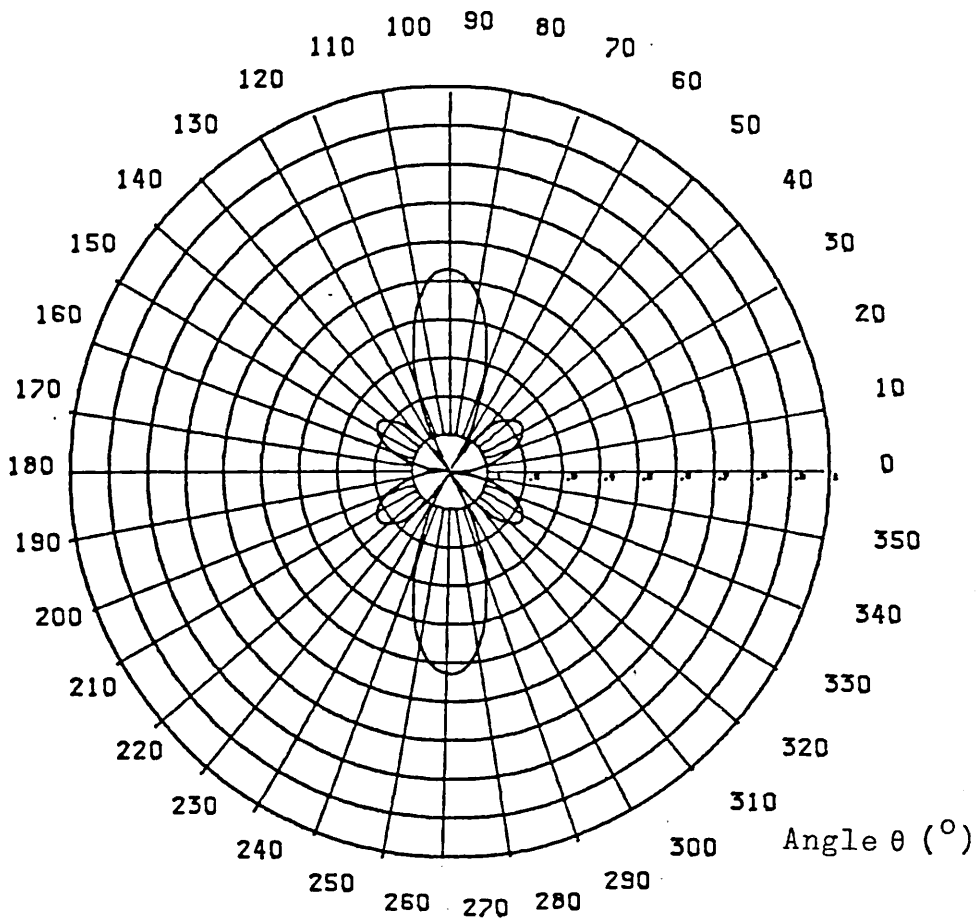
Figure 9.22. (b). Variation of electric field distribution  $E(\theta)/E_0$  with azimuthal angle  $\theta$  for a transmitting antenna of halflength  $0.55\lambda$ .





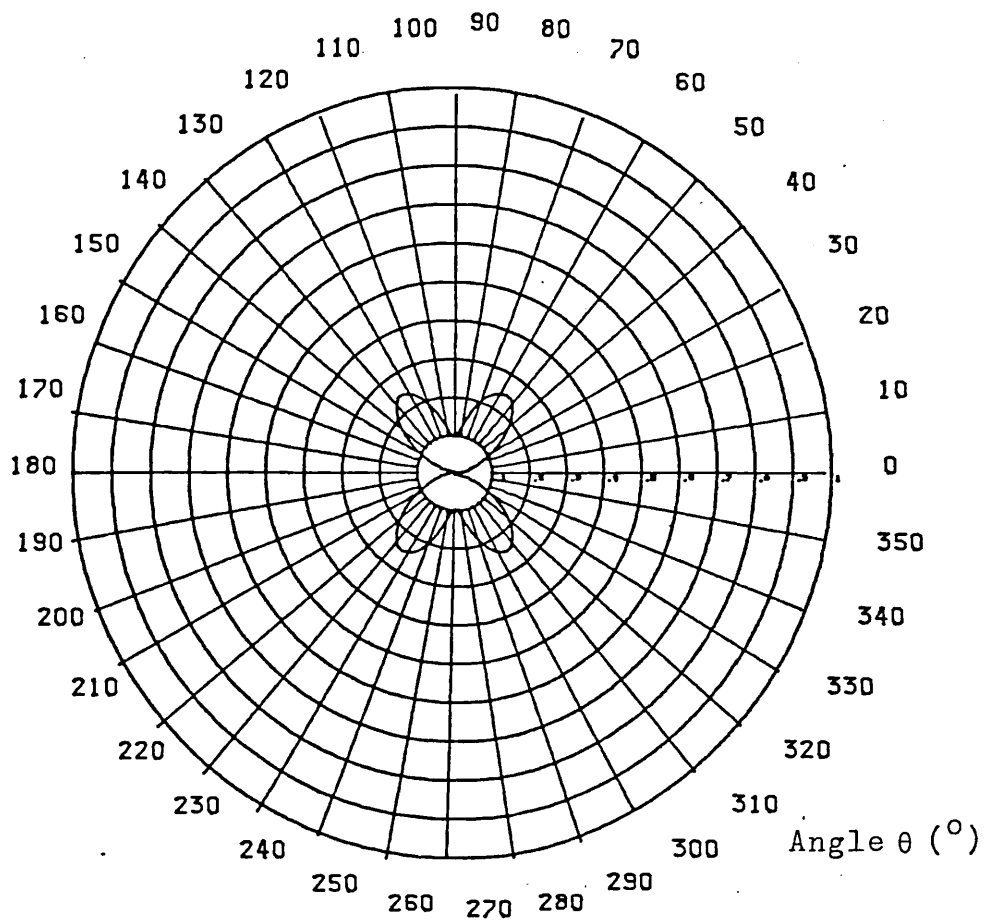
HALFLENGTH=0.65λ

Figure 9.23. (a) Variation of the backscattered electric field  $E(\theta)/E_0$  with angle of incidence  $\theta$  for a short circuited dipole element of halflength  $0.65\lambda$ .



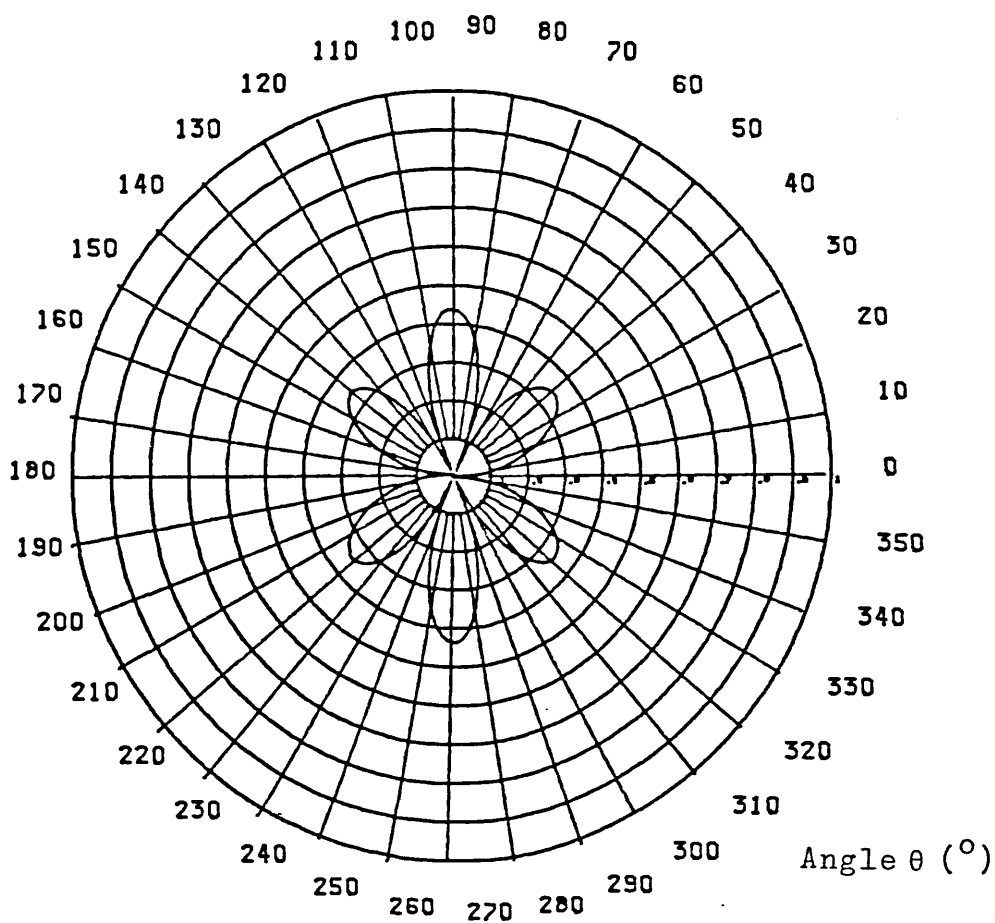
HALFLENGTH=0.65λ

Figure 9.23. (b). Variation of the electric field distribution  $E(\theta)/E_0$  with azimuthal angle  $\theta$  for a transmitting antenna of halflength  $0.65\lambda$ .



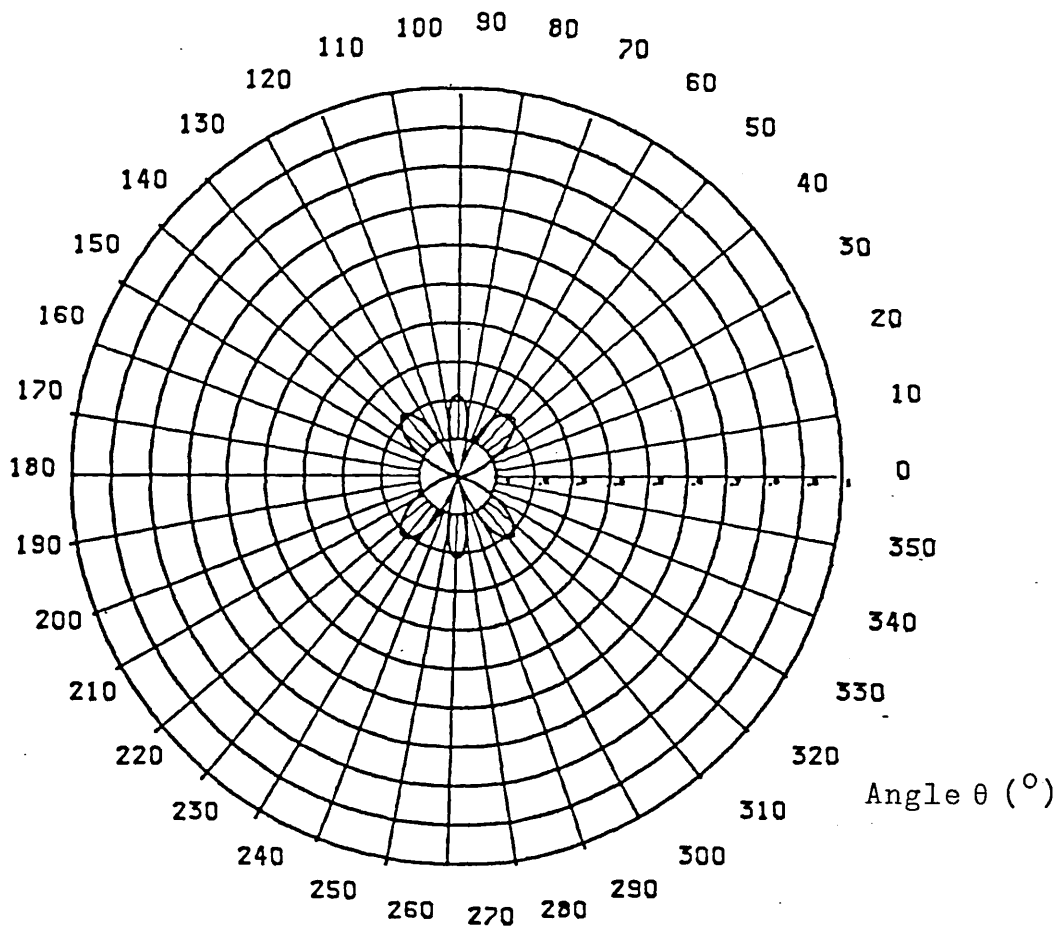
HALFLENGTH=0.7 $\lambda$

Figure 9.24. (a) Variation of the backscattered electric field  $E(\theta)/E_0$  with angle of incidence  $\theta$  for a short circuited dipole element of halflength  $0.7\lambda$ .



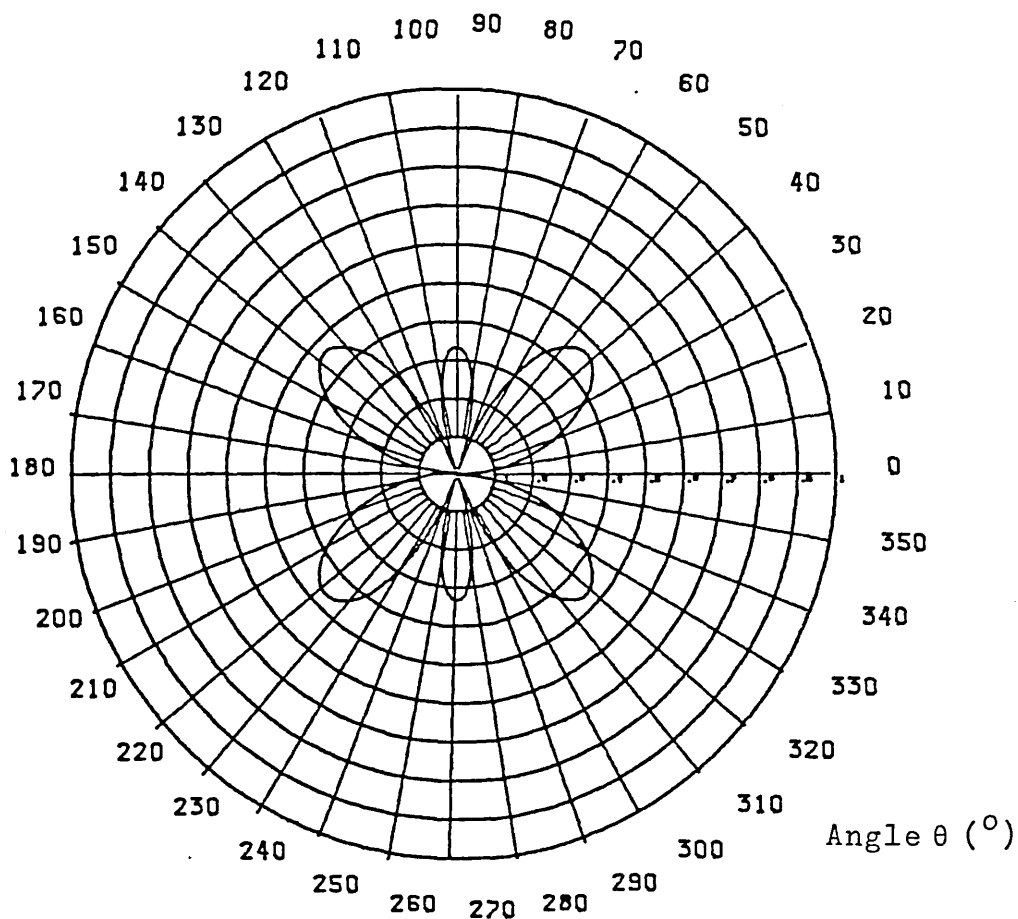
HALFLENGTH=0.7λ

Figure 9.24. (b). Variation of electric field distribution  $E(\theta)/E_0$  with azimuthal angle  $\theta$  for a transmitting antenna of halflength  $0.7\lambda$ .



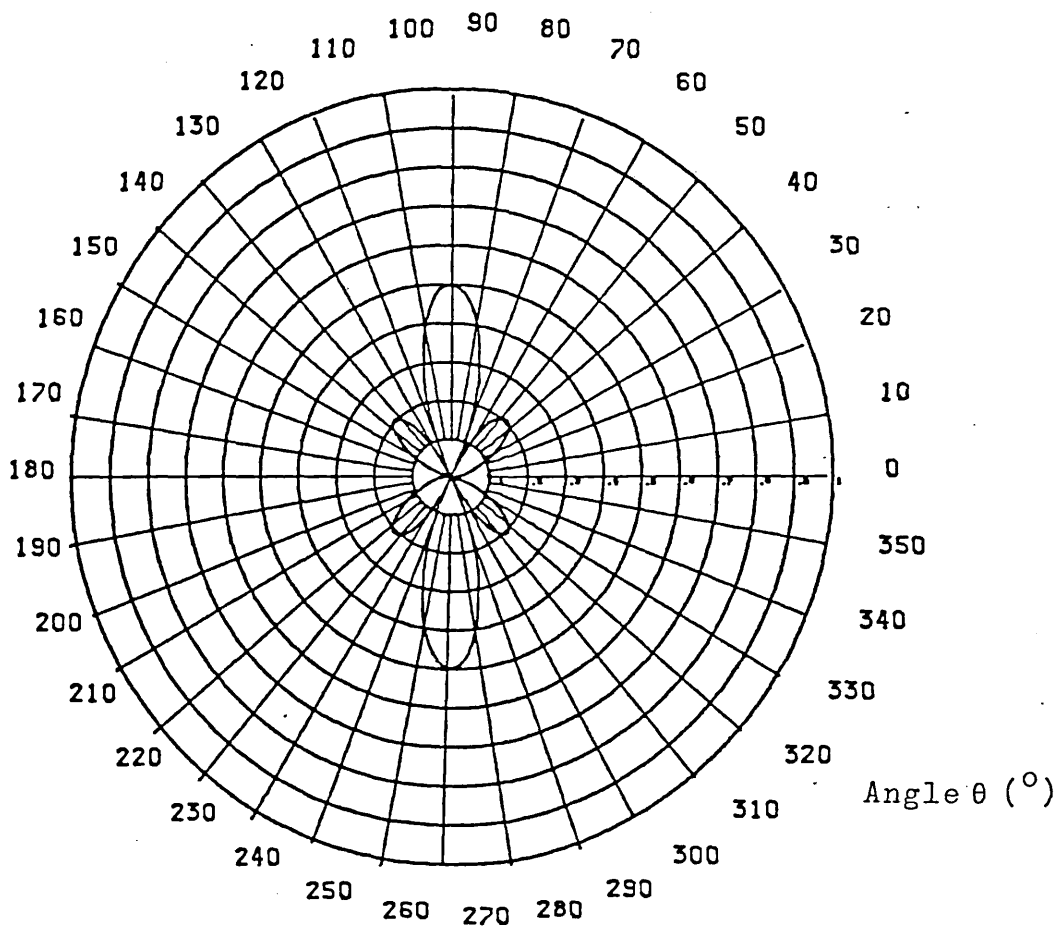
HALFLENGTH= $0.75\lambda$

Figure 9.25. (a). Variation of the backscattered electric field  $E(\theta)/E_0$  with angle of incidence  $\theta$  for a short circuited dipole element of half-length  $0.75\lambda$ .



HALFLENGTH= $0.75\lambda$

Figure 9.25. (b). Variation of electric field distribution  $E(\theta)/E_0$  with azimuthal angle  $\theta$  for a transmitting antenna of halflength  $0.75\lambda$ .



HALFLENGTH= $0.8\lambda$

Figure 9.26 (a). Variation of the backscattered electric field  $E(\theta)/E_0$  with angle of incidence  $\theta$  for a short-circuited dipole element of halflength  $0.8\lambda$ .

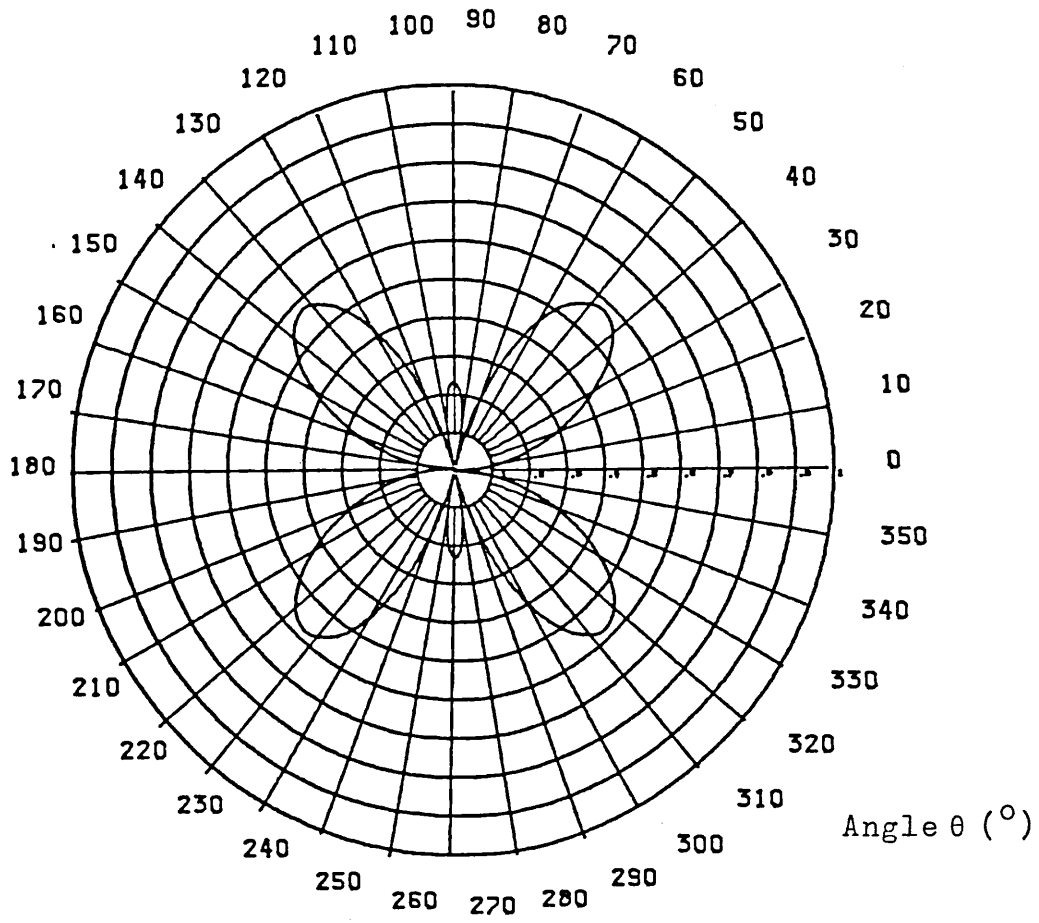
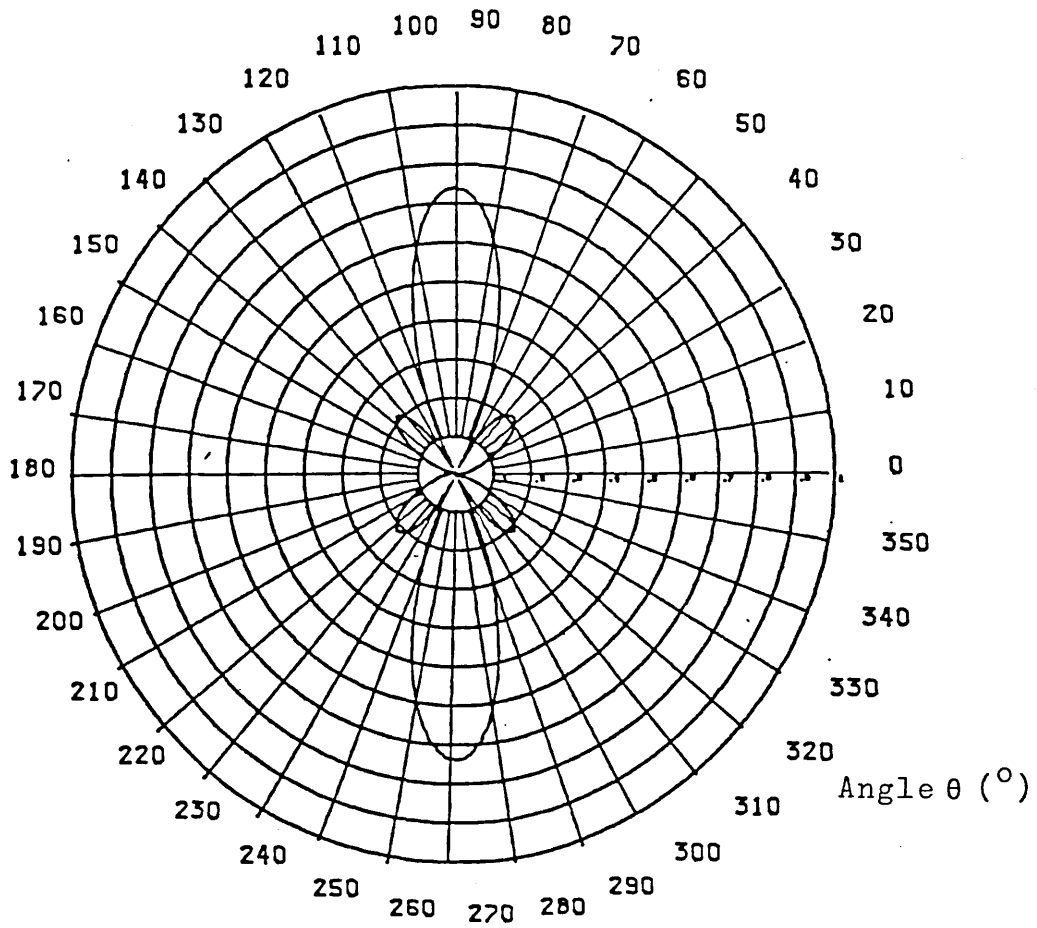


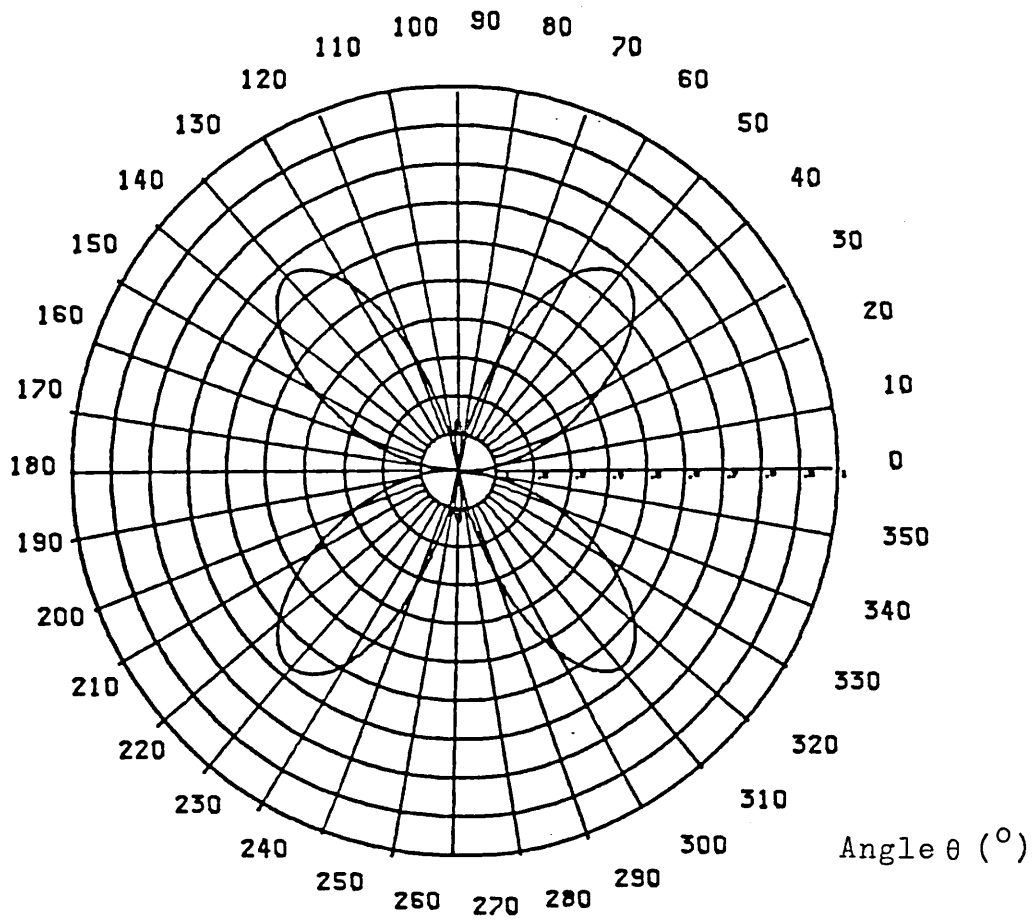
Figure 9.26 (b). Variation of electric field distribution  $E(\theta)/E_0$  with azimuthal angle  $\theta$  for a transmitting antenna of halflength  $0.8\lambda$ .





HALFLENGTH=0.85λ

Figure 9.27 (a). Variation of the backscattered electric field  $E(\theta)/E_0$  with angle of incidence  $\theta$  for a short circuited dipole element of halflength  $0.85\lambda$ .



HALFLENGTH=0.85 $\lambda$

Figure 9.27 (b). Variation of electric field distribution  $E(\theta)/E_0$  with azimuthal angle  $\theta$  for a transmitting antenna of halflength  $0.85\lambda$ .

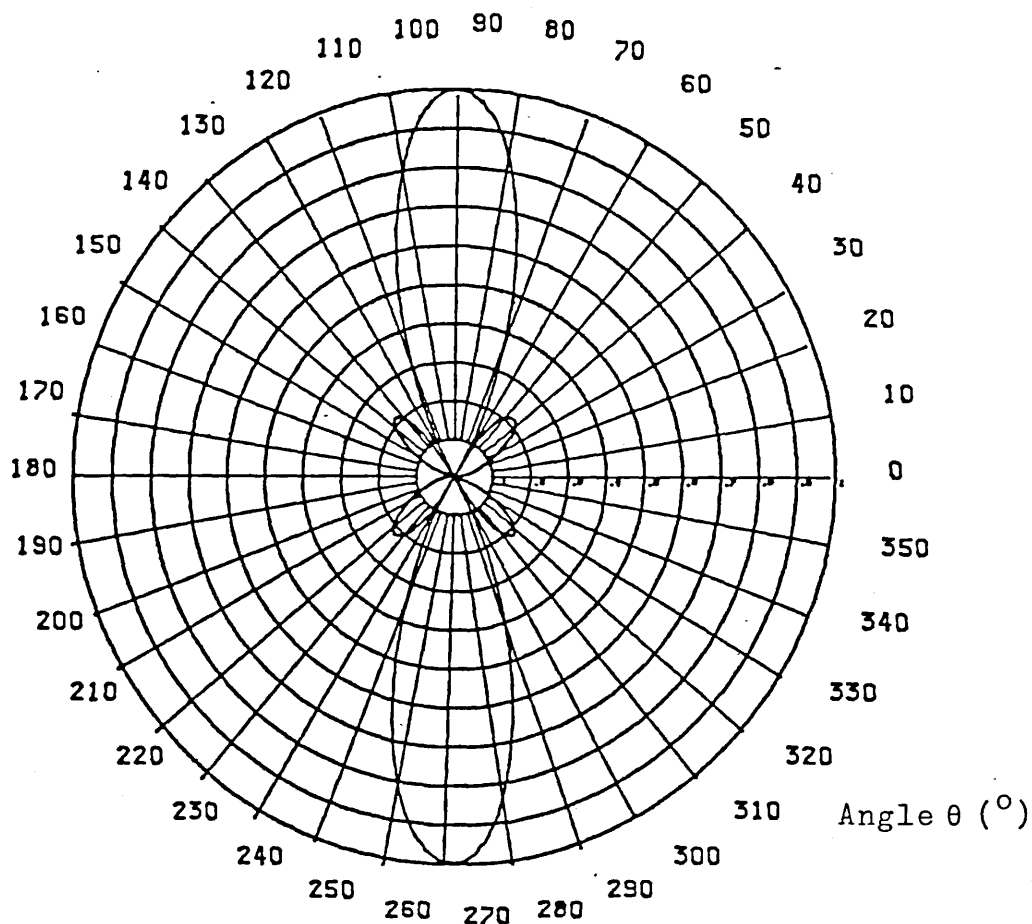
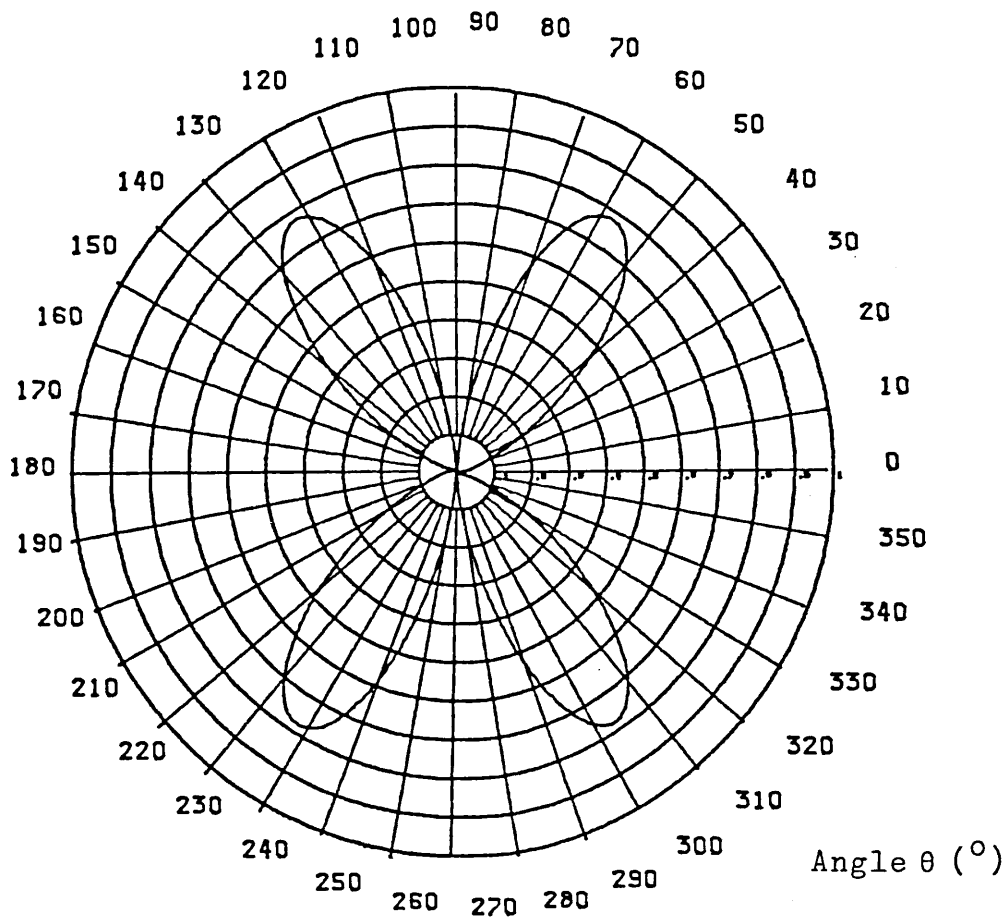
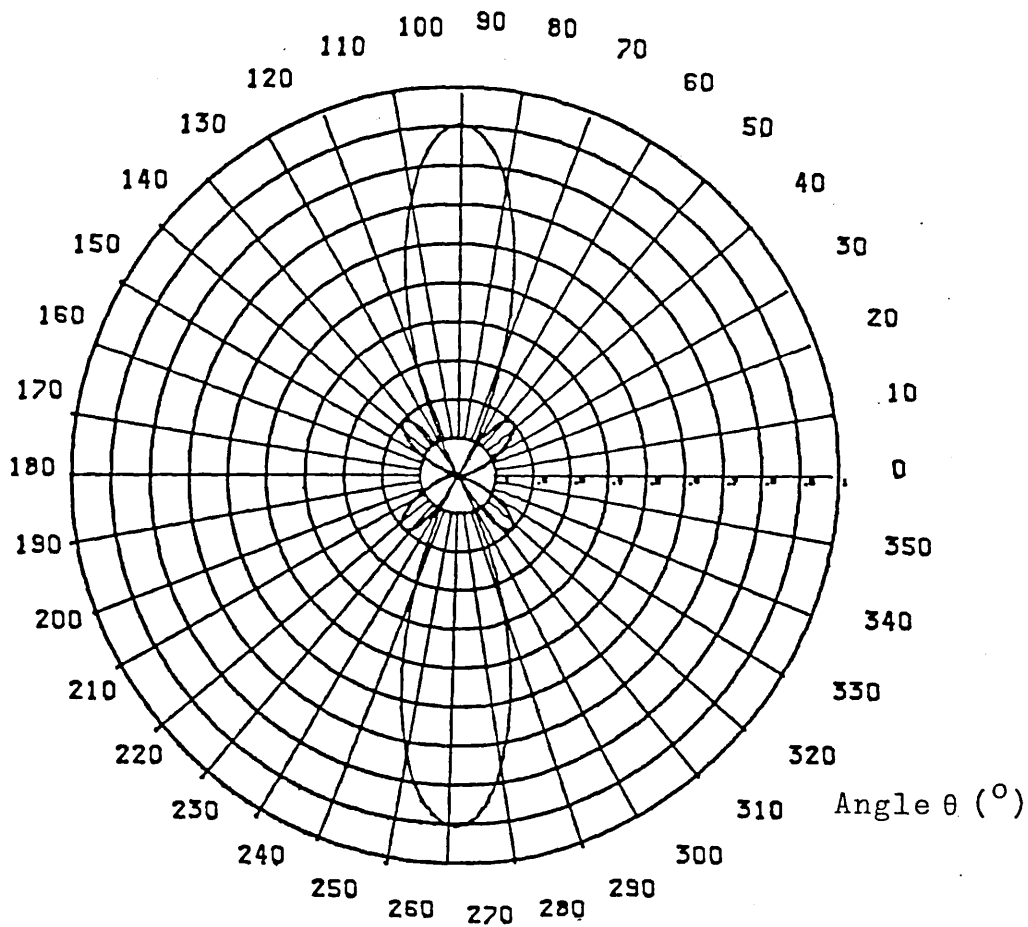


Figure 9.28 (a). Variation of the backscattered electric field  $E(\theta)/E_0$  with angle of incidence  $\theta$  for a short circuited dipole element of halflength  $1.0\lambda$ .



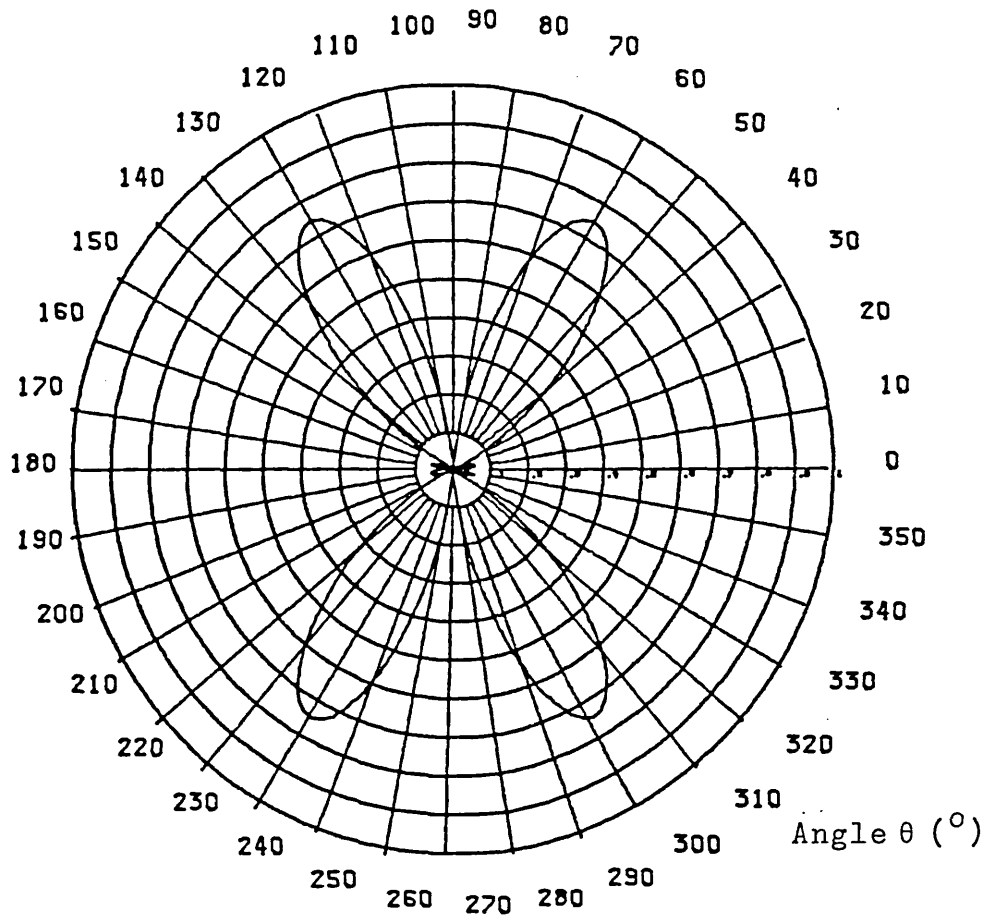
HALFLENGTH= $1.0\lambda$

Figure 9.28 (b). Variation of electric field distribution  $E(\theta)/E_0$  with azimuthal angle  $\theta$  for a transmitting antenna of halflength  $1.0\lambda$ .



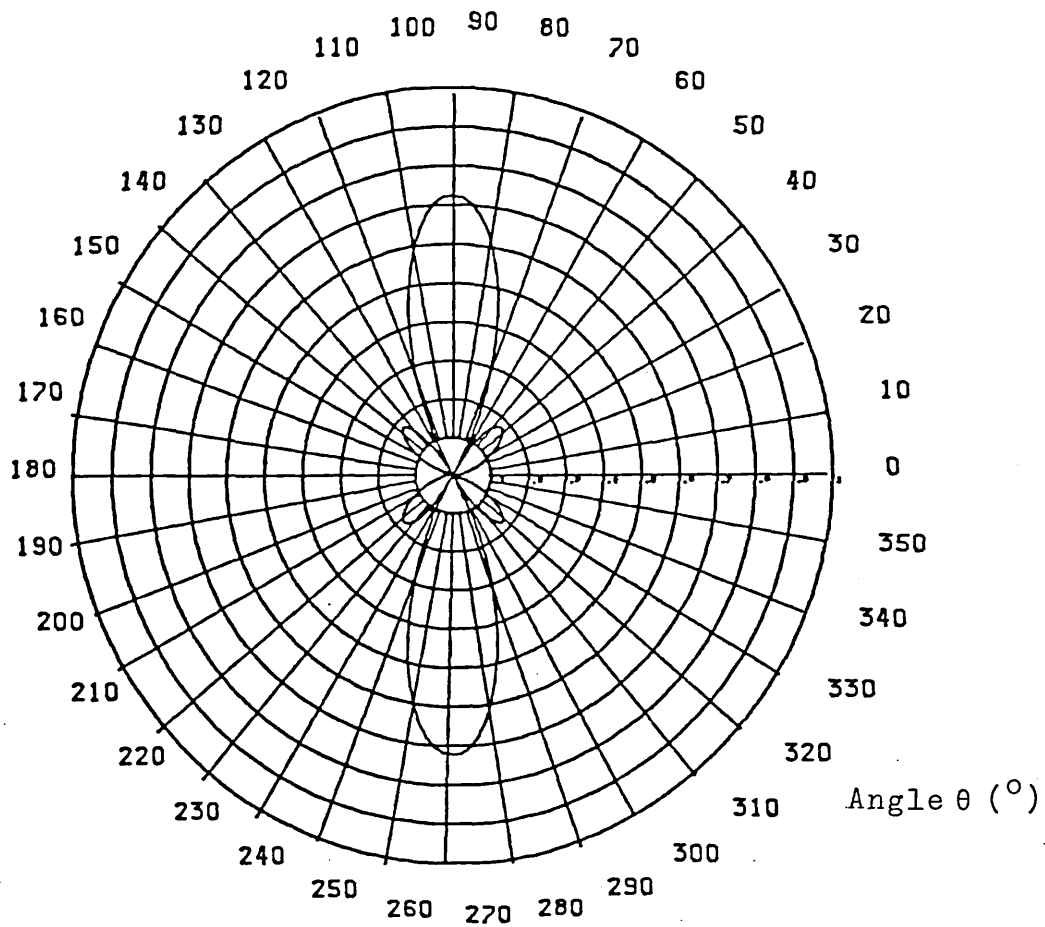
HALFLENGTH=1.05λ

Figure 9.29 (a). Variation of the backscattered electric field  $E(\theta)/E_0$  with angle of incidence  $\theta$  for a short circuited dipole element of halflength  $1.05\lambda$ .



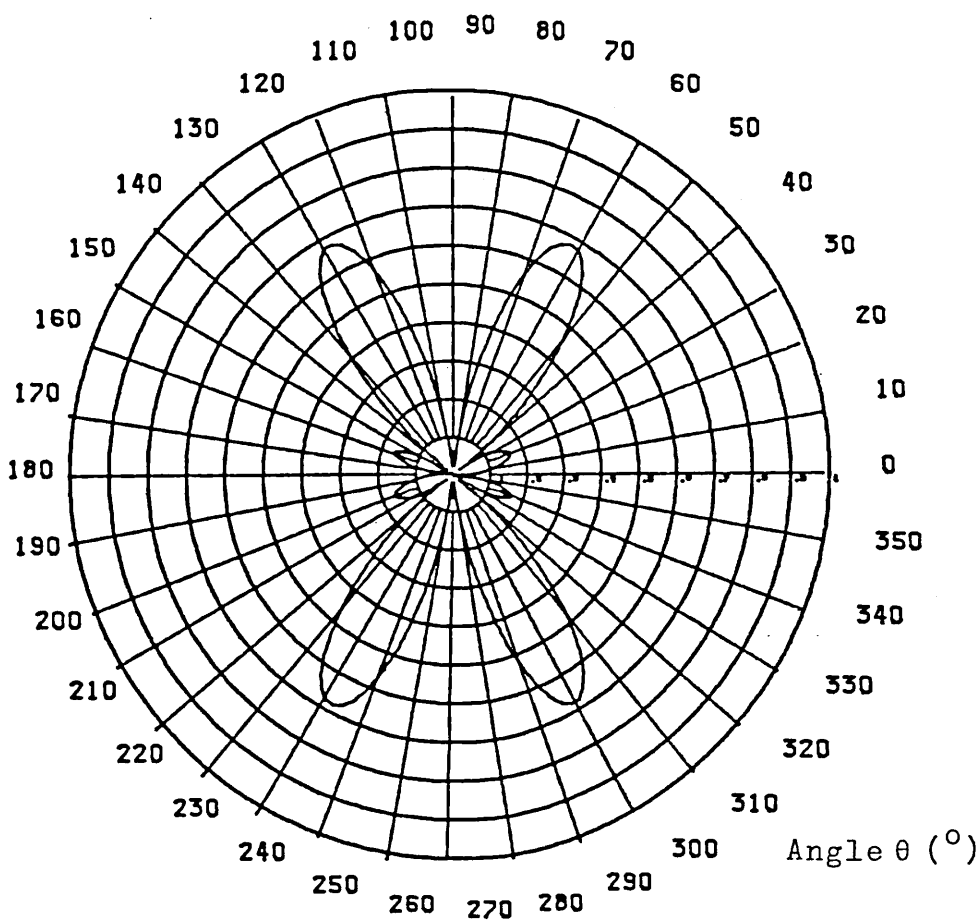
HALFLENGTH= $1.05\lambda$

Figure 9.29 (b). Variation of electric field distribution  $E(\theta)/E_0$  with azimuthal angle  $\theta$  for a transmitting antenna of halflength  $1.05\lambda$ .



HALFLENGTH=1.1λ

Figure 9.30 (a). Variation of the backscattered electric field  $E(\theta)/E_0$  with angle of incidence  $\theta$  for a short circuited dipole element of halflength  $1.1\lambda$ .



HALFLENGTH= $1.1\lambda$

Figure 9.30 (b). Variation of electric field distribution  $E(\theta)/E_0$  with azimuthal angle  $\theta$  for a transmitting antenna of halflength  $1.1\lambda$ .



Figure 9.31. E-plane backscattering pattern for a linear array of 10 short circuited dipole elements of halflength  $0.25 \lambda$ . Inter-element spacing =  $0.25\lambda$ , element width =  $0.03\lambda$ .

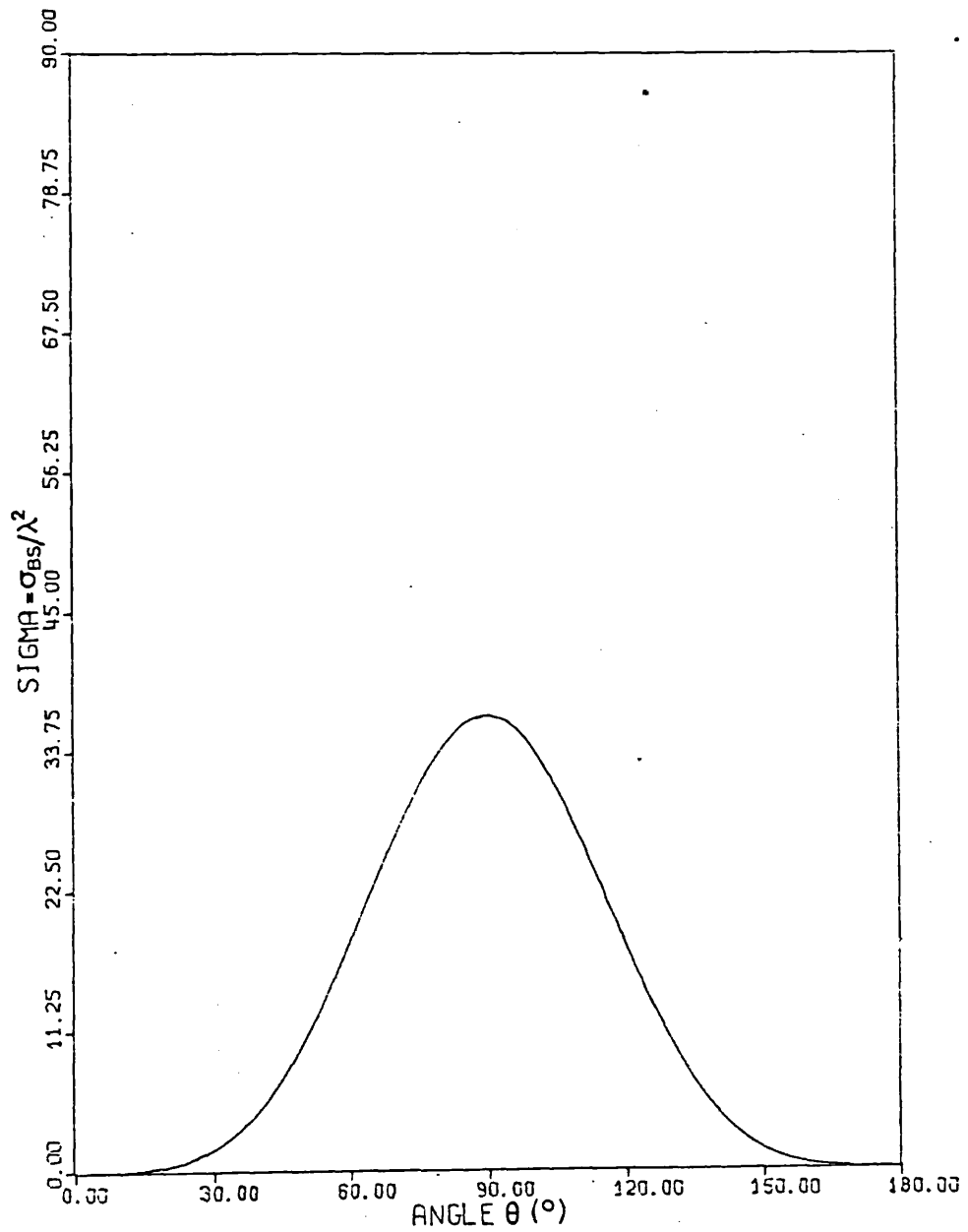


Figure 9.32. E-plane backscattering pattern for a linear array of 10 short circuited dipole elements of halflength  $0.5\lambda$ . Inter-element spacing =  $0.25\lambda$ , element width =  $0.03\lambda$ .

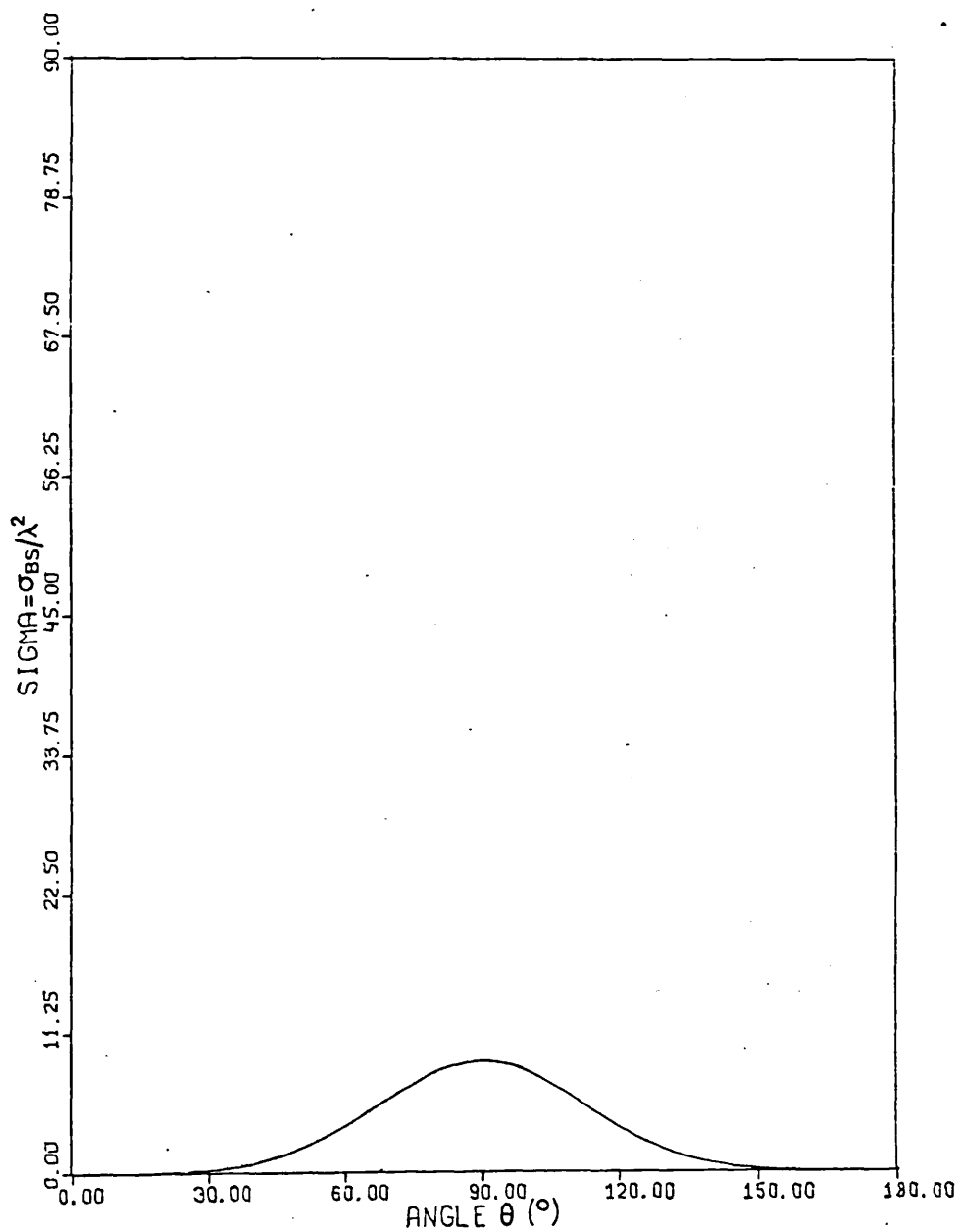


Figure 9.33. E-plane backscattering pattern for a linear array of 10 short circuited dipole elements of halflength  $0.75\lambda$ . Inter-element spacing =  $0.25\lambda$ , element width =  $0.03\lambda$ .

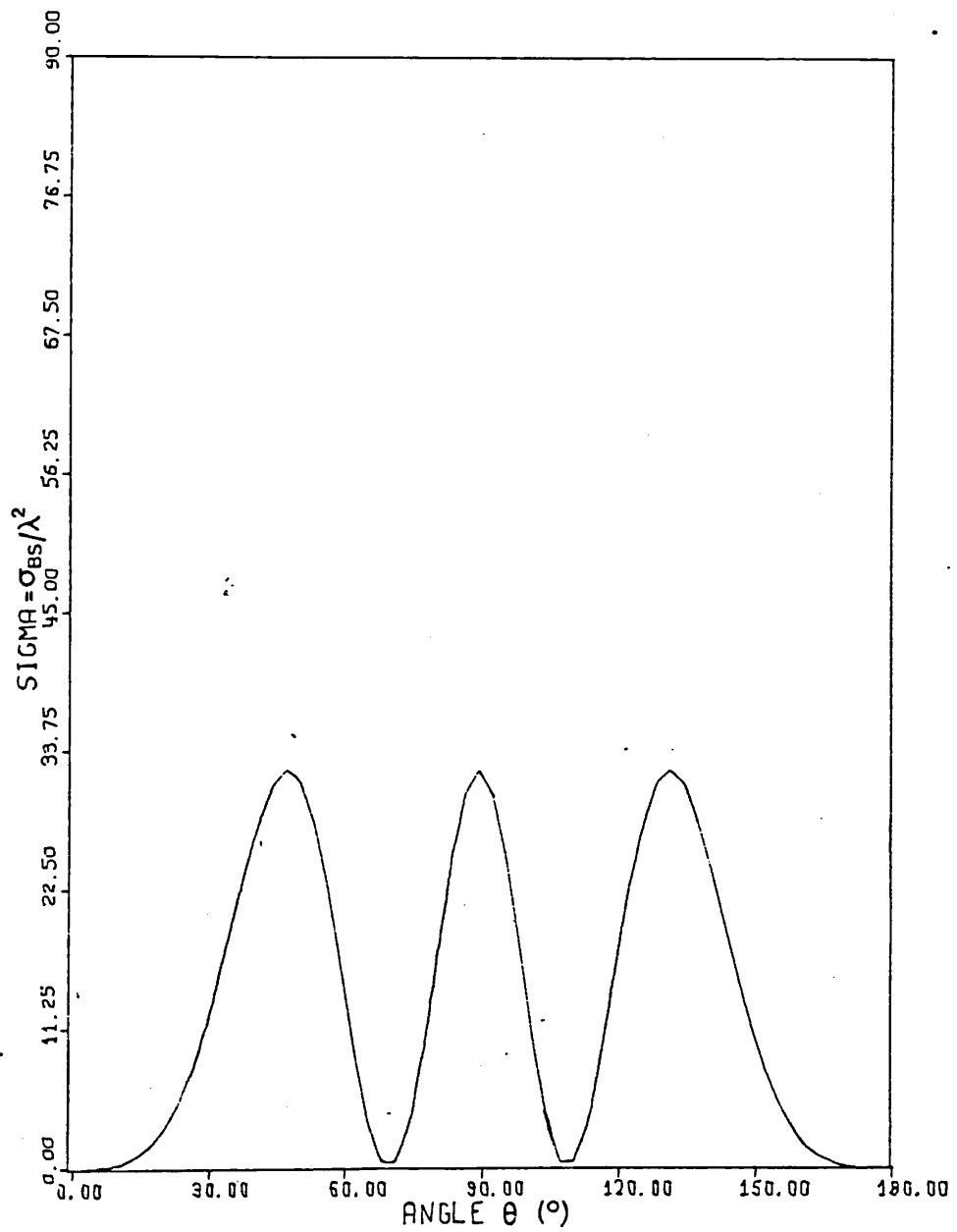
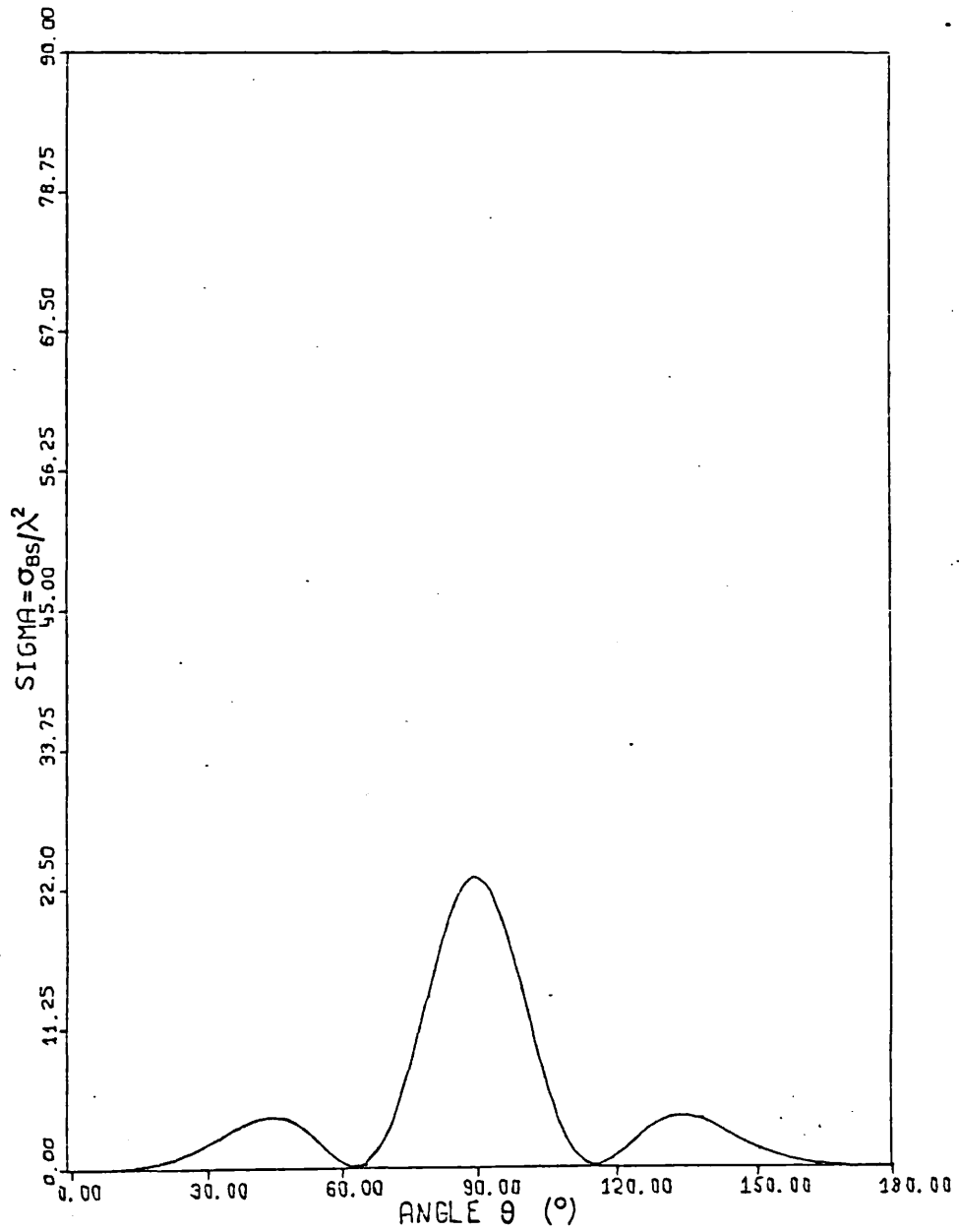


Figure 9.34. E-plane backscattering pattern for a linear array of 10 short circuited dipole elements of halflength  $0.8\lambda$ . Inter-element spacing =  $0.25\lambda$ , element width =  $0.03\lambda$ .



co-ordinate system is given by<sup>82</sup>

$$\frac{E(\theta)}{E_0} = \left[ \frac{\cos(kL \cos \theta) - \cos kL}{\sin \theta} \right] \quad (9.25.)$$

The various forms of the current distribution on array elements will be discussed more fully in Chapter 11.

The square of the angular term in the parenthesis in equation 9.22 was required to obtain the angular power distribution. Figure 9.31 to 9.34 show a sample of the theoretical E-plane variations for the backscattering cross-sections of arrays of 10 short-circuited elements of separation 0.25 wavelengths, and for various dipole half-lengths. These were calculated by multiplying the backscattering cross-sections for normal incidence, obtained from the theory presented in Chapter 3, by the factor  $|E(\theta) / E(\theta = 90^\circ)|^2$ . It is evident that the backscattering patterns give much information about the resultant current distributions on the array elements.

9.3.2. Experimental Investigation of the Variation of E-plane backscattering from Antenna Arrays at 891 GHz.

Figures 9.35 to 9.43 show the experimental E-plane backscattering patterns obtained for linear arrays of 10 short-circuited dipole antennas of various halflengths ranging from 0.25 to 1.0 wavelength. The width of the elements was 10  $\mu\text{m}$  ( $\lambda/34$  at 891 GHz) and they were reproduced on 3.5  $\mu\text{m}$  mylar substrates. The halfpower beamwidths of the lobes are indicated. The theoretical and experimental results are listed in Table 9.4.

It is evident from the results given in Table 9.4 and the patterns shown in Figures 9.35 to 9.43, that the experimental main lobe halfwidths are generally narrower than those predicted by theory. For the halflength of  $0.65\lambda$ , the beamwidth is much narrower than expected. The spike at normal incidence is possibly due to reflection from the substrate. Also the experimental E-plane backscattering patterns occur at progressively shorter half-lengths than predicted by the theory as the halflengths increase. It can be seen from Figures 9.33 and 9.39 that an array of elements of halflength  $0.7\lambda$  exhibits an experimental E-plane pattern similar to that predicted theoretically for elements of  $0.75\lambda$  halflength. This suggests that the velocity factor of the current on the elements is less than the free space value. The velocity factor  $V/C$  of the current propagating on the elements is given by

$$\frac{V}{C} = \frac{\text{experimental resonant halflength}}{\text{free space resonant halflength}} \quad (9.26.)$$

Hence  $V/C = 0.7/0.75 = 0.933$ . It is evident from Figure 7.15 in Chapter 7 that the first experimental resonance occurs at a halflength of  $0.25\lambda$  whereas that predicted theoretically occurs at an element halflength of  $0.266\lambda$ . This indicated a  $V/C$  value 0.94. Similarly the second experimentally observed resonance occurs at a halflength of  $0.71\lambda$ . The theoretically predicted half-length for the second resonance is  $0.76\lambda$ . Hence the velocity factor was calculated to be 0.934. Taking the average of these three values, the velocity factor of the

TABLE 9.4.

E-Plane Backscattering results for linear arrays of 10 short-circuited dipole elements. Inter-element separation is $0.25\lambda$						
Element Half-length	Main Lobe Halfwidth		Secondary Lobe Position		Secondary Lobe Intensity	
	Theoretical	Experimental	Theoretical	Experimental	Theoretical	Experimental
0.25 $\lambda$	60°	75 ± 3°	None	None	None	None
0.50 $\lambda$	54°	45 ± 3°	None	None	None	None
0.55 $\lambda$	56°	40 ± 3°	None	None	None	None
0.65 $\lambda$	76°	20 ± 3°	None	—	None	0.5 ± 0.03
0.70 $\lambda$	—	23 ± 3°	36°	45 ± 3°	2.5	0.9 ± 0.03
0.75 $\lambda$	20°	26 ± 3°	42°	40° ± 3°	1.0	0.32 ± 0.03
0.80 $\lambda$	22°	18 ± 3°	45°	35 ± 3°	0.16	0.167 ± 0.03
0.85 $\lambda$	26°	15 ± 3°	45°	38 ± 3°	0.086	0.21 ± 0.03
1.00 $\lambda$	26°	14 ± 3°	45°	38 ± 3°	0.048	0.205 ± 0.03
1.05 $\lambda$	26°	—	46°	—	0.05	—
1.10 $\lambda$	26°	—	48°	—	0.056	—

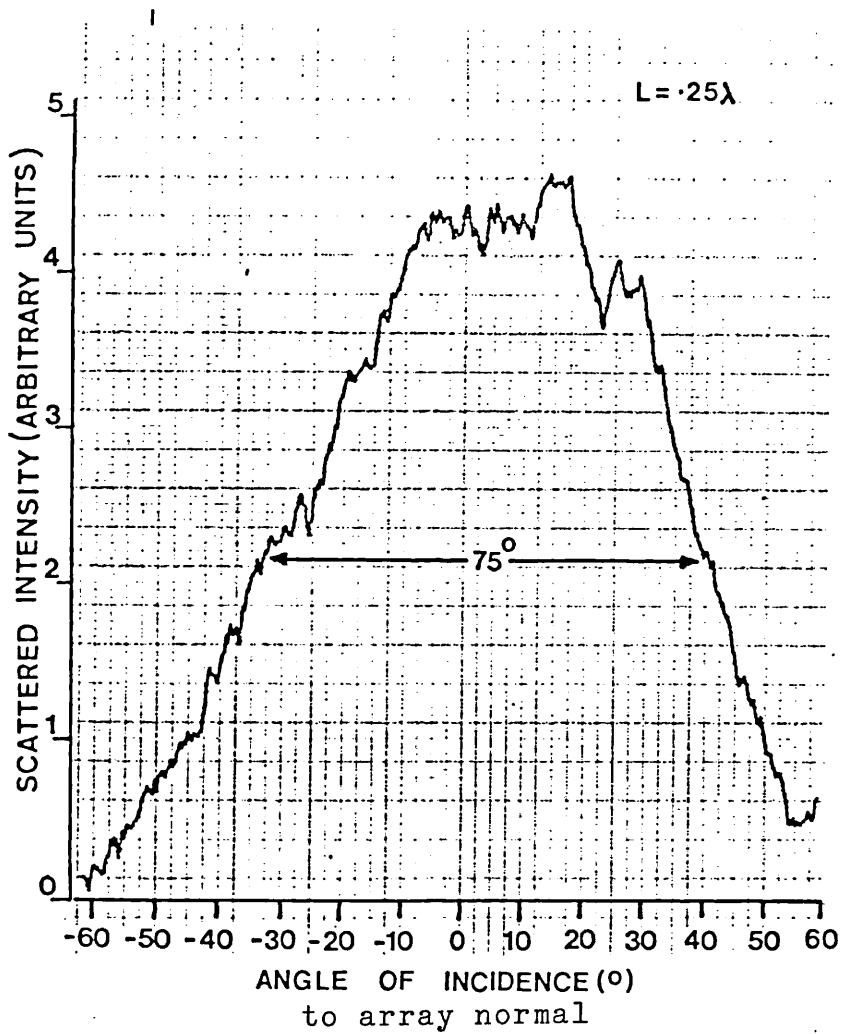


Figure 9.35. Experimental E-plane backscattering pattern for a linear array of 10 short-circuited dipole elements of halflength  $0.25\lambda$  separated by  $0.25\lambda$ . Element width =  $10 \mu\text{m}$ .



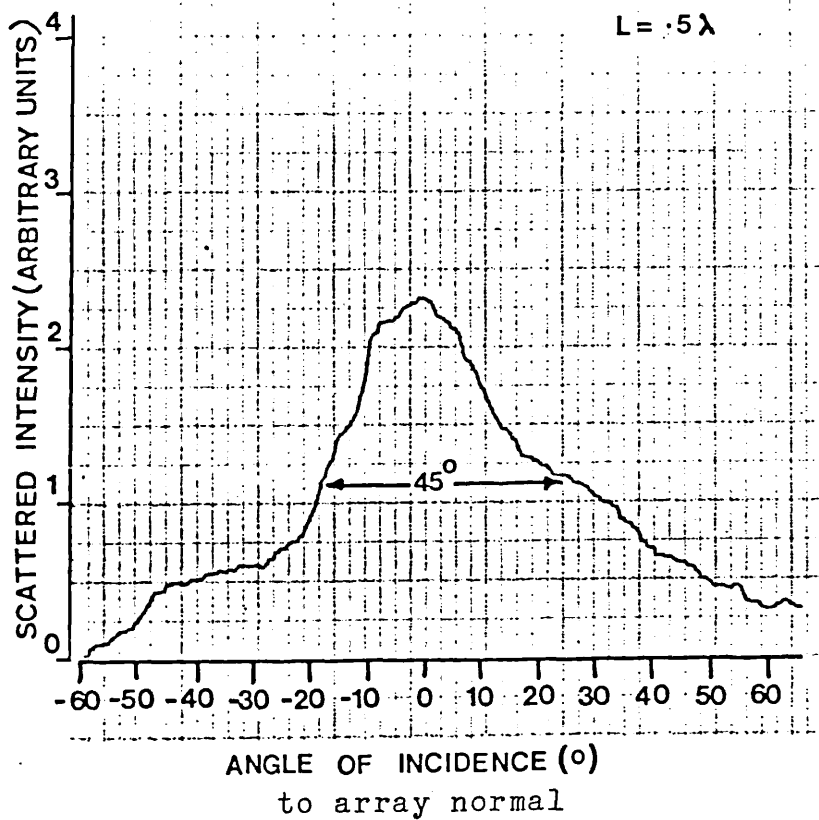


Figure 9.36. Experimental E-plane backscattering pattern for a linear array of 10 short-circuited dipole elements of halflength  $0.5\lambda$  separated by  $0.25\lambda$ . Element width =  $10 \mu\text{m}$ .

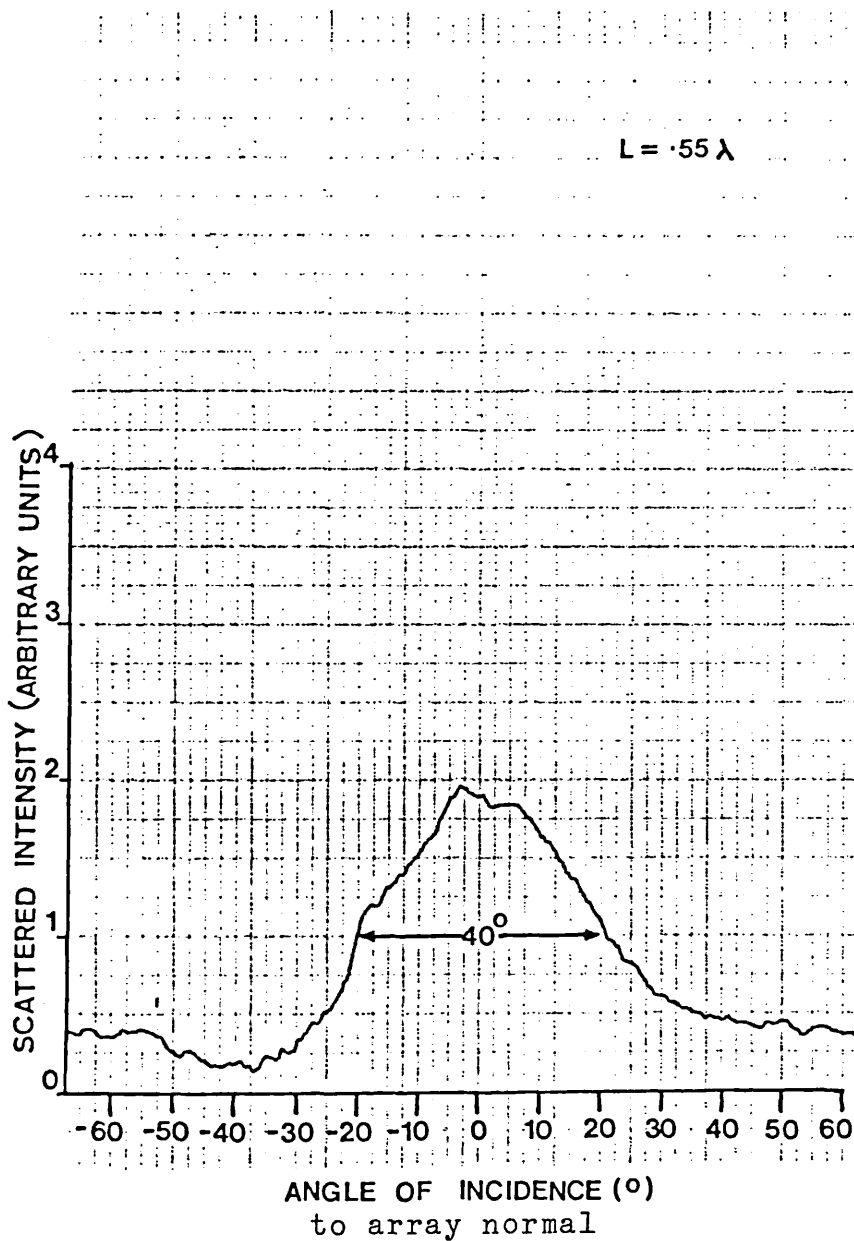


Figure 9.37. Experimental E-plane backscattering pattern for a linear array of 10 short circuited dipole elements of halflength  $0.55\lambda$ . Element width  $w = 10 \mu\text{m}$ .

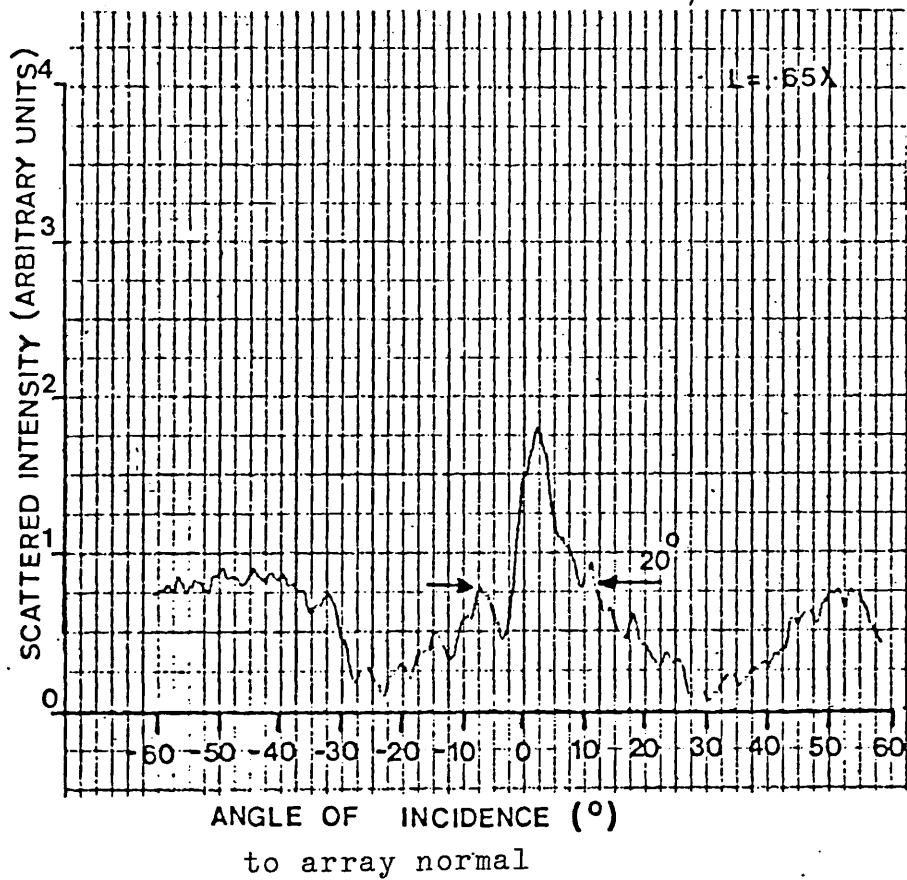


Figure 9.38. Experimental E-plane backscattering pattern for a linear array of 10 short-circuited dipole elements of halflength  $0.65\lambda$ . Element width =  $10 \mu\text{m}$ .

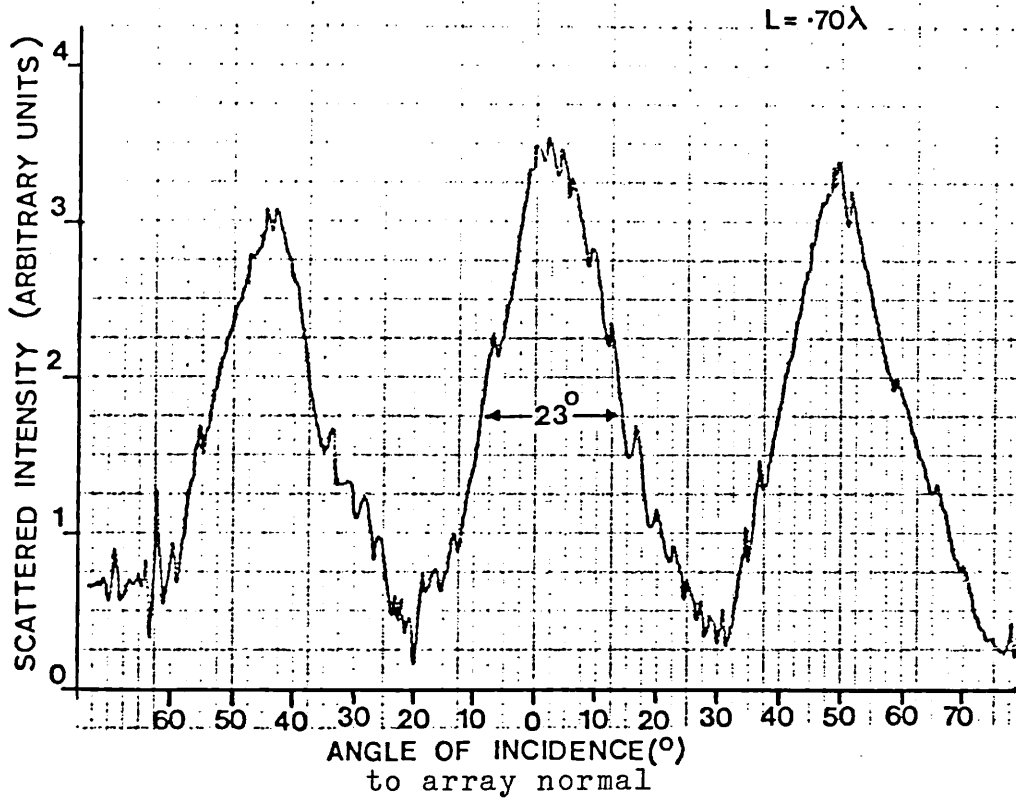


Figure 9.39. Experimental E-plane backscattering pattern for a linear array of 10 short-circuited dipole elements of half-length  $0.7\lambda$ . Element width  $= 10 \mu\text{m}$ .

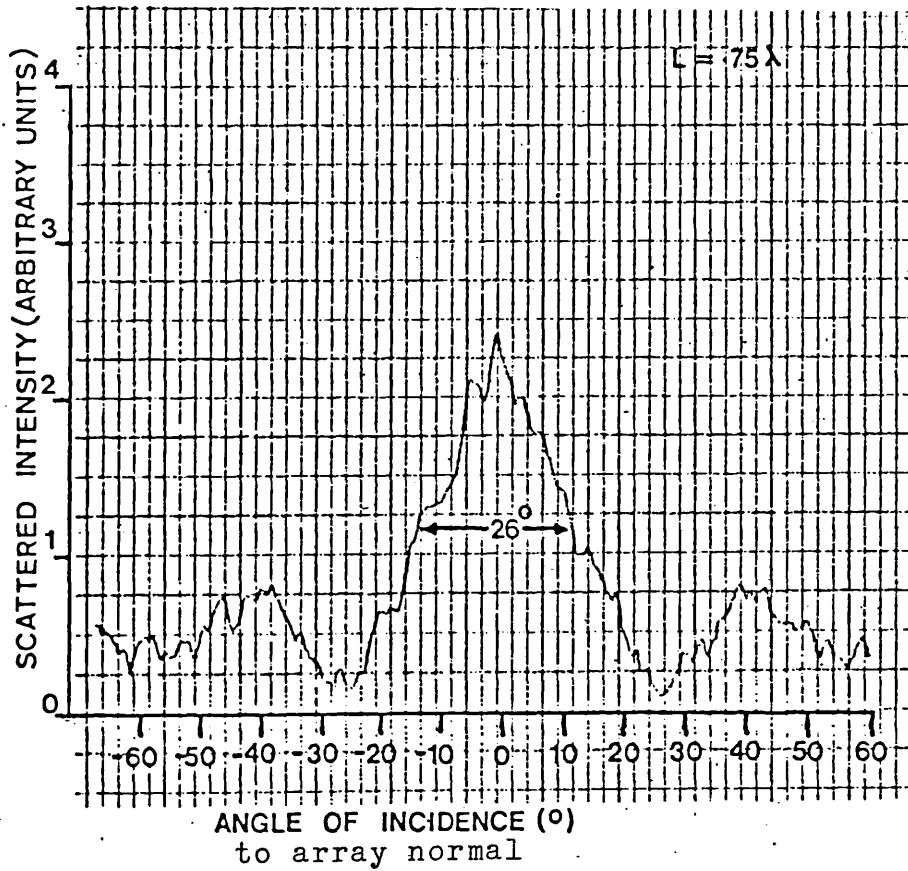


Figure 9.40. Experimental E-plane backscattering pattern for a linear array of 10 short circuited dipole elements of half length  $0.75\lambda$ . Element width =  $10\mu\text{m}$ .

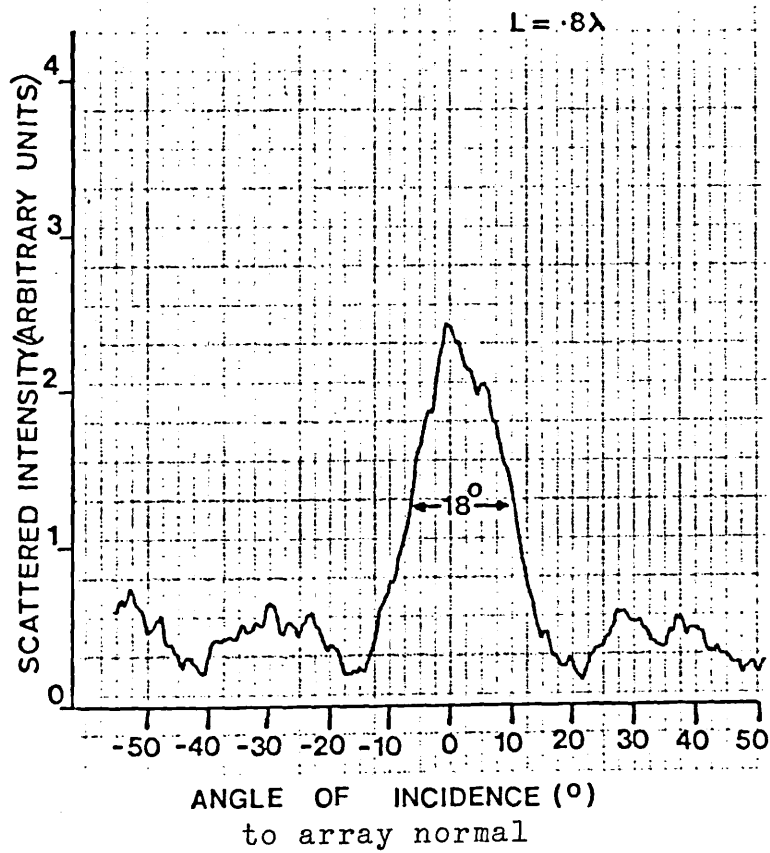


Figure 9.41. Experimental E-plane backscattering pattern for a linear array of 10 short circuited dipole elements of halflength  $0.8\lambda$  separated by  $0.25\lambda$ . Element width =  $10 \mu\text{m}$ .

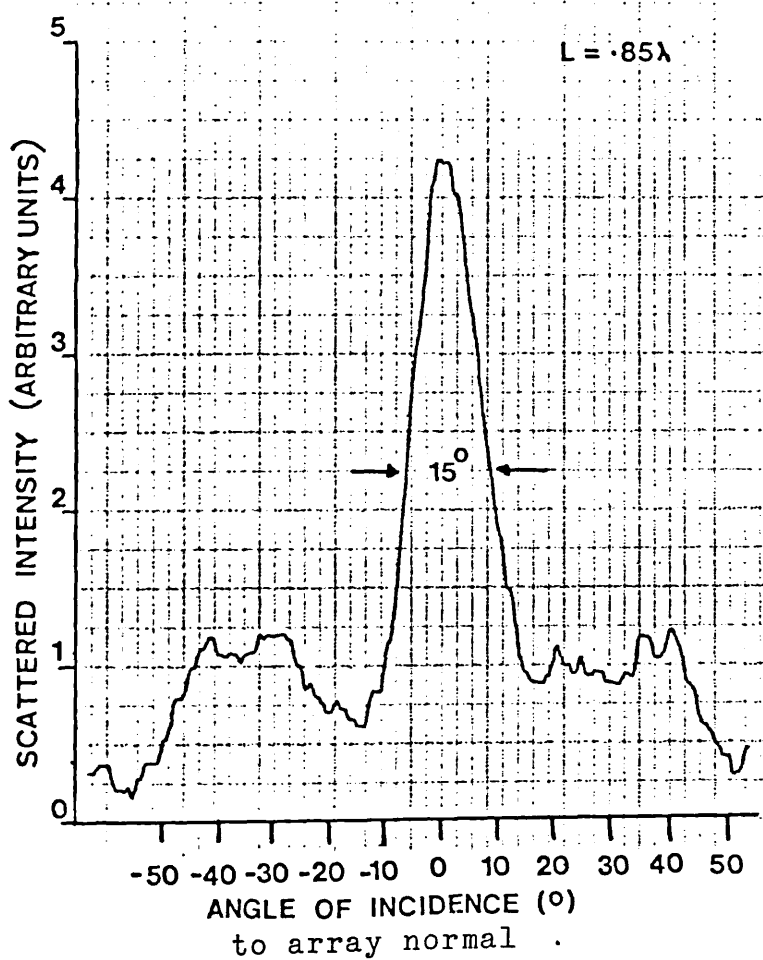


Figure 9.42. Experimental E-plane backscattering pattern for a linear array of 10 short-circuited dipole elements of halflength  $0.85\lambda$  separated by  $0.25\lambda$ . Element width =  $10 \mu\text{m}$ .

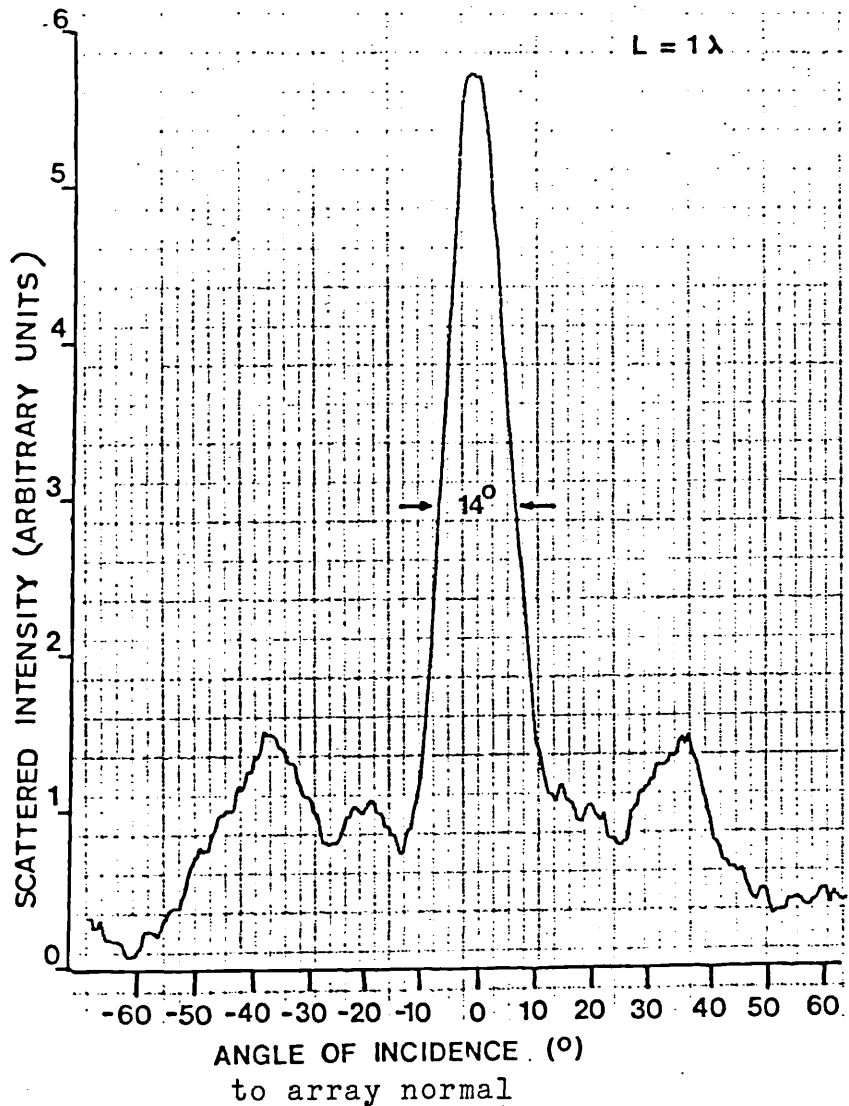


Figure 9.43. Experimental E-plane backscattering pattern for a linear array of 10 short-circuited dipole elements of halflength  $1.0\lambda$  separated by  $0.25\lambda$ . Element width =  $10 \mu\text{m}$ .



current was calculated to be  $0.935 \pm 0.003$ . The experimental velocity factor consequently represents a 6.5% reduction of the free space value. This reduction may be due to either the reactive component of the surface impedance of the antenna causing a slowing of the current or the effect of the substrate itself. From equations 2.14 and 2.15 in Chapter 2 a reduction in the velocity factor of 0.7% was calculated for a halfwave dipole of width  $\lambda/30$  at 891 GHz due to the surface reactance of the silver metallisation. Clearly this does not account for the observed reduction.

The effect of the substrate may be calculated from the results obtained by Mizuno et al<sup>29</sup>. Figure 9.44 shows the velocity factors for the current as a function of an effective thickness  $t_{\text{eff}}$  of the substrate for various relative permittivities. The curves for  $\epsilon_r = 3.7, 5, 6.9$  and  $9.8$  are those obtained experimentally by Mizuno et al<sup>29</sup> for a resonant dipole. The curve for  $\epsilon_r = 3.1$  (corresponding to a mylar substrate at 891 GHz) was extrapolated from the above results. The effective thickness of the substrate is given by

$$t_{\text{eff}} = \sqrt{\epsilon_r} \frac{t}{\lambda} \quad (9.27.)$$

where  $\epsilon_r$  is the relative permittivity of the substrate,  $t$  is the real thickness of the substrate and  $\lambda$  is the free space wavelength. Hence for a  $3.5 \mu\text{m}$  mylar substrate  $t_{\text{eff}} = 0.018$ . From Figure 9.44 the velocity factor of the current was estimated to be 0.95. Therefore, the experimentally observed reduction in the velocity factor can be fully accounted for in terms of the effect of the substrate alone.

It was found that the amplitude and the position of the secondary lobes did not agree as well for arrays of dipoles over  $0.85\lambda$  in halflength. This disagreement may possibly be due to mutual impedance effects between the elements causing a change in the form of the current distribution rather than just a change in the amplitude as previously assumed. However, such effects have not been documented to the author's knowledge. It has also been assumed that

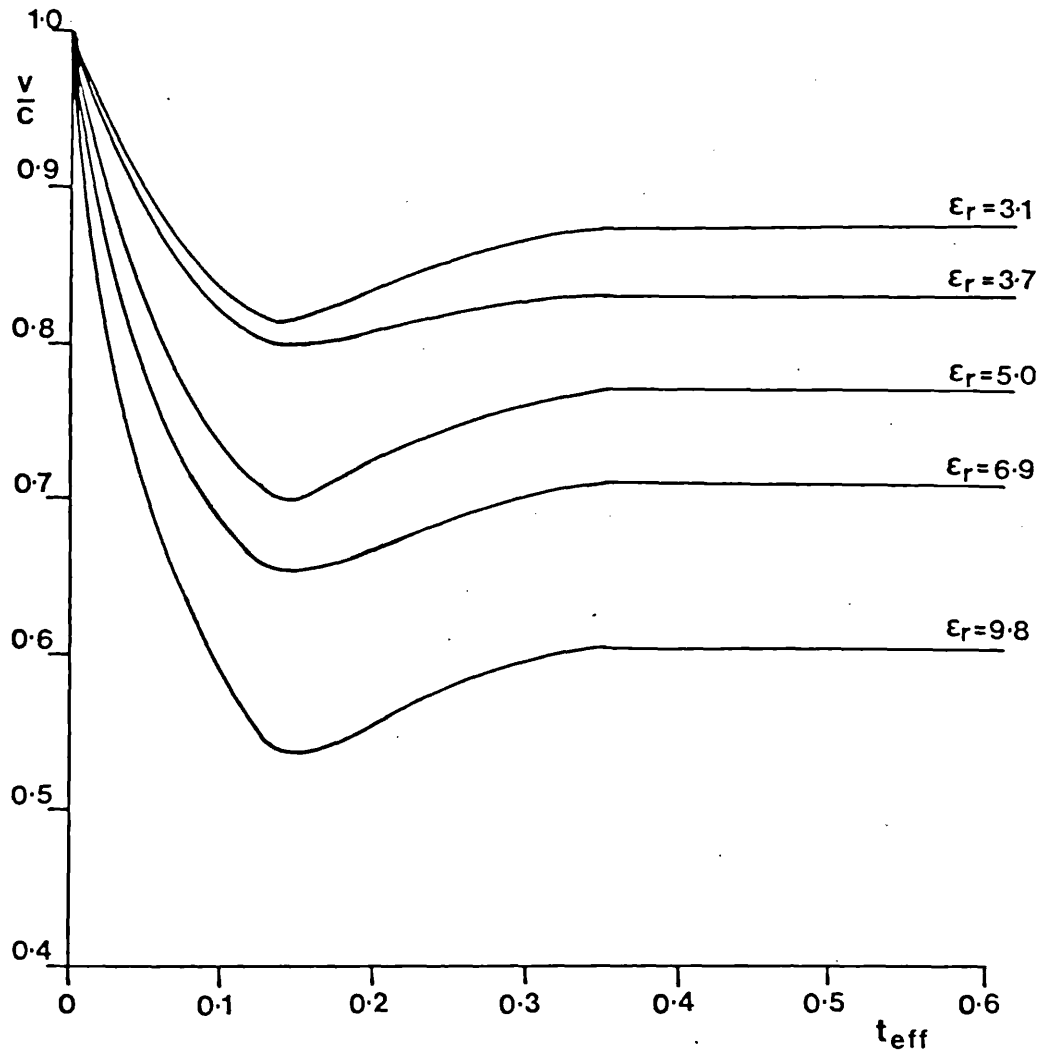


Figure 9.44. Variation of the velocity factor  $V/C$  for the current on a dipole plotted against the effective thickness  $t_{eff}$  of the supporting substrate for various substrate relative permittivities,  $\epsilon_r$ .

the form of the current distribution is unaffected by the angle of incidence of the incident radiation in the E-plane. However, the general form of the E-plane radiation patterns agreed quite well with those predicted theoretically. The fact that the major details of these patterns appear to be consistent with accepted theory is encouraging. In order to proceed with a full design some method of feeding current to or extracting current from the array is necessary. Consequently there is an obvious need for a low-loss transmission line structure that would be compatible with the thin film technology. Even if the active device could be attached directly to the antenna terminals, a length of transmission line would probably be required for constructing a matching stub in order to match out any reactive component of the active device impedance. Transmission lines are investigated in the next Chapter, along with the scattering properties of vee antennas which were also found useful in the study of the properties of transmission lines at these frequencies.

CHAPTER TEN

PROPERTIES OF COPLANAR TRANSMISSION  
LINES AT 891 GHz

10.1. Transmission Line Analysis from Scattering  
Measurements.

A transmission line of carefully selected impedance is an essential and integral part of the overall antenna design. The characteristic impedance of the line should match the feed point impedance of the antenna to obtain a maximum transmission of power to the load. In order to investigate the properties of thin-film transmission lines free of possible complications due to the antenna itself, backscattering measurements were made on arrays of simple dipole elements each terminated with an individual length of short-circuited coplanar transmission line. The vee-antenna, owing to its larger backscattering cross-section, obviated the need for replicating arrays for the study of transmission lines.

For an antenna of transmitting gain  $G_t (\theta_t, \phi_t)$ , receiving gain  $G_r (\theta_r, \phi_r)$ , terminal impedance  $Z_{ss} = R_{ss} + j X_{ss}$  and terminated by a load impedance  $Z_L$ , the backscattering cross-section,  $\sigma_{BS}$ , is given by<sup>20</sup>

$$\sigma_{BS} = \frac{\lambda^2}{\pi} G_r (\theta_r, \phi_r) G_t (\theta_t, \phi_t) \left| \frac{R_{ss}}{Z_{ss} + Z_L} \right|^2 \quad (10.1.)$$

If the antenna is terminated with a length,  $L$ , of short-circuited transmission line of characteristic impedance  $Z_0$  and propagation constant  $\gamma = \alpha + j\beta$ , then the load impedance seen by the antenna  $Z_L = R_L + j X_L$  would depend on the properties of the transmission line.

For a transmission line of characteristic impedance  $Z_0$  terminated by a load impedance  $Z_T$  and of length  $L$

with a propagation constant  $\gamma$ , the input impedance  $Z_i$  is given by

$$Z_i = Z_o \left[ \frac{Z_T + Z_o \tanh \gamma L}{Z_o + Z_T \tanh \gamma L} \right] \quad (10.2.)$$

For a short-circuited line  $Z_T = 0$  and equation (10.2.) becomes

$$Z_i = Z_o \tanh \gamma L \quad (10.3.)$$

or

$$Z_i = Z_o \tanh (\alpha + j\beta)L \quad (10.4.)$$

$$\text{Now } \tanh (A + B) = \frac{\tanh A + \tanh B}{1 + \tanh A \tanh B} \quad (10.5.)$$

Hence equation 10.4 becomes

$$Z_i = Z_o \left[ \frac{\tanh \alpha L + \tanh j\beta L}{1 + \tanh \alpha L \tanh j\beta L} \right] \quad (10.6.)$$

$$\text{Now, as } \tanh j\beta L = j \tan \beta L \quad (10.7.)$$

then equation (10.6) becomes

$$Z_i = Z_o \left[ \frac{\tanh \alpha L + j \tan \beta L}{1 + j \tanh \alpha L \tan \beta L} \right] \quad (10.8.)$$

Simplifying, equation 10.8 becomes

$$Z_i = \frac{Z_o (\tanh \alpha L (1 + \tan^2 \beta L) + j \tan \beta L (1 - \tanh^2 \alpha L))}{(1 + \tanh^2 \alpha L \tan^2 \beta L)} \quad (10.9.)$$

Separating the real and imaginary parts of the input impedance  $Z_i = R_i + j X_i$

$$R_i = \frac{Z_o \tanh \alpha L (1 + \tan^2 \beta L)}{1 + \tanh^2 \alpha L \tan^2 \beta L} \quad (10.10.)$$

$$X_i = \frac{Z_o \tan \beta L (1 - \tanh^2 \alpha L)}{1 + \tanh^2 \alpha L \tan^2 \beta L} \quad (10.11.)$$

Since  $\lambda$ ,  $G_r$  ( $\theta_r$ ,  $\phi_r$ ) and  $G_t$  ( $\theta_t$ ,  $\phi_t$ ) are constant for a given antenna, the backscattering cross-section  $\sigma_{BS}$  may be written as

$$\sigma = \text{CONSTANT} \times \left| \frac{R_{ss}}{(R_{ss} + R_L) + j (X_{ss} + X_L)} \right|^2 \quad (10.12.)$$

If the load is a length of short-circuited transmission line of input impedance  $Z_i = R_i + j X_i$  then  $R_L = R_i$  and  $X_L = X_i$ .  $R_i$  and  $X_i$  being given by equations 10.10 and 10.11 respectively. The term on the right-hand side of equation 10.12 is a periodic function of the transmission line length,  $L$ . The ratios of the maxima of this function to the value at  $L = 0$ , depend upon the line attenuation  $\alpha$ . The separation of these maxima is half a guidewavelength and is dependent on the velocity factor,  $V/C$ . The position of these maxima depend on the line impedance,  $Z_0$ , and the dipole input reactance  $X_{ss}$ .

### 10.2. Transmission Lines for Submillimetre Wavelengths.

At millimetre wavelengths, dielectric waveguide type integrated circuits have been employed for circumventing the difficulties conventional microwave integrated circuitry technology encounters at higher frequencies, namely high conductor loss and small structural dimensions. Figure 10.1 shows the cross-sections of typical dielectric waveguide structures used for millimetre wave systems.<sup>90</sup>

The cross-sectional dimensions of single-mode dielectric waveguides are typically of the order of the wavelength, whereas they are required to be about one tenth of the wavelength for microstrip lines. The wave-propagation mechanism in dielectric waveguides does not depend on the existence of metallic conductors, but rather on the total internal reflection at the dielectric boundaries. Instead of conductor loss, the main contribution to the wave attenuation comes from dielectric loss and radiation loss. At the millimetre wavelengths these losses are less than the conductor losses and so this type of waveguiding structure is desirable. However, at sub-millimetre wavelengths dielectric loss is usually high. It is found that the losses in dielectric waveguides are comparable with those of microstrip in the submillimetre, being of the order of 0.5 to 2dB per guide

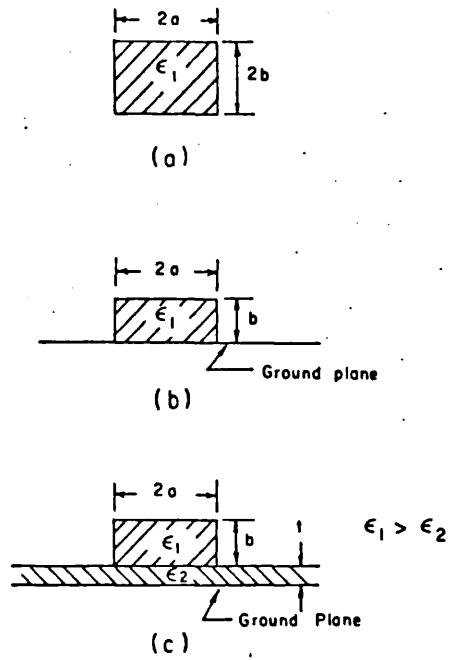


Figure 10.1. Cross-section of typical dielectric waveguides for millimetre wave integrated circuits (a) rod guide (b) image guide (c) insular guide. Taken from Reference 90)

wavelength. Because microstrip type lines provide greater spatial control of the field distributions and can be directly coupled to antenna structures they are preferred where efficient coupling between antennas and lines are required. This is a primary consideration at submillimetre wavelengths where power is limited.

Figure 10.2 illustrates the various types of strip transmission lines<sup>8,2</sup> with the relationships used to calculate their characteristic impedances. It was found that conductors having the dimensions required for strip transmission lines at a wavelength of 337  $\mu\text{m}$  could be reproduced using the photolithographic techniques described in Chapter 8, and so there was no reason why these structures could not be reproduced experimentally and their characteristics calculated theoretically.

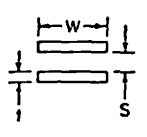
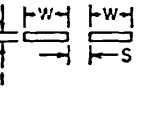
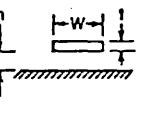
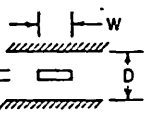
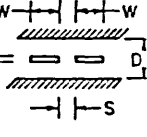
#### 10.2.1. Coplanar Transmission Line.

Figure 10.3 illustrates the coplanar line geometry employed. This type of transmission line is very suitable for use with planar arrays reproduced on thin substrates as it is a balanced line and therefore does not require a ground plane. Coplanar line has the lowest dielectric loss of all the types of strip line. It is a factor of 2.5 better in this respect than conventional stripline<sup>8,5</sup> as the electric fields between the conductors are not so strongly confined to the substrate in coplanar line. Also, as the metalisation for both the antenna and the line are on the same side of the substrate complicated double sided production procedures, requiring careful alignment of masks, are unnecessary. Consequently the metallic tracks can be reproduced from a single mask contact printed onto the substrate.

#### 10.2.2. Theoretical Analysis of Coplanar Transmission Line.

The velocity factor  $V/C$  for the coplanar transmission



	CHARACTERISTIC IMPEDANCE	
	EXACT FOR $\epsilon=0^*$	APPROXIMATE
	$Z_0 = \frac{377}{\sqrt{\epsilon}} \frac{K}{K'}$ $\text{MAX } z_n(u,k) = \frac{\pi W}{2KS}$	$Z_0 \approx \frac{377}{\sqrt{\epsilon}} \frac{S}{W}, S \ll W$ $Z_0 \approx \frac{276}{\sqrt{\epsilon}} \log_{10} \frac{4S}{W}, S \gg W$
	$Z_0 = \frac{377}{\sqrt{\epsilon}} \frac{K}{K'}$ $k = \frac{S}{S+2W}$	$Z_0 \approx \frac{257}{\sqrt{\epsilon} \log_{10} (4 + \frac{6W}{S})}, S \ll W, \epsilon=0$ $Z_0 \approx \frac{276}{\sqrt{\epsilon}} \log_{10} (8 + \frac{4S}{W}), S \gg W, \epsilon=0$
	$Z_0 = \frac{189}{\sqrt{\epsilon}} \frac{K}{K'}$ $\text{MAX } z_n(u,k) = \frac{\pi W}{4Kh}$	$Z_0 \approx \frac{377}{\sqrt{\epsilon}} \frac{h}{W}, h \ll W$ $Z_0 \approx \frac{138}{\sqrt{\epsilon}} \log_{10} \frac{8h}{W}, h \gg W$
	$Z_0 = \frac{94}{\sqrt{\epsilon}} \frac{K}{K'}$ $k = \text{sech} \frac{\pi W}{2D}$	$Z_0 = \frac{94}{\sqrt{\epsilon}} \frac{1 - \frac{1}{D}}{\frac{W}{D} + 0.47 + 0.65 \frac{1}{D} - 1.12 (\frac{1}{D})^2}, 1 \leq .5D, W \geq .35(D-1)$ $Z_0 = \frac{138}{\sqrt{\epsilon}} \log_{10} \left( \frac{\frac{6}{\pi}}{\frac{W}{D} + 1.4 \frac{1}{D}} \right), 1 \leq .25D, W \leq .35(D-1)$
	<p>BALANCED</p> $Z_0 = \frac{189}{\sqrt{\epsilon}} \frac{K'}{K}$ $k = \tanh \left( \frac{\pi W}{2D} \right) \cdot \coth \left( \frac{\pi [W+S]}{2D} \right)$	<p>FOR APPROXIMATE FORMULAS IN THE CASE <math>\epsilon &gt; 0</math>, SEE REFERENCE 8</p>

\*K(k) IS THE COMPLETE ELLIPTIC INTEGRAL OF THE FIRST KIND,  $K'=K(K')$  WHERE  $k'^2=1-k^2$ .  $z_n(u,k)$  IS THE JACOBI ZETA-FUNCTION.

Figure 10.2. Strip transmission lines.  
 (Taken from Reference 82)

line is given by

$$\frac{V}{C} = \frac{1}{\sqrt{\epsilon_{re}}} \quad (10.13.)$$

where  $\epsilon_{re}$  is the effective permittivity of the substrate. The characteristic impedance of the line,  $Z_0$ , is given by<sup>82</sup>

$$Z_0 = \frac{377}{\sqrt{\epsilon_{re}}} \frac{K(k)}{K'(k)} \quad (10.14.)$$

$K(k)$  is the complete elliptic integral of the first kind and  $K'(k) = K(k')$  where  $k'^2 = 1 - k^2$ .  $K(k)$  and  $K'(k)$  are tabulated in Reference 86.  $k$  is given by,

$$k = \frac{S}{S + 2W} \quad (10.15.)$$

$W$  being the conductor width and  $S$  the gap between the conductors (see Figure 10.3.)

The effective dielectric constant for the substrate is dependent upon the substrate thickness  $h$ . If  $\epsilon_r$  is the relative permittivity of the substrate then the capacitance per unit length of line  $C$  is given by the integral

$$\frac{1}{C} = \frac{1}{\pi \epsilon_r \epsilon_0} \int_0^\infty \frac{\tilde{F}(\beta)}{\beta} \left| \frac{f(\beta)}{Q} \right|^2 d\beta \quad (10.16.)$$

where

$$\tilde{F}(\beta) = \frac{\epsilon_r \{ \epsilon_r \cosh(\beta h) + \sinh(\beta h) \}}{\{ \epsilon_r^2 + 1 \} \sinh(\beta h) + 2\epsilon_r \cosh(\beta h)} \quad (10.17.)$$

$$\left| \frac{f(\beta)}{Q} \right| = \frac{4}{\beta \omega} \sin\left(\frac{\beta \omega}{2}\right) \sin\left(\frac{\beta a}{2}\right) \quad (10.18.)$$

$\omega = 2\pi f$  and  $\epsilon_0$  is the permittivity of free space and is  $8.854 \times 10^{-2}$  pF  $\text{cm}^{-1}$ . The distance between the centres of the two conductors is  $a$  and is equal to  $S + W$ . If  $\lambda_g$  is the guide wavelength and  $\lambda_0$  the free space

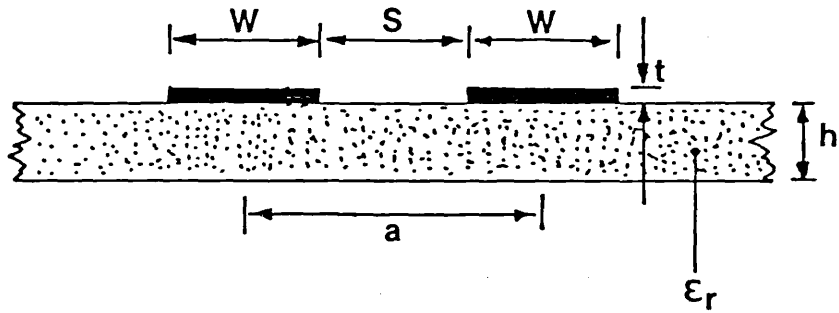


Figure 10.3 Coplanar line geometry.

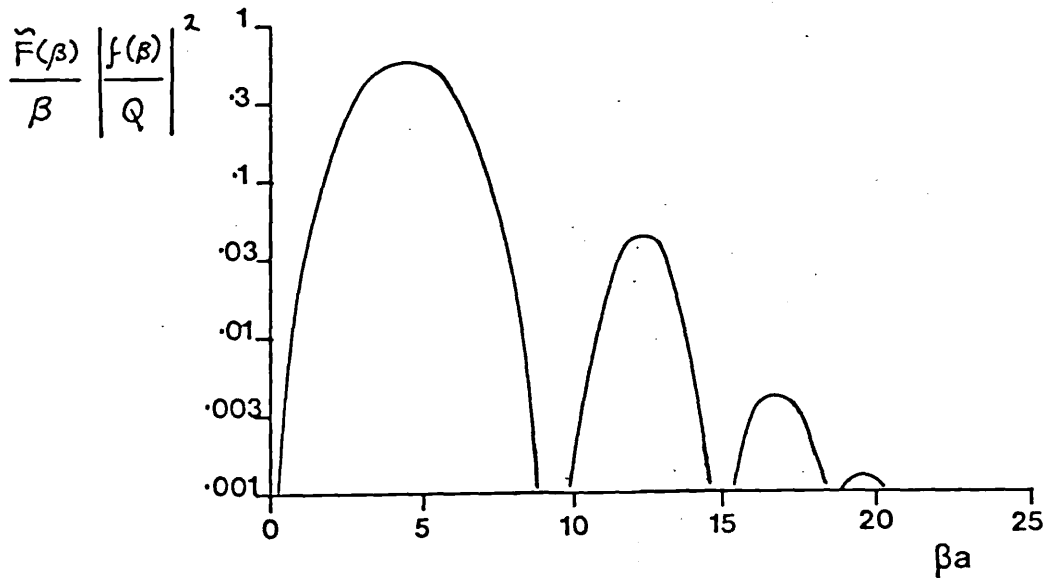


Figure 10.4. Numerical value of  $\frac{\tilde{F}(\beta)}{\beta} \left| \frac{f(\beta)}{Q} \right|^2$  plotted against  $\beta a$ .

wavelength then

$$\frac{\lambda_g}{\lambda_0} = \frac{V}{C} = \frac{1}{\sqrt{\epsilon_{re}}} = \sqrt{\frac{C_0}{C}} \quad (10.19.)$$

where  $C_0$  is the capacitance per unit length of the unsupported transmission line taking  $\epsilon_r = 1$  and  $C$  is the capacitance per unit length when supported by a substrate of relative permittivity  $\epsilon_r$ . When  $\epsilon_r = 1$   $\tilde{F}(\beta) = 0.5$  and is independent of  $h$  which would be expected. The integral given in equation 10.16 must be solved by numerical integration. The graph shown in Figure 10.4 shows the variation of the numerical value of the integrand of equation 10.16 plotted against  $\beta a$ , for a typical case, where  $h = 0.35$ ,  $W = 0.5$  and  $a = 1.5$ . It is evident from this graph that the value of the integrand decreases rapidly with  $\beta a$ . Hence it is only necessary to numerically evaluate the integral to the limit  $\beta a = 25$  in order to obtain sufficient accuracy.

If the bulk attenuation constant of the substrate upon which the coplanar transmission line is deposited is  $\alpha_s$ , then the loss tangent of the substrate material

$$\text{is} \quad \tan \delta = 2 \alpha_s / K \quad (10.20.)$$

where  $K$  is the propagation constant in the infinite dielectric. The dielectric loss factor,  $\alpha_d$ , per guide wavelength,  $\lambda_g$ , for a coplanar transmission line is given by<sup>88</sup>

$$\alpha_d = 27.3 \frac{\epsilon_r}{\epsilon_{re}} \frac{(\epsilon_{re} - 1)}{(\epsilon_r - 1)} \tan \delta \quad \text{dB}/\lambda_g \quad (10.21.)$$

The conductor loss,  $\alpha_c$ , per guide wavelength is given by<sup>89</sup>

$$\alpha_c = \frac{8.686 R_s q \lambda_0}{2 Z_0 W \sqrt{\epsilon_{re}}} \quad \text{dB}/\lambda_g \quad (10.22.)$$

where  $\lambda_0$  is the free space wavelength and  $R_s$  is the surface resistance of the conductor. The quantity  $q$  is dimensionless and accounts for the fact that the

surface current is not distributed evenly over the two conductors.

$$q = \frac{2W}{|I|^2} \int_0^L |J|^2 dL \quad (10.23.)$$

$I$  is the current and  $J$  the current density for the lossless guide.

For coplanar guide<sup>89</sup>

$$q = \frac{1}{2[K(\sqrt{1-k^2})]} \left\{ \frac{1}{k} \left[ \text{Ln} \left( \frac{4\pi s}{kt} \frac{(1-k)}{(1+k)} \right) + \pi \right] - \frac{\text{Ln}k}{1+k} \right\} \quad (10.24.)$$

The total guide loss,  $\alpha_T$ , per guide wavelength,  $\lambda_g$ , is given by

$$\alpha_T = \alpha_d + \alpha_c \quad \text{dB}/\lambda_g \quad (10.25.)$$

### 10.3. Experimental Investigation of Coplanar Lines from Backscattering Measurements.

Backscattering measurements were made on linear arrays of identical dipole elements, terminated in lengths of short-circuited coplanar transmission line, of the type shown in Figure 8.5. The lengths of transmission lines were identical for a given array but were varied for different arrays. Hence the variation of backscattering with transmission line length was ascertained.

The experimental measurements were made using the backscattering apparatus shown in Figure 9.1. The phase sensitive detector output was measured with a Digital voltmeter (DVM) for the broadside backscattering response of the array. The phase sensitive detector output integration time constant was 10 seconds and 3 separate measurements were taken for each array. The DVM readings were all normalised to a monitor beam detector signal of 1 mV to compensation for the small amount of residual laser output power drift.

Figure 10.5(a) and (b) show the variation of dipole

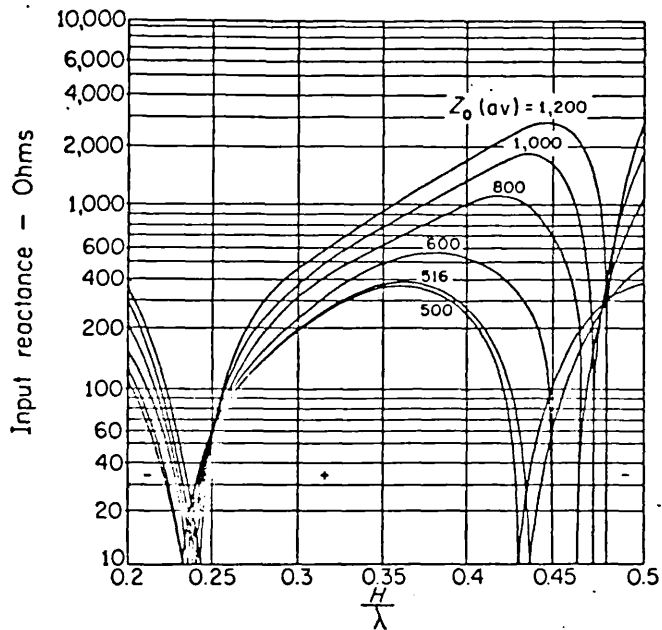


Figure 10.5.(a) Variation of input reactance with dipole halflength  $H$ . (Taken from Reference 43)

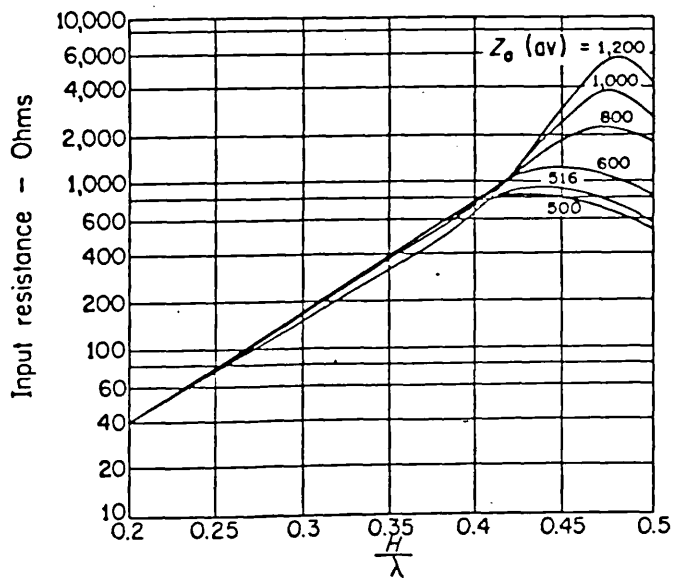


Figure 10.5.(b) Variation of input resistance with dipole halflength  $H$ . (Taken from Reference 43)

input reactance and resistance with dipole halflength for free standing dipoles<sup>43</sup>. The characteristic impedance,  $Z_0$  (av), of a planar dipole of width  $W$  and halflength  $H$  is given by<sup>43</sup>

$$Z_0 \text{ (av)} = 120 \left\{ \text{Ln} \left( \frac{8H}{W} \right) - 1 \right\} \quad (10.26.)$$

Two types of array were investigated experimentally. These arrays were reproduced on 3.5  $\mu\text{m}$  thick mylar substrates. In the first type, each consisted of 10 identical dipoles of width 10  $\mu\text{m}$  and halflength 0.25 wavelengths. Each dipole was connected to a length of coplanar transmission line short-circuited at the far end. The characteristic impedance of the line on a 3.5  $\mu\text{m}$  thick mylar substrate was 115  $\Omega$ . From Figure 10.5 it can be seen that the input resistance and reactance of a dipole of halflength 0.25 $\lambda$  is weakly dependent upon the characteristic impedance  $Z_0$  (av).

The input impedance of the halfwave dipoles was taken to be 73 + j 42  $\Omega$ . The impedance mismatch between the dipole and the transmission line was small, the calculated VSWR was 1.89.

The second type of arrays investigated again consisted of 10 identical dipoles of width 10  $\mu\text{m}$  but the half-length was now 0.31 wavelengths. The characteristic impedance of the coplanar transmission line connected to each dipole was 138  $\Omega$  on a 3.5  $\mu\text{m}$  thick mylar substrate. Each line was short-circuited at the far end as before. The characteristic impedance,  $Z_0$  (av), of a dipole antenna of halflength 0.31 wavelengths at 891 GHz and of width 10  $\mu\text{m}$  is ~500  $\Omega$  and so the corresponding input impedance found from Figure 10.5 is 200 + j 300  $\Omega$ . The mismatch between the transmission line and antenna impedances produced a calculated VSWR of 4.33. The mismatch was more severe in this case.

Figure 8.4 in Chapter 8 shows a photomicrograph of a typical array employed in this investigation and Figure 8.5 shows a photomicrograph of an individual element from the array in Figure 8.4. The width of the coplanar

conductors in the case of the  $115\ \Omega$  line was  $10\ \mu\text{m}$  and the gap between the conductors  $2.5\ \mu\text{m}$ . For the  $138\ \Omega$  line the conductor width was again  $10\ \mu\text{m}$  but the gap between these was now  $5\ \mu\text{m}$ . Because the conductor gaps in each case were comparable with the substrate thickness, the fields were well confined within the substrate. Hence the effective permittivity was taken to be the mean of that of the substrate and free space. For mylar  $\epsilon_r = 3.1$  at  $891\ \text{GHz}$ . The effective permittivity of the substrate,  $\epsilon_{re}$ , was  $2.05$  and so the velocity factor for both types of line was  $0.7$ .

Figure 10.6 and 10.7 show the variation of the effective backscattering cross-section  $F$ , defined by equation 10.27

$$F = \left| \frac{R_{ss}}{(R_{ss} + R_L) + j(X_{ss} + X_L)} \right|^2 \quad (10.27.)$$

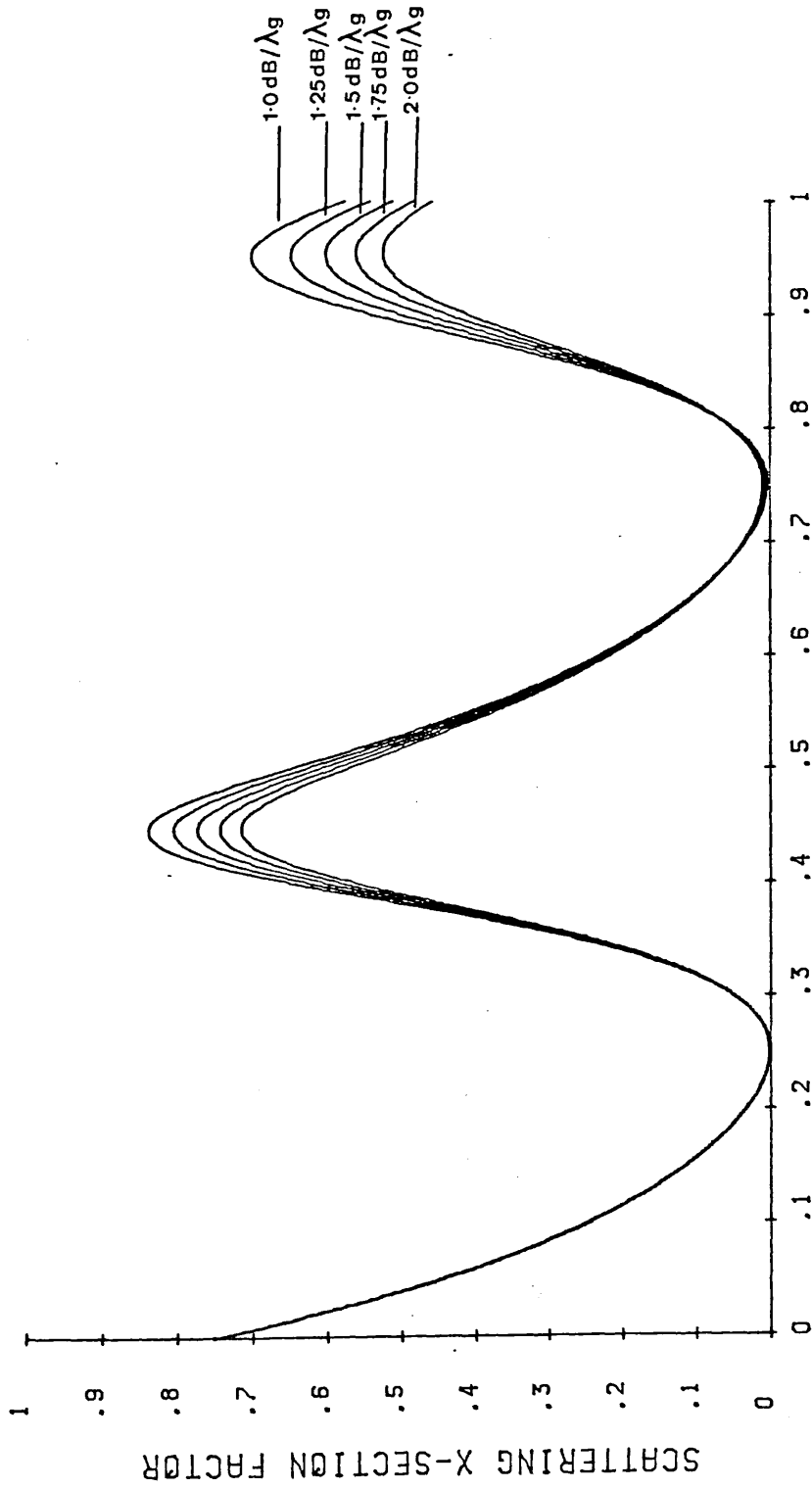
with the length of short-circuited transmission line measured in guide wavelengths and also as a function of the line attenuation specified in dB's per guide wavelength. In equation 10.27,  $R_L$  is set equal to the resistive component of the input impedance of the short-circuited transmission line given by equation 10.10, and  $X_L$  is set equal to the reactive component of the input impedance of the short-circuited line, given by equation 10.11.

Figure 10.6 shows the variation of the effective backscattering cross-section  $F$ , in terms of the length of the short-circuited coplanar line measured in guide wavelengths, for the  $115\ \Omega$  line connected to a halfwave dipole with an input impedance of  $73 + j\ 42\ \Omega$ . The dependence on line attenuation is also shown.

Figure 10.7 shows the variation of  $F$  when a  $138\ \Omega$  transmission line is connected to a  $0.62\ \lambda$  length dipole having an input impedance of  $200 + j\ 300\ \Omega$  as a function of the line attenuation.



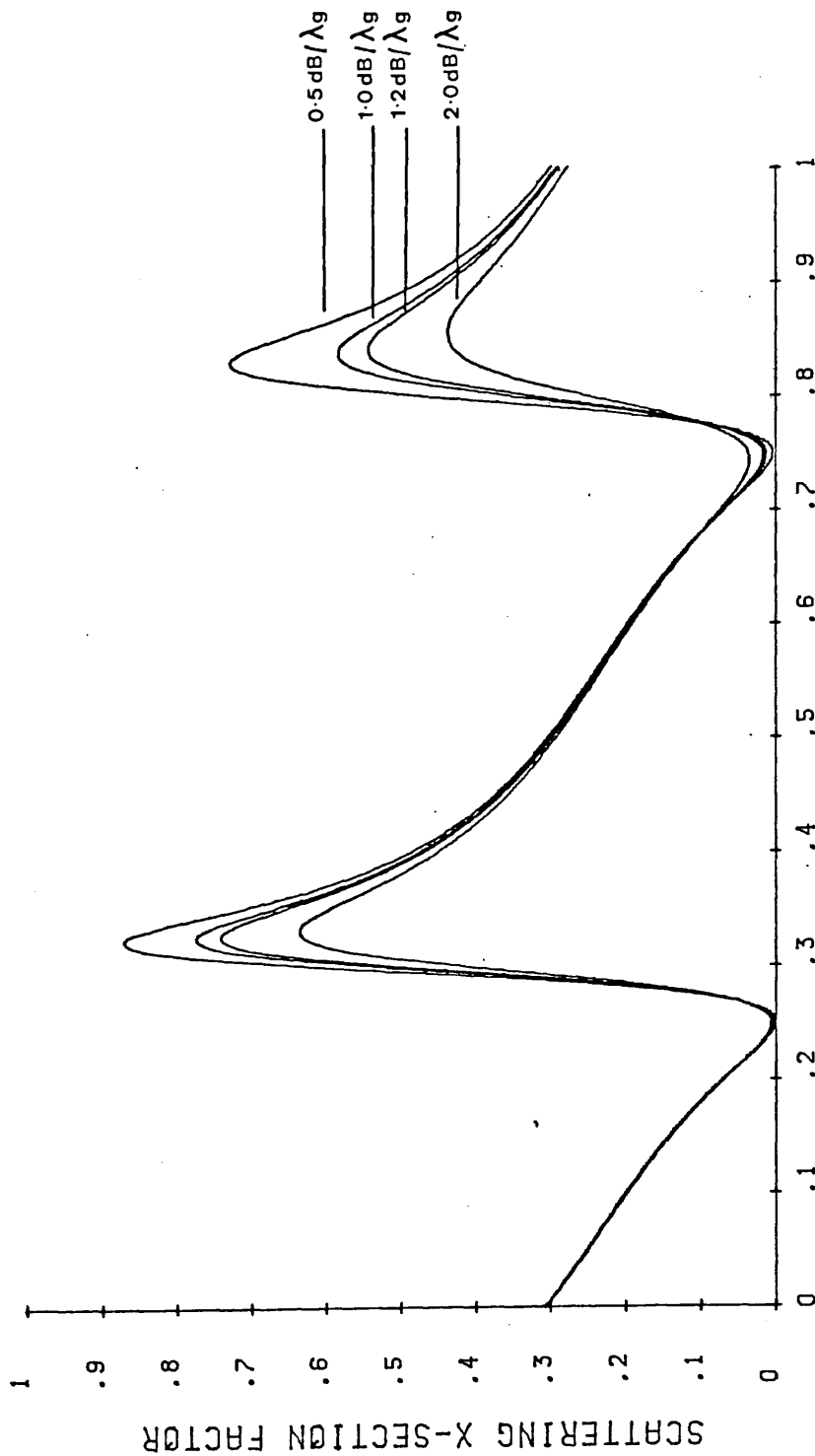
$Z_0=115 \text{ OHMS}$ ,  $R_{SS}=73 \text{ OHMS}$ ,  $X_{SS}=42 \text{ OHMS}$



TX LINE GUIDE WAVELENGTH

Figure 10.6. Variation of effective backscattering cross-section,  $F$ , with the length of a short-circuited  $115 \Omega$  transmission line loading a halfwave dipole of input impedance  $73 + j 42 \Omega$ . The length of line is expressed in guide wavelengths and the variation for various line attenuations is given.

$Z_0=138 \text{ OHMS}$ ,  $R_{SS}=200 \text{ OHMS}$ ,  $X_{SS}=300 \text{ OHMS}$



TX LINE GUIDE WAVELENGTH

Figure 10.7. Variation of effective backscattering cross-section,  $F$ , with the length of a short circuited  $138 \Omega$  transmission line loading a  $0.62 \lambda$  length dipole of input impedance  $200 + j 300 \Omega$ . The length of line is expressed in guide wavelengths and the variation for various line attenuations is given.

Figures 10.8 and 10.9 show the experimental results obtained respectively for arrays of  $0.5\lambda$  length dipoles terminated by  $115\Omega$  short-circuited coplanar transmission lines and  $0.62\lambda$  length dipoles terminated by  $138\Omega$  coplanar lines. As previously stated, each experimental point is an average over 3 separate measurements and the size of the dots represents the experimental uncertainty. The baseline level in each case was due to reflection by the substrate itself and the structure used to support the Golay detector. The Golay detector support was covered with a microwave absorber (Ecosorb AN-73) but in spite of this treatment still gave rise to a small amount of reflected power.

From measurements of the peak amplitudes, and their position, both the line attenuation and velocity factor has been determined. The results are summarised in Table 10.1 and the agreement between theory and experiment is satisfactory. The actual shape of the two curves do not agree very well with those calculated theoretically, and this may possibly be due to mutual interaction between elements which has not been taken into account. The line attenuation is higher for the  $115\Omega$  coplanar line than for the  $138\Omega$  line because the conductor loss is greater in the former case due to closer proximity of the conductors.

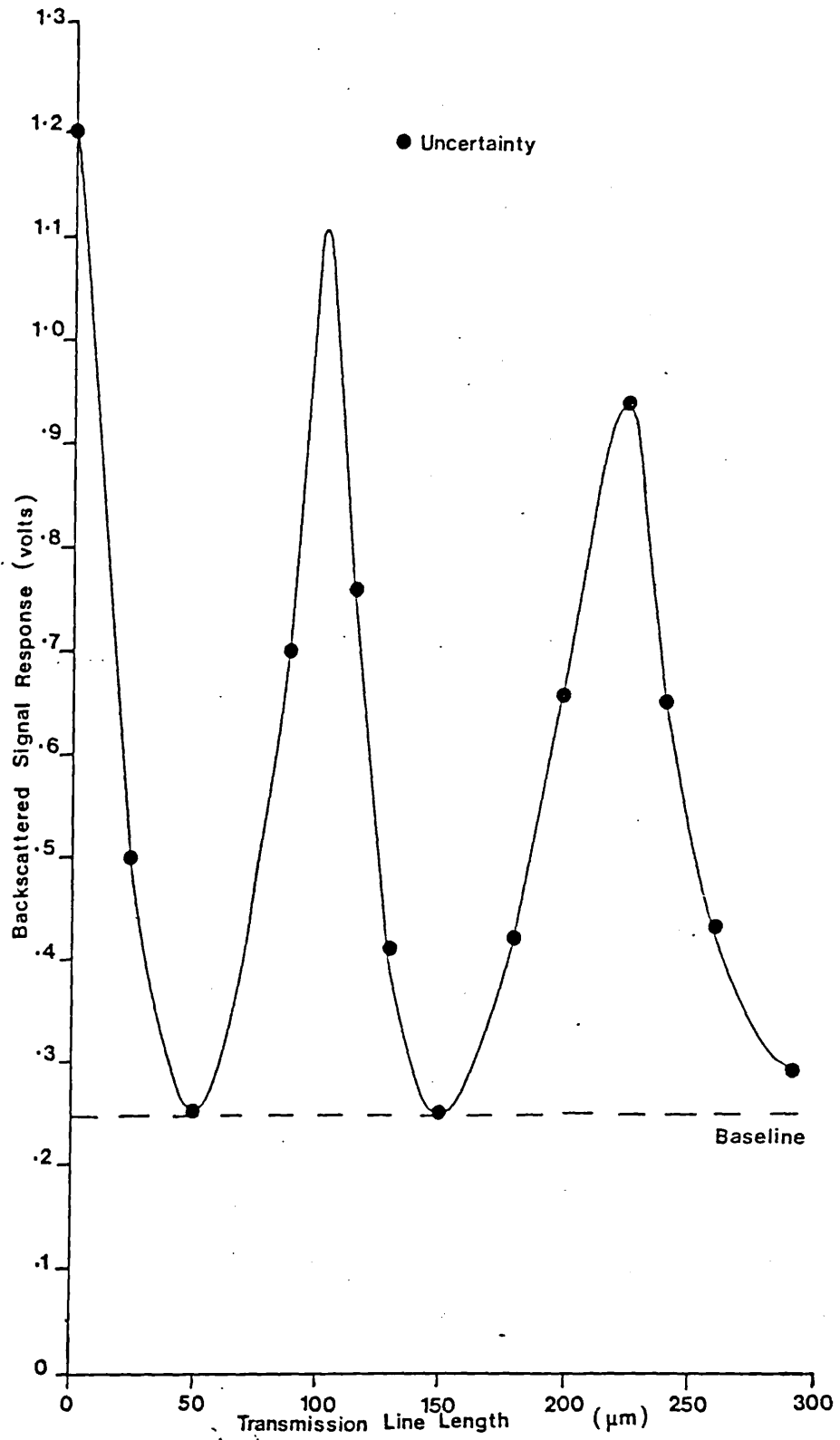


Figure 10.8. Variation of backscattered signal response with length of transmission line for an array of 10,  $0.5\lambda$  length dipoles connected to  $115\Omega$  short circuited coplanar transmission line.

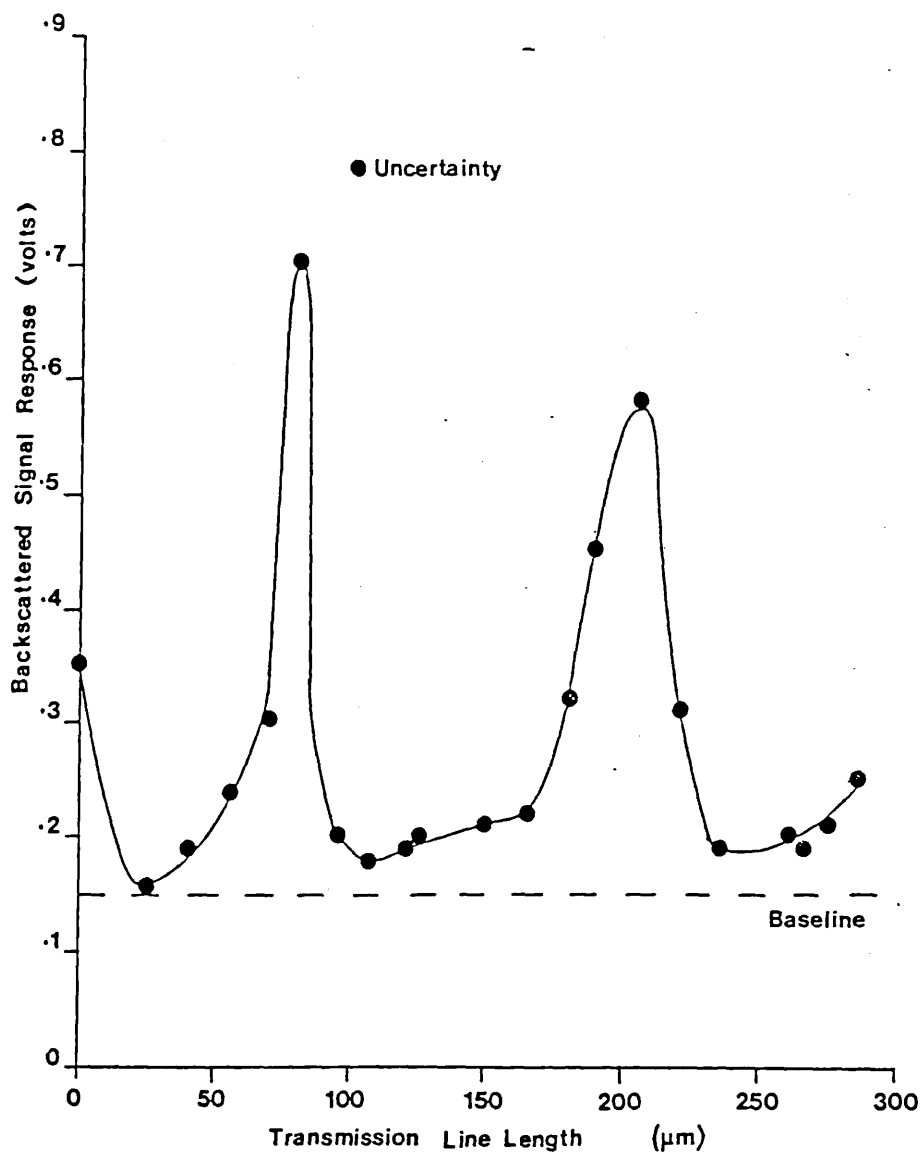


Figure 10.9. Variation of backscattered signal response with length of transmission line for an array of 10,  $0.62\lambda$  length dipoles connected to  $138\Omega$  short circuited coplanar transmission line.

TABLE 10.1.

EXPERIMENTAL RESULTS OBTAINED FROM DIPOLE ARRAYS TERMINATED WITH COPLANAR TRANSMISSION LINES																		
Element Length	Element Terminal Impedance $Z_{ss}$ ( $\Omega$ )	Transmission Line Characteristic Impedance $Z_0$ ( $\Omega$ )	Peak positions ( $x\lambda g$ )				Velocity Factors		Line attenuation (dB/ $\lambda$ g)						Coplanar Line Parameters			
			1st		2nd		Theo.	Exp.	Theo.			Exp.			S ( $\mu m$ )	W ( $\mu m$ )	T ( $\mu m$ )	t ( $\mu m$ )
			Theo.	Exp.	Theo.	Exp.	Theo.	Exp.	$\alpha_c$	$\alpha_d$	$\alpha_T$	$\alpha_T$	$\alpha_T$					
0.5 $\lambda$	73+j42	115 $\Omega$	0.45	0.44 $\pm 0.01$	0.95	0.94 $\pm 0.01$	0.7	0.71 $\pm 0.03$	1.48	0.25	1.73	1.76 $\pm 0.05$		2.5	10	3.5	0.1	
0.62 $\lambda$	200+j300	138 $\Omega$	0.33	0.32 $\pm 0.01$	0.83	0.82 0.01	0.7	0.74 $\pm 0.03$	0.82	0.25	1.07	0.93 $\pm 0.07$		5	10	3.5	0.1	

10.4. Experimental Investigation of the Variation of Velocity Factor of Coplanar Lines with Substrate thickness using Vee-Antennas.

Vee antennas have been previously described by Rutledge et al<sup>37</sup>. Figure 10.10 shows the type of vee antennas that the above authors found suitable for use in the submillimetre region. The conductors spread radially to reduce conductor loss and also to keep the distributed impedance of the conductor constant. Owing to the consistency of the impedance, the input impedance of the antenna must be purely resistive and the reactive component is negligible. This has certain advantages as will be seen later.

The antenna design parameters are, the length of the arms, the angle between them, the angular width of the arms and the thickness of the conductors. These determine the antenna directivity and feed impedance.

The impedance itself depends upon the length of the arms, and for a very long antenna it will be close to the characteristic impedance for the lowest order transmission mode. The technique employed to calculate the antenna feed impedance is presented in Appendix VI.

The optimum length of the arms and the directivity can be estimated from long-wire antenna theory. For maximum directivity, the arms should be equal in length to that required for a single long wire antenna to have a principal lobe on the axis of symmetry. The angle  $\theta_s$  of the principal lobe of a single long wire antenna is given by the following expression derived from conventional "long wire" theory

$$\theta_s = 2 \sin^{-1} \left\{ \frac{0.431}{\sqrt{L/\lambda}} \right\} \quad (10.28.)$$

In this expression  $L$  is the conductor length. For maximum directivity the angle  $\theta_s$  for the principal lobe should be half the angle between the centre line of the two conductors. The directivity,  $D(\theta, \phi)$ , of an antenna

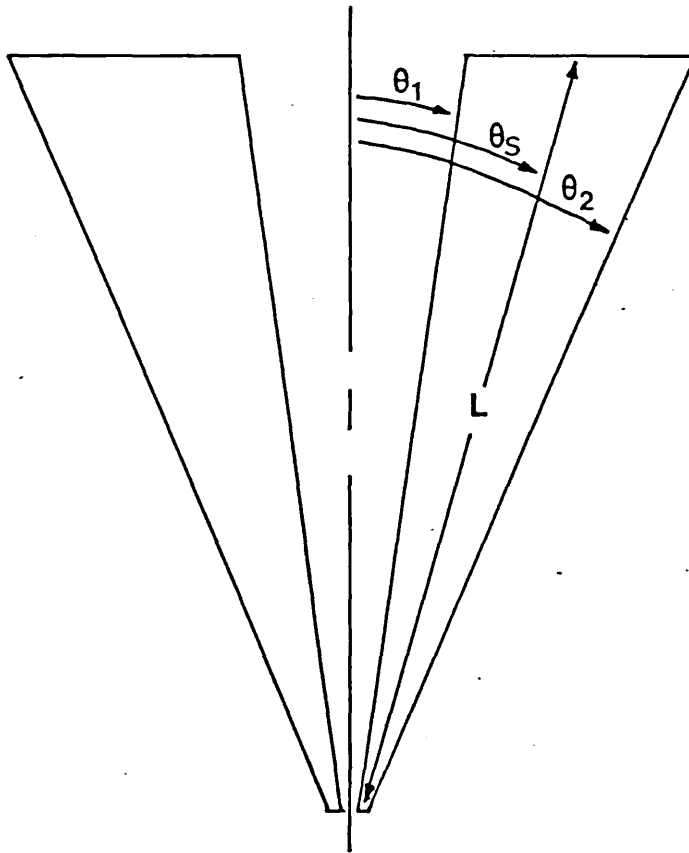


Figure 10.10. Geometry of the vee-antenna.



as a function of the angles  $(\theta, \phi)$  is given by the expression

$$D(\theta, \phi) = \frac{4 \times \text{Power radiated per unit solid angle in the direction } \theta, \phi}{\text{Total radiated power}} \quad (10.29.)$$

Since the radiation from two conductors add in phase on the symmetry axis, an optimistic estimate of the directivity,  $D_v$ , of the vee would be four times that for a single long wire,  $D_s$ , given approximately by the formula

$$D_s = \frac{3.95 L/\lambda}{\log_{10}(L/\lambda) + 0.915} \quad (10.30)$$

Therefore the directivity,  $D_v$ , of the vee antenna becomes

$$D_v = 4 D_s \quad (10.31.)$$

A photomicrograph of the vee antenna used in these investigations is shown in Figure 8.6 in Chapter 8. The angular width of the conductors was  $30^\circ$  and the angular separation of the centres was  $50^\circ$ . These dimensions resulted in an antenna terminal impedance of  $200 \Omega$ . Using equation 10.28 it was calculated that an arm length of  $3.96 \lambda$  or  $1.336 \text{ mm}$  (for  $\lambda = 337 \mu\text{m}$ ) was required to obtain maximum directivity. This result was obtained by taking  $\theta_s = 25^\circ$ . The single wire directivity for this arm length was found to be 10.34 from equation 10.30 and hence the directivity of the vee antenna was expected to be 41.4 (16.2 dB).

The vee antennas were reproduced by the lithography technique described in Chapter 8. After replication, the vee antenna substrates were transferred from the circular rings necessary for the lithographic procedure to a horseshoe shaped support. This transfer was essential because the vee antenna has an "end fire" radiation pattern and so the direction of maximum response lies in the plane of the substrate. The open portion of the horseshoe support ring allowed clear access to the vee, whilst reflection from the curved

surface was minimised by coating with microwave absorbing material (Ecosorb AN-73). The technique for supporting the vee is illustrated in Figure 10.11. The E and H-plane backscattering patterns for vee antennas reproduced on 1.5  $\mu\text{m}$  and 3.5  $\mu\text{m}$  thick mylar substrates are shown in Figures 10.12 to 10.15. An equation relating the E and H plane half power beamwidths to the directivity of an antenna can be obtained from the generalised equation for the directivity, given in equation 10.34<sup>40</sup>. Let the radiation-intensity pattern be expressed by

$$U = U_a f(\theta, \phi) \quad (10.32.)$$

and its maximum value by

$$U_m = U_a f(\theta, \phi)_{\text{max}} \quad (10.33.)$$

The directivity is given by

$$D = \frac{U_m}{U_o} \quad (10.34.)$$

where  $U_o$  is the average radiation intensity

$$U_o = \frac{\int \int U_a f(\theta, \phi) d\Omega}{4\pi} \quad (10.35.)$$

where  $d\Omega$  is an element of solid angle.

The directivity is given by

$$D = \frac{U_a f(\theta, \phi)_{\text{max}}}{\int \int \frac{U_a f(\theta, \phi) d\Omega}{4\pi}} \quad (10.36.)$$

$$= \frac{4\pi f(\theta, \phi)_{\text{max}}}{\int \int f(\theta, \phi) d\Omega} \quad (10.37.)$$

Equation 10.37 can be re-expressed as

$$D = \frac{4\pi}{B} \quad (10.38.)$$

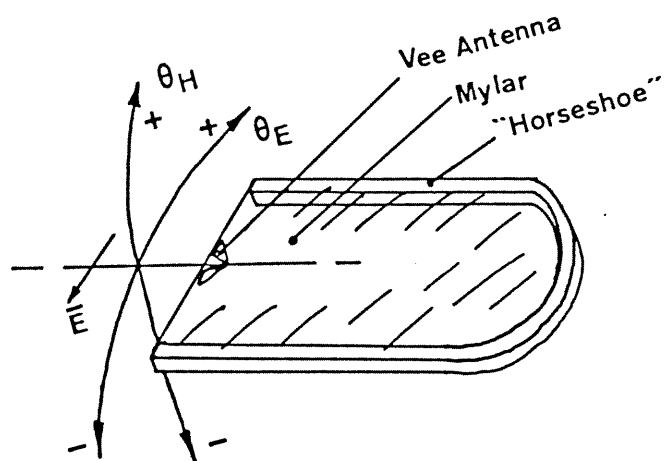


Figure 10.11. Technique employed to support the vee antennas.

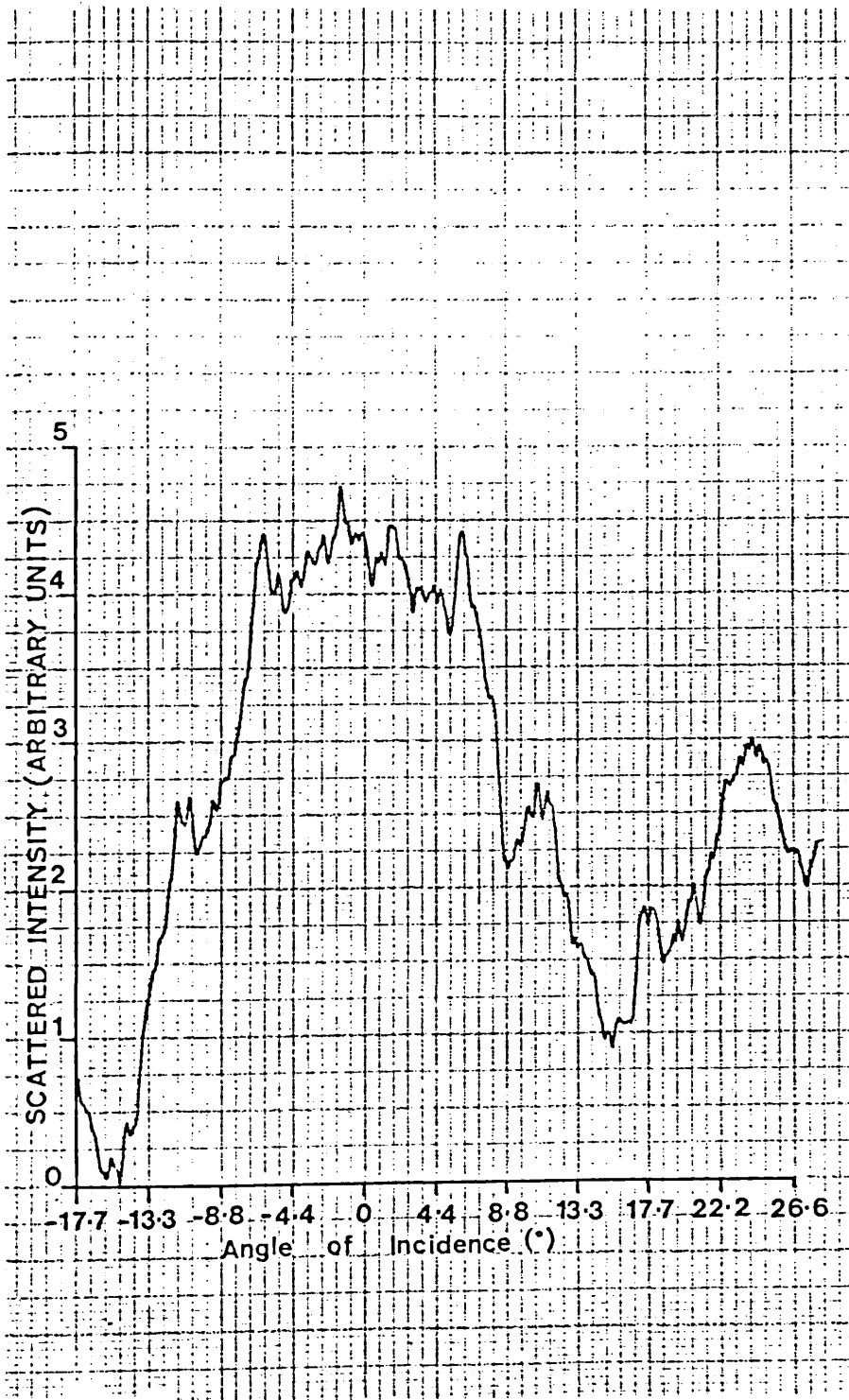


Figure 10.12. H-Plane backscattering pattern for a vee antenna reproduced on a 1.5 $\mu$ m thick mylar substrate.

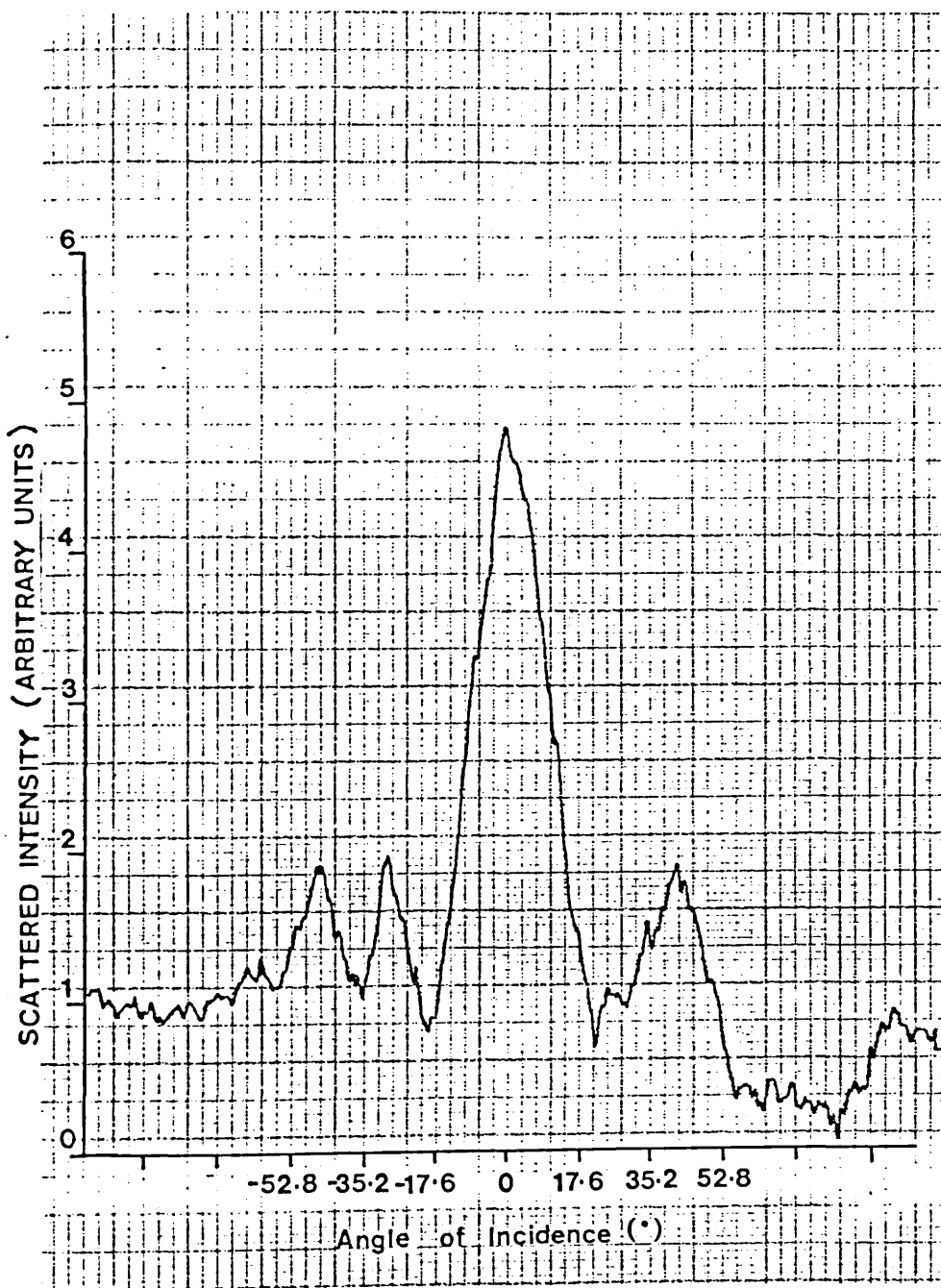


Figure 10.13. E-Plane backscattering pattern for a vee antenna reproduced on a 1.5  $\mu\text{m}$  thick mylar substrate.

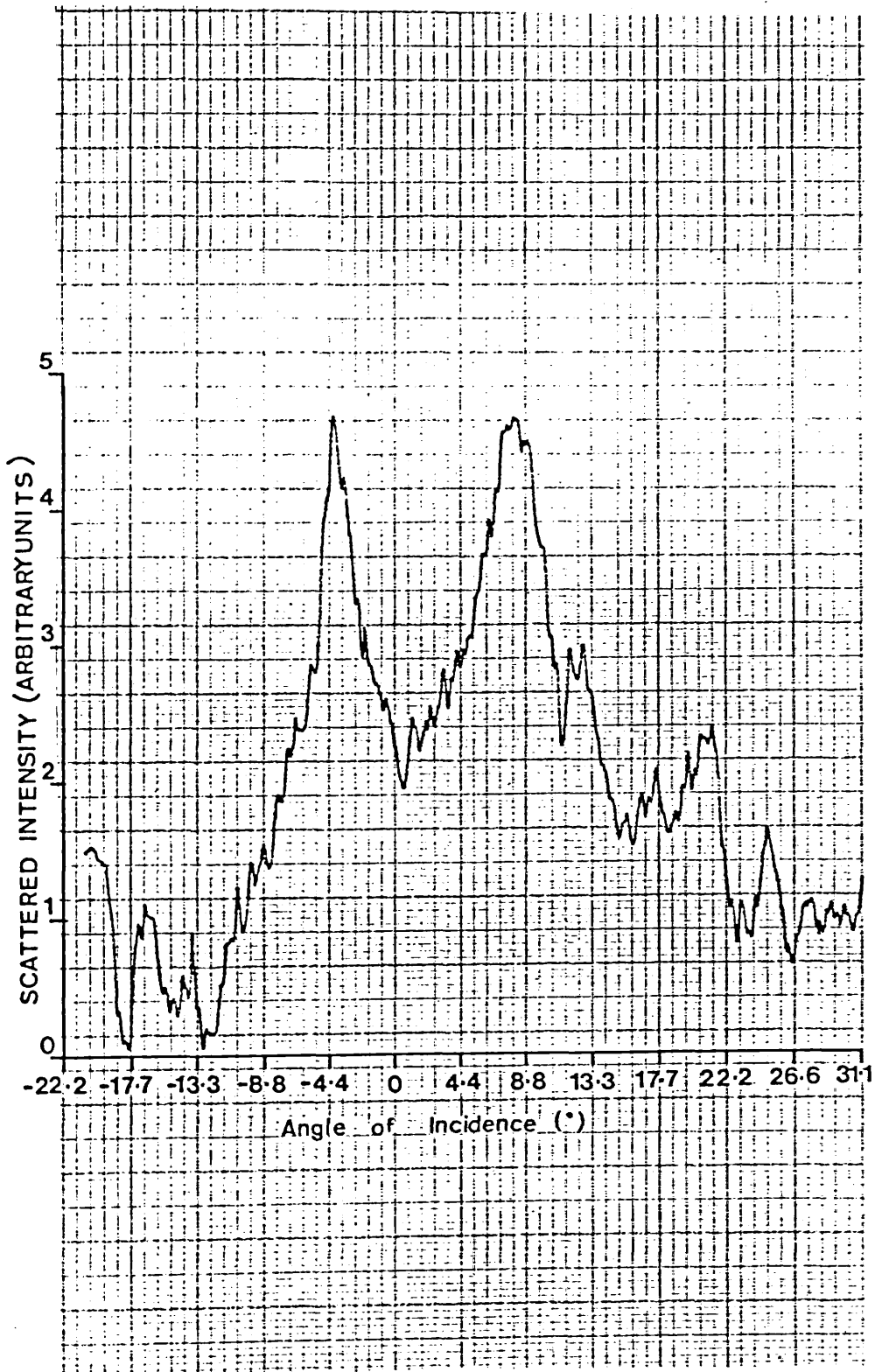


Figure 10.14. H-Plane backscattering pattern for a vee antenna reproduced on a 3.5  $\mu$ m thick mylar substrate.

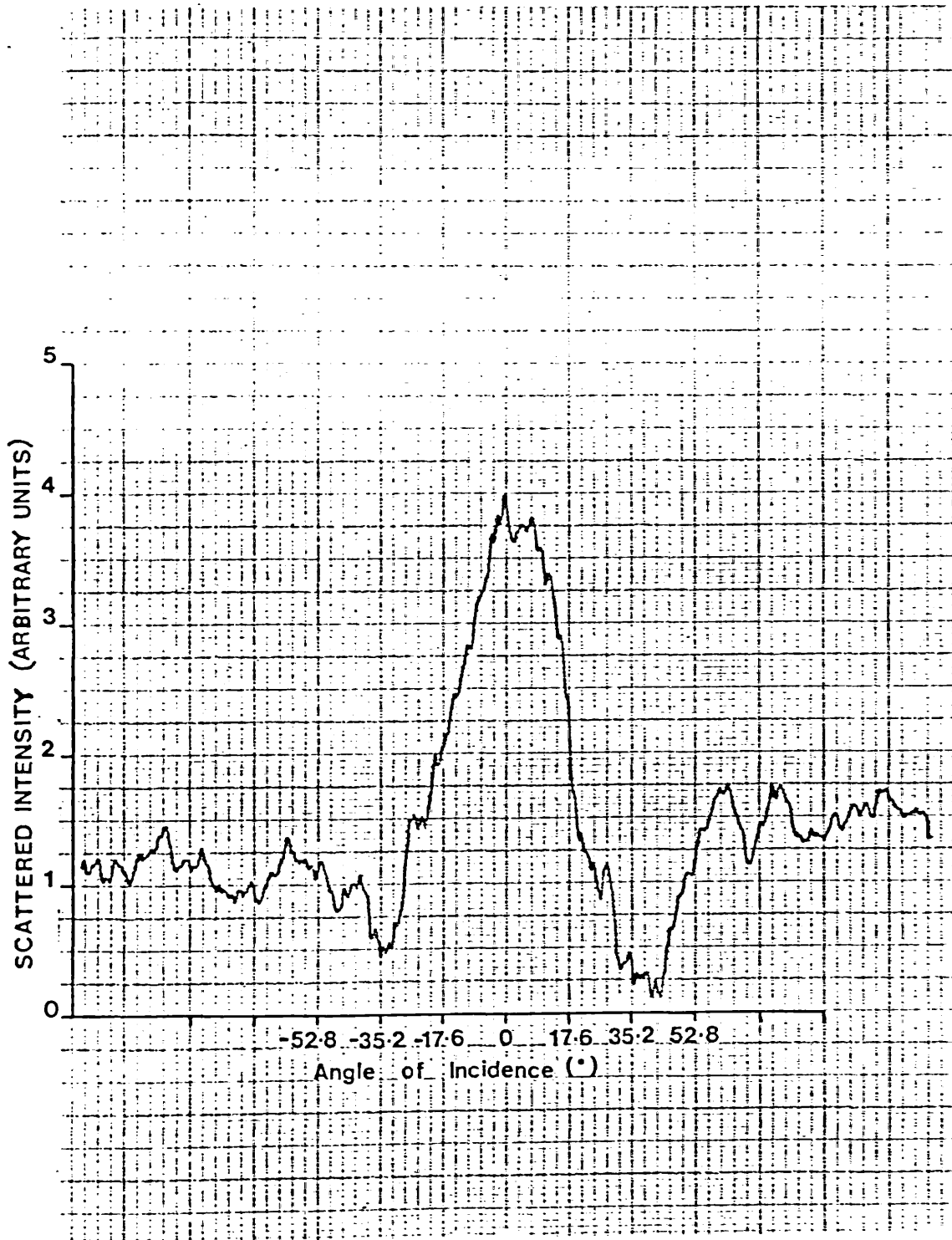


Figure 10.15 E-Plane backscattering pattern for a vee antenna reproduced on a 3.5  $\mu\text{m}$  thick mylar substrate.

where  $B$  is defined as the beam area. It is given by

$$B = \frac{\iint f(\theta, \phi) d\Omega}{f(\theta, \phi)_{\max}} \quad (10.39.)$$

$$D = \frac{41,253}{B} \quad (10.40.)$$

where  $B$  is in square degrees.  $B$  is approximately  $1.5 \theta_E \theta_H$  where  $\theta_E$  and  $\theta_H$  are the E and H-plane halfpower beamwidths in degrees. Therefore <sup>82</sup>

$$D = \frac{27000}{\theta_E \theta_H} \quad (10.41.)$$

The value obtained in this fashion will generally be accurate to within 25 percent, particularly for high gain antennas.

For the vee antennas reproduced on 1.5  $\mu\text{m}$  thick mylar, the experimentally measured values for the E and H plane halfpower beamwidths were  $\theta_E = 27.0^\circ$  and  $\theta_H = 21.2^\circ$  yielding an experimental value for the directivity of 47.6 (16.8 dB) from equation 10.41. The E and H plane halfpower beamwidths for the vee antenna reproduced on 3.5  $\mu\text{m}$  thick mylar were found to be  $\theta_E = 33.2^\circ$  and  $\theta_H = 18.8^\circ$ . This yielded a directivity of 43.2 (16.4 dB). However, for the vee antenna reproduced on 3.5  $\mu\text{m}$  thick mylar, the H-plane scattering pattern was found to exhibit a deep trough about the point where the angle of incidence was  $0^\circ$ . The H-plane pattern for the identical antenna reproduced on 1.5  $\mu\text{m}$  thick mylar did not, however, exhibit this effect.

Because the incident and scattered components of electric field lie in the plane of the substrate it is conceivable that TE guided wave modes may become excited <sup>36</sup>. The  $TE_0$  mode is the dominant mode for the plane dielectric sheet of thickness  $2d$ . The critical thickness below which the  $n^{\text{th}}$  mode cannot propagate is given by <sup>36</sup>

$$\frac{2d}{\lambda} = \frac{n}{2\sqrt{\epsilon_r - 1}} \quad (10.42.)$$



Therefore the  $TE_0$  mode has no cut-off. Figure 10.16 shows the variation of velocity factor for the  $TE_0$  mode with substrate thickness for a mylar substrate at 337  $\mu\text{m}$ . The velocity factor of the TE wave in the substrate is less than that on the conductor, which would be expected to be approximately equal to that of free space. Hence the conductor will tend to radiate into the dielectric.<sup>37</sup> For a 1.5  $\mu\text{m}$  thick substrate the velocity factor is nearly that of free space so a  $TE_0$  mode will not be strongly excited. However, for the 3.5  $\mu\text{m}$  thick substrate the velocity factor is 0.98 which is significantly different from that of free space. Hence it would be expected that a  $TE_0$  mode would be excited. The trough in the H-plane about  $0^\circ$  may be explained as being a result of some of the radiation exciting a  $TE_0$  mode in the substrate and so becoming trapped.

The measured directivities are higher than the theoretically predicted values. This is possibly due to the supporting substrate acting as a dielectric plate antenna.<sup>21</sup> Because the velocity factor of the  $TE_0$  mode excited in the substrate is less than that of free space the substrate acts as a slow wave structure<sup>36</sup>. The incident electromagnetic wave will excite the  $TE_0$  mode and some of the incident radiation will couple to the substrate and this will enhance the coupling to the vee antenna. Therefore, the directivity of the vee will be increased.

Figure 10.17 shows the variation of the effective back-scattering cross section,  $F$ , for a vee antenna of input impedance  $200\ \Omega$  with a length of short circuited transmission line connected at the apex of the vee. Neglecting attenuation, the dependence of the effective back-scattering cross-section on line impedance has also been computed. The terminal impedance of the vee antenna used in these investigations was designed to be  $200\ \Omega$ . It can be seen that, owing to the reactive component of the antenna impedance being zero, the relative

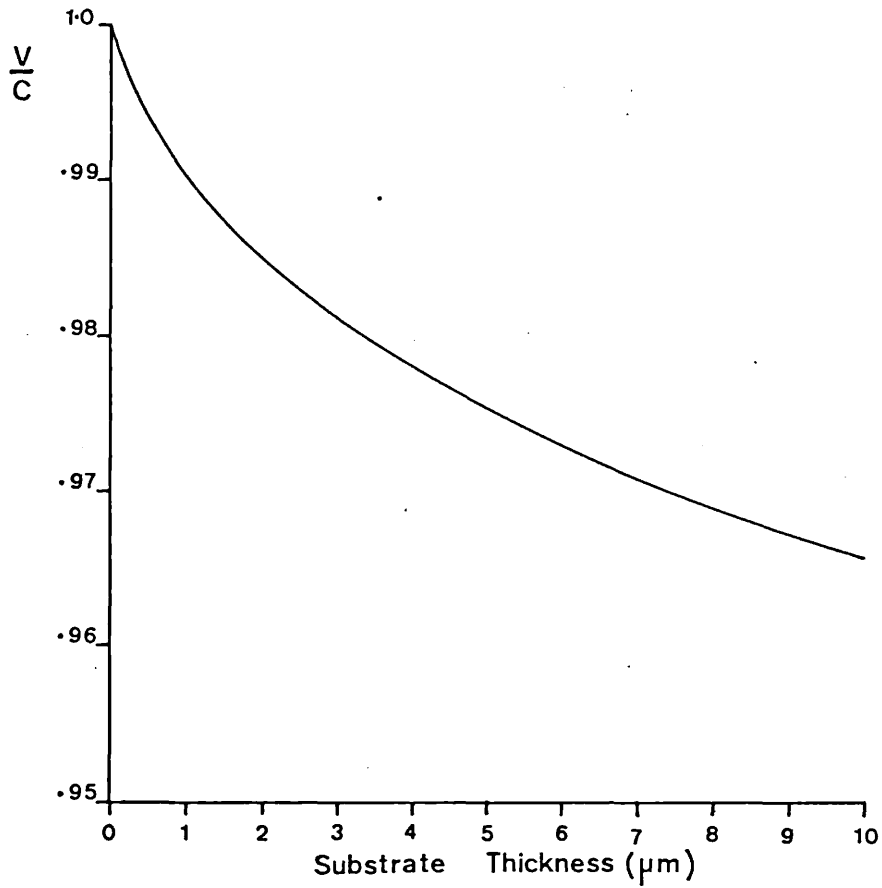
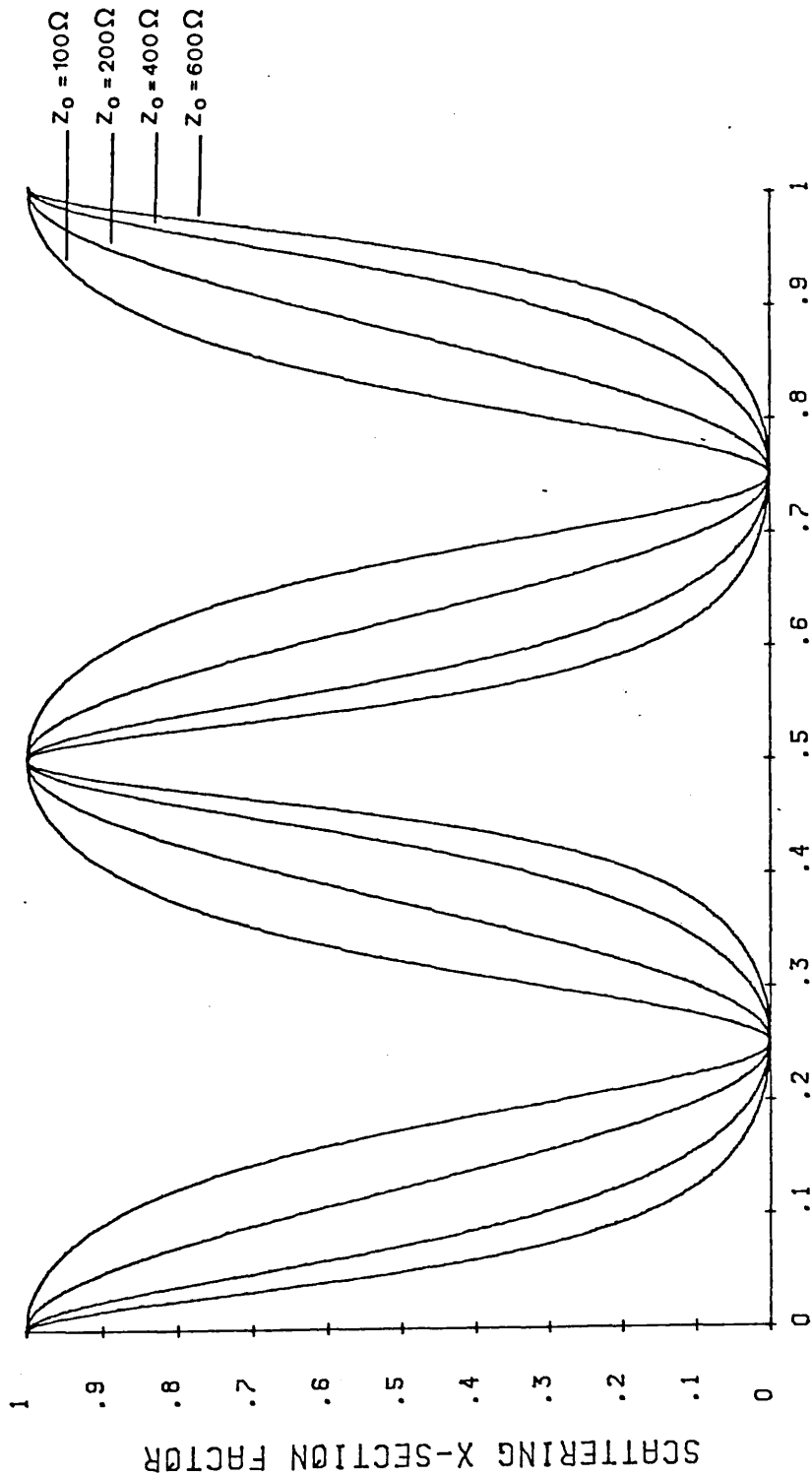


Figure 10.16. Variation of velocity factor with substrate thickness for a  $\text{TE}_0$  mode excited on a mylar substrate<sup>o</sup> ( $\epsilon_r = 3.1$ ) at 891 GHz (337  $\mu\text{m}$ ). (Calculated from relationships given in reference<sup>36</sup>).

VEE ANTENNA, RSS=200 OHMS, XSS=0 OHMS.



TX LINE GUIDE WAVELENGTH

Figure 10.17. Variation of scattering cross section factor with the length of short circuited transmission lines of various characteristic impedance connected to a vee antenna of input impedance 200  $\Omega$ . The length of line is expressed in guide wavelengths. Attenuation is ignored.

positions of the minima and maxima of the effective backscattering cross-section,  $F$ , are independent of the line impedance, when the line length is normalised to the guide wavelength,  $\lambda_g$ . The first minima always occurs at  $0.25 \lambda_g$ , and the first maxima at  $0.5 \lambda_g$ . The effect of changing the thickness of the substrate is to modify its effective permittivity and consequently change the values of the velocity factor,  $V/c$ , and characteristic impedance,  $Z_0$ , for the line. The position of the maxima and minima only depend upon the guide wavelength and hence  $V/c$ . Consequently the functional dependence of the guide wavelength on substrate thickness can be determined from a study of back-scattering measurements. This enables a velocity factor to be found for each substrate thickness.

Figures 10.18 to 10.24 show the variation of backscattered power with the length of the terminated line for various substrate thicknesses. From experimental values of the line lengths  $\lambda_g/2$  and  $\lambda_g/4$  corresponding to maximum and minimum values of the cross-section the velocity factor could easily be determined.

Figure 10.25 shows the variation of velocity factor  $V/c$  with substrate thickness. The solid line is the theoretical variation obtained by numerically integrating equation 10.16 on a Casio FX-602P programmable calculator and using the relationship given by equation 10.19 to obtain the velocity factor. The experimental points obtained are plotted with the uncertainty indicated by the error bars. The width of the conductors forming the coplanar line were  $5 \mu\text{m}$  and the gap between the conductors was  $10 \mu\text{m}$ . The relative permittivity of the bulk mylar substrate material was taken to be 3.1.

The agreement between theory and experiment is quite good. The effects of line attenuation were not considered in the theoretical analysis. The effect of line attenuation on the positions of the minima and maxima were small and estimated to be of the order of  $\pm 1\%$  of a guide wavelength

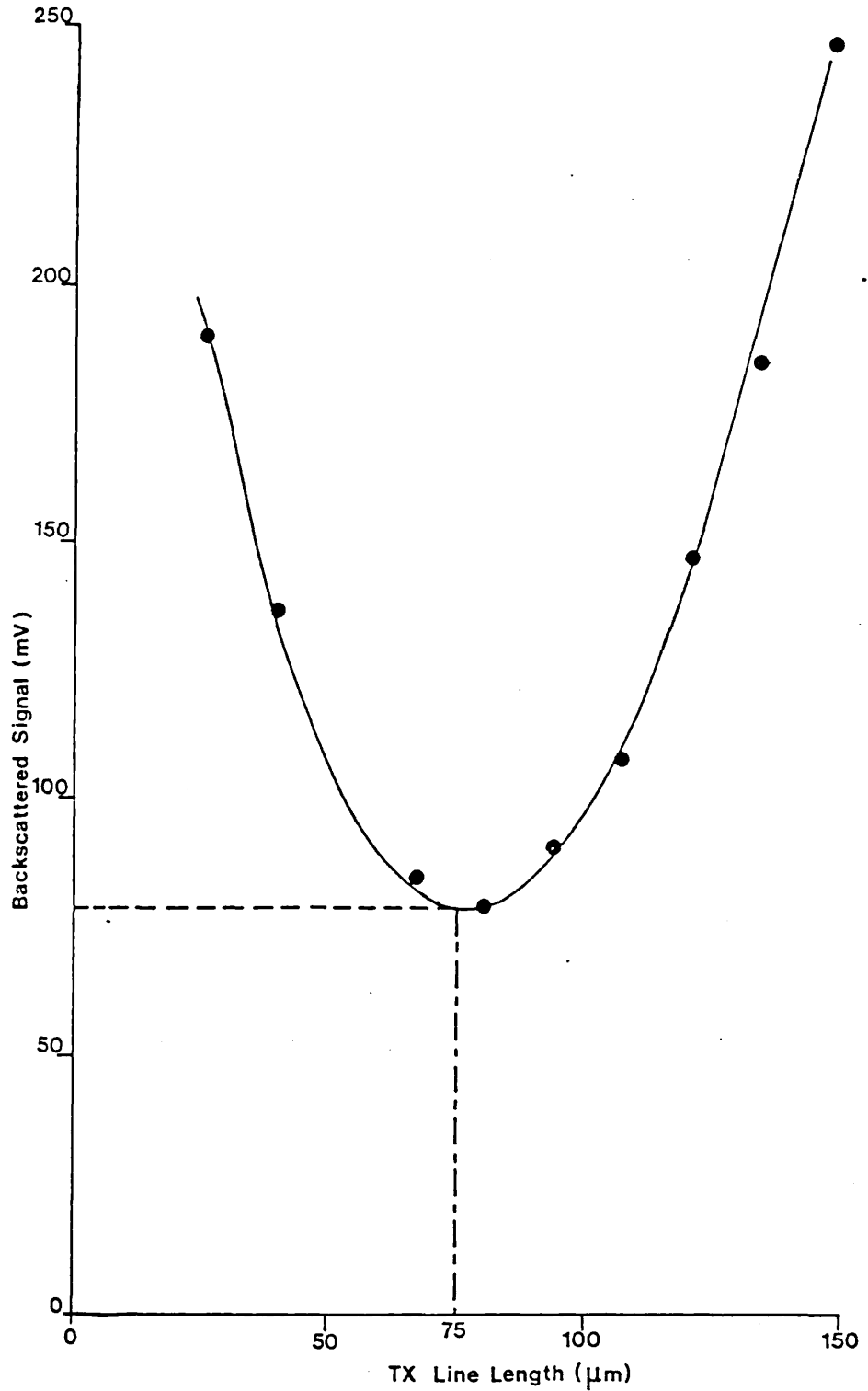


Figure 10.18. Variation of backscattered signal from a vee antenna with the length of terminating short circuited transmission line reproduced on 1.5 μm thick mylar.

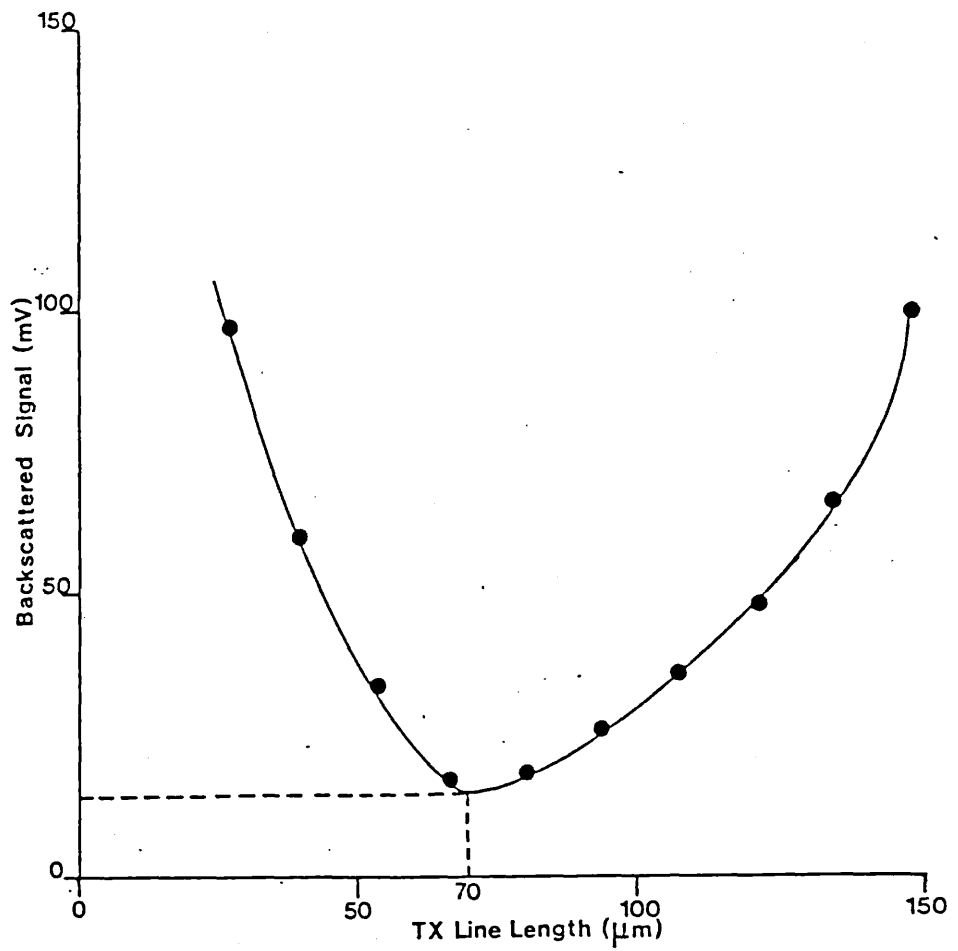


Figure 10.19. Variation of backscattered signal from a vee antenna with the length of terminating short circuited transmission line reproduced on 3.5 μm thick mylar.

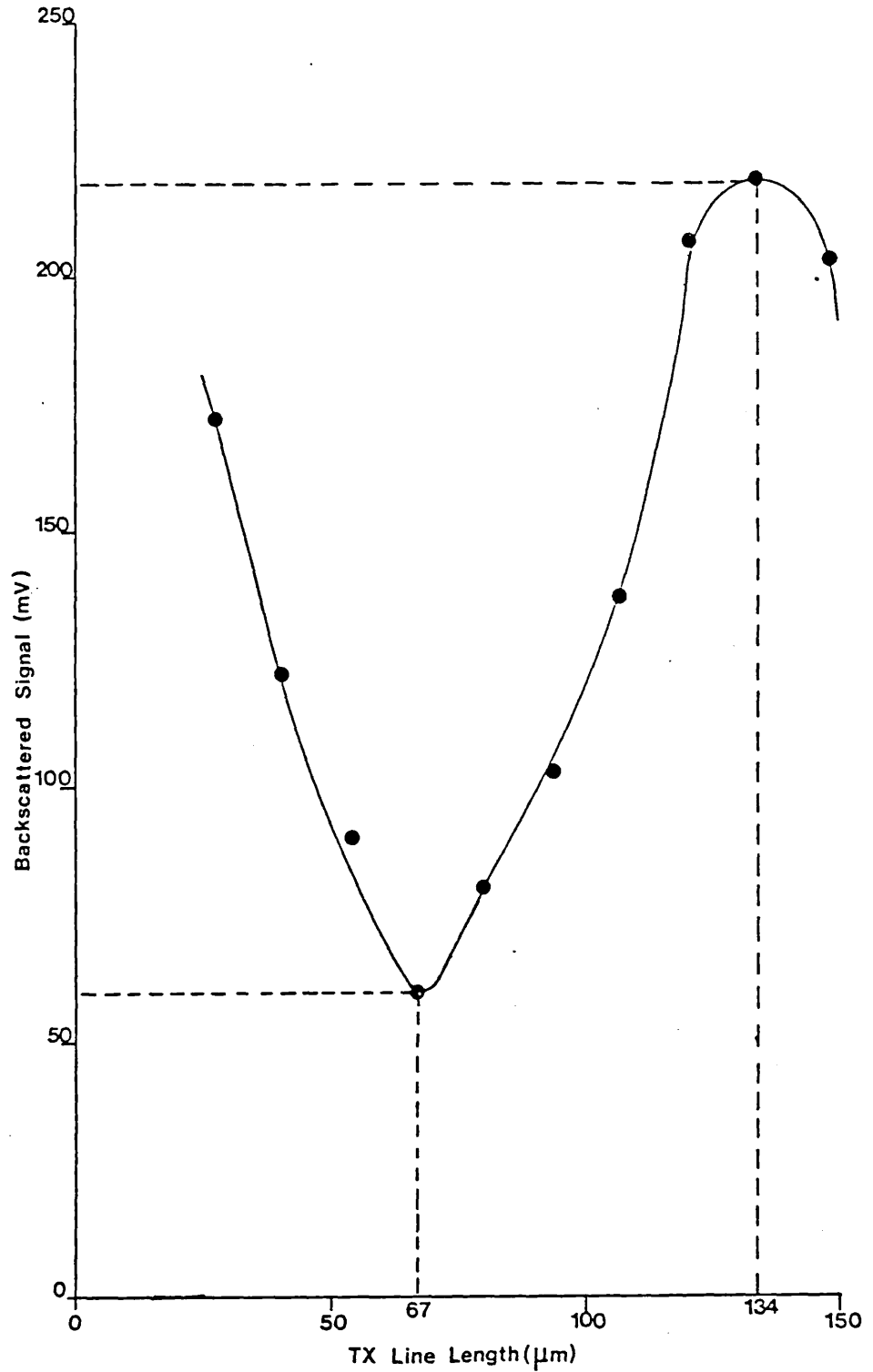


Figure 10.20. Variation of backscattered signal from a vee antenna with the lengths of terminating short circuited transmission line reproduced on 4 μm thick mylar.

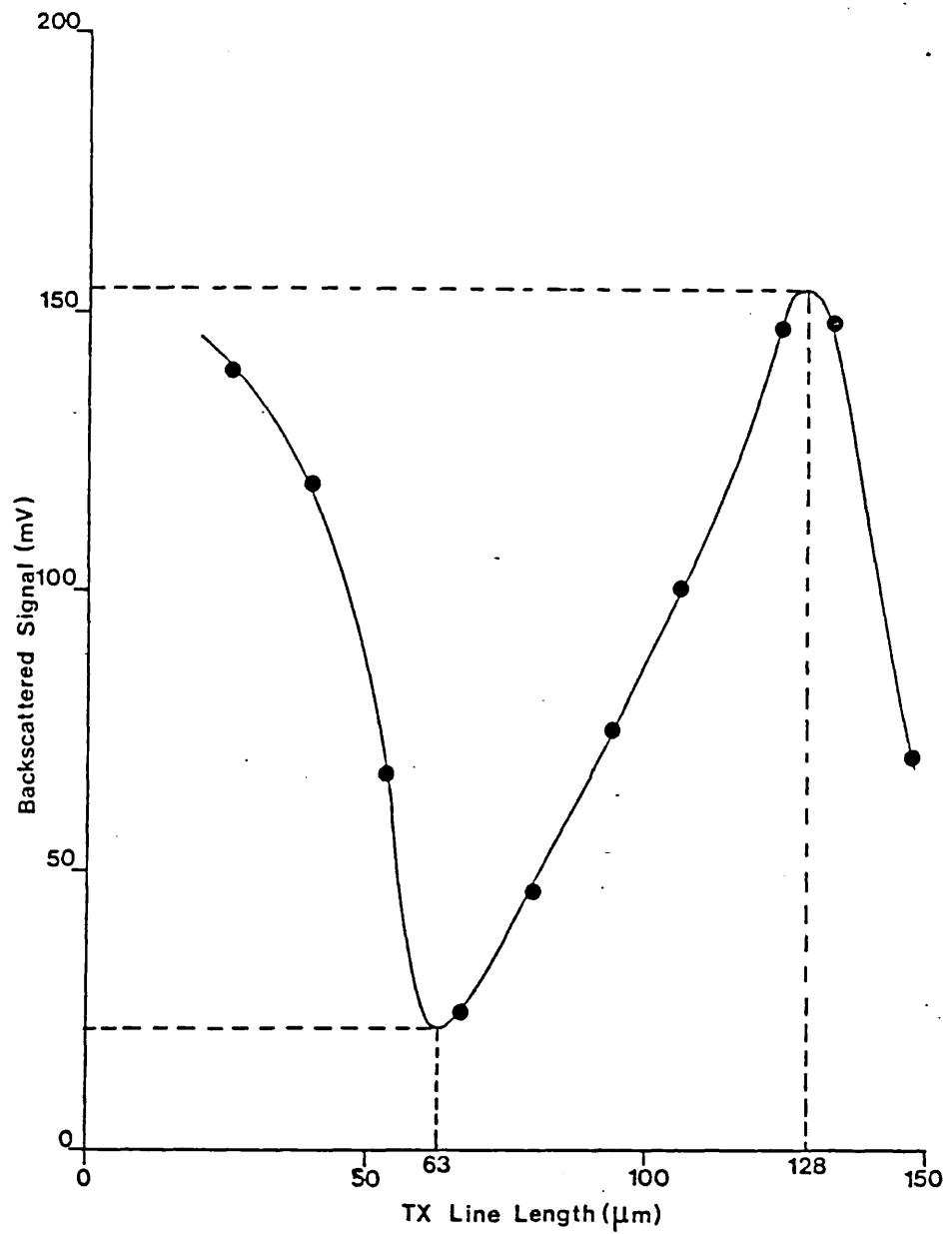


Figure 10.21. Variation of backscattered signal from a vee antenna with the length of terminating short circuited transmission line reproduced on 6 μm thick mylar.



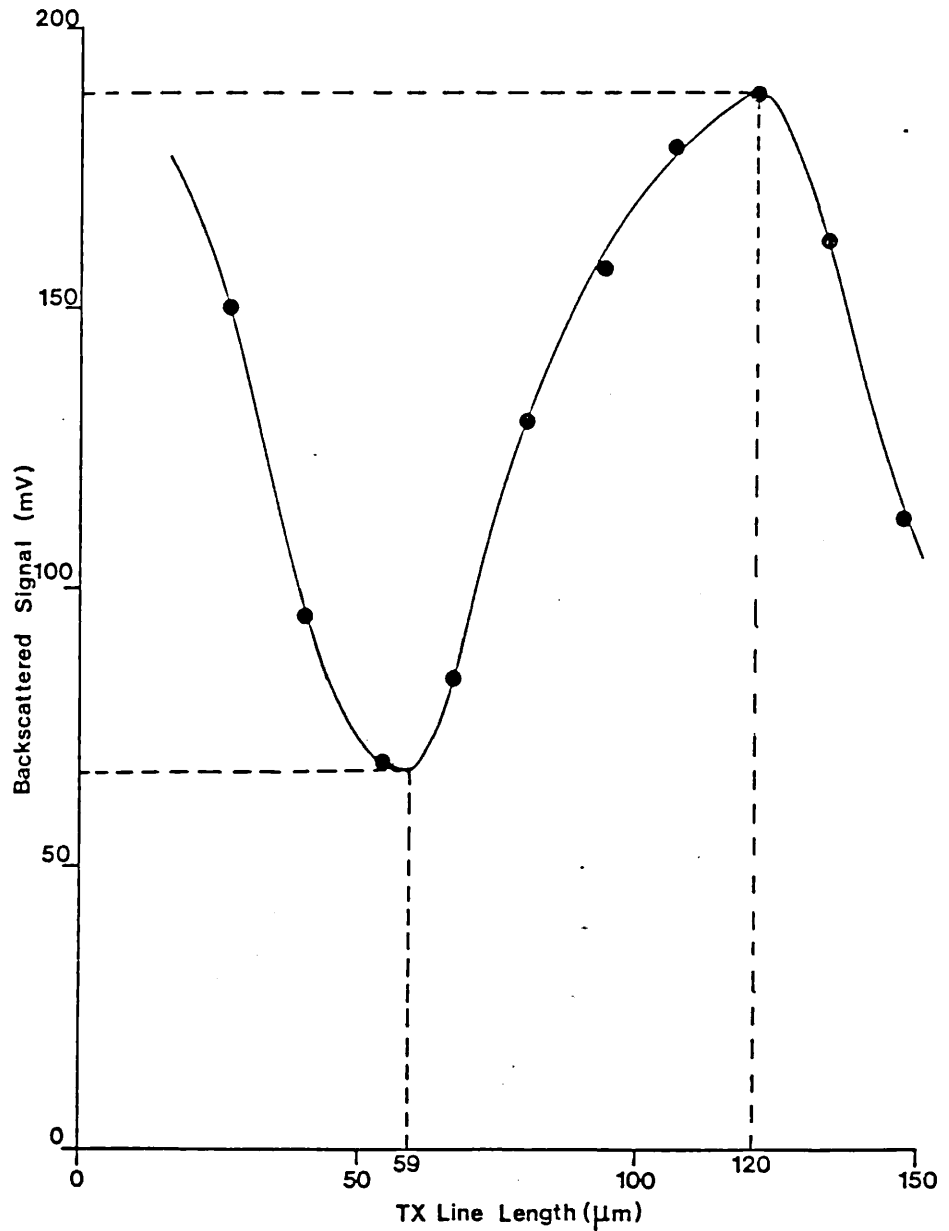


Figure 10.22. Variation of backscattered signal from a vee antenna with the length of terminating short circuited transmission line reproduced on 8 μm thick mylar.

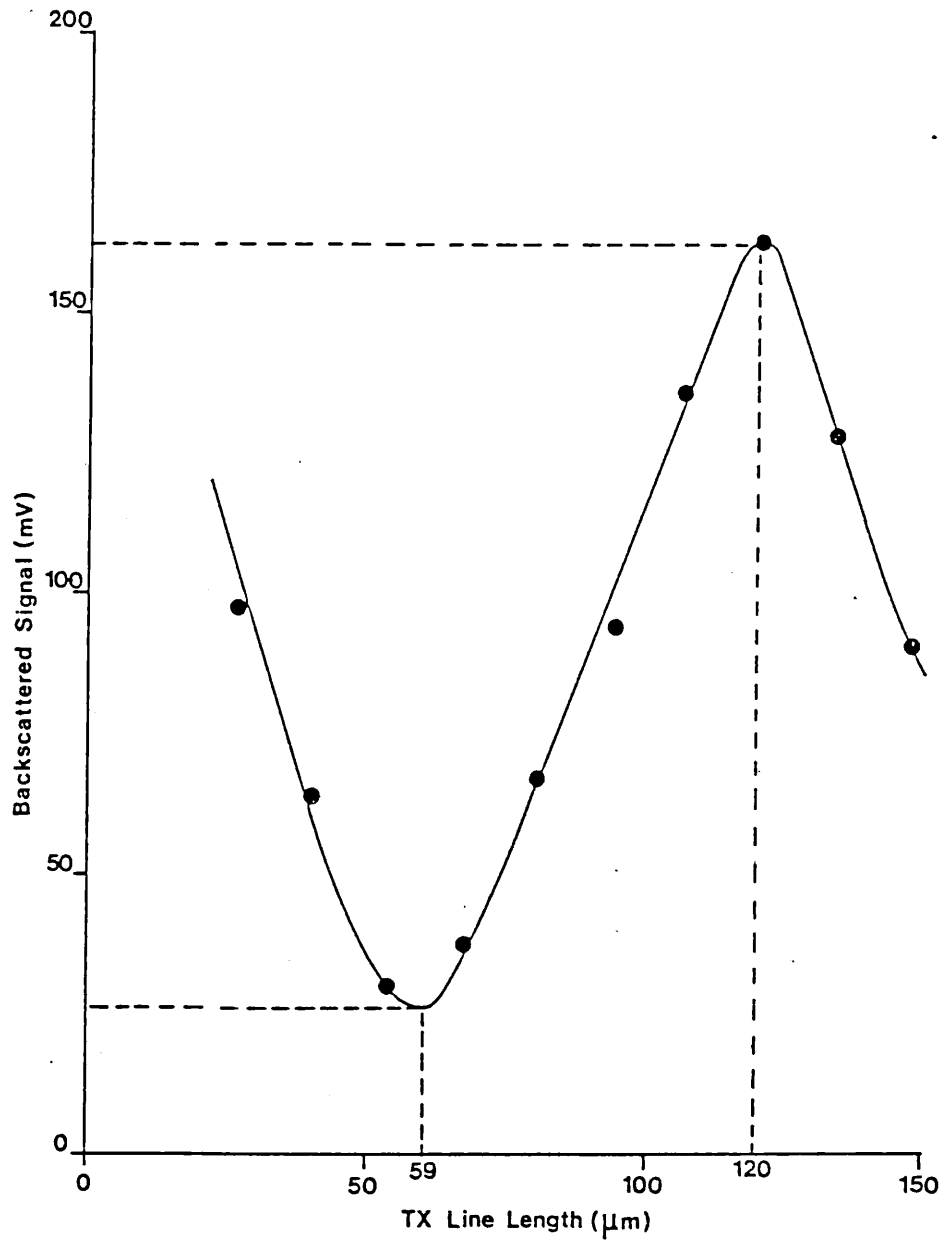


Figure 10.23. Variation of backscattered signal from a vee antenna with the length of terminating short circuited transmission line reproduced on a 8.9 μm thick mylar.

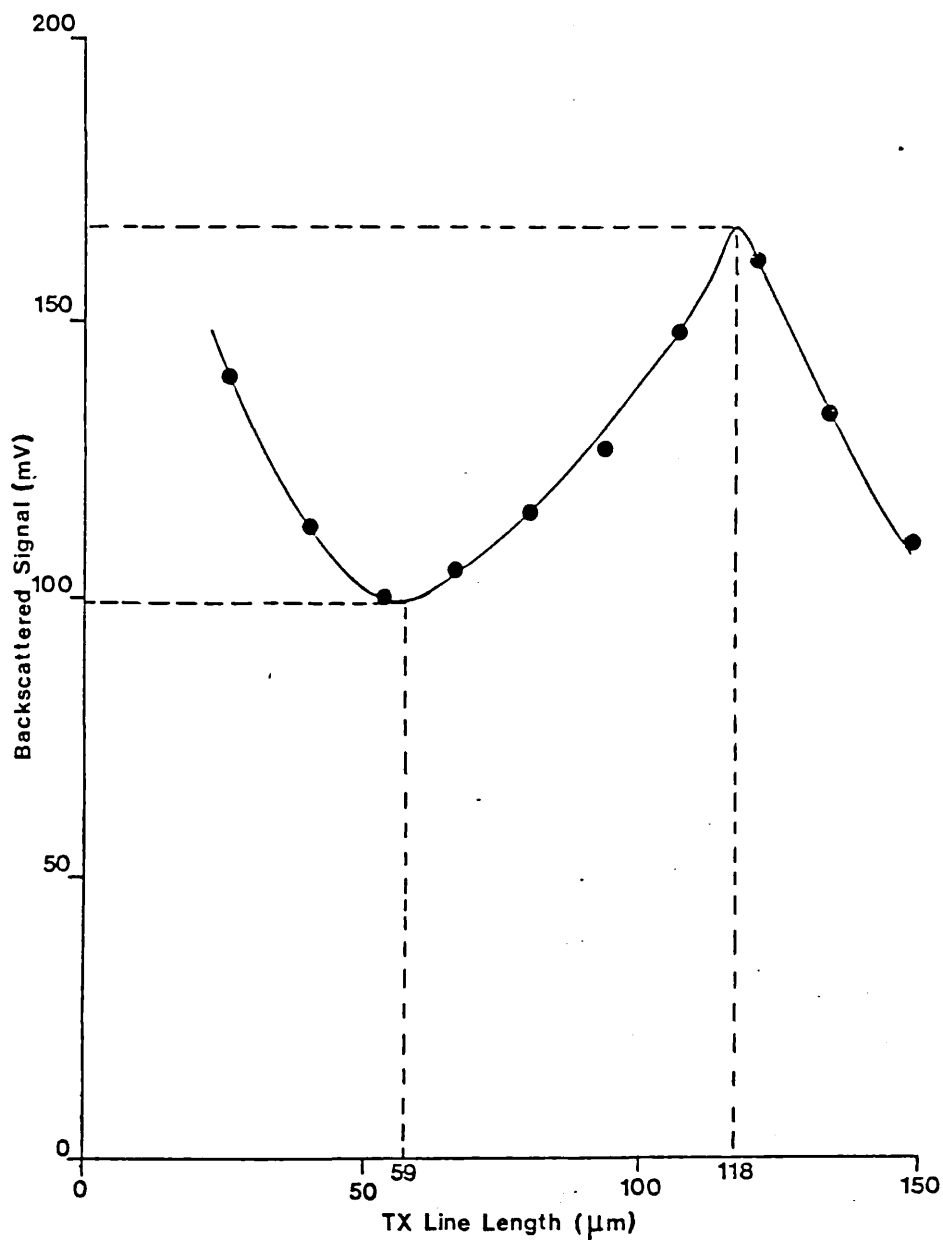


Figure 10.24. Variation of backscattered signal from a vee antenna with the length of terminating short circuited transmission line reproduced on 12.5 μm thick mylar.

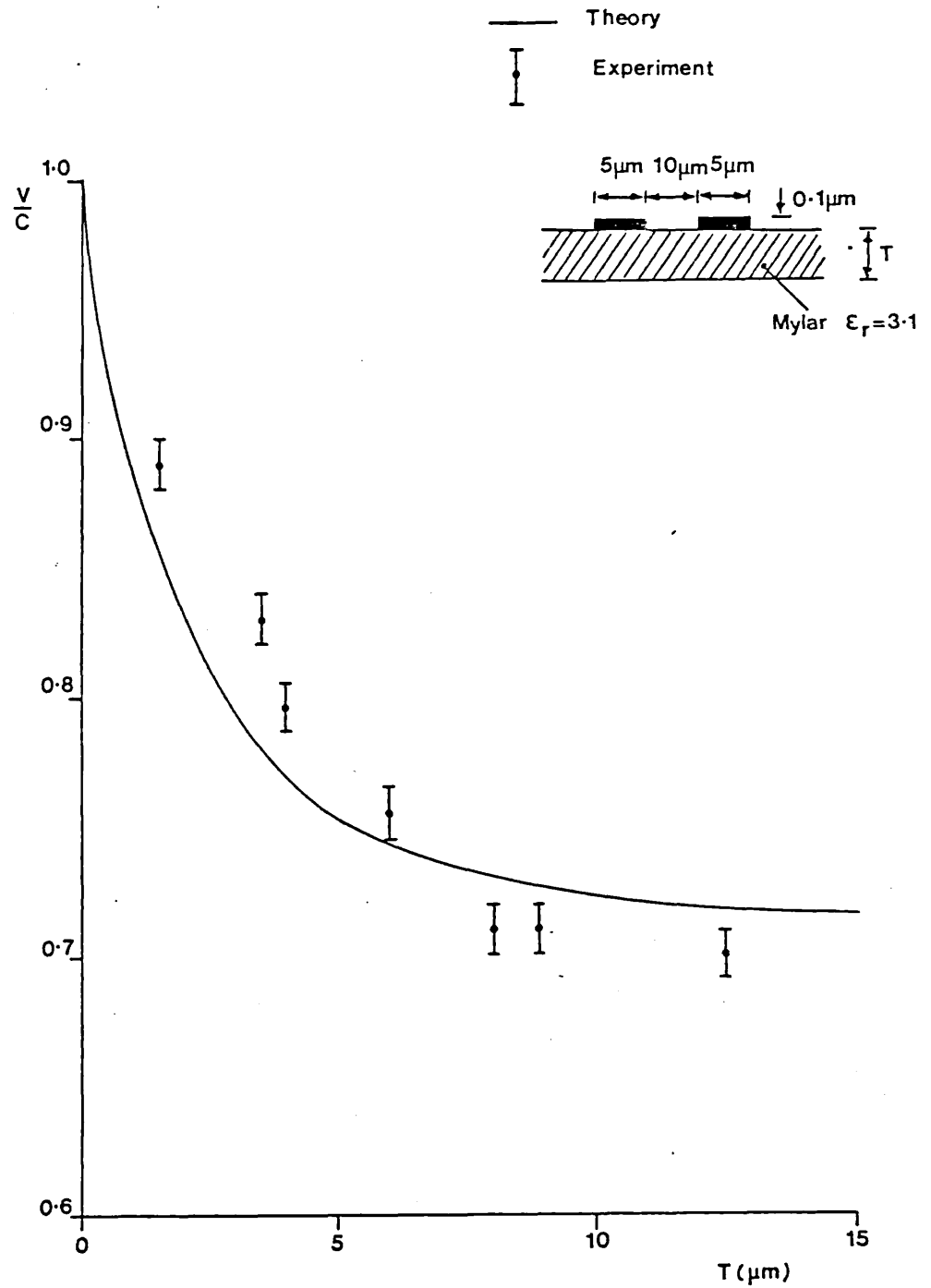


Figure 10.25. Variation of the velocity factor  $V/C$  with the substrate thickness  $T$  for the above coplanar line geometry.

for an attenuation of 2dB per guide wavelength. This error produces an uncertainty in  $V/C$  of  $\pm 5\%$ . It can be seen from Figure 10.25 that when the substrate thickness becomes comparable to the gap width between the transmission lines the velocity factor approaches the value it would have on a semi-infinite substrate where the effective relative permittivity is then the mean of the bulk value and the free space value.

It has been demonstrated that coplanar transmission lines are viable at submillimetre wavelengths, even on a substrate such as mylar which has relatively high absorption. The geometry of the coplanar line is fully compatible with the thin film technology employed. Also, the characteristic impedances obtainable with such lines are suitable for achieving a good impedance match with the dipole and vee structures. The range of impedances available is also compatible with devices such as planar Schottky barrier diodes which have impedances of typically  $70\ \Omega$  to  $100\ \Omega$  and also with microbolometers.

## CHAPTER ELEVEN

### CONCLUSIONS AND FURTHER WORK

The investigations made in this programme of work were approached with the aim of studying the fundamental physical behaviour of standing wave antennas at submillimetre wavelengths. To obtain rugged devices, that would be suitable for practical applications, it is necessary to support the antennas on a suitable substrate. It was felt that array structures, in which the elements of the arrays possessed resonant properties, would be more useful than travelling wave antennas because the main lobe of the array could be designed to lie in a direction perpendicular to the plane of the substrate, which is more convenient than the "end-fire" geometry.

These arrays were investigated from the standpoint of their scattered energy distribution which is determined by the currents flowing in the antenna conductors. Knowledge of the antenna current distributions is essential if antenna structures are to be designed and implemented in practical applications with confidence. Large aperture arrays possessing large electrical cross-sections could then be produced. Such arrays could be used for transducing radiation in the beam waist of a free space beam mode propagation system into a conduction current flowing in small active or passive devices connected across the antenna terminals.

From the studies of vee antennas (which are travelling wave structures) it was found that, provided the substrate was kept sufficiently thin ( $\approx 1.5 \mu\text{m}$  for mylar), the antenna pattern was not seriously affected by the substrate itself. However, in thicker  $3.5 \mu\text{m}$  mylar substrates a trough appeared in the H-plane scattering pattern of the vee antenna. This trough was thought to be the result of waves becoming excited within and guided by the substrate. Consequently, dipole arrays with broadside or

"end-fire" patterns are both practicable on sufficiently thin substrates. Clearly, in order to achieve an "end-fire" radiation pattern it would be necessary to produce phase differences of the order of  $180^\circ$  between successive elements<sup>92</sup>. This could be achieved by interconnecting the elements with lengths of transmission line, and reversing the polarity of the elements between successive elements. A possible design for such an array, realised in planar geometry, is shown in Figure 11.1. An alternative approach would be to use a Yagi array where the mutual impedances existing between elements provide the necessary phase of excitation to produce an "end-fire" pattern.

Returning to the broadside arrays which were initially investigated, the results obtained for the total scattering cross-sections of the parasitically coupled dipole arrays indicated that a conductor loss of the order of 0.11 dB per wavelength did not seriously modify the current distribution in practice. It was also found that the greater part of the antenna element velocity factor was due to the effect of the substrate itself.

The E and H-plane backscattering patterns agreed well with those predicted theoretically, and this suggested that the form of the current distributions and the mutual coupling between elements had been accurately accounted for. Particularly good agreement was obtained for arrays with element halflengths ranging from  $0.25\lambda$  to  $0.5\lambda$  which were of greatest practical interest.

Even in the simplest cases, the exact current distribution in the array elements is complex. Approximations are usually unavoidable, and it is essential that the relative importance of various factors affecting the current distribution be well understood. The factors affecting the current distribution may be grouped as follows :-

- (1) Effects of size, shape and proximity of conductors.
- (2) Effects of discontinuities, such as sudden changes in radius of the antenna, or sudden divergence of

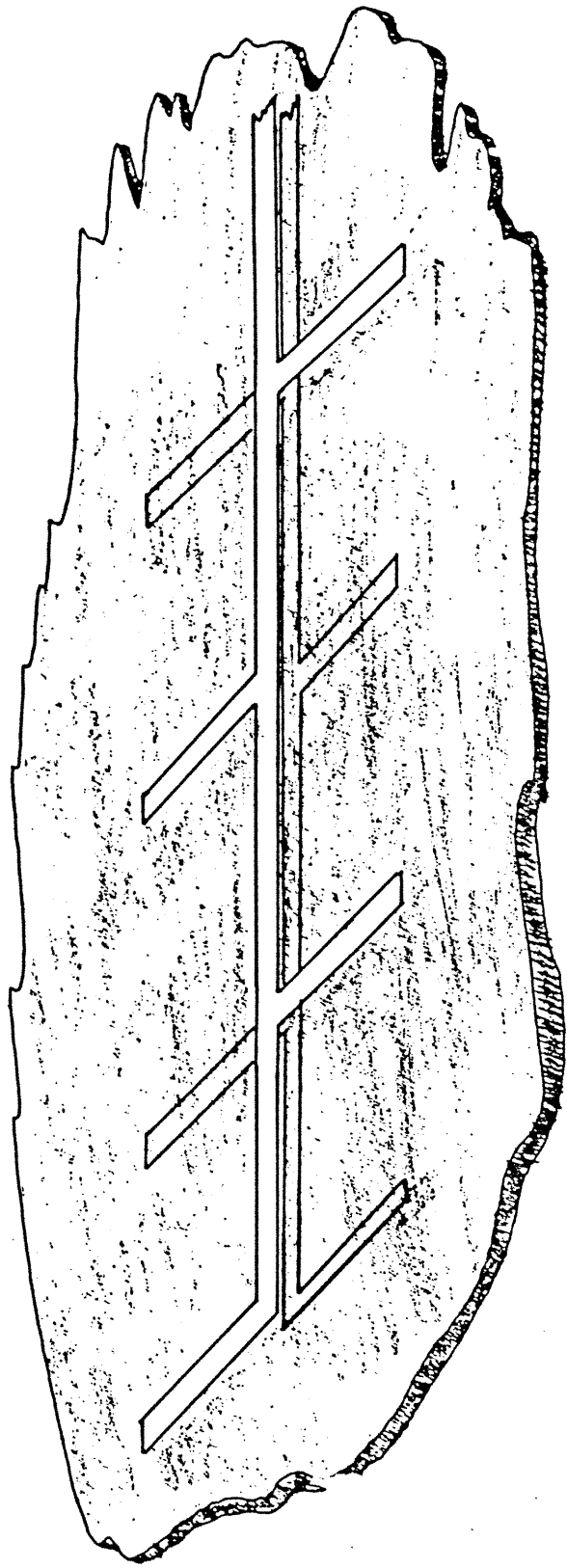


Figure 11.1. End-fire antenna array structure on thin-dielectric substrate.



previously closely spaced wires.

- (3) Effects due to the distribution of power.
- (4) Effects due to the distribution of generators or to the impressed field.
- (5) Effects due to the resistance of conductors.
- (6) Effects of proximity between the antenna terminals.

In the first approximation it was assumed that the current in a thin antenna was distributed exactly as in a transmission line and was therefore sinusoidal. This assumption, first made by Pocklington<sup>93</sup>, states that the source of excitation is localised, such as a voltage generator connected across the antenna terminals. However, the current distribution due to several localised sources or to a continuous distribution of the impressed field is obtained by superposition of sinusoidally distributed currents, and thus will not appear sinusoidal, even approximately.

Therefore, the current in a transmitting antenna may be described quite accurately by a sinusoid, but the distribution will be quite different when the same configuration is used as a receiving or scattering antenna. For a current distribution flowing in the Z direction  $I(Z)$ , centred symmetrically about the origin of a spherical polar co-ordinate system in free space, the far field radiation density,  $K$ , is given by

$$K = \frac{\eta}{8 \lambda^2} \left| \int_{-L}^{+L} I(Z) \cos k_0 Z \cos \theta \, dZ \right|^2 \sin^2 \theta \quad (11.1.)$$

where  $2L$  is the total linear extent of the current distribution,  $\eta$  is the intrinsic impedance of free space,  $\lambda$  is the free space wavelength and  $k_0 = 2\pi/\lambda$ . It is evident that the radiation pattern  $K(\theta, \phi)$  will be strongly dependent upon the current distribution  $I(Z)$ .

The asymptotic current distributions<sup>25</sup> are simple and are determined from boundary conditions at the generator, at the junctions, and at the end of the wire. For a dipole antenna shown in Figure 11.2, connected to a generator by a parallel wire transmission line, the current is sinusoidally distributed. A general equation for the current

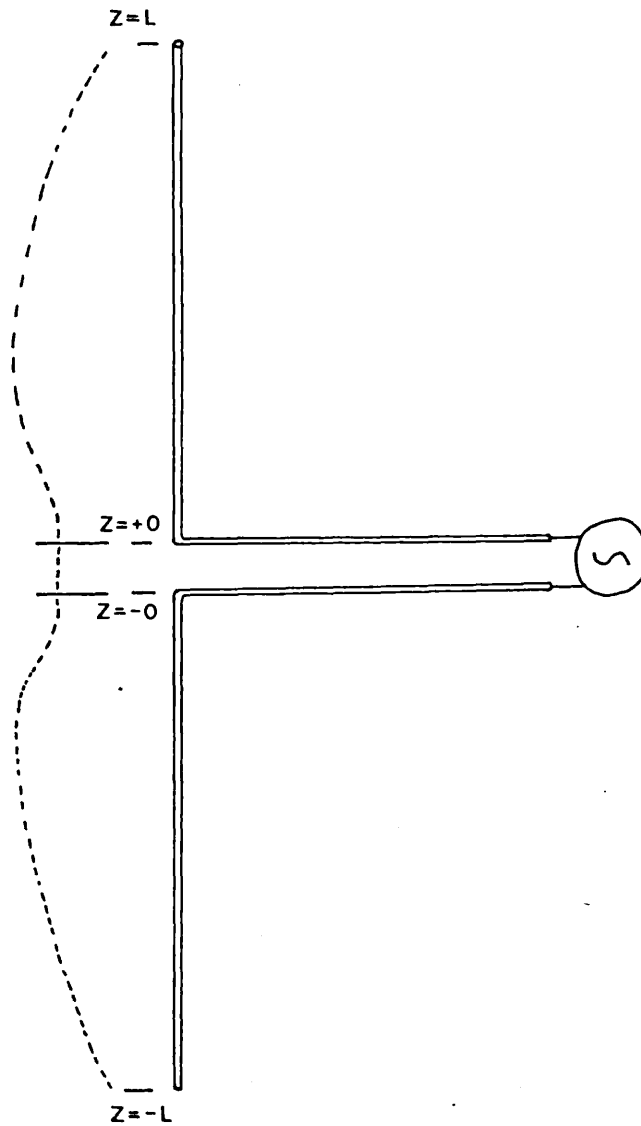


Figure 11.2. Asymptotic current distribution in a symmetrically fed dipole antenna of halflength  $L$ .

distribution is

$$\begin{aligned} I(Z) &= A_1 \cos \beta Z + B_1 \sin \beta Z & Z > + 0 \\ &= A_2 \cos \beta Z + B_2 \sin \beta Z & Z < - 0 \end{aligned} \quad (11.2.)$$

where the propagation constant in the wire is  $\beta$ . At the end of the wires,  $Z = \pm L$ , the current must vanish in the limit.

$$I(L) = I(-L) = 0 \quad (11.3.)$$

It also follows since the generator and the transmission line form a balanced system.

$$I(+0) = I(-0) \quad (11.4.)$$

Hence from equations 11.2 and 11.3

$$\begin{aligned} A_1 \cos \beta L + B_1 \sin \beta L &= 0 \\ A_2 \cos \beta L - B_2 \sin \beta L &= 0 \end{aligned} \quad (11.5.)$$

In the first of equations (11.5.) we can express  $B_1$  in terms of  $A_1$  or both in terms of some new constant  $I_1$ . The second equation is similar. Thus

$$\begin{aligned} A_1 &= I_1 \sin \beta L & B_1 &= -I_1 \cos \beta L \\ A_2 &= I_2 \sin \beta L & B_2 &= -I_2 \cos \beta L \end{aligned} \quad (11.6.)$$

substituting into equation 11.2

$$\begin{aligned} I(Z) &= I_1 \sin \beta (L - Z) & Z > + 0 \\ &= I_2 \sin \beta (L + Z) & Z < - 0 \end{aligned} \quad (11.7.)$$

From equation 11.4  $I_2 = I_1 = I_0$  and so

$$\begin{aligned} I(Z) &= I_0 \sin \beta (L - Z) & Z > + 0 \\ &= I_0 \sin \beta (L + Z) & Z < - 0 \end{aligned} \quad (11.8.)$$

A reflecting antenna is simply a wire in an electromagnetic field (which is equivalent to a short-circuited receiving antenna). The current in a reflecting antenna is obtained by noting that the current in a infinitely long wire in a uniform field parallel to the wire is constant. In a finite wire the current must vanish at the ends, which must, therefore, act as virtual sources of waves on the wire. The electric charge associated with the uniform current would tend to concentrate at the ends, and the

increasing force due to it would oppose the flow of charge. The ends of the wire act as point generators and the current distribution due to them is therefore sinusoidal. The total current in a wire extending from  $Z = -L$  to  $Z = +L$  due to a uniform field parallel to the wire is thus

$$I(Z) = A + B \cos \beta Z \quad (11.9.)$$

There can be no sine term because  $I(-Z) = I(Z)$ . Since  $I(-L) = I(L) = 0$ , then

$$A = -B \cos \beta L \quad B = \frac{-A}{\cos \beta L} \quad (11.10.)$$

hence

$$\begin{aligned} I(Z) &= B (\cos \beta Z - \cos \beta L) \\ &= \frac{A (\cos \beta L - \cos \beta Z)}{\cos \beta L} \end{aligned} \quad (11.11.)$$

In terms of the current at the centre of the wire

$$I(Z) = I(0) \frac{\cos \beta Z - \cos \beta L}{(1 - \cos \beta L)} \quad (11.12.)$$

For short dipoles  $L \leq \lambda/4$  the current distributions in transmitting and reflecting antennas are alike, to the present order of approximation, but similarity disappears for longer lengths. Figure 11.3 illustrates some of the differences between the transmitting and the scattering patterns for various lengths of the element.

In a receiving antenna there is in addition a load impedance  $Z$ . The voltage across the load is  $ZI$ , and the load acts as a virtual generator with an output voltage of  $-ZI$ . Therefore, the current in a receiving antenna in response to a uniform field parallel to the antenna will be the sum of a current distribution of the form existing in a scattering antenna and a current distribution of the form existing in a transmitting antenna. Thus for a load in the centre,  $Z = 0$ , the current is

$$\begin{aligned} I(Z) &= I_0 \sin \beta (L - |Z|) \\ &\quad + B (\cos \beta Z - \cos \beta L) \end{aligned} \quad (11.13.)$$

the constants  $I_0$  and  $B$  depend on the impressed field, the wire length, the wavelength, the wire radius and the

Transmitting antenna.  
 (Current distribution assumed  
 sinusoidal  $I_z = I_0 \sin(\beta|L-Z|)$ )

Reflecting antenna.  
 (Assumed current distri-  
 bution  $I_z = I_0 \frac{\cos \beta Z - \cos \beta L}{1 - \cos \beta L}$ )

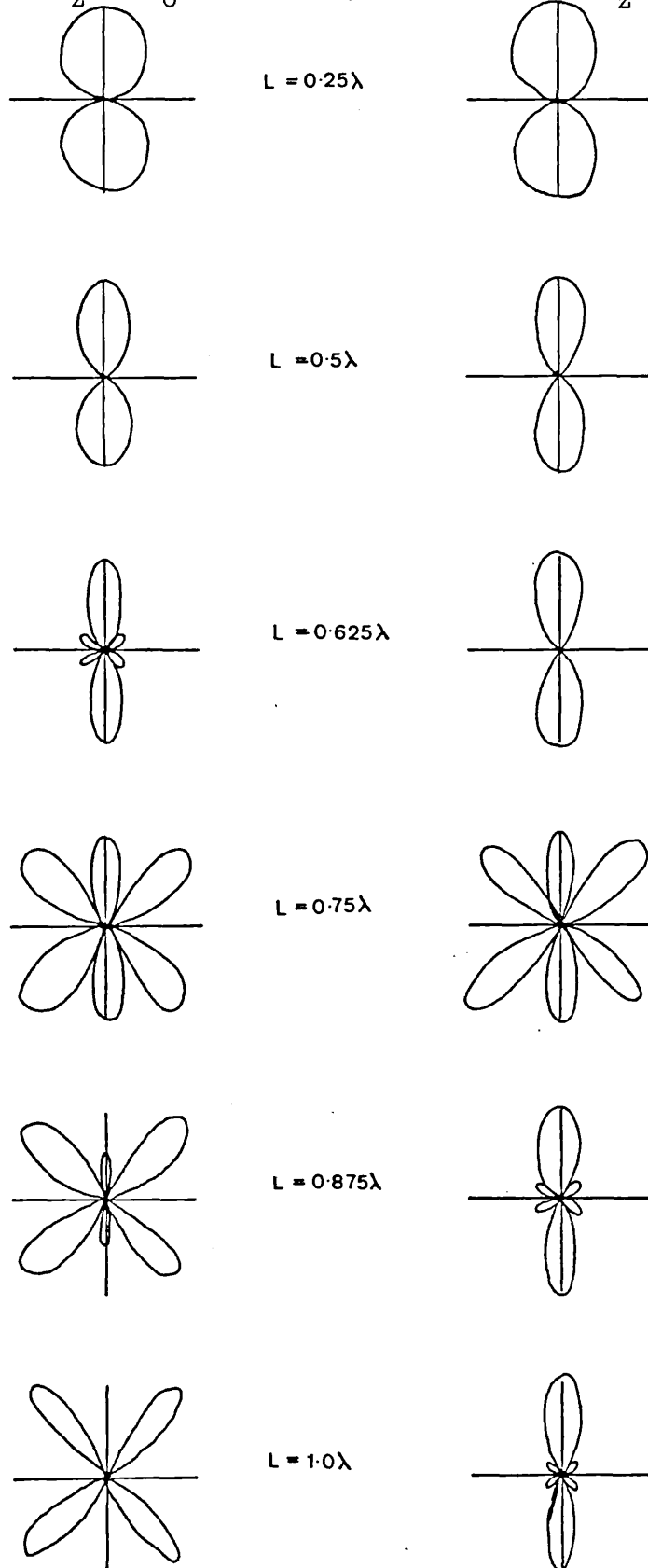


Figure 11.3 Radiation (electric field) patterns for transmitting and reflecting dipole antennas of halflength  $L$ . (Reference 82).

load impedance. The pattern for a receiving dipole is usually similar to its transmitting pattern.

It has been demonstrated that the geometry of the coplanar transmission line is well suited to the thin film technology employed and its properties and calculable at submillimetre wavelengths. Furthermore it was possible to achieve a good impedance match to a single dipole or an array with halflengths in the range  $0.25\lambda$  and  $0.5\lambda$  with these lines. Therefore, there arose the possibility of constructing an antenna coupled video receiver based upon the technology developed here. Microbolometers of the type developed by Rutledge et al<sup>94,95</sup> are an obvious choice for detector elements. These would be eminently suitable for integrating onto thin mylar films. A possible antenna geometry is shown in Figure 11.4. A co-linear dipole array would be the most suitable because the outputs of the individual microbolometers could be connected in series or parallel to produce a high output signal or low output impedance. The stages required to produce such an array is illustrated in Figures 11.5 (a), (b), (c) and (d). Using this technique the device could be produced from a single mask. This would eliminate the need for multiple mask alignments. However, it has been found that the differential etch rate of the two metals employed, bismuth and silver, in the most suitable wet chemical etches, results in a "lifting off" of the silver metallisation. This is because bismuth is much more reactive than silver.

Radio frequency sputter etching<sup>80,96, 97,98</sup> of the substrate in argon gas at low pressure ( $< 10^{-4}$ Pa) has been proposed as a possible solution to this problem. It is a non-specific etching technique and relies on ion bombardment to remove the unwanted metallisation from an insulating substrate. The photoresist that was employed for the wet chemical etching process would still be suitable as a protective layer in the sputter etching process. The etch rate of the photoresist is comparable to that of most metals. As the resist thickness is typically in the range

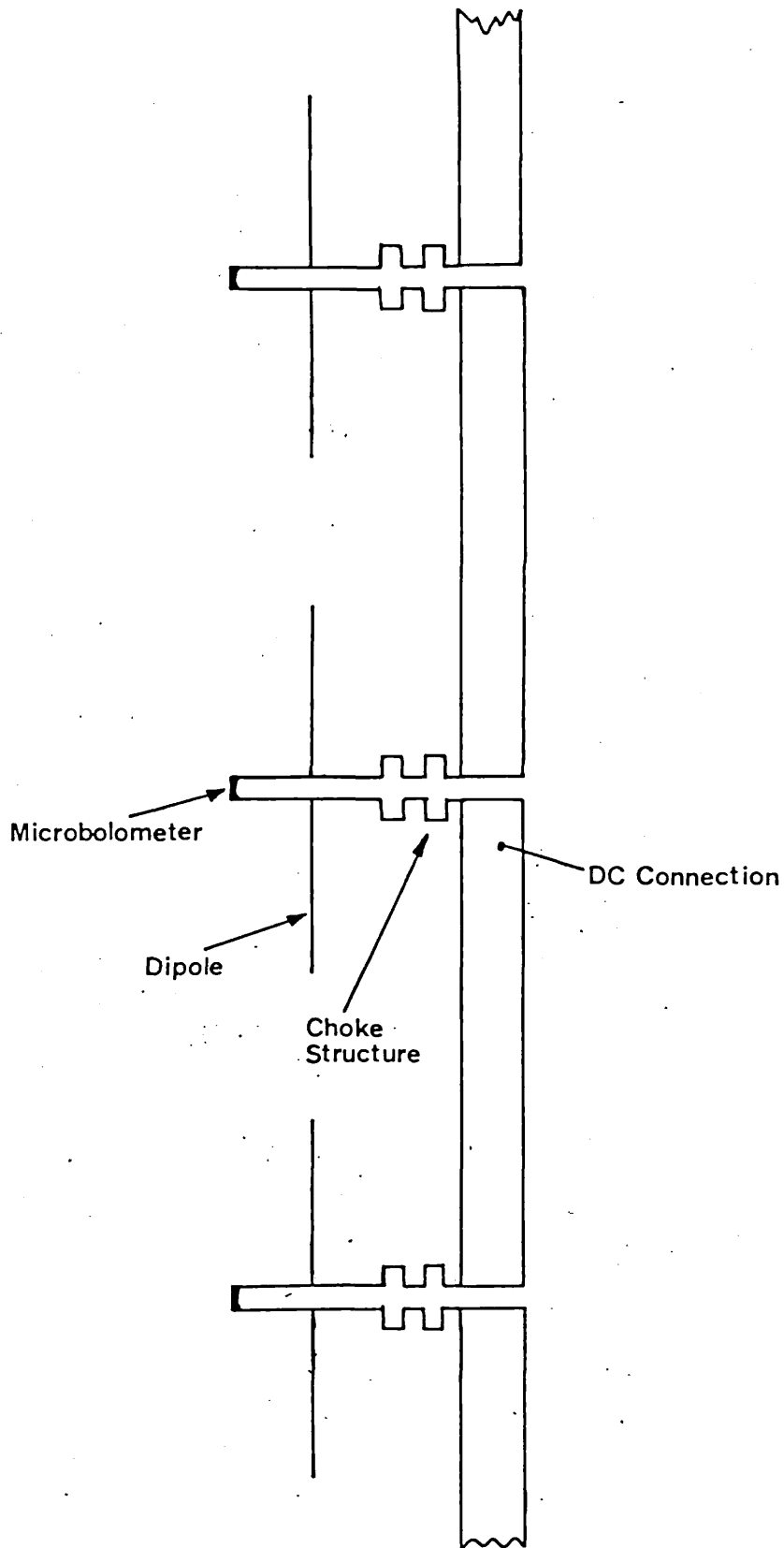


Figure 11.4. Proposed design for a co-linear dipole array with series connected microbolometers.

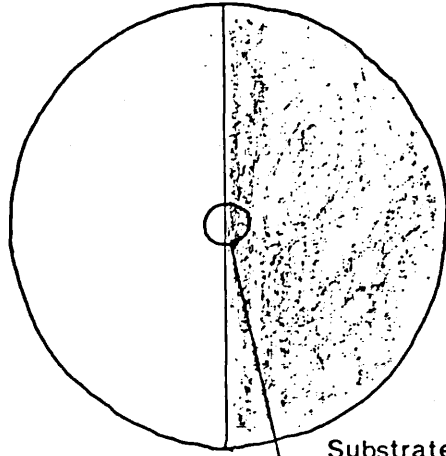


Figure 11.5(a). A bismuth layer is deposited on substrate. A silver layer is deposited over the bismuth and covers half of the substrate.

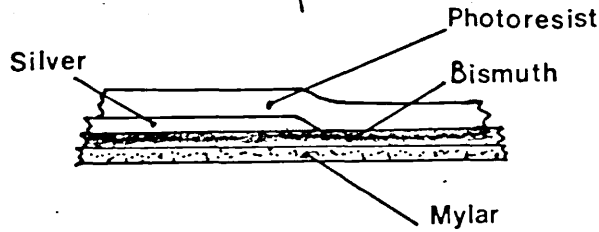


Figure 11.5. (b). Detail of substrate layers. A photoresist layer covers the metalisation.

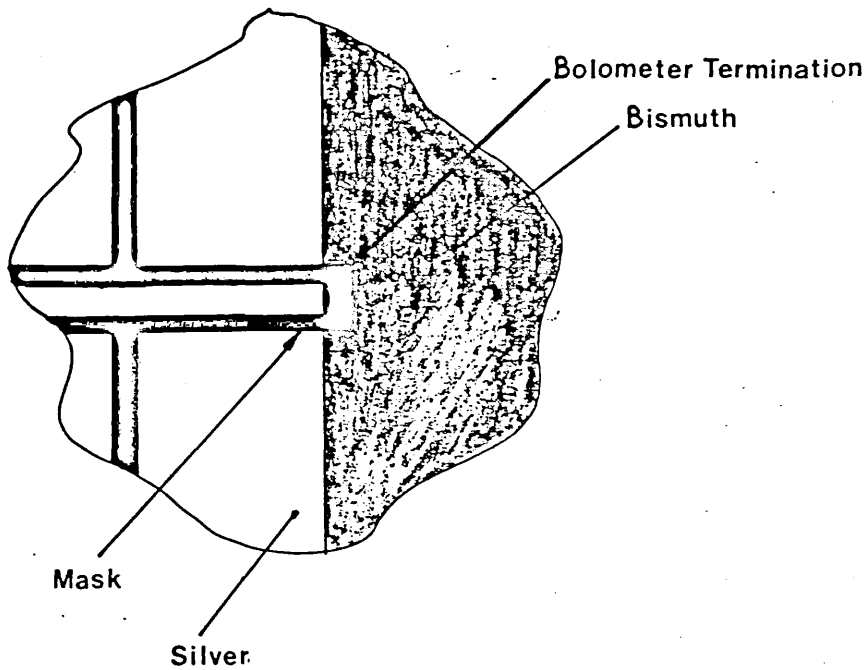


Figure 11.5. (c) The mask is aligned over the substrate so that the microbolometer elements lie on the bismuth side of the bismuth/silver interface.



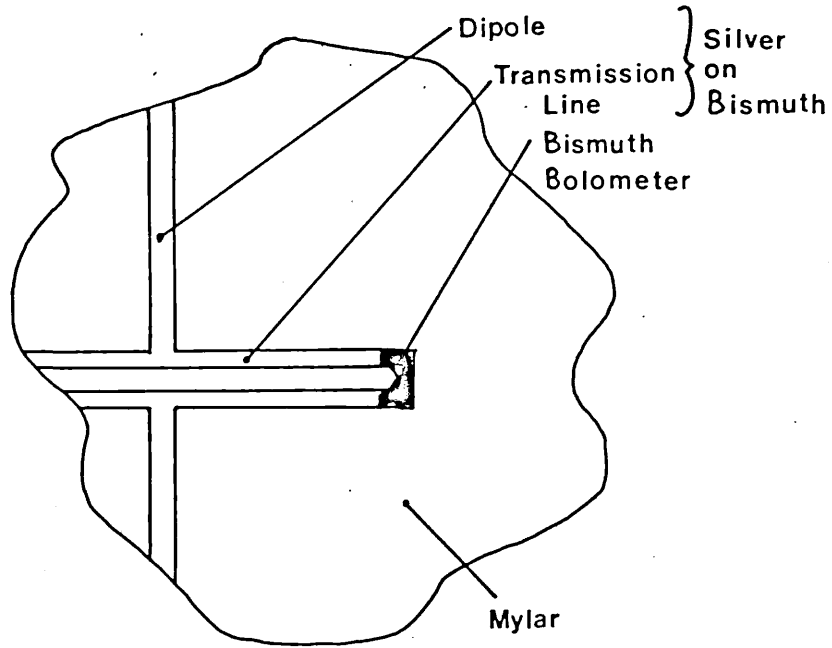


Figure 11.5. (d) The finished antenna/bolometer structure after etching and resist removal.

1 to 3  $\mu\text{m}$  and that of the metallisation 0.1 to 0.2  $\mu\text{m}$ , then the unwanted metallisation should be removed before the resist mask was appreciably attacked. The R.F. sputter etching technique is also free from undercutting because the ions impinge normally onto the substrate. A schematic representation of a R.F. sputter etching plant is shown in Figure 11.6.

To achieve a viable design for a microbolometer, it is necessary to consider the thermodynamic principles underlying its action. Consider a bolometer of area  $A$  lying on a substrate. Currents produced by the radiation incident upon the bolometer/antenna increase the temperature of the bolometer from  $T_0$  to  $T_0 + \Delta T$ . If the frequency of the incoming radiation is  $f$ , then the heat balance equation for the bolometer is

$$2\pi j f C \Delta T + G(f) \Delta T = W \quad (11.14.)$$

where  $C$  is the thermal capacity of the bolometer,  $G(f)$  is the thermal conductance between the bolometer and the environment and the incoming signal power is  $W$ . The output voltage obtained,  $V$ , is given by

$$V = \alpha V_B \Delta T \quad (11.15.)$$

where  $\alpha$  is the temperature co-efficient of resistance for the bolometric material.  $V_B$  is the bias voltage and it is assumed that the load resistance is approximately equal to the bolometer resistance

$$\alpha = \frac{1}{\rho} \left\{ \frac{d\rho}{dT} \right\} \quad (11.16.)$$

$\rho$  is the resistivity of the bolometric material. From equations 11.14 and 11.15

$$V = \frac{\alpha V_b W}{2\pi j f C + G(f)} \quad (11.17.)$$

Usually  $2\pi j f C \ll G(f)$  and so may be neglected.

The thermal conductance,  $G$ , between the bolometer and its environment is the sum of that between the bolometer and air,  $G_A$ , the substrate,  $G_S$ , and the metal conductors,  $G_M$ .

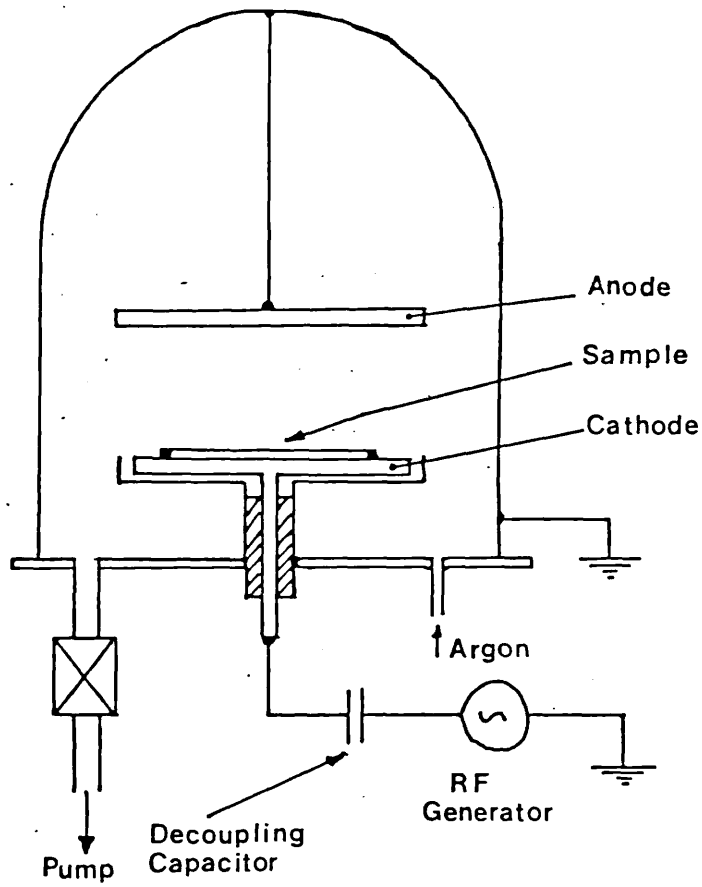


Figure 11.6. Schematic diagram of a R.F. sputter etching plant. (From Reference 80.)

Therefore

$$G = G_A + G_S + G_M \quad (11.18.)$$

As the thermal conductance between the bolometer and air,  $G_A$ , is so small it can be neglected.

$$G(f) = G_S(f) = G_M(f) \quad (11.19.)$$

For the substrate

$$G_S(f) = \frac{K_S}{\Delta T} \int \nabla T \cdot dS \quad (11.20.)$$

where  $K_S$  is the thermal conductivity of the substrate and  $T$  the substrate temperature. The bolometer must obey the heat diffusion equation

$$K_S \nabla^2 T - 2\pi j f H_S T = 0 \quad (11.21.)$$

where  $H_S$  is the heat capacity per unit volume of the substrate and is equal to the product of the specific heat capacity and the density of the substrate. If the bolometer/substrate contact is modelled as a hemisphere of radius  $a$ , of surface area equal to that of the actual contact then  $A = 2\pi a^2$ . At low frequencies, the substrate temperature will obey Laplace's equation so

$$T = T_0 + \Delta T (a/r) \quad (11.22.)$$

and 
$$G_S(0) = 2\pi a K_S \quad (11.23.)$$

As the frequency,  $f$ , increases the heat flow is still radial but

$$T = T_0 + \Delta T (a/r) \exp(-(r-a)/L_S) \quad (11.24.)$$

where  $L_S$  is the complex heat diffusion length and is given by

$$L_S = (K_S/2\pi j f H_S)^{\frac{1}{2}} \quad (11.25.)$$

Provided that  $|L_S| \gg a$ , which is true for low frequencies, then the new exponential factor has little effect on  $\nabla T$  at or near  $r = a$  and so

$$G_S(f) \approx G_S(0) \quad (11.26.)$$

The frequency  $f_1$  at which  $|L_S| = a$  is the -3dB response frequency of the bolometer and is given by

$$f_1 = \frac{K_S}{2\pi a^2 H_S} \quad (11.27.)$$

When  $f \gg f_1$

$$G \approx 2 \pi a^2 \frac{K_s}{L_s} \quad (11.28.)$$

The component of thermal conductance, arising due to the thermal contacts,  $G_M$ , is hard to calculate exactly, because thermal conductivity of the metal is much larger than that of the substrate. Hence the diffusion length in the metal,  $L_M$ , is much larger than that of the substrate,  $L_s$ . Hence, as an upper limit

$$|G_M| \approx \frac{K_M A'}{|L_s|} \quad (11.29.)$$

where  $K_M$  is the thermal conductivity of the metal and  $A'$  is the effective cross-sectional area of the metal contacts.

The heat capacity of the bolometer,  $C$ , is given by

$$C = p A t C_s \quad (11.30.)$$

where  $p$  is the density of the bolometer material,  $t$  is the bolometer thickness and  $C_s$  is the specific heat capacity of the bolometric material. Because the bolometer is purely resistive, the noise component will be due to Johnson noise. Hence the noise equivalent power (NEP) of the bolometer is given by

$$NEP = \frac{(4 K T R_o)^{\frac{1}{2}}}{V/W} = \frac{(4 K T R_o)^{\frac{1}{2}}}{S} \quad (11.31.)$$

where  $S$  is the voltage responsivity of the bolometer.

Figure 11.7 shows the proposed geometry of the bolometer. Table 11.1 lists the physical constants, relevant to the bolometer and substrate materials, which were used to calculate the values given below. The -3dB point for the bolometer,  $f_1$ , was calculated to be 375 Hz. The best case prediction for the responsivity and NEP of the bolometer was made by ignoring metallic conduction arising from the transmission line. The best case voltage responsivity was then found to be  $7.4 \text{ V Watt}^{-1}$  and the

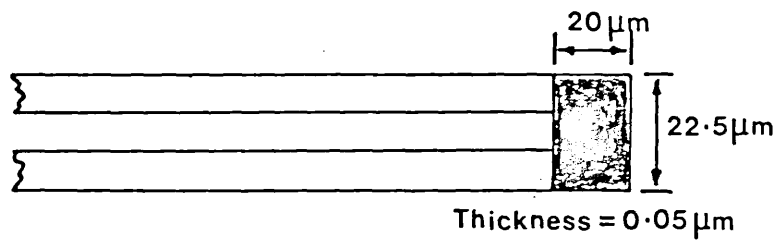


Figure 11.7. Proposed microbolometer geometry.

TABLE 11.1.

---

Physical Constants for a Bismuth Bolometer  
on a Mylar Substrate used in the Calculations.

---

BISMUTH

Density*	9800 Kg m <sup>-3</sup>	
Specific Heat Capacity*		124 J Kg <sup>-1</sup> K <sup>-1</sup>
Temperature Coefficient of Resistancet	-3.3 x 10 <sup>-3</sup> K <sup>-1</sup>	
Thermal Conductivity*		8.4 W m <sup>-1</sup> K <sup>-1</sup>
Thin Film Resistivity†		5.98 x 10 <sup>-6</sup> Ω m

MYLAR

Density*	1375 kg m <sup>-3</sup>	
Specific Heat Capacity*		1250 J Kg <sup>-1</sup> K <sup>-1</sup>
Thermal Conductivity*		0.29 W m <sup>-1</sup> K <sup>-1</sup>

---

\* "Tables of Physical and Chemical Constants"  
Kaye G.W.C. and Laby T. 14th Ed. Longman 1975

† Reference 94

NEP for this case was  $2.13 \times 10^{-10} \text{ Watt Hz}^{-\frac{1}{2}}$ . The worse case predictions were calculated by allowing for a metal conductor contact area equal to that of the bolometer. The voltage responsivity was calculated to be  $1.16 \text{ V Watt}^{-1}$  and the NEP was  $1.36 \times 10^{-9} \text{ Watt Hz}^{-\frac{1}{2}}$ . The above predictions were made assuming that the temperature co-efficient of resistance,  $\alpha$ , for bismuth was that obtained by Rutledge et al<sup>94</sup> and was  $-3.3 \times 10^{-3} \text{ K}^{-1}$ , and the DC bias voltage applied to the bolometre was 35 mV. Measurements made on scaled up bolometers over the range  $0^\circ\text{C}$  to  $140^\circ\text{C}$  suggests that  $\alpha$  is  $-2.49 \pm 0.53 \times 10^{-3} \text{ K}^{-1}$  for bismuth films with thicknesses in the range 200 to 800 Å.

From the above predictions it can be seen that a video detector array possessing a useful responsivity could be produced.

It was found that the vee antenna with radially spreading conductors, which has previously been studied by Rutledge et al<sup>95,37</sup> at  $119 \mu\text{m}$  in a dielectric sandwich structure, also exhibited useful antenna patterns when reproduced on thin substrates. This type of antenna has the advantage that a single device can have appreciable power gain. Also, due to the radial spread of the conductors, the reactive component of the terminal impedance is negligible and so the problems of matching purely resistive devices to the antenna are reduced. An optimization study of the vee antenna structure at these frequencies, where surface impedance effects produce losses in the antennas, is worthy of further consideration.

With regard to possible further work on theoretical analysis of submillimetre antennas, it is worth considering in more detail the effect of the substrate on the element currents and on the mutual coupling between the array elements and hence the effect upon the resultant radiation patterns. This would be more important when designing antennas for integration on the surface of semiconductor substrates which tend to be relatively thick and possess high relative permittivities (for example Si,  $\epsilon_r = 11.6$



and Ga As,  $\epsilon_r = 12.4$ ). However, by the use of chemical etching techniques it is possible to thin down semiconductor substrates to thicknesses of the order of 10  $\mu\text{m}$ . The mathematical treatment of antennas on substrates of finite thickness is complicated and involves contour integration over a Riemann surface. The substrate itself could be used to help shape the radiation pattern by acting as a dielectric sheet<sup>21</sup> or rod antenna<sup>89</sup>. Anisotropic etch solutions can be employed to create quite complex three dimensional structures in silicon and other semiconducting materials. High resistivity silicon and gallium arsenide act as good dielectrics at submillimetre frequencies. The principal absorption mechanism in semiconductors at submillimetre wavelengths is free carrier absorption. The absorption length  $K$  for radiation with a free space wavelength  $\lambda$  is given by the expression<sup>99</sup>

$$K = \frac{\lambda^2 e^2}{4 \pi^2 C^3 n \epsilon_0} \left\{ \frac{N_d}{m_e^{*2} \mu_e} + \frac{N_a}{m_h^{*2} \mu_h} \right\} \quad (11.32.)$$

where  $n$  is the refractive index of the material,  $C$  is the velocity of light,  $\epsilon_0$  is the permittivity of free space and  $e$  is the electronic charge. The number density of donor impurities is  $N_d$ , the effective mass of the electrons is  $m_e^*$  and the electron mobility is  $\mu_e$ . The number density of acceptor impurities is  $N_a$ , the effective mass of the holes is  $m_h^*$  and the hole mobility is  $\mu_h$ .

Figures 11.8 and 11.9 show the variation of absorption length  $K$  with impurity concentration for p - type and n - type silicon respectively. Table 11.2 lists the parameters used to calculate these absorption lengths. It can be seen that for a given impurity concentration n - type silicon has a lower absorption length than p - type. This is because the electron mobility is higher than the hole mobility. For n -type silicon

$$K (\text{cm}^{-1}) = N_d (\text{cm}^{-3}) \times 4.2 \times 10^{-15}$$

TABLE 11.2.  
SEMICONDUCTOR PROPERTIES

---

Silicon (Si)	$\epsilon_r$	= 11.6
Electron mobility $\mu_e$		= $0.13 \text{ m}^2 \text{ V}^{-1} \text{ S}^{-1}$
Electron effective mass $m_e^*$		= $0.58 m_e$
Hole mobility $\mu_h$		= $0.05 \text{ m}^2 \text{ V}^{-1} \text{ S}^{-1}$
Hole effective mass $m_h^*$		= $0.3 m_e$
Gallium Arsenide (GaAs)	$\epsilon_r$	= 12.4
Electron mobility $\mu_e$		= $0.88 \text{ m}^2 \text{ V}^{-1} \text{ S}^{-1}$
Electron effective mass $m_e^*$		= $0.067 m_e$
Hole mobility $\mu_h$		= $0.05 \text{ m}^2 \text{ V}^{-1} \text{ S}^{-1}$
Hole effective mass $m_h^*$		= $0.5 m_e$
Free electron mass $m_e$		= $0.91 \times 10^{-30} \text{ Kg}$

---

Taken from Reference 99.

---

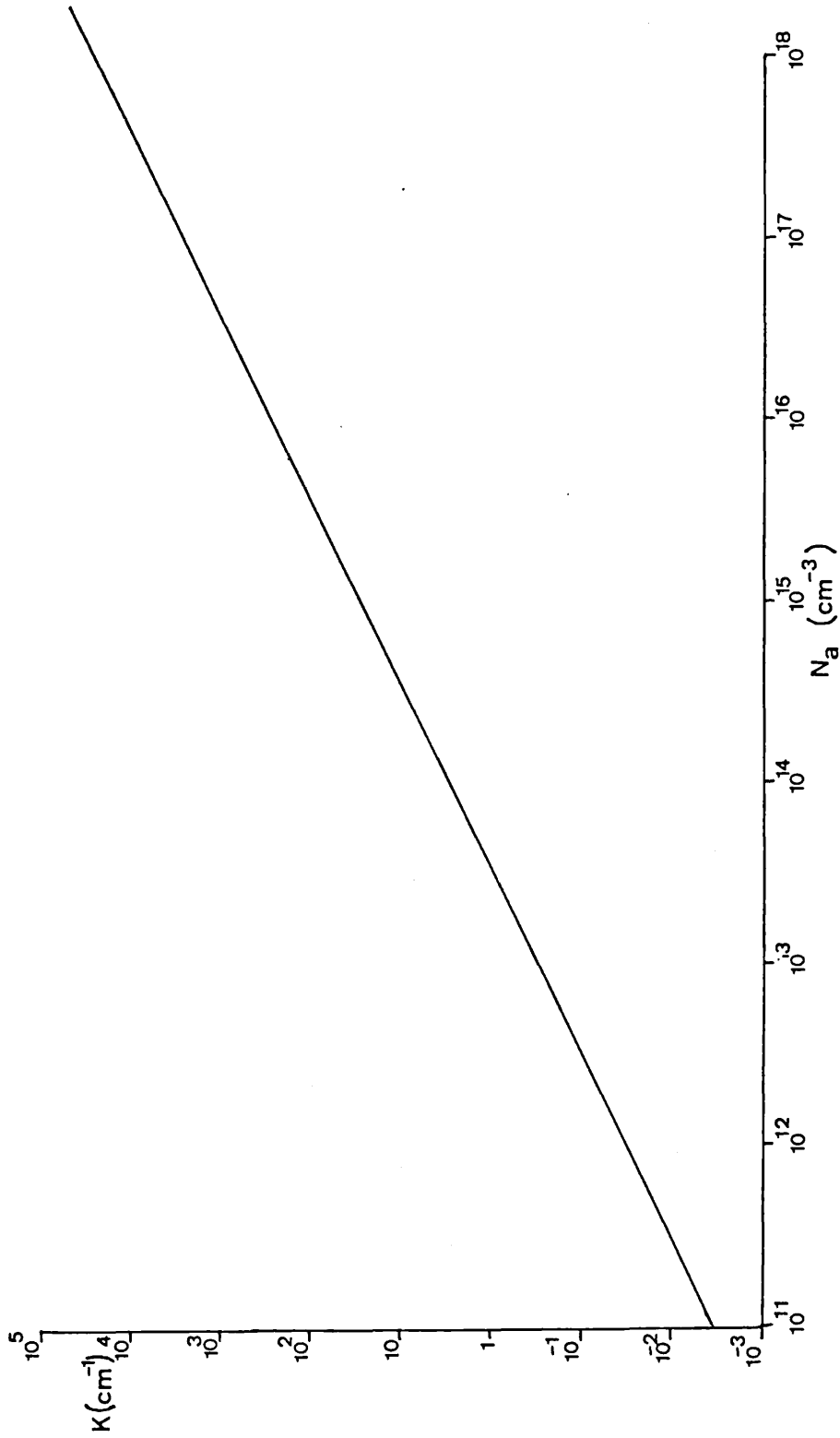


Figure 11.8. Variation of radiation absorption length,  $K$ , with acceptor impurity concentration in p - type silicon.

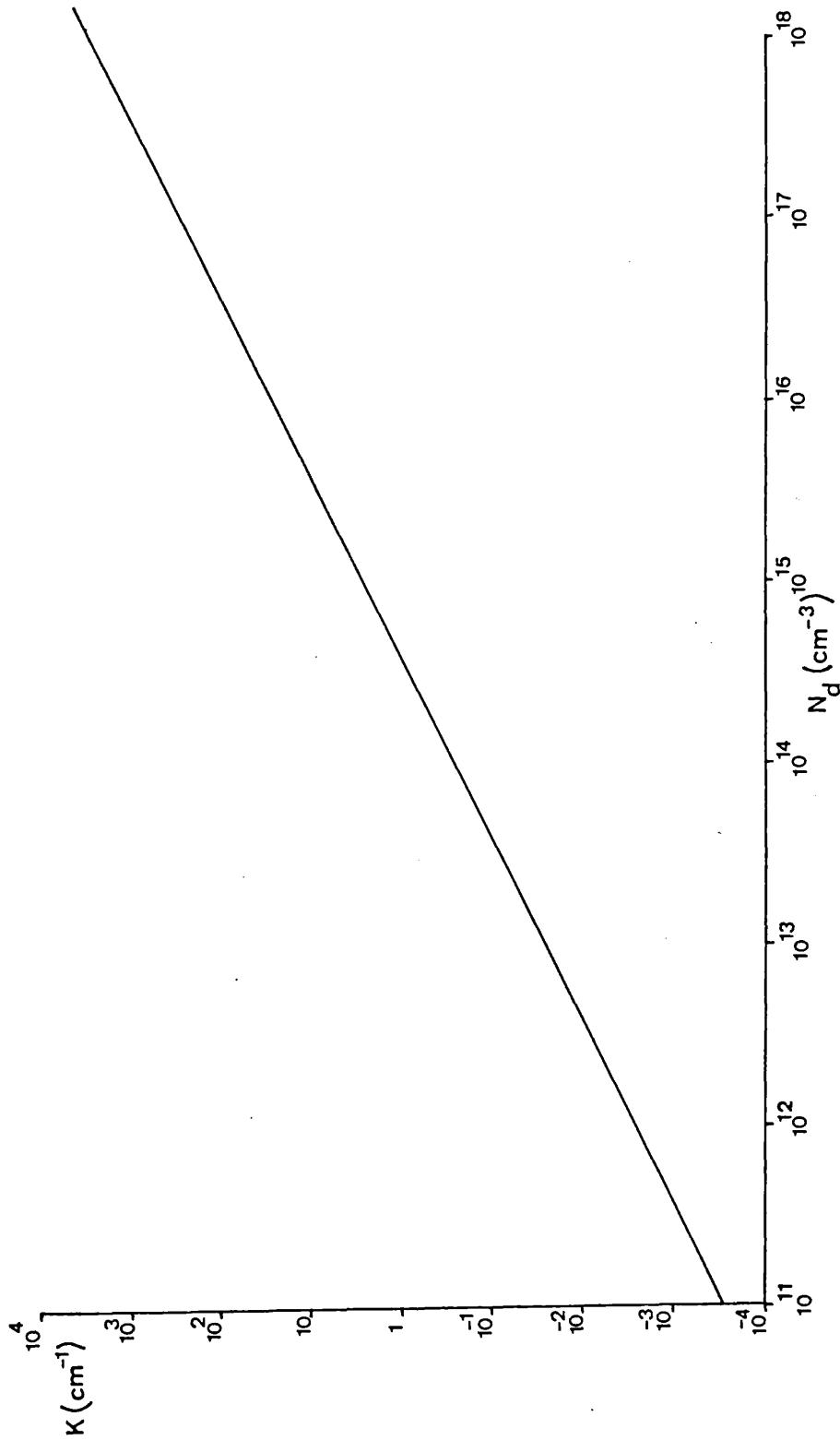


Figure 11.9. Variation of radiation absorption length,  $K$ , with donor impurity concentration in n - type silicon.

and for p - type silicon

$$K (\text{cm}^{-1}) = N_a (\text{cm}^{-3}) \times 3.7 \times 10^{-14}$$

The lowest impurity concentrations obtainable in silicon are  $\sim 10^{13}$  to  $10^{14}$  per  $\text{cm}^3$ . The lowest absorption lengths one can expect are in the range 0.1 to 1  $\text{cm}^{-1}$ . For gallium arsenide (GaAs), the absorption lengths for a given impurity concentration are approximately the same for both n and p - type materials. For n - type GaAs

$$K (\text{cm}^{-1}) = N_d (\text{cm}^{-3}) \times 4.6 \times 10^{-14}$$

and for p - type GaAs

$$K (\text{cm}^{-1}) = N_a (\text{cm}^{-3}) \times 3.9 \times 10^{-14}$$

The parameters employed to calculate these values are listed in Table 11.2. The variation of absorption with impurity concentration is similar to that of p - type silicon.

The relatively low absorption of high resistivity silicon has enabled it to be used as a dielectric rod antenna and waveguiding structure in the submillimetre region<sup>89</sup>.

Transmitting antenna structures are not recommended at submillimetre wavelengths unless the radiating structure can be integrated with the generator in order to minimise Ohmic loss. The transmission line structures developed so far possess too much loss to produce efficient long length feeds. Since beam mode propagation is more desirable the antenna comes into its own as a beam mode to RF current transducer, and as such could find many applications in a complete system. Radiation possessing Gaussian beam profiles can be adequately produced with horn, lens and reflector antenna systems, so the need for transmitting arrays at submillimetre wavelengths is limited. Many of the structures developed here could also be employed at lower frequencies. At the boundary between millimetre and submillimetre waves these structures may be of use in radio astronomy and fusion plasma diagnostics. Therefore, a study of arrays at lower frequencies (using IMPATTS, carcinatrons or optically pumped molecular gas

lasers as sources) is also worthy of consideration.

The open resonator instrument developed for this investigation would be of use for studying arrays in which the elements are terminated with resistive loads. These loads could be produced using the same techniques as those proposed for making the microbolometers, but using nichrome instead of bismuth to achieve thermal stability. As the extinction cross-section of an antenna depends upon the load impedance the open resonator is a valuable diagnostic tool. It may be used to ascertain whether or not an antenna is perfectly matched to its load.

The open resonator measures the extinction cross-section of an obstacle placed within it. If the output terminals of an antenna are short circuited then, provided that the intrinsic losses are low, the extinction cross-section is equal to the total scattering cross-section. When the antenna is perfectly matched to its load the scattering cross-section is equal to the absorption cross-section. Also the scattering cross-section of a perfectly matched antenna is equal to a quarter of that of a short-circuited antenna. Hence the extinction cross-section of a perfectly matched antenna is exactly half that of an identical short-circuited antenna.

The open resonator could also be used at lower frequencies, and the low frequency cut-off of the instrument would then be governed by the aperture of the Golay detector input window.

REFERENCES

1. DeTemple, T.A. Infrared and Millimetre Waves, vol.1, chapt.3, 1979
2. Kneübuhl, F.K. and Sturzenegger, Ch. Infrared and Millimetre Waves, vol.3, chapt.5, 1980
3. Preissner, J. Symp. Millimeter Submillimetre Wave Propag. Circuits, AGARD Conf. Proc. No.245, chapt.37, 1978
4. "Principles of Military Communication Systems" D.J. Torrieri, Artech House Inc. 1981
5. Beckman, J.E. and Harries, J.E., Appl. Optics. 14 pp.470-485, 1975
6. Harries, J.E., Swann, N.R.W., Carruthers, G.P. and Robinson, G.A. Infrared Physics 13, pp.149-155, 1973
7. Fleming, J.W. Infrared Physics, vol.18, pp.791-797, 1978
8. Chamberlain, J., Gebbie, H.A. George, A. and Beynon, J.D.E. J. Plasma Phys. 3, pp.75-79, 1969
9. Parkinson, G.J., Dangor, A.E. and Chamberlain, J. Appl. Phys. Lett., 13, pp.233-235, 1968
10. Brossier, P. and Blanken, R.A., IEEE Trans., MTT-22, pp.1053-1056, 1974
11. Cram, L.A. and Woolcock, S.C., Symp. Millimeter Submillimetre Wave propag. Circuits; AGARD Conf. Proc. No. 245, sect. 6, 1978
12. Vershinina, L.N. and Shevchenko, V.V., Instrum. Exper. Tech. (USSR) 14, pp 1120-1122 1971 (Translation)
13. Martin, D.H. and Lesurf, J. Infrared Physics 18 pp.405-412, 1978
14. Murphy, R.A., Bozler, C.O., Parker, C.D. Fetterman, H.R., Tannenwald, P.E., Clifton, B.J., Donnelly, J.P. and Lindley, W.Y., IEEE Trans. Micro. Theor. Techn. MTT-25, p.494, 1977

15. Schwarz, S.E. and Ulrich, B.T. Jour. Appl. Phys.  
vol. 48 (5) pp.1870-1873 1977
16. Tien-Lai Hwang, Schwarz, S.E., and Rutledge, D.B.  
Appl. Phys. Lett. 34 (11) pp.773-776 1979
17. Matarresse, L.M. and Evenson, K.M. Appl. Physc.  
Lett. 17 (1) pp.8-10 1970
18. Krautle, H., Sauter, E., and Schultz, G.V. Infrared  
Physics vol. 18 pp.705-712 1978
19. Burroughs, W.J., Pyatt, E.C. and Gebbie, H.A.,  
Nature 1966 212 pp.387-388
20. Harrington, R.F., Proc IEE Vol 111 No. 4  
pp.617-623 1964
21. Daiku, Y., Mizuno, K. and Ono, S. Infrared Physics  
vol. 18 pp.679-682 1978
22. Tai, C.T. IRE Trans. Ant. and Prop. AP-9, Part 2,  
pp.224-225 1961
23. Casimir, H.G.C. and Ubbink, G., Phillips Technical  
Review vol. 28 No. 10 pp.300-315 1967
24. "Solid State Physics", Ashcroft, N.W. and Mermin,  
N.P., Holt, Rienhart & Winston 1977
25. "Electromagnetic Waves", Schelkunoff, S.A., Van  
Nostrand, 1948
26. Hansen, W.W. and Woodyard, J.R. Proc. IRE vol.26  
p.333 1938
27. "Fields and Waves in Communication Electronics"  
Ramo, S., Whinnery, J.R., and Van Duzer, T. Wiley 1965
28. Mizuno, K., Daiku, Y. and Ono, S. IEEE Trans. Micro.  
Theor. Tech. vol MTT-25 No. 6, p.470 1977
29. Small, J.G. Elchinger, G.M., Javan, A., Antonio  
Sanchez, Bachner, F.J. and Smythe, D.L. Appl. Phys.  
Lett. vol.24 p.275 1974
30. Wang, S.Y., Izawa, T., and Gustafson, T.K. Appl.  
Phys. Lett. vol.27 p.481 1975
31. Heiblum, M., Wang, S., Whinnery, J.R. and Gustafson,  
T.K., IEEE J. Quant. Electron. QE-14 p.159 1978



32. Coleman, B.L. Phil. Mag. 41 p.276 1950
33. Wait, J.R. Rad. Sci., 7, p.675 1972
34. "Antennas in Inhomogeneous Media" Galejs, J.  
Pergamon Press 1969
35. Brewitt-Taylor, C.R. Gunton, D.J. and Rees, H.D.  
Electron Lett. vol. 17 No. 20 pp.729-730 1981
36. "Travelling Wave Antennas" Walter, C.H., Dover, 1965
37. Rutledge, D.B., Schwarz, S.E., and Adams, A.T.  
Infrared Physics vol. 18 pp.713-729 1978
38. "Antenna Theory, Part I" Collin, R.E., and Zucker,  
F.J. McGraw Hill 1969
39. Friis, H.T. Proc. Inst. Radio Engrs. 34 p.254 1946
40. "Antennas", Kraus, J.D. McGraw Hill 1950
41. "Field Computation by Moment Methods" Harrington, R.F.,  
MacMillan Company, New York 1968
42. Hu Y.Y. IRE Trans. AP-6 pp.140-148 1958
43. "Electromagnetic Waves and Radiating Systems" Jordan,  
E.C. and Balmain, K.G. Prentice Hall 1968
44. Hansen, R.C. and Brunner, G., Microwave Journal vol.  
22, No.12 pp.54-56 1979
45. "Synthesis of Planar Antenna Sources" Rhodes, P.H.  
Clarendon Press, Oxford 1974
46. Brown, G., and King, R. Proc. Inst. Radio Engrs.,  
22 pp.457-480 1934
47. King, H.E. Trans. IRE AP-5 pp.300-313 1957
48. Cullen, A.L. Electron. Lett. Vol. 3 No. 12  
pp.557-558 1967
49. Cullen, A.L., and Kumar, A. Proc. Roy. Soc.Lond.  
A315 pp.217-230 1970
50. Cullen, A.L., and Tang, C.M. Electron. Lett. vol.14  
No. 8 pp.245-246 1978
51. Bryant, D.L., and Auchterlonie, L.J. Electron. Lett.  
vol.14 pp.475-476 1978

52. Bryant, D.L., and Auchterlonie, L.J. Electron. Lett. vol. 15 pp.52-53 1979
53. Harris, D.J., and Teo, T.M. Electron. Lett. vol.16 pp.500-501 1980
54. Cullen, A.L., and Yu, P.K. Proc. Roy. Soc. Lond. A325 pp.493-509 1971
55. Batt, R.J., and Harris, D.J. Infrared Physics vol.16 pp.325-327 1976
56. Schulten, G. Phillips Technical Review vol. 26 No. 11/12 pp.350-356 1965
57. Breeden, K.H., and Langley, J.B. Rev. Sci. Inst. vol.40 No. 9 pp.1162-1163 1969
58. Kogelnik, H., and Li, T. Proc. IEEE. 54 pp.1312-1329 1966
59. Cullen, A.L. Electron. Lett. vol.16 No. 8 pp.243-244 1970
60. Harris, D.J.; Teo, T.M.; Batt, R.J. and Luk, S.C. Internat. Jour. Infrared and Millimeter Waves. vol.1 No. 3 pp.339-349 1980
61. Marshal, T. Practical Electronics, December 1978 pp.1252-1253
62. Cummins, H.J. and Frayne, P.G. J. Phys.. E. Sci. Instrum. vol.15 No. 1 pp.50-52 1982
63. Adde, R. and Lourtioz, J.M. Rev. Phys. Appl. vol.11 pp.533-40 1976
64. Kang, C.S. and Venderkooy, J. Infrared Physics vol.16 pp.627-38 1976
65. Belland, P. and Veron, D. Opt. Commun. vol.9 pp.146-8 1973
66. Batt, R.J., Luk, S.C., White, B.S. and Teo, T.M. Infrared Physics vol.19 pp.309-312 1979
67. Tang, C.M., and Cullen, A.L. Electron. Lett. vol.14 No.8 pp.245-246
68. "The Scattering and Diffraction of Waves", King, R.W.P., and Wu, T.T. Harvard University Press 1959

69. Degenford, J.E. and Coleman, P.D., Proc. IEEE  
vol.54 pp.520-522 1966
70. Coleman, P.D., Sherman, G., Parsons, D. and Akitt, D.  
Proceedings of the Symposium on Submillimeter Waves,  
pp.694-701 New York 1970
71. Loewenstein, E.V. and Smith, D.R., Appl. Optics,  
vol.10 No. 3 pp.577-583 1970
72. "American Institute of Physics Handbook" Third  
Edition. Gray, D.E. Ed. McGraw Hill 1972
73. James, D.J. and Ring, J. Jour. De Physique C2  
No.3-4 pp.150-152 1967
74. Loewenstein, E.V. Jour. de Physique C2 No.3-4  
pp.153-155 1967
75. "Gaelic Language Compiler User Guide" Compeda  
Limited 1979
76. "Gaelic Language" Boyd, D.R.S., Rutherford Labor-  
atory, GUN002, issue 1, 1979
77. "Tables of Physical and Chemical Constants" Kaye,  
G.W.C. and Laby, T.H. Longman 1973
78. "'Kodak' Photosensitive Resist Techniques". Kodak  
Limited London
79. "AZ-1350 Photo Resist Process Instructions" Shipley  
Chemical Limited 1969
80. Dimigen, H. and Lüthje, H. Philips Tech. Rev. vol.35  
No. 7/8 pp.199-208 1975
81. "Experimental Microwaves" Cross, A.W. Marconi  
Instrument Publications 1977
82. "Antenna Engineering Handbook" Jasik, H. McGraw-  
Hill Book Company 1971
83. "Introduction to Radar Systems" Skolnik, M.I.  
McGraw-Hill 1962
84. Van Vleck, J.H., Bloch, F. and Hamermesh, M. Jour.  
Appl. Phys. vol.18 pp.274-294 1947
85. Nestic, A. Proceedings of Second International  
Conference on Antennas and Propagation (IEE Con.Pub.  
No. 195) 13-16 April 1981 York

86. Abramowitz, M. and Stegun, I.A. Eds. "Handbook of Mathematical Functions" NBS Applied Mathematics Series 1966
87. Yamashita, E. and Yamazaki, S. IEEE Trans. Micro. Theor. and Techn. MTT-16 No. 11 pp.972-973 1968
88. "Microwave Integrated Circuits" Gupta, K.C., and Amarjit Singth Eds. Wiley Eastern Ltd. 1974
89. Rutledge, D.B. Schwarz, S.E., Hwang, T.L. Angelakos, D.J., Mei, K.K. and Yokota, S. IEEE Jour. Quant. Electron. QE-16 No. 5 1980
90. "Infrared and Millimetre Waves" Button, K.J. and Wiltse, J.C. Eds. vol.4 Millimetre Wave Systems Academic Press 1981
91. "The Physics of Transmission Lines at High and Very High Frequencies" Grivet, P. vol. 1 Academic Press 1970
92. "Antenna Theory and Design" Elliot, R.S., Prentice-Hall 1981
93. Pocklington, H.E. Phil. Soc. Proc. 9 October 25 1897 pp.324-332
94. Tien-Lai Hwang, Schwarz, S.E. and Rutledge, D.B. Appl. Phys. Lett. vol. 34 No. 11 pp.773-776 1979
95. Tien-Lai Hwang, Rutledge, D.B. and Schwarz, S.E. Appl. Phys. Lett. vol. 34 No. 1 pp.9-11 1979
96. Koenig, H.R. and Maissel, L.I. IBM Journ. Res. Develop. March 1970 pp.168-171
97. Logan, J.S. IBM Jour. Res. Develop. March 1970, pp.172-175
98. Maissel, L.I., Standley, C.L. and Gregor, L.V. IBM Jour. Res. Develop. January 1972 pp.67-70
99. "Optical Properties of Semi-Conductors" Moss, T.S. Butterworths Scientific Publications 1959

#### ACKNOWLEDGEMENTS

Grateful thanks are due to Dr. P.G. Frayne for his help and encouragement during the course of this work and also for his persistence in obtaining the supporting grants.

I would like to thank the Science and Engineering Research Council for providing a research studentship and electron beam lithography facilities at the Rutherford Appleton Laboratory.

The open resonator instrument developed and employed in this investigation was supported by a grant made available by the Paul Instrument Fund of The Royal Society.

I would also like to acknowledge the assistance of Mr. A. Grant and the technical staff of the Physics Department, Royal Holloway College.

Thanks are due to Mr. R. Elton and his staff in the departmental mechanical workshops, particularly Mr. W.F. Hawkins whose care in constructing the mechanical aspects of the open resonator contributed greatly to its success.

The help Mr. M. Thyer who carried out the countless vacuum evaporations required during the project is gratefully acknowledged.

Thanks are due to Mr. L. Ellison for his work on the stabilised power supply for the HCN laser and Mr. B. Tait for the photographic work in this thesis.

Last but not least I wish to thank my mother, Mrs. Joyce Cummins, for her dedication and patience in typing this thesis.

APPENDIX I

For a centre fed dipole antenna of halflength  $L$  carrying a current with propagation constant  $\beta$ , the current distribution has a sinusoidal variation with distance  $Z$  along the antenna of the form

$$\begin{aligned} I &= I_m \sin \beta (L - Z) \quad Z \geq 0 \\ I &= I_m \sin \beta (L + Z) \quad Z < 0 \end{aligned} \quad (A.1.1.)$$

The geometry of the antenna is illustrated in Figure 2.2. As the currents are all flowing in the  $Z$  - direction, the radiation vector,  $N_z$ , for the dipole antenna is given by

$$N_z = 2 I_m \int_0^L \sin \beta (L-Z) \cos (k_0 Z \cos \theta) dz \quad (A.1.2.)$$

integrating this yields

$$N_z = 2 I_m \beta \left[ \frac{\cos (k_0 L \cos \theta) - \cos \beta L}{\beta^2 - k_0^2 \cos^2 \theta} \right] \quad (A.1.3.)$$

If the currents in a radiating system all flow in one direction then

$$K = \frac{\eta}{8 \lambda^2} |N_z|^2 \sin^2 \theta \quad (A.1.4.)$$

hence, from equations A.1.3 and A.1.4

$$K = 120 k_0^2 \beta^2 I_m^2 \left[ \frac{\sin^2 |L(\beta+k_0 \cos \theta)| \sin^2 |L(\beta-k_0 \cos \theta)|}{(\beta^2 - k_0^2 \cos^2 \theta)^2 \sin^2 \theta} \right] \quad (A.1.5.)$$

The effect of changing the phase velocity is found by evaluating the derivative of the maximum power density with respect to  $\beta$ .

$$\left. \frac{dK(\beta, \theta)}{d\beta} \right|_{\theta \text{ max}} = \frac{\partial K}{\partial \beta} + \frac{\partial K}{\partial \theta} \frac{d\theta \text{ max}}{d\beta} \quad (A.1.6.)$$

Partially differentiating K with respect to  $\theta$  gives

$$\begin{aligned} \frac{\partial K}{\partial \theta} &= \frac{2K \sin \theta \cos \theta}{\sin^2 \theta} + \left[ \frac{K 4k_0^2 \cos \theta \sin \theta}{(\beta^2 - k_0^2 \cos^2 \theta) k_0 \sin \theta} \right. \\ &\quad \left. - \frac{2K \sin \theta \cos \theta}{\sin^2 \theta k_0 \sin \theta} \right] k_0 \sin \theta \\ &\quad - \frac{4K k_0^2 \cos \theta \sin \theta}{(\beta^2 - k_0^2 \cos^2 \theta)} \end{aligned} \tag{A.1.7.}$$

hence

$$\frac{\partial K}{\partial \theta} = 0 \tag{A.1.8.}$$

partially differentiating K with respect to  $\beta$  gives

$$\begin{aligned} \frac{\partial K}{\partial \beta} &= \frac{2K}{\beta} + \frac{K 4 k_0 \cos \theta}{\beta^2 - k_0^2 \cos^2 \theta} - \frac{2K \cos \theta}{k_0 \sin^2 \theta} \\ &\quad - \frac{K 4 \beta}{(\beta^2 - k_0^2 \cos^2 \theta)} \end{aligned} \tag{A.1.9.}$$

therefore

$$\frac{\partial K}{\partial \beta} = \frac{2K}{\beta} - \frac{2K \cos \theta}{k_0 \sin^2 \theta} - \frac{4(\beta - k_0 \cos \theta)}{\beta^2 - k_0^2 \cos^2 \theta} \tag{A.1.10.}$$

Re-arranging equation A.1.10

$$\frac{\partial K}{K} = \frac{2\partial \beta}{\beta} - \frac{\partial \beta}{k_0} \left\{ \frac{2 \cos \theta}{\sin^2 \theta} \right\} - \frac{4 \partial \beta (\beta - k_0 \cos \theta)}{(\beta^2 - k_0^2 \cos^2 \theta)} \tag{A.1.11.}$$

APPENDIX II  
FORTAN PROGRAM LISTINGS

The programs listed in this Appendix calculated the scattering response of single cylindrical antenna elements and arrays and were based on the theory presented in Chapter 3.

The general graph plotting program plotted the dependent variable on the Y-axis for 60 incremental steps of the independent variable plotted on the X-axis within a preset range of values XMAX, XMIN, YMAX and YMIN. The value of the dependent variable was obtained through calling the appropriate subroutine and passing the independent variable to it.

Subroutine BACK calculated the parameters  $Z_{11}'$ ,  $Z_{12}'$  and  $Z_{22}'$  for a cylindrical antenna along with the value of its total and backscattering cross sections. These parameters were calculated within this subroutine using the expressions derived by Hu<sup>42</sup>.

Subroutine MUTUAL calculated the mutual impedance between pairs of non staggered dipoles of equal length and arbitrary separation and was based upon the expressions obtained by Brown and King<sup>46</sup>.

Subroutine ARRAY calculated the total and backscattering cross sections of linear arrays of cylindrical dipoles with various parameters such as element length, element separation and broadside angle of incidence. This was done by setting up the self and mutual impedance matrices with values obtained from subroutines BACK and MUTUAL and solving these using the technique described by Harrington<sup>20</sup>. In this way the backscattering and total scattering cross-sections were obtained for the linear dipole arrays.

Subroutines developed by the Numerical Algorithms Group



(NAG routines), which were available on library files, were employed to numerically evaluate the integrals required in the calculation of the self and mutual impedance terms and for obtaining the inverse of the complex matrices which were required in the solution of the matrix equations. The library routines are listed below.

NAG routine	Function
S13ACF	Ci (x)
S13ADF	Si (x)
F04ADF	complex matrix inverse

Program listing for the calculation of  
total and backscattering cross sections  
of cylindrical antennas

```
1      PROGRAM TEST(INPUT,TAPE1=INPUT,OUTPUT,
          TAPE2=OUTPUT)
C GENERAL GRAPH PLOTTING PROGRAM MK IIIA.
      XMAX=6.
      XMIN=0.
5      YMAX=1.5
      YMIN=0.
      RADIUS=3.5E-3
      READ(1,10)IXNAME,IYNAME
10     FORMAT(A8)
10    C CALCULATE STEPS FOR AXES 8 BY 6 IN 1 INCH STEPS.
      STEPX=(XMAX-XMIN)/6.0
      STEPY=(YMAX-YMIN)/8.0
C PLOT AXES.
      CALL START
15     CALL PLOT(1.0,1.0,-3)
      CALL AXIS(0.0,0.0,IXNAME,-8,6.0,0.0,XMIN,STEPX)
      CALL AXIS(0.0,0.0,IYNAME,8,8.0,90.0,YMIN,STEPY)
      CALL PLOT(0.0,8.0,3)
      CALL PLOT(6.0,8.0,2)
20     CALL PLOT(6.0,0.0,2)
      DIFF=ABS(XMAX-XMIN)
      SUMM=ABS(XMAX+XMIN)
      IF(DIFF.LE.SUMM)GOTO 15
      DIFF=(0.0-XMIN)*6.0/(XMAX-XMIN)
25     CALL PLOT(DIFF,0.0,3)
      CALL PLOT(DIFF,8.0,2)
15     DIFF=ABS(YMAX-YMIN)
      SUMM=ABS(YMAX+YMIN)
      IF (DIFF.LE.SUMM)GOTO 20
30     DIFF=(0.0-YMIN)*8.0/(YMAX-YMIN)
      CALL PLOT(0.0,DIFF,3)
      CALL PLOT(6.0,DIFF,2)
20     CONTINUE
C AXES COMPLETE
35     DELTAX=STEPX/10.0
      YY=YMAX-YMIN
      IG=0
      DO 25 I=1,60
      X=XMIN+I*DELTAX
40    C MAKE X THE INDEPENDENT VARIABLE OF THE EQUATION.
      CALL BACK(X,RADIUS,Z)
      WRITE(2,100)Z
100   FORMAT(1H ,E14.7)
      IF(Z.GT.YMAX.OR.Z.LT.YMIN)GOTO 24
45     X=FLOAT(I)/10.0
      Z=(Z-YMIN)*8.0/YY
      IF(IG.EQ.0.)CALL PLOT(X,Z,3)
      IF=1
      CALL PLOT(X,Z,2)
50     GOTO 25
24     IG=0
25     CONTINUE
      CALL ENPLOT(1.0)
      STOP
55     END
```

```
1      SUBROUTINE BACK(L,RADIUS,SIGMA)
      REAL LN2,LN4,L
      COMPLEX HC,EC,FC,GC,CC,DC,AC,BC,J30,Z11,
              Z12,Z22

      PI=3.1415926
5      ALPHA=2.*PI*RADIUS
      COSL=COS(L)
      SINL=SIN(L)
      COS2L=COS(2.*L)
      SIN2L=SIN(2.*L)
10     LN2=ALOG(2.*L/ALPHA)
      LN4=ALOG(4.*L/ALPHA)
      G=.5772=566
      IFAIL=0
      CL=G+ALOG(L)-S13ACF/(L,IFAIL)
15     C2L=G+ALOG(2.*L)-S13ACF(2.*L,IFAIL)
      C4L=G+ALOG(4.*L)-S13ACF(4.*L,IFAIL)
      SL=S13ADF(L,IFAIL)
      S2L=S13ADF(2.*L,IFAIL)
      S4L=S13ADF(4.*L,IFAIL)
20     S=1./(1.-COSL)
      S2=S*S
      A=S2*(S4L+4.*COSL*(L*COSL-SINL)*(LN4-C2L)
      C-(8.*ALPHA*SINL**2(/PI-2.*COSL**2*SIN2L)
      B=S26(-C4L-(4.*L*COSL**2-2*SIN2L)*S2L+SIN2L**2)
      C=S*(SINL *S4L+(1.-COSL)*C4L+4.*COSL*(1.-COSL-L
              *SINL)*C2L
      C+4.*COSL*(1.-COSL)*CL+4.*SINL*(L*COSL-SINL)*LN4
      C+4.*(1.-COSL)**2*LN2
      C-(8.*ALPHA*SINL*(1.-COSL))/PI-SIN2L**2)
      D=S*((1.-COSL)*S4L-SINL*C4L+4.*COSL*(1.-COSL-L
              *SINL)*S2L
30     C+4.*COSL*(1.-COSL)*SL+2.*SINL**2*SIN2L)
      E=2.*COSL*(1.-COSL)*S4L+2.*SINL*(1.-COSL)*C4L
      C+4.*(1.-COSL)**2*S2L-4.*L*SINL**2*C2L
      C+8.*SINL*(1.-COSL)*CL+(4.*L*SINL**2-8.*SINL*
              (1.-COSL))*LN4
      C-(24.*ALPHA*(1.-COSL)**2)/PI-2.*SINL**2*SIN2L
35     F=2.*SINL*(1.-COSL)*S4L-2.*COSL*(1.-COSL)*C4L
      C-4.*L*SINL**2*S2L-4.*(1.-COSL)**2*C2L
      C+8.*SINL*(1.-COSL)*SL+4.*SINL**4
      G=2.*S*(SINL-L*COSL)
      H=2.*(2.*(1.-COSL)-L*SINL)
40     HC=COMPLX(H,0.)
      EC=COMPLX(E,0.)
      FC=COMPLX(0.,F)
      GC=COMPLX(G,0.)
      CC=COMPLX(C,0.)
45     DC=COMPLX(0.,D)
      AC=COMPLX(A,0.)
      BC=COMPLX(0.,B)
      J30=COMPLX(0.,30.)
      Z11=(-J30*HC**2)/(EC+FC)
50     Z12+J30*(GC-HC*(CC+DC)/EC+FC)
      Z22=J30*((AC+BC)-(CC+DC)**2/(EC+FC))
      SIGMA=(1./(PI*900.))*(CABS(Z11-Z12**2/Z22))**2
      WRITE(2,100)SIGMA,L
100    FORMAT(' SIGMA=',E14.7,' KH=',F10.6)
55     RETURN
      END
```

Program listing for the calculation of  
total broadside scattering cross-sections  
of linear arrays of cylindrical antennas

```
1      PROGRAM TEST(INPUT,TAPE1=INPUT,OUTPUT,
          TAPE2=OUTPUT)
C GENERAL GRAPH PLOTTING PROGRAM MK IIIA.
      XMAX=6.
      XMIN=0.
5      YMAX=1.5
      YMIN=0.
      RADIUS=3.5E-3
      READ(1,10)IXNAME,IYNAME
10     FORMAT(A8)
10    C CALCULATE STEPS FOR AXES 8 BY 6 IN 1 INCH STEPS.
      STEPX=(XMAX-XMIN)/6.0
      STEPY=(YMAX-YMIN)/8.0
C PLOT AXES.
      CALL START
15     CALL PLOT(1.0,1.0,-3)
      CALL AXIS(0.0,0.0,IXNAME,-8,6.0,0.0,XMIN,STEPX)
      CALL AXIS(0.0,0.0,IYNAME,8,8.0,90.0,YMIN,STEPY)
      CALL PLOT(0.0,8.0,3)
      CALL PLOT(6.0,8.0,2)
20     CALL PLOT(6.0,0.0,2)
      DIFF=ABS(XMAX-XMIN)
      SUMM=ABS(XMAX+XMIN)
      IF(DIFF.LE.SUMM)GOTO 15
      DIFF=(0.0-XMIN)*6.0/(XMAX-XMIN)
25     CALL PLOT(DIFF,0.0,3)
      CALL PLOT(DIFF,8.0,2)
      DIFF=ABS(YMAX-YMIN)
      SUMM=ABS(YMAX+YMIN)
      IF (DIFF.LE.SUMM)GOTO 20
30     DIFF=(0.0-YMIN)*8.0/(YMAX-YMIN)
      CALL PLOT(0.0,DIFF,3)
      CALL PLOT(6.0,DIFF,2)
20     CONTINUE
C AXES COMPLETE
35     DELTAX=STEPX/10.0
      YY=YMAX-YMIN
      IG=0
      DO 25 I=1,60
      X=XMIN+I*DELTAX
40    C MAKE X THE INDEPENDENT VARIABLE OF THE EQUATION.
      CALL BACK(X,RADIUS,Z)
      WRITE(2,100)Z
100   FORMAT(1H ,E14.7)
      IF(Z.GT.YMAX.OR.Z.LT.YMIN)GOTO 24
45     X=FLOAT(I)/10.0
      Z=(Z-YMIN)*8.0/YY
      IF(IG.EQ.0.)CALL PLOT(X,Z,3)
      IF=1
      CALL PLOT(X,Z,2)
50     GOTO 25
24     IG=0
25     CONTINUE
      CALL ENPLOT(1.0)
      STOP
55     END
```

```
1      SUBROUTINE ARRAY(D,SIGMA)
      COMPLEX ZSS(20,20),ZSSIN(20,20),UNIT(20,20),Z11,
          Z12,Z22,ZST(20),CZZ,Z(20),ZA
      REAL WKSPCE(20),K
5      THETA=ANGLE*0.01745
      X=0.
      YO=.25
      RADIUS=3.SE-3
      P1=6.283-85306=1
10     K=120.*ALOG(2.*D/RADIUS)
      DO 100 I=1,20
      DO 100 J=1,20
      UNIT(I,J)=(0.,0.)
      IF(I.EQ.J)UNIT(I,J)=(1.,0.)
15     100 CONTINUE
      CALL BACK(PI*D,RADIUS,Z11,Z12,Z22)
      WRITE(2,170)Z11,Z12,Z22
170    FORMAT(' Z11=',2E15.7,' Z12=',2E15.7,' Z22=',2E15.7)
      DO 200 I=1,20
20     200 ZST(I)=Z12
      CONTINUE
      DO 300 I=1,20
      DO 300 J=1,20
      IF(I.EQ.J)GOTO 400
25     Y=ABS((I-J)*YO)
      CALL MUTUAL (D,Y,ZSS(I,J))
      GOTO 300
400    ZSS(I,J)=Z22
300    CONTINUE
30     CALLF04ADF(ZSS,20,UNIT,20,20,20,ZSSIN,20,WKSPCE,0)
      DO 600 I=1,20
      Z(I)=(0.,0.)
      DO 600 J=1,20
      Z(I)=Z(I)+ZSSIN(I,J)*ZST(J)
35     600 CONTINUE
      ZZ=(0.,0.)
      DO 700 I=1,20
      ZZ=ZZ+Z(I)*ZST(I)
700    CONTINUE
40     SIGMA=3.537E-4*(CABS(20.*Z11-ZZ)**2)
      SIGMA=SQRT(2.*SIGMA/PI)
      WRITE(2,70)K
70     FORMAT(' K=',E15.7)
      WRITE(2,800)D,SIGMA
45     800 FORMAT(' D=',F10.6,' SCATTERING X-SECTION=',E15.7)
      RETURN
      END
```

```
1      SUBROUTINE BACK(L,RADIUS,SIGMA)
      REAL LN2,LN4,L
      COMPLEX HC,EC,FC,GC,CC,DC,AC,BC,J30,Z11,
              Z12,Z22

      PI=3.1415926
5      ALPHA=2.*PI*RADIUS
      COSL=COS(L)
      SINL=SIN(L)
      COS2L=COS(2.*L)
      SIN2L=SIN(2.*L)
10     LN2=ALOG(2.*L/ALPHA)
      LN4=ALOG(4.*L/ALPHA)
      G=.5772=566
      IFAIL=0
      CL=G+ALOG(L)-S13ACF/(L,IFAIL)
15     C2L=G+ALOG(2.*L)-S13ACF(2.*1,IFAIL)
      C4L=G+ALOG(4.*L)-S13ACF(4.*L,IFAIL)
      SL=S13ADF(L,IFAIL)
      S2L=S13ADF(2.*L,IFAIL)
      S4L=S13ADF(4.*L,IFAIL)
20     S=1./(1.-COSL)
      S2=S*S
      A=S2*(S4L+4.*COSL*(L*COSL-SINL))*(LN4-C2L)
      C-(8.*ALPHA*SINL**2/(PI-2.*COSL**2*SIN2L)
      B=S26*(-C4L-(4.*L*COSL**2-2*SIN2L)*S2L+SIN2L**2)
      C=S*(SINL *S4L+(1.-COSL)*C4L+4.*COSL*(1.-COSL-L
              *SINL)*C2L
      C+4.*COSL*(1.-COSL)*CL+4.*SINL*(L*COSL-SINL)*LN4
      C+4.*(1.-COSL)**2*LN2
      C-(8.*ALPHA*SINL*(1.-COSL))/PI-SIN2L**2)
      D=S*((1.-COSL)*S4L-SINL*C4L+4.*COSL*(1.-COSL-L
              *SINL)*S2L
30     C+4.*COSL*(1.-COSL)*SL+2.*SINL**2*SIN2L)
      E=2.*COSL*(1.-COSL)*S4L+2.*SINL*(1.-COSL)*C4L
      C+4.*(1.-COSL)**2*S2L-4.*L*SINL**2*C2L
      C+8.*SINL*(1.COSL)*CL+(4.*L*SINL**2-8.*SINL*
              (1.COSL))*LN4
      C-(24.*ALPHA*(1.-COSL)**2)/PI-2.*SINL**2*SIN2L
35     F=2.*SINL*(1.-COSL)*S4L-2.*COSL*(1.-COSL)*C4L
      C-4.*L*SINL**2*S2L-4.*(1.-COSL)**2*C2L
      C+8.*SINL*(1.-COSL)*SL+4.*SINL**4
      G=2.*S*(SINL-L*COSL)
      H=2.*(2.*(1.-COSL)-L*SINL)
40     HC=COMPLX(H,0.)
      EC=COMPLX(E,0.)
      FC=COMPLX(0.,F)
      GC=COMPLX(G,0.)
      CC+COMPLX(C,0.)
45     DC=COMPLX(0.,D)
      AC=COMPLX(A,0.)
      BC=COMPLX(0.,B)
      J30=COMPLX(0.,30.)
      Z11=(-J30*HC**2)/(EC+FC)
50     Z12+J30*(GC-HC*(CC+DC)/EC+FC)
      Z22=J30*((AC+BC)-(CC+DC)**2/(EC+FC))
      SIGMA=(1./(PI*900.))*(CABS(Z11-Z12**2/Z22))**2
      WRITE(2,100)SIGMA,L
100    FORMAT(' SIGMA=',E14.7,' KH=',F10.6)
55     RETURN
      END
```



```
1      SUBROUTINE MUTUAL(A,D,Z)
      COMPLEX Z
      PI=6.283185306
      AO=PI*D
5      A1=PI*(SORT(D*D+A*A)-A)
      A2=PI*(SORT(D*D+A*A)+A)
      A3=PI*(SORT(D*D+4.*A*A)-2.*A)
      A4=PI*(SORT(D*D+4.*A*A)+2.*A)
      IFAIL=0
10     SA0=S13ADF(AO,IFAIL)
      SA1=S13ADF(A1,IFAIL)
      SA2=S13ADF(A2,IFAIL)
      SA3=S13ADF(A3,IFAIL)
      SA4=S13ADF(A4,IFAIL)
15     G=.57721566
      CA0=S13ACF(AO,IFAIL)
      CA1=S13ACF(A1,IFAIL)
      CA2=S13ACF(A2,IFAIL)
      CA3=S13ACF(A3,IFAIL)
20     CA4=S13ACF(A4,IFAIL)
      G=PI*A
      SG=SIN(G)
      CG=COS(G)
      C2G=COS(2.*G)
25     S2G=SIN(2.*G)
      RM=2.*(2.+C2G)*CA0-4.*CG*CG*(CA1+CA2)+C2G*(CA3+CA4)
           C+S2G*(SA4-SA3-2.*SA2+2.*SA1)
      RM=RM*15./(SG*SG)
      XM=-2.*(2.+C2G)*SA0+4.*CG*CG*(SA1+SA2)-C2G*(SA3+SA4)
           C+S2G*(CA4-CAB-2.*CA2+2.*CA1)
      XM=XM*15./(SG*SG)
      Z=2.*CMLX(RM, XM)
      RETURN
      END
```

Program listing for the calculation of  
the variation of total and backscattering  
patterns for linear arrays of cylindrical  
antennas

```
1      PROGRAM TEST(INPUT,TAPE1=INPUT,OUTPUT,
          TAPE2=OUTPUT)
      C GENERAL GRAPH PLOTTING PROGRAM MK IIIA.
        XMAX=6.
        XMIN=0.
5       YMAX=1.5
        YMIN=0.
        RADIUS=3.5E-3
        READ(1,10)IXNAME,IYNAME
10      FORMAT(A8)
10     C CALCULATE STEPS FOR AXES 8 BY 6 IN 1 INCH STEPS.
        STEPX=(XMAX-XMIN)/6.0
        STEPY=(YMAX-YMIN)/8.0
      C PLOT AXES.
        CALL START
15      CALL PLOT(1.0,1.0,-3)
        CALL AXIS(0.0,0.0,IXNAME,-8,6.0,0.0,XMIN,STEPX)
        CALL AXIS(0.0,0.0,IYNAME,8,8.0,90.0,YMIN,STEPY)
        CALL PLOT(0.0,8.0,3)
        CALL PLOT(6.0,8.0,2)
20      CALL PLOT(6.0,0.0,2)
        DIFF=ABS(XMAX-XMIN)
        SUMM=ABS(XMAX+XMIN)
        IF(DIFF.LE.SUMM)GOTO 15
        DIFF=(0.0-XMIN)*6.0/(XMAX-XMIN)
25      CALL PLOT(DIFF,0.0,3)
        CALL PLOT(DIFF,8.0,2)
15     DIFF=ABS(YMAX-YMIN)
        SUMM=ABS(YMAX+YMIN)
        IF (DIFF.LE.SUMM)GOTO 20
30     DIFF=(0.0-YMIN)*8.0/(YMAX-YMIN)
        CALL PLOT(0.0,DIFF,3)
        CALL PLOT(6.0,DIFF,2)
20     CONTINUE
      C AXES COMPLETE
35     DELTAX=STEPX/10.0
        YY=YMAX-YMIN
        IG=0
        DO 25 I=1,60
          X=XMIN+I*DELTAX
40     C MAKE X THE INDEPENDENT VARIABLE OF THE EQUATION.
        CALL BACK(X,RADIUS,Z)
        WRITE(2,100)Z
100    FORMAT(1H ,E14.7)
        IF(Z.GT.YMAX.OR.Z.LT.YMIN)GOTO 24
45     X=FLOAT(I)/10.0
        Z=(Z-YMIN)*8.0/YY
        IF(IG.EQ.0.)CALL PLOT(X,Z,3)
        IF=1
        CALL PLOT(X,Z,2)
50     GOTO 25
24     IG=0
25     CONTINUE
        CALL ENPLOT(1.0)
        STOP
55     END
```

```
1      SUBROUTINE ARRAY(ANGLE,SIGMA)
      COMPLEX ZSS(20,20),ZSSIN(20,20),UNIT(20,20),Z11,
          Z12,Z22,ZST(20),CAA,Z(20),ZA
      REAL WKSPCE(20),K
5      THETA=ANGLE*0.01745
      X=0.
      D=.25
      YO=1.0
      RADIUS=3.50-3
10     PI=6.283185306
      K=120.*ALOG(2.*D/RADIUS)
      DO 100 I=1,20
      DO 100 J=1,20
      UNIT (I,J)=(0.,0.)
15     IF(I.EQ.J)UNIT(I,J)=(1.,0.)
      CONTINUE
      CALL BACK(PI*D,RADIUS,Z11,Z12,Z22)
      WRITE(2,170)Z11,Z12,Z22
170    FORMAT(' Z11=',2L15.7,' Z12='2E15.7,' Z22='2E15.7)
      DO 200 I=1,20
      ZST(I)=Z12*CEXP(COMPLX(0.00,((I-1)*PI*YO*COS(THETA))))
200    CONTINUE
      DO 300 I=1,20
      DO 300 J=1,20
25     IF(I.EQ.J)GOTO 400
      Y=ABS(I-J*YO)
      CALL MUTUAL(D,Y,ZSS(I,J))
      GOTO 300
      400 ZSS(I,J)=Z22
30     300 CONTINUE
      CALL FO4ADF(ZSS,20,UNIT,20,20,20,ZSSIN,20,WKSPCE,0)
      DO 600 I=1,20
      Z(I)=(0.,0.)
      DO 600 J=1,20
35     Z(I)=Z(I)+ZSSIN(I,J)*ZST(J)
      600 CONTINUE
      ZZ=(0.,0.)
      DO 700 I=1,20
      ZZ=ZZ+Z(I)*ZST(I)
40     700 CONTINUE
      SIGMA=3.537E-4*(CABS(ZZ))**2
      SIGMA=SQRT(2.*SIGMA/PI)
      WRITE(2,70)K
      70  FORMAT('K=',E15.7)
45     WRITE(2,800)ANGLE,SIGMA
899    FORMAT(' ANGLE=',-10.6.' DEGREES', ' SCATTERING CROSS
          SECTION=',E15.7,' M2')
      RETURN
      END
```

```
1      SUBROUTINE BACK(L,RADIUS,SIGMA)
      REAL LN2, LN4, L
      COMPLEX HC, EC, FC, GC, CC, DC, AC, BC, J30, Z11,
              Z12, Z22

      PI=3.1415926
5      ALPHA=2.*PI*RADIUS
      COSL=COS(L)
      SINL=SIN(L)
      COS2L=COS(2.*L)
      SIN2L=SIN(2.*L)
10     LN2=ALOG(2.*L/ALPHA)
      LN4=ALOG(4.*L/ALPHA)
      G=.5772=566
      IFAIL=0
      CL=G+ALOG(L)-S13ACF/(L, IFAIL)
15     C2L=G+ALOG(2.*L)-S13ACF(2.*L, IFAIL)
      C4L=G+ALOG(4.*L)-S13ACF(4.*L, IFAIL)
      SL=S13ADF(L, IFAIL)
      S2L=S13ADF(2.*L, IFAIL)
      S4L=S13ADF(4.*L, IFAIL)
20     S=1./(1.-COSL)
      S2=S*S
      A=S2*(S4L+4.*COSL*(L*COSL-SINL))*(LN4-C2L)
      C=(8.*ALPHA*SINL**2/(PI-2.*COSL**2*SIN2L))
      B=S26*(-C4L-(4.*L*COSL**2-2*SIN2L)*S2L+SIN2L**2)
      C=S*(SINL *S4L+(1.-COSL)*C4L+4.*COSL*(1.-COSL-L
              *SINL)*C2L
      C+4.*COSL*(1.-COSL)*CL+4.*SINL*(L*COSL-SINL)*LN4
      C+4.*(1.-COSL)**2*LN2
      C-(8.*ALPHA*SINL*(1.-COSL))/PI-SIN2L**2)
      D=S*((1.-COSL)*S4L-SINL*C4L+4.*COSL*(1.-COSL-L
              *SINL)*S2L
30     C+4.*COSL*(1.-COSL)*SL+2.*SINL**2*SIN2L)
      E=2.*COSL*(1.-COSL)*S4L+2.*SINL*(1.-COSL)*C4L
      C+4.*(1.-COSL)**2*S2L-4.*L*SINL**2*C2L
      C+8.*SINL*(1.-COSL)*CL+(4.*L*SINL**2-8.*SINL*
              (1.-COSL))*LN4
      C-(24.*ALPHA*(1.-COSL)**2)/PI-2.*SINL**2*SIN2L
35     F=2.*SINL*(1.-COSL)*S4L-2.*COSL*(1.-COSL)*C4L
      C-4.*L*SINL**2*S2L-4.*(1.-COSL)**2*C2L
      C+8.*SINL*(1.-COSL)*SL+4.*SINL**4
      G=2.*S*(SINL-L*COSL)
      H=2.*(2.*(1.-COSL)-L*SINL)
40     HC=COMPLX(H, 0.)
      EC=COMPLX(E, 0.)
      FC=COMPLX(0, , F)
      GC=COMPLX(G, 0.)
      CC=COMPLX(C, 0.)
45     DC=COMPLX(0, , D)
      AC=COMPLX(A, 0.)
      BC=COMPLX(0, , B)
      J30=COMPLX(0, , 30.)
      Z11=(-J30*HC**2)/(EC+FC)
50     Z12+J30*(GC-HC*(CC+DC)/EC+FC)
      Z22=J30*((AC+BC)-(CC+DC)**2/(EC+FC))
      SIGMA=(1./(PI*900.))*(CABS(Z11-Z12**2/Z22))**2
      WRITE(2, 100) SIGMA, L
100    FORMAT(' SIGMA=', E14.7, ' KH=', F10.6)
55     RETURN
      END
```

```
1      SUBROUTINE MUTUAL(A,D,Z)
      COMPLEX Z
      PI=6.283185306
      AO=PI*D
5      A1=PI*(SORT(D*D+A*A)-A)
      A2=PI*(SORT(D*D+A*A)+A)
      A3=PI*(SORT(D*D+4.*A*A)-2.*A)
      A4=PI*(SORT(D*D+4.*A*A)+2.*A)
      IFAIL=0
10     SA0=S13ADF(AO,IFAIL)
      SA1=S13ADF(A1,IFAIL)
      SA2=S13ADF(A2,IFAIL)
      SA3=S13ADF(A3,IFAIL)
      SA4=S13ADF(A4,IFAIL)
15     G=.57721566
      CAO=S13ACF(AO,IFAIL)
      CA1=S13ACF(A1,IFAIL)
      CA2=S13ACF(A2,IFAIL)
      CA3=S13ACF(A3,IFAIL)
20     CA4=S13ACF(A4,IFAIL)
      G=PI*A
      SG=SIN(G)
      CG=COS(G)
      C2G=COS(2.*G)
      S2G=SIN(2.*G)
25     RM=2.*(2.+C2G)*CAO-4.*CG*CG*(CA1+CA2)+C2G*(CA3+CA4)
           C+S2G*(SA4-SA3-2.*SA2+2.*SA1)
      RM=RM*15./(SG*SG)
      XM=-2.*(2.+C2G)*SA0+4.*CG*CG*(SA1+SA2)-C2G*(SA3+SA4)
           C+S2G*(CA4-CAB-2.*CA2+2.*CA1)
      XM=XM*15./(SG*SG)
      Z=2.*CMPLX(RM,XM)
      RETURN
      END
```

APPENDIX III

Details the circuit diagrams, operating details and relevant program listings relating to the open resonator electronics and computer control system described in Chapter 5.

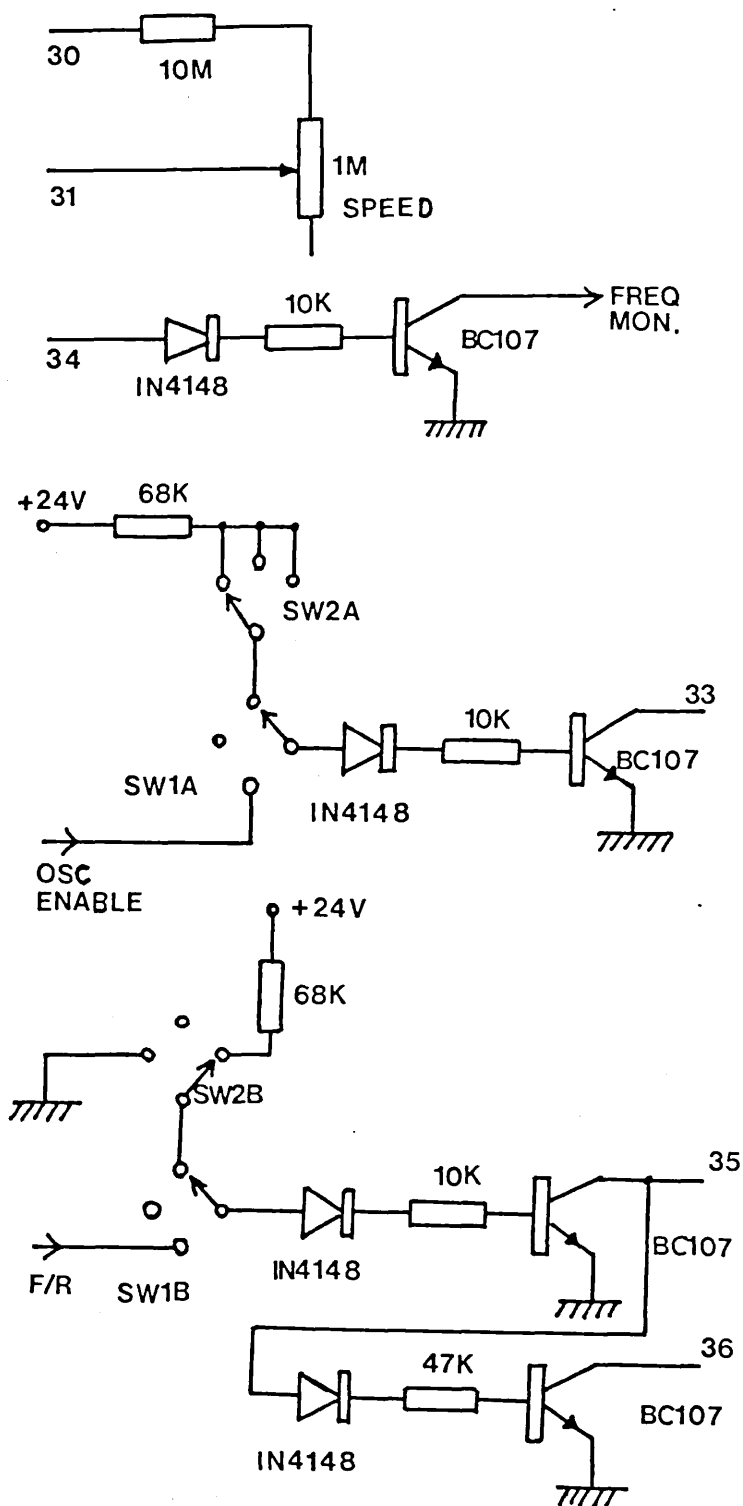


Figure A.3.1. TTL to ADC 117 drive board interface (for 4 step/rev stepping motors). Numbers refer to the board edge connector.



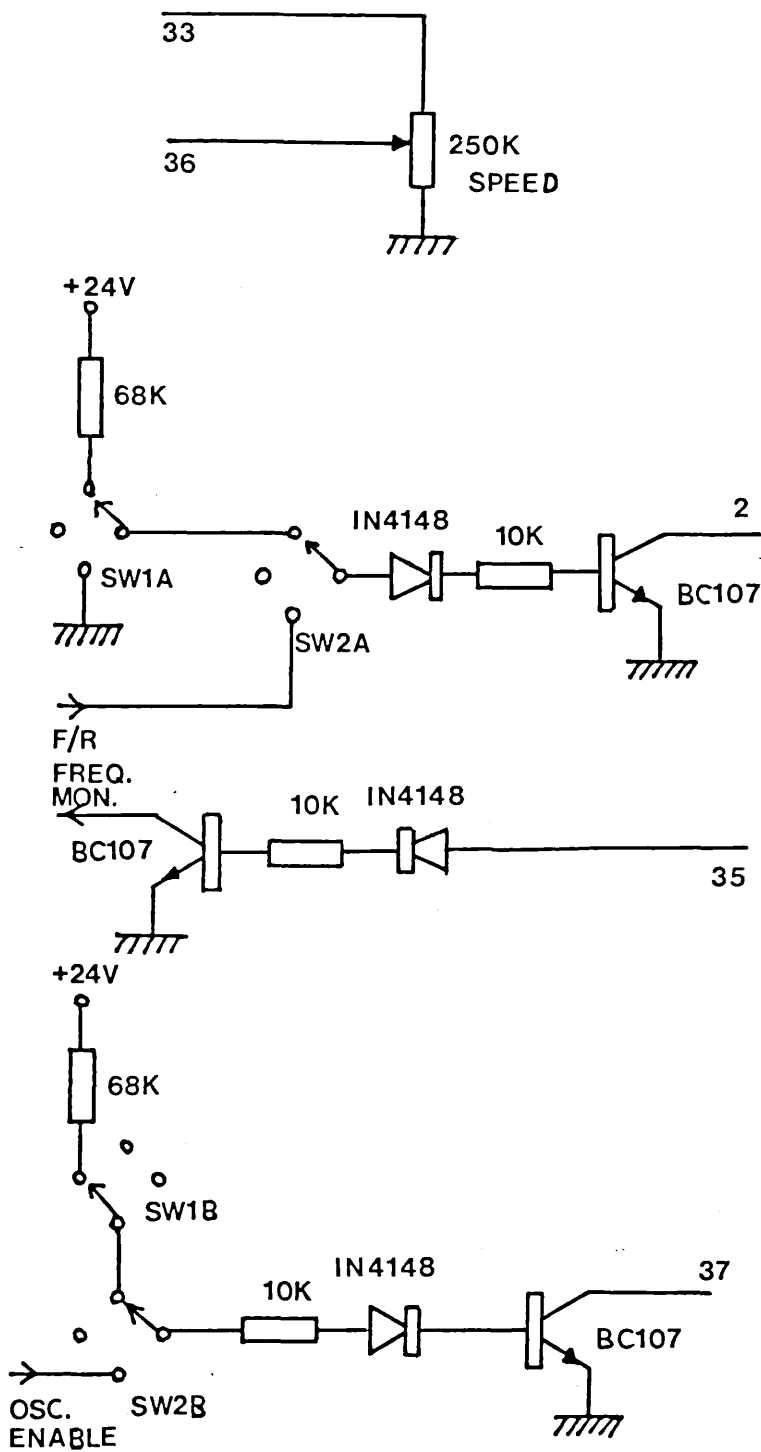


Figure A.3.2. TTL to ADC 800 drive board interface (for 800 step/rev stepping motors). Numbers refer to the board edge connector.

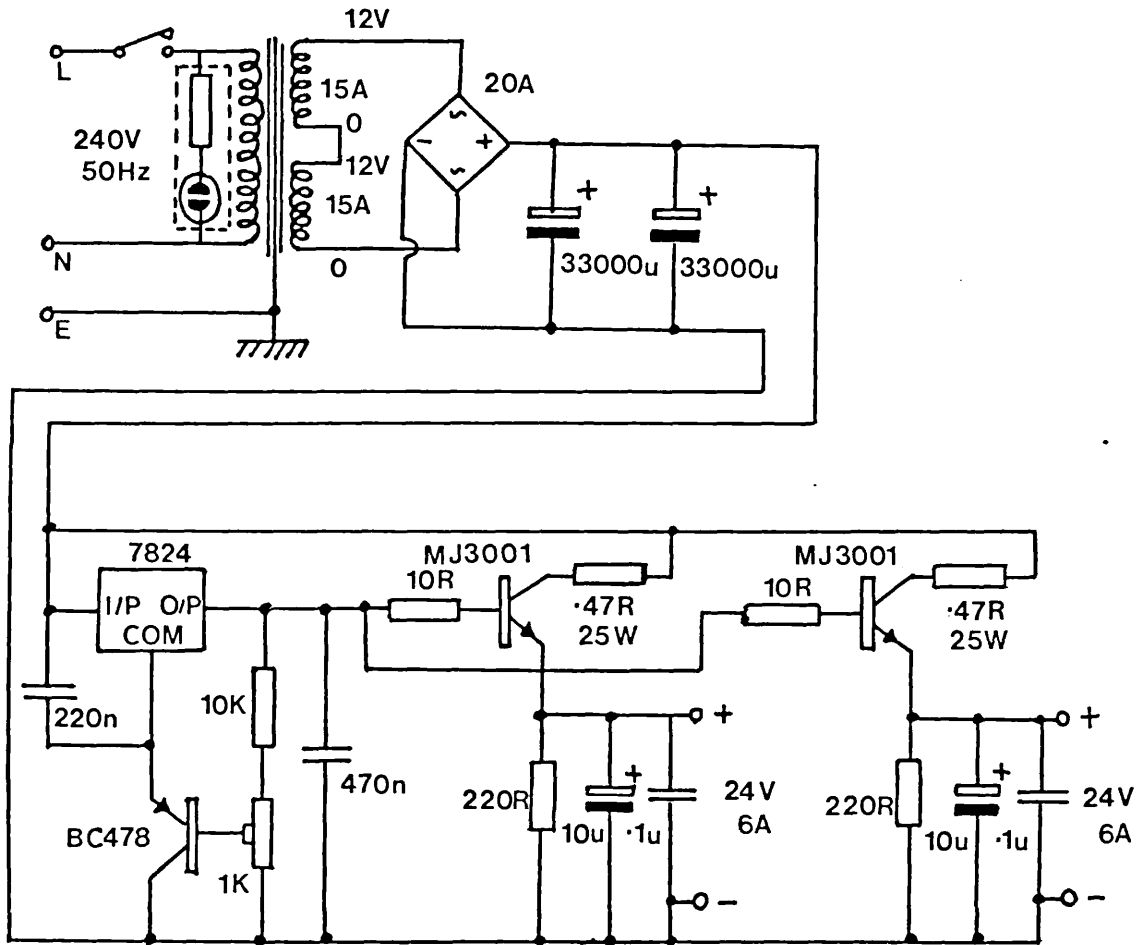


Figure A.3.3. Dual 24 volt 6 amp power supply circuit diagram. Each output fed one ADC 117 and one ADC 800 drive board.

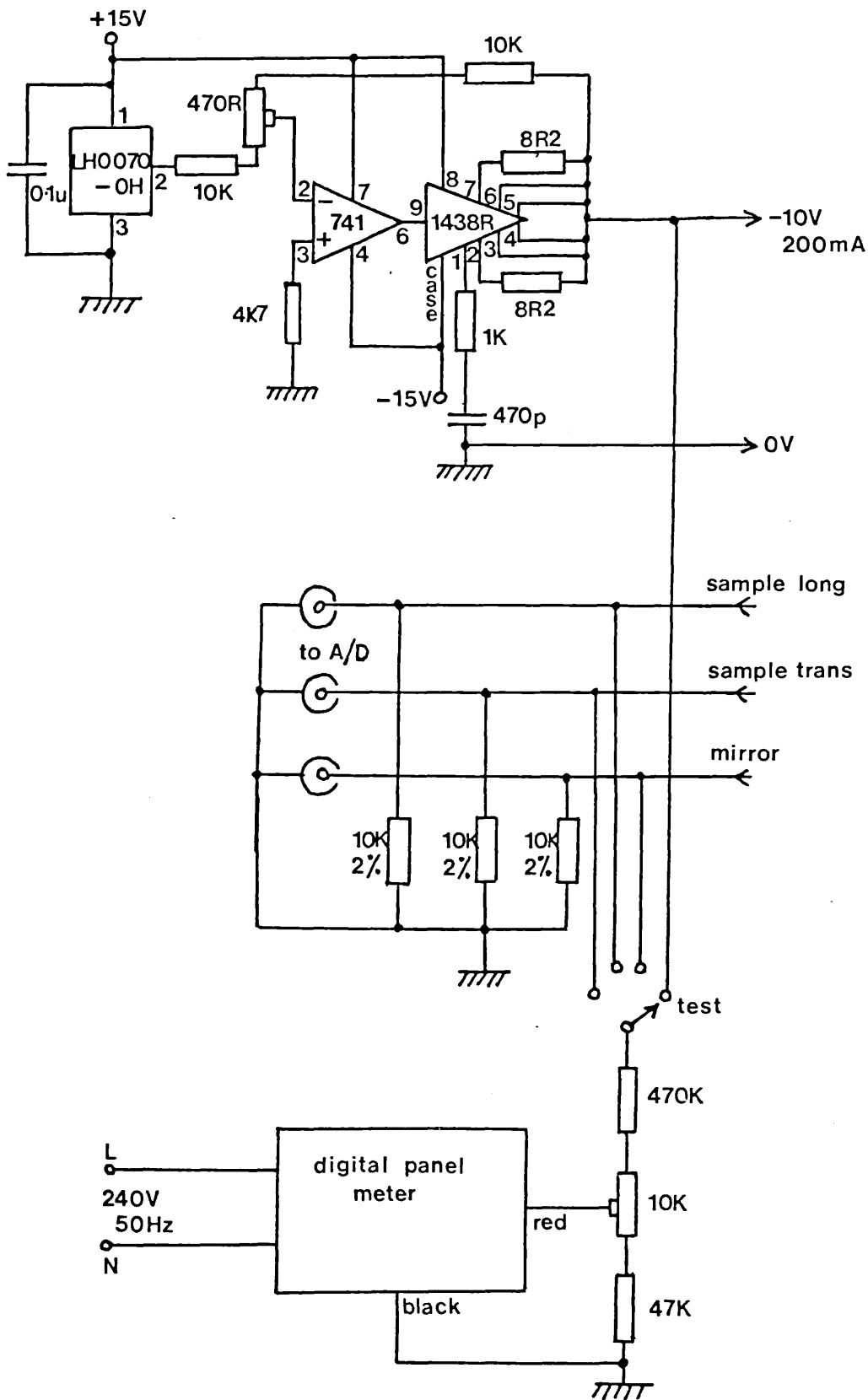
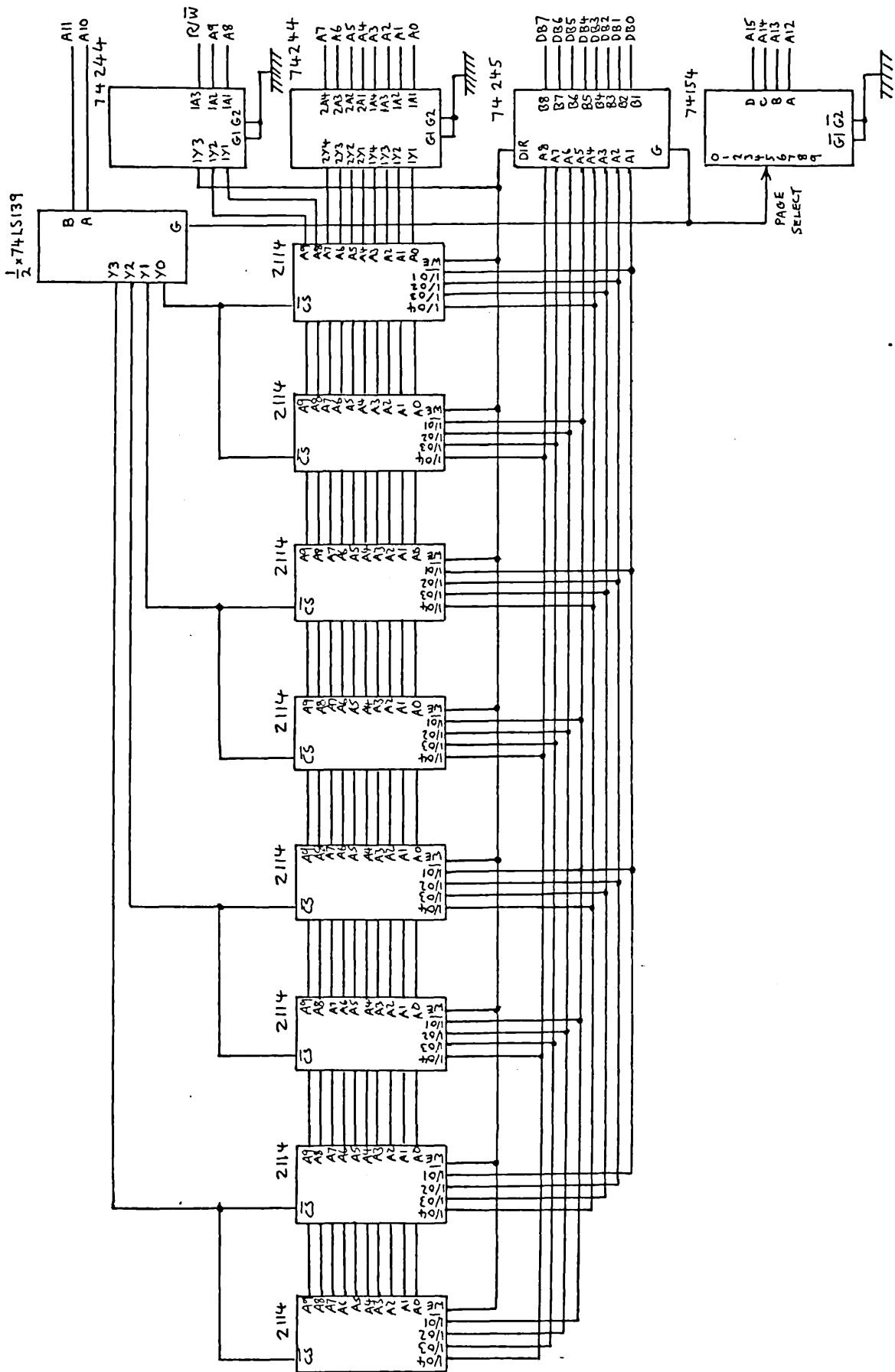
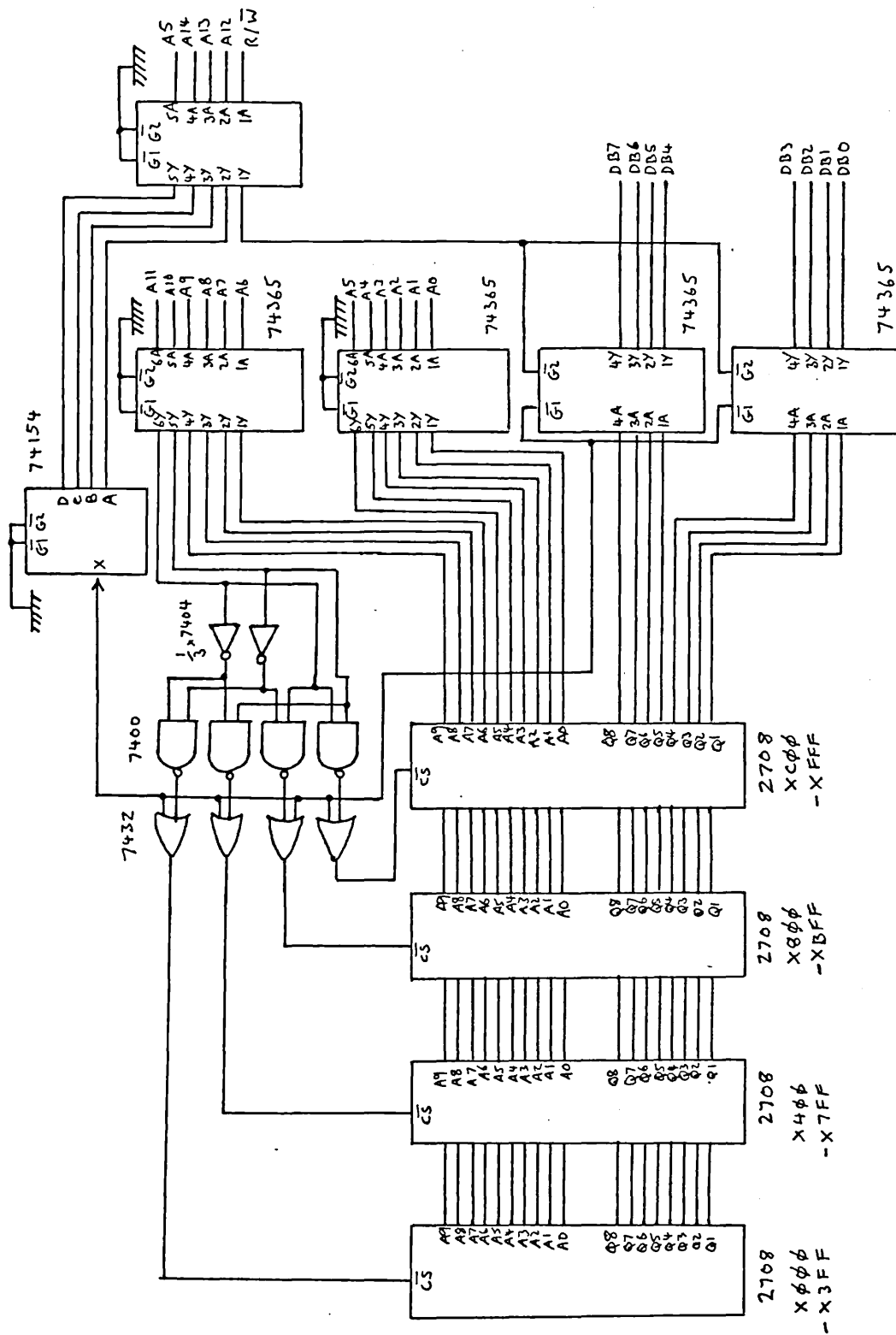


Figure A.3.4. Circuit diagram for the linear variable differential transformer displacement transducer power supply and meter unit.





A.3.6. 4K RAM board.



A.3.7. 4K EPROM board.

8 Channel 12 bit analogue to digital converter.

Address allocations

Input 8020<sub>16</sub> = 32800<sub>10</sub> - start conversion  
Output 8021<sub>16</sub> = 32801<sub>10</sub> - conversion status  
Output 8022<sub>16</sub> = 32802<sub>10</sub> - lower order byte  
Output 8023<sub>16</sub> = 32803<sub>10</sub> - higher order byte

Basic Commands

To start a conversion on channel X, the command in BASIC would be

POKE 32800, X

X could take a value in the range 0 through to 7 inclusive. While the conversion was in progress, bit 0 of address 32801<sub>10</sub>(8021<sub>16</sub>) was set to 1 and was reset to 0 when the conversion was completed. The status of the A - D could be tested with the command

WAIT 32801, 1, 1

Upon completion of the conversion the next line in BASIC would be executed. The lower order byte was read with the command

LB = PEEK (32802)

and the higher order byte with

HB = PEEK (32803)

As bits 6 and 7 were always 1 a mask was employed to screen off these bits using the command

HB = HB AND 63

this set bits 6 and 7 to zero and left bits 0 through 5 intact.

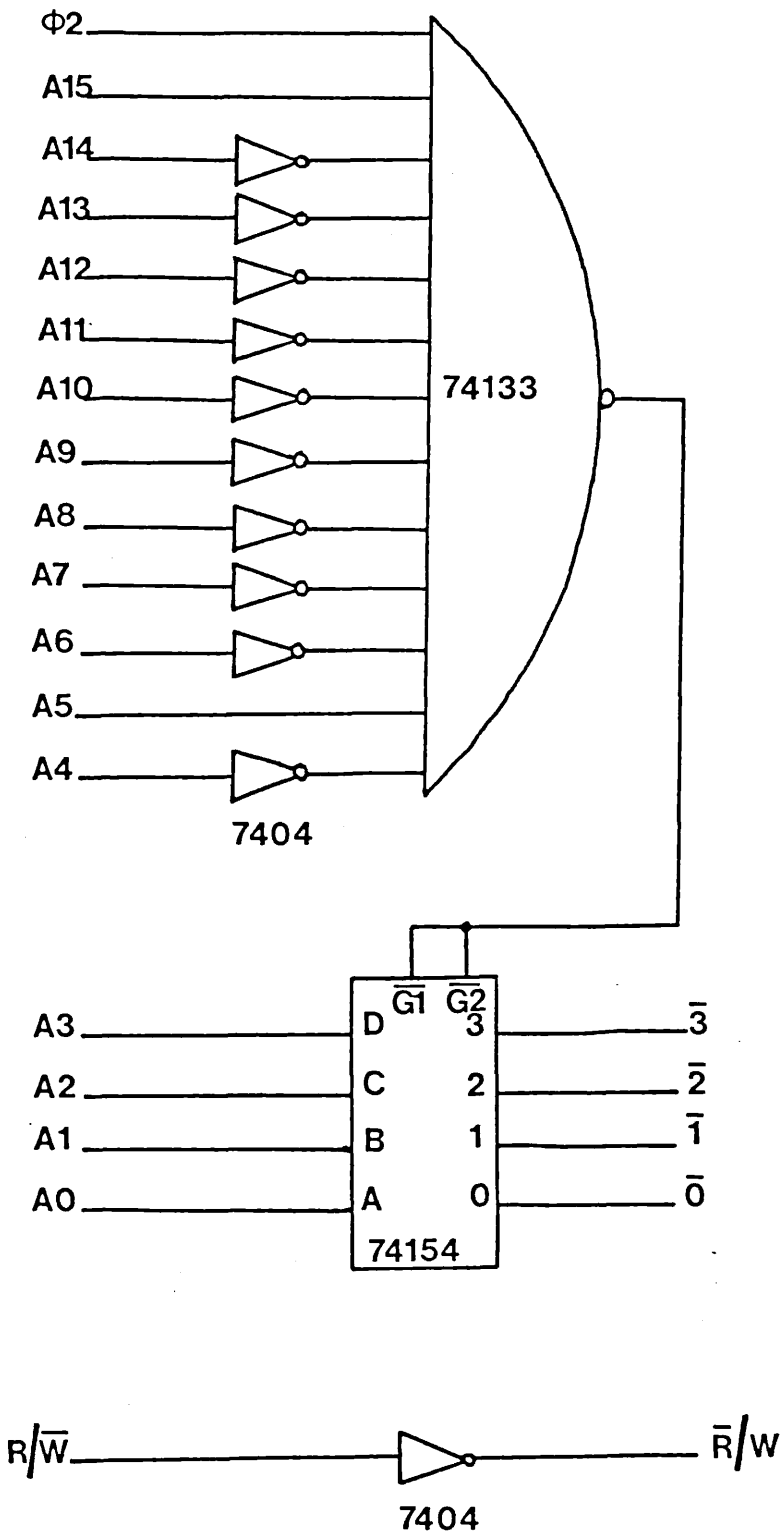


Figure A.3.8 (a). 8 Channel 12 bit A - D converter address decoding circuitry.



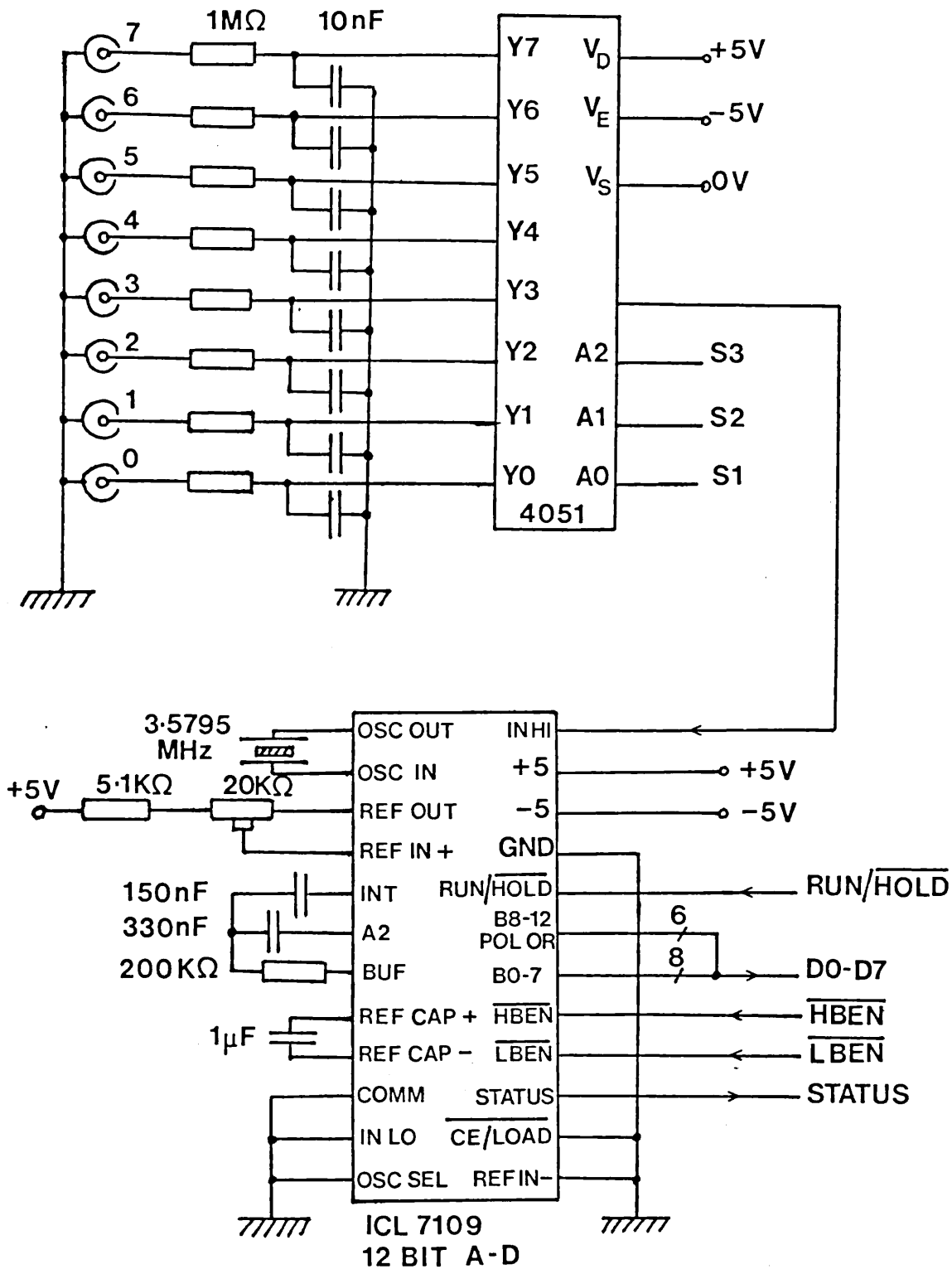


Figure A.3.8.(b). 8 channel 12 bit A - D converter.  
8 channel input analogue multiplexer  
and converter IC circuit.

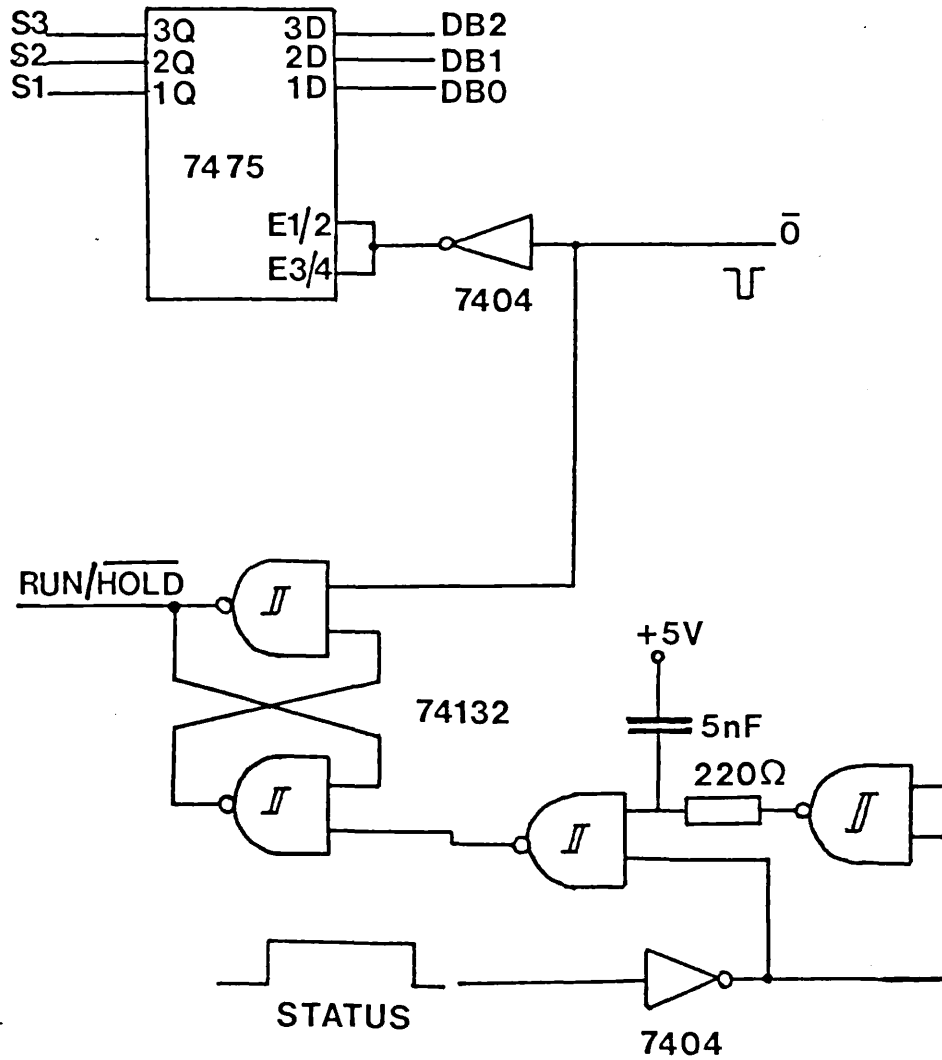


Figure A.3.8 (c). 8 channel 12 bit A - D converter. Analogue channel address select and status latching circuitry.



Dual Stepping Motor Interface.

Address allocations

Input 8001<sub>16</sub> = 32769<sub>10</sub> - motor 1 step counter  
 Input 8002<sub>16</sub> = 32770<sub>10</sub> - motor 1 forward/reverse  
 Input 8003<sub>16</sub> = 32771<sub>10</sub> - motor 2 step counter  
 Input 8004<sub>16</sub> = 32772<sub>10</sub> - motor 2 forward/reverse  
 Output 8005<sub>16</sub> = 32773<sub>10</sub> - status register

BASIC Commands

The BASIC commands given below were used to control the stepping motor interface. To control the number of steps made by motor 1 the command POKE 32769,X was used, where X was the number of steps motor 1 was to make. The BASIC command employed to control the number of steps made by motor 2 was POKE 32770,X, where X was the number of steps motor 2 was to make. The direction of rotation of motor 1 was controlled with the command POKE 32770,Y, Y was 0 or 1 corresponding to the forward or reverse settings of motor 1. The command POKE 32772,Y was used to control the direction of motor 2. Y was 0 or 1 corresponding to the forward or reverse setting of motor 2. The status register was examined with the command, Z = PEEK (32773). Z was then equal to the value of the status register.

Status Register

D7	D6	D5	D4	D3	D2	D1	D0
0	0	0	0	X	X	X	X

D0 X = 0 Motor 1 not stepping  
 X = 1 Motor 1 stepping  
 D1 X = 0 Motor 2 not stepping  
 X = 1 Motor 2 stepping  
 D2 X = Data stored in 8002<sub>16</sub> (i.e. 0 or 1)  
 D3 X = Data stored in 8004<sub>16</sub> (i.e. 0 or 1)

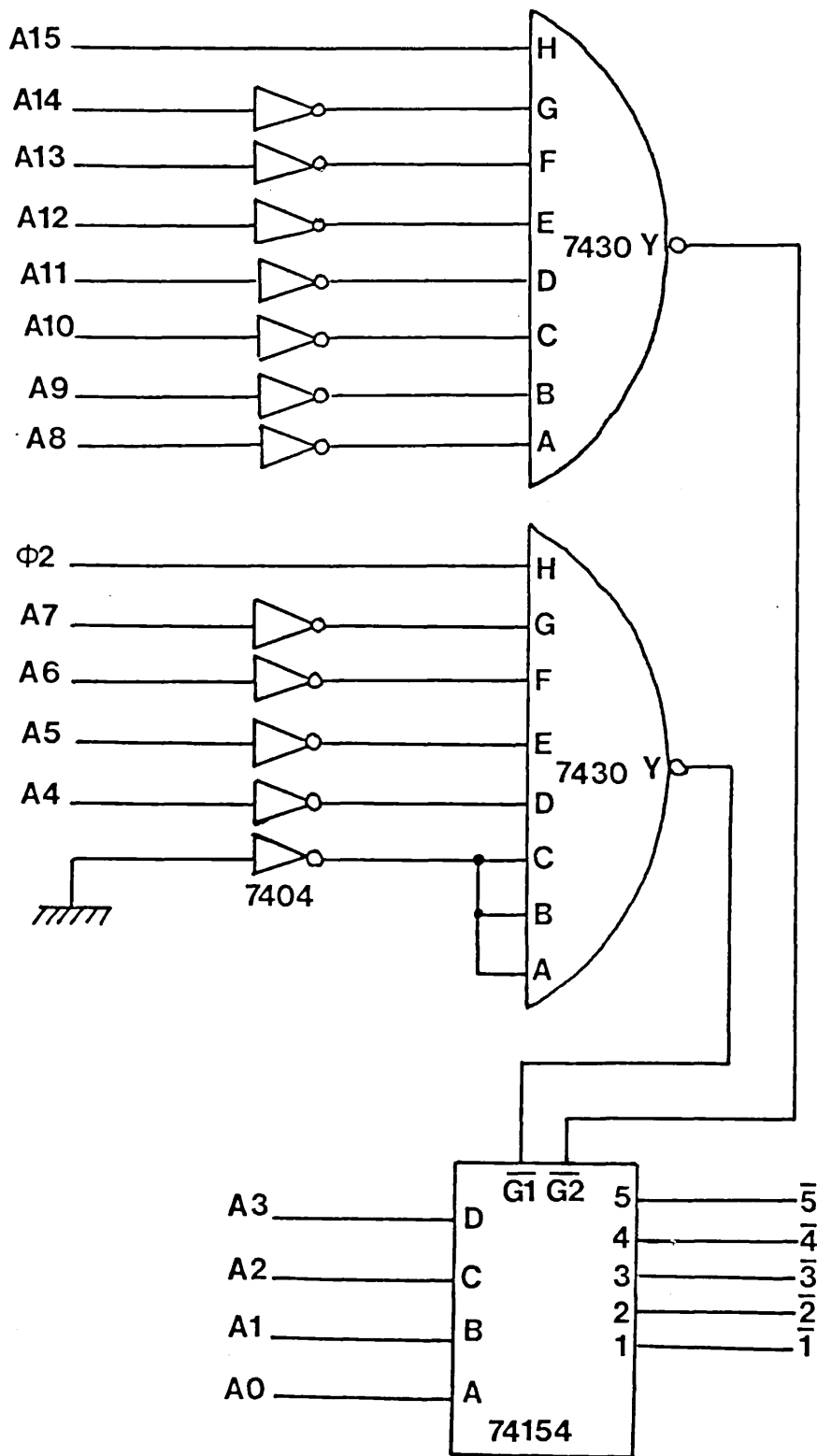


Figure A.3.9 (a). Dual stepping motor interface address decoder.



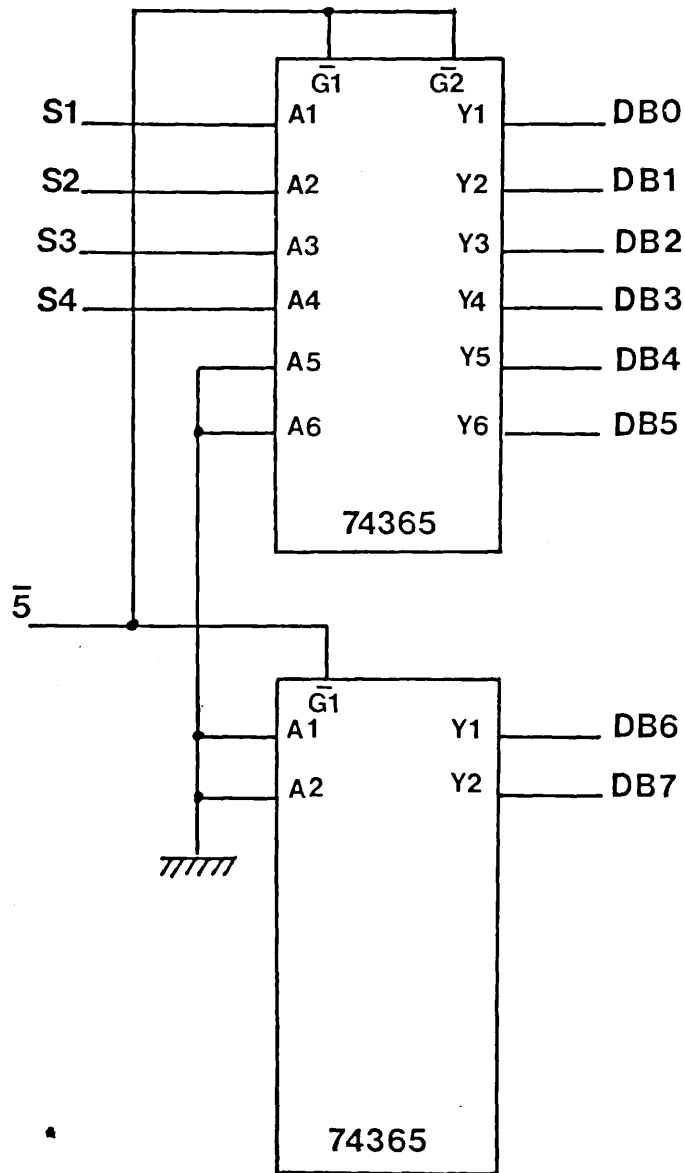


Figure A.3.9. (c). Dual stepping motor interface peripheral status register tristate output buffer.

Quad Stepping Motor Interface.

Address allocations

Input 8010<sub>16</sub> = 32784<sub>10</sub> - motor 1 step counter  
Input 8011<sub>16</sub> = 32785<sub>10</sub> - motor forward/reverse  
Input 8012<sub>16</sub> = 32786<sub>10</sub> - motor 2 step counter  
Input 8013<sub>16</sub> = 32787<sub>10</sub> - motor 2 forward/reverse  
Input 8014<sub>16</sub> = 32788<sub>10</sub> - motor 3 step counter  
Input 8015<sub>16</sub> = 32789<sub>10</sub> - motor 3 forward/reverse  
Input 8016<sub>16</sub> = 32790<sub>10</sub> - motor 4 step counter  
Input 8017<sub>16</sub> = 32791<sub>10</sub> - motor 4 forward/reverse  
Output 8018<sub>16</sub> = 32792<sub>10</sub> - status register

BASIC Commands

For example, to cause motor 1 to take 200 steps the BASIC command would be

POKE 32784, 199

The direction of stepping motor 1 was controlled by the command

POKE 32785, X

where X was 0 or 1 corresponding to the forward or reverse directions. By reading the contents of address 32792<sub>10</sub> the status of the peripheral could be ascertained. For example, to wait for motor N to complete a stepping sequence the command sequence

Y = 2 ↑ (N - 1)

WAIT 32792, Y, Y

would be used. N could take the value 1 to 4.



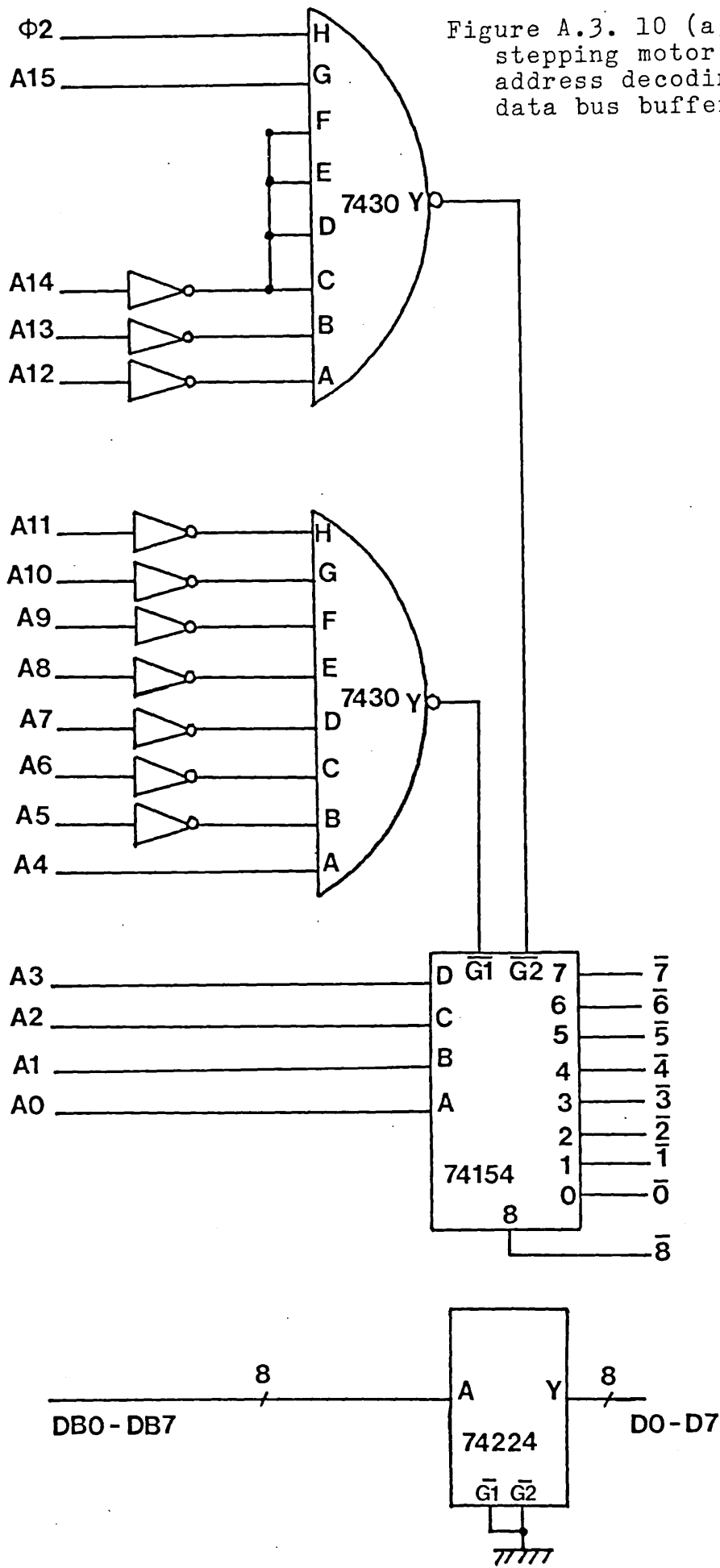


Figure A.3. 10 (a). Quad stepping motor interface address decoding and input data bus buffering circuitry.

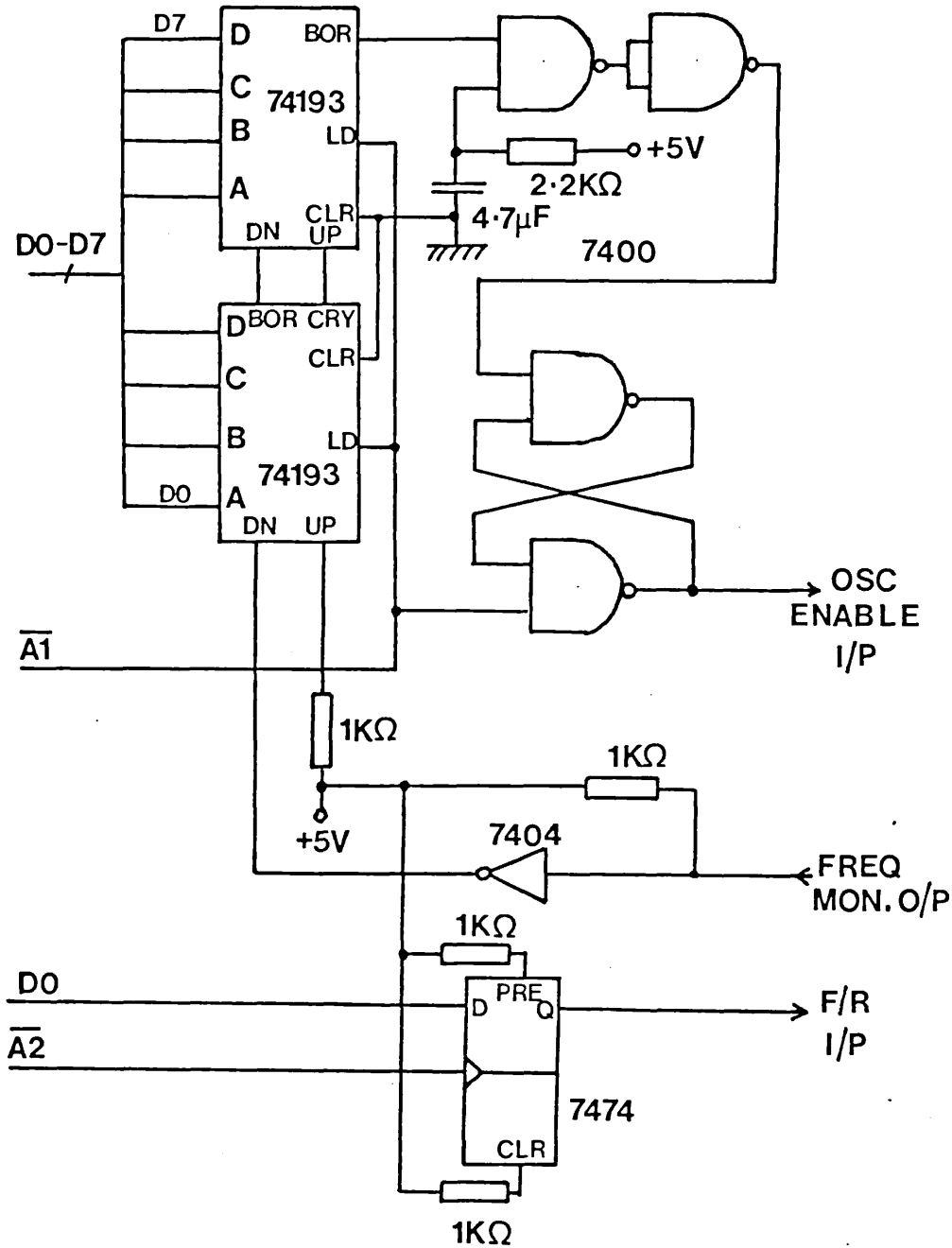


Figure A.3.10. (b). Stepping motor interface parallel loaded down counter, motor drive board oscillator enable latching and forward/reverse latch circuitry. There are 4 such circuits in the quad interface. The connection table is given below.

Motor	$\overline{A1}$	$\overline{A2}$
1	0	1
2	2	3
3	4	5
4	6	7

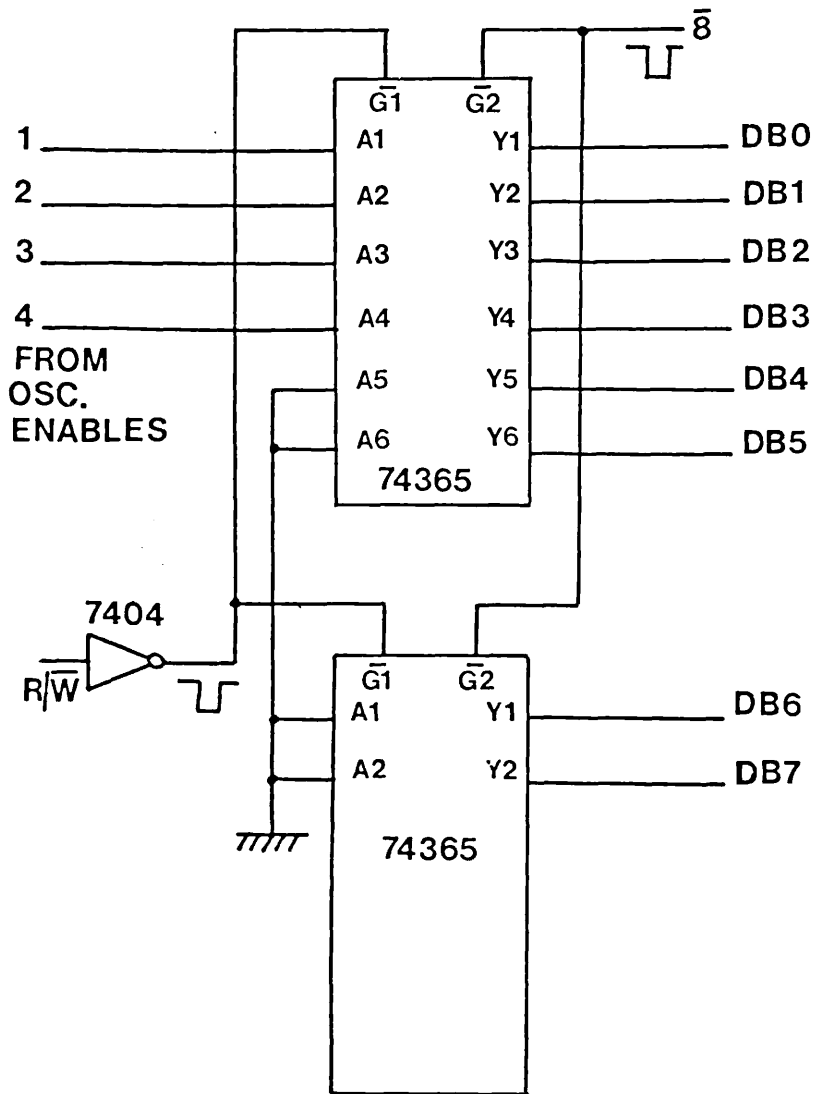


Figure A.3.10. (c) Quad stepping motor interface peripheral status register tristate buffering.

Rotary Position Transducer Interface.

Address allocation

The rotary position transducer interface was available at address  $603F_{16} = 24639_{10}$  and was read only.

BASIC Commands

The peripheral could be read by using the following commands. From command level

? PEEK (24639)

and from program level

X = PEEK (24639)

the number returned was an integer between 0 and 255 inclusive.

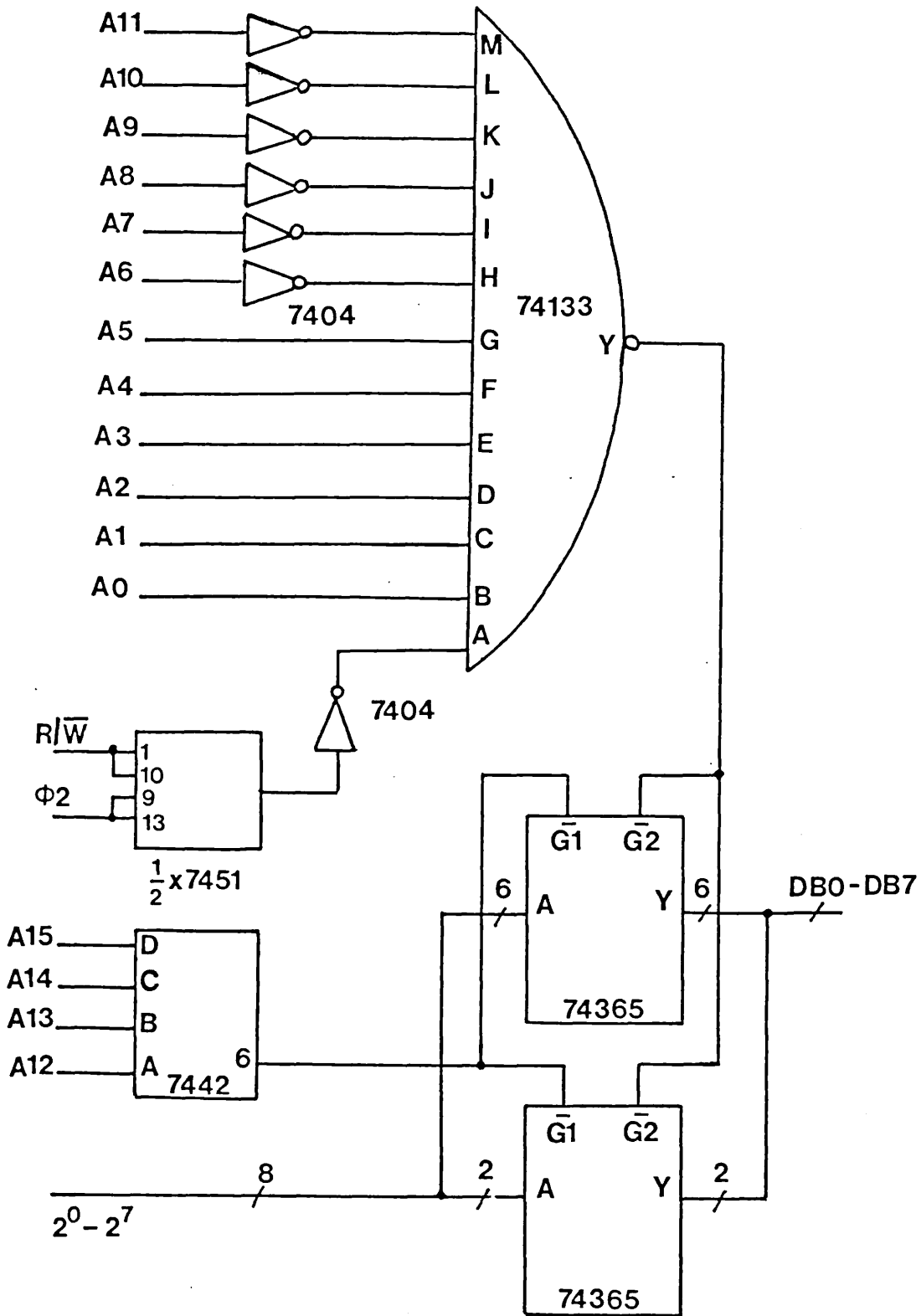
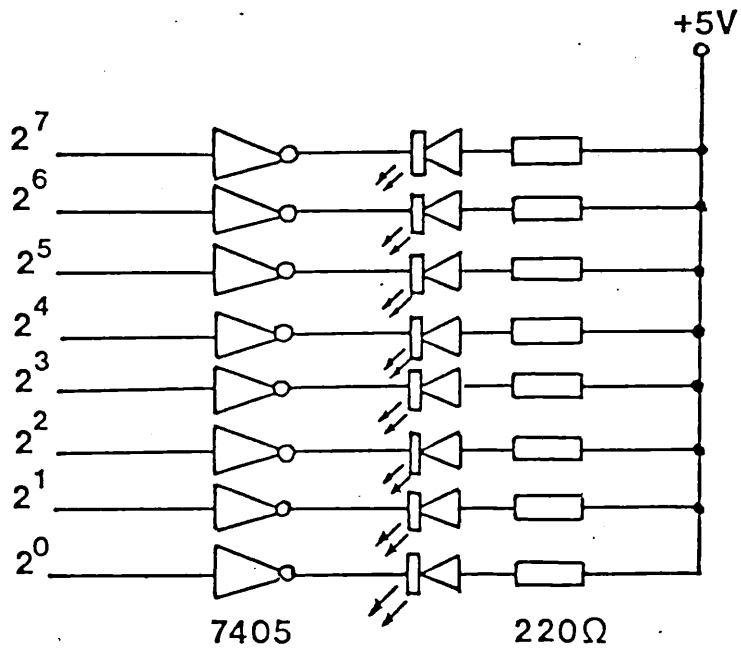
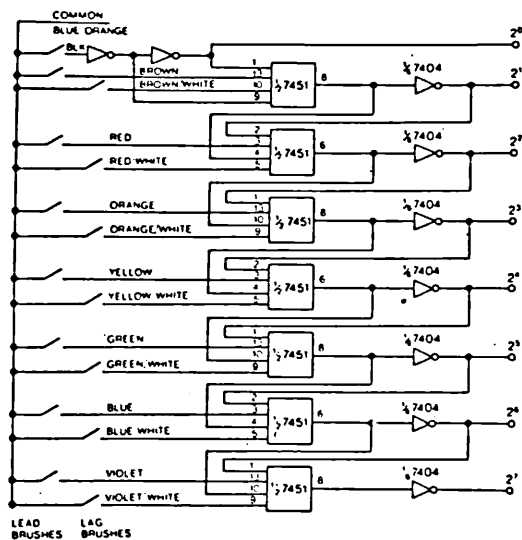


Figure A.3.11. (a) Rotary position transducer interface address decoding and output tristate buffering circuitry.



led binary display



code converter

Figure A.3.11 (b). Rotary position transducer V-scan to natural binary decoding and display circuitry.

Visual Display Unit Interface.

Address allocation

The address allocated to the VDU interface was  $800B_{16}$  ( $32779_{10}$ ). It was a write only interface, and as no busy signal was generated, software delays using the timer in the system VIA were employed. This allowed sufficient time for the VDU to process the current data and instructions before the next one was sent.

VDU Interface program

The monitor on the AIM 65 allowed one to echo a character to an external peripheral before it was displayed on the onboard display and/or printer. The linkage vector to the external display routine was stored in RAM at addresses A406 and A407. These memory locations were set to the starting address of the VDU display routine. The monitor program would then make a jump to the external display routine. After completion of the external display routine, control was then returned to the monitor printer/display routines. The VDU display routine was stored in EPROM starting at address 7C20. This echoed the displayed character to the VDU interface before returning to the monitor display routines. The accumulator and other registers in the microprocessor had to be returned to the values they had upon entry into the external display routine. The VDU interface program is listed below.

7C00	LDA	7C	}	Set DILINK to echo to VDU before display and return to monitor.
7C02	STA	A407		
7C05	LDA	20		
7C07	STA	A406		
7COA	BRK			
7C20	PHA			- Save accumulator (ACC).
7C21	JSR	EB9E		- Save X and Y registers.
7C24	TAY			- Transfer ACC to Y register.
7C25	CPY	0C		- If clear screen and cursor
7C27	BEQ	7C66		home instruction branch to 7C66.
7C29	CPY	1C		- If cursor home instruction
7C2B	BEQ	7C66		branch to 7C66.
7C2D	CPY	0D		- If carriage return instruction
7C2F	BEQ	7C37		branch to 7C37.
7C31	CPY	8D		- If VDU carriage return
7C33	BEQ	7C37		instruction branch to 7C37.
7C35	BNE	7C52		- Not any of above branch 7C52.

7C37	LDY	0D	- Carriage return routine.
7C39	STY	800B	- Store chracter in VDU
7C3C	LDX	28	- memory and initiate a
7C3E	JSR	7C77	- 10.4 ms delay.
7C41	LDY	1B	- Line feed/cursor down
7C43	STY	800B	- routine, store chracter in
7C46	LDX	28	- VDU memory and initiate
7C48	JSR	7C77	- a 10.4 ms delay.
7C4B	JSR	EBAC	- Restore X and Y registers.
7C4E	PLA		- Restore accumulator.
7C4F	JMP	EF05	- Jump to AIM 65 display routine.
7C52	TSX		- Test for a delete
7C53	LDA	0105,X	- character. If a
7C56	CMP	E7	- delete then stack
7C58	BNE	7C43	- should contain address
7C5A	LDA	0104,X	- of delete subroutine
7C5D	CMP	F2	- at 0105,X and
7C5F	BNE	7C43	- 0104,X. X is stack pointer.
7C61	LDY	08	- Cursor left command.
7C63	JMP	7C43	
7C66	STY	800B	- Store chracter in
7C69	LDX	FF	VDU memory and
7C6B	JSR	7C77	initiate a 150 ms
7C6E	JSR	7C77	delay.
7C71	JSR	7C77	
7C74	JMP	7C4B	Return to monitor.
7C77	LDA	00	} Delay routine entered with X register containing most significant byte of delay in X register.
7C79	STA	A00B	
7C7C	STA	A008	
7C7F	STX	A009	
7C82	LDA	20	} Delayed for MSB LSB Hex clock pulses
7C84	BIT	A00D	
7C87	BEQ	0C84	
7C89	LDA	A008	
7C8C	RTS		

The VDU routine was initialised, after powering up the AIM 65, with the commands

\* = 7C00  
G

The screen could then be cleared and the cursor homed by holding down the control key and pressing the L key.



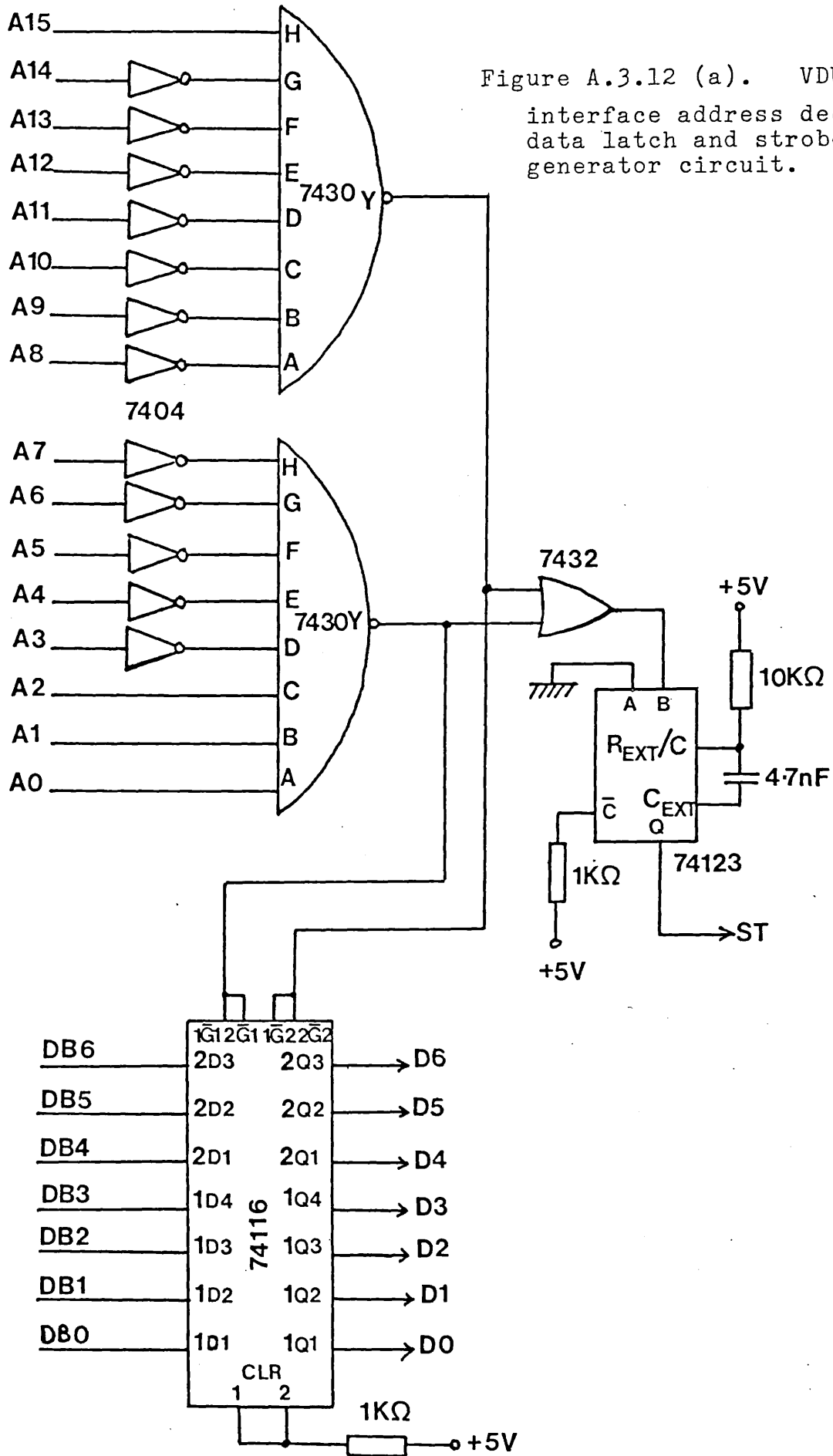


Figure A.3.12 (a). VDU interface address decoder, data latch and strobe generator circuit.

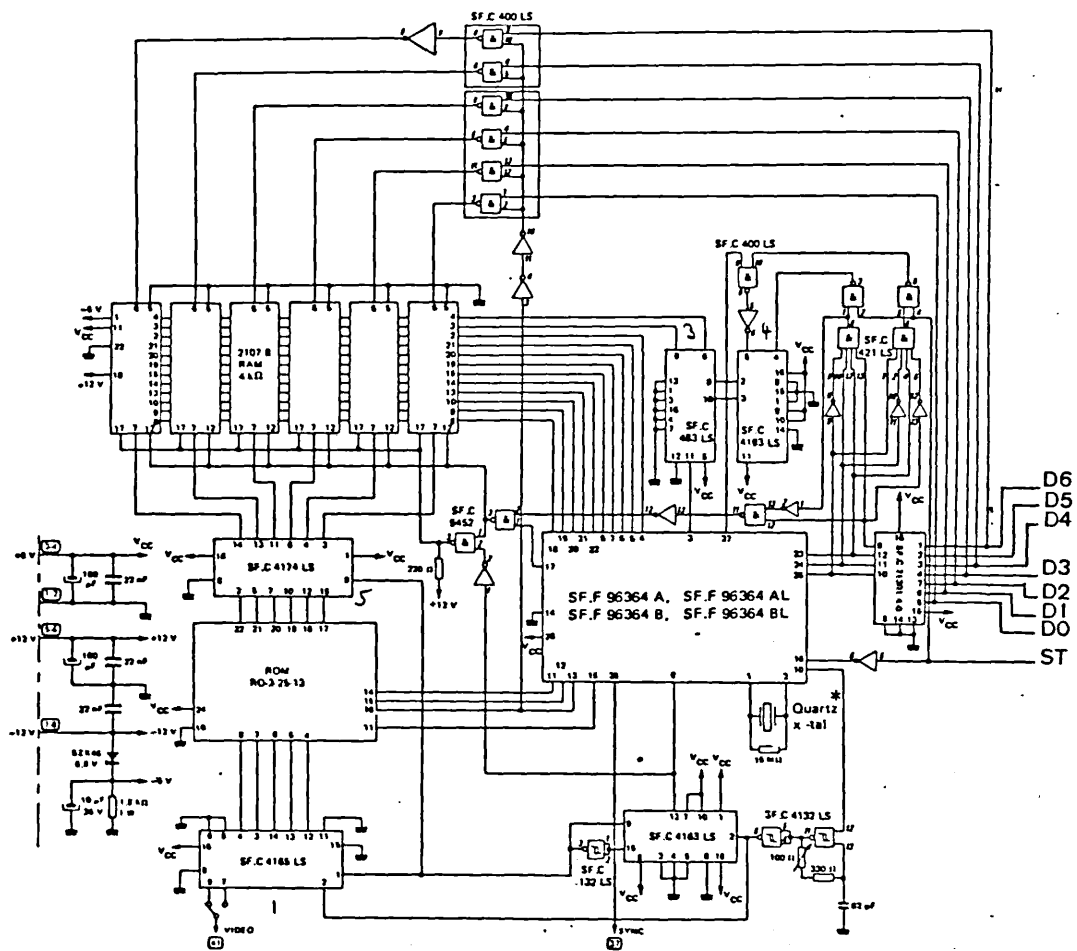


Figure A.3.12 (b). CRT controller circuit.

Digital Plotter Interface

Address allocation

Input/output  $800A_{16}$  =  $32778_{10}$  ASCII Input Data/Busy  
Signal

BASIC Commands

The peripheral could be tested to see if the digital plotter was busy by using the command

X = PEEK (32778)

if it returned X as 0 then the plotter was not busy. If X was 1 then the plotter was busy. If the plotter was not busy a data word could be transferred to the digital plotter with the command

POKE 32778,Y

where Y corresponds to the required decimalised ASCII code word.

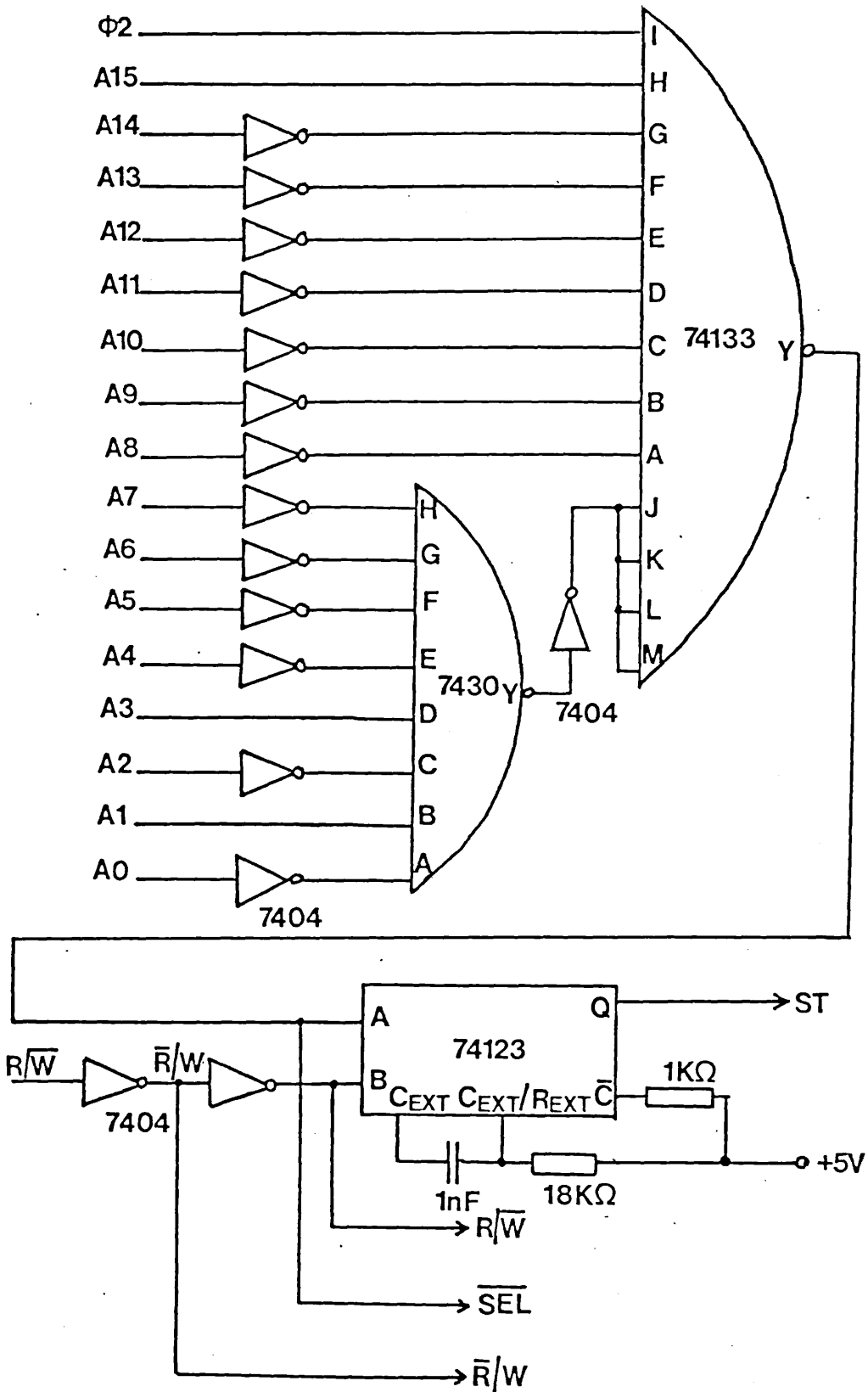
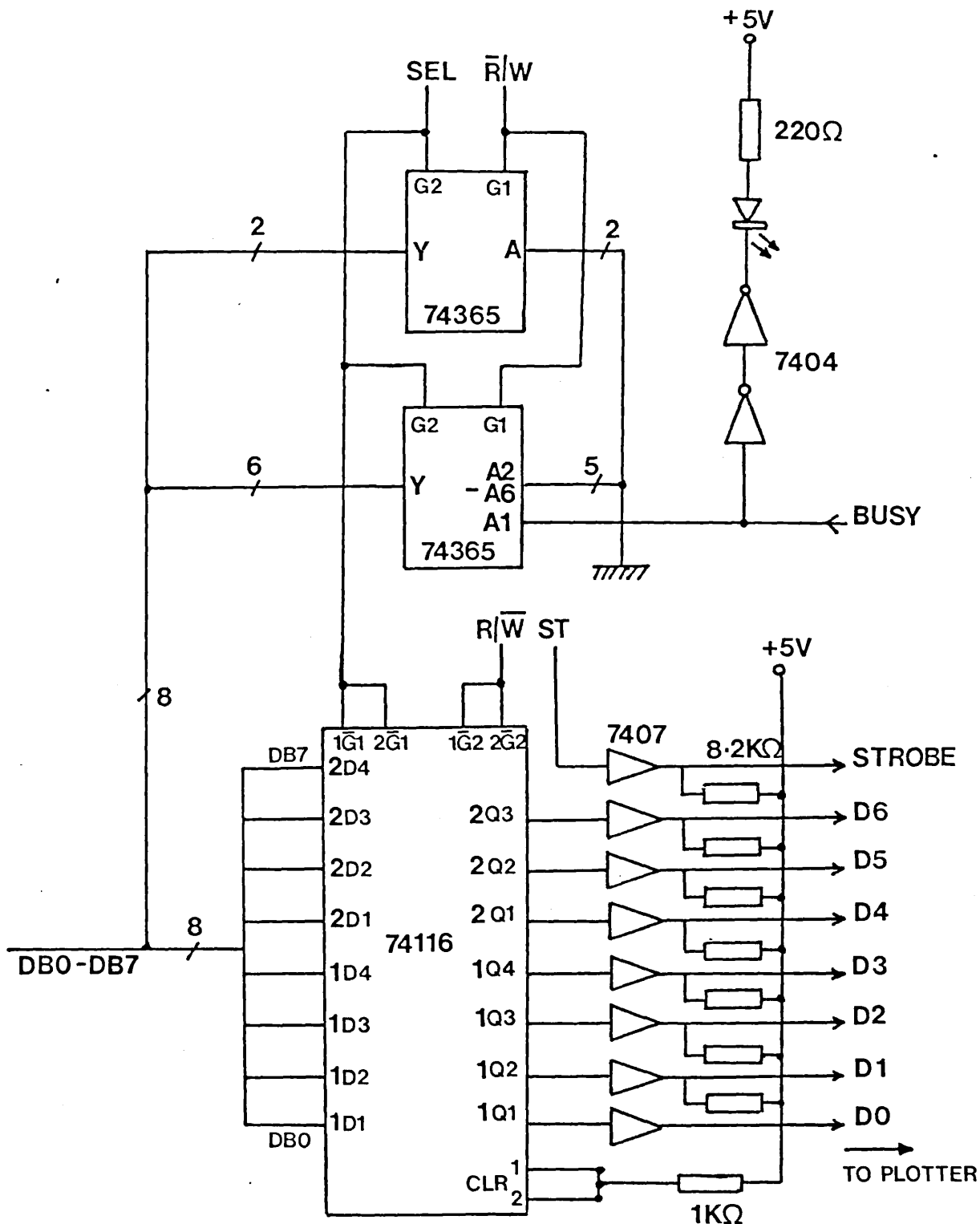


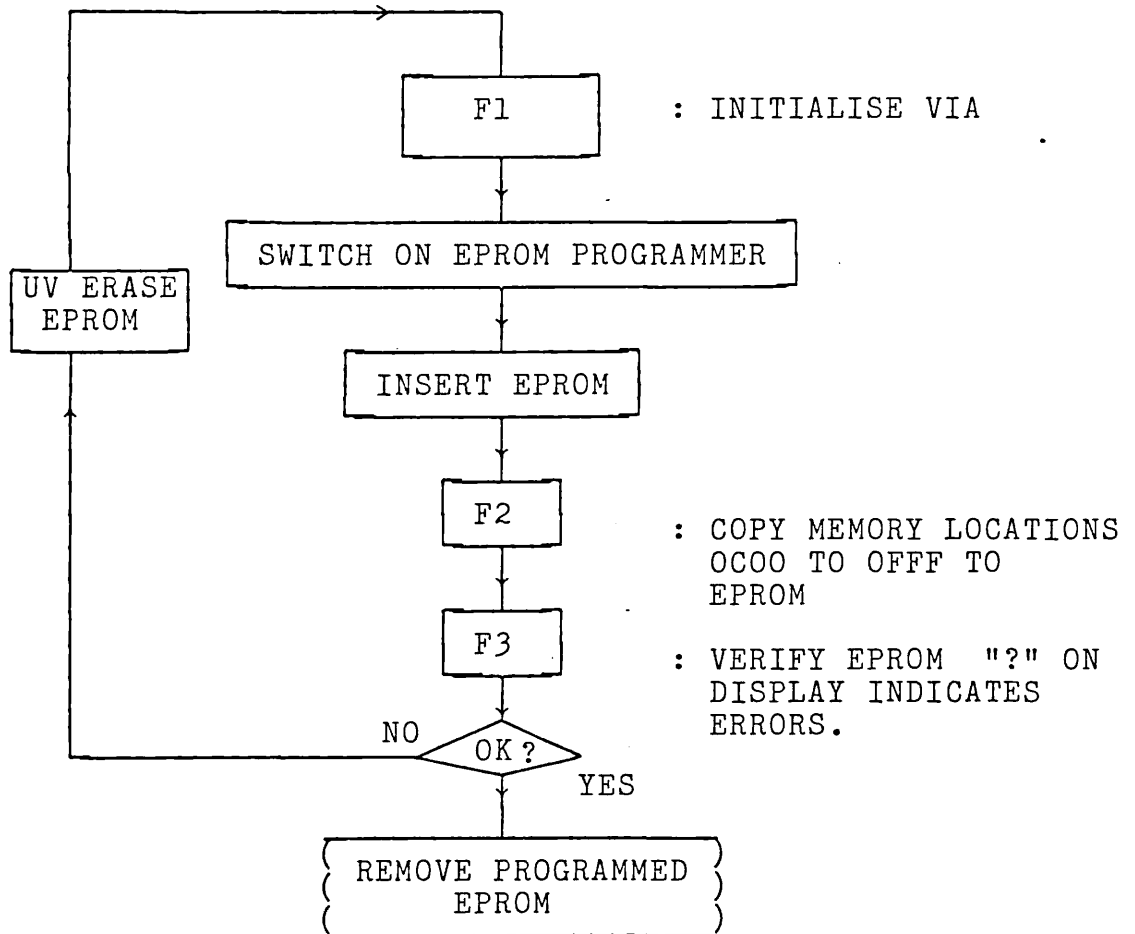
Figure A.3.13. (a) Digital plotter interface address decoder and data strobe circuitry.

Figure A.3.13. (b) Digital plotter interface data latch and busy output tristate buffer.



2708 EPROM Programmer.

The EPROM programmer was used in conjunction with a software package, filename EPROM, which was stored on cassette tape. The program operations were initialised using the function keys F1 to F3 on the AIM 65. The EPROM programming sequence flowchart is given below, along with the machine code programming listing.

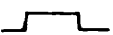


EPROM Programmer Program Listing

Filename: EPROM

Medium : Cassette

```
F1 0800 LDA CE : SET CA2 = 1 SET CB2 = 0
    0802 STA A00C : IN EPROM PROGRAM MODE
    0805 LDA FF : SET PORT B TO 0/P
    0807 STA A002 : SET PORT A TO 0/P
    080A STA A003 :
    080D LDA 30 : SET PB4, PB5 to 0/P
    080F STA A802 : ON SYSTEM VIA
    0812 RTS : RETURN TO MONITOR

F2 0813 LDX 00 : DO 1K TRANSFER SUBROUTINE
    0815 JSR 082A : 216 TIMES
    0818 INX
    0819 CPX D8
    081B BEQ 02
    081D BNE F6
    081F LDA EE : SET CB2 = 1, CA2 = 1
    0821 STA A00C : EPROM IN READ ONLY MODE
    0824 LDA 00
    0826 STA A003 : SET PORT A TO 1/P
    0829 BRK : HALT
    082A LDA 00 : SET UP INDIRECT ADDRESS LINKAGE
    082C STA 0000 : AT ZERO PAGE ADDRESS 0000
    082F LDA 0C :
    0831 STA 0001 :
    0834 LDA 30 : SET TAPE 1A = 0
    0836 STA A800 : AND TAPE 2A = 0
    0839 JSR 0864 : TRANSFER 0C00 - 0CFF TO EPROM
    083C LDA 0D
    083E STA 0001 : MODIFY ZERO PAGE ADDRESS
    0841 LDA 20 : SET TAPE 1A = 1
    0843 STA 0001 : AND TAPE 2A = 0
    0846 JSR 0864 : TRANSFER 0D00 - 0DFF TO EPROM
    0849 LDA 0E
    084B STA 0001 : MODIFY ZERO PAGE ADDRESS
    084E LDA 10 : SET TAPE 1A = 0
    0850 STA A800 : AND TAPE 2A = 1
    0853 JSR 0864 : TRANSFER 0E00 - 0EFF TO E
    0856 LDA 0F
    0858 STA 0001 : MODIFY ZERO PAGE ADDRESS
    085B LDA 00 : SET TAPE 1A = 1
    085D STA A800 : AND TAPE 2A = 1
    0860 JSR 0864 : TRANSFER 0F00 - 0FFF TO EPROM
    0863 RTS
    0864 LDY 00 : INITIALISE Y TO 00
    0866 STY A000 : STORE Y IN PORT B
    0869 LDA (00),Y : GET CONTENTS OF (INDIRECT
    086B STA A00F : STORE MEM LOC IN PORT A ADDRESS + Y)
    086E LDA 14
    0870 STA 08A2
    0873 DEC 08A2 : >
    0876 BNE FB : ~ 20 µS DELAY LOOP
    0878 LDA CC : 500 µS 30V PROGRAM PULSE 
    087A STA A00C : SET CA2 = 0
    087D LDA 00 : 500 µS DELAY
    087F STA A00B :
    0882 STA A008 :
```

```
0885 LDA 02 :  
0887 STA A009 :  
088A LDA 20 :  
088C BIT A00D :  
088F BEQ FB :  
0891 LDA A008 :  
0894 LDA CE :  
0896 STA A00C : SET CA2 = 1 AGAIN  
0899 CPY FF : INCREMENT Y REGISTER  
089B BEQ 04 : IF Y = 256 RETURN  
089D INY :  
089E JMP 0866 :  
08A1 RTS :  
08A2 : > 20 μS DELAY LOCATION
```

F3

```
08A3 LDA 0C : SET UP INDIRECT ADDRESS .  
LINKAGE  
08A5 STA 0001 : AT ZERO PAGE ADDRESS  
08A8 LDA 30 : SET TAPE 1A = 0  
08AA STA A800 : SET TAPE 2A = 0  
08AD JSR 08D8 : COMPARE FIRST 256 BYTES  
08B0 LDA 0D :  
08B2 STA 0001 : MODIFY ZERO PAGE ADDRESS  
08B5 LDA 20 : SET TAPE 1A = 1  
08B7 STA A800 : AND TAPE 2A = 0  
08BA JSR 08D8 : COMPARE 2nd 256 BYTES  
08BD LDA 0E :  
08BF STA 0001 : MODIFY ZERO PAGE ADDRESS  
08C2 LDA 10 : SET TAPE 1A = 0  
08C4 STA A800 : AND TAPE 2A = 1  
08C7 JSR 08D8 : COMPARE 3rd 256 BYTES  
08CA LDA 0F :  
08CC STA 0001 : MODIFY ZERO PAGE ADDRESS  
08CF LDA 00 : SET TAPE 1A = 1  
08D1 STA A800 : AND TAPE 2A = 1  
08D4 JSR 08D8 : COMPARE LAST 256 BYTES  
08D7 BRK : HALT  
08D8 LDY 00 : INITIALISE Y TO 00  
08DA STY A000 : STORE Y IN PORT B  
08DD LDA (00),Y : GET CONTENTS OF (INDIRECT  
ADDRESS + Y)  
08DF CMP A00F : COMPARE WITH CONTENTS OF PORT A  
08E2 BNE 09 : BRANCH TO "?" IF NOT EQUAL  
08E4 CPY FF : SEE IF 256 BYTES CHECKED  
08E6 BEQ 04 : IF SO RETURN FROM SUBROUTINE  
08E8 INY : INCREMENT Y REGISTER  
08E9 JMP 08DA :  
08EC RTS :  
08ED JSR E7D4 : IF ERROR DISPLAY A "?"  
08F0 JMP 08DA :
```



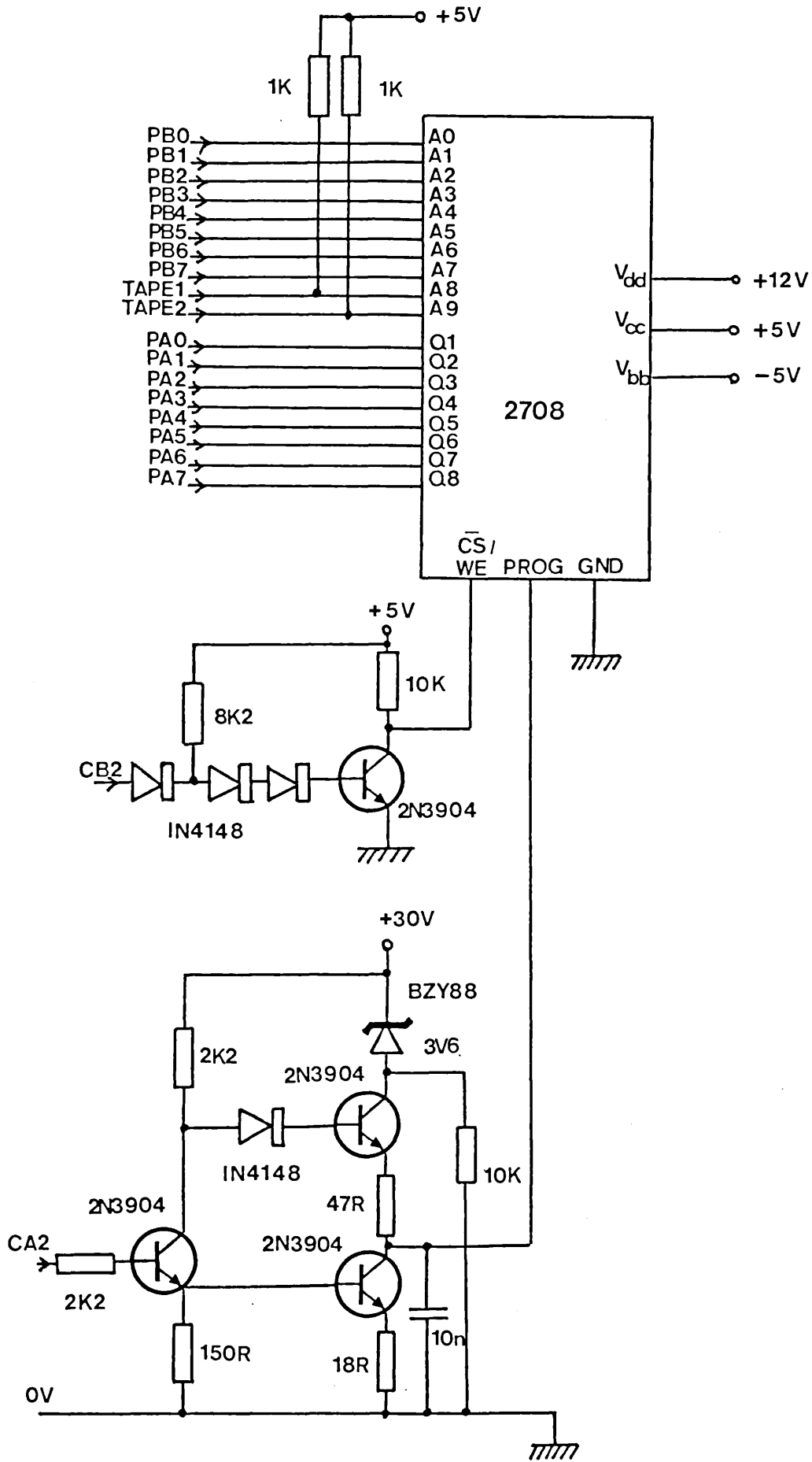


Figure A.3.14 EPROM programmer circuit.

APPENDIX IV

Scattering Cross Section Measurement Program Listing.

10 INPUT"CHANNEL";C	Measures and displays
20 GOSUB1010	voltage on channel No.
30 GOSUB1140	C of A-D converter.
40 GOTO20	
50 INPUT"LEVEL=":LV	Input routine for detec-
60 INPUT"BASELINE=";BL	tor voltage level above
70 INPUT"NO.OFSCANS=" ;TI	which data from Golay
	detector should be stored,
	baseline and number of
	scans per mode.
75 DIMA(300),B(300),QM(5,2)	
80 W1=1:GOSUB200	Measure Q's at Z for
85 FORJ=1TO6000:NEXTJ	each sample setting
90 L0=84.25:ER=.2:GOSUB1400	Move sample $\lambda/4$
100 GOSUB1600	Measure Q's at Z + $\lambda/4$
110 W1=2:GOSUB200	for each sample setting
120 D=.17:R0=.768:GOSUB1320	Resonator dimensions.
125 INPUT"Q0=";Q0	Input unloaded Q
130 FORW=1TO5	Retrieve measured Q's and
140 Q1=QM(W,1 ):Q2=QM(W,2 ): GOSUB1300	calculate scattering cross-sections.
150 PRINT!"INCIDENCE=", (W-1) *4;"DEGREES"	Prints out measurement
160 PRINT!"SCATTERING X-SECTION =" ,ES;"M2"	results.
170 NEXTW	
180 STOP	
200 D8=0	
205 FORW=1TO5	
210 GOSUB900	Adjust angle of inci-
220 M=2:DI=0:ST=8 GOSUB1160	dence of the sample
225 QM (W,W1)=QT	
230 NEXTW	
235 FORJ=1TO6000:NEXTJ	
240 M=2;DI=1:ST=40:GOSUB1160	
250 RETURN	
300 C=A(1)	Calculated resonator
305 FORN=2TOI	Q for halfwidth
310 IFA(N) < OTHEN320	of resonant curve

```
315 J=N:C=A(N)
320 NEXTN
330 PRINT!"PEAK POSITION=":
    115*B(J);"MICRONS"
350 P=(A(J)+BL)*.5
360 FORI=2TOJ
370 IFA(I)<=PANDA(I-1)>=P
    THEN410
380 NEXTI
390 PRINT"HP1 NOT FOUND"
400 RETURN
410 GOSUB530
420 H1=H
430 FORI=JTO299
440 IFA(I+1)<=PANDA(I)>=P
    THEN480
450 NEXTI
460 PRINT"HP2 NOT FOUND"
470 RETURN
480 GOSUB530
490 H2=H
500 Q+17/1.15E-7*ABS(H2-H1))
510 PRINT!"RESONATOR Q=";Q
520 RETURN
```

obtained from stored  
Golay detector response  
and mirror position  
data using data  
interpolation routine.

```
530 H=B(I)+(B(I+1)-B(I))*(P-A
    (I))/(A(I+1)-A(I))
540 RETURN
600 FORJ=1TO2000:NEXTJ
```

Data interpolation  
routine

```
610 C=0:GOSUB1010
620 GOSUB1140
630 VA=V
640 C=1:GOSUB1010
650 GOSUB1140
660 VB=V
670 RETURN
700 GOSUB1160
720 GOSUB600
730 IFVA>LVTHEN750
740 GOTO700
750 FORI=1TO300
760 A(I)=VA:B(I)=VB
770 GOSUB1160
780 GOSUB600
790 IFVA<.9*LVANDI>8THEN840
800 PRINTI
810 NEXTI
820 PRINT"ARRAY OVERLOAD"
830 STOP
840 GOSUB300
850 RETURN
860 SS=ST:ST=15
870 GOSUB1160
880 ST=SS
890 RETURN
900 M=4:ST=2:DI=D8:QT=0:F=0
910 Q=0:GOSUB860
920 GOSUB700
930 IFDI=0THEN950
```

This routine first  
locates the nearest  
mode to the current  
mirror position and  
scans it the required  
number of times,  
storing the data  
of the detector  
signal and the  
mirror position,  
provided it exceeds  
the baseline level  
by a preset amount  
entered at the  
start of the program.

```
940 DI=0:GOTO960
950 DI=1
960 IFQ=0THEN910
970 QT=QR+Q:F=F=1:IFF=TITHEN990
980 GOTO910
990 QT=QT/TI:PRINT!"Q-AV=";QT
995 D8=DI
1000 RETURN
```

```
1010 POKE32800,C
1020 WAIT32801,1,1
1030 LB=PEEK(32802)
1040 HB=PEEK(32803)
1050 R=HBAND16
1060 IFR=0THEN1090
1070 PRINT"**OVERRANGE**"
1080 RETURN
1090 S=HBAND32
1100 HB=HBAND15
1110 V=HB*256+LB
1120 IFS=0THENV=-V
1130 RETURN
1140 PRINTV;"MV"
1150 RETURN
```

Measures and displays the voltage on Channel C of multi-channel A-D converter. Detects polarity and overrange conditions.

Voltage displayed in millivolts with correct sign

```
1160 IFM=5THEN1230
1170 Z=2 (M-1)
1180 X=32783+2*M
1190 POKEX,DI
1200 POKEX-1,ST
1210 WAIT32792,Z,Z
1220 RETURN
1230 POKE32771,DI
1240 POKE32769,ST
1250 WAIT32773,1,1
1260 RETURN
```

Causes stopping motor M to execute ST steps in direction set by DI

Motor 3 = mirror  
Motor 4 = sample longitudinal  
Motor 2 = incidence  
Motor 1 = polarisation  
Motor 5 = sample transverse.

```
1300 ES=KO*(1/Q1+1/Q2-2/Q0)
1310 RETURN
1320 KO=7854*D*5QR(D*(2*RO-D))
1330 RETURN
1400 GOSUB1550
1405 CD=.11455
1410 D1=V:ER=INT(ER/OD)
1420 PRINT"INITIALPOSITION=",
D1*DC;"MICRONS"
1430 DT=INT(D1+(LO/OD)):M=3
1440 SP=DT-D1
1444 PRINT"TARGET POSITION=",
DT*CD;"MICRONS"
1445 PRINT"ACTUAL POSITION=",
D1*CD;"MICRONS"
1446 PRINT"POSITIONING ERROR=",
ABS(SP)*OD;"MICRONS"
1450 IFABS(SP)<=ERTHEN1540
1460 DI=SGN(SP)
1470 IFDI=1THEN1490
1480 DI=0
1490 ST=INT(ABS(5*CD*SP))
1500 IFST>255THENST=255
1510 GOSUB1160
```

Calculates the resonator constant K from the resonator dimensions.

Moves sample LO microns and positions to within an error of ER microns. LO may be positive or negative corresponding to a movement forward or backwards.

```
1520 GOSUB1550
1530 DI=V:GOTO1440
1540 PRINT"POSITIONED TO WITHIN
      ERROR: RETURN
1550 FORJ=1TO3000:NEXTJ
1560 C=2:GOSUB1010
1570 RETURN

1600 M=4:ST=40:DI=0:H=0
1610 FORK=1TO100
1615 GOSUB1160
1620 GOSUB600
1630 IFVA<HGOTO1650
1640 PP=VB:H=VA
1650 NEXTK
1655 PRINT"PEAK AMPLITUDE=",H
1656 PRINT"PEAK POSITION=",PP
1657 PP=PP-100
1660 GOSUB1790
1670 P=V
1680 SP=PP-P
1690 IFABS(SP)<5THEN1770
1770 DI=SGN(SP)
1710 IFDI=1THEN1730
1720 DI=0
1730 ST=INT(ABS(SP*2 3))
1740 IFST>255THENST=255
1750 GOSUB1160
1760 GOTO1660
1770 PRINT"PEAK OFF SET POSITION
      LOCATED
1780 RETURN
```

This routine locates a mode and positions the mirror so it is at the required position to start a forward scan of the mode.

APPENDIX V

The theoretical Variation of E-Plane backscattered electric field for a short circuited dipole.

A current distribution of the form given in equation A.5.1 is assumed. The propagation constant for the current on the wire is taken to be the free space value  $k = 2\pi/\lambda$  in order to simplify the mathematics.

$$I(Z) = \frac{I_0 (\cos kZ - \cos kL)}{(1 - \cos kL)} \quad (A.5.1.)$$

Figure 9.19 in Chapter 9 illustrates the geometry. The azimuthal field component produced by a current element  $I(Z) dZ$  is given by

$$dE_\theta = \frac{j\eta k I(Z) dZ e^{-jkr''} \sin\theta''}{4\pi r''} \quad (A.5.2.)$$

Since the far-field is to be computed the approximations

$$r'' \approx r - Z \cos\theta \quad (A.5.3.)$$

$$1/r'' \approx 1/r \quad (A.5.4.)$$

and  $\theta'' \approx \theta$  (A.5.5.)

are valid. Now  $E_\theta = \int_{-L}^{+L} dE_\theta$  (A.5.6.)

hence 
$$E_\theta = \frac{j\eta k I_0 \sin\theta e^{-jkr}}{4\pi r (1 - \cos kL)} \int_{-L}^{+L} e^{jkZ \cos\theta} (\cos kZ - \cos kL) dZ \quad (A.5.7.)$$

The current induced by the incident field will vary as  $\sin\theta$  as

$$\bar{E}_Z(\theta) = \hat{Z} E_{INC}(\theta = 90^\circ) \sin\theta \quad (A.5.8.)$$

From Ohm's law  $\bar{J} = \sigma \bar{E}$  and so

$$I_0(\theta) = I_0(\theta = 90^\circ) \sin\theta \quad (A.5.9.)$$

Now 
$$\int_{-L}^{+L} e^{jkZ \cos\theta} (\cos kZ - \cos kL) dZ$$

$$= \int_{-L}^{+L} e^{jkZ \cos\theta} \cos kZ dZ - \cos kL \int_{-L}^{+L} e^{jkZ \cos\theta} dZ \quad (A.5.10.)$$

$$\text{As } \int e^{ax} \cos bx \, dx = \frac{e^{ax}}{a^2 + b^2} (a \cos bx + b \sin bx) \quad (\text{A.5.11.})$$

$$\text{and } \int e^{ax} \, dx = \frac{e^{ax}}{a} \quad (\text{A.5.12.})$$

then integration of equation A.5.10 yields

$$\left[ \frac{e^{jkz} \cos \theta}{k^2(1-\cos^2 \theta)} (j k \cos \theta \cos kz + k \sin kz) \right]_{-L}^{+L} - \cos kL \left[ \frac{e^{jkz} \cos \theta}{j k \cos \theta} \right]_{-L}^{+L} \quad (\text{A.5.13.})$$

hence the above integral becomes

$$\frac{e^{jkL} \cos \theta}{k^2 \sin^2 \theta} (j k \cos \theta \cos kL + k \sin kL) - \frac{e^{-jkL} \cos \theta}{k^2 \sin^2 \theta} (j k \cos \theta \cos kL - k \sin kL) - \cos kL \left\{ \frac{e^{jkL} \cos \theta - e^{-jkL} \cos \theta}{j k \cos \theta} \right\} \quad (\text{A.5.14.})$$

Simplifying equation A.5.14 the result shown in equation A.5.15 is obtained

$$\frac{2 \cos kL \cos \theta \sin kL}{k \sin^2 \theta} - \frac{2 \sin (kL \cos \theta) \cos kL}{k \sin^2 \theta \cos \theta} \quad (\text{A.5.15.})$$

substituting A.5.15 into equation A.5.7

$$E_{\theta} = E_0 \left\{ \cos (kL \cos \theta) \sin kL - \frac{\sin (kL \cos \theta) \cos kL}{\cos \theta} \right\} \quad (\text{A.5.16.})$$

where

$$E_0 = \frac{j 2 \eta I_0 e^{-jkr}}{4 \pi r (1 - \cos kL)} \quad (\text{A.5.17.})$$

When  $\theta = 90^\circ$  the last term in the parenthesis in equation A.5.16 becomes uncertain as  $\cos \theta = 0$ . Using a MacLaurin series expansion for  $(\sin ax)/x$ , in the limit as  $x$  tends to zero

$$\begin{aligned} & \lim_{x \rightarrow 0} \left| \frac{\sin ax}{x} \right. \\ &= \lim_{x \rightarrow 0} \left[ a - \frac{a^3 x^2}{3!} + \frac{a^5 x^4}{5!} - \frac{a^7 x^6}{7!} + \dots \right] \\ &= a \end{aligned} \tag{A.5.18.}$$

Hence 
$$\lim_{\theta \rightarrow 90^\circ} \left| \frac{\sin (kL \cos \theta)}{\cos \theta} \right. = kL \tag{A.5.19.}$$

therefore 
$$E_\theta (\theta = 90^\circ) = E_o (\sin kL - kL \cos kL) \tag{A.5.20.}$$



APPENDIX VI

Calculation of the input impedance of a vee antenna with radially spreading conductors.

The geometry of the vee antenna considered here is illustrated in Figure A.6.1. If it is assumed that the conductors have negligible thickness and surface impedance then the transmission mode excited on the vee will be a spherical TEM mode. For the TEM mode both the electric field and magnetic field lines lie in a plane transverse to the direction of propagation, and so the field distribution may be obtained by a solution for static fields in the transverse plane. In such a case the characteristic impedance of the transmission line may be obtained from the electrostatic capacitance per unit length of the line by using the following simple relation

$$Z_0 = 1 / V_p C \quad (\text{A.6.1.})$$

where  $Z_0$  is the characteristic impedance of the line,  $V_p$  is the phase velocity for the wave and  $C$  is the capacitance per unit length of the line.

Calculation of capacitance for the geometry encountered in the present problem may be simplified by using a set of conformal transformations to convert the geometry to one where the capacitance is accurately known. The transformations used convert the vee geometry to a coplanar geometry and the capacitance for this is the same as that derived for a coplanar transmission line. Hence the characteristic impedance of the vee antenna, which is equal to its feed point impedance, is equal to the characteristic impedance of the coplanar line geometry which results from the transformation.

The use of conformal transformation for calculation of capacitance is based upon the fact that the real and imaginary parts of an analytic function of a

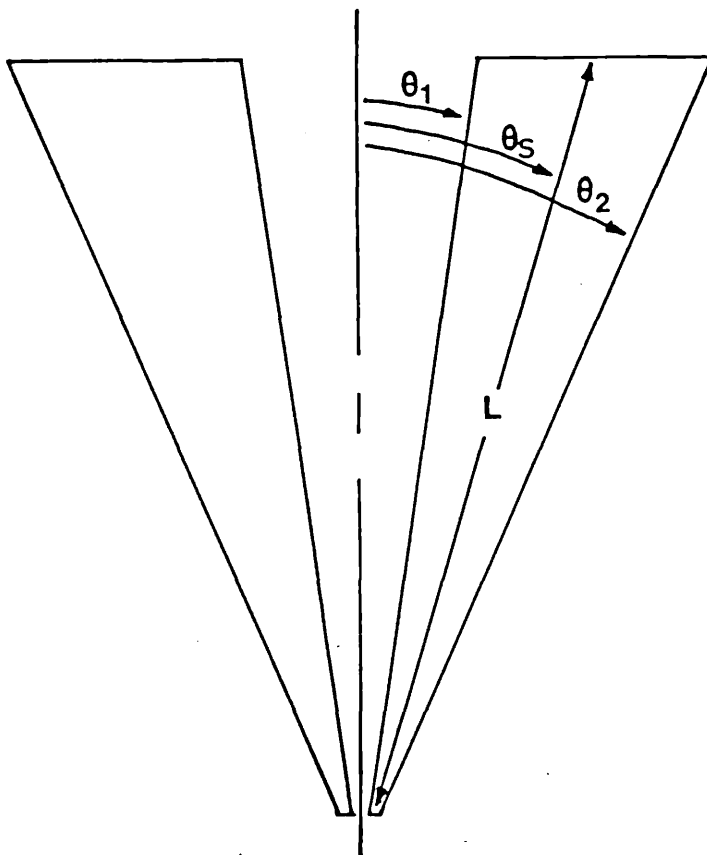


Figure A.6.1. Geometry of the vee-antenna.

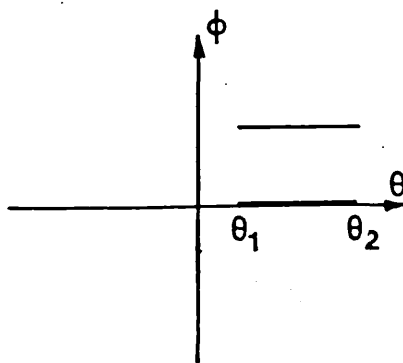


Figure A.6.2.(a) Vee-antenna conductors mapped into spherical-polar co-ordinates.

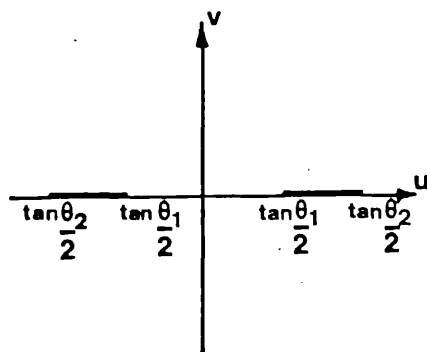


Figure A.6.2.(b) Vee-antenna conductors mapped into  $u + iv$  co-ordinates. ( $u + iv = \tan \frac{\theta}{2} \exp i \phi$ )

complex variable satisfy Laplace's equation. Not only that, the real and imaginary parts of an analytic function are also related by Cauchy - Reimann relations. This is expressed by saying that they are "conjugate" in the sense of complex variable theory. In electrostatics, electric potential  $V(x,y)$  and flux  $\phi(x,y)$  of the displacement vector ( $\vec{D} = \epsilon \vec{E}$ ) also have the same properties.

$$\nabla^2 V(x,y) = 0 \quad \nabla^2 \phi(x,y) = 0 \quad (A.6.2.)$$

and

$$\frac{\partial V}{\partial x} = \frac{\partial \phi}{\partial y} \quad \text{and} \quad -\frac{\partial V}{\partial y} = \frac{\partial \phi}{\partial x} \quad (A.6.3.)$$

In view of the linearity and uniqueness of the solution of Laplace's equation in electrostatics, real and imaginary parts of an analytic function may be used to represent the potential and electric field displacement functions (apart from a scalar factor). Since the capacitance between the electrodes is defined as the ratio of the total electric flux (from one electrode to the other) to the potential difference between the two electrodes, it can be shown that transformation from one complex plane to another keeps the capacitance invariant<sup>91</sup>.

In spherical co-ordinates, the conductor surfaces map into contours shown in Figure A.6.2(a). The contours repeat with a period of  $2\pi$  along both the  $\theta$  and  $\phi$  axes. Since the contours are independent of the radius, the potential will be independent of the radius, and the Laplace equation for the potential  $V$  becomes

$$\sin \theta \frac{\partial}{\partial \theta} \left\{ \sin \theta \frac{\partial V}{\partial \theta} \right\} + \frac{\partial^2 V}{\partial \phi^2} = 0 \quad (A.6.4.)$$

By making the substitution  $u + iv = \tan \frac{\theta}{2} \exp i \phi$ , this equation reduces to the two dimensional Laplace equation in rectangular co-ordinates

$$\frac{\partial^2 V}{\partial u^2} + \frac{\partial^2 V}{\partial v^2} = 0 \quad (A.6.5.)$$

and the conductor contours are transformed from a doubly-periodic system to a single pair of contours on the  $u$  axis, as shown in Figure A.6.2.(b). The impedance of the vee is the same as the impedance of the transformed contours which is

$$Z = \frac{377}{\sqrt{\epsilon_r}} \frac{K(k)}{K'(k)} \quad (\text{A.6.6.})$$

where  $k = (\tan \theta_1/2) / (\tan \theta_2/2)$   
and  $K(k)$  is the complete elliptic integral of the first kind, and  $K' = K(k')$  where  $k'^2 = 1 - k^2$ .  
Provided that the antenna is on a thin substrate,  $< \lambda/15$  thick, then  $\epsilon_r$  can be taken to be that of free space, namely unity.

## A calibration technique for a computer-controlled photoelectron spectrometer

P H Cannington and W Fock

CSIRO Division of Chemical Physics, PO Box 160, Clayton, Victoria, Australia 3168

Received 22 December 1980, in final form 14 July 1981

**Abstract.** A new method for calibrating the energy scale of photoelectron spectra, using the  $\text{He}^+$  peak at 24.59 eV, is shown to be satisfactory for both the He I and the He II spectra produced by spectrometers fitted with He I/He II photon sources.

Calibration of the energy scale of a photoelectron spectrum cannot be derived from instrumental parameters as the energy of the electrons entering the analyser is affected by the contact potentials within the ionisation chamber, and these are sensitive to the pressure and chemical nature of the sample. In practice, calibration must be achieved by using the known ionisation energies of reference compounds, and it has become established practice to record the spectrum of a mixture of sample and calibrant, or to record alternately the separate spectra of sample and calibrant.

In He I/He II spectrometers with hollow cathode discharge sources a small amount of helium gas is always present in the ionisation chamber and some of this is ionised by  $\text{He II}_\alpha$  (40.81 eV) photons. The resulting 16.22 eV photoelectrons produce a sharp peak at an ionisation energy of 24.59 eV. This makes the  $\text{He}^+$  peak an ideal one for calibrating the energy scale, especially as it eliminates the inconvenience of adding calibrant gas.

For calibration to be based on only the  $\text{He}^+$  peak, it must first be established that the energy scale shift, defined as the difference between the uncalibrated and true ionisation energy, is independent of ionisation energy. Then any shift can be eliminated at the end of data acquisition by setting the ionisation energy scale of the spectrum so that the  $\text{He}^+$  peak is located at 24.59 eV.

Our modified Perkin-Elmer PS 16/18 He I/He II spectrometer (Cannington 1980) has been interfaced to a Hewlett-Packard 21MX minicomputer, which controls the

sweeping of the analyser potential and allows accumulation of repetitive scans. The analyser potential is generated via a 12-bit digital-to-analogue converter, the linearity of which has been measured to be better than 1 part in  $10^4$ . With this DAC the transmission energy of the analyser can be incremented in 10 meV steps from 0 to 40.95 eV, thus spanning both the 40.81 eV He II and the 21.22 eV He I ionisation regions.

He I and He II spectra of several samples with well known ionisation energies were obtained, and the energy scale shifts of these spectra are presented in figure 1. This shows that the shift of each peak in any one spectrum is the same and that the shifts are independent of ionisation energy over the range 19.7 eV He I to 9.1 eV He II, i.e. for electron energies from 1.5 to 30.7 eV. The criterion for use of the  $\text{He}^+$  peak alone for calibration is therefore satisfied.

It should be noted that the nonlinearity reported using an earlier version of our type of spectrometer (Lloyd 1970) is not observed with the present computer-controlled spectrometer.

Accumulation of scans requires the shift in the ionisation energy scale to be constant during this period. In practice, it has been found that drifts are less than or about 10 meV during a 30 min period, which is sufficient to record 25 He I or He II scans in steps of 10 meV. Each scan comprises an 0.2 eV sweep over the  $\text{He}^+$  peak in 10 meV steps followed by a sweep over the specified scan range with the chosen step size. After 25 scans, but prior to storage on disc, the resulting spectrum has its energy scale shifted so that the cumulative  $\text{He}^+$  peak occurs at 24.59 eV. Scanning is continued until the sum of these calibrated spectra provides an acceptable spectrum.

### Acknowledgments

The authors wish to express their thanks to Dr N S Ham and to Dr A J C Nicholson for helpful discussions concerning this paper.

### References

- Cannington P H 1980 Improvements to a commercial uv photoelectron spectrometer  
*J. Phys. E: Sci. Instrum.* **13** 1344
- Gardner J L and Samson J A R 1976 Calibration of electron-energy spectrometers  
*J. Electron Spectrosc.* **8** 469
- Lloyd D R 1970 Calibration of a He (I) photoelectron spectrometer  
*J. Phys. E: Sci. Instrum.* **3** 629
- Turner D W, Baker C, Baker A D and Brundle C R 1970 *Molecular Photoelectron Spectroscopy* (London: Wiley-Interscience)

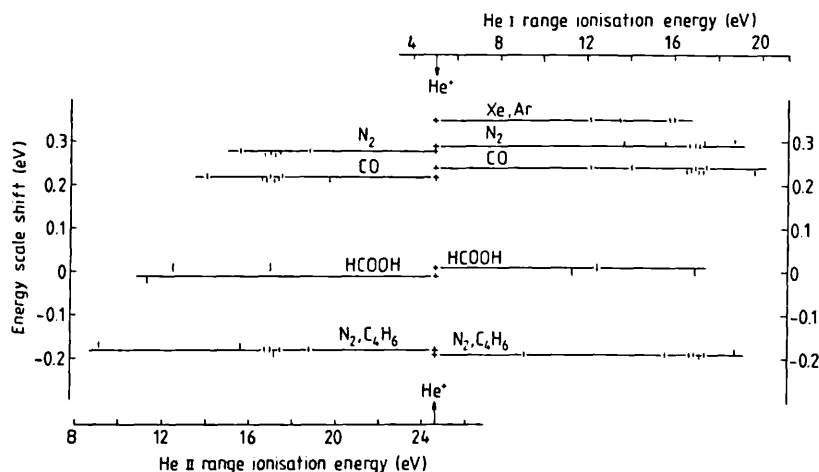


**Figure 1.** Energy scale shift (uncalibrated ionisation energy - true ionisation energy) as a function of ionisation energy for He I and He II spectra of several samples. The ionisation energies were taken from the literature (Gardner and Samson 1976, Lloyd 1970, Turner *et al* 1970). Spectra were recorded in 10 meV steps for carbon monoxide, nitrogen, a nitrogen-butadiene mixture and a xenon-argon mixture and in 20 meV steps for formic acid.

## Cavity length stabilisation of a 10 mW cw 337 $\mu\text{m}$ HCN laser

H J Cummins and P G Frayne

Department of Physics, Royal Holloway College, Egham, Surrey, TW20 0EX, UK

Received 18 June 1981

**Abstract.** A servo system has been developed for cavity stabilisation of a far infrared HCN laser operating at 337  $\mu\text{m}$ . It has advantages over previous methods in that accurate temperature control of the laser cavity is not required. The technique should be applicable to other types of far infrared lasers.

### 1. Introduction

In order to obtain useful output powers from far infrared molecular lasers (such as the HCN laser) it is necessary to employ cavity lengths in excess of a metre as the gain per unit length tends to be low, being of the order of  $0.01\text{--}0.1\text{ m}^{-1}$  (Adde and Lourtioz 1976). One of the main factors affecting the stability of a continuous wave (cw) HCN laser comes from instability in the cavity length arising from thermal expansion of the laser body structure due to fluctuating ambient temperature. This can be overcome by employing temperature regulated silica or steel spacing rods (Kang and Venderkooy 1976, Belland and Veron 1973). Although very effective, these techniques are however complicated and expensive, especially if the laser is of appreciable length.

### 2. Laser details

The laser used in these experiments is a 7.6 m long 15 cm tube diameter cw HCN laser, with beamsplitter output coupling operating from a current stabilised power supply. The laser is excited by a discharge current of 1 A through a continuous flow methane, nitrogen and helium mixture (partial pressures 1:2:10 respectively). The total tube pressure is 66.7 Pa (0.5 Torr) and the corresponding voltage drop is 2.2 kV. A stable striated discharge is obtained using a water cooled hollow cathode situated in a tube sidearm. Although fixed by four Invar spacers the cavity length varies by up to 100  $\mu\text{m}$  per hour due to thermal expansion. As a result the laser drifts off tune, making long term measurements difficult.

### 3. Stabilisation technique

The laser cavity is stabilised by locking it to the mode peak by employing a cavity modulation technique. This is achieved by using a hemispherical laser cavity configuration with the lighter 3" diameter plane mirror supported in the cone of a 5" loudspeaker. The DC correction voltage generated by the servo system is applied to the loudspeaker to correct for changes in the cavity length. A small AC modulating voltage is also applied to the loudspeaker to achieve cavity modulation. The modulation voltage applied to the loudspeaker causes modulation of the laser output of a few per cent. The detected modulation is amplified and applied to a phase sensitive detector along with the modulating signal which acts as the reference. The correction voltage generated by the phase sensitive detector is fed back to the loudspeaker along with the modulating signal. A modulation frequency of 40 Hz was chosen as this is high enough to lie outside the bandwidth of the golay detectors used in the instrumentation for which the laser is the radiation source. The output of one of the laser beam output ports is focused on to a Mullard RPY 89 pyroelectric detector to detect the modulated output from the laser. A block diagram of the servo system is shown in figure 1. To prevent the plasma discharge from

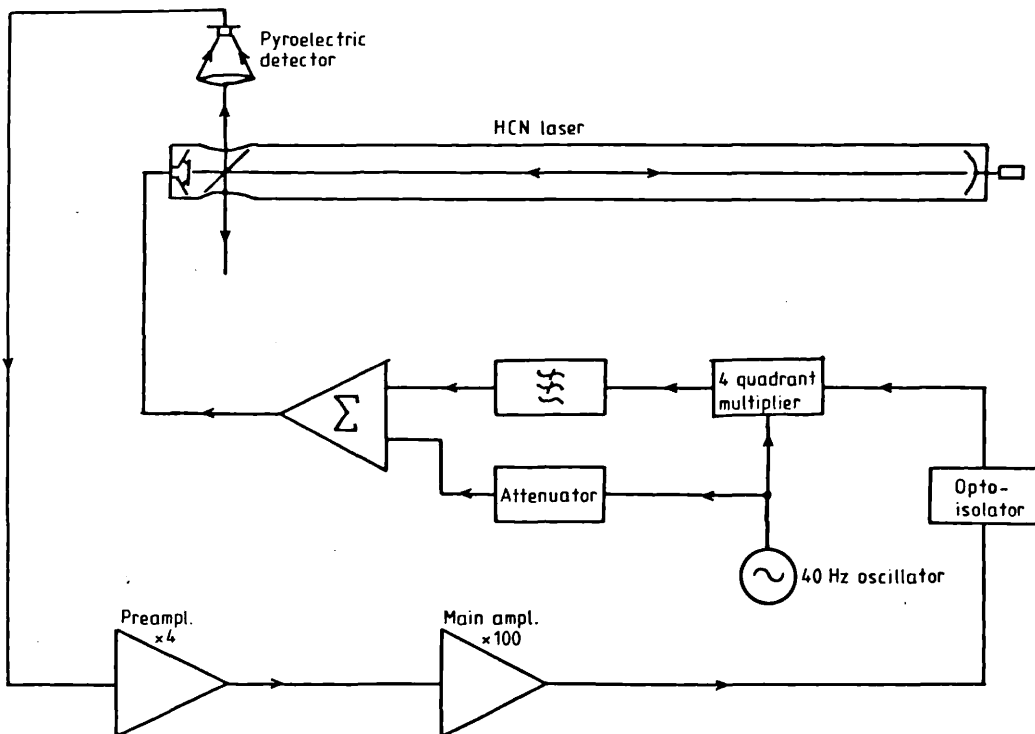


Figure 1. Block diagram of the servo loop.

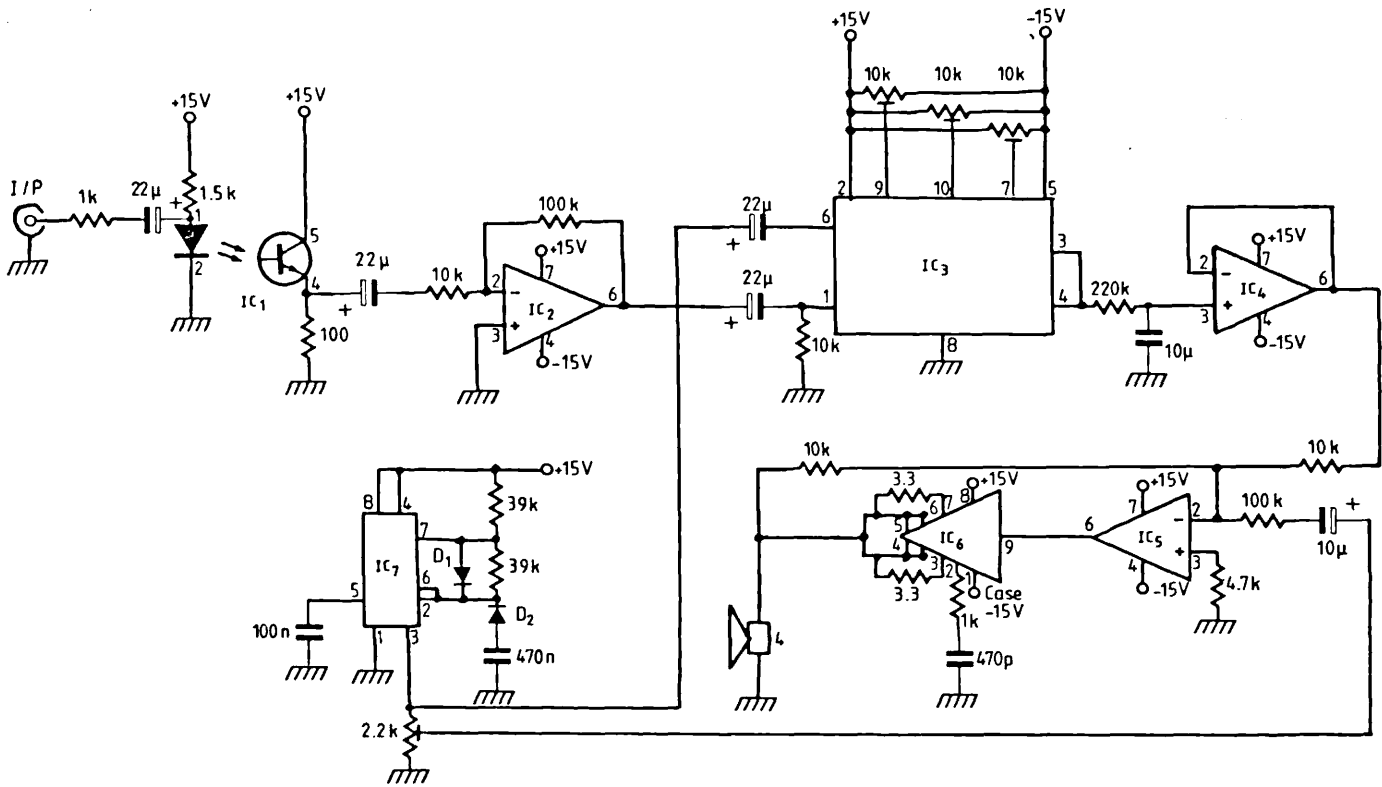


Figure 2. Circuit diagram. IC<sub>1</sub>, opto-isolator; IC<sub>2,5</sub>, µA741; IC<sub>3</sub>, ICL8013; IC<sub>4</sub>, CA3140E; IC<sub>6</sub>, MC1438R; IC<sub>7</sub>, NE555; D<sub>1,2</sub>, 1N4148.

running on to the loudspeaker, the servo loop circuitry is floating and the amplified detector signal is coupled into this using an opto-isolator. A full circuit is shown in figure 2.

#### 4. Theory

The cavity mode resonance curve can be approximated to a parabola of the form

$$I = I_0(1 - ax^2) \quad (1)$$

where  $I$  is the laser intensity when the mirror is displaced a distance  $x$  from the mode peak mirror separation.  $I_0$  is the peak laser intensity and  $a$  is a constant ( $a = 2.5 \times 10^9 \mu\text{m}^{-2}$  for our laser). The loudspeaker is modulated by a small AC signal of frequency  $\omega_m$  giving rise to mechanical modulation of the mirror,  $m$ , which is given by

$$m = m_0 \cos \omega_m t. \quad (2)$$

If the mirror is displaced from resonance by a distance  $e$  then from equations (1) and (2) the output intensity is given by

$$I = I_0[1 - a(e + m_0 \cos \omega_m t)^2]. \quad (3)$$

After detection the AC component of this signal is

$$V_{\text{SIG}} = KI_0 a(e^2 + 2em_0 \cos \omega_m t + m_0^2 \cos^2 \omega_m t) \quad (4)$$

where  $K$  is the detector sensitivity.

After voltage amplification  $A_v$ , the signal is then multiplied by a reference signal,  $V_{\text{REF}}$ , by a four quadrant multiplier.

$$V_{\text{REF}} = V_R \cos \omega_m t. \quad (5)$$

The output of the four quadrant multiplier is given by

$$V_0 = V_R A_v K I_0 a (e^2 \cos \omega_m t + 2em_0 \cos^2 \omega_m t + m_0^2 \cos^3 \omega_m t). \quad (6)$$

The  $\cos^2 \omega_m t$  term gives rise to a DC error signal, which is

proportional to  $e$ , given by

$$V_{\text{DC}} = V_R A_v K I_0 a e m_0. \quad (7)$$

The error signal is extracted by feeding the four quadrant multiplier output through a low pass filter with  $f_c = 0.07$  Hz. The output from the filter is buffered and fed back to the loudspeaker so as to compensate for the displacement error.

For this particular servo loop the open loop DC output voltage corresponding to an error of  $1 \mu\text{m}$  is  $0.84$  V. Hence the amplification factor for the loop,  $A$ , is equal to  $0.84 \text{ V } \mu\text{m}^{-1}$ . The feedback factor  $B$  is supplied by the loudspeaker sensitivity which is  $168 \mu\text{m V}^{-1}$ .

The stability factor for the servo loop,  $S = (AB)^{-1}$ , is thus equal to  $0.7\%$ . The loop time constant, which is governed by the low pass filter time constant used after the four quadrant multiplier, is  $2.2$  s.

#### 5. Performance

To ascertain the performance of the laser stabilisation system the experimental arrangement shown in figure 3 was employed. The phase sensitive detector output was monitored on a chart recorder and an integration time constant of  $10$  s was employed. Figure 4 shows the output of the laser against time for both the unstabilised and the stabilised cases. The servo loop stability of the system was measured and found to be  $0.9\%$ . The servo loop technique reduced the output drift rate from  $44\%$  per hour to  $4.8\%$  per hour. The amplitude modulation produced by the  $40$  Hz cavity modulation was also measured and found to be  $5\%$  of the total output amplitude. The cavity modulation gives rise to a theoretical residual frequency modulation of  $26$  KHz.

Clearly this technique offers a marked improvement in the output stability of the laser provided a small amount of amplitude modulation on top of the laser output can be tolerated. The frequency of modulation could be made higher

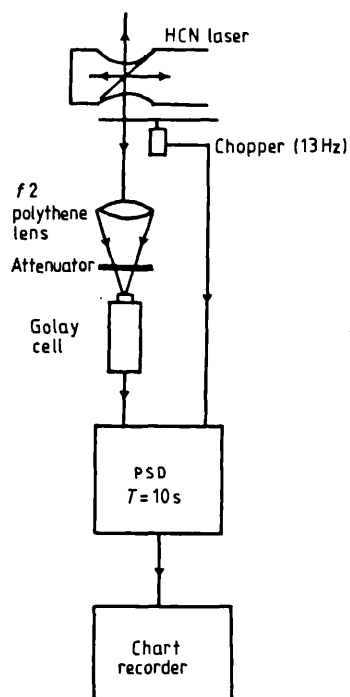


Figure 3. Laser output monitoring arrangement.

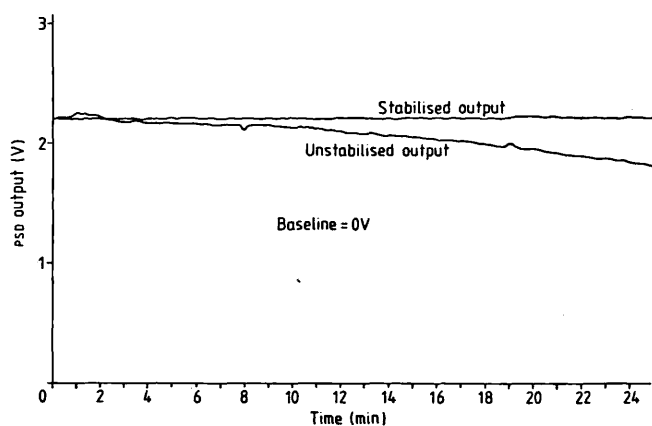


Figure 4. Variation of laser output with time for both stabilised and unstabilised cases.

but is limited here by the frequency response of the monitor detector. In applications where the laser is employed as a local oscillator the degree of frequency modulation produced by the stabiliser may prove detrimental. However, in applications where good amplitude stability is the only requirement this technique is most successful.

**References**

Adde R and Lourtioz J M 1976 Design of a stable cw HCN laser for far infrared frequency synthesis  
*Rev. Phys. Appl.* **11** 533-40

Kang C S and Venderkooy J 1976 Design and characteristics of a 2m continuous wave HCN laser  
*Infrared Phys.* **16** 627-37

Belland P and Veron D 1973 A compact cw HCN laser with high stability and power output  
*Opt. Commun.* **9** 146-8